PROCEEDINGS OF THE INTERNATIONAL SCHOOL ON MAGNETIC RESONANCE AND BRAIN FUNCTION - XIII WORKSHOP

EDITED BY: Itamar Ronen, Marta Bianciardi and Federico Giove
PUBLISHED IN: Frontiers in Neuroscience, Frontiers in Physics,
Frontiers in Physiology and Frontiers in Neural Circuits

frontiers Research Topics

frontiers

ISSN 1664-8714
ISBN 978-2-88971-199-4
DOI 10.3389/978-2-88971-199-4

About Frontiers

Frontiers is more than just an open-access publisher of scholarly articles: it is a pioneering approach to the world of academia, radically improving the way scholarly research is managed. The grand vision of Frontiers is a world where all people have an equal opportunity to seek, share and generate knowledge. Frontiers provides immediate and permanent online open access to all its publications, but this alone is not enough to realize our grand goals.

Frontiers Journal Series

The Frontiers Journal Series is a multi-tier and interdisciplinary set of open-access, online journals, promising a paradigm shift from the current review, selection and dissemination processes in academic publishing. All Frontiers journals are driven by researchers for researchers; therefore, they constitute a service to the scholarly community. At the same time, the Frontiers Journal Series operates on a revolutionary invention, the tiered publishing system, initially addressing specific communities of scholars, and gradually climbing up to broader public understanding, thus serving the interests of the lay society, too.

Dedication to Quality

Each Frontiers article is a landmark of the highest quality, thanks to genuinely collaborative interactions between authors and review editors, who include some of the world's best academicians. Research must be certified by peers before entering a stream of knowledge that may eventually reach the public - and shape society; therefore, Frontiers only applies the most rigorous and unbiased reviews.
Frontiers revolutionizes research publishing by freely delivering the most outstanding research, evaluated with no bias from both the academic and social point of view. By applying the most advanced information technologies, Frontiers is catapulting scholarly publishing into a new generation.

What are Frontiers Research Topics?

Frontiers Research Topics are very popular trademarks of the Frontiers Journals Series: they are collections of at least ten articles, all centered on a particular subject. With their unique mix of varied contributions from Original Research to Review Articles, Frontiers Research Topics unify the most influential researchers, the latest key findings and historical advances in a hot research area! Find out more on how to host your own Frontiers Research Topic or contribute to one as an author by contacting the Frontiers Editorial Office: frontiersin.org/about/contact

PROCEEDINGS OF THE INTERNATIONAL SCHOOL ON MAGNETIC RESONANCE AND BRAIN FUNCTION - XIII WORKSHOP

Topic Editors:
Itamar Ronen, Leiden University Medical Center, Netherlands
Marta Bianciardi, Harvard Medical School, United States
Federico Giove, Centro Fermi - Museo storico della fisica e Centro studi e ricerche Enrico Fermi, Spain

Citation: Ronen, I., Bianciardi, M., Giove, F., eds. (2021). Proceedings of the International School on Magnetic Resonance and Brain Function - XIII Workshop. Lausanne: Frontiers Media SA. doi: 10.3389/978-2-88971-199-4

Table of Contents

05 ***Awake Rat Brain Functional Magnetic Resonance Imaging Using Standard Radio Frequency Coils and a 3D Printed Restraint Kit***
Petteri Stenroos, Jaakko Paasonen, Raimo A. Salo, Kimmo Jokivarsi, Artem Shatillo, Heikki Tanila and Olli Gröhn

19 ***Identifying Respiration-Related Aliasing Artifacts in the Rodent Resting-State fMRI***
Patricia Pais-Roldán, Bharat Biswal, Klaus Scheffler and Xin Yu

33 ***Tuning Neuromodulation Effects by Orientation Selective Deep Brain Stimulation in the Rat Medial Frontal Cortex***
Lauri J. Lehto, Pavel Filip, Hanne Laakso, Alejandra Sierra, Julia P. Slopsema, Matthew D. Johnson, Lynn E. Eberly, Walter C. Low, Olli Gröhn, Heikki Tanila, Silvia Mangia and Shalom Michaeli

43 ***Myelin and Modeling: Bootstrapping Cortical Microcircuits***
Robert Turner

54 **In vivo** ***Probabilistic Structural Atlas of the Inferior and Superior Colliculi, Medial and Lateral Geniculate Nuclei and Superior Olivary Complex in Humans Based on 7 Tesla MRI***
María G. García-Gomar, Christian Strong, Nicola Toschi, Kavita Singh, Bruce R. Rosen, Lawrence L. Wald and Marta Bianciardi

69 ***Brain Functional Connectivity Through Phase Coupling of Neuronal Oscillations: A Perspective From Magnetoencephalography***
Laura Marzetti, Alessio Basti, Federico Chella, Antea D'Andrea, Jaakko Syrjälä and Vittorio Pizzella

90 ***Brain Networks Underlying Eye's Pupil Dynamics***
Mauro DiNuzzo, Daniele Mascali, Marta Moraschi, Giorgia Bussu, Laura Maugeri, Fabio Mangini, Michela Fratini and Federico Giove

103 ***Myelin Water Imaging and Transcranial Magnetic Stimulation Suggest Structure-Function Relationships in Multiple Sclerosis***
Eric Y. Zhao, Irene M. Vavasour, Marjan Zakeri, Michael R. Borich, Cornelia Laule, Alexander Rauscher, Anthony Traboulsee, David K. B. Li, Lara A. Boyd and Alex L. MacKay

113 ***Apparent Diffusion Coefficient Assessment of Brain Development in Normal Fetuses and Ventriculomegaly***
Maria Giovanna Di Trani, Lucia Manganaro, Amanda Antonelli, Michele Guerreri, Riccardo De Feo, Carlo Catalano and Silvia Capuani

122 ***Influence of Repetitive Transcranial Magnetic Stimulation on Human Neurochemistry and Functional Connectivity: A Pilot MRI/MRS Study at 7 T***
Heidi Gröhn, Bernadette T. Gillick, Ivan Tkáč, Petr Bednařík, Daniele Mascali, Dinesh K. Deelchand, Shalom Michaeli, Gregg D. Meekins, Michael J. Leffler-McCabe, Colum D. MacKinnon, Lynn E. Eberly and Silvia Mangia

135 ***Mild Propofol Sedation Reduces Frontal Lobe and Thalamic Cerebral Blood Flow: An Arterial Spin Labeling Study***
Neeraj Saxena, Tommaso Gili, Ana Diukova, Danielle Huckle, Judith E. Hall and Richard G. Wise

141 ***Mini Review on Anomalous Diffusion by MRI: Potential Advantages, Pitfalls, Limitations, Nomenclature, and Correct Interpretation of Literature***
Silvia Capuani and Marco Palombo

148 ***Probabilistic Template of the Lateral Parabrachial Nucleus, Medial Parabrachial Nucleus, Vestibular Nuclei Complex, and Medullary Viscero-Sensory-Motor Nuclei Complex in Living Humans From 7 Tesla MRI***
Kavita Singh, Iole Indovina, Jean C. Augustinack, Kimberly Nestor, María G. García-Gomar, Jeffrey P. Staab and Marta Bianciardi

159 ***Multiscale Imaging Approach for Studying the Central Nervous System: Methodology and Perspective***
Michela Fratini, Ali Abdollahzadeh, Mauro DiNuzzo, Raimo A. Salo, Laura Maugeri, Alessia Cedola, Federico Giove, Olli Gröhn, Jussi Tohka and Alejandra Sierra

167 ***Assessment of the Effects of Aerobic Fitness on Cerebrovascular Function in Young Adults Using Multiple Inversion Time Arterial Spin Labeling MRI***
Catherine Foster, Jessica J. Steventon, Daniel Helme, Valentina Tomassini and Richard G. Wise

178 ***Cerebral Metabolic Changes During Visuomotor Adaptation Assessed Using Quantitative fMRI***
Catherine Foster, Jessica J. Steventon, Daniel Helme, Valentina Tomassini and Richard G. Wise

190 ***Brain Network Modularity During a Sustained Working-Memory Task***
Marta Moraschi, Daniele Mascali, Silvia Tommasin, Tommaso Gili, Ibrahim Eid Hassan, Michela Fratini, Mauro DiNuzzo, Richard G. Wise, Silvia Mangia, Emiliano Macaluso and Federico Giove

200 ***Temperature Measurements in the Vicinity of Human Intracranial EEG Electrodes Exposed to Body-Coil RF for MRI at 1.5T***
Hassan B. Hawsawi, Anastasia Papadaki, John S. Thornton, David W. Carmichael and Louis Lemieux

frontiers in Neuroscience

ORIGINAL RESEARCH
published: 20 August 2018
doi: 10.3389/fnins.2018.00548

Awake Rat Brain Functional Magnetic Resonance Imaging Using Standard Radio Frequency Coils and a 3D Printed Restraint Kit

*Petteri Stenroos[1], Jaakko Paasonen[1], Raimo A. Salo[1], Kimmo Jokivarsi[1], Artem Shatillo[2], Heikki Tanila[1] and Olli Gröhn[1]**

[1] Kuopio Biomedical Imaging Unit, A.I.V. Institute for Molecular Sciences, University of Eastern Finland, Kuopio, Finland,
[2] Charles River Discovery Research Services Finland Oy, Kuopio, Finland

Functional magnetic resonance imaging (fMRI) is a powerful noninvasive tool for studying spontaneous resting state functional connectivity (RSFC) in laboratory animals. Brain function can be significantly affected by generally used anesthetics, however, rendering the need for awake imaging. Only a few different awake animal habituation protocols have been presented, and there is a critical need for practical and improved low-stress techniques. Here we demonstrate a novel restraint approach for awake rat RSFC studies. Our custom-made 3D printed restraint kit is compatible with a standard Bruker Biospin MRI rat bed, rat brain receiver coil, and volume transmitter coil. We also implemented a progressive habituation protocol aiming to minimize the stress experienced by the rats, and compared RSFC between awake, lightly sedated, and isoflurane-anesthetized rats. Our results demonstrated that the 3D printed restraint kit was suitable for RSFC studies of awake rats. During the short 4-day habituation period, the plasma corticosterone concentration, movement, and heart rate, which were measured as stress indicators, decreased significantly, indicating adaptation to the restraint protocol. Additionally, 10 days after the awake MRI session, rats exhibited no signs of depression or anxiety based on open-field and sucrose preference behavioral tests. The RSFC data revealed significant changes in the thalamo-cortical and cortico-cortical networks between the awake, lightly sedated, and anesthetized groups, emphasizing the need for awake imaging. The present work demonstrates the feasibility of our custom-made 3D printed restraint kit. Using this kit, we found that isoflurane markedly affected brain connectivity compared with that in awake rats, and that the effect was less pronounced, but still significant, when light isoflurane sedation was used instead.

Keywords: awake imaging, fMRI, rat, BOLD, resting state, 3D printing, restraint kit

OPEN ACCESS

Edited by:
Federico Giove, Centro Fermi - Museo Storico della Fisica e Centro Studi e Ricerche Enrico Fermi, Italy

Reviewed by:
Xin Yu, Max-Planck-Institut für Biologische Kybernetik, Germany
Jack A. Wells, University College London, United Kingdom

***Correspondence:**
Olli Gröhn
olli.grohn@uef.fi

Specialty section:
This article was submitted to Brain Imaging Methods, a section of the journal Frontiers in Neuroscience

Received: *18 May 2018*
Accepted: *20 July 2018*
Published: *20 August 2018*

Citation:
Stenroos P, Paasonen J, Salo RA, Jokivarsi K, Shatillo A, Tanila H and Gröhn O (2018) Awake Rat Brain Functional Magnetic Resonance Imaging Using Standard Radio Frequency Coils and a 3D Printed Restraint Kit. Front. Neurosci. 12:548. doi: 10.3389/fnins.2018.00548

INTRODUCTION

Functional magnetic resonance imaging (fMRI) is a modern imaging modality enabling noninvasive measurements of neuronal activity. The detection is typically based on the blood oxygenation-level dependent (BOLD) contrast (Ogawa et al., 1990), which exploits the neurovascular coupling cascade to provide an indirect measure of brain activity. Traditionally,

fMRI is used to detect local activation changes induced by a precise stimulus, but advanced fMRI techniques, such as resting-state fMRI (Biswal et al., 1995), have enabled studies of resting state functional connectivity in large-scale brain networks.

Despite the fMRI method being fully compatible with clinical settings, experimental rodent studies are still irreplaceable, as they not only provide a means to scrutinize the neurovascular coupling mechanisms, but also allow for controlled genetic, electrical, and pharmacologic manipulations, and more invasive monitoring that enables mechanistic studies of normal and abnormal brain functions. In the majority of preclinical fMRI studies, however, anesthetics complicate interpretations of the results. Anesthesia is required to prevent the animals from moving as well as to decrease discomfort and stress in the animals, but it also has significant undesirable effects on fMRI responses to stimuli or drugs (Paasonen et al., 2016, 2017) and resting state activity (Hamilton et al., 2017; Paasonen et al., 2018) by interfering with normal brain function and neurovascular coupling (Franks and Lieb, 1994; Martin et al., 2006; Zhao et al., 2007; Ferron et al., 2009; Gao et al., 2016).

To avoid the disrupting effects of anesthetics, several groups have implemented awake animal fMRI imaging protocols (King et al., 2005; Zhang et al., 2010; Becerra et al., 2011; Febo, 2011; Tsurugizawa et al., 2012; Brydges et al., 2013; Chang et al., 2016; Kenkel et al., 2016). Awake animals are likely to move and experience stress during fMRI, which raises the demand for carefully optimized restraint and habituation protocols. Several studies have demonstrated, based on physiologic markers of stress, that rats are able to adapt to the level of restraint required for fMRI (King et al., 2005; Tsurugizawa et al., 2010; Reed et al., 2013; Chang et al., 2016).

Despite the advantages provided by awake animal imaging, the method is still relatively rarely exploited, partly due to several methodologic issues. First, there are only a few readily available solutions for restraint implementation, leading to a demand for custom-made restraint kits and beds. Second, the custom-made restraint parts are typically not compatible with standard radiofrequency coils. If large volume coils are used for signal reception, decreases in the signal-to-noise ratio hinder the detection of fMRI signal changes. Third, the habituation protocols can last up to 8 days (King et al., 2005) making the approach very time-consuming. Therefore, there is a clear demand for fast, easily implemented, low-stress, and low-cost approaches that could be performed using standard hardware available in the preclinical MRI laboratory.

To address some of the essential methodologic limitations in awake rat imaging, the first aim of this study was to construct an open-access 3D printable restraint kit that is fully compatible with a standard Bruker rat bed and surface coil. The second aim of this study was to investigate the possibility of performing a habituation protocol under very light sedation that would minimally affect brain function, but at the same time allow for a short habituation period. The developed restraint kit and habituation protocol were implemented into fMRI studies to obtain RSFC data from awake and lightly sedated (0.5% isoflurane) rats, and the RSFC data were subsequently compared with corresponding data obtained from anesthetized (1.3% isoflurane) rats.

MATERIALS AND METHODS

Restraint Parts

The custom-made 3D printed (with Zmorph 2.0 SX) restraint kit (**Figure 1**), compatible with an existing Bruker Pharmascan rat bed and quadrature surface receiver coil (Bruker Biospin, Ettlingen, Germany), was designed for rat brain imaging. The restraint kit, printed from acrylonitrile styrene acrylate (other materials e.g., acrylonitrile butadiene styrene can be also used), comprises a foam-padded arc-shaped shoulder and neck support, padded cheek supports, and a sliding sledge with a padded nose cone, which functions as a gas mask. The sliding sledge also includes a bite bar. Thus, the contact points for the restraint are neck area, shoulders, muzzle and cheeks of the rat. The RF-coil is attached on top of the head making little physical contact.

The 3D printed restraint kit was designed with CAD software (Autodesk 123D Design), and the kit requires no additional modifications (e.g., screw threads) to the animal bed. The 3D printing files (file format: STL), excluding the MRI bed, are available in the electronic **Supplementary Material**. For the cheek supports, we provide a 3D printable model for the whole support and separately for a curved plate (presses against the cheek) but we recommend to use a tougher carbon fiber bar that can be fixed to the plastic plate. In 3D printing, we used layer thickness of 200 μm for all parts except for the cheek support bars 50–100 μm layer thickness is recommended. Also, we advise to use support material in 3D printing. In addition to 3D printed parts, plastic screws (diameter 3.8 mm, length 20 mm) and compatible plastic nuts (outer diameter 7 mm) were used for attaching the restraint parts, and foam pad was used to soften points of restraint.

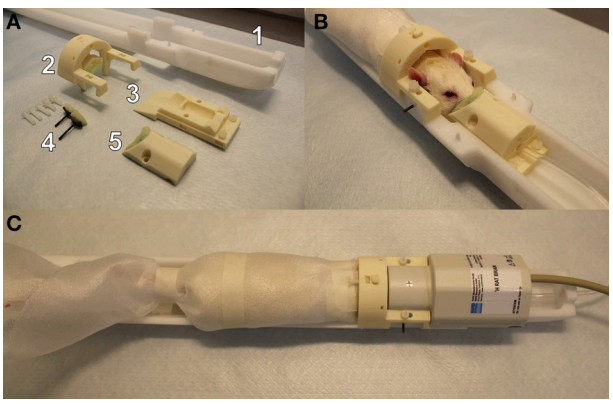

FIGURE 1 | A custom-made 3D printed rat restraint kit **(A)**, a rat restrained in the bed with the developed restraint kit **(B)**, and a restrained rat in the bed with a Bruker quadrature receiver coil attached **(C)**. The rat restraint kit **(A)** consists of a standard Bruker rat bed **(A1)**, a padded shoulder/neck support **(A2)**, a sliding sledge including a bite bar **(A3)**, padded cheek supports **(A4)**, and a padded nose cone **(A5)**. A replicate of Bruker bed was used in mock scanner.

Animals

All animal procedures were approved by the Animal Experiment Board in Finland, and conducted in accordance with the guidelines set by the European Commission Directive 2010/63/EU.

A total of 23 adult male rats were used (RccHan Wistar, 320 ± 25 g, purchased from Laboratory Animal Centre, University of Eastern Finland). Rats were divided into three groups: awake ($n = 8$), lightly sedated (isoflurane 0.5%, $n = 7$), or anesthetized (isoflurane 1.3%, $n = 8$). The rats in the 1.3% isoflurane group were group-housed in cages, while rats in the awake and lightly sedated groups were individually housed because the rats were also individually habituated. All animals were maintained on a 12/12 h light-dark cycle at room temperature of 22 ± 2°C with humidity of 50–60%. Food and tap water were available *ad libitum*.

Habituation and Imaging Schedule for Awake and Lightly Sedated Rats

Habituation sessions were gradually increased from 15 to 45 min (**Figure 2**). Rats in the lightly sedated group were habituated for 4 consecutive days prior to fMRI. Rats in the awake group were habituated and imaged in two 5-day periods. During the first week, we used a protocol identical to that for the lightly sedated group. In the following week, training was continued for another 4 days with fixed 45-min sessions, followed by a second fMRI session. Rats were habituated daily and imaged (two rats sequentially at one session) at the same time of day (9.00–12.00 a.m.) to control for circadian rhythm variations.

Habituation Protocol for Awake and Lightly Sedated Rats

Rats were habituated for imaging in a mock scanner mimicking the real MRI environment. Located in a separate habituation room, the mock scanner comprised a plastic tube (ID = 72 mm) mimicking a magnet bore, a rat bed, a standard platform for the rat bed, a web camera for recording movement, and a speaker (JBL LSR308, Harman International Industries, Stamford, CT, USA). We measured the sound level using a microphone (MT830R, Audio-Technica, Leeds, England) positioned inside the real MRI bore and played the sounds of the MRI at the same sound pressure as that inside an actual animal scanner.

At the beginning of each habituation session, the rats were first anesthetized with 5% isoflurane (Baxter, Lessines, Belgium; in a carrier gas mixture of N_2/O_2 [70/30]), weighed, and transferred to a hood where anesthesia was maintained with 1.5–2.0% isoflurane. The restraint protocol described below is also available in video format (**Supplementary Video 1**). A piezoelectric pneumatic sensor (M2M, Cleveland, OH, USA) was taped onto the belly and adhesive electrocardiography (ECG) electrodes (3M, St. Paul, MN, USA) were secured to the limbs. The forepaws were attached with masking tape along the sides of the rat without allowing the adhesive surface of the tape to come into contact with the rat fur. The hind paws were tied together with the tail with masking tape.

A sheet of foam plastic was wrapped around the rat from the shoulders to the hind paws to restrain body movement. Foam plastic assured a tight, but flexible and warm environment that allowed the rat to breathe normally. Foam plastic was secured with tape around the shoulders and hind paws. Silicone plugs were used to protect hearing from the MRI scanner sounds, thus increasing comfort.

Next, the rat was transferred to the animal bed in the mock scanner. Isoflurane was maintained at 1.5–2.0%. The head was placed on the sliding sledge and the upper teeth were secured behind the bite bar. The nose cone was tightened to the sledge to prevent muzzle movement in the vertical direction. The padded cheek supports, positioned on the both sides of the head, were gently tightened below the ears to prevent lateral movement of the head. The head was further secured by adjusting the shoulder and neck support; this also reduces the effects of lower body movements on the head. The nose cone, cheek supports, and shoulder/neck support also suppressed rotational movement of the head. To minimize body movement, tape was placed around the rear part of the body and attached to the bed.

ECG electrodes and a breathing sensor were connected to an amplifier (Biovet CT1 system, m2m imaging, Corp., USA). A heating pad was placed on top of the rat and connected to a Biovet CT1 temperature regulation unit to keep the body warm. To minimize discomfort, a rectal probe was not used but thermometer was placed under the animal to monitor temperature.

Finally, a Bruker rat surface quadrature receiver coil was placed on top of the head, and the animal bed was pushed inside the mock MRI tube. The receiver coil used in the habituation sessions was similar to the one used during the actual fMRI session.

The pre-habituation preparations lasted approximately 8 min per rat, excluding the induction of anesthesia. After the preparations, isoflurane was decreased to either 0.5% in the lightly sedated group or turned off in the awake group.

MRI sounds, starting with the sounds of pilot imaging and shimming, and then continuing with continuous EPI scanning, were played for a given time (15–45 min, see **Figure 2**), while simultaneously monitoring the physiologic parameters, i.e., the respiratory rate and heart rate. Movement was monitored and recorded through a web camera. If the rat was moving excessively, defined as continuous movement >30 s, or more than a third of the time used for the session, the habituation protocol was ceased and continued the next day.

After reaching the desired habituation session length (see **Figure 2**), isoflurane was raised to 2%. When physiologic parameters indicated a sufficient depth of anesthesia, the rat was released from the kit and transferred back to the hood where the plastic foam and tape were removed. Blood samples (total of 150 μl) were obtained from the lateral tail vein. Next, the rat was returned to the cage and chocolate cereal balls were given as a reward. Blood samples were centrifuged at 3,500 RPM for 10 min, after which plasma was collected and samples were stored at −70°C for corticosterone analysis.

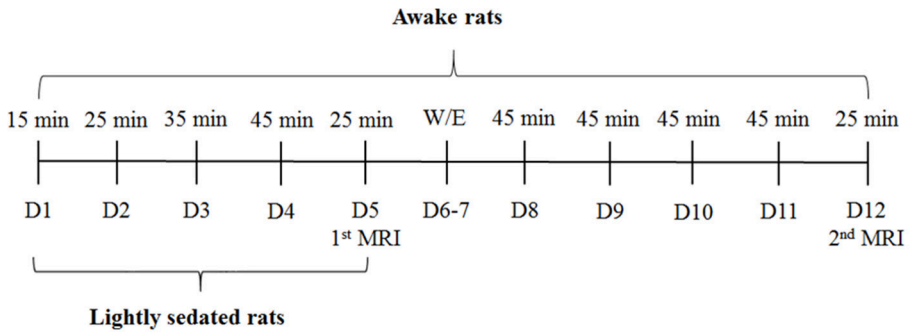

FIGURE 2 | Rat habituation and imaging schedule. D, days, W/E, weekend.

fMRI Protocol

MRI was performed with a 7T/16cm horizontal Bruker Pharmascan system and ParaVision 5.1 software. A standard Bruker quadrature resonator volume coil (ID = 72 mm) and a rat brain quadrature surface coil were used. A 3D field-map based shimming method was used to optimize the field homogeneity.

Functional imaging was performed with single-shot spin-echo echo planar imaging sequence with the following parameters: repetition time 2,000 ms, echo time 45 ms, matrix size 64 × 64, field-of-view 2.5 × 2.5 cm, 9–11 slices of 1.5 mm thickness, and a bandwidth of 250 kHz. The same imaging parameters were used with all animals, except that 300 fMRI volumes (10 min) were acquired from anesthetized rats and 600–750 fMRI (20–25 min) volumes were acquired from awake and lightly sedated rats. Despite habituation, awake animals tend to move slightly. Therefore, a longer period was obtained from awake and lightly sedated rats to ensure a continuous motion-free 10-min period for analysis.

Anatomic images were acquired after the fMRI scans with fast spin-echo sequence with the following parameters: repetition time 4,680 ms, echo spacing 16.1 ms, 8 echoes, effective echo time 48.4 ms, matrix size 512 × 512, field-of-view 5.0 × 5.0 cm, 30 slices of 0.75 mm thickness, and bandwidth of 46.875 kHz. The restraint preparations for the awake and lightly sedated rats were similar to those for the habituation protocol, except that heart rate was measured using a pulse oximetry sensor.

Physiologic parameters (heart rate, respiration, and temperature) were monitored continuously during the imaging, and movement was estimated from the real-time reconstructed EPI images. Rats were kept warm using a water circulation heated animal bed. After measurements, blood samples for corticosterone level analysis were collected as in the habituation sessions.

The protocol for imaging anesthetized rats (isoflurane 1.3%) was describer earlier (Paasonen et al., 2018). Briefly, small cannulas (BD Intramedic™ PE-10, Franklin Lakes, NJ, USA) were inserted into the femoral artery and vein, and tracheostomy was performed under 2% isoflurane anesthesia. As isoflurane anesthesia suppresses respiratory function and easily leads to hypercapnia, mechanical ventilation (Inspira, Harvard Apparatus) was used to maintain normal blood gas values (pCO_2 45.1 ± 2.0; i-STAT Model 300, Abbott Point of Care Inc., Princeton, NJ, USA) measured from the arterial blood sample (150 µl). Muscle relaxant (∼1 mg/kg/h i.v., pancuronium bromide, Pavulon (R), Actavis) was given while connecting the animal to the ventilator. Rats were killed immediately after the measurements.

fMRI Analysis

First, a 10-min motion-free fMRI data period was selected from each subject. Next, the fMRI data were converted to NIfTI (http://aedes.uef.fi), slice-timing corrected, motion-corrected, spatially smoothed, and co-registered to a reference brain (SPM8).

Regions of interest (ROIs) were drawn according to an anatomic atlas (Paxinos and Watson, 1998). The 12 ROIs for whole brain analysis were the medial prefrontal cortex (mPFC), motor cortex (MC), somatosensory cortex (SC), visual cortex (VC), auditory cortex (AC), retrosplenial cortex (RC), nucleus accumbens (NAc), striatum (Str), hippocampus (HC), medial thalamus (ThM), ventrolateral thalamus (ThVL), and hypothalamus (HTH) (**Supplementary Figure 1A**).

Additional ROIs were drawn for the default mode network (DMN) analysis, based on the article by Lu et al. (2012): medial frontal cortex (including prelimbic cortex and anterior cingulate cortex), temporal association cortex, orbitofrontal cortex, auditory cortex, retrosplenial cortex, posterior parietal/visual cortex and hippocampus (**Supplementary Figure 1B**).

RSFC was estimated with ROI-based Pearson correlation (r) analysis. Prior to correlation calculations, data were band-pass filtered at 0.01–0.15 Hz. Subsequently, the *r*-values were transformed to Z-scores prior to calculating group averages and statistical comparisons. After performing the calculations, the mean Z-scores were returned to *r*-values. Correlation coefficients between the 12 ROIs were used to form functional connectivity (FC) matrices (**Figure 4**) and the same ROIs were used as seed regions in correlation maps. Voxel-wise correlation maps for the awake group were calculated by using somatosensory cortex, striatum, and medial thalamus as seed regions (**Figure 5A**). Subsequently, difference maps between the awake and 0.5 and 1.3% isoflurane groups were calculated (**Figure 5B**). Mean correlation values (**Supplementary Figure 2**) from each of the 12 ROIs were additionally calculated to obtain mean connectivity of

the brain regions. Correlation coefficients within the rat DMN were also calculated (**Figure 6**). Moreover, we calculated partial correlation coefficients by using mass center displacement values (x, y, z and roll, pitch, yaw) as a regression for motion.

Statistical group-level differences ($p < 0.05$) in DMN and mean functional connectivity were calculated using a one-way ANOVA and Tukey's multiple comparison *post-hoc* test. FDR-corrected *t*-tests ($p < 0.05$) were applied to FC matrices. FDR-corrected, one-sample *t*-test ($p < 0.001$) was performed to obtain functional connectivity map from the awake rats. Two-sample *t*-test ($p < 0.05$) was performed to compare 0.5 and 1.3% isoflurane groups to the awake rats. Statistical testing was performed with GraphPad Prism (Version 5.03, GraphPad Software Inc., La Jolla, CA, USA) or Matlab (R2011a), Natick, MA, USA.

Analysis of Movement During fMRI

In addition to visually estimated movement incidents, motion correction parameters, obtained from SPM8, were analyzed to evaluate the movement of the head during the fMRI session. Translational (x-y-z-directions) and rotational (roll, pitch, and yaw) movements were calculated.

First, co-registered translational and rotational mass center displacement values, given by SPM8, were detrended and normalized. Movement was evaluated from these values during the awake fMRI session by subtracting every subsequent time-point from the preceding value. After removing visible movement incidents (sharp peaks in mass center displacement) from a selected 10-min fMRI period, we preprocessed the data again to obtain 10-min motion-free fMRI periods. In these periods the motion was substantially lower in relation to voxel size (**Supplementary Figure 3A**). Of 16 awake datasets, 2 (2/16) were excluded from the analysis due to excessive movement.

Each subtracted translational and rotational movement was then converted to absolute values. These absolute values were summated over 10-min MRI sessions to obtain summated translational and rotational movement (**Supplementary Figure 3B**). Additionally, absolute maximum translational displacement in the y-direction, in which most of the movement happened, was calculated to estimate overall displacement of the animal head in the restraint kit (**Supplementary Figure 4**). This displacement value represents maximum displacement of the animal head from the starting position and does not inform of the separate movement incidents.

Estimation of Stress

Physiologic values (plasma corticosterone level, respiratory rate, heart rate, movement, and weight) were monitored during the habituation and fMRI sessions to estimate stress. Plasma corticosterone concentrations were quantified by a corticosterone immunoassay (Corticosterone rat/mouse ELISA Cat. No.: RTC002R, Demeditec Diagnostics, Kiel, Germany). Corticosterone concentrations were measured with a microtiter plate reader (Labsystems Multiskan MS, Vantaa, Finland) at an absorbance of 405 nm. Average respiratory and heart rates were calculated from values during habituation and fMRI sessions. Only values from 6 min onwards were included to minimize the possible influence of anesthesia on arousal. If the interval between two visually estimated movement indicents was $\geq$4 s (two fMRI volumes), they were considered separate incidents.

Additionally, we estimated the potential habituation-induced depression and anxiety by conducting open-field and sucrose preference behavioral tests with a small subgroup of awake habituated rats ($n = 5$). Control rats ($n = 5$) were anesthetized daily with isoflurane for the same amount of time that the habituated rats were anesthetized.

In the open-field test we used a circular plastic arena (ID = 100 cm) placed in a quiet room. Color of the arena was black to distinguish white Wistar rats from the environment. We used a lux meter (TR-710, Trifitek Finland Oy, Alajärvi, Finland) to confirm homogenous lighting conditions (19.3 $\pm$ 1.1 lx, 9 measurement points) across the test arena. Test was performed 10 days after the last procedure. In the test, rat was placed on the arena edge having its nose toward the wall. Movement and other activities were video-recorded for 10 min. Data were analyzed with Ethovision XT 7.1 (Noldus, Wageningen, The Netherlands), where the arena was divided into center (circle with 40 cm diameter) and edge (up to 10 cm from borders) zones. Distance traveled, activities (rearing and grooming), and time spent in different zones were subsequently calculated.

In the sucrose preference test, rats were first habituated to 1% sucrose water, which was made available *ad libitum* for 2 days next to regular tap water. During the next 2 days, the bottles with sweetened and regular water were weighed to calculate consumption during each day. The positioning of the bottles was switched each day.

The plasma corticosterone level, respiratory rate, heart rate, movement, and weight measurements were analyzed with ANOVA for repeated measures and Dunnett's *post-hoc* test in GraphPad Prism. Statistical comparison of corticosterone levels between days was done by comparing each day to baseline level. Comparison of respiratory rate, heart rate, movement and weight between days were done by comparing each day to habituation day 1. Statistical testing for the open field and sucrose preference tests was performed with a two-sample, two-tailed *t*-test assuming equal variances.

RESULTS

Stress Level Indicators

The measured values for stress level indicators (plasma corticosterone level, heart rate, respiratory rate, and movement) obtained from awake and lightly anesthetized rats during the habituation protocol are summarized in **Figure 3**.

Plasma corticosterone concentrations on the MRI day 1 did not differ statistically from the baseline concentrations in the awake or lightly sedated groups ($p = 0.25$ and $p = 0.36$, respectively, paired *t*-test). In the awake group, corticosterone concentrations significantly increased from the baseline level on habituation day 1 ($p = 0.014$, paired, *t*-test). However, concentrations returned to baseline level on the habituation day 4 (baseline: 95 $\pm$ 43 ng/ml, day 4: 102 $\pm$ 30 ng/ml, $p = 0.75$, paired, *t*-test). Also corticosterone concentration did not appear to differ statistically on MRI day 2 from MRI day 1 ($p = 0.064$,

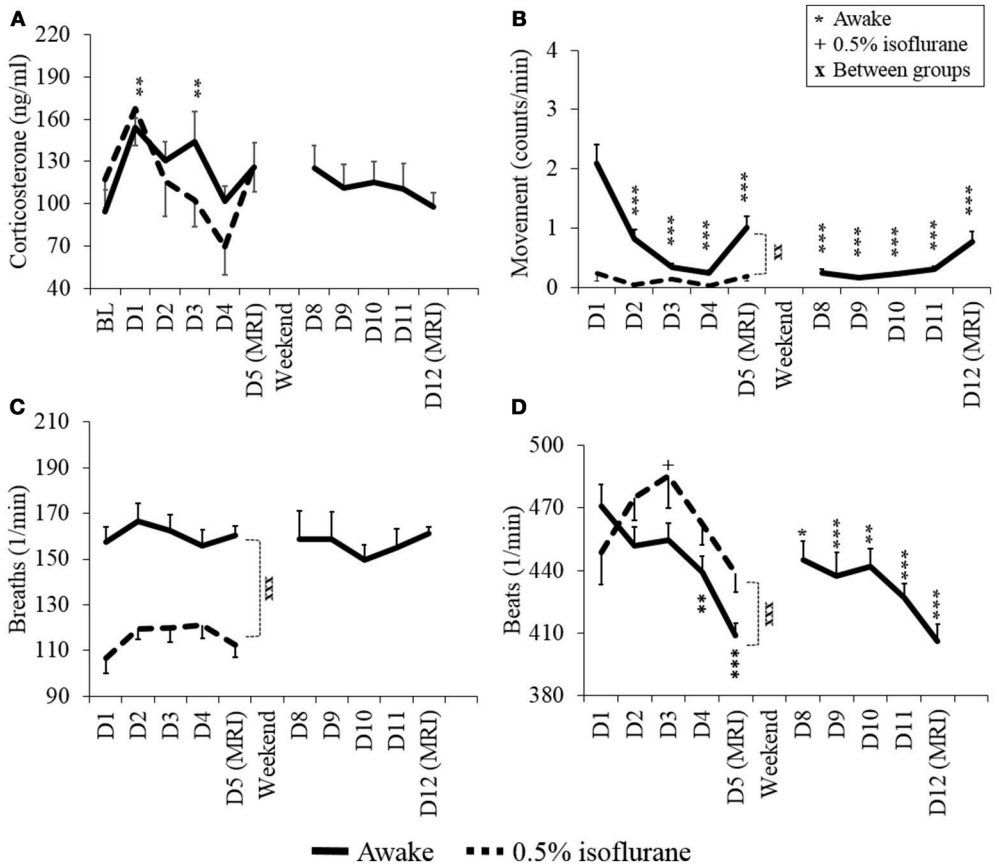

FIGURE 3 | Stress level indicators of plasma corticosterone **(A)**, movement **(B)**, respiratory rate **(C)**, and heart rate **(D)** of awake and lightly sedated rats during habituation and fMRI. Mean values ± SEM of corticosterone (ng/ml), movement (counts/min), respiration (breaths/min) and heart rate (beats/min) are presented ($n = 7$–8 in each group). Statistical testing between days was done with ANOVA for repeated measures and Dunnett's *post-hoc* test, and between groups with a two-sample *t*-test. Significant differences of each time point are co mpared to either BL **(A)** or D1 **(B–D)** values. One symbol equals $p < 0.05$, two symbols equal $p < 0.01$, three symbols equal $p < 0.001$.

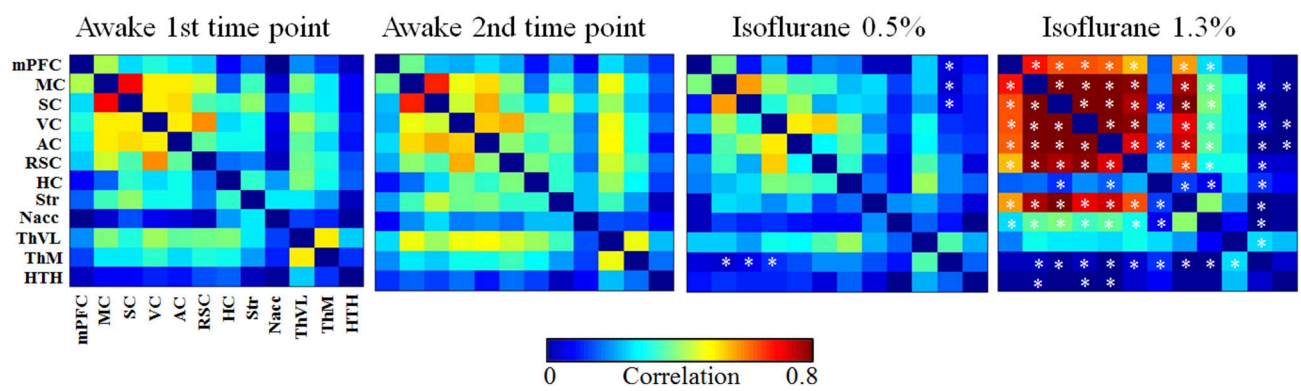

FIGURE 4 | The group-level functional connectivity (FC) obtained from the 1st ($n = 8$) and 2nd ($n = 6$) awake time points, lightly sedated rats ($n = 7$), and anesthetized rats ($n = 8$). The connectivity data were analyzed from 300 volumes from 12 regions of interests. Statistical testing was done by using FDR-corrected *t*-test, $^{*}p < 0.05$, $^{**}p < 0.01$, $^{***}p < 0.001$. Significant differences against 1st awake time point are presented. AC, auditory cortex; HC, hippocampus; HTH, hypothalamus; mPFC, medial prefrontal cortex; ThM, medial thalamus; MC, motor cortex; Nacc, nucleus accumbens; RSC, retrosplenial cortex; SC, somatosensory cortex; Str, striatum; ThVL, ventrolateral thalamus; VC, visual cortex.

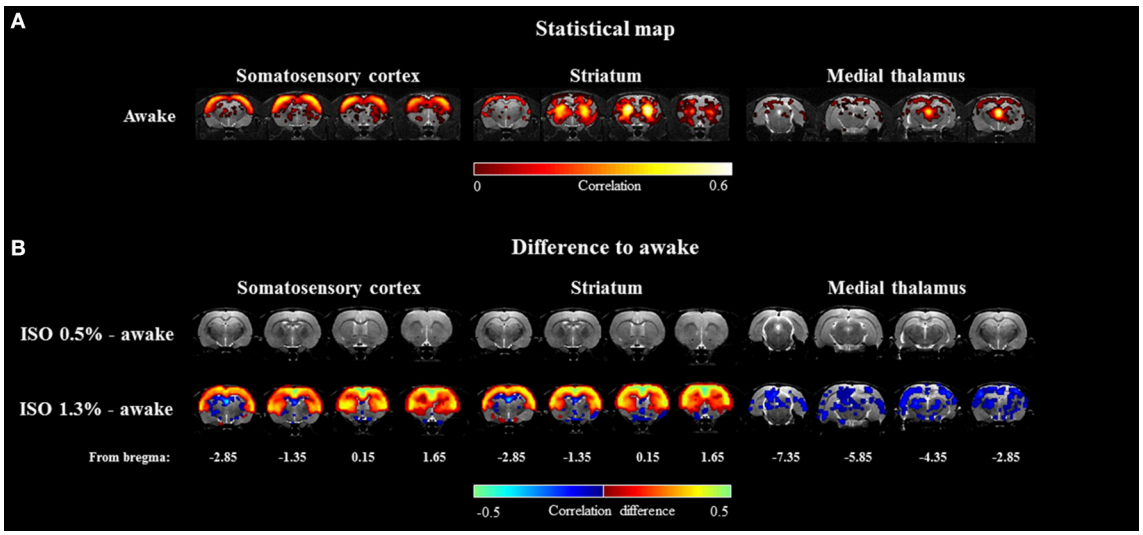

FIGURE 5 | The group-level seed-based statistical correlation maps obtained from the awake group **(A)** and group-level differences compared to the awake group **(B)** obtained from three representative brain regions. Brain regions of somatosensory cortex, striatum, and medial thalamus were selected. Statistically significant voxels were obtained with one-sample *t*-test **(A)** ($p < 0.001$) and two-sample *t*-test **(B)** ($p < 0.05$).

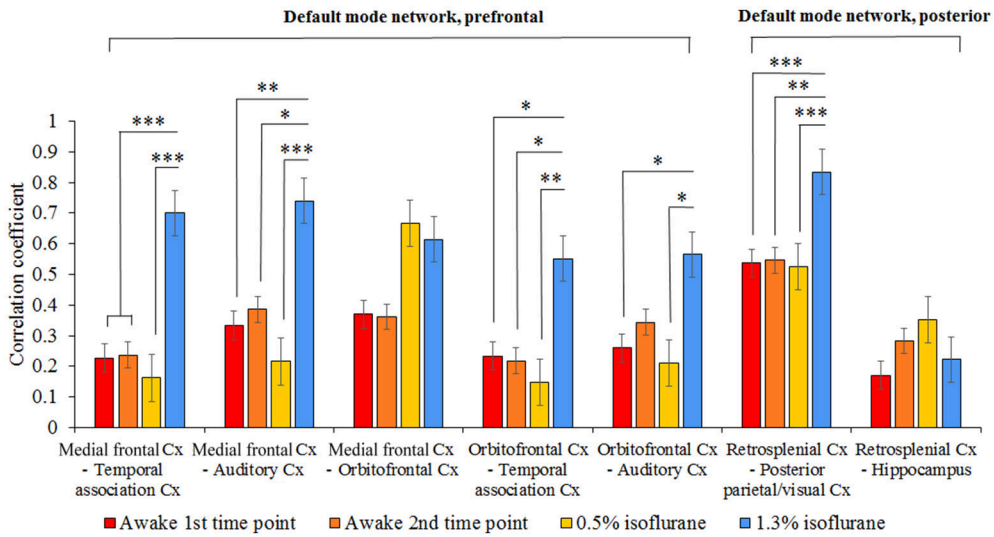

FIGURE 6 | The group level mean correlation coefficients (± SEM) between the seven pathways in the rat DMN. The 300-volume data (10 min) were obtained under two awake time points, lightly sedated and anesthetized conditions. Statistical testing was done by one-way ANOVA and Tukey's multiple comparison *post-hoc* test, $^{*}p < 0.05$, $^{**}p < 0.01$, $^{***}p < 0.001$. Cx, cortex.

paired *t*-test). Noticeably, in the lightly sedated group, there was no clear difference between the baseline (117 ± 20 ng/ml) or the 1st habituation day (168 ± 27 ng/ml) ($p = 0.066$, paired *t*-test).

Movement of awake rats decreased significantly already during habituation day 2 ($p = 0.002$, paired *t*-test) and, from thereon, differed significantly in each habituation and MRI days from habituation day 1. Importantly, there was no further decrease in movement on MRI day 2 (0.77 ± 0.18 counts/min) compared with MRI day 1 (1.0 ± 0.20 counts/min) ($p = 0.20$, paired *t*-test). In the lightly sedated group, movement did not differ significantly between days but rats moved significantly less during MRI day 1 compared to awake rats ($p < 0.001$, two-sample *t*-test).

The heart rate of awake rats was significantly lower during habituation day 4 and MRI day 1 compared with habituation day 1 ($p = 0.018$ and $p < 0.001$, respectively, paired *t*-test). Heart rates during MRI day 2 did not differ significantly from MRI day 1 ($p = 0.67$, paired *t*-test). In the lightly sedated group there was no significant difference in the heart rates between habituation day 1 and MRI day 1 ($p = 0.49$, paired *t*-test).

The breathing rate was significantly lower during MRI day 1 in lightly sedated group compared with the awake group ($p < 0.001$, two-sample t-test) but the levels did not change significantly in either group between the habituation days. Additionally, average body weight of animals remained stable during the habituation (varied between 316 to 325 ± 4.2 g in awake rats and 319 to 320 ± 5.1 g in lightly sedated rats) (data not shown).

Results from the open field and sucrose preference tests are illustrated in the **Supplementary Figures 5, 6**. There were no differences in locomotor activity, time spent in different zones, rearing activity, or sucrose preference between the groups ($p > 0.05$, two-sample t-test). However, habituated rats spent more time grooming than control rats (20.2 ± 3.6 s vs. 4.9 ± 2.8 s, $p = 0.01$, two-sample t-test).

Movement During fMRI

Generally, the awake rats moved more compared with the other groups. For example, there was a significant difference in the summated movement in X- (1st awake time-point 988 μm, 1.3% group 339 μm, $p < 0.001$, two-sample t-test) and Y- (1st awake time-point 3,330 μm, 1.3% group 423 μm, $p < 0.001$, two-sample t-test) directions, and in rotational directions of roll (1st awake time-point 18.3°, 1.3% group 11.0°, $p < 0.01$, two-sample t-test) and yaw (1st awake time-point 9.11°, 1.3% group 3.40°, $p < 0.001$, two-sample t-test) between the 1st awake time-point and 1.3% isoflurane groups. Maximum displacement from the mass center was also significantly higher in the 1st (253 μm) and 2nd (271 μm) awake time-points compared with the 1.3% isoflurane group (51 μm; $p < 0.001$ and $p < 0.01$, respectively, two-sample t-test). Notably, lightly sedated rats did not move significantly more than anesthetized rats based on summated movement or displacement values. Movement incidents, summated movement and displacement values during 10-min fMRI sessions are illustrated in **Supplementary Figures 3** and **4**.

Resting State Functional Connectivity

Functional Connectivity Matrices

Functional connectivity matrices are shown in **Figure 4**. FC matrices obtained from the awake animals after the first and second habituation week were almost identical with no significant difference between them ($p > 0.99$, t-test, FDR adjusted). In the lightly sedated group, connectivity was significantly weaker in the three pathways compared with that in the first awake group: between medial thalamus and motor, somatosensory, and visual cortex.

In the anesthetized group, correlation values were significantly higher in several (21/66) cortico-cortical and cortico-striatal connections compared with the first awake group ($p < 0.05$, t-test, FDR adjusted). In addition, statistically stronger connectivity in anesthetized rats was observed in mean connectivity values in the medial frontal cortex (0.41), motor (0.61), somatosensory (0.60), visual (0.59), auditory (0.57) cortices, and in the striatum (0.49) compared with the first awake group (medial frontal cortex [0.20], motor [0.37], somatosensory [0.37], visual [0.37], auditory [0.33] cortices, and striatum [0.26]) ($p < 0.05$, **Supplementary Figure 2**).

In contrast, the correlation was significantly lower in several subcortical-cortical (22/66) connections in anesthetized rats compared with the awake rats ($p < 0.05$, t-test, FDR adjusted). Further, the mean correlation was significantly lower in the medial thalamus ($p < 0.01$) in anesthetized rats than in awake rats.

Seed-based partial correlation, with motion as a regression, did not differ statistically from correlation values calculated without motion regression ($p > 0.05$ t-test, FDR adjusted). Therefore, the possible remaining motion artifacts were not affecting the results obtained with functional connectivity analyses.

Voxel-Wise Correlation Maps

The seed-based mean correlation map and group difference maps obtained from three representative ROIs are shown in **Figure 5**. In the 1.3% isoflurane group, the connectivity of the somatosensory cortex and the striatum was more widespread and stronger compared to the awake group, while thalamo-cortical connectivity was clearly suppressed. In the lightly sedated group, we did not find statistically significant voxel-wise correlation differences compared to the awake group after multiple comparison correction.

Default Mode Network

The functional connectivity of seven pathways in the rat DMN is illustrated in **Figure 6**. In the 1.3% isoflurane group, connectivity was stronger in almost all DMN connections ($p < 0.05$), excluding medial frontal–orbitofrontal and retrosplenial cortex–hippocampus connections, when compared with the first awake time-point. In the lightly sedated group, the DMN connectivity did not differ statistically from those in the awake groups.

DISCUSSION

It has become increasingly recognized that anesthesia is a major confounding factor in animal fMRI studies, especially when assessing functional connectivity in the brain (Liang et al., 2012, 2015; Liu and Duyn, 2013; Paasonen et al., 2018). Awake animal imaging offers the possibility of avoiding the drawbacks of anesthesia, and robust, practical, and low-stress awake imaging methods are in high demand. Indeed, a number of different approaches are available for awake fMRI (**Table 1**).

The existing awake imaging methods, however, have several shortcomings with regard to both technical feasibility and animal welfare. Many of these approaches require dedicated beds and/or receiver coils, with poor filling factors, making the replication of protocols by others practically impossible. Additionally, the use of possibly painful ear bars, the lack of ear protection, the lack of soft padding materials, and the use of long non-progressive habituation times (**Table 1**) may induce major acute pain or long-term stress.

In the present work, we aimed to avoid several of these shortcomings by implementing novel ideas and adopting known best practices to create a significantly improved approach for awake fMRI. We designed a 3D printable restraint kit compatible with a common rat bed type and standard RF-coil with good

TABLE 1 | Different rat restraint and habituation methods from literature.

Publications	Species	Type of MRI receiver coil	Restraint of the head	Restraint of the body	Habituation protocol	Padded holder parts	Ear bars	Ear plugs	Corticosterone levels	MRI applications
Current study	**Wistar**	**Quadrature surface coil**	**3D printed restraint kit compatible to standard rat beds and coils**	**Elastic plastic foam**	**15–45 min with increments of 10 min/day, 4–9 days**	**Yes**	**No**	**Yes**	**Decrease in corticosterone, 126 ± 18 ng/ml after fMRI (D5)**	**Resting state fMRI**
King et al., 2005	Sprague-Dawley	Single loop, surface coil	Cylindrical head holder	Body tube	90 min/day, 4–8 days	No, but topical analgesic	Yes+ topical analgesic	No	Decrease in corticosterone, ∼120 ng/ml after fMRI (D5)	Resting state fMRI
Febo, 2011	Sprague-Dawley	Quadrature surface coil (transmit/receive)	Cylindrical head holder	Body tube, limbs free	20 min to a maximum of 50 min, 5 days	No, but topical analgesic	Yes+ topical analgesic	No	–	fMRI, stress-evoking stimulus
Tsurugizawa et al., 2012	Sprague-Dawley	Surface coil compatible to head fixation mount	Head fixation acrylic mount	Rubber bands	30 min on first day and 90 min from thereon, 5 days	Head fixation	No	Yes	–	fMRI, reward anticipation
Brydges et al., 2013	Lister hooded rats	Single loop, surface coil	Cylindrical head holder	Body tube	90 min/day, 3 days	No	Yes	No	–	fMRI, conditioned fear circuitry
Kenkel et al., 2016	Sprague-Dawley	Quadrature volume coil (transmit/receive)	Head holder	Body tube	30 min/day, 4–5 days	Yes	No	No	–	fMRI, reward processing
Chang et al., 2016	Sprague-Dawley	Surface coil compatible to head fixation mount	Head fixation mount	Snuggle sack	30 min, 8–10 days	Head fixation	No	No	Decrease in corticosterone ∼1,200 ng/ml after fMRI	Resting state fMRI, stimulus fMRI (air puff)

filling factor. In the kit design, we aimed to take the comfort of animal into account, to reduce the amount stress experienced by the animal, and to minimize the required habituation period, while still maintaining robust fixation of the head. Indeed, the physiologic markers of stress indicate that fully awake rats were able to adapt to the measurement environment in 4 days, showing very low peak concentrations of plasma corticosterone throughout the habituation period. Additionally, we show that by using light sedation, the habituation protocol could be shortened to 2 days. After the 4-day habituation period, the RSFC pattern of lightly sedated rats better resembled the pattern obtained under the awake state than that under an anesthetized state. Thalamo-cortical connectivity, however, was significantly suppressed in the lightly sedated state compared with the awake state.

3D Printed Restraint Kit

The 3D printed restraint kit and protocol described here was robust and easy to use during the *in vivo* experiments. The initial preparations and fixation of the rat to the bed typically took less than 10 min under isoflurane anesthesia. The restraint kit was confirmed to be suitable for a wide range of rat sizes, as rats weighting from 200 to 480 g were tested in the pilot experiments. Because no dedicated surface coil or animal bed is required, our protocol provides an affordable option for any awake rat fMRI study design. We provide the restraint kit template (STL-file, **Supplementary Material**) for public use and for further modifications.

Movement During fMRI

In fMRI studies, it is crucial that patients or animals remain motionless during the imaging for acquisition of artifact-free data, as movement can compromise the fMRI analysis (Power et al., 2012, 2014). In our habituation protocol, rats adapted quickly to the restraint environment and movement decreased rapidly. Importantly, the occasional lower body movement did not typically affect the head position, indicating robust fixation achieved by our restraint kit.

Furthermore, we assume the 3D-printed kit can be helpful to reduce head motion also in lightly sedated animals, as our 3D-printed kit has more fixation points compared to a standard rat head fixation setting and we do not use ear bars causing possible pain in ear canals.

Our analyses indicated that the awake rats, as expected, tended to move more frequently than the lightly sedated and anesthetized rats. Typically, head movement of the awake rats occurred in vertical Y-direction, which seemed to be due to shifts in the teeth positioning. Nevertheless, the amount of movement of awake rats in the present study was relatively equal to that of human movement in a clinical fMRI (Power et al., 2012, 2014). Based on the results reported by Power et al. (2012, 2014) we estimated the mean position change relative to voxel size ($4 \times 4 \times 4$ mm) to be 4–10% in humans, while in our rat experiments position change was 2.8 ± 0.2% relative to voxel size (0.391 mm shortest dimension).

Stress

Based on the observed decreases in the stress indicators (plasma corticosterone level, movement, and heart rate), the custom-made restraint kit with the applied habituation protocol was well-suited for the acclimatization of both awake and lightly sedated rats.

The plasma corticosterone concentration, perhaps the most reliable stress marker, returned to the baseline level by habituation day 4 in the awake group. Similar trend was observed already by habituation day 2 in the lightly sedated group. Generally, corticosterone concentrations remained surprisingly low even after habituation day 1, as several groups report concentrations in the range of 240–550 ng/ml on the first habituation day (King et al., 2005; Chang et al., 2016). In our study, the corresponding value was 162 ng/ml in the awake group. This observation strongly indicates that the animals were more gently introduced to the measurement environment compared with several previous reports.

Moreover, movement, as an indicator of adaptation, decreased rapidly during the habituation period to very low levels compared with previous reports (King et al., 2005; Chang et al., 2016). Movement of the brain in our study was in the range of 0–350 μm, while previous studies reported movement in the range of 0–550 μm or 0–1,300 μm (King et al., 2005; Chang et al., 2016).

Heart rate decreased to close to 400 beats per minute in awake animals after the 4-day habituation period. This is considered to be within the normal heart rate range in adult Wistar rats during the active day phase (Zhang and Sannajust, 2000).

Among the awake and lightly sedated groups, body weight did not decrease during the habituation weeks, which is in line with other observations, suggesting only minor stress induced by the habituation protocol. In the awake group, weight increased in a normal manner already over the weekend, further supporting the normal behavior.

Breathing rate and movement pointed to clear differences in the brain state between rats in the awake and lightly sedated groups. Breathing rates of lightly sedated rats were notably lower than those of awake rats on the MRI day 1. Movement was already minimal in lightly sedated rats from the starting day and also differed from that of awake rats on the MRI day 1.

In both animal groups, plasma corticosterone concentrations and movement levels tended to increase slightly on the imaging day compared with the 4th habituation session, indicating a small difference between the habituation and scanning conditions. Certain properties of the MRI device, such as possible sounds that may mimic ultrasonic communication between rats (>20 kHz), could not be reproduced in our mock scanner. Furthermore, small mechanical vibrations coming from the gradient set could not be mimicked in the habituation environment. Nevertheless, the slight increases in the stress indicators did not reach statistical significance.

In addition to acute stress, rats can develop chronic stress after the habituation protocol. Low et al. (2016) demonstrated that long-lasting elevated plasma corticosterone concentrations, reduced nociceptive behavior, and increased activation of the central amygdala are observed following

commonly applied habituation protocols (30 min, 3 days). Therefore, chronic stress can mask or compromise fMRI results, especially those obtained at later time-points. To address this issue, we evaluated depression- and anxiety-like behavior in habituated rats with well-known open-field and sucrose preference behavioral tests (Brenes Sáenz et al., 2006). Our results suggested no differences between habituated and control rats in locomotor activity, rearing, or center time in the open-field, or in the sucrose preference test, which speaks against major anxiety or depression-like behavior due to the habituation. In contrast, the habituated rats groomed more often than the control rats. This could indicate that the habituated rats felt more comfortable, as they were used to handling and experiencing new environments, thus making their adaptation faster. However, we recognize that the relatively small group sizes in behavioral tests may have hindered the detection of potential differences.

Habituation Time

The shortest required training period for awake and lightly sedated rats based on the measured indicators for stress was estimated to be 4 and 2 days for the awake and lightly sedated rats, respectively, to achieve a low amount of movement and low corticosterone concentrations. Additionally, heart rate decreased significantly in the awake group during the 4-day period. Importantly, our RSFC data show similar connectivity at the end of the first and second week of habituation. Thus, the additional week of habituation yielded no additional benefit for connectivity analysis.

A protocol in which rats are completely restrained for a prolonged time, i.e., several hours, is widely used to study chronic stress (Chiba et al., 2012; Stepanichev et al., 2014). To avoid chronic stress, habituation sessions in different awake MRI studies typically last only in the range of 30–90 min. To elaborate this protocol further, in our study, the restraint session times started as a very short period of 15 min and progressively increased up to a maximum of 45 min on the day 4.

Resting State Connectivity

Overall, the measured functional connectivity differed significantly between brain states. Even with a sub-anesthetic dose of isoflurane, the connectivity was significantly modulated compared with awake rats.

Strong connectivity across the cortical regions in the 1.3% isoflurane group is likely due to the anesthesia-induced burst suppression activity, which is characterized by alternation of silent brain states with almost no electrical activity (suppression) and active states with high-amplitude activity (bursts) (Derbyshire et al., 1936). Isoflurane induces burst suppression activity at a wide range of doses (e.g., 1.25–2.0%) (Hudetz and Imas, 2007; Vincent et al., 2007; Liu et al., 2013). The cycling between silent and active states is directly reflected by the hemodynamics and therefore is also visible in the fMRI BOLD signal (Liu et al., 2011, 2013). This cycling is likely to induce strong cortico-cortical and cortico-striatal correlations. Similar strong cortico-cortical or cortico-striatal connectivity in rats under high isoflurane anesthesia has been also observed previously (Williams et al., 2010; Liu et al., 2011, 2013; Kalthoff et al., 2013). When the cortical and cortico-striatal burst suppression synchronization is the most dominant feature in the brain, it is evident that the intrinsic connectivity is heavily masked.

The effect of burst suppression was also evident in the DMN in the 1.3% isoflurane group. While DMN is generally suppressed under anesthesia (Deshpande et al., 2010; Liu et al., 2015), brain regions associated with the DMN exhibited increased connectivity under 1.3% isoflurane anesthesia compared with awake rats. By contrast, isoflurane anesthesia induced heavy disruption of cortico-subcortical connectivity, mainly affecting connections between the cortex and medial thalamus. As the thalamus works as a key hub for controlling sensory information flow to the cortex, disrupted thalamo-cortical connectivity is considered to be the central mechanism regulating consciousness (Nallasamy and Tsao, 2011).

In the lightly sedated group, there were no abnormally high cortico-striatal correlations indicating burst suppression activity, which is consistent with previous reports (Liu et al., 2013), enabling more detailed analysis of intrinsic connectivity. Indeed, the FC matrices and maps in the cortex and striatum were fairly similar between the lightly sedated and awake rats, although global connectivity tended to be slightly suppressed. Suppression of connectivity most likely originates from reduced excitatory activities or increased inhibitory activities (Franks, 2008) induced by the low isoflurane dose. Additionally, we observed significantly suppressed connectivity in three medial thalamo-cortical connections in the seed-based connectivity analysis. In the voxel-wise analysis, however, this phenomenon was not detected after correcting for multiple comparisons. In summary, light sedation protocol allows two-times faster habituation protocol, but its drawbacks are the anesthesia-induced effects on RSFC that appear to be emphasized in the thalamo-cortical connectivity.

Effect of Physiology and Methodologic Considerations

In this study, we used a spin echo EPI sequence to study resting state networks. We have used spin echo EPI (SE-EPI) to have comparable results obtained from our previous EEG/fMRI studies which are conducted using SE-EPI to reduce susceptibility artifacts caused by electrodes. However, most of the fMRI studies today are conducted with a gradient echo EPI. While fMRI BOLD contrast in spin echo EPI has more specificity to small capillaries, gradient echo EPI is more sensitive to larger venules giving more detectable fMRI contrast (Lee et al., 1999). This can potentially influence comparison of rsfMRI maps obtained from studies implementing gradient echo EPI sequences. It is also worth noting that the current study was conducted with a 7T magnet, and with the higher magnetic fields, motion related artifacts can increase.

Because of local availability, Wistar rats were used in this study instead of Sprague-Dawley rats, despite SD rats are known to be less anxious and easier to habituate (Rex et al., 2004). Moreover, despite from results indicating female rats being more adaptable to restraint (Albonetti and Farabollini, 1992), we used male

Wistar rats instead of female rats as the majority of biomedical research is conducted using male rats to avoid possible bias caused by hormonal rhythm variations.

As physiologic parameters such as breathing and heart rates differ between awake, lightly sedated, and anesthetized animals, they must be taken into account in the connectivity analysis. For this purpose, both high-pass and low-pass filters were used for the BOLD signals. A low-pass filter at 0.15 Hz was used to minimize the effect of physiologic noise, like respiratory and heart rate artifacts, on the BOLD signal. The high-pass filter at 0.01 Hz reduces the possible false-positive correlation of extremely low fluctuations of the BOLD signal originating from, e.g., hardware-related drifts. Nevertheless, the low sampling rate (0.5 Hz) does not allow for the complete removal of physiologic noise, and the effect on the connectivity analysis remains unclear.

Spontaneous behavioral changes, such as changes in eye state (open vs. closed), variations in respiratory and olfactory activity of awake animals can influence dynamic connectivity (Liu and Duyn, 2013; Di and Biswal, 2015). During the habituation sessions, rats kept their eyes open and blinked normally. Once rats woke up from the initial anesthesia, breathing rate remained mostly stable during the habituation and fMRI sessions. In addition, based on respiratory rates, rats did not spontaneously fall asleep (possible due to slight stress and noise) during the scanning. Spontaneous olfactory stimulation was controlled by cleaning the animal beds after imaging each rat, and the scanner room was kept clean from other animal odors. In this study, we used standard EPI sequence causing significant sound pressure. The current experimental setup can be clearly improved by using pulse sequences with sound optimized gradient wave form design (Hutter et al., 2018) or radial acquisition (Lehto et al., 2017).

As rats were initially anesthetized and prepared under isoflurane, we cannot completely ignore the possible residual effects of isoflurane on functional connectivity in awake animals. The effect of isoflurane is short, however, and it is eliminated rather quickly from the body as rats usually wake within 2–4 min after the cessation of isoflurane, depending on the dose and duration. Also, isoflurane was turned off already during the shimming stage. Therefore, animals had several minutes to wake up from the anesthesia before the functional scanning started. Furthermore, the first minute from each functional dataset was excluded from analysis.

Finally, in the sub-cohort open field and sucrose preference studies, the relatively small animal numbers could possibly prevent the detection of small differences between groups, however, it rules out possible robust long-term anxiety or depression caused by stress.

SUMMARY AND CONCLUSION

We present a novel and easily implemented approach for awake rat fMRI. Our method introduces a 3D printed rat restraint kit compatible with a standard Bruker rat MRI bed, and quadrature surface receiver and transmitter coils. By using this kit and a modified habituation protocol, we were able to perform low-stress RSFC studies in fully awake rats. Based on measured physiologic markers for stress and the amount of movement, a 4-day acclimatization period was sufficient for awake rats, and the habituation protocol can be shortened to 2 days when 0.5% isoflurane is used. Additionally, we demonstrated that 1.3% isoflurane anesthesia in rats markedly affected brain connectivity compared with that in the awake state, and that the effect was significant, albeit less marked, for cortico-thalamic connections when 0.5% isoflurane was used. Overall the proposed approach is likely to make awake fMRI studies in rat more common in future, and thus increase the reliability and translatability of the results from rat fMRI studies.

AUTHOR CONTRIBUTIONS

PS and JP contributed in data collection and analysis. RS contributed in data analysis. KJ contributed in the 3D printing process. HT was consulted in the behavioral tests. OG contributed in the study design. PS contributed in writing of the manuscript and all authors took part in reading and revision of the manuscript.

ACKNOWLEDGMENTS

This work was supported by Academy of Finland (grant # 298007) and the Doctoral Program in Molecular Medicine of University of Eastern Finland. Partial support was provided by Charles River Discovery. We like to thank MP for technical assistance in animal preparations. The funding sources had no further role in study design or in the collection, analysis, or interpretation of data.

SUPPLEMENTARY MATERIAL

The Supplementary Material for this article can be found online at: https://www.frontiersin.org/articles/10.3389/fnins.2018.00548/full#supplementary-material

REFERENCES

Albonetti, M. E., and Farabollini, F. (1992). Behavioural responses to single and repeated restraint in male and female rats. *Behav. Processes* 28, 97–109.

Becerra, L., Pendse, G., Chang, P. C., Bishop, J., and Borsook, D. (2011). Robust reproducible resting state networks in the awake rodent brain. *PLoS ONE* 6:e25701. doi: 10.1371/journal.pone.0025701

Biswal, B., Yetkin, F. Z., Haughton, V. M., and Hyde, J. S. (1995). Functional connectivity in the motor cortex of resting human brain using echo-planar MRI. *Magn. Reson. Med.* 34, 537–541.

Brenes Sáenz, J. C., Villagra, O. R., and Fornaguera Trías, J. (2006). Factor analysis of forced swimming test, sucrose preference test and open field test on enriched, social and isolated reared rats. *Behav. Brain Res.* 169, 57–65. doi: 10.1016/j.bbr.2005.12.001

Brydges, N. M., Whalley, H. C., Jansen, M. A., Merrifield, G. D., Wood, E. R., Lawrie, S. M., et al. (2013). Imaging conditioned fear circuitry using awake rodent fMRI. *PLoS ONE* 8:e54197. doi: 10.1371/journal.pone.0054197

Chang, P. C., Procissi, D., Bao, Q., Centeno, M. V., Baria, A., and Apkarian, A. V. (2016). Novel method for functional brain imaging in awake minimally restrained rats. *J. Neurophysiol*. 116, 61–80. doi: 10.1152/jn.01078.2015

Chiba, S., Numakawa, T., Ninomiya, M., Richards, M. C., Wakabayashi, C., and Kunugi, H. (2012). Chronic restraint stress causes anxiety- and depression-like behaviors, downregulates glucocorticoid receptor expression, and attenuates glutamate release induced by brain-derived neurotrophic factor in the prefrontal cortex. *Prog. Neuropsychopharmacol. Biol. Psychiatry* 39, 112–119. doi: 10.1016/j.pnpbp.2012.05.018

Derbyshire, A. J., Rempel, B., Forbes, A., and Lambert, E. F. (1936). The effects of anesthetics on action potentials in the cerebral cortex of the cat. *Am. J. Physiol. Legacy Content* 116, 577–596.

Deshpande, G., Kerssens, C., Sebel, P. S., and Hu, X. (2010). Altered local coherence in the default mode network due to sevoflurane anesthesia. *Brain Res.* 1318, 110–121. doi: 10.1016/j.brainres.2009.12.075

Di, X., and Biswal, B. B. (2015). Dynamic brain functional connectivity modulated by resting-state networks. *Brain Struct. Funct.* 220, 37–46. doi: 10.1007/s00429-013-0634-3

Febo, M. (2011). Technical and conceptual considerations for performing and interpreting functional mri studies in awake rats. *Front. Psychiatry* 2:43. doi: 10.3389/fpsyt.2011.00043

Ferron, J. F., Kroeger, D., Chever, O., and Amzica, F. (2009). Cortical inhibition during burst suppression induced with isoflurane anesthesia. *J. Neurosci.* 29, 9850–9860. doi: 10.1523/JNEUROSCI.5176-08.2009

Franks, N. P. (2008). General anaesthesia: from molecular targets to neuronal pathways of sleep and arousal. *Nat. Rev. Neurosci*. 9, 370–386. doi: 10.1038/nrn2372

Franks, N. P., and Lieb, W. R. (1994). Molecular and cellular mechanisms of general anaesthesia. *Nature* 367, 607–614.

Gao, Y. R., Ma, Y., Zhang, Q., Winder, A. T., Liang, Z., Antinori, L., et al. (2016). Time to wake up: studying neurovascular coupling and brain-wide circuit function in the un-anesthetized animal. *Neuroimage* 153, 382–398. doi: 10.1016/j.neuroimage.2016.11.069

Hamilton, C., Ma, Y., and Zhang, N. (2017). Global reduction of information exchange during anesthetic-induced unconsciousness. *Brain Struct. Funct*. 222, 3205–3216. doi: 10.1007/s00429-017-1396-0

Hudetz, A. G., and Imas, O. A. (2007). Burst activation of the cerebral cortex by flash stimuli during isoflurane anesthesia in rats. *Anesthesiology* 107, 983–991. doi: 10.1097/01.anes.0000291471.80659.55

Hutter, J., Price, A. N., Cordero-Grande, L., Malik, S., Ferrazzi, G., Gaspar, A., et al.(2018). Quiet echo planar imaging for functional and diffusion MRI. *Magn. Reson. Med.* 79, 1447–1459. doi: 10.1002/mrm.26810

Kalthoff, D., Po, C., Wiedermann, D., and Hoehn, M. (2013). Reliability and spatial specificity of rat brain sensorimotor functional connectivity networks are superior under sedation compared with general anesthesia. *NMR Biomed.* 26, 638–650. doi: 10.1002/nbm.2908

Kenkel, W. M., Yee, J. R., Moore, K., Madularu, D., Kulkarni, P., Gamber, K., et al. (2016). Functional magnetic resonance imaging in awake transgenic fragile X rats: evidence of dysregulation in reward processing in the mesolimbic/habenular neural circuit. *Transl. Psychiatry* 6:e763. doi: 10.1038/tp.2016.15

King, J. A., Garelick, T. S., Brevard, M. E., Chen, W., Messenger, T. L., Duong, T. Q., et al. (2005). Procedure for minimizing stress for fMRI studies in conscious rats. *J. Neurosci. Methods* 148, 154–160. doi: 10.1016/j.jneumeth.2005.04.011

Lee, S. P., Silva, A. C., Ugurbil, K., and Kim, S. G. (1999). Diffusion-weighted spin-echo fMRI at 9.4 T: microvascular/tissue contribution to BOLD signal changes. *Magn. Reson. Med.* 42, 919–928.

Lehto, L. J., Idiyatullin, D., Zhang, J., Utecht, L., Adriany, G., Garwood, M., et al. (2017). MB-SWIFT functional MRI during deep brain stimulation in rats. *Neuroimage* 159, 443–448. doi: 10.1016/j.neuroimage.2017.08.012

Liang, Z., King, J., and Zhang, N. (2012). Intrinsic organization of the anesthetized brain. *J Neurosci.* 32, 10183–10191. doi: 10.1523/JNEUROSCI.1020-12.2012

Liang, Z., Liu, X., and Zhang, N. (2015). Dynamic resting state functional connectivity in awake and anesthetized rodents. *NeuroImage* 104, 89–99. doi: 10.1016/j.neuroimage.2014.10.013

Liu, X., and Duyn, J. H. (2013). Time-varying functional network information extracted from brief instances of spontaneous brain activity. *Proc. Natl. Acad. Sci. U.S.A.* 110, 4392–4397. doi: 10.1073/pnas.1216856110

Liu, X., Li, H., Luo, F., Zhang, L., Han, R., and Wang, B. (2015). Variation of the default mode network with altered alertness levels induced by propofol. *Neuropsychiatr. Dis. Treat* 11, 2573–2581. doi: 10.2147/NDT.S88156

Liu, X., Zhu, X. H., Zhang, Y., and Chen, W. (2011). Neural origin of spontaneous hemodynamic fluctuations in rats under burst–suppression anesthesia condition. *Cereb. Cortex* 21, 374–384. doi: 10.1093/cercor/bhq105

Liu, X., Zhu, X. H., Zhang, Y., and Chen, W. (2013). The change of functional connectivity specificity in rats under various anesthesia levels and its neural origin. *Brain Topogr.* 26, 363–377. doi: 10.1007/s10548-012-0267-5

Low, L. A., Bauer, L. C., Pitcher, M. H., and Bushnell, M. C. (2016). Restraint training for awake functional brain scanning of rodents can cause long-lasting changes in pain and stress responses. *Pain* 157, 1761–72. doi: 10.1097/j.pain.0000000000000579

Lu, H., Zou, Q., Gu, H., Raichle, M. E., Stein, E. A., and Yang, Y. (2012). Rat brains also have a default mode network. *Proc. Natl. Acad. Sci. U.S.A.* 109, 3979–3984. doi: 10.1073/pnas.1200506109

Martin, C., Martindale, J., Berwick, J., and Mayhew, J. (2006). Investigating neural-hemodynamic coupling and the hemodynamic response function in the awake rat. *Neuroimage* 32, 33–48. doi: 10.1016/j.neuroimage.2006.02.021

Nallasamy, N., and Tsao, D. Y. (2011). Functional connectivity in the brain: effects of anesthesia. *Neuroscientist* 17, 94–106. doi: 10.1177/1073858410374126

Ogawa, S., Lee, T. M., Kay, A. R., and Tank, D. W. (1990). Brain magnetic resonance imaging with contrast dependent on blood oxygenation. *Proc. Natl. Acad. Sci. U.S.A.* 87, 9868–9872.

Paasonen, J., Salo, R. A., Huttunen, J. K., and Gröhn, O. (2017). Resting-state functional MRI as a tool for evaluating brain hemodynamic responsiveness to external stimuli in rats. *Magn. Reson. Med.* 78, 1136–1146. doi: 10.1002/mrm.26496

Paasonen, J., Salo, R. A., Shatillo, A., Forsberg, M. M., Närväinen, J., Huttunen, J. K., et al. (2016). Comparison of seven different anesthesia protocols for nicotine pharmacologic magnetic resonance imaging in rat. *Eur. Neuropsychopharmacol.* 26, 518–531. doi: 10.1016/j.euroneuro.2015.12.034

Paasonen, J., Stenroos, P., Salo, R. A., and Gröhn, O. (2018). Functional connectivity under six anesthesia protocols and the awake condition in rat brain. *Neuroimage* 172, 9–20. doi: 10.1016/j.neuroimage.2018.01.014

Paxinos, G., and Watson, C. (1998). *The Rat Brain in Stereotaxic Coordinates, 4th edn*. San Diego, CA: Academic Press.

Power, J. D., Barnes, K. A., Snyder, A. Z., Schlaggar, B. L., and Petersen, S. E. (2012). Spurious but systematic correlations in functional connectivity MRI networks arise from subject motion. *Neuroimage* 59, 2142–2154. doi: 10.1016/j.neuroimage.2011.10.018

Power, J. D., Mitra, A., Laumann, T. O., Snyder, A. Z., Schlaggar, B. L., and Petersen, S. E. (2014). Methods to detect, characterize, and remove motion artifact in resting state fMRI. *NeuroImage* 84, 320–341. doi: 10.1016/j.neuroimage.2013.08.048

Reed, M. D., Pira, A. S., and Febo, M. (2013). Behavioral effects of acclimatization to restraint protocol used for awake animal imaging. *J. Neurosci. Methods* 217, 63–66. doi: 10.1016/j.jneumeth.2013.03.023

Rex, A., Voigt, J. P., Gustedt, C., Beckett, S., and Fink, H. (2004). Anxiolytic-like profile in Wistar, but not Sprague Dawley rats in the social interaction test. *Psychopharmacology* 177, 23–34. doi: 10.1007/s00213-004-1914-7

Stepanichev, M., Dygalo, N. N., Grigoryan, G., Shishkina, G. T., and Gulyaeva, N. (2014). Rodent models of depression: neurotrophic and neuroinflammatory biomarkers. *biomed. Res. Int.* 2014:932757. doi: 10.1155/2014/932757

Tsurugizawa, T., Uematsu, A., Uneyama, H., and Torii, K. (2010). Effects of isoflurane and alpha-chloralose anesthesia on BOLD fMRI responses to ingested L-glutamate in rats. *Neuroscience* 165, 244–251. doi: 10.1016/j.neuroscience.2009.10.006

Tsurugizawa, T., Uematsu, A., Uneyama, H., and Torii, K. (2012). Functional brain mapping of conscious rats during reward anticipation. *J. Neurosci. Methods* 206, 132–137. doi: 10.1016/j.jneumeth.2012.02.014

Vincent, J. L., Patel, G. H., Fox, M. D., Snyder, A. Z., Baker, J. T., Van Essen, D. C., et al. (2007). Intrinsic functional architecture in the anaesthetized monkey brain. *Nature* 447, 83–86. doi: 10.1038/nature 05758

Williams, K. A., Magnuson, M., Majeed, W., LaConte, S. M., Peltier, S. J., Hu, X., et al. (2010). Comparison of alpha-chloralose, medetomidine and isoflurane anesthesia for functional connectivity mapping in the rat. *Magn. Reson. Imaging* 28, 995–1003. doi: 10.1016/j.mri.2010. 03.007

Zhang, B., and Sannajust, F. (2000). Diurnal rhythms of blood pressure, heart rate, and locomotor activity in adult and old male Wistar rats. *Physiol. Behav*. 70, 375–380.

Zhang, N., Rane, P., Huang, W., Liang, Z., Kennedy, D., Frazier, J. A., et al. (2010). Mapping resting-state brain networks in conscious animals. *J. Neurosci. Methods* 189, 186–196. doi: 10.1016/j.jneumeth.2010.04.001

Zhao, F., Jin, T., Wang, P., and Kim, S. G. (2007). Isoflurane anesthesia effect in functional imaging studies. *Neuroimage* 38, 3–4. doi: 10.1016/j.neuroimage.2007.06.040

Conflict of Interest Statement: The authors declare that the research was conducted in the absence of any commercial or financial relationships that could be construed as a potential conflict of interest.

frontiers in Neuroscience

ORIGINAL RESEARCH
published: 02 November 2018
doi: 10.3389/fnins.2018.00788

Identifying Respiration-Related Aliasing Artifacts in the Rodent Resting-State fMRI

*Patricia Pais-Roldán[1,2], Bharat Biswal[3], Klaus Scheffler[1,4] and Xin Yu[1,5]**

[1] High-Field Magnetic Resonance Department, Max Planck Institute for Biological Cybernetics, Tuebingen, Germany, [2] Graduate Training Centre of Neuroscience, International Max Planck Research School, University of Tuebingen, Tuebingen, Germany, [3] Department of Biomedical Engineering, New Jersey Institute of Technology, Newark, NJ, United States, [4] Department for Biomedical Magnetic Resonance, University of Tuebingen, Tuebingen, Germany, [5] Athinoula A. Martinos Center for Biomedical Imaging, Massachusetts General Hospital and Harvard Medical School, Charlestown, MA, United States

Resting-state functional magnetic resonance imaging (rs-fMRI) combined with optogenetics and electrophysiological/calcium recordings in animal models is becoming a popular platform to investigate brain dynamics under specific neurological states. Physiological noise originating from the cardiac and respiration signal is the dominant interference in human rs-fMRI and extensive efforts have been made to reduce these artifacts from the human data. In animal fMRI studies, physiological noise sources including the respiratory and cardiorespiratory artifacts to the rs-fMRI signal fluctuation have typically been less investigated. In this article, we demonstrate evidence of aliasing effects into the low-frequency rs-fMRI signal fluctuation mainly due to respiration-induced B0 offsets in anesthetized rats. This aliased signal was examined by systematically altering the fMRI sampling rate, i.e., the time of repetition (TR), in free-breathing conditions and by adjusting the rate of ventilation. Anesthetized rats under ventilation showed a significantly narrower frequency bandwidth of the aliasing effect than free-breathing animals. It was found that the aliasing effect could be further reduced in ventilated animals with a muscle relaxant. This work elucidates the respiration-related aliasing effects on the rs-fMRI signal fluctuation from anesthetized rats, indicating non-negligible physiological noise needed to be taken care of in both awake and anesthetized animal rs-fMRI studies.

Keywords: rat fMRI, physiological noise, EPI, ventilation rate, repetition time, resting state networks

OPEN ACCESS

Edited by:
Federico Giove, Centro Fermi – Museo Storico della Fisica e Centro Studi e Ricerche Enrico Fermi, Italy

Reviewed by:
Cornelius Faber, Universitätsklinikum Münster, Germany
Pasquina Marzola, Università degli Studi di Verona, Italy

***Correspondence:**
Xin Yu
xin.yu@tuebingen.mpg.de

Specialty section:
This article was submitted to Brain Imaging Methods, a section of the journal Frontiers in Neuroscience

Received: *27 August 2018*
Accepted: *12 October 2018*
Published: *02 November 2018*

Citation:
Pais-Roldán P, Biswal B, Scheffler K and Yu X (2018) Identifying Respiration-Related Aliasing Artifacts in the Rodent Resting-State fMRI. Front. Neurosci. 12:788. doi: 10.3389/fnins.2018.00788

INTRODUCTION

Low-frequency (< 0.1 Hz) fMRI signal fluctuation (LFF) related to spontaneous brain dynamic signaling has been observed using a number of different brain imaging modalities (Biswal et al., 1995; Obrig et al., 2000). Applying a series of data analysis including correlation, coherence and independent component analysis of LFF during resting state scans has revealed distinct "resting-state" networks (RSN) that represent potential functional connectivity across regions in the brain (De Luca et al., 2005; Fox et al., 2009). The "default mode" network (DMN) is one of the RSNs that has been reliably identified from resting-state fMRI (rs-fMRI) in the human brain (Raichle et al., 2001; Greicius et al., 2003). Similar DMN spatial correlation patterns have been detected in both anesthetized monkeys and rodents, using fMRI (Vincent et al., 2007; Mantini et al., 2011;

Lu et al., 2012; Cabral et al., 2014; Stafford et al., 2014; Paasonen et al., 2018). This has allowed translational studies to specify the potential neuronal basis/underpins of the RSNs detected by fMRI in animal models. Animal fMRI has played a critical role in mapping the brain dynamics across multiple scales (Logothetis, 2002; Airaksinen et al., 2010; Hyder and Rothman, 2010; Mishra et al., 2011; Pan et al., 2011; Schulz et al., 2012; Yu et al., 2016; Yu, 2017; Albers et al., 2018; Wang et al., 2018). Multi-modal animal fMRI platform has been developed by merging fMRI with optogenetics (Lee et al., 2010; Liang et al., 2015; Yu et al., 2016; Albers et al., 2018), for cell/circuit specific activation, and with concurrent electrophysiological recordings (Goense and Logothetis, 2008; Shmuel and Leopold, 2008; Scholvinck et al., 2010; Pan et al., 2013). Also, fMRI brain mapping has been performed with parallel fiber optic measurements of the brain dynamic signals through genetically encoded sensors (e.g., detection of calcium with GCaMP or even of glutamate with GluSnRf) for identification of the LFF neural correlates (Schulz et al., 2012; Xie et al., 2016; Schwalm et al., 2017; Albers et al., 2018; He et al., 2018; Jiang et al., 2018; Wang et al., 2018). Thus, the multi-modal animal fMRI offers the possibility of studying the multi-site neural components underlying the RSNs.

Extensive efforts have been made to elucidate the confounding issues of LFF in the human brain, especially in the correction of motion artifacts from varied sources (Biswal et al., 1996; Welvaert and Rosseel, 2012; Murphy et al., 2013; Chen et al., 2015a; Jorge et al., 2015; Bright and Murphy, 2017). Besides the head motion-caused artifacts (Yang et al., 2005), the cardiorespiratory (CR) interference, e.g., the respiration-induced B0 field offset and cardiac pulsation etc., are the most dominant physiological noise source to a broad frequency range of the fMRI signal fluctuation (Hu et al., 1995; Noll et al., 1998; Van de Moortele et al., 2002; Razavi et al., 2008; Birn et al., 2008a; Starck et al., 2010; Birn, 2012; Murphy et al., 2013; Cordes et al., 2014). The CR-relevant parameters including arteriole CO2 (Wise et al., 2004), respiratory volume per time (RVT) (Birn et al., 2006, 2008b), and heart rate variability (HRV) (Shmueli et al., 2007), oscillate at frequencies < 0.1 Hz and directly interfere with the rs-fMRI signal correlation features. In addition, the slow sampling rate of fMRI could alias the high-frequency oscillation of the cardiac signal, and even the respiration artifacts at TR > 2 s, which can contaminate the low frequency range in human rs-fMRI studies (Biswal et al., 1996; Lowe et al., 1998; Noll et al., 1998; Dagli et al., 1999; Frank et al., 2001; De Luca et al., 2006). To solve the aliasing problem, high sampling rate imaging schemes or fMRI with specific TRs are needed to avoid the aliased oscillatory signals in the < 0.1 Hz low frequency range (Frank et al., 2001; De Luca et al., 2006; Posse et al., 2013; Cordes et al., 2014; Tong et al., 2014; Reynaud et al., 2017). Advanced imaging schemes and signal denoising methods have been developed to reduce these artifacts in human rs-fMRI studies (Biswal et al., 1996; Kiviniemi et al., 2003, 2005; Feinberg et al., 2010; Murphy et al., 2013; Feinberg and Setsompop, 2013; Liu, 2016; Abreu et al., 2017; Bright and Murphy, 2017; Caballero-Gaudes and Reynolds, 2017).

The CR-relevant confounding issues have been less concerned in animal rs-fMRI studies, especially in anesthetized animals with head-fixation to remove a large portion of the motion-relevant artifacts that are usually observed in awake human subjects (Kannurpatti et al., 2008; Zhao et al., 2008; Biswal and Kannurpatti, 2009; Pawela et al., 2010; Williams et al., 2010; Majeed et al., 2011). The respiratory rates of animals at different anesthesia vary largely, which can alter the respiration-related neck/chest motion patterns across different cases (Zhao et al., 2008; Williams et al., 2010; Bukhari et al., 2017). In many rs-fMRI studies using 2D-EPI sequences with different TRs (0.1 s -single slice- to 2 s), the CR-relevant aliasing effect was either reported negligible, or could be filtered out from the < 0.1 Hz LFF (Zhao et al., 2008; Biswal and Kannurpatti, 2009; Williams et al., 2010). Under the same anesthesia (e.g., medetomidine), the respiration-relevant motion artifacts have been reported to have different spatial patterns by different studies, either located only at the brain edge voxels using 300 ms TR (Magnuson et al., 2015), or to spread through the whole brain structure with severe aliasing interference at 3 s TR (Kalthoff et al., 2011). To better interpret the RSNs in animal rs-fMRI studies, the potential aliasing effect needs to be characterized carefully to avoid confounding the < 0.1 Hz LFF (Kalthoff et al., 2011). This is particularly critical for multi-modal fMRI studies that adopt 3D-EPI sequences to achieve even higher spatiotemporal resolution, so that more refined functional patterns from smaller brain nuclei can be matched with other imaging modalities in multi-scales (e.g., Wang et al., 2018) or even in awake animal fMRI studies (Ferenczi et al., 2016). Thus, for the implementation of a multi-modal fMRI methodology, a quality control to prevent or correct the physiological-related noise in the animal rs-fMRI signal is crucial to reliably investigate the neural basis of the RSNs detected in the animal brain.

In this study, we focused on deciphering the confounding rs-fMRI signal oscillation due to the respiration-related artifacts in anesthetized rats freely breathing or under ventilation with or without a muscle relaxant. By systematically varying the TR and the ventilation rates during the rs-fMRI acquisition, we characterized the aliasing effects, showing altered interference at different conditions. In addition, the frequency-specific power map demonstrated the voxel-specific sensitivity to the respiration-related motion artifacts with unique spatiotemporal dynamic interference. Because the ventilation mechanism enforces sinusoidal signals at very specific frequencies, it helps narrow the broad respiratory bandwidth of the free-breathing conditions, providing an efficient solution to avoid the overlap of the aliased oscillation to the < 0.1 Hz fMRI signal fluctuation. Furthermore, the muscle relaxant can significantly reduce the respiratory-induced B0 distortion and its corresponding aliasing artifacts to the LFF. In summary, this work provides a detailed view on aliasing effects of the rs-fMRI signal fluctuation from anesthetized rats, indicating a crucial CR interference issue needed to be taken care of in both awake and anesthetized animal rs-fMRI studies.

MATERIALS AND METHODS

Simulations of the Physiological Noise Sampling at Different TR for fMRI

In order to simulate the aliasing effect of the respiratory motion in the fMRI signal acquired at a certain TR, a cosine wave oscillating at frequencies near the common rat ventilatory rate was created using Matlab (Mathworks, Natick, MA, United States). The generated signal was then down-sampled at frequencies equivalent to potential volume acquisition times (TR). The resulting waves were plotted to illustrate the effect of sampling an intruder ventilatory-driven signal at a certain TR.

Mathematical Explanation of the Observed Aliasing Effects

The function $f(TR)$ calculates the frequency *freqS* of a signal *S* that results from sampling an original signal *S*0 at a given *TR*.

$$f(TR) = abs(freqS0 - k^* \frac{1}{TR}) = freqS$$

with $k = 1,2,3 \ldots .$

Supplementary Figure S1B shows an example of how a signal (e.g., motion from breathing at 60.1 breaths per minute) can be aliased by using typical TRs (i.e., TR > 0.5 s). When using a sampling frequency equal to the peak frequency S0, the resampled signal (S) is flat (frequency = 0) (see **Supplementary Figure S1A** middle inferior panel). In the practice, complete cancelation of the signal is often not possible, when dealing with analog devices, but by getting very close to the peak frequency, an extremely slow aliased signal can remain, which would lie out of the rs-fMRI analysis (freqS $< < <$ 0.01 Hz, **Supplementary Figure S1B**). By knowing the specific rate at which the animals breathe (e.g., by imposing a respiration rate with ventilatory support) it is possible to choose an appropriate TR that minimizes the interference of the aliased signal with the spectrum of interest (e.g., 0.01–0.1 Hz).

Animal Subjects, Procedures, and Experimental Design

In order to test whether aliasing occurs in the fMRI signal upon spontaneous breathing, nine adult (300–400 g) male Sprague Dawley rats were included in the study and their fMRI signal was assessed under anesthesia at three different conditions: (1) spontaneous breathing through a mask; (2) ventilated, not paralyzed; and (3) ventilated and paralyzed. All animal procedures were approved by the Animal Protection Committee of Tübingen (Regierungspräsidium Tübingen).

All animals were initially anesthetized with 5% isoflurane in chamber. In order to track changes in the blood pressure, the femoral artery was catheterized and connected to a blood pressure transducer (Biopac, Goleta, CA, United States). As in further steps the effect of a muscle relaxant was to be assessed, the femoral vein was also catheterized and connected to an infusion pump. The inner ear cavity was filled with paste to avoid air-tissue interfaces near the brain. A closed-loop heating system was used to keep the rectal temperature at 37°C during the entire experiment, ensuring stable physiological conditions. The end-tidal CO2 was also controlled throughout the experiment using a Respironics-Novametric monitor. A chest transducer was placed under the chest of the animal and constantly used to monitor breathing through a Biopac acquisition system, at 5000 samples per second.

During acquisition of the fMRI, 6 animals were kept anesthetized with 1.5–2% isoflurane, 1 animal was anesthetized with alpha-chloralose (25 mg/Kg·h), 1 with urethane (1 dose of 1–2 g/Kg) and 1 with medetomidine (0.05–0.5 mg/Kg·h), to rule out the contribution of a specific anesthetic to the observed effects. First, the not-yet-intubated animals were transferred to the 12 cm horizontal bore of a 14T MRI scanner and breathed oxygen-enhanced air (∼30% oxygen) through a mask. In the second part of the study, animals were intubated and maintained at a constant ventilatory rate that could be varied between scans. A last study was carried out in animals anesthetized with isoflurane with concurrent intravenous infusion (∼1–2 mg/Kg·h) of the muscle paralyzer agent Pancuronium (typical fMRI setup). All animals were euthanized right after the fMRI study based on the termination procedure from the approved protocols.

fMRI Acquisition

To detect the BOLD signal in the anesthetized animals, 2D and 3D Echo Planar Imaging (EPI) sequences were used, covering a field of view (FOV) of 2.24 cm × 1.92 cm × 1.92 cm with a matrix size of 56 × 48 × 32, achieving a resolution of 400 μm × 400 μm ×600 μm (all the data shown in the main figures correspond to 3D EPI, unless stated otherwise - **Supplementary Figure S7** is an example of a 2D EPI-). In order to determine whether different TRs modified the frequency of the aliased signal, the TR was varied between scans (TE was kept at 9.75 ms). A phantom containing Phosphate Buffered Saline (PBS) was located over the animal's head to compare the signal detected inside the brain with a signal experiencing similar motion in an inert tissue. A surface coil of diameter 2.2 cm was used to transmit and receive the RF signals. For anatomical registration purposes, RARE images were also acquired using a TR of 4000 ms, TE of 9.025 ms, FOV of 2.24 × 1.92 × 1.92 and matrix size of 128x128x32 (resolution of 175 μm × 150 μm × 600 μm). **Table 1** summarizes the conditions and fMRI parameters used in our study.

Analysis of the Data

The purpose of the analysis was to determine the influence of the respiration in the fMRI time course. Therefore, both signals (i.e., the chest–derived motion trace and the fMRI time-course), were considered for analysis.

Assessment of the Spatial Distribution of the Interference

The amplitude of the fluctuations in the BOLD signal was considered as an indicator of the level of contamination in the data. In order to detect the brain areas most vulnerable to the respiration-related interference, a power map was created in AFNI (Cox, 1996), by calculating the BOLD signal change at

TABLE 1 | Experimental conditions.

TR (s)	No V	V-54	V-56	V-58	V-59	V-60	V-61	V-62	V-64	V-66
0.5	wo P					w & o P				
0.8	wo P					w & o P				
0.9	wo P					w & o P				
1	wo P	wo P	wo P	wo P	wo P	w & o P	w & o P	w & o P	w & o P	w & o P
1.1	wo P					w & o P				
1.2	wo P					w & o P				
1.5	wo P					w & o P				
2	wo P					w & o P				

The table summarizes the parameters used in our study in terms of ventilatory frequency (in beats per minute), TR, and the use of a muscle relaxant (Pancuronium). No V, not ventilated (using mask); V-N, Ventilated (at the rate N, in breaths per minute); P, Pancuronium (wo: without, w & o, with and without).

each voxel. The function 3dPeriodogram was used to obtain 1024 frequency components and their corresponding power in each functional scan. 3dTstat was used to average the power of the frequencies in the range of 0.005 to 0.4 Hz in each voxel, resulting in a color-coded power map. In order to compare different animals and to average maps together, all scans were registered to a template using 3dAllineate. First, the anatomical datasets were aligned, and later the registration matrix was applied to the functional scans.

Comparative Analysis Between Chest Motion and fMRI Signal

In order to compare the respiratory-driven chest motion and the fMRI time-course, both signals were plotted in temporal and frequency domains. fMRI time courses were extracted by manually drawing a mask of 4 voxels from inside the brain and from a phantom placed over the animal's head. The AFNI function 3dMaskave was used to compute the average of the 4 voxels and output a 1D file. To extract single voxel time courses, the AFNI function 3dmaskdump was implemented. The time courses were then read in matlab using dlmread. In order to create a signal that simulates the chest motion detected from the fMRI, chest movement traces were down-sampled to 1/TR for each fMRI acquisition and included in the analysis. The fast Fourier transform (fft) function of matlab was used to calculate the power spectral density (PSD) from the original chest movement trace, from the down-sampled chest trace, and from the fMRI time courses. The full width at half maximum (FWHF) of the peak aliased frequency was calculated on the enveloped chest and fMRI spectra using matlab, to assess their similarity in terms of bandwidth and differentiate between mask and ventilation conditions. A two-tailed not-paired *t*-test was performed to assess the differences between groups. Errors in figures represent standard error of the mean.

Analysis of the Variance

To quantify the degree of variability that is incorporated to a group of scans solely based on the aliasing effect (i.e., variability of the fMRI signal upon using different ventilatory rates or TRs), spectral signal similarity was evaluated for each pair of conditions (e.g., time course acquired at TR = 1 vs. TR = 1.2 s, or time course acquired from the animal ventilated at 60 bpm vs. 61 bpm) by using the corr2 function in matlab applied to the PSDs. Correlation matrices were built to visualize the effect across all different conditions. Signal amplitude (i.e., BOLD signal change) was calculated as the standard deviation within the time course. A two-tailed not-paired *t*-test was performed to assess the difference in averaged signal amplitude (indicative of signal contamination) between fMRI time courses from spontaneously breathing animals vs. paralyzed animals. Errors in figures represent standard error of the mean.

Power Spectrum Characterization

In order to have a measure of the spectral specificity of the respiration-induced interference at different conditions (i.e., how wide the contaminated frequency range is or how much it spreads from a center frequency in an animal breathing through mask or mechanically ventilated), a map showing the fractional amplitude of low frequency fluctuations (fALFF) at specific frequency bands was generated using the function 3dRSFC (Zou et al., 2008), to cover a bandwidth of 0.01 Hz at the peak aliased frequency and the immediate lower and higher spectral components. To further verify the effect of ventilating the animals on the width of the frequency range subjected to respiratory-driven interference, the matlab function bandpower was used to calculate the average power within a 0.01 Hz bandwidth centered at the peak aliased frequency or the immediate superior and inferior neighbors. A two-tailed paired *t*-test was performed to assess the difference in power between the peak and the neighbor frequencies. Errors in figures represent standard error of the mean.

Table 2 provides the *p*-values obtained from the different *t*-tests performed during analysis.

RESULTS

Identification of the Aliased Respiration-Driven Artifact in Anesthetized Rats

A 3D EPI-fMRI method was used to study the potential interference between the animal respiration and the rs-fMRI signal in anesthetized rats. **Figure 1** illustrates the potential disruption of B0 field homogeneity due to the respiration-induced movement of the chest/neck, which results in distorted

TABLE 2 | *p*-values.

Figure 2E	**Mask chest**	**Mask brain**	**Vent,noP chest**	**Vent,no P brain**		
Mask chest		0.70	2.52*10^−8			
Mask brain	0.70			7.00*10^−6		
Vent, noP chest	2.52*10^−8			0.015		
Vent, no P brain		7.00*10^−6	0.015			
Figure 2F	**Mask-peak**	**Mask-neigh**	**Vent,noP-peak**	**Vent,noP-neigh**	**Vent,P-peak**	**Vent,P-neigh**
Mask- Peak		2.5*10^−2	0.90		4.02*10^−12	
Mask- neigh	2.5*10^−2			9.68*10^−11		2.83*10^−14
Vent,noP-peak	0.90			8.91*10^−4	2.97*10^−4	
Vent,noP-neigh		9.68*10^−11	8.91*10^−4			1.10*10*−3
Vent,P-peak	4.02*10^−12		2.97*10^−4			4.40*10^−4
Vent,P-neigh		2.83*10^−14		1.10*10*−3	4.40*10^−4	
Figure 5D	**noP**	**P**				
noP		1.13*10^−5				
P	1.13*10^−5					

The table summarizes the p-values obtained from the t-tests performed during analysis, organized by figures.

EPI images with characteristic periodic patterns in ventilated rats without muscle relaxant. It is worth noting that the periodic motion artifacts can be detected in animals under different anesthesia (e.g., medetomidine, urethane, isoflurane, and alpha-chloralose) (**Supplementary Figure S2**). Since muscle relaxants avoid the movement of the chest/neck, they reduce the respiration-induced B0 offset during fMRI acquisition, therefore, 3D EPI images show little distortion in paralyzed rats under ventilation (**Figure 1C**).

To specify the aliasing effect that occurs when the respiratory cycle is sampled at a given TR (see simulated data in **Supplementary Figure S1**), the respiratory signal (i.e., the chest movement) was recorded simultaneously with the rs-fMRI signal in anesthetized rats under three conditions: (1) not-ventilated, spontaneously breathing through mask, (2) ventilated, without muscle relaxant (i.e., not paralyzed), and (3) ventilated, with muscle relaxant (i.e., paralyzed). In **Figure 2**, the TR of the 3D EPI-fMRI was 1.2 s, i.e., 0.83 Hz. As shown in the PSD of the respiratory signal, the freely breathing rat (i.e., not ventilated -breathing through mask-) exhibits a broad frequency peak centered at ∼1 Hz ("chest", **Figure 2A**). The FWHM of this broad peak in non-ventilated rats is ∼0.06 Hz ± 0.004 Hz (**Figure 2E**). The aliasing effect of this respiratory signal at a sampling rate of 0.83 Hz causes a slow oscillatory signal at the 0.17 Hz ± 0.03 Hz, which is observed in both, brain voxels and phantom voxels positioned at the top of the rat head (**Figure 2A**). A strong correlation between the peak frequency observed from the aliased (i.e., down-sampled) chest motion and the fMRI time course of both, brain and phantom voxels, suggests that the artifacts originate from the respiratory-induced B0 offset and not from brain functional dynamic signals. Similarly, the fMRI signal from rats ventilated at 1 Hz shows clear aliasing effect at 0.17 Hz, but the bandwidth of the aliased signal, assessed as the FWHM of the aliased peak, is much sharper than the observed in not-ventilated animals (**Figure 2E**, p-value = 7*10^−6), in both brain and phantom voxels (**Figure 2B**). The aliased signal is significantly reduced in paralyzed ventilated rats (**Figures 2C,F**).

Prevalence and Characteristics of the Aliased Signal Across Different Ventilatory Conditions

To specify the spatial distribution of the respiration-related motion artifacts on the 3D EPI images, the mean voxel-wise power map (0.005–0.4 Hz) was calculated for each group (**Figure 2D**), showing that dorsal cortical areas and ventral brain regions are more sensitive to the motion artifacts. However, no generalized spatial patterns of motion artifacts can be achieved; instead, the respiratory-related motion and, hence, the interferential signal, varies across animals (**Supplementary Figure S3**). The significantly lower power estimate at the peak frequency in the paralyzed group (p-value = 2.9*10^−4, compared to the non-paralyzed ventilated condition) suggests a reduced aliasing effect in animals without spontaneous breathing (**Figure 2D**, bottom map, and **Figure 2F**). **Figure 2F** and **Supplementary Figure S4** demonstrate the differences in power between the aliased center frequency and the collateral frequency bands at three conditions (mask, ventilated and ventilated paralyzed). **Figure 2F** shows the averaged power within a bandwidth of 0.01 Hz calculated at the peak and the neighbor frequencies across different animals, showing a significantly sharper effect (i.e., less contribution of the neighbor frequencies) in ventilated animals, compared to freely breathing rats (p-value = 9.68*10^−11). **Supplementary Figure S4** provides the fALFF maps specific for the peak and neighbor frequency bands in a representative animal. The power estimates in the adjacent frequency bands are much lower when the animal is ventilated, in comparison to the free-breathing condition. This indicates that ventilation can prevent the spread of respiratory-motion aliasing

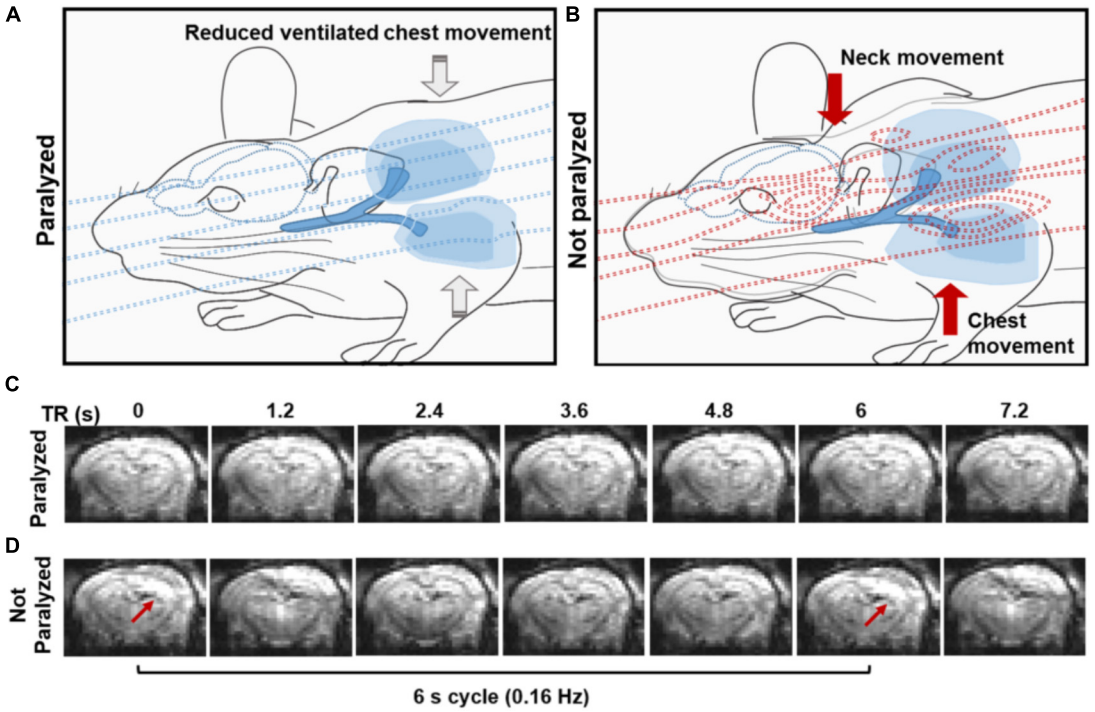

FIGURE 1 | Effect of the spontaneous respiration on the B0 field. **(A,B)** The schemes illustrate the B0 field at the iso-center of the MR bore in the presence of a paralyzed **(A)** or a non-paralyzed animal **(B)**. Note how the B0 is relatively homogeneous when a paralyzed animal is passively ventilated due to the lack of large body motion and how B0 inhomogeneities emerge upon active breathing involving diaphragm, intercostal and neck muscle movement during the respiration **(B)**. **(C,D)** Coronal sections from a 3D EPI sequence acquired at 1.2 s TR, showing the effect of the B0 (in)homogeneity in a paralyzed **(C)** and spontaneously breathing animal **(D)**. Note the distortions in the images acquired from the non-paralyzed animal, compared to the paralyzed condition.

effects along a broader frequency bandwidth (**Figures 2E,F** and **Supplementary Figure S4**). This is particularly important when the conventional TR at 1s is used, which causes the aliasing oscillatory effect at < 0.1 Hz to directly interfere with the low-frequency rs-fMRI signal fluctuation (**Supplementary Figure S5**). This result demonstrates that ventilation can be used to confine the aliasing oscillatory effect to a sharp frequency range.

Characterization of the Spatial and Temporal Patterns of the Respiration-Driven Aliasing Effects on rs-fMRI: Influence of the TR and the Ventilatory Rate

The features of the aliased oscillation were evaluated in non-paralyzed animals at multiple voxels across different parts of the brain and a phantom located over the animal's head. Different voxels exhibited different signal interference, in both, mask-breathing and non-paralyzed ventilated animals (**Figures 3B,C**, **4A,B**), which demonstrates a highly varied effect of the respiration on the rat fMRI signal. In order to reduce the potential interference of the aliased respiration on the LFF (< 0.1 Hz), different TRs were used (0.5 s to 2 s), demonstrating that the aliasing oscillation can be shifted along the spectrum in non-ventilated animals (e.g., to be out of the < 0.1 Hz low-frequency range) (**Figure 3D** and **Supplementary Figures S1B**, **S5**). Similarly, to avoid the interference to the < 0.1 Hz rs-fMRI signal fluctuation, the ventilation rate could be altered in mechanically ventilated animals with fixed TR (1 s, **Figure 4C** and **Supplementary Figure S1A**), as an alternative strategy for anesthetized animal rs-fMRI studies without employing muscle relaxant agents.

Examination of the Variability and Magnitude of the Aliasing Effect on the rs-fMRI in Ventilated Rats: Influence of Muscle Relaxants

The fMRI signal is an indirect measure of neuronal activation and therefore, any variability introduced by external sources is undesired and should be minimized. In order to assess the degree of variability between data acquired under different ventilatory rates or different TRs (i.e., different aliasing effects), and to determine whether the use of a paralyzer agent could reduce the differences across scans, fMRI time courses were acquired at different sampling and ventilatory conditions with and without the muscle relaxant Pancuronium (**Figure 5**). In ventilated rats anesthetized with constant 2% isoflurane and without muscle relaxant, the fMRI time courses acquired at different TRs exhibited a large between-scan spectral variability, compared to groups of scans performed during infusion of the

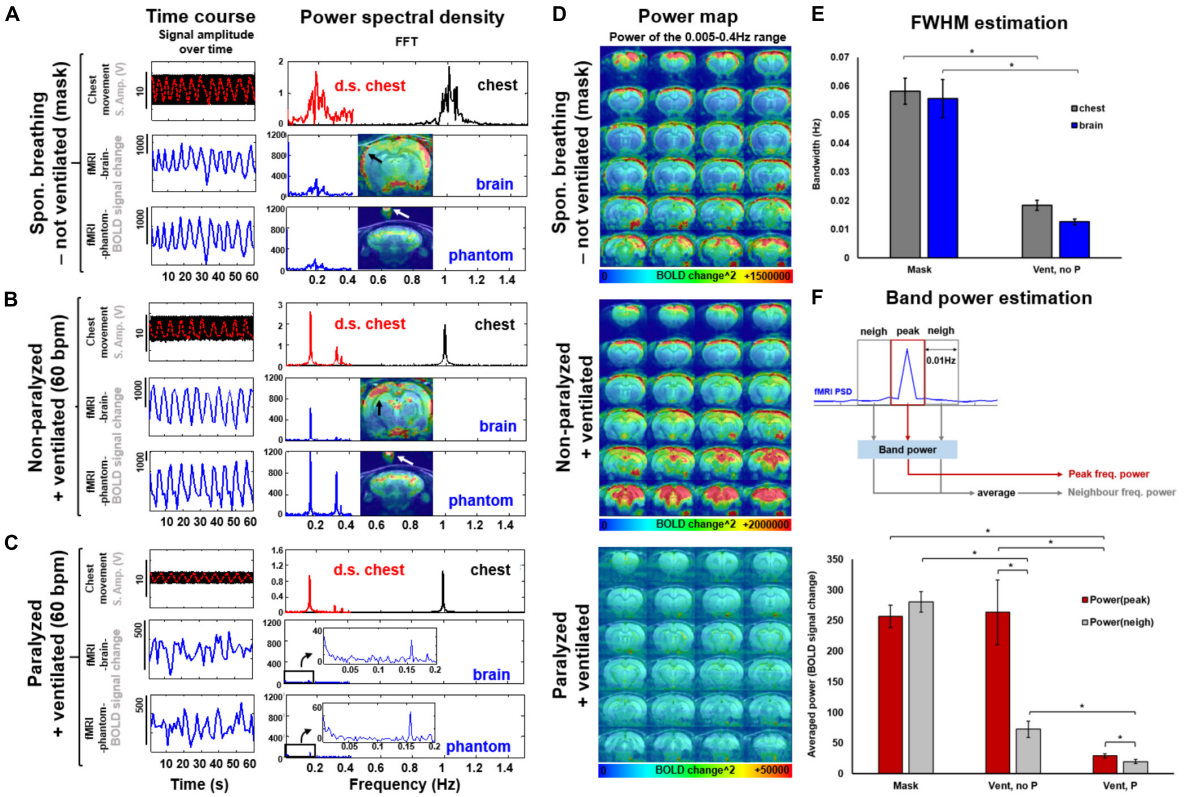

FIGURE 2 | Spectral and spatial characterization of the respiratory interference at 3 conditions: spontaneously breathing through a mask, ventilated and ventilated while paralyzed. **(A,B,C)** The original chest movement recorded at a sampling rate of 5000 is shown as a black trace. The down-sampled chest-motion (resampled at 1/TR) is shown in red. Note the smaller amplitude of this signal in the paralyzed condition **(C**, vs. **A** or **B)**. The fMRI time course of a voxel in the brain or in a phantom (over the animal's head) is shown in blue. The frequency decomposition of the signals is shown on the right. Note the similarity between the spectra of the aliased chest and fMRI signal. **(D)** The power maps show the distribution of the interference for each condition (averaged from 5 different animals). Note the low power scale in paralyzed animals. **(E)** The graph shows the spectral FWHM (i.e., spreading) of the peak breathing frequency and the aliased signal in the fMRI time course for non-intubated (mask, $N = 26$) and ventilated non-paralyzed animals ($N = 17$). **(F)** The graphs show the averaged power calculated within a frequency range that contains either the peak frequency (i.e. aliased from chest motion) or the limiting/neighbor frequency bands. N(Mask) = 16 trials from 4 animals, N(Vent,noP) = 16 trials from 3 animals, N(Vent,P) = 14 trials from 4 animals. Statistical test within conditions: two-tailed paired t-test. Statistical test between conditions: two-tailed not-paired t-test. (*): p-value < 0.005.

paralyzer agent (**Figure 5B**). Similarly, the spectral correlation between scans acquired at different ventilatory rates was lower in spontaneously breathing animals (**Figure 5F**). The magnitude of the aliased-motion artifact, estimated as the standard deviation within the fMRI time course, was calculated across animals, revealing a significantly lower contamination of the fMRI signal in the paralyzed condition (**Figure 5E**, p-value = 1.13*10^−5). These experiments demonstrate that the respiration-induced interference on the fMRI signal and the subsequent inter-scan variability can be ameliorated by providing a muscle relaxant during the fMRI study. In agreement with this, the seed-based correlation analysis of rs-fMRI acquired from ventilated rats without muscle relaxant (no denoising procedure) showed highly varied correlation patterns throughout the brain, in contrast to the more specific correlation pattern observed from rats ventilated and paralyzed with a muscle relaxant, which identifies RSNs more reliably (**Supplementary Figure S6**), as previously reported (Williams et al., 2010; Lu et al., 2012; Hsu et al., 2016; Bajic et al., 2017).

DISCUSSION

In this study, the aliasing effect due to respiration-induced B0 distortion was systematically characterized in the rs-fMRI of anesthetized rats at varied fMRI imaging and respiratory controlling conditions: different TRs, altered respiration rates, free-breathing vs. ventilation (with or without muscle relaxant). The ventilation scheme was found to significantly narrow the broad respiratory frequency bandwidth of the free-breathing anesthetized rats (from FWHM≅0.06 Hz to FWHM≅0.01 Hz) and reduce the potential aliasing interference on the < 0.1 Hz fMRI signal fluctuation, which can be further reduced by the muscle relaxant. The characterization of the spatial and temporal dynamic features of the aliasing effects due to B0 distortion from individual animals allows choosing appropriate TRs or ventilation rates to avoid the aliased oscillation within the 0.01–0.1 Hz range of the fMRI signal. This may be particularly useful in fMRI studies intended to study brain dynamics in awake animals, which are becoming a common platform to investigate

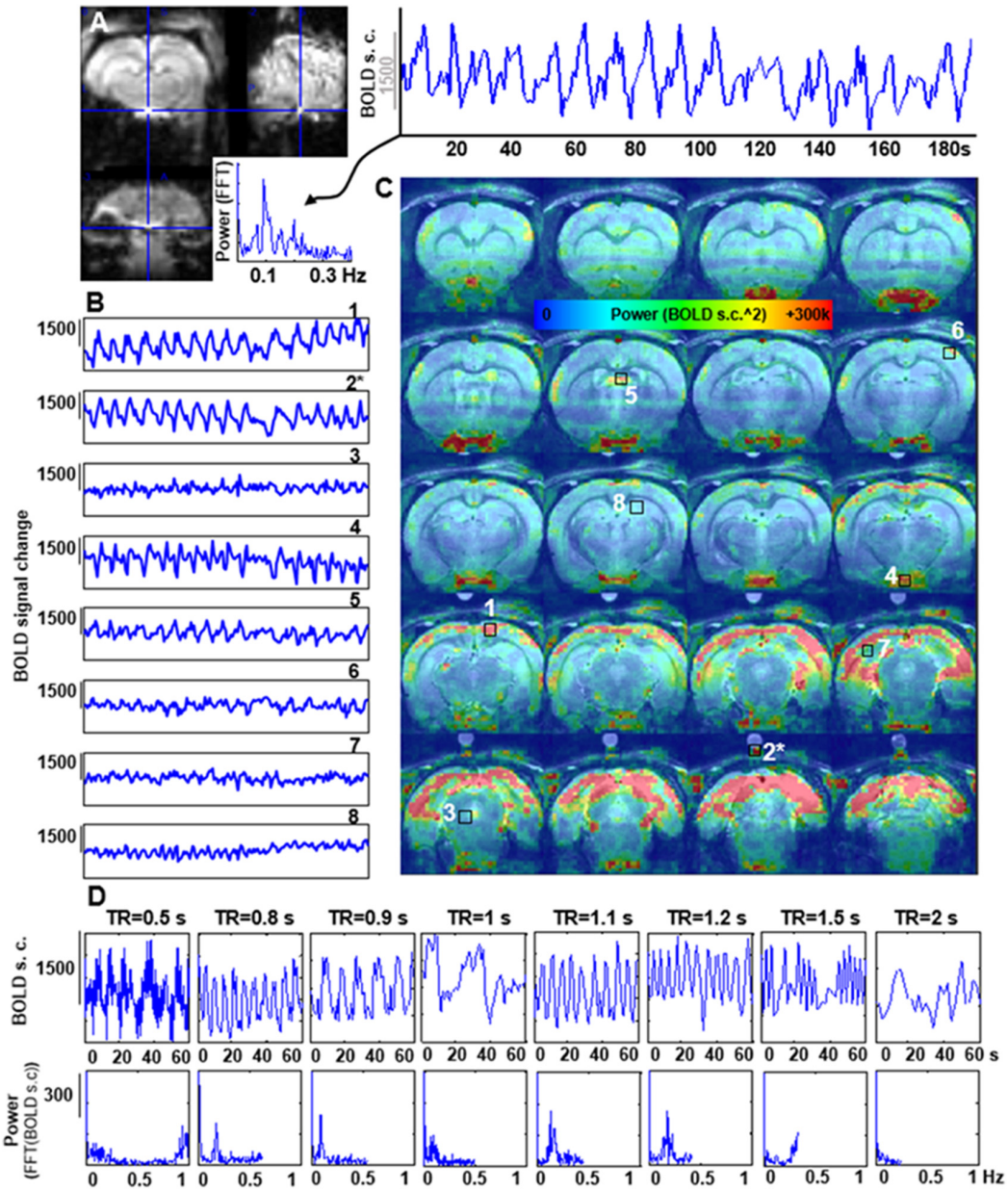

FIGURE 3 | Artifactual slow fMRI waves and TR dependency. **(A)** Location of the extracted voxel, fMRI time course and PSD from a 3D EPI acquired in an animal breathing spontaneously through a mask, showing an artifactual slow wave with peak frequency of ∼0.09 Hz (TR = 0.9 s). **(B)** The graphs show 180 s of fMRI time course from 8 different voxels in a spontaneously breathing animal (TR = 0.9 s). Numbers indicate the location of the voxels (see **C**). (*) indicates a phantom voxel (registration is not perfect due to misalignment between the anatomical and functional scan). **(C)** The map shows the distribution of the power of frequencies within the range 0.005–0.4 Hz. **(D)** fMRI time courses acquired at eight different TRs in a spontaneously breathing animal (not ventilated). Note how the frequency of the artifactual oscillations changes according to the chosen TR.

neurological processes without the potential confounder effects from general anesthetics. Despite the benefit of being anesthetic-free, imaging the awake brain involves the need of coping with other sources of confusion variables like potential stress or spontaneous voluntary movement of the limbs or body and, inevitably, spontaneous breathing. While the stress and voluntary motion can be avoided by exhaustive training with the animal, the last one is a factor inherent to and inseparable of the awake condition. Therefore, faced the unfeasibility of applying a muscle relaxant to these animals, it is critical to understand the implications of imaging a spontaneously breathing rodent before acquiring rs-fMRI data and, if possible, choose adequate parameters that allow an easy discrimination between neurological and artifactual signals (e.g., deviating the aliased signal from the spectral range intended for analysis by choosing a convenient TR). Given the physiological noise of the

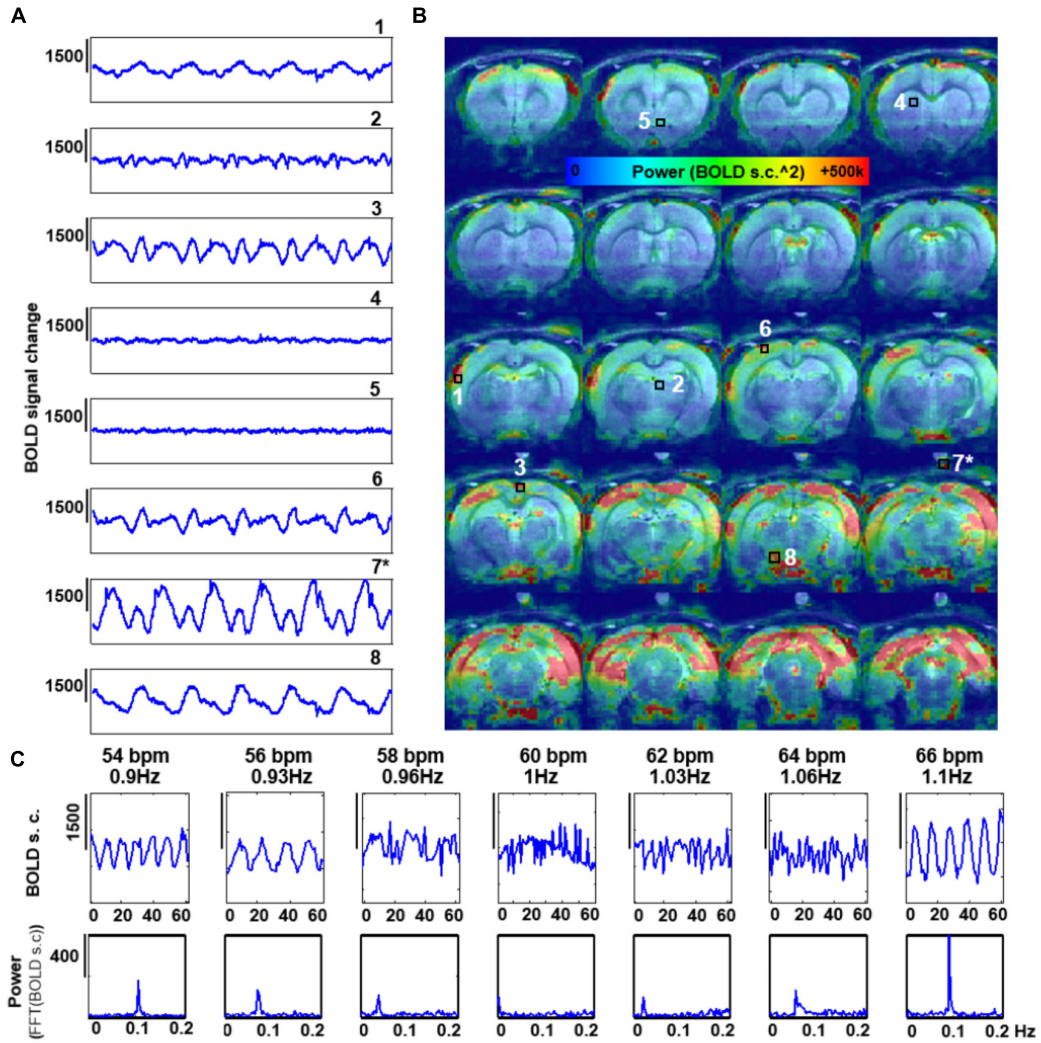

FIGURE 4 | Effect of the rate of artificial ventilation on the fMRI time-course. **(A)** The graphs show 300 s of fMRI time course from 8 different voxels, extracted from a 3D EPI in an animal ventilated at 59 bpm (0.96 Hz) (TR = 1 s). Numbers indicate the location of the voxels (see C). (*) indicates a phantom voxel (registration is not perfect due to misalignment between the anatomical and functional scan). **(B)** The map shows the distribution of the power of frequencies in the range 0.005–0.4 Hz. **(C)** fMRI time courses acquired with TR = 1s in a non-paralyzed animal ventilated at seven different rates.

rs-fMRI detected from anesthetized rats, this work suggests that the denoising methods developed for human fMRI (Hu et al., 1995; Glover et al., 2000; Birn et al., 2014; Caballero-Gaudes and Reynolds, 2017) should be adapted and implemented in the routine rs-fMRI animal studies.

Divergence Between the Aliasing Interference in Humans and Rodents

Human cardiovascular and respiratory signals in the young adult fluctuate at 0.66–1.66 Hz and 0.16–0.33 Hz, respectively (Fleming et al., 2011). Human respiration can, therefore, be sampled if relatively short TRs are used (< 1.5 s), preventing aliasing. In contrast, the cardiovascular oscillations constitute a clear source of aliasing in human fMRI (TR needs to be ∼0.3 s to sample the human heart rate appropriately) (Hu et al., 1995; Kiviniemi et al., 2005; Feinberg et al., 2010; Hugger et al., 2011). Despite the similarity between the neurological signals of human and rodents (e.g., EEG spectrum), the heart and respiratory rates are approximately 5 times faster in the rat (5–8 Hz and 0.9–1.5 Hz, respectively), with their respiratory cycle matching the human cardiac cycle (Zhao et al., 2008; Williams et al., 2010). The spectral features of the rat cardio-respiratory signals imply the need of correction methods to avoid aliasing in the 0.01–0.1 Hz fMRI signal. Here, we have shown how the respiratory interference can be detected and shifted away from the rs-fMRI analysis by changing the ventilatory rate or the rate of fMRI sampling (i.e., TR). This is possible due to the fact that the aliased frequency depends on the frequency of the interference (i.e., the respiratory rate) and on the sampling rate (i.e., the TR), which is a consequence of the Nyquist Sampling Theorem, stating that if the rate of sampling is less than twice the signal frequency,

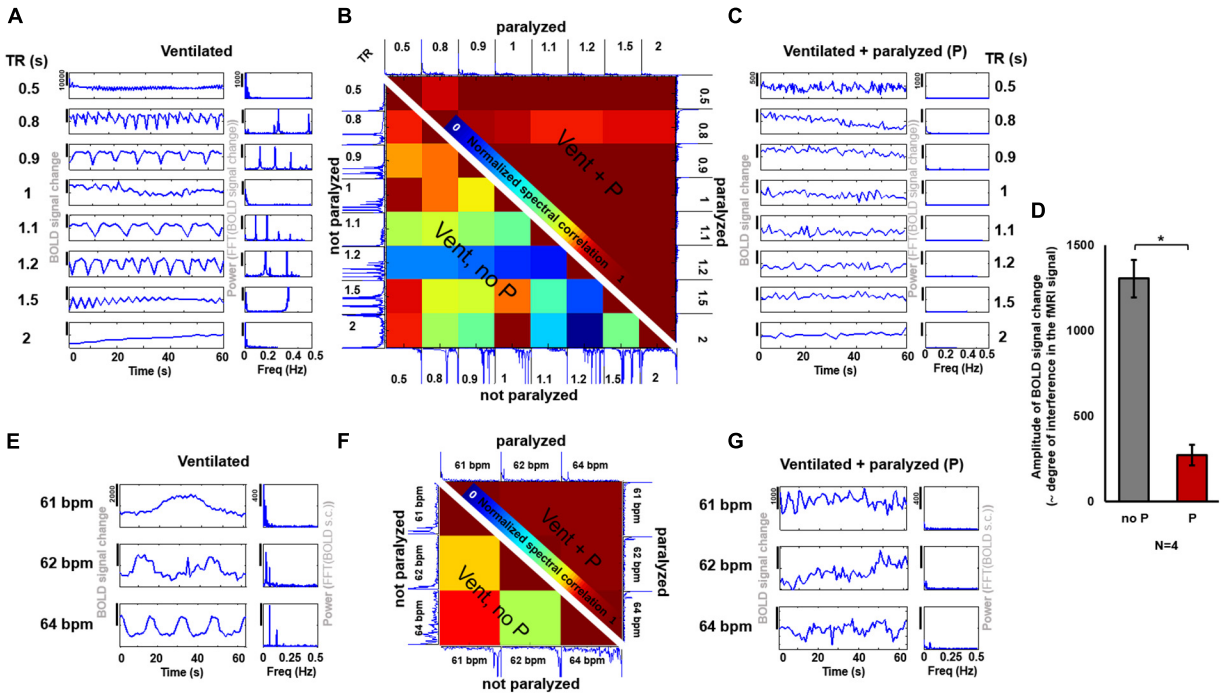

FIGURE 5 | Effect of a muscle relaxant on the emergence of artefactual oscillations. **(A**,**C)** The graphs show the time courses and PSDs of the fMRI signal from an animal ventilated at 1 Hz, acquired at 8 different TRs, when the animal is not paralyzed **(A)** and when it is paralyzed with a muscle relaxant **(C)**. **(B)** The matrix shows the correlation values between the spectra from the different time courses acquired at different TRs (under the same ventilatory rate) in a spontaneously breathing animal (i.e., ventilated not paralyzed, as in "**A**"), shown on the lower left half of the matrix, and in a ventilated paralyzed animal (as in "**C**"), shown on the upper right half of the matrix (the matrix is not symmetric, instead it incorporates one half of the "non-paralyzed" matrix and one half of the "paralyzed" matrix, to avoid redundancy). High values indicate a higher correlation between time courses (i.e., low variability, as observed between time courses from paralyzed animals). **(D)** The bar plot shows the averaged amplitude of the BOLD signal change (indicative of the level of interference) in non-paralyzed ventilated animals and in paralyzed ventilated animals (N = 26 time courses, acquired at variable TRs, from 4 animals, for each of the two conditions). (P) Pancuronium. **(E**,**G)** The graphs show the time courses and PSDs of the fMRI signal from an animal ventilated at 3 different rates, acquired at TR = 1 s, with **(G)** and without **(E)** a paralyzer. **(F)** The matrix shows the correlation between the spectra of the signals acquired at different ventilatory rates (same TR) while the animal had spontaneous breath (i.e., ventilated not paralyzed, as in "**E**"), shown on the lower left half of the matrix, and of signals acquired while the animal was ventilated and paralyzed (as in "**G**"), shown on the upper right half of the matrix (the matrix is not symmetric, instead it incorporates one half of the "non-paralyzed" matrix and one half of the "paralyzed" matrix, to avoid redundancy). High values indicate a higher correlation between time courses (i.e., low variability). (*): p-value < 0.005.

aliasing occurs, with $f_{alias} = |f_{resp}\text{-}n^{*}f_{sample}|$, $n = 1, 2, \ldots$, $f_{sample} = 1/TR$ (Holst, 1996; Kiviniemi et al., 2005). Future studies using fast imaging schemes (e.g., line scanning with 50 ms TR Yu et al., 2014) could be used to characterize the cardiovascular contributions to the fMRI signal in rodent studies.

3D vs. 2D EPI fMRI Methods

In this work, we demonstrated the aliasing effect of the respiratory-driven artifacts in the rat rs-fMRI acquired as 3D EPI, which is a highly efficient sequence to acquire whole-brain fMRI signal. Nevertheless, a significant portion of the animal and human fMRI studies are performed with multi-slice (2D) EPI (Keilholz et al., 2004; Bruno et al., 2010; Magnuson et al., 2010; Williams et al., 2010; Lu et al., 2012; D'Arceuil et al., 2013; Chen et al., 2015b), which is less sensitive to physiological noise than its 3D counterpart (Lutti et al., 2013). While 2D EPI slices are acquired consecutively within ∼30 ms, with each slice sensing a different dynamic B0 field during a small portion of the respiratory cycle, 3D EPI schemes sample the whole brain slab in an additional phase encoding step, which incorporates the B0 field distortion through the whole respiratory cycle. This difference will certainly make the 3D EPI method more sensitive to the B0 field distortions due to respiration. To account for the potential differences between both imaging schemes, multi-slice 2D EPI was acquired in animals to demonstrate the presence of a similar aliased respiratory signal in both rs-fMRI paradigms (**Supplementary Figure S7**). Although the abovementioned aliased signals could be detected in both imaging schemes, the aliased signal interference remains but is reduced in the 2D EPI method in comparison to the 3D EPI [a more exhaustive comparison between the sensitivity of both methodologies is beyond the purpose of the current study, for a discussion on the topic see: (Goerke et al., 2005)]. While physiological noise can be regressed out retrospectively from 2D EPI datasets by slice-selective correction methods (Glover et al., 2000; Hutton et al., 2011), other strategies, e.g., ICA-based artifact removal (Griffanti et al., 2014), may be applied to 3D EPIs to diminish the noise generated by the aliased cardiorespiratory interference (Caballero-Gaudes and Reynolds, 2017).

Complexity of the Respiration-Induced B0 Distortion Aliased Signal Throughout the Brain

The B0 offset induced by respiration-related motion causes dynamic B0 spatial distortion through the respiratory phasic cycles. **Figures 2D**, **3C**, **4B** show how the oscillatory signals due to motion-related artifacts dominate the fMRI signal fluctuation of the cerebellum, cortex and hypothalamic area across a frequency bandwidth (0.005–0.4Hz). Despite a major susceptibility of the dorsal, occipital and ventral regions, the distribution of the artifactual signals can vary between animals with different respiratory motion (**Supplementary Figure S3**), which shows the challenges of the generalized correction method. Paralysis of the ventilated animal resulted in a significantly reduced interference, as passive ventilation does not involve recruitment of accessory muscles in the chest or neck of the animal, which are the major contributors to the B0 inhomogeneities (Raj et al., 2001; Van de Moortele et al., 2002). However, other physiological variables not coupled to motion, such as the arterial CO2 signal (Wise et al., 2004), can change with each respiratory cycle and its direct vascular interference can be aliased into the rs-fMRI signal, even in paralyzed animals. The aliasing of these signals would cause a strong correlation between large vessels (Dagli et al., 1999). Besides the breathing-related physiological variables, an enveloped blood pressure signal of frequency ∼0.01–0.04 Hz (Meyer waves, dependent on sympathetic activity) may also appear and contaminate the BOLD signal near large vessels (Diehl et al., 1995; Pfurtscheller et al., 2017). Importantly these signals would not be a consequence of aliasing (e.g., generated due to insufficient sampling) but may be caused by real cardiac-induced slow fluctuations (Bhattacharyya and Lowe, 2004). The ventral area (i.e., near the circle of Willis) highlighted in the power map of **Figures 3**, **4** may also potentially indicate a contribution of an aliased cardiorespiratory signal in the rs-fMRI data.

Spontaneous vs. Imposed Ventilation

Free-breathing subjects may exhibit a broad respiratory frequency bandwidth (FWHM≅0.06 Hz) along the acquisition time (**Figures 2A,E** and **Supplementary Figures S5**, **S7**, black and red traces of the mask condition). This produces an equally broad bandwidth of frequencies aliased into the fMRI signal (**Figures 2A,E** and **Supplementary Figures S5**, **S7**, blue traces of the mask condition). In 2D EPI, different slices within the volume may be acquired at different phases of the varied respiratory cycles along the scan time, which leads to mild aliasing periodic patterns that could be diminished with slice-selective denoising methods (Glover et al., 2000; Hutton et al., 2011). In 3D EPI, the B0-offset throughout the varied respiratory cycles may produce artifacts along the second phase encoding direction that is harder to be corrected using the existing regression methods. Ventilation of animals at constant rates during scans forces the respiratory cycle to remain unvaried, therefore avoiding phase difference between cycles and sharpening the spectrum of the respiratory-derived motion within functional scans (**Figure 2E** and **Supplementary Figure 4b**). By providing ventilation at specific rates, the process of identification of the aliased frequency is optimized, allowing to exclude the given spectral components with band-stop filters. Furthermore, paralyzer agents could be used to further dampen the respiratory interference.

CONCLUSION

Here, we present evidence for an interference in the rs-fMRI signal fluctuation from the respiration-related motion in animals breathing through mask or artificially ventilated, which can be observed as waves within a large frequency range depending on the length of the particular respiratory cycle and on the TR used to sample the fMRI signal (i.e., aliasing effect). The artifacts can be significantly dampened by using muscle paralyzers like Pancuronium for anesthesied animals of terminal studies. For the chronic or longitudinal studies, post-processing methods with retrospective regression (Hu et al., 1995; Glover et al., 2000), e.g., RETROICOR, can be used to attenuate the respiration-induced artifacts, as has been routinely used for human fMRI studies. Additionally, the use of a convenient TR may further simplify the cleaning process by shifting the aliased respiratory-driven artifacts to a specific frequency range that can be filtered out from the analysis. Our observations suggest that recording of respiratory cycles and blood pressure in parallel to fMRI and data cleaning (i.e., removal of physiological noise) constitutes a necessary step in small animal fMRI as well, especially in awake or non-paralyzed anesthetized rodent studies.

AUTHOR CONTRIBUTIONS

XY led the research. XY, KS, and PP-R designed the experiments. PP-R and XY performed the experiments. PP-R XY and BB guided the analysis. PP-R performed the analysis. XY, PP-R, and BB wrote the manuscript. All authors reviewed the manuscript.

ACKNOWLEDGMENTS

This work is supported by the US-Germany joint grant (BMBF:01GQ1702 and NIH:R01 AT009829) and also the internal fund of the Max Planck Society and the Graduate Training Centre of Neuroscience in Tübingen. We thank Dr. N. Avdievitch, R. Pohmann and K. Buckenmaier for MR technical support. We thanks Ms. H. Schulz, S. Fischer and M. Pitscheider and Dr. E. Weiler on animal experiment, welfare and maintenance support. We also thank the team in AFNI for software support.

SUPPLEMENTARY MATERIAL

The Supplementary Material for this article can be found online at: https://www.frontiersin.org/articles/10.3389/fnins.2018.00788/full#supplementary-material

REFERENCES

Abreu, R., Nunes, S., Leal, A., and Figueiredo, P. (2017). Physiological noise correction using ECG-derived respiratory signals for enhanced mapping of spontaneous neuronal activity with simultaneous EEG-fMRI. *Neuroimage* 154, 115–127. doi: 10.1016/j.neuroimage.2016.08.008

Airaksinen, A. M., Niskanen, J. P., Chamberlain, R., Huttunen, J. K., Nissinen, J., Garwood, M., et al. (2010). Simultaneous fMRI and local field potential measurements during epileptic seizures in medetomidine-sedated rats using raser pulse sequence. *Magn. Reson. Med.* 64, 1191–1199. doi: 10.1002/mrm.22508

Albers, F., Wachsmuth, L., Van Alst, T. M., and Faber, C. (2018). multimodal functional neuroimaging by simultaneous BOLD fMRI and fiber-optic calcium recordings and optogenetic control. *Mol. Imaging Biol.* 20, 171–182. doi: 10.1007/s11307-017-1130-6

Bajic, D., Craig, M. M., Mongerson, C. R. L., Borsook, D., and Becerra, L. (2017). Identifying rodent resting-state brain networks with independent component analysis. *Front. Neurosci.* 11:685. doi: 10.3389/fnins.2017.00685

Bhattacharyya, P. K., and Lowe, M. J. (2004). Cardiac-induced physiologic noise in tissue is a direct observation of cardiac-induced fluctuations. *Magn. Reson. Imaging* 22, 9–13. doi: 10.1016/j.mri.2003.08.003

Birn, R. M. (2012). The role of physiological noise in resting-state functional connectivity. *Neuroimage* 62, 864–870. doi: 10.1016/j.neuroimage.2012.01.016

Birn, R. M., Cornejo, M. D., Molloy, E. K., Patriat, R., Meier, T. B., Kirk, G. R., et al. (2014). The influence of physiological noise correction on test-retest reliability of resting-state functional connectivity. *Brain Connect.* 4, 511–522. doi: 10.1089/brain.2014.0284

Birn, R. M., Diamond, J. B., Smith, M. A., and Bandettini, P. A. (2006). Separating respiratory-variation-related neuronal-activity-related fluctuations in fluctuations from fMRI. *Neuroimage* 31, 1536–1548. doi: 10.1016/j.neuroimage.2006.02.048

Birn, R. M., Murphy, K., and Bandettini, P. A. (2008a). The effect of respiration variations on independent component analysis results of resting state functional connectivity. *Hum. Brain Mapp.* 29, 740–750. doi: 10.1002/hbm.20577

Birn, R. M., Smith, M. A., Jones, T. B., and Bandettini, P. A. (2008b). The respiration response function: the temporal dynamics of fMRI signal fluctuations related to changes in respiration. *Neuroimage* 40, 644–654. doi: 10.1016/j.neuroimage.2007.11.059

Biswal, B., Deyoe, E. A., and Hyde, J. S. (1996). Reduction of physiological fluctuations in fMRI using digital filters. *Magn. Reson. Med.* 35, 107–113. doi: 10.1002/mrm.1910350114

Biswal, B., Yetkin, F. Z., Haughton, V. M., and Hyde, J. S. (1995). Functional connectivity in the motor cortex of resting human brain using echo-planar MRI. *Magn. Reson. Med.* 34, 537–541. doi: 10.1002/mrm.1910340409

Biswal, B. B., and Kannurpatti, S. S. (2009). Resting-state functional connectivity in animal models: modulations by exsanguination. *Methods Mol. Biol.* 489, 255–274. doi: 10.1007/978-1-59745-543-5_12

Bright, M. G., and Murphy, K. (2017). Cleaning up the fMRI time series: Mitigating noise with advanced acquisition and correction strategies. *Neuroimage* 154, 1–3. doi: 10.1016/j.neuroimage.2017.03.056

Bruno, M. A., Soddu, A., Demertzi, A., Laureys, S., Gosseries, O., Schnakers, C., et al. (2010). Disorders of consciousness: moving from passive to resting state and active paradigms. *Cogn. Neurosci.* 1, 193–203. doi: 10.1080/17588928.2010.485677

Bukhari, Q., Schroeter, A., Cole, D. M., and Rudin, M. (2017). Resting state fMRI in mice reveals anesthesia specific signatures of brain functional networks and their interactions. *Front. Neural Circuits* 11:5. doi: 10.3389/fncir.2017.00005

Caballero-Gaudes, C., and Reynolds, R. C. (2017). Methods for cleaning the BOLD fMRI signal. *Neuroimage* 154, 128–149. doi: 10.1016/j.neuroimage.2016.12.018

Cabral, J., Kringelbach, M. L., and Deco, G. (2014). Exploring the network dynamics underlying brain activity during rest. *Prog. Neurobiol.* 114, 102–131. doi: 10.1016/j.pneurobio.2013.12.005

Chen, L., Beckett, A., Verma, A., and Feinberg, D. A. (2015a). Dynamics of respiratory and cardiac CSF motion revealed with real-time simultaneous multi-slice EPI velocity phase contrast imaging. *Neuroimage* 122, 281–287. doi: 10.1016/j.neuroimage.2015.07.073

Chen, L., Vu, A. T., Xu, J., Moeller, S., Ugurbil, K., Yacoub, E., et al. (2015b). Evaluation of highly accelerated simultaneous multi-slice EPI for fMRI. *Neuroimage* 104, 452–459. doi: 10.1016/j.neuroimage.2014.10.027

Cordes, D., Nandy, R. R., Schafer, S., and Wager, T. D. (2014). Characterization and reduction of cardiac- and respiratory-induced noise as a function of the sampling rate (TR) in fMRI. *Neuroimage* 89, 314–330. doi: 10.1016/j.neuroimage.2013.12.013

Cox, R. W. (1996). AFNI: software for analysis and visualization of functional magnetic resonance neuroimages. *Comput. Biomed. Res.* 29, 162–173. doi: 10.1006/cbmr.1996.0014

Dagli, M. S., Ingeholm, J. E., and Haxby, J. V. (1999). Localization of cardiac-induced signal change in fMRI. *Neuroimage* 9, 407–415. doi: 10.1006/nimg.1998.0424

D'Arceuil, H., Coimbra, A., Triano, P., Dougherty, M., Mello, J., Moseley, M., et al. (2013). Ferumoxytol enhanced resting state fMRI and relative cerebral blood volume mapping in normal human brain. *Neuroimage* 83, 200–209. doi: 10.1016/j.neuroimage.2013.06.066

De Luca, M., Beckmann, C. F., De Stefano, N., Matthews, P. M., and Smith, S. M. (2006). fMRI resting state networks define distinct modes of long-distance interactions in the human brain. *Neuroimage* 29, 1359–1367. doi: 10.1016/j.neuroimage.2005.08.035

De Luca, M., Smith, S., De Stefano, N., Federico, A., and Matthews, P. M. (2005). Blood oxygenation level dependent contrast resting state networks are relevant to functional activity in the neocortical sensorimotor system. *Exp. Brain Res.* 167, 587–594. doi: 10.1007/s00221-005-0059-1

Diehl, R. R., Linden, D., Lucke, D., and Berlit, P. (1995). Phase relationship between cerebral blood flow velocity and blood pressure. A clinical. test of autoregulation. *Stroke* 26, 1801–1804. doi: 10.1161/01.STR.26.10.1801

Feinberg, D. A., Moeller, S., Smith, S. M., Auerbach, E., Ramanna, S., Gunther, M., et al. (2010). Multiplexed echo planar imaging for sub-second whole brain FMRI and fast diffusion imaging. *PLoS One* 5:e15710. doi: 10.1371/journal.pone.0015710

Feinberg, D. A., and Setsompop, K. (2013). Ultra-fast MRI of the human brain with simultaneous multi-slice imaging. *J. Magn. Reson.* 229, 90–100. doi: 10.1016/j.jmr.2013.02.002

Ferenczi, E. A., Zalocusky, K. A., Liston, C., Grosenick, L., Warden, M. R., Amatya, D., et al. (2016). Prefrontal cortical regulation of brainwide circuit dynamics and reward-related behavior. *Science* 351:aac9698. doi: 10.1126/science.aac9698

Fleming, S., Thompson, M., Stevens, R., Heneghan, C., Pluddemann, A., Maconochie, I., et al. (2011). Normal ranges of heart rate and respiratory rate in children from birth to 18 years of age: a systematic review of observational studies. *Lancet* 377, 1011–1018. doi: 10.1016/S0140-6736(10)62226-X

Fox, M. D., Zhang, D., Snyder, A. Z., and Raichle, M. E. (2009). The global signal and observed anticorrelated resting state brain networks. *J. Neurophysiol.* 101, 3270–3283. doi: 10.1152/jn.90777.2008

Frank, L. R., Buxton, R. B., and Wong, E. C. (2001). Estimation of respiration-induced noise fluctuations from undersampled multislice fMRI data. *Magn. Reson. Med.* 45, 635–644. doi: 10.1002/mrm.1086

Glover, G. H., Li, T. Q., and Ress, D. (2000). Image-based method for retrospective correction of physiological motion effects in fMRI: RETROICOR. *Magn. Reson. Med.* 44, 162–167. doi: 10.1002/1522-2594(200007)44:1<162::AID-MRM23>3.0.CO;2-E

Goense, J. B., and Logothetis, N. K. (2008). Neurophysiology of the BOLD fMRI signal in awake monkeys. *Curr. Biol.* 18, 631–640. doi: 10.1016/j.cub.2008.03.054

Goerke, U., Moller, H. E., Norris, D. G., and Schwarzbauer, C. (2005). A comparison of signal instability in 2D and 3D EPI resting-state fMRI. *NMR Biomed.* 18, 534–542. doi: 10.1002/nbm.987

Greicius, M. D., Krasnow, B., Reiss, A. L., and Menon, V. (2003). Functional connectivity in the resting brain: a network analysis of the default mode hypothesis. *Proc. Natl. Acad. Sci. U.S.A.* 100, 253–258. doi: 10.1073/pnas.0135058100

Griffanti, L., Salimi-Khorshidi, G., Beckmann, C. F., Auerbach, E. J., Douaud, G., Sexton, C. E., et al. (2014). ICA-based artefact removal and accelerated fmri acquisition for improved resting state network imaging. *Neuroimage* 95, 232–247. doi: 10.1016/j.neuroimage.2014.03.034

He, Y., Wang, M., Chen, X., Pohmann, R., Polimeni, J. R., Scheffler, K., et al. (2018). Ultra-Slow Single-Vessel BOLD and CBV-Based fMRI spatiotemporal dynamics and their correlation with neuronal intracellular calcium signals. *Neuron* 97, 925–939.e5. doi: 10.1016/j.neuron.2018.01.025

Holst, G. C. (1996). Sampling, aliasing, and target appearance. *Infrared Phys. Technol.* 37, 627–634. doi: 10.1016/S1350-4495(97)80356-8

Hsu, L. M., Liang, X., Gu, H., Brynildsen, J. K., Stark, J. A., Ash, J. A., et al. (2016). Constituents and functional implications of the rat default mode network. *Proc. Natl. Acad. Sci. U.S.A.* 113, E4541–E4547. doi: 10.1073/pnas.1601485113

Hu, X. P., Le, T. H., Parrish, T., and Erhard, P. (1995). Retrospective estimation and correction of physiological fluctuation in functional Mri. *Magn. Reson. Med.* 34, 201–212. doi: 10.1002/mrm.1910340211

Hugger, T., Zahneisen, B., Levan, P., Lee, K. J., Lee, H. L., Zaitsev, M., et al. (2011). Fast undersampled functional magnetic resonance imaging using nonlinear regularized parallel image reconstruction. *PLoS One* 6:e28822. doi: 10.1371/journal.pone.0028822

Hutton, C., Josephs, O., Stadler, J., Featherstone, E., Reid, A., Speck, O., et al. (2011). The impact of physiological noise correction on fMRI at 7 T. *Neuroimage* 57, 101–112. doi: 10.1016/j.neuroimage.2011.04.018

Hyder, F., and Rothman, D. L. (2010). Neuronal correlate of BOLD signal fluctuations at rest: err on the side of the baseline. *Proc. Natl. Acad. Sci. U.S.A.* 107, 10773–10774. doi: 10.1073/pnas.1005135107

Jiang, Y., Chen, X., and Yu, X. (2018). Fiber optic mediated extracellular glutamate and intracellular calcium recording with simultaneous fMRI. *Int. Soc. Magn. Reson. Med.*

Jorge, J., Grouiller, F., Ipek, O., Stoermer, R., Michel, C. M., Figueiredo, P., et al. (2015). Simultaneous EEG-fMRI at ultra-high field: artifact prevention and safety assessment. *Neuroimage* 105, 132–144. doi: 10.1016/j.neuroimage.2014.10.055

Kalthoff, D., Seehafer, J. U., Po, C., Wiedermann, D., and Hoehn, M. (2011). Functional connectivity in the rat at 11.7T: Impact of physiological noise in resting state fMRI. *Neuroimage* 54, 2828–2839. doi: 10.1016/j.neuroimage.2010.10.053

Kannurpatti, S. S., Biswal, B. B., Kim, Y. R., and Rosen, B. R. (2008). Spatio-temporal characteristics of low-frequency BOLD signal fluctuations in isoflurane-anesthetized rat brain. *Neuroimage* 40, 1738–1747. doi: 10.1016/j.neuroimage.2007.05.061

Keilholz, S. D., Silva, A. C., Raman, M., Merkle, H., and Koretsky, A. P. (2004). Functional MRI of the rodent somatosensory pathway using multislice echo planar imaging. *Magn. Reson. Med.* 52, 89–99. doi: 10.1002/mrm.20114

Kiviniemi, V., Kantola, J. H., Jauhiainen, J., Hyvarinen, A., and Tervonen, O. (2003). Independent component analysis of nondeterministic fMRI signal sources. *Neuroimage* 19, 253–260. doi: 10.1016/S1053-8119(03)00097-1

Kiviniemi, V., Ruohonen, J., and Tervonen, O. (2005). Separation of physiological very low frequency fluctuation from aliasing by switched sampling interval fMRI scans. *Magn. Reson. Imaging* 23, 41–46. doi: 10.1016/j.mri.2004.09.005

Lee, J. H., Durand, R., Gradinaru, V., Zhang, F., Goshen, I., Kim, D. S., et al. (2010). Global and local fMRI signals driven by neurons defined optogenetically by type and wiring. *Nature* 465, 788–792. doi: 10.1038/nature09108

Liang, Z., Watson, G. D., Alloway, K. D., Lee, G., Neuberger, T., and Zhang, N. (2015). Mapping the functional network of medial prefrontal cortex by combining optogenetics and fMRI in awake rats. *Neuroimage* 117, 114–123. doi: 10.1016/j.neuroimage.2015.05.036

Liu, T. T. (2016). Noise contributions to the fMRI signal: an overview. *Neuroimage* 143, 141–151. doi: 10.1016/j.neuroimage.2016.09.008

Logothetis, N. K. (2002). The neural basis of the blood-oxygen-level-dependent functional magnetic resonance imaging signal. *Philos. Trans. R. Soc. Lond. B Biol. Sci.* 357, 1003–1037. doi: 10.1098/rstb.2002.1114

Lowe, M. J., Mock, B. J., and Sorenson, J. A. (1998). Functional connectivity in single and multislice echoplanar imaging using resting-state fluctuations. *Neuroimage* 7, 119–132. doi: 10.1006/nimg.1997.0315

Lu, H., Zou, Q., Gu, H., Raichle, M. E., Stein, E. A., and Yang, Y. (2012). Rat brains also have a default mode network. *Proc. Natl. Acad. Sci. U.S.A.* 109, 3979–3984. doi: 10.1073/pnas.1200506109

Lutti, A., Thomas, D. L., Hutton, C., and Weiskopf, N. (2013). High-resolution functional MRI at 3 T: 3D/2D echo-planar imaging with optimized physiological noise correction. *Magn. Reson. Med.* 69, 1657–1664. doi: 10.1002/mrm.24398

Magnuson, M., Majeed, W., and Keilholz, S. D. (2010). Functional connectivity in blood oxygenation level-dependent and cerebral blood volume-weighted resting state functional magnetic resonance imaging in the rat brain. *J. Magn. Reson. Imaging* 32, 584–592. doi: 10.1002/jmri.22295

Magnuson, M. E., Thompson, G. J., Schwarb, H., Pan, W. J., Mckinley, A., Schumacher, E. H., et al. (2015). Errors on interrupter tasks presented during spatial and verbal working memory performance are linearly linked to large-scale functional network connectivity in high temporal resolution resting state fMRI. *Brain Imaging Behav.* 9, 854–867. doi: 10.1007/s11682-014-9347-3

Majeed, W., Magnuson, M., Hasenkamp, W., Schwarb, H., Schumacher, E. H., Barsalou, L., et al. (2011). Spatiotemporal dynamics of low frequency BOLD fluctuations in rats and humans. *Neuroimage* 54, 1140–1150. doi: 10.1016/j.neuroimage.2010.08.030

Mantini, D., Gerits, A., Nelissen, K., Durand, J. B., Joly, O., Simone, L., et al. (2011). Default mode of brain function in monkeys. *J. Neurosci.* 31, 12954–12962. doi: 10.1523/JNEUROSCI.2318-11.2011

Mishra, A. M., Ellens, D. J., Schridde, U., Motelow, J. E., Purcaro, M. J., Desalvo, M. N., et al. (2011). Where fMRI and electrophysiology agree to disagree: corticothalamic and striatal activity patterns in the WAG/Rij rat. *J. Neurosci.* 31, 15053–15064. doi: 10.1523/JNEUROSCI.0101-11.2011

Murphy, K., Birn, R. M., and Bandettini, P. A. (2013). Resting-state fMRI confounds and cleanup. *Neuroimage* 80, 349–359. doi: 10.1016/j.neuroimage.2013.04.001

Noll, D. C., Genovese, C. R., Vazquez, A. L., O'brien, J. L., and Eddy, W. F. (1998). Evaluation of respiratory artifact correction techniques in multishot spiral functional MRI using receiver operator characteristic analyses. *Magn. Reson. Med.* 40, 633–639. doi: 10.1002/mrm.1910400417

Obrig, H., Neufang, M., Wenzel, R., Kohl, M., Steinbrink, J., Einhaupl, K., et al. (2000). Spontaneous low frequency oscillations of cerebral hemodynamics and metabolism in human adults. *Neuroimage* 12, 623–639. doi: 10.1006/nimg.2000.0657

Paasonen, J., Stenroos, P., Salo, R. A., Kiviniemi, V., and Grohn, O. (2018). Functional connectivity under six anesthesia protocols and the awake condition in rat brain. *Neuroimage* 172, 9–20. doi: 10.1016/j.neuroimage.2018.01.014

Pan, W. J., Thompson, G., Magnuson, M., Majeed, W., Jaeger, D., and Keilholz, S. (2011). Broadband local field potentials correlate with spontaneous fluctuations in functional magnetic resonance imaging signals in the rat somatosensory cortex under isoflurane anesthesia. *Brain Connect.* 1, 119–131. doi: 10.1089/brain.2011.0014

Pan, W. J., Thompson, G. J., Magnuson, M. E., Jaeger, D., and Keilholz, S. (2013). Infraslow LFP correlates to resting-state fMRI BOLD signals. *Neuroimage* 74, 288–297. doi: 10.1016/j.neuroimage.2013.02.035

Pawela, C. P., Biswal, B. B., Hudetz, A. G., Li, R., Jones, S. R., Cho, Y. R., et al. (2010). Interhemispheric neuroplasticity following limb deafferentation detected by resting-state functional connectivity magnetic resonance imaging (fcMRI) and functional magnetic resonance imaging (fMRI). *Neuroimage* 49, 2467–2478. doi: 10.1016/j.neuroimage.2009.09.054

Pfurtscheller, G., Schwerdtfeger, A., Brunner, C., Aigner, C., Fink, D., Brito, J., et al. (2017). Distinction between neural and vascular BOLD oscillations and intertwined heart rate oscillations at 0.1 Hz in the resting state and during movement. *PLoS One* 12:e0168097. doi: 10.1371/journal.pone.0168097

Posse, S., Ackley, E., Mutihac, R., Zhang, T., Hummatov, R., Akhtari, M., et al. (2013). High-speed real-time resting-state FMRI using multi-slab echo-volumar imaging. *Front. Hum. Neurosci.* 7:479. doi: 10.3389/fnhum.2013.00479

Raichle, M. E., Macleod, A. M., Snyder, A. Z., Powers, W. J., Gusnard, D. A., and Shulman, G. L. (2001). A default mode of brain function. *Proc. Natl. Acad. Sci. U.S.A.* 98, 676–682. doi: 10.1073/pnas.98.2.676

Raj, D., Anderson, A. W., and Gore, J. C. (2001). Respiratory effects in human functional magnetic resonance imaging due to bulk susceptibility changes. *Phys. Med. Biol.* 46, 3331–3340. doi: 10.1088/0031-9155/46/12/318

Razavi, M., Eaton, B., Paradiso, S., Mina, M., Hudetz, A. G., and Bolinger, L. (2008). Source of low-frequency fluctuations in functional MRI signal. *J. Magn. Reson. Imaging* 27, 891–897. doi: 10.1002/jmri.21283

Reynaud, O., Jorge, J., Gruetter, R., Marques, J. P., and Van Der Zwaag, W. (2017). Influence of physiological noise on accelerated 2D and 3D resting state

functional MRI data at 7 T. *Magn. Reson. Med.* 78, 888–896. doi: 10.1002/mrm.26823

Scholvinck, M. L., Maier, A., Ye, F. Q., Duyn, J. H., and Leopold, D. A. (2010). Neural basis of global resting-state fMRI activity. *Proc. Natl. Acad. Sci. U.S.A.* 107, 10238–10243. doi: 10.1073/pnas.0913110107

Schulz, K., Sydekum, E., Krueppel, R., Engelbrecht, C. J., Schlegel, F., Schroter, A., et al. (2012). Simultaneous BOLD fMRI and fiber-optic calcium recording in rat neocortex. *Nat. Methods* 9, 597–602. doi: 10.1038/nmeth.2013

Schwalm, M., Schmid, F., Wachsmuth, L., Backhaus, H., Kronfeld, A., Aedo Jury, F., et al. (2017). Cortex-wide BOLD fMRI activity reflects locally-recorded slow oscillation-associated calcium waves. *Elife* 6:e27602. doi: 10.7554/eLife.27602

Shmuel, A., and Leopold, D. A. (2008). Neuronal correlates of spontaneous fluctuations in fMRI signals in monkey visual cortex: Implications for functional connectivity at rest. *Hum. Brain Mapp.* 29, 751–761. doi: 10.1002/hbm.20580

Shmueli, K., Van Gelderen, P., De Zwart, J. A., Horovitz, S. G., Fukunaga, M., Jansma, J. M., et al. (2007). Low-frequency fluctuations in the cardiac rate as a source of variance in the resting-state fMRI BOLD signal. *Neuroimage* 38, 306–320. doi: 10.1016/j.neuroimage.2007.07.037

Stafford, J. M., Jarrett, B. R., Miranda-Dominguez, O., Mills, B. D., Cain, N., Mihalas, S., et al. (2014). Large-scale topology and the default mode network in the mouse connectome. *Proc. Natl. Acad. Sci. U.S.A.* 111, 18745–18750. doi: 10.1073/pnas.1404346111

Starck, T., Remes, J., Nikkinen, J., Tervonen, O., and Kiviniemi, V. (2010). Correction of low-frequency physiological noise from the resting state BOLD fMRI–Effect on ICA default mode analysis at 1.5 *T. J. Neurosci. Methods* 186, 179–185. doi: 10.1016/j.jneumeth.2009.11.015

Tong, Y., Hocke, L. M., and Frederick, B. (2014). Short repetition time multiband echo-planar imaging with simultaneous pulse recording allows dynamic imaging of the cardiac pulsation signal. *Magn. Reson. Med.* 72, 1268–1276. doi: 10.1002/mrm.25041

Van de Moortele, P. F., Pfeuffer, J., Glover, G. H., Ugurbil, K., and Hu, X. (2002). Respiration-induced B0 fluctuations and their spatial distribution in the human brain at 7 Tesla. *Magn. Reson. Med.* 47, 888–895. doi: 10.1002/mrm.10145

Vincent, J. L., Patel, G. H., Fox, M. D., Snyder, A. Z., Baker, J. T., Van Essen, D. C., et al. (2007). Intrinsic functional architecture in the anaesthetized monkey brain. *Nature* 447, 83–86. doi: 10.1038/nature05758

Wang, M., He, Y., Sejnowski, T. J., and Yu, X. (2018). Brain-state dependent astrocytic Ca(2 +) signals are coupled to both positive and negative BOLD-fMRI signals. *Proc. Natl. Acad. Sci. U.S.A.* 115, E1647–E1656. doi: 10.1073/pnas.1711692115

Welvaert, M., and Rosseel, Y. (2012). How ignoring physiological noise can bias the conclusions from fMRI simulation results. *J. Neurosci. Methods* 211, 125–132. doi: 10.1016/j.jneumeth.2012.08.022

Williams, K. A., Magnuson, M., Majeed, W., Laconte, S. M., Peltier, S. J., Hu, X., et al. (2010). Comparison of alpha-chloralose, medetomidine and isoflurane anesthesia for functional connectivity mapping in the rat. *Magn. Reson. Imaging* 28, 995–1003. doi: 10.1016/j.mri.2010.03.007

Wise, R. G., Ide, K., Poulin, M. J., and Tracey, I. (2004). Resting fluctuations in arterial carbon dioxide induce significant low frequency variations in BOLD signal. *Neuroimage* 21, 1652–1664. doi: 10.1016/j.neuroimage.2003.11.025

Xie, Y., Chan, A. W., Mcgirr, A., Xue, S., Xiao, D., Zeng, H., et al. (2016). Resolution of high-frequency mesoscale intracortical maps using the genetically encoded glutamate sensor iglusnfr. *J. Neurosci.* 36, 1261–1272. doi: 10.1523/JNEUROSCI.2744-15.2016

Yang, S., Ross, T. J., Zhang, Y., Stein, E. A., and Yang, Y. (2005). Head motion suppression using real-time feedback of motion information and its effects on task performance in fMRI. *Neuroimage* 27, 153–162. doi: 10.1016/j.neuroimage.2005.02.050

Yu, X. (2017). "When photons meet protons: Optogenetics, Calcium signal detection, and fMRI in small animals," in *Small Animal Imaging Basics and Practical Guide*, eds F. Kiessling, B. Pichler, and P. Hauff (Berlin: Springer International Publishing).

Yu, X., He, Y., Wang, M., Merkle, H., Dodd, S. J., Silva, A. C., et al. (2016). Sensory and optogenetically driven single-vessel fMRI. *Nat. Methods* 13, 337–340. doi: 10.1038/nmeth.3765

Yu, X., Qian, C., Chen, D. Y., Dodd, S. J., and Koretsky, A. P. (2014). Deciphering laminar-specific neural inputs with line-scanning fMRI. *Nat. Methods* 11, 55–58. doi: 10.1038/nmeth.2730

Zhao, F., Zhao, T., Zhou, L., Wu, Q., and Hu, X. (2008). BOLD study of stimulation-induced neural activity and resting-state connectivity in medetomidine-sedated rat. *Neuroimage* 39, 248–260. doi: 10.1016/j.neuroimage.2007.07.063

Zou, Q. H., Zhu, C. Z., Yang, Y., Zuo, X. N., Long, X. Y., Cao, Q. J., et al. (2008). An improved approach to detection of amplitude of low-frequency fluctuation (ALFF) for resting-state fMRI: fractional ALFF. *J. Neurosci. Methods* 172, 137–141. doi: 10.1016/j.jneumeth.2008.04.012

Conflict of Interest Statement: The authors declare that the research was conducted in the absence of any commercial or financial relationships that could be construed as a potential conflict of interest.

frontiers in Neuroscience

ORIGINAL RESEARCH
published: 13 December 2018
doi: 10.3389/fnins.2018.00899

Tuning Neuromodulation Effects by Orientation Selective Deep Brain Stimulation in the Rat Medial Frontal Cortex

Lauri J. Lehto[1†], Pavel Filip[1,2†], Hanne Laakso[1,3], Alejandra Sierra[3], Julia P. Slopsema[4], Matthew D. Johnson[4], Lynn E. Eberly[5], Walter C. Low[6], Olli Gröhn[3], Heikki Tanila[3], Silvia Mangia[1‡] and Shalom Michaeli[1‡]*

[1] Center for Magnetic Resonance Research, University of Minnesota, Minneapolis, MN, United States, [2] First Department of Neurology, Faculty of Medicine, St. Anne's Teaching Hospital, Masaryk University, Brno, Czechia, [3] A.I. Virtanen Institute for Molecular Sciences, University of Eastern Finland, Kuopio, Finland, [4] Department of Biomedical Engineering, University of Minnesota, Minneapolis, MN, United States, [5] Division of Biostatistics, University of Minnesota, Minneapolis, MN, United States, [6] Department of Neurosurgery, University of Minnesota, Minneapolis, MN, United States

OPEN ACCESS

Edited by:
Marta Bianciardi,
Harvard Medical School,
United States

Reviewed by:
Natalia Gudino,
National Institutes of Health (NIH),
United States
Laleh Golestanirad,
University of Toronto, Canada

***Correspondence:**
Shalom Michaeli
micha042@umn.edu

[†]These authors have contributed equally to this work as shared first authorship

[‡]Shared senior authorship

Specialty section:
This article was submitted to Brain Imaging Methods, a section of the journal Frontiers in Neuroscience

Received: 24 August 2018
Accepted: 19 November 2018
Published: 13 December 2018

Citation:
Lehto LJ, Filip P, Laakso H, Sierra A, Slopsema JP, Johnson MD, Eberly LE, Low WC, Gröhn O, Tanila H, Mangia S and Michaeli S (2018) Tuning Neuromodulation Effects by Orientation Selective Deep Brain Stimulation in the Rat Medial Frontal Cortex. Front. Neurosci. 12:899. doi: 10.3389/fnins.2018.00899

Previous studies that focused on treating major depressive disorder with conventional deep brain stimulation (DBS) paradigms produced inconsistent results. In this proof-of-concept preclinical study in rats (n = 8), we used novel paradigms of orientation selective DBS for stimulating the complex circuitry crossing the infralimbic cortex, an area considered analogous to human subgenual cingulate cortex. Using functional MRI at 9.4 T, we monitored whole brain responses to varying the electrical field orientation of DBS within the infralimbic cortex. Substantial alterations of functional MRI responses in the amygdala, a major node connected to the infralimbic cortex implicated in the pathophysiology of depression, were observed. As expected, the activation cluster near the electrode was insensitive to the changes of the stimulation orientation. Hence, our findings substantiate the ability of orientation selective stimulation (OSS) to recruit neuronal pathways of distinct orientations relative to the position of the electrode, even in complex circuits such as those involved in major depressive disorder. We conclude that OSS is a promising approach for stimulating brain areas that inherently require individualisation of the treatment approach.

Keywords: deep brain stimulation, infralimbic cortex, fMRI, orientation selective, depression

INTRODUCTION

Despite best efforts of psychiatrists, the results of the mainstay treatment strategies in major depressive disorders (MDD) are often disappointing, labeling nearly a third of patients as therapy-refractory (Warden et al., 2007). This stalemate situation is not surprising, considering our lack of deeper insight in the exact neurophysiology of MDD. However, over the years several neural nodes have emerged as possible major culprits (Koenigs and Grafman, 2009), paving a path for possible

Abbreviations: Amyg, amygdala; CP, caudate putamen; fMRI, functional magnetic resonance imaging; IL, infralimbic cortex; LS, lateral septum; MB-SWIFT, multi-band sweep imaging with fourier transformation; mFC, medial frontal cortex; NAc, nucleus accumbens; PL, prelimbic cortex; ROI, region of interest; sgACC, subgenual cingulate cortex.

targeted, even curative interventions, with high hopes invested mainly in deep brain stimulation (DBS) therapy. Since its renaissance in the 1990s, DBS has confidently risen to the position of a safe and effective therapeutic option for various movement disorders, epilepsy and even obsessive-compulsive disorder (Greenberg et al., 2006; Bari et al., 2018). Yet, the encouraging results yielded in several small, open-label MDD DBS studies targeting various structures failed to be replicated in two randomized, sham-controlled trials (Dougherty et al., 2015; Youngerman and Sheth, 2017). However, this was recently countered by another randomized clinical trial proving MDD DBS efficacy in the anterior limb of the internal capsule (Bergfeld et al., 2016). These disparate results call for better understanding not only of the targeted neural circuitry, but also of the interindividual variability in clinical and cognitive phenotypes (Widge et al., 2016), which may be directly relevant for optimizing the stimulation parameters and the implantation site (Morishita et al., 2014).

Advances in electrode design (Tsai et al., 2015) and stimulation paradigms (Martens et al., 2011; Chaturvedi et al., 2012) are promising venues for expanding and optimizing the stimulation outcomes. In particular, the recently introduced paradigms of orientation selective stimulation (OSS) (Lehto et al., 2017b) generate orientation dependent electric field gradients based on multichannel leads with independently driven channels, and can provide optimal stimulation of axonal pathways with distinct orientations relative to the position of the electrode. OSS was shown to be effective in more selectively stimulating axonal pathways crossing a highly organized structure such as the corpus callosum, but its effectiveness in more complex, cognitive-related circuitry has not been investigated.

Here, we aimed at characterizing, by fMRI, the involvement of neural circuitry during real-time DBS of a rat brain region that is relevant to major depression. Despite the considerable variations of the anatomy of the prefrontal cortex across species, and hence the somewhat controversial correspondence of various structures (Heidbreder and Groenewegen, 2003), the cytoarchitectonics and anatomical connections of the ventral aspect of the medial prefrontal cortex in rats are homologous to the sgACC in humans. More specifically, the infralimbic subregion (IL) has been implied in the mechanisms of stress (Diorio et al., 1993; Ostrander et al., 2003), and is one of the main candidates in MDD DBS in humans (Takagishi and Chiba, 1991; Gabbott et al., 2003; Hamani et al., 2010b). In addition, sgACC/IL is a good example of crossroads of several major fiber tracts. Within one hemisphere strong connections are sent to the mFC, medial thalamus, NAc, amygdala and hypothalamus. In addition, the ascending serotonergic and noradrenergic pathways pass through the sgACC/IL before diverging all over the cortical mantle. Undoubtedly, conventional electric stimulation even with bipolar electrodes would touch all these connections and thus influence all these networks to a variable extent (Hamani et al., 2011). The objective of this study was to compare the network-level responses to infralimbic DBS across multiple electric field orientations employing OSS and across multiple DBS frequencies. We hypothesized that OSS would titrate the fMRI responses in the ipsilateral limbic system, including the amygdala and NAc.

MATERIALS AND METHODS

Animals

For DBS-fMRI, Sprague-Dawley rats (Envigo, Madison, WI, United States; n = 8, male, 295–327 g) were housed in pairs in a temperature and humidity-controlled vivarium with a 12-h light-dark cycle with food and water *ad libitum*. These animal procedures were approved by the Institutional Animal Care and Use Committee (IACUC) of the University of Minnesota.

Electrode Implantation

After the induction of isoflurane anesthesia (5% induction, 2–3% maintenance; carrier gas O_2/N_2O 30/70%), the animals were placed on a heating pad and into a stereotactic frame (Stoelting, Wood Dale, IL, United States). Temperature was monitored via a rectal probe and maintained at 37°C, while respiration rate was monitored using a plastic pressure sensor and maintained at 70–80 per min. Burr hole with a diameter of 0.7 mm was performed over the implantation target and a tripolar electrode composed of tightly braided three polyimide-insulated (30 μm thickness) tungsten electrodes (PlasticsOne, MS333T/3C-C 3TW, Roanoke, VA, United States) with tip-only contact diameter of 127 μm was inserted unilaterally in the right IL (**Figure 1A**; rostrocaudal 3.0 mm, mediolateral 0.6 mm and dorsoventral 5.2 mm). The orientation of the electrode tip (**Figure 1B**) was controlled using a microscope, identifying each channel with a multi-meter. The burr hole around the electrode was filled with gelatin foam (SPONGOSTAN^{TM}, Søborg, Denmark) and covered using dental acrylic (Lang Dental, Jet Acrylic, Wheeling, IL, United States) to secure the tripolar electrode to the cranium. An Ag/AgCl grounding wire (4 cm long, diameter of 1 mm) was inserted below the skin, with the tip located at the base of the neck. Prior to the transfer to the MRI system, anesthesia was switched to urethane (four consecutive intraperitoneal injections with the dose of 1.25–1.50 g/kg of body weight, 15 min apart) while gradually decreasing the isoflurane level and discontinuing it at the last urethane injection. Optical rectal temperature probe and pressure respiration sensor were employed to monitor body temperature and respiration (Small Animal Instruments Inc., New York, NY, United States), respectively, during the MRI scan. The body temperature was maintained at the level of 37°C using heated water circulation and heated air.

MRI Acquisition

All MRI scans were conducted with a 9.4-T 31-cm horizontal-bore magnet equipped with Agilent DirecDRIVE console (Palo Alto, CA, United States) using a quadrature radio frequency coil designed for full rat brain coverage. The coil was composed of ^{1}H MRI invisible materials, thus ensuring that no unwanted signal would fold into the Field of View (FOV) from the coil itself. Prior to fMRI, anatomical images were acquired using a Fast Spin-Echo (FSE) sequence: repetition time (TR) = 3 s, effective echo time = 48 ms, number of echoes = 8, matrix size = 192^2,

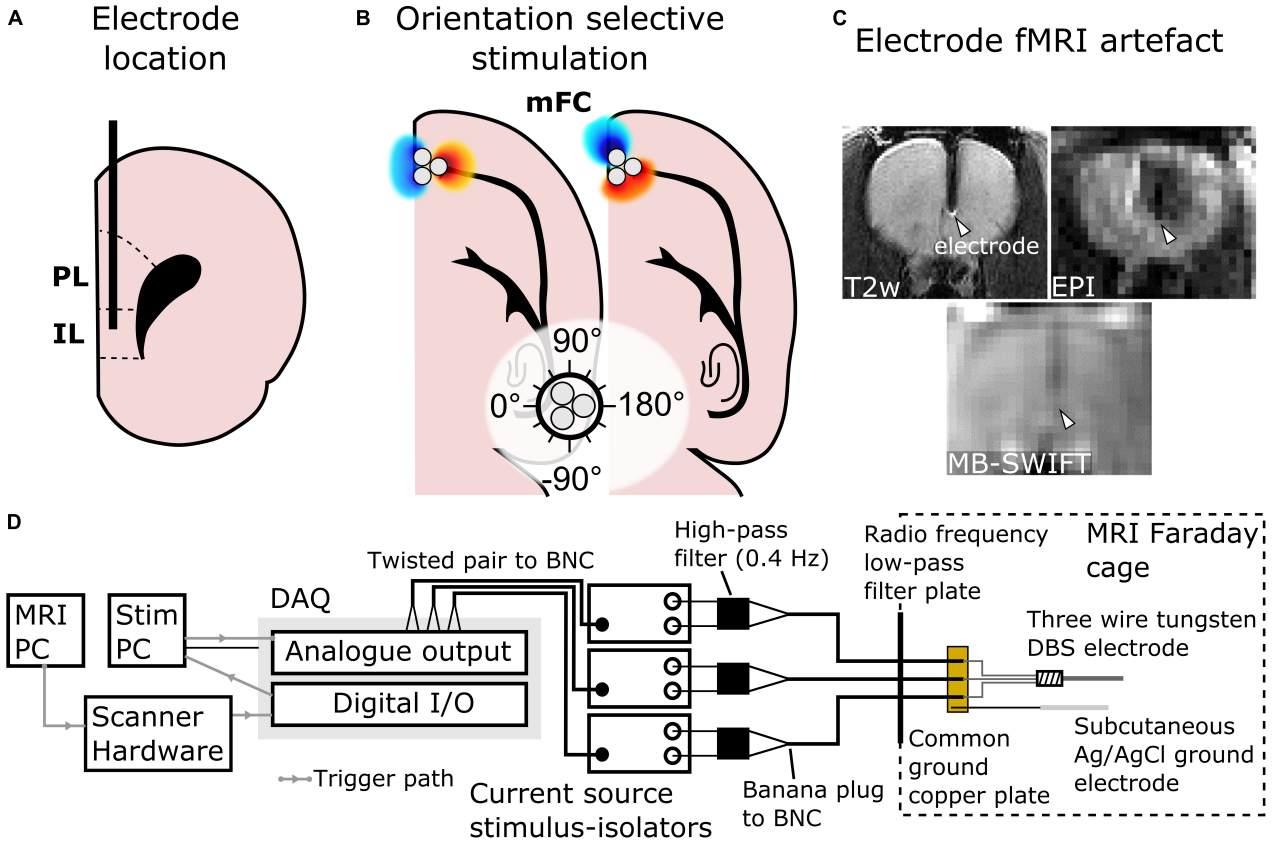

FIGURE 1 | Schematic representation of the main features of the study design, including site of electrode implantation in IL. **(A)** Placement of the electrode in IL (PL, prelimbic cortex) shown in a coronal schematic drawing. **(B)** 0° and 60° orientations of dipoles in OSS to target different fibers, depicted in a horizontal schematic drawing. In this study, the stimulation angles 0° and 180° were chosen to be in the mediolateral direction and angles 90° and –90° were chosen to be in the rostrocaudal direction (white circle). **(C)** Metallic electrodes interfere with the magnetic field used for MRI leading to a susceptibility artifact (white arrowheads). The artifact is especially severe when using traditional Echo Planar Imaging (EPI) fMRI, whereas MB-SWIFT technique provides artifact-free fMRI. **(D)** Diagram of the stimulation system.

FOV = 3.2 × 3.2 cm^2, slice thickness = 1 mm, number of slices = 15, no interslice gap and number of averages = 4. Next, MB-SWIFT fMRI was conducted using the following parameters: TR = 0.97 ms, 3094 spokes per volume, resulting in temporal resolution of 3 s, bandwidth (BW) = 192 kHz, matrix size = 64^3, FOV = 3.5 × 3.5 × 6.4 cm^3 and flip angle = 6°. Excitation was performed with a chirp pulse gapped into four 2.6-μs sub-pulses (Idiyatullin et al., 2006, 2015). Two-fold oversampling was used during acquisition in the gaps of 32/BW duration. The post-correlation FID (Idiyatullin et al., 2006) consisted of 32 points. MB-SWIFT was chosen instead of conventional Echo Planar Imaging (EPI) as it provides images virtually free of magnetic susceptibility artifacts (**Figure 1C**) at high magnetic field of 9.4 T caused by the implanted electrode and it does not require magnetic field distortion correction (Lehto et al., 2017a).

Functional Paradigms of Deep Brain Stimulation

All stimulation paradigms consisted of three blocks of 60 s of rest and 18 s of stimulation, ending with an additional rest period, resulting in 4 min 54 s of total paradigm. To avoid adaptation to stimulus, 2-min breaks were taken between trials. To seek for stimulation frequency ($n = 6$) with the strongest fMRI response, monopolar, biphasic symmetric 180-μs square pulses without interphase delay were delivered, with total current of 1.4–1.7 mA distributed equally among the three electrode channels. The current was chosen as the minimal current that produced amygdala activation. The tested stimulation frequencies were 20, 35, 70, 100, 130, 160, and 200 Hz in randomized order.

OSS was achieved by controlling the orientation of an electric dipole under the tip of the electrode. As the strongest electric field gradient of a dipole is aligned with its primary axis, an axon is the most excitable when the primary axis of a dipole is aligned with the axon (Rattay, 1989; Lehto et al., 2017b). The orientation of the dipole was controlled by changing the current amplitudes of the individual channels relative to each other by choosing the amplitudes from phase offset sinusoids (Lehto et al., 2017b). The OSS was applied using the same square pulses and current amplitudes as described above with a stimulation frequency of 20 Hz ($n = 8$) based on the results of monopolar stimulation with different stimulation frequencies. The stimulation angles were

chosen in 30° steps resulting in 12 separate OSS experiments. The angles of stimulation were set such that 0°/180° corresponded to the mediolateral direction and −90°/90° corresponded to rostrocaudal direction (**Figure 1B**).

The stimulation waveforms were computed and delivered using MATLAB 2016a (Mathworks; Natick, MA, United States) through National Instruments digital-to-analog converter (cDAQ-9174 chassis, 9263 analog output module, 9402 digital input/output module; Austin, TX, United States) and three stimulus-isolators (A-M Systems; Carlsborg, WA, United States) ran as current sources enabling the same peak current through each contact regardless of potential inter-contact impedance differences. The analog output module was used to drive the stimulus isolators (voltage to current conversion), while the digital input/output module was used to software trigger a MATLAB based stimulation script by detecting a TTL voltage from the scanner hardware with the onset of MB-SWIFT MRI pulse sequence (Lehto et al., 2017a). Analog high-pass filters with cut-off frequencies of 0.4 Hz (A-M Systems; Carlsborg, WA, United States) were attached to the outputs of the stimulus-isolators to remove DC drift in the stimulus-isolator output voltages. The stimulus isolators were connected to the electrodes via three 10 m coaxial cables (RG223/U; Pasternack Enterprises, Irvine, CA, United States) and routed through a radiofrequency low-pass filter plate into the MRI scanner Faraday cage to reduce radiofrequency noise of the MRI acquisition. The ends of the three coaxial cables were stripped exposing the shielding and the center conductor. The shielding was soldered to a small copper plate connected to the aforementioned subcutaneous Ag/AgCl ground electrode. The center conductors were soldered to the electrode connector (PlasticsOne, 335-000; Roanoke, VA, United States). Diagram of the stimulation system is shown in **Figure 1D**.

MRI Data Processing and Analysis

MB-SWIFT images were reconstructed using gridding and iterative fast iterative shrinkage/thresholding algorithm (Beck and Teboulle, 2009) with three iterations. The resulting data were analyzed in SPM8[1] and MATLAB 2013b. The pre-processing included motion correction, smoothing with a [2 2 1] pixel FWHM Gaussian kernel, and coregistration and normalization to an animal without an electrode outside the fMRI group based on FSE images. The general linear model consisted of a block design model convolved with a rat hemodynamic function (Silva et al., 2007) and the baseline. For individual analysis, threshold for statistical significance of the activation maps were set to $p < 10^{-5}$ (family-wise error corrected). Due to the significant interindividual differences and relatively limited size of the cohort, the standard second level analysis as implemented in SPM8 was not performed. Instead, for group analysis the overlap maps were created (Spiridon et al., 2006), where for each voxel, after coregistration and normalization, the fraction of animals with a statistically significant activation at individual level was calculated. Aggregates of MB-SWIFT fMRI data were then obtained in anatomically defined regions of interest (ROIs) drawn manually with Aedes[2] based on a rat brain atlas (Paxinos and Watson, 1998). The ROIs were chosen based on the major clusters found during monopolar IL stimulation in the functionally and anatomically relevant areas according to the main hypothesis and included the IL, NAc, CP, and amygdala (**Figure 2A**). For each ROI and condition, the time series of all voxels in an individual ROI were averaged and the corresponding fMRI response amplitude was assessed by averaging the peak values of the three stimulation periods from the ROI mean time series. On the other hand, the extent of activation was estimated by the number of activated voxels inside the ROIs as calculated from the individual *t*-maps using the individual thresholds for the *t*-values.

Statistical analysis was conducted using one tailed paired *t*-test to compare fMRI amplitudes of monopolar 20 Hz stimulation to those acquired with other frequencies and to compare the OSS angle with the highest mean response to the other stimulation angles. Wilcoxon signed-rank test was used correspondingly to compare the mean number of activated voxels. For one animal OSS angle 90° was missing, and for one animal a single missing frequency dataset (70 Hz) was imputed by the mean of the dataset of other five animals. Correction for multiple comparisons was conducted using false discovery rate (FDR) at ROI level.

After fMRI, rats were sacrificed using a pentobarbital overdose (100 mg/kg; Fatal-Plus, Dearborn, MI, United States). The head was harvested by decapitation and immersion fixed and stored in 10% formalin. The brains were extracted, post-fixed in 10% formalin followed by 10% sucrose. Brains were mounted on to a cryostat for cutting coronal sections at a thickness of 10 μm. Brain tissue sections were placed on to glass slides, and stained with hematoxylin and eosin for visualization of the electrode tract. Finally, confirmation of the implantation of the electrodes into the IL was assessed by light microscopy independently by three experienced researchers.

RESULTS

The electrode tips were verified to be situated in the IL. Responses to the IL stimulation in individual rats are illustrated in **Supplementary Figure 1**. In general, the stimulation activated widespread networks or brain regions known to be connected with the IL. These included the local mFC (PL, IL), medial orbitofrontal cortex, anterior cingulate cortex, anterior insula, olfactory tubercle and piriform cortex, basal forebrain structures (bed nucleus of stria terminalis, substantial innominata, diagonal band of Broca), LS, amygdala (basal and cortical nuclei), ventral hippocampus and entorhinal cortex. In addition, we found a robust activation in NAc, which receives strong projections from PL but not IL. From these, the brain regions with the most robust responses were chosen for the ROI analysis including the IL itself, NAc, CP, LS, and amygdala. The ROI analysis of the fMRI response using different stimulation frequencies (**Figure 2B**) revealed that while the extent of activation did not statistically differ among different frequencies, maximum

[1] http://www.fil.ion.ucl.ac.uk/spm

[2] http://aedes.uef.fi

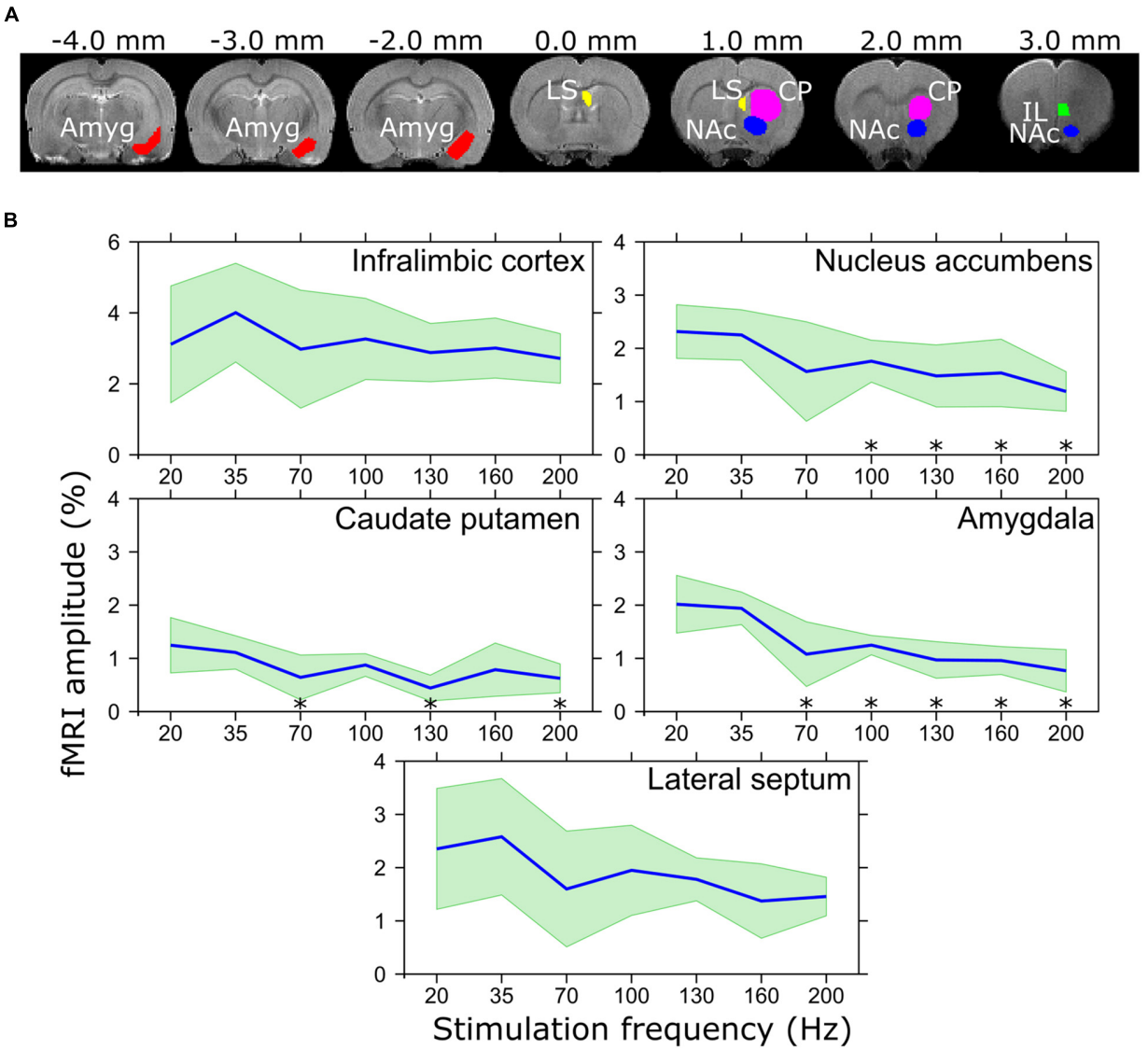

FIGURE 2 | (A) Regions of interest representing the IL, NAc, CP, amygdala, and LS, and **(B)** corresponding BOLD amplitudes in response to different stimulation frequencies. $^{*}p_{FDR} < 0.05$ mean amplitude is smaller than that of 20 Hz stimulation frequency, paired *t*-test. Mean values are shown using blue lines and the standard deviation is shown with green filling.

amplitude of the activation in amygdala was achieved in the lower frequency range (20 and 35 Hz) with a clear declining pattern in higher frequencies and statistically significantly smaller amplitude using 70 ($p_{FDR} = 0.014$), 100 ($p_{FDR} < 0.001$), 130 ($p_{FDR} < 0.001$), 160 ($p_{FDR} < 0.001$), and 200 Hz ($p_{FDR} < 0.001$) as compared to 20 Hz. Similar results were observed in NAc where 100 ($p_{FDR} = 0.048$), 130 ($p_{FDR} = 0.048$), 160 ($p_{FDR} = 0.048$), and 200 Hz ($p_{FDR} = 0.029$) resulted in smaller responses as compared to 20 Hz, while the amplitude in CP was only lower using 70 ($p_{FDR} = 0.037$), 130 ($p_{FDR} = 0.006$), and 200 Hz ($p_{FDR} = 0.029$). In the IL and LS, a similar trend of lower response with higher stimulation frequencies was detected, while no statistically significant differences were found.

In the analysis of OSS-fMRI overlap maps, a clear dependence on the angle of stimulation was observed. Multiple angles led to an activation in the amygdala (**Figure 3A**) and CP, NAc, and LS (**Figure 3B**), with varying extent of activation and a maximum in the range of 150° and 180°. On the other hand, the activation in the mFC in the vicinity of the electrode exhibited no significant OSS dependence (**Figure 3C**). On the individual level, one animal out of the eight exhibited negative responses in the thalamus using 60°, 90°, −120°, and −30° stimulation angles (slice not shown).

The ROI analysis of the OSS-fMRI responses confirmed statistically significant differences in the number of activated pixels observed with different orientations, although differences in amplitude of the fMRI responses did not reach statistical

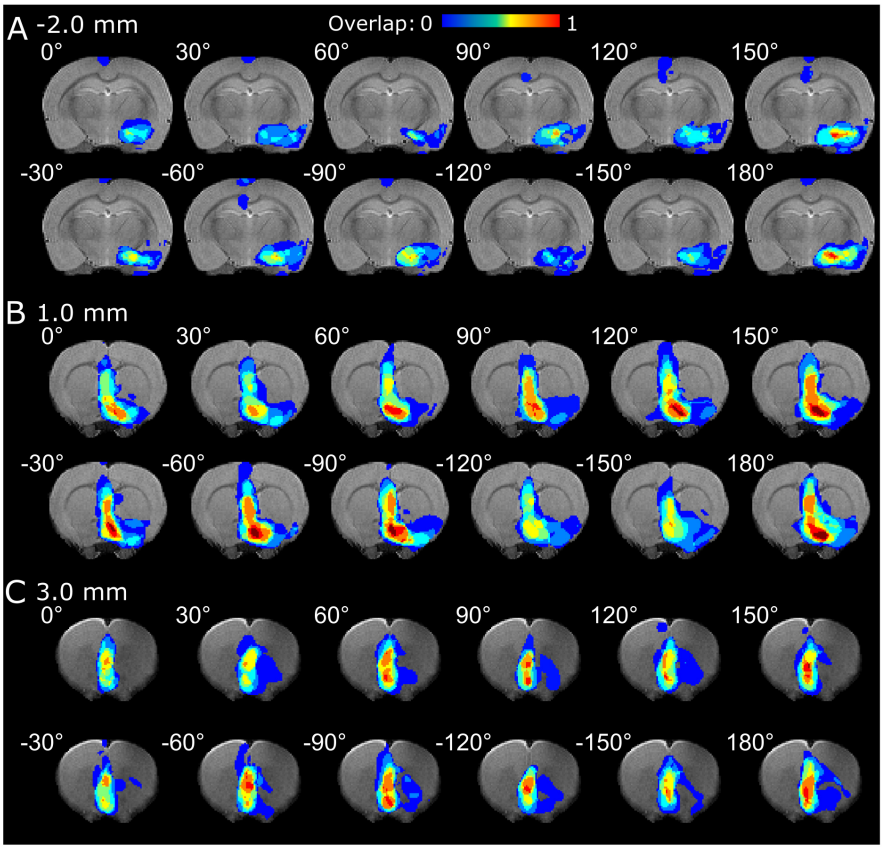

FIGURE 3 | fMRI overlap maps summarizing the responses of the **(A)** amygdala, **(B)** CP, LS and NAc, and **(C)** mFC to OSS of the IL upon different orientations of the OSS.

significance. In particular, the number of activated voxels in different ROIs (**Figure 4**) showed clear orientation dependence in the amygdala, with the main peak at 150° having statistically significantly higher value compared to angles 60° and 90° (p_{FDR} = 0.043), while trending at 30°, 120°, −150°, and −120° (p_{FDR} = 0.051). Maximum response at 150° showed 89 ± 59 activated voxels whereas minimum at 60° had 23 ± 27 activated voxels. Standard deviation of the number of activated voxels was also clearly higher at the angle of −60°, indicating inter-animal differences in response to OSS. Although OSS led to a clear trend of orientation dependence of the activation, no statistically significant differences were reached in CP (0°, 60°–120°, −90°, −60°; p_{FDR} = 0.086) or LS (0°–60°, −120°, −60°, −30°; p_{FDR} = 0.086), while the IL and NAc showed virtually no dependence on stimulation angle with no statistically significant differences.

DISCUSSION

The main rationale for the present study was not only to delineate the neural network activated during IL DBS in rats, but also, and more importantly, to investigate an advanced neuromodulation strategy that can exceed standard DBS programming approaches employed in clinical practice. The complexity of virtually all conceivable MDD DBS targets necessitates highly discriminatory modulation of desired, clinically relevant pathways, while ideally evading various high-risk neural circuits.

Rodent IL, a viable correlate of human sgACC (Diorio et al., 1993; Ostrander et al., 2003), has been reported to receive afferent projections from other medial frontal structures, insula, claustrum, basal forebrain (substantia innominata, diagonal band of Broca, LS), midline thalamic nuclei, hypothalamus, basal amygdala, ventral hippocampus, perirhinal and entorhinal cortex and some midline brainstems structures, including the serotonergic raphe nuclei (Hoover and Vertes, 2007). IL sends efferent projections to medial and orbital frontal cortex, insula, olfactory forebrain, basal forebrain (especially to bed nucleus of stria terminalis), medial thalamus, hypothalamus, basal and medial nuclei of amygdala, and parabrachial and solitary nuclei of brainstem (Saper, 1982; Hurley et al., 1991; Vertes, 2004, 2006). This is consistent with the observed pattern of fMRI activation in the present study with two notable exceptions. First, we found a strong activation in NAc which should not receive major projections from IL. This may result from simultaneous activation of nearby PL with strong projections to NAc (Vertes, 2004) or potentially from current spread. Second,

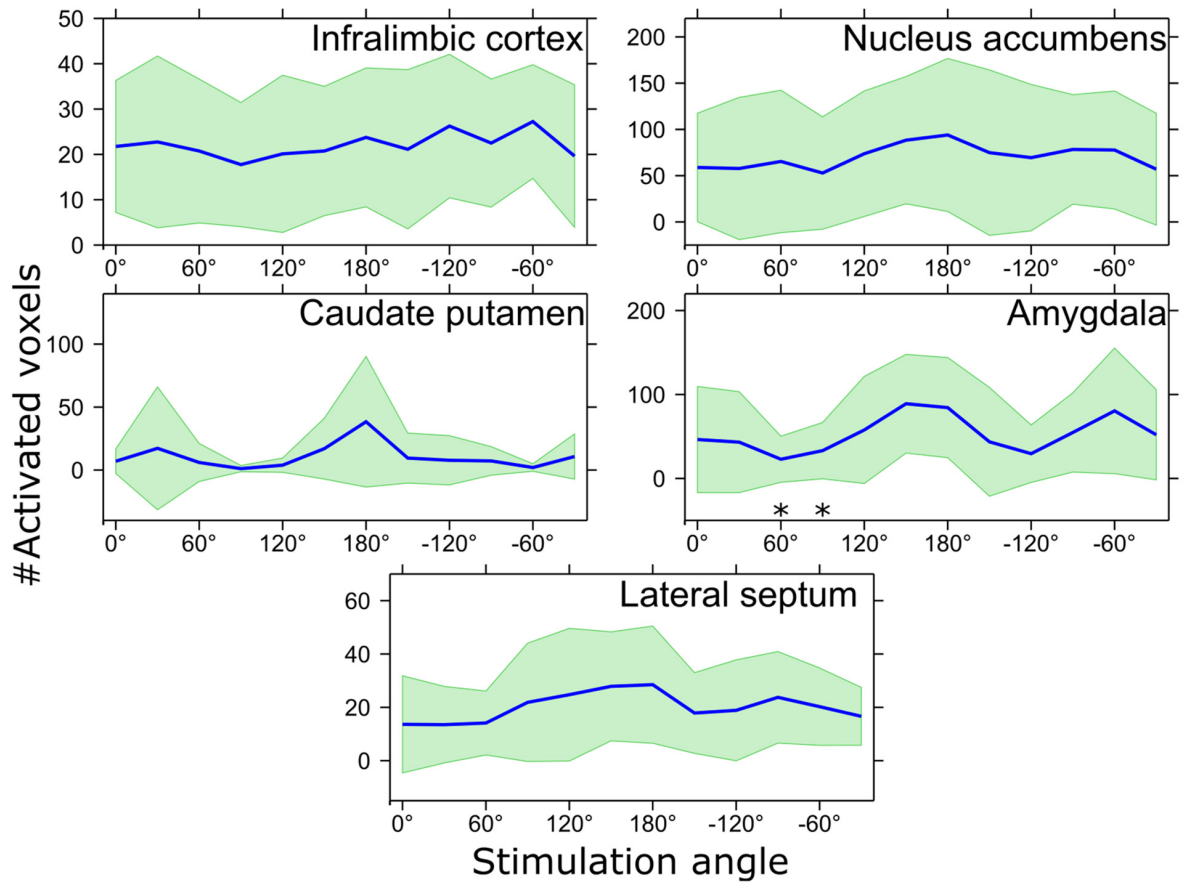

FIGURE 4 | The number of activated voxels in response to various stimulation angles inside the ROIs shown in **Figure 3**. $*p_{FDR} < 0.05$ mean number of activated voxels is smaller than that of 150° stimulation angle, Wilcoxon signed-rank test. Mean values are shown using blue lines and the standard deviation is shown with green filling.

we found no activation in mediodorsal thalamic nucleus which had strong bidirectional connections with IL. Furthermore, the anatomical projections and cytoarchitectural characteristics of IL exhibit significant homologies to clinically relevant human correlates and its stimulation elicits antidepressant-like effects in various behavioral testing paradigms (Hamani et al., 2010b, 2014; Rea et al., 2014), providing both predictive and construct validity of this animal model for translational DBS studies.

Deep brain stimulation effects have been initially explained as a mere functional inactivation of stimulated targets (Benabid et al., 1998; Okun and Vitek, 2004). However, according to the most recent findings, DBS invokes neuromodulation also in brain regions distant from the stimulated target due to the release of various neurotransmitters (Nambu and Chiken, 2015; Florence et al., 2016). These distant effects, specifically selective antidromic stimulation of afferent axons, have even been implicated as the major drivers behind the clinical efficacy of subthalamic nucleus DBS in movement disorders (Gradinaru et al., 2009). Analogous results have been seen as markedly good antidepressant-like effect of IL DBS even after destroying neuronal bodies and sparing axons using ibotenic acid in a rat model (Hamani et al., 2010b). This major role of axons in the DBS effect in IL is of utmost importance for our advanced OSS paradigms capable of angle-dependent axonal stimulation based on the direction of electrical field gradient (Lehto et al., 2017b), thus providing a further dimension for the optimisation and individualisation of DBS parameters.

The exact mechanisms underlying antidepressant effects of various possible DBS targets are still obscure. Partially overlapping but also different neural circuits are likely modulated when stimulation is applied to different common DBS target areas (Hamani et al., 2014). Indeed, IL DBS in rats was shown to reduce anhedonia-like behavior (Rea et al., 2014) and exert anxiolytic effects (Edemann-Callesen et al., 2015), while e.g., DBS of medial forebrain bundle significantly interacts also with the reward system (Edemann-Callesen et al., 2015). Targeting specific DBS parameters, including the stimulation frequency of the individual nodes, advanced electrode configurations (Martens et al., 2011; Tsai et al., 2015) and OSS (Lehto et al., 2017b), might be highly beneficial for eliciting desired outcomes. Even though the therapeutic relevance of the circuits recruited in the present study could not be directly tested

due to the use of normal, healthy rats, and the translational nature of animal model networks to psychiatric disorders is also indirect, preclinical models allow us to appraise the activation patterns specific to advanced DBS paradigms in comparable settings.

While the fMRI results of this initial study on rats are highly promising in demonstrating that novel DBS paradigms can effectively modulate distinct circuitries without changing the stimulation sites, any inference on clinical effects would be an oversimplification, neglecting differences between two distinct mammalian species and uncertain correlation of fMRI-detected responses and the desired clinical effect. Moreover, OSS outcomes demonstrated a non-negligible interindividual variability. The origin of this discrepancy may stem from the deviations in the location of the stimulated area, as well as from inherent minor anatomical variability to be expected even in laboratory conditions. Our implantation precision is in the range of previous DBS studies in IL (Hamani et al., 2010a) and outcomes have similar variability as expected in clinical practice. It should be noted that deflections of even mere 0.5 mm in an inherently complex rat mFC with the volume of 1.7–1.9 mm^3 (Hamani and Nobrega, 2012) unavoidably lead to different responses in individual animals, which could eventually be attenuated using a more advanced, high-density electrode design corresponding to the spatial constraints of the stimulated area and allowing for precise location selection (Tsai et al., 2015). Further caveat must be considered with regard to our results. Bearing in mind the dimensions of the rodent IL and the configuration of our stimulation electrode, including the high currents necessary to overcome fMRI response suppression in anesthetised animals, certain level of current spread seems unavoidable. Notably, comparable current strengths have been successfully implemented in other DBS studies (Dunn et al., 2009; Lai et al., 2014), without any detected electric current related tissue damage. Moreover, the current spill-over to adjacent areas could be of interest as well, since more significant antidepressant-like response was reported in prelimbic (PL) DBS (Hamani et al., 2010a), even though other authors rather associate IL with antidepressant-like functions and relevant projections (Hurley et al., 1991; Gabbott et al., 2003; Edemann-Callesen et al., 2015). Nonetheless, the potential stimulation spread under these current amplitudes prohibits more complex deductions on the specific networks activated during stimulation.

Given the large stimulation spread due to the relatively strong stimulation current and the large size of the electrode in respect to the stimulated area, and high interconnectivity of the regions in the immediate vicinity to the implanted lead, significant OSS effects were not expected in the IL, PL or in the regions with the strongest connections such as NAc, although the trend of sensitivity to OSS was observed in the CP and LS. It was expected that connections to these regions were stimulated at every stimulation angle. On the other hand, the effect of OSS in amygdala was more expected as its connection to the IL is more defined. Previous studies observed the strongest anti-depressant effects in the range of 100–130 Hz (Hamani and Nóbrega, 2010; Lim et al., 2015), however, the aim of using OSS-DBS was to show differential network level responses using fMRI. Hence, monopolar stimulation frequency eliciting the highest fMRI response in the amygdala (20 Hz) was chosen based on preliminary studies. As DBS induces a combination of inhibitory and excitatory effects, strong fMRI response and treatment response do not necessarily go hand in hand. Finally, in our previous work stimulating the corpus callosum (Lehto et al., 2017b), symmetry in the strength of fMRI response was shown between 0° and 180° stimulation angles while in the current study similar effect was not observed. This is likely related to the much more complicated local anatomy of the IL as compared to the corpus callosum and the size of the electrodes used for stimulation. In the corpus callosum, the electrode tip was embedded inside the structure with very well defined fiber orientation in all of its surrounding, while in the IL the orientation distribution and geometry of fibers relative to the electrode is likely much more complex. To better target specific fiber orientations near the electrode, high-density electrode designs are needed with more flexible capability of orienting electric field gradient in space rather than on the plane, which limited in part the effect of the OSS for stimulating IL/PL areas of the brain.

CONCLUSION

Our findings show adjustable activation of the rat limbic system when applying OSS to the IL, a homologue to the human sgACC identified as a DBS target for treating MDD. OSS may offer a new avenue for stimulus parameter optimization using DBS so that only relevant pathways are stimulated, while simultaneously avoiding crossing pathways associated with possible adverse events. In combination with pre-implantation MRI could be invaluable for individualization of DBS treatment in complex brain areas such as the sgACC, where OSS strategies could be beneficial for expanding capabilities of DBS. High-density electrodes with clearly smaller contact size and pitch as compared to the present study are likely needed, as they will allow separating small distinct fiber bundles with different orientations. Finally, although our study is a first demonstration of the capabilities of orientation selective DBS in stimulating areas relevant to MDD, further technological developments of multielectrode arrays and additional studies are required to substantiate the potential of our findings as a direction for treatment therapy of MDD.

AUTHOR CONTRIBUTIONS

LL and PF participated in design of the work, acquisition, analysis, interpretation of data and preparing the manuscript. HL participated in design of the work, acquisition and preparing the manuscript. AS participated in interpretation of data and preparing the manuscript. JS participated in design of the work and preparing the manuscript. MJ participated in analysis, interpretation of data and preparing

the manuscript. LE participated in analysis and preparing the manuscript. WL participated in design of the work, interpretation of data and preparing the manuscript. OG, HT, SMa, and SMi participated in design of the work, analysis, interpretation of data and preparing the manuscript.

FUNDING

This work was supported by the National Institutes of Health U01-NS103569-01, the Center for Magnetic Resonance Research NIH core grant P41-EB015894, NIH R01-NS094206, NIH R01-NS094206, the EU H2020 Marie Skłodowska RISE project #691110 (MICROBRADAM), Erkko foundation (OG), Academy of Finland (AS), and The Emil Aaltonen Foundation (LL). The content is solely the responsibility of the authors and does not necessarily represent the official views of the funding bodies.

ACKNOWLEDGMENTS

The authors are grateful to Lynn Utecht for technical assistance with animal experiments and to Maple Shiao for processing of histological tissue sections.

SUPPLEMENTARY MATERIAL

The Supplementary Material for this article can be found online at: https://www.frontiersin.org/articles/10.3389/fnins.2018.00899/full#supplementary-material

REFERENCES

Bari, A. A., Thum, J., Babayan, D., and Lozano, A. M. (2018). "Current and expected advances in deep brain stimulation for movement disorders," in *Current Concepts in Movement Disorder Management*, eds A. Niranjan, L. D. Lunsford, and R. M. Richardson (Basel: Karger Publishers), 222–229. doi: 10.1159/000481106

Beck, A., and Teboulle, M. (2009). Fast gradient-based algorithms for constrained total variation image denoising and deblurring problems. *IEEE Trans. Image Process.* 18, 2419–2434. doi: 10.1109/TIP.2009.2028250

Benabid, A. L., Benazzouz, A., Hoffmann, D., Limousin, P., Krack, P., and Pollak, P. (1998). Long-term electrical inhibition of deep brain targets in movement disorders. *Mov. Disord.* 13, 119–125. doi: 10.1002/mds.870131321

Bergfeld, I. O., Mantione, M., Hoogendoorn, M. L. C., Ruhé, H. G., Notten, P., Van Laarhoven, J., et al. (2016). Deep brain stimulation of the ventral anterior limb of the internal capsule for treatment-resistant depression. *JAMA Psychiatry* 73, 456–464. doi: 10.1001/jamapsychiatry.2016.0152

Chaturvedi, A., Foutz, T. J., and McIntyre, C. C. (2012). Current steering to activate targeted neural pathways during deep brain stimulation of the subthalamic region. *Brain Stimul. Basic Transl. Clin. Res. Neuromodul.* 5, 369–377. doi: 10.1016/j.brs.2011.05.002

Diorio, D., Viau, V., and Meaney, M. J. (1993). The role of the medial prefrontal cortex (cingulate gyrus) in the regulation of hypothalamic-pituitary-adrenal responses to stress. *J. Neurosci.* 13, 3839–3847. doi: 10.1523/JNEUROSCI.13-09-03839.1993

Dougherty, D. D., Rezai, A. R., Carpenter, L. L., Howland, R. H., Bhati, M. T., O'Reardon, J. P., et al. (2015). A randomized sham-controlled trial of deep brain stimulation of the ventral capsule/ventral striatum for chronic treatment-resistant depression. *Biol. Psychiatry* 78, 240–248. doi: 10.1016/j.biopsych.2014.11.023

Dunn, J. F., Tuor, U. I., Kmech, J., Young, N. A., Henderson, A. K., Jackson, J. C., et al. (2009). Functional brain mapping at 9.4 T using a new MRI-compatible electrode chronically implanted in rats. *Magn. Reson. Med.* 61, 222–228. doi: 10.1002/mrm.21803

Edemann-Callesen, H., Voget, M., Empl, L., Vogel, M., Wieske, F., Rummel, J., et al. (2015). Medial forebrain bundle deep brain stimulation has symptom-specific anti-depressant effects in rats and as opposed to ventromedial prefrontal cortex stimulation interacts with the reward system. *Brain Stimul.* 8, 714–723. doi: 10.1016/j.brs.2015.02.009

Florence, G., Sameshima, K., Fonoff, E. T., and Hamani, C. (2016). Deep brain stimulation: more complex than the inhibition of cells and excitation of fibers. *Neuroscientist* 22, 332–345. doi: 10.1177/1073858415591964

Gabbott, P. L. A., Warner, T. A., Jays, P. R. L., and Bacon, S. J. (2003). Areal and synaptic interconnectivity of prelimbic (area 32), infralimbic (area 25) and insular cortices in the rat. *Brain Res.* 993, 59–71. doi: 10.1016/j.brainres.2003.08.056

Gradinaru, V., Mogri, M., Thompson, K. R., Henderson, J. M., and Deisseroth, K. (2009). Optical deconstruction of parkinsonian neural circuitry. *Science* 324, 354–359. doi: 10.1126/science.1167093

Greenberg, B. D., Malone, D. A., Friehs, G. M., Rezai, A. R., Kubu, C. S., Malloy, P. F., et al. (2006). Three-year outcomes in deep brain stimulation for highly resistant obsessive–compulsive disorder. *Neuropsychopharmacology* 31, 2384–2393. doi: 10.1038/sj.npp.1301165

Hamani, C., Amorim, B. O., Wheeler, A. L., Diwan, M., Driesslein, K., Covolan, L., et al. (2014). Deep brain stimulation in rats: different targets induce similar antidepressant-like effects but influence different circuits. *Neurobiol. Dis.* 71, 205–214. doi: 10.1016/j.nbd.2014.08.007

Hamani, C., Diwan, M., Isabella, S., Lozano, A. M., and Nobrega, J. N. (2010a). Effects of different stimulation parameters on the antidepressant-like response of medial prefrontal cortex deep brain stimulation in rats. *J. Psychiatr. Res.* 44, 683–687. doi: 10.1016/j.jpsychires.2009.12.010

Hamani, C., Diwan, M., Macedo, C. E., Brandão, M. L., Shumake, J., Gonzalez-Lima, F., et al. (2010b). Antidepressant-like effects of medial prefrontal cortex deep brain stimulation in rats. *Biol. Psychiatry* 67, 117–124. doi: 10.1016/j.biopsych.2009.08.025

Hamani, C., Mayberg, H., Stone, S., Laxton, A., Haber, S., and Lozano, A. M. (2011). The subcallosal cingulate gyrus in the context of major depression. *Biol. Psychiatry* 69, 301–308. doi: 10.1016/j.biopsych.2010.09.034

Hamani, C., and Nóbrega, J. N. (2010). Deep brain stimulation in clinical trials and animal models of depression. *Eur. J. Neurosci.* 32, 1109–1117. doi: 10.1111/j.1460-9568.2010.07414.x

Hamani, C., and Nobrega, J. N. (2012). Preclinical studies modeling deep brain stimulation for depression. *Biol. Psychiatry* 72, 916–923. doi: 10.1016/j.biopsych.2012.05.024

Heidbreder, C. A., and Groenewegen, H. J. (2003). The medial prefrontal cortex in the rat: evidence for a dorso-ventral distinction based upon functional and anatomical characteristics. *Neurosci. Biobehav. Rev.* 27, 555–579. doi: 10.1016/j.neubiorev.2003.09.003

Hoover, W. B., and Vertes, R. P. (2007). Anatomical analysis of afferent projections to the medial prefrontal cortex in the rat. *Brain Struct. Funct.* 212, 149–179. doi: 10.1007/s00429-007-0150-4

Hurley, K. M., Herbert, H., Moga, M. M., and Saper, C. B. (1991). Efferent projections of the infralimbic cortex of the rat. *J. Comp. Neurol.* 308, 249–276. doi: 10.1002/cne.903080210

Idiyatullin, D., Corum, C., Park, J. Y., and Garwood, M. (2006). Fast and quiet MRI using a swept radiofrequency. *J. Magn. Reson.* 181, 342–349. doi: 10.1016/j.jmr.2006.05.014

Idiyatullin, D., Corum, C. A., and Garwood, M. (2015). Multi-Band-SWIFT. *J. Magn. Reson.* 251, 19–25. doi: 10.1016/j.jmr.2014.11.014

Koenigs, M., and Grafman, J. (2009). The functional neuroanatomy of depression: distinct roles for ventromedial and dorsolateral prefrontal cortex. *Behav. Brain Res.* 201, 239–243. doi: 10.1016/j.bbr.2009.03.004

Lai, H.-Y., Younce, J. R., Albaugh, D. L., Kao, Y.-C. J., and Shih, Y.-Y. I. (2014). Functional MRI reveals frequency-dependent responses during deep brain stimulation at the subthalamic nucleus or internal globus pallidus. *Neuroimage* 84, 11–18. doi: 10.1016/j.neuroimage.2013.08.026

Lehto, L. J., Idiyatullin, D., Zhang, J., Utecht, L., Adriany, G., Garwood, M., et al. (2017a). MB-SWIFT functional MRI during deep brain stimulation in rats. *Neuroimage* 159, 443–448. doi: 10.1016/j.neuroimage.2017.08.012

Lehto, L. J., Slopsema, J. P., Johnson, M. D., Shatillo, A., Teplitzky, B. A., Utecht, L., et al. (2017b). Orientation selective deep brain stimulation. *J. Neural Eng.* 14:016016. doi: 10.1088/1741-2552/aa5238

Lim, L. W., Prickaerts, J., Huguet, G., Kadar, E., Hartung, H., Sharp, T., et al. (2015). Electrical stimulation alleviates depressive-like behaviors of rats: investigation of brain targets and potential mechanisms. *Transl. Psychiatry* 5:e535. doi: 10.1038/tp.2015.24

Martens, H. C. F., Toader, E., Decré, M. M. J., Anderson, D. J., Vetter, R., Kipke, D. R., et al. (2011). Spatial steering of deep brain stimulation volumes using a novel lead design. *Clin. Neurophysiol.* 122, 558–566. doi: 10.1016/j.clinph.2010.07.026

Morishita, T., Fayad, S. M., Higuchi, M. A., Nestor, K. A., and Foote, K. D. (2014). Deep brain stimulation for treatment-resistant depression: systematic review of clinical outcomes. *Neurotherapeutics* 11, 475–484. doi: 10.1007/s13311-014-0282-1

Nambu, A., and Chiken, S. (2015). "Mechanism of DBS: inhibition, excitation, or disruption?" in *Deep Brain Stimulation for Neurological Disorders*, ed. T. Itakura (Berlin: Springer), 13–20.

Okun, M. S., and Vitek, J. L. (2004). Lesion therapy for Parkinson's disease and other movement disorders: update and controversies. *Mov. Disord.* 19, 375–389. doi: 10.1002/mds.20037

Ostrander, M. M., Richtand, N. M., and Herman, J. P. (2003). Stress and amphetamine induce Fos expression in medial prefrontal cortex neurons containing glucocorticoid receptors. *Brain Res.* 990, 209–214. doi: 10.1016/j.brainres.2003.07.001

Paxinos, G., and Watson, C. (1998). *The Rat Brain Atlas in Stereotaxic Coordinates*. San Diego, CA: Academic Press.

Rattay, F. (1989). Analysis of models for extracellular fiber stimulation. *IEEE Trans. Biomed. Eng.* 36, 676–682. doi: 10.1109/10.32099

Rea, E., Rummel, J., Schmidt, T. T., Hadar, R., Heinz, A., Mathé, A. A., et al. (2014). Anti-anhedonic effect of deep brain stimulation of the prefrontal cortex and the dopaminergic reward system in a genetic rat model of depression: an intracranial self-stimulation paradigm study. *Brain Stimul.* 7, 21–28. doi: 10.1016/j.brs.2013.09.002

Saper, C. B. (1982). Convergence of autonomic and limbic connections in the insular cortex of the rat. *J. Comp. Neurol.* 210, 163–173. doi: 10.1002/cne.902100207

Silva, A. C., Koretsky, A. P., and Duyn, J. H. (2007). Functional MRI impulse response for BOLD and CBV contrast in rat somatosensory cortex. *Magn. Reson. Med.* 57, 1110–1118. doi: 10.1002/mrm.21246

Spiridon, M., Fischl, B., and Kanwisher, N. (2006). Location and spatial profile of category-specific regions in human extrastriate cortex. *Hum. Brain Mapp.* 27, 77–89. doi: 10.1002/hbm.20169

Takagishi, M., and Chiba, T. (1991). Efferent projections of the infralimbic (area 25) region of the medial prefrontal cortex in the rat: an anterograde tracer PHA-L study. *Brain Res.* 566, 26–39. doi: 10.1016/0006-8993(91)91677-S

Tsai, D., John, E., Chari, T., Yuste, R., and Shepard, K. (2015). High-channel-count, high-density microelectrode array for closed-loop investigation of neuronal networks. *Conf. Proc. IEEE Eng. Med. Biol. Soc.* 2015, 7510–7513. doi: 10.1109/EMBC.2015.7320129

Vertes, R. P. (2004). Differential projections of the infralimbic and prelimbic cortex in the rat. *Synapse* 51, 32–58. doi: 10.1002/syn.10279

Vertes, R. P. (2006). Interactions among the medial prefrontal cortex, hippocampus and midline thalamus in emotional and cognitive processing in the rat. *Neuroscience* 142, 1–20. doi: 10.1016/j.neuroscience.2006.06.027

Warden, D., Rush, A. J., Trivedi, M. H., Fava, M., and Wisniewski, S. R. (2007). The STAR*D project results: a comprehensive review of findings. *Curr. Psychiatry Rep.* 9, 449–459. doi: 10.1007/s11920-007-0061-3

Widge, A. S., Deckersbach, T., Eskandar, E. N., and Dougherty, D. D. (2016). Deep brain stimulation for treatment-resistant psychiatric illnesses: what has gone wrong and what should we do next? *Biol. Psychiatry* 79, e9–e10. doi: 10.1016/j.biopsych.2015.06.005

Youngerman, B. E., and Sheth, S. A. (2017). Deep brain stimulation for treatment-resistant depression: optimizing interventions while preserving valid trial design. *Ann. Transl. Med.* 5(Suppl. 1):S1. doi: 10.21037/atm.2017.03.40

Conflict of Interest Statement: The authors declare that the research was conducted in the absence of any commercial or financial relationships that could be construed as a potential conflict of interest.

frontiers in Neural Circuits

REVIEW
published: 08 May 2019
doi: 10.3389/fncir.2019.00034

Myelin and Modeling: Bootstrapping Cortical Microcircuits

Robert Turner[1,2,3]*

[1]Department of Neurophysics, Max Planck Institute for Human Cognitive and Brain Sciences, Leipzig, Germany, [2]Sir Peter Mansfield Imaging Centre, University of Nottingham, Nottingham, United Kingdom, [3]Spinoza Centre for Neuroimaging, University of Amsterdam, Amsterdam, Netherlands

Histological studies of myelin-stained sectioned cadaver brain and *in vivo* myelin-weighted magnetic resonance imaging (MRI) show that the cerebral cortex is organized into cortical areas with generally well-defined boundaries, which have consistent internal patterns of myelination. The process of myelination is largely driven by neural experience, in which the axonal passage of action potentials stimulates neighboring oligodendrocytes to perform their task. This bootstrapping process, such that the traffic of action potentials facilitates increased traffic, suggests the hypothesis that the specific pattern of myelination (myeloarchitecture) in each cortical area reveals the principal cortical microcircuits required for the function of that area. If this idea is correct, the observable sequential maturation of specific brain areas can provide evidence for models of the stages of cognitive development.

Keywords: brain, myelin, MRI, cortical microcircuitry, develoment, modeling

OPEN ACCESS

Edited by:
Marta Bianciardi,
Massachusetts General Hospital,
Harvard Medical School,
United States

Reviewed by:
Iole Indovina,
Saint Camillus International University of Health and Medical Sciences, Italy
Fabrizio Fasano,
Siemens Healthcare Limited,
United Kingdom

***Correspondence:**
Robert Turner
turner@cbs.mpg.de

Received: *09 March 2019*
Accepted: *25 April 2019*
Published: *08 May 2019*

Citation:
Turner R (2019) Myelin and Modeling: Bootstrapping Cortical Microcircuits. Front. Neural Circuits 13:34. doi: 10.3389/fncir.2019.00034

INTRODUCTION

Mammalian cerebral cortex invariably shows localized functional specialization, such that the performance of specific actions is associated with specific and reproducible patterns of increased and decreased neural activity on a spatial scale of a few millimetres, often organized in larger scale networks across the brain. Anatomically, the cortex comprises relatively distinct areas, on a similar same spatial scale, each with quite uniform cytoarchitecture and myeloarchitecture. These areas form the basis of parcellations such as those of Brodmann (1909), Vogt and Vogt (1919) and many more recent studies (reviewed in Caspers et al., 2013), amounting in human brain to an inventory of perhaps 200 cortical areas which are distinguishable in every normal brain. Studies of chemoarchitecture (reviewed in Palomero-Gallagher and Zilles, 2018), using staining and autoradiographic techniques specific to particular neuroreceptors, also reveal sharply bounded cortical areas. For some simple tasks, such as visual (Bridge et al., 2005) and auditory (Dick et al., 2012; De Martino et al., 2015) perception, good congruence has been observed between the anatomically and functionally defined boundaries of the relevant cortical areas, and these boundaries often coincide with chemoarchitectonic boundaries. In describing their hybrid cortical parcellation scheme, Glasser and Van Essen (2011) furthermore assert that the boundaries they observe, using a crude magnetic resonance imaging (MRI) measure of cortical myelination, coincide with those they derive from maps of functional connectivity in the so-called "resting state," in those cortical regions where

both types of boundary are clearly definable. For a more quantitative MRI measure of myelin, see Geyer et al. (2011), Stüber et al. (2014) and Callaghan et al. (2015).

The simple question naturally arises: what is special about each cortical area? Putting it another way, does each cortical area have an identifiable particular processing competence? The idea is by no means new that brain function can be explained mechanistically at the systems level (for example, Logothetis et al., 2010; Turner, 2016) and considerable progress has recently been made, with such concepts as voxel encoding (Naselaris et al., 2011) and representational similarity (Diedrichsen and Kriegeskorte, 2017) in using functional MRI (fMRI) experiments to identify feature spaces that specific neural architecture may be responsible for parsing.

When axonal fibers have been tracked using chemical tracing techniques, or diffusion-weighted MRI, it has been established that the connectivity of some areas is dominated by a particular set of input or output pathways (Felleman and Van Essen, 1991). However, recent work by Han et al. (2018) has demonstrated that even in primary visual cortex, the most strikingly specialized cortical area, neurons make a wide range of connections to other cortical and subcortical regions. It would be surprising if other cortical areas had simpler connectivity. Such repertoires of long-range connections shared as a connectional fingerprint (Gorbach et al., 2011) within any particular area and established during the later stages of gestation, may explain the relative uniformity of cellular architecture within each cortical area. The cytoarchitecture characteristic of a particular cortical area is also genetically prescribed during early development (Burt et al., 2018; Gomez et al., 2018; Wen et al., 2018), as neuronal cell bodies of various types find their layer-dependent destinations at the end of their long traverse from their birthplaces. Recent work by Burt et al. (2018) found a close resemblance between MRI-based myelin maps of the cortex (which reliably index the cortical functional hierarchy) and the dominant pattern of transcriptomic variation across the cortex. Gradients in the profiles of gene expression could be related to microcircuit function and neuropsychiatric disorders.

But the functionality of neurons within a cortical area must critically depend on the pattern of connections local to that area—connections which are formed, re-formed and consolidated throughout an organism's life—in other words, its microcircuitry. While for some purposes a "canonical microcircuit" (Shipp, 2007) can crudely represent the intracortical wiring diagram, there is considerable diversity of cyto- and myeloarchitecture across the cortex, which may well provide a key to much improved modeling of brain function.

At stake is a continuing controversy in systems neuroscience, with qualitatively different approaches to cognitive modeling and its plausibility in regard to empirical evidence. In a recent article, Turkheimer et al. (2019) argue as follows. "Drawing on the epistemological literature, we observe that due to their loose mechanistic links with the underlying biology, models based on strong forms of emergence (such as those of Friston, using the idea of free energy) are at risk of metaphysical implausibility. This, in practical terms, translates into the over-determination that occurs when the proposed model becomes only one of a large set of possible explanations for the observable phenomena. On the other hand, computational models that start from biologically plausible elementary units, hence are weakly emergent, are not limited by ontological faults and, if scalable and able to realistically simulate the hierarchies of brain output, represent a powerful vehicle for future neuroscientific research programmes." Research springing from the proposals in the present article may provide a firmly grounded ontology for realistic modeling of brain function.

I address the question whether cortical microcircuits can be defined and differentiated using the mesoscopic tools of MRI, and thus investigated as they develop *in vivo*. The argument rests on the key histological observations of Smith (1907), Vogt and Vogt (1919), Flechsig (1920), and those of more recent researchers using MRI to quantitatively assess the distribution of myelin in the cerebral cortex (Geyer et al., 2011; Glasser and Van Essen, 2011; Lutti et al., 2014). The fundamental points are: (a) myelination is generally driven by a neuron's experience; (b) it is only once the relevant axons have reached an appropriate level of myelination that cortical microcircuits can be considered to be consolidated, and thus available for routine later use; and (c) the distribution of myelin in the white matter and cerebral cortex is observable *in vivo* with a spatial resolution of about 300 microns using MRI techniques at high magnetic field.

BENEFITS OF MYELINATION

It is worth listing the advantages conferred by the myelination of axons, an expedient evolved hundreds of millions of years ago and first noted in cartilaginous fish.

Perhaps most importantly, myelination speeds up the conduction velocity of action potentials by 10–50-fold for an axon of a given diameter, by enabling salutatory conduction (reviewed in Nave and Werner, 2014). It also makes transmission of action potentials more efficient, increases robustness of axons (Staal and Vickers, 2011), enhances the arrival synchrony of action potentials, reduces electrical crosstalk between axons and other nearby neurites (Hull et al., 2015), enables neural regeneration after damage (Jessen and Mirsky, 2016), and, last but not least, myelination suppresses synaptic plasticity in gray matter by inhibiting neurite growth (Lozano et al., 1995; Thallmair et al., 1998) and preventing the formation of synaptic contacts on already-myelinated axons (Braitenberg, 1962).

It is this final property of myelination, well discussed by Glasser et al. (2014), that is of greatest relevance in the present work. It is reasonable to suppose that in gray matter the axons that become myelinated are those which are most important in providing dedicated cortical microcircuits. Myelination confers durability and reliability, the basic requirements for the observed specialization of function. Study of the variations in myeloarchitecture across the cortex may thus provide unique insights into the specific competencies of different cortical areas. Before such variations are discussed,

some points need to be made regarding how myelination comes about.

THE PROCESS OF MYELINATION

The main networks of peripheral nerves and neurons are established during gestation, but in humans at birth very few of the axons in the brain are already myelinated (Flechsig, 1920), mostly in the optic radiation and the cerebrospinal tract. Brain tissue is rich in oligodendrocyte precursor cells, which transform into mature oligodendrocytes when appropriately stimulated, and proceed to wrap adjacent axons with a sheet of myelin (Snaidero et al., 2014), which may be up to about 16 layers thick. For a given oligodendrocyte and local stretch of axon, this process takes about 5 h (Czopka et al., 2013) and the oligodendrocyte involved generally continues to support the myelin sheath that it has generated until the neuron concerned dies from damage or old age (Yeung et al., 2014).

By adulthood, most white matter axons are myelinated, although a few unmyelinated axons can still be found even in early-myelinated axonal bundles such as the optic radiation, and some WM regions, such as the prefrontal lobes, are slow to mature in human brains (Giedd et al., 2015) reaching their plateau myelination level in people more than 30 years old (Yeatman et al., 2014). Short association fiber bundles, including U-fibers, are generally unmyelinated at birth and become myelinated in a well-defined order (Brody et al., 1987; Kinney et al., 1988). The topic of white matter maturation is well reviewed by Dubois et al. (2014). In a similar way, gray matter axons are progressively myelinated (Guillery, 2005; Lebenberg et al., 2019) cortical area by area.

Extensive recent research has focused on the mechanism of myelination, especially on its relationship to neural activity (well reviewed in Chorghay et al., 2018; Almeida and Lyons, 2017). Oligodendrocytes commence the myelination of a nearby axon when: (a) the axon has a larger diameter than roughly 0.5 micrometres (Nave and Werner, 2014); and/or (b) a sufficient number of action potentials have passed along the unmyelinated axon. The passage of action potentials itself can promote an increase of axon diameter (Costa et al., 2018) so that activity might be ultimately considered the primary driver of myelination. Once an axon is myelinated, several mechanisms are available to fine-tune the conduction velocity, a control needed to ensure the arrival-time synchrony of action potentials at synaptic destinations. These mechanisms include the axon diameter (Chéreau et al., 2017), myelin thickness (Rushton, 1951; Waxman, 1975; Campbell et al., 2018), length of continuous axonal segment that is wrapped (Rushton, 1951; Brill et al., 1977), as well as the nodal geometry itself (Arancibia-Cárcamo et al., 2017).

In the light of these findings, it can be fairly claimed that neural experience shapes the patterns of myelination that develop as a brain matures (Hill et al., 2018; Hughes et al., 2018; Stedehouder et al., 2018) and learns new skills (McKenzie et al., 2014; Xiao et al., 2016). It follows that the neural circuits which are thus preferentially constructed, as self-organizing networks, are requisite for the appropriate performance of the specific brain area where they are located. Because myelination protects the axons included in these circuits from additional synaptic connections and renders them more durable, their configuration may provide clues regarding the transformational operations that each brain area is equipped to perform.

MYELOARCHITECTURE

The surprisingly sparse histological literature on myeloarchitecture has been brilliantly reviewed by Nieuwenhuys (2013) and Nieuwenhuys et al. (2015). Much of the most careful and detailed histological work was performed by Oscar and Cecile Vogt and their team between 1905 and 1955, although a significant number of their publications have not yet been translated from their original German. By creating a feature-based terminology, the Vogts were able unambiguously to discriminate cortical areas from each other and claimed that the boundaries they discovered were sharp. This confirmed Elliot Smith's observation (1907) that "there is a very widespread belief that the characters of one area merge gradually and imperceptibly into those of the neighboring areas, but this is entirely mistaken. The changes in structure occur with the utmost abruptness so that it is possible to determine with absolute precision the exact boundaries of each area. If the reader needs convincing of the accuracy of this statement let him cut a fresh brain at right angles to the calcarine, intraparietal (any part), central, inferior frontal, or parallel sulci, and he will find all the confirmation that is necessary." Recent work by Nieuwenhuys et al. (2015) and Nieuwenhuys and Broere (2017) has transferred the drawings of myeloarchitectonic areas made by the Vogts and their team to the modern Montreal Neurological Institute template brain (Colin27).

Even a cursory examination of a cadaver human brain section (**Figure 1A**) stained using the Gallyas technique (Gallyas, 1979) for myelin demonstrates the strength of the Vogts' claim. Here, several distinct gray matter areas are easily distinguishable by eye, as described by Clarke and Miklossy (1990), with boundaries which are sharp compared with the cortical thickness, by the density and distribution of the cortical myelin—even allowing for the variations of the angle between the cutting plane and the cortical sheet. **Figure 2A** shows two cortical areas that are easily identifiable in this section. Lacking complete deformable 3D atlases of human brain myeloarchitecture, it is not yet possible to match these sections precisely.

Most of the myelinated axonal fibers in gray matter are radial or horizontal (see **Figure 3**). Radial fibers emerge from the white matter with a myelin sheath that can extend as far as cytoarchitectonic Layer II (depending on cortical area). In some areas, such as motor cortex, these fibers are strikingly bunched into groups of 12–16 axons. Horizontal fibers are mostly clustered into the two bands of Baillarger (1840) lying in cortical Layers IV and V, and in the Exner stripe, in cortical Layer I (Lam and Sherman, 2018; Schuman et al., 2019). The bands of Baillarger, between 100 and 300 micrometres thick and often visible by naked eye in fresh cadaver brain without tissue staining (Smith, 1907), vary in density, thickness and depth, again

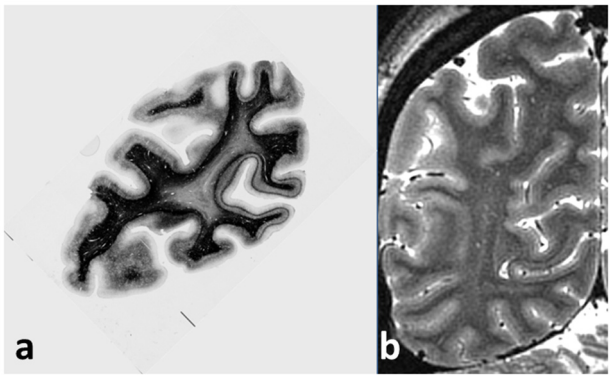

FIGURE 1 | (A) Coronal section of cadaver human brain, stained for myelin using the Gallyas stain. The stria of Gennari, located in the calcarine sulcus, is easily visible on the right, and a cortical area with a pronounced band of Baillarger (probably MT/V5) appears at the left. Note the sharpness of the boundaries between areas with different myeloarchitecture, and the uniformity of the architecture within each area. **(B)** Coronal magnetic resonance imaging (MRI) section of live occipital human brain at 7T, GRASE imaging sequence, 0.5 mm isotropic voxels, obtained at the Leipzig Max Planck Institute for Human Cognitive and Brain Sciences. The same two cortical areas with a visible myelinated layer can easily be picked out, together with other areas also showing a band of Baillarger.

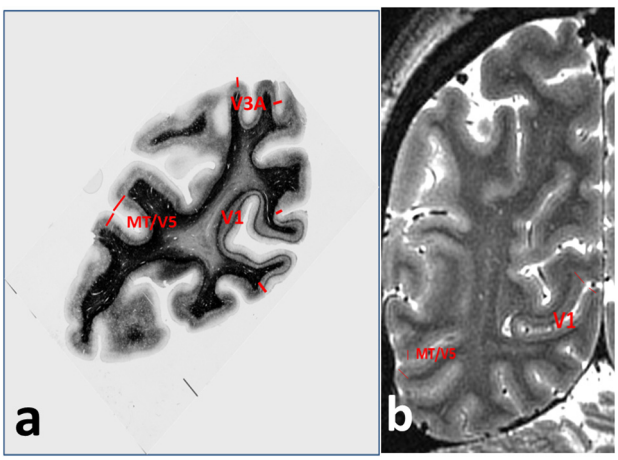

FIGURE 2 | Annotations for **Figure 1**, showing **(A)** cortical areas V1, V3A and MT/V5 on the myelin-stained histological section, and **(B)** V1 and MT/V5 on the MRI section.

depending on cortical area, while the thinner Exner stripe is remarkably uniform across the entire cortical surface.

It is a reasonable assumption that myelinated axons play the most important roles in local neural activity, due to their three advantageous properties of high conduction speed, precise control of conduction speed, and invulnerability. Tonotopy is destroyed in mouse brain primary auditory cortex when the brain is demyelinated by administration of cuprizone (Cerina et al., 2017). The pathways that can comprise important cortical microcircuits fall into four classes. Besides the radial fibers, there are three types of horizontal pathways: the Exner stripe, the bands of Baillarger, and the late-myelinated U-fibers, which lie just outside the gray matter within the surface layer of the white matter. Two crucial questions can be raised in regard to each of these types of connection. The first is, are the fibers carrying inhibitory or excitatory signals? The second question relates to origins and destinations: are the fibers carrying signal traffic internal to each specific cortical area, or signals between separate cortical areas?

Generally speaking, at cortical area boundaries, the bands of Baillarger are discontinuous, changing their cortical depth from one area to the next within a fraction of the cortical thickness (as in **Figure 3**). Plainly, the axons comprising these bands play a much more important role within each cortical area and do not function as inter-areal connections. Less is known regarding the intra-areal and trans-areal connections of the other horizontal connections, although experimental techniques are available to investigate these questions.

IN VIVO VISUALIZATION OF MYELOARCHITECTURE

It was recognized in the initial development of MRI that much of the contrast observed in brain tissue arose from the presence of myelin (for example Bydder and Steiner, 1982). Maps of the MRI parameters proton density and longitudinal relaxation time T1 each show a striking resemblance to myelin-stained sections of the brain. Initially, it was thought that T1 was dominated by the water content of the tissue, but that can be only part of the explanation because the fractional difference of T1 between gray and white matter (70%) is much larger than their ratio of water content (15%). NMR studies of model membranes made by Koenig (1991) and others in the 1990s revealed that T1 is strongly dependent on membrane composition. Essentially, the sink with which the spin magnetization of free water equilibrates after radiofrequency excitation, a process defining T1 relaxation, is comprised of the lipid content of the brain. The molecules cholesterol and cerebroside, in which myelin is rich, are particularly effective in T1 relaxation (Koenig, 1991; Kucharczyk et al., 1994). This finding has been confirmed unequivocally in studies (Leuze et al., 2017; Morawski et al., 2018) of the effect of lipid removal from brain tissue using CLARITY (Chung and Deisseroth, 2013) and related techniques. Clearing the lipid content, which includes all of the myelin sheaths except for a skeleton of hydrophilic proteins, entirely removes T1-based contrast between gray and white matter (Leuze et al., 2017). Independently, Stüber et al. (2014) showed that T1 measured in cadaver brain samples showed a linear dependence on myelin content, which was inferred from proton beam microscopy analysis of sections from the same tissue samples.

Although maps of T1 may not provide a fully quantitative measure of myelin content (see Callaghan et al., 2015; O'Muircheartaigh et al., 2019) and indeed depend slightly on the relative angle between axonal fiber direction and the static magnetic field (Knight et al., 2018), T1 is easy to measure accurately and quantitatively *in vivo* (Marques et al., 2010; Lutti et al., 2014), and thus offers itself as a reliable guide (Dubois et al., 2014) to the presence of

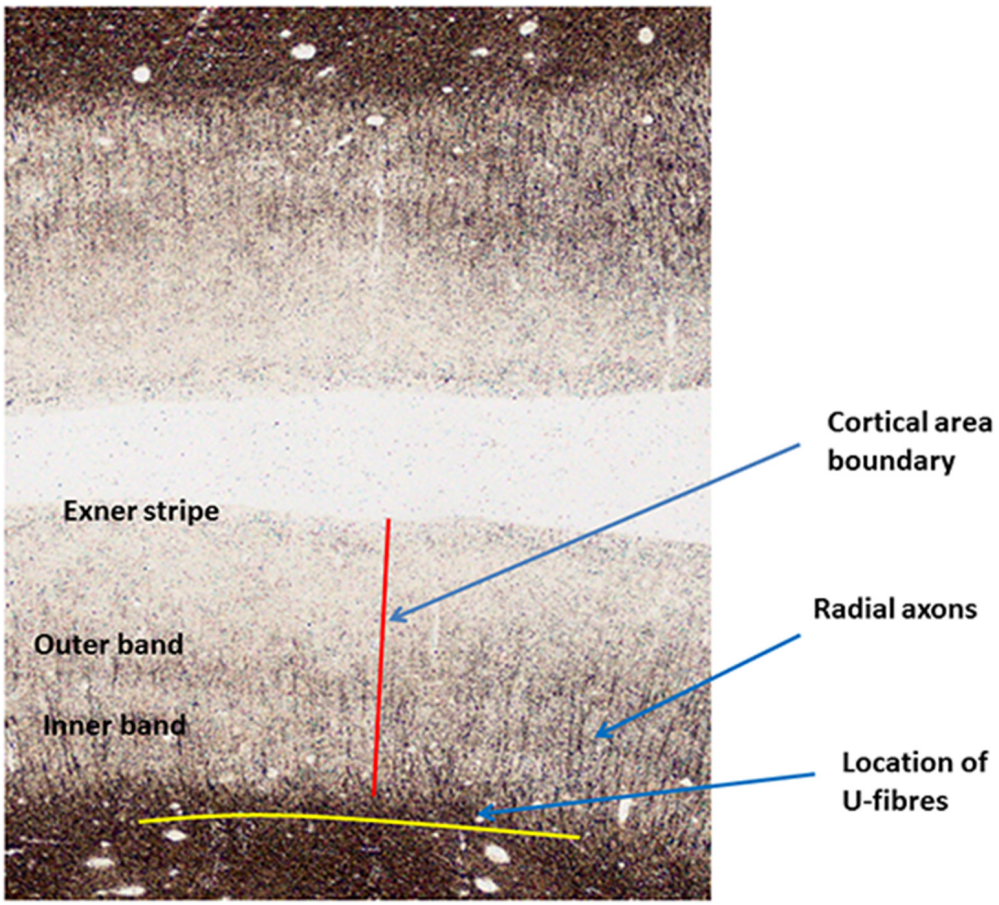

FIGURE 3 | Annotated Gallyas-stained histological section of human parietal cortex. Positions are indicated for the Exner stripe, the bands of Baillarger, radial myelinated axons and U-fibers.

myelin in brain tissue voxels, and as a quantitative means for comparing brains in longitudinal and cross-sectional studies. At magnetic fields of 7T and above, MRI has sufficient signal to noise ratio to resolve structures of less than 300 microns in size in an acceptable imaging time, provided that the effects of subject head motion are mitigated by prospective motion correction methods (e.g., Schulz et al., 2012). This has enabled the depiction of the entire primary visual cortex (Geyer et al., 2011), characterized by the well-defined Stria of Gennari (Gennari, 1782; Trampel et al., 2011), and several other cortical areas with prominent bands of Baillarger (Dinse et al., 2015; Fracasso et al., 2016). **Figure 1B** shows a coronal MRI section of occipital brain with good T1 contrast and 0.5 mm isotropic resolution, obtained in 2011 at 7T field strength. Several areas show cortical layering attributable to bands of Baillarger. Areas corresponding to those identified in the histological section are indicated in **Figure 2B**. At lower field strengths the spatial resolution is insufficient to discriminate cortical areas by means of their intensity profiles but still allows perhaps 15 myeloarchitectonically defined areas to be parcellated (Sereno et al., 2013).

Using the ratio of two MR image acquisitions with inverse T1 intensity weightings (one of these inappropriately named "T2-weighted"), Glasser and Van Essen (2011) were also able to discriminate several cortical areas. Techniques for mapping quantitative T1, and hence myelin density, continue to be rapidly developed by several groups. Of particular promise is a segmented simultaneous multi-slice inversion recovery echo-planar technique, MS-IR-EPI (Sanchez Panchuelo et al., 2018), which may provide 350 micron isotropic resolution images of volunteer subject brains with sharp definition of cortical myelin, given multiple imaging sessions and prospective motion correction to provide sufficient signal to noise ratio.

MYELOARCHITECTONIC AREAS

The most definitive compilation of anatomically distinguishable cortical areas in human brain can be found, as already mentioned, in the work of Nieuwenhuys (2013), who analyzed the findings of Oscar and Cecile Vogt and their team, published in 20 articles between 1910 and 1954. These findings together provided a parcellation of the cortex (here termed the "Vogt parcellation") into a total of 180 distinguishable areas, a figure

reflected by the hybrid parcellation scheme of Glasser et al. (2016). The general picture is as follows: (a) primary brain areas, both sensory and motor, show a greater degree of myelination; (b) higher association areas in superior parietal cortex and prefrontal cortex have strikingly fewer myelinated axons, although no areas are devoid of either radial or horizontal myelinated axons; and (c) in those studies, such as Sanides (1964), which gave parcellations using both cytoarchitecture and myeloarchitecture, a precise congruence of boundaries was found.

In vivo myelin maps of the cortex using MRI are entirely consistent with these histological studies, although due to the lower SNR and poorer spatial resolution of MRI, only a small fraction of the Vogt parcellation has yet been unambiguously determined.

CORTICAL MICROCIRCUITS

In the light of the observation that myelination is driven by a neuron's experience, the uniformity of the myeloarchitecture within a cortical area carries a very interesting implication. A shared pattern of myelination may well imply shared experience. This suggests two linked hypotheses. The first is that each anatomically definable cortical area has a specific set of computational competencies—algorithms by which inputs to an area of cortex are transformed into outputs. The second hypothesis—which goes back to Flechsig's early writings—is that stages in motor and cognitive development are reflected in episodes of more rapid myelination of specific cortical areas, as their axons myelinate and their neurons "come on stream," thus becoming dramatically more effective participants in brain-wide neural networks. Cadaver brain studies of neonatal and infant myelination (Brody et al., 1987; Kinney et al., 1988) showed wide area-specific variations in the onset of myelination in short association fibers. Yeatman et al. (2014) have already shown that the MRI parameter T1, a quantitative measure of myelination, varies between white matter fascicles while remaining relatively uniform within each fascicle, and that each fascicle has a distinguishable longitudinal time course over the life span.

The hard wiring intrinsic to myelination surely results in privileged microcircuits specific to each cortical area. Techniques for modeling the performance of cortical microcircuits are well developed in the computational neuroscience literature (for example Potjans and Diesmann, 2014). Such microcircuits are protected from interference by unwanted additional synapse formation, they are made fast and durable, and the synchrony with which they carry action potentials is amenable to fine tuning using the adjustments available in the number of myelin layers and the internode spacing.

There are still few MRI studies of the relationship between cortical myelination and motor and cognitive performance. Ideally, such studies should be longitudinal, following a cohort of subjects over several years as they acquire new testable skills, such as reading. To resolve the bands of Baillarger, the highest possible spatial resolution would be needed, with 0.5 mm isotropic voxels or better, entailing the use of ultra-high field MRI of 7T or greater.

However, at lower resolution using 1.5 T MRI with 1 mm isotropic voxels, early work by Su et al. (2008) showed that the intensity of turbo-spin-echo images (erroneously described as "T2-weighted') in language areas (including Broca's Area) of the brains of children was correlated with their developmental stage. The results of Grydeland et al. (2013) at 3T using Glasser's non-quantitative measure of myelin are also promising, showing a correlation of apparent net cortical myelination with performance in a speeded cognitive task. Kwon et al. (2018) also show the regional development of cortical myelination, although the inadequate technical standards of their study do not allow many important conclusions to be drawn; they use a non-quantitative myelin measure, unnecessary averaging of brain images across subjects, and excessive spatial smoothing, so that the details specific to actual cortical areas become entirely unobservable. Using MRI cortical maps of T1 in a group of infants between 3 and 21 weeks old, Lebenberg et al. (2019) identified five clusters of cortical areas with distinguishable development trajectories, confirming and extending the findings of Flechsig (1920). Very surprisingly, there is no mention of myeloarchitecture in this article, and no histological sections are shown. The level of superficial white matter myelination was found to correspond well to that of the adjacent cortex, suggesting that parallel processes take place within the cortex and in its white matter connections.

In a comprehensive study involving 484 participants, Grydeland et al. (2019) have explored the trajectory of myelination in more detail, showing waves of intracortical myelinogenesis and age-related demyelination, in which the age at which a plateau was reached was found to vary across the cortex. Age at peak growth had a bimodal distribution comprising a pre-pubertal wave of myelination in primary sensory and motor cortices, and a post-pubertal wave in association, insular and limbic cortices. The MR image resolution was insufficient in this study to allow greater specificity regarding the myeloarchitectonic areas involved in each of these waves.

A recent study (Andrews et al., 2017) examined differences in tissue contrast between gray and white matter in 98 adults diagnosed with autism spectrum disorder (ASD), and 98 typically developing controls. Although the authors were reticent regarding the interpretation of their data, the results indicated quite consistent hypermyelination of several cortical areas, mainly in the medial prefrontal region and in the ventral lateral temporal lobe. This suggests that a fundamental feature of autism is the premature maturation of a range of cortical microcircuits which cannot later be properly adapted for the processes required in social communication. This idea, which might provide further insights into the private world of the autistic brain, and indeed other refractory disorders that might be associated with structural slow learning processes, could be investigated using functional imaging that explored not only the responses to basic stimuli, but also feature spaces, especially the semantic feature space, and related this to the abnormalities in cortical myelination. Again, in the Andrews study, the spatial resolution was insufficient to enable the detailed analysis of cortical profiles needed to explore this further.

For evidence regarding the role of myelinated axons in cortical microcircuits, one must, therefore, turn to the relatively scanty cellular-level neuroscience studies using animal models. It is important to distinguish studies of horizontal and radial myelinated cortical axons. The recent work of Micheva et al. (2016) using tracer methods in mouse brain investigated the paths of myelinated horizontal cortical axons, making the important discovery that these interneurons mostly originate in basket cells, stain for parvalbumin, and are primarily inhibitory in their activity. This is inconsistent with earlier speculations that such axons are mainly collateral branches of excitatory axons of pyramidal cells in cortical layer IV (for example Braitenberg, 1962). This work has been replicated by Stedehouder et al. (2017). Micheva makes the crucial point that the myelination of horizontal cortical axons is unlikely to come about purely to increase their conduction velocity, because such axons are relatively short, and myelination would make very little difference to the transit time of an action potential. In corresponding work (2018) in human cortex, with cadaver brain samples from lightly myelinated cortical regions, Micheva et al. (2018) were able to confirm the presence of inhibitory myelinated parvalbumin axons, although with lower density than in mouse brain. It is worth commenting that if these workers had been able to study cortical areas with pronounced bands of Baillarger, they may have found a much higher proportion of inhibitory horizontal myelinated axons.

There has been a recent resurgence of interest in the neural connectivity of cortical Layer I. Here neuronal cell bodies are relatively scarce, and mostly GABA-ergic, but there is a dense neuropil consisting of dendritic arbors of pyramidal cells in deeper layers, and the horizontal myelinated axons of the Exner Stripe. Lam and Sherman (2018) review the scanty literature. In mouse brain, it appears that thalamocortical projections originating in nonspecific "thalamic matrix" nuclei and terminating in Layer I have the generic role of controlling and modulating cortical excitability (Cruikshank et al., 2012), a role which might explain the omnipresence of the Exner Stripe across the entire cortex. The results of Lam and coworkers suggested a wide range of modulatory control of Layer I neurons by metabotropic glutamate receptors and long range subcortical pathways.

Cauller et al. (1998) used a retrograde tracking method to investigate the paths of long horizontal fibers in Layer I of the rat somatosensory cortex, finding an isotropic distribution within the layer. In human cadaver brain primary visual cortex, however, using diffusion-weighted MRI, Leuze et al. (2014) provide evidence that the axons in Layer I have a preferred orientation within the layer, while the deeper myelinated layer known as the Stria of Gennari appears to show no preferential axonal orientation. Thus it remains unknown whether long myelinated fibers within Layer I link separate cortical areas, or form collaterals of thalamocortical axons, or simply serve to provide robust connections within a given cortical area.

In general, cellular neuroscience literature inexplicably fails to comment on the relatively prevalent myelination of horizontal axons lying in Layer I. Similarly, puzzlingly little research has ever been performed in regard to the functional role of the myelination of the axons comprising the horizontal bands of Baillarger, although this myelination is strikingly obvious anatomically, and energetically costly for the oligodendrocytes to produce. Few neuroanatomists have even been willing to speculate on the functional role of the Stria of Gennari in primary visual cortex. This feature, likely to consist largely of parvalbumin inhibitory axons arising from basket cells surrounding Layer IV pyramidal cells (Micheva et al., 2016), would seem to be a prime candidate both for the required "fast wipe" of the primary visual cortex needed to avoid the image streaking and blurring that would otherwise result from saccades, and for the well-established wide-scale center-surround inhibition that is driven by attentional focusing (Shmuel et al., 2006).

The appearance of the radial myelinated cortical axons is also highly characteristic for specific cortical areas (Vogt and Vogt, 1919), as **Figure 1A** clearly illustrates. Rowley et al. (2015) have already used the apparent depth of cortical myelin, visualized in relatively low-resolution MRI scans, as a crude index for cortical parcellation. Higher resolution structural MRI mapping of T1 is likely to provide better data for cortical profiling of myelin concentration, which will enable the histological details of specific myeloarchitectural areas to be associated unambiguously with the observed functional activity of each area in response to imposed tasks (Turner and Geyer, 2014; Turner, 2016).

The length of myelination of radial axons within gray matter is never more than about 2 mm, a small fraction of their typical myelinated length within white matter, so its presence cannot be easily explained by the need for rapid conduction velocity. Could the variability of this distance across cortical areas, together with the prevalence and degree of myelination of horizontal axons, be better explained by the varying needs between cortical areas for privileged microcircuits? To function effectively, some areas may require a high proportion of unmyelinated radial axons that in response to non-recurrent experience can easily participate in temporary synaptic connections to local dendritic arborizations, as needed for transitional computational operations. In mouse brain, many synapses have been observed to form and regress in a dynamic turnover (Loewenstein et al., 2015). On the other hand, other areas, such as primary motor cortex, may need very robustly defined output pathways that must not be modulated by extraneous connections.

CAN THE STUDY OF MYELOARCHITECTURAL DEVELOPMENT BE THE KEY FOR UNDERSTANDING CORTICAL MICROCIRCUITS?

The foregoing remarks suggest the following interlinked research questions:

(1) Can high-resolution quantitative structural MRI (hqsMRI) at ultra-high field show the bands of Baillarger in many cortical areas, and thus provide an extensive structural parcellation?
(2) Does cortical myelination indeed proceed synchronously within each cortical area?

(3) Can hqsMRI track intracortical developmental changes in myelination?
(4) Do onsets or bursts of myelination in specific cortical areas coincide with transitions in cognitive development?
(5) Can components of the feature spaces revealed by machine learning analysis of functional imaging studies (such as voxel encoding Naselaris et al., 2011 or representational similarity Diedrichsen and Kriegeskorte, 2017) be associated with specific cortical areas?
(6) Can the hard wiring defined by the myelination pattern of each cortical area be used to model the operation of that area's particular microcircuits?
(7) Can models based on such area-specific microcircuits predict the observed feature space components of that area?

The functional operation of cortical microcircuits may be experimentally observed using fMRI methods. Following the insights of Felleman and Van Essen (1991) and Callaway (2004), many studies (e.g., Harel et al., 2006) have used blood oxygenation level dependent (BOLD) and vascular space occupancy (VASO) fMRI with sufficiently high resolution to discriminate activity in different layers of the cerebral cortex (for a recent review, see Larkum et al., 2018). Pioneering work in 2010 by Polimeni (personal communication) showed that very high-resolution resting-state fMRI at 7T magnetic field could be used to investigate the correlation between activity in different cortical layers of separate cortical areas (in his work V1 and MT). This inspired later work (e.g., Huber et al., 2017; Trampel et al., 2017) which used layer-dependent fMRI together with experimental paradigms differentially emphasizing input and output activity in the same cortical area, in order to distinguish the roles of cortical input and output layers. Such experiments can infer causal directionality within brain networks at the systems level. Once the insights gained from detailed knowledge of local myeloarchitecture have been incorporated into such fMRI studies, the answers to the list of questions above may provide a dramatic advance in our understanding of human brain function.

AUTHOR CONTRIBUTIONS

RT wrote this entire article.

FUNDING

This work was supported by Max-Planck-Institut für Kognitions- und Neurowissenschaften.

ACKNOWLEDGMENTS

We would like to thank Rudolf Nieuwenhuys for his advice and encouragement in the preparation of this article.

REFERENCES

Almeida, R. G., and Lyons, D. A. (2017). On myelinated axon plasticity and neuronal circuit formation and function. *J. Neurosci.* 37, 10023–10034. doi: 10.1523/JNEUROSCI.3185-16.2017

Andrews, D. S., Avino, T. A., Gudbrandsen, M., Daly, E., Marquand, A., Murphy, C. M., et al. (2017). *In vivo* evidence of reduced integrity of the gray-white matter boundary in autism spectrum disorder. *Cereb. Cortex* 27, 877–887. doi: 10.1093/cercor/bhw404

Arancibia-Cárcamo, I. L., Ford, M. C., Cossell, L., Ishida, K., Tohyama, K., and Attwell, D. (2017). Node of Ranvier length as a potential regulator of myelinated axon conduction speed. *Elife* 6:e23329. doi: 10.7554/eLife.23329

Baillarger, J. (1840). Recherches sur la structure de la couche corticale des circonvolutions du cerveau. *Mem. Acad. R. Med.* 8, 149–183.

Braitenberg, V. (1962). A note on myeloarchitectonics. *J. Comp. Neurol.* 118, 141–156. doi: 10.1002/cne.901180202

Bridge, H., Clare, S., Jenkinson, M., Jezzard, P., Parker, A. J., and Matthews, P. M. (2005). Independent anatomical and functional measures of the V1/V2 boundary in human visual cortex. *J. Vis.* 5, 93–102. doi: 10.1167/5.2.1

Brill, M. H., Waxman, S. G., Moore, J. W., and Joyner, R. W. (1977). Conduction velocity and spike configuration in myelinated fibres: computed dependence on internode distance. *J. Neurol. Neurosurg. Psychiatry* 40, 769–774. doi: 10.1136/jnnp.40.8.769

Brodmann, K. (1909). *Vergleichende Lokalisationslehre der Grosshirnrinde in ihren Prinzipien Dargestellt auf Grund des Zellenbaues.* Leipzig: J. A. Barth.

Brody, B. A., Kinney, H. C., Kloman, A. S., and Gilles, F. H. (1987). Sequence of central nervous system myelination in human infancy. *J. Neuropathol. Exp. Neurol.* 46, 283–301. doi: 10.1097/00005072-198705000-00005

Burt, J. B., Demirtaş, M., Eckner, W. J., Navejar, N. M., Ji, J. L., Martin, W. J., et al. (2018). Hierarchy of transcriptomic specialization across human cortex captured by structural neuroimaging topography. *Nat. Neurosci.* 21, 1251–1259. doi: 10.1038/s41593-018-0195-0

Bydder, G. M., and Steiner, R. E. (1982). NMR imaging of the brain. *Neuroradiology* 23, 231–240.

Callaghan, M. F., Helms, G., Lutti, A., Mohammadi, S., and Weiskopf, N. (2015). A general linear relaxometry model of R1 using imaging data. *Magn. Reson. Med.* 73, 1309–1314. doi: 10.1002/mrm.25210

Callaway, E. M. (2004). Feedforward, feedback and inhibitory connections in primate visual cortex. *Neural. Netw.* 17, 625–632. doi: 10.1016/j.neunet.2004.04.004

Campbell, J. S. W., Leppert, I. R., Narayanan, S., Boudreau, M., Duval, T., Cohen-Adad, J., et al. (2018). Promise and pitfalls of G-ratio estimation with MRI. *Neuroimage* 182, 80–96. doi: 10.1016/j.neuroimage.2017.08.038

Caspers, S., Eickhoff, S. B., Zilles, K., and Amunts, K. (2013). Microstructural grey matter parcellation and its relevance for connectome analyses. *Neuroimage* 80, 18–26. doi: 10.1016/j.neuroimage.2013.04.003

Cauller, L. J., Clancy, B., and Connors, B. W. (1998). Backward cortical projections to primary somatosensory cortex in rats extend long horizontal axons in layer I. *J. Comp. Neurol.* 390, 297–310. doi: 10.1002/(SICI)1096-9861(19980112)390:2%3C297::AID-CNE11%3E3.0.CO;2-V

Cerina, M., Narayanan, V., Göbel, K., Bittner, S., Ruck, T., Meuth, P., et al. (2017). The quality of cortical network function recovery depends on localization and degree of axonal demyelination. *Brain Behav. Immun.* 59, 103–117. doi: 10.1016/j.bbi.2016.08.014

Chéreau, R., Saraceno, G. E., Angibaud, J., Cattaert, D., and Nägerl, U. V. (2017). Superresolution imaging reveals activity-dependent plasticity of axon morphology linked to changes in action potential conduction velocity. *Proc. Natl. Acad. Sci. U S A* 114, 1401–1406. doi: 10.1073/pnas.1607541114

Chung, K., and Deisseroth, K. (2013). CLARITY for mapping the nervous system. *Nat. Methods* 10, 508–513. doi: 10.1038/nmeth.2481

Chorghay, Z., Káradóttir, R. T., and Ruthazer, E. S. (2018). White matter plasticity keeps the brain in tune: axons conduct while glia wrap. *Front. Cell. Neurosci.* 12:428. doi: 10.3389/fncel.2018.00428

Clarke, S., and Miklossy, J. (1990). Occipital cortex in man: organization of callosal connections, related myelo- and cytoarchitecture and putative boundaries of functional visual areas. *J. Comp. Neurol.* 298, 188–214. doi: 10.1002/cne.902980205

Costa, A. R., Pinto-Costa, R., Sousa, S. C., and Sousa, M. M. (2018). The regulation of axon diameter: from axonal circumferential contractility to activity-dependent axon swelling. *Front. Mol. Neurosci.* 11:319. doi: 10.3389/fnmol.2018.00319

Cruikshank, S. J., Ahmed, O. J., Stevens, T. R., Patrick, S. L., Gonzalez, A. N., Elmaleh, M., et al. (2012). Thalamic control of layer 1 circuits in prefrontal cortex. *J. Neurosci.* 32, 17813–17823. doi: 10.1523/JNEUROSCI.3231-12.2012

Czopka, T., Ffrench-Constant, C., and Lyons, D. A. (2013). Individual oligodendrocytes have only a few hours in which to generate new myelin sheaths *in vivo*. *Dev. Cell* 25, 599–609. doi: 10.1016/j.devcel.2013.05.013

De Martino, F., Moerel, M., Xu, J., van de Moortele, P. F., Ugurbil, K., Goebel, R., et al. (2015). High-resolution mapping of myeloarchitecture *in vivo*: localization of auditory areas in the human brain. *Cereb. Cortex* 25, 3394–3405. doi: 10.1093/cercor/bhu150

Dick, F., Tierney, A. T., Lutti, A., Josephs, O., Sereno, M. I., and Weiskopf, N. (2012). *In vivo* functional and myeloarchitectonic mapping of human primary auditory areas. *J. Neurosci.* 32, 16095–16105. doi: 10.1523/JNEUROSCI.1712-12.2012

Diedrichsen, J., and Kriegeskorte, N. (2017). Representational models: a common framework for understanding encoding, pattern-component and representational-similarity analysis. *PLoS Comput. Biol.* 13:e1005508. doi: 10.1371/journal.pcbi.1005508

Dinse, J., Härtwich, N., Waehnert, M. D., Tardif, C. L., Schäfer, A., Geyer, S., et al. (2015). A cytoarchitecture-driven myelin model reveals area-specific signatures in human primary and secondary areas using ultra-high resolution *in vivo* brain MRI. *Neuroimage* 114, 71–87. doi: 10.1016/j.neuroimage.2015.04.023

Dubois, J., Dehaene-Lambertz, G., Kulikova, S., Poupon, C., Hüppi, P. S., and Hertz-Pannier, L. (2014). The early development of brain white matter: a review of imaging studies in fetuses, newborns and infants. *Neuroscience* 276, 48–71. doi: 10.1016/j.neuroscience.2013.12.044

Felleman, D. J., and Van Essen, D. C. (1991). Distributed hierarchical processing in the primate cerebral cortex. *Cereb. Cortex* 1, 1–47. doi: 10.1093/cercor/1.1.1

Flechsig, P. (1920). *Anatomie des Menschlichen Gehirns und Rückenmarks auf Myelogenetischer Grundlage*. Leipzig: G. Thieme.

Fracasso, A., van Veluw, S. J., Visser, F., Luijten, P. R., Spliet, W., Zwanenburg, J. J. M., et al. (2016). Lines of Baillarger *in vivo* and *ex vivo*: myelin contrast across lamina at 7T MRI and histology. *Neuroimage* 133, 163–175. doi: 10.1016/j.neuroimage.2016.02.072

Gallyas, F. (1979). Silver staining of myelin by means of physical development. *Neurol. Res.* 1, 203–209. doi: 10.1080/01616412.1979.11739553

Gennari, F. (1782). *De Peculiari Structura Cerebri Nonnulisque Ejus Morbis*. Parma: Ex Regio.

Geyer, S., Weiss, M., Reimann, K., Lohmann, G., and Turner, R. (2011). Microstructural parcellation of the human cerebral cortex-from Brodmann's post-mortem map to *in vivo* mapping with high-field magnetic resonance imaging. *Front. Hum. Neurosci.* 5:19. doi: 10.3389/fnhum.2011.00019

Giedd, J. N., Raznahan, A., Alexander-Bloch, A., Schmitt, E., Gogtay, N., and Rapoport, J. L. (2015). Child psychiatry branch of the National Institute of Mental Health longitudinal structural magnetic resonance imaging study of human brain development. *Neuropsychopharmacology* 40, 43–49. doi: 10.1038/npp.2014.236

Glasser, M. F., Coalson, T. S., Robinson, E. C., Hacker, C. D., Harwell, J., Yacoub, E., et al. (2016). A multi-modal parcellation of human cerebral cortex. *Nature* 536, 171–178. doi: 10.1038/nature18933

Glasser, M. F., Goyal, M. S., Preuss, T. M., Raichle, M. E., and Van Essen, D. C. (2014). Trends and properties of human cerebral cortex: correlations with cortical myelin content. *Neuroimage* 93, 165–175. doi: 10.1016/j.neuroimage.2013.03.060

Glasser, M. F., and Van Essen, D. C. (2011). Mapping human cortical areas *in vivo* based on myelin content as revealed by T1- and T2-weighted MRI. *J. Neurosci.* 31, 11597–11616. doi: 10.1523/JNEUROSCI.2180-11.2011

Gomez, J., Zhen, Z., and Weiner, K. S. (2018). Human visual cortex is organized along two genetically opposed hierarchical gradients with unique developmental and evolutionary origins. *BioRxiv* doi: 10.1101/495143 [Preprint].

Gorbach, N. S., Schütte, C., Melzer, C., Goldau, M., Sujazow, O., Jitsev, J., et al. (2011). Hierarchical information-based clustering for connectivity-based cortex parcellation. *Front. Neuroinform.* 5:18. doi: 10.3389/fninf.2011.00018

Grydeland, H., Vértes, P. E., Váša, F., Romero-Garcia, R., Whitaker, K., Alexander-Bloch, A. F., et al. (2019). Waves of maturation and senescence in microstructural MRI markers of human cortical myelination over the lifespan. *Cereb. Cortex* 29, 1369–1381. doi: 10.1093/cercor/bhy330

Grydeland, H., Walhovd, K. B., Tamnes, C. K., Westlye, L. T., and Fjell, A. M. (2013). Intracortical myelin links with performance variability across the human lifespan: results from T1- and T2-weighted MRI myelin mapping and diffusion tensor imaging. *J. Neurosci.* 33, 18618–18630. doi: 10.1523/JNEUROSCI.2811-13.2013

Guillery, R. W. (2005). Is postnatal neocortical maturation hierarchical? *Trends Neurosci.* 28, 512–517. doi: 10.1016/j.tins.2005.08.006

Han, Y., Kebschull, J. M., Campbell, R. A. A., Cowan, D., Imhof, F., Zador, A. M., et al. (2018). The logic of single-cell projections from visual cortex. *Nature* 556, 51–56. doi: 10.1038/nature26159

Harel, N., Lin, J., Moeller, S., Ugurbil, K., and Yacoub, E. (2006). Combined imaging-histological study of cortical laminar specificity of fMRI signals. *Neuroimage* 29, 879–887. doi: 10.1016/j.neuroimage.2005.08.016

Hill, R. A., Li, A. M., and Grutzendler, J. (2018). Lifelong cortical myelin plasticity and age-related degeneration in the live mammalian brain. *Nat. Neurosci.* 21, 683–695. doi: 10.1038/s41593-018-0120-6

Huber, L., Handwerker, D. A., Jangraw, D. C., Chen, G., Hall, A., Stüber, C., et al. (2017). High-resolution CBV-fMRI allows mapping of laminar activity and connectivity of cortical input and output in human M1. *Neuron* 96, 1253–1263.e7. doi: 10.1016/j.neuron.2017.11.005

Hughes, E. G., Orthmann-Murphy, J. L., Langseth, A. J., and Bergles, D. E. (2018). Myelin remodeling through experience-dependent oligodendrogenesis in the adult somatosensory cortex. *Nat. Neurosci.* 21, 696–706. doi: 10.1038/s41593-018-0121-5

Hull, M. J., Soffe, S. R., Willshaw, D. J., and Roberts, A. (2015). Modelling the effects of electrical coupling between unmyelinated axons of brainstem neurons controlling rhythmic activity. *PLoS Comput. Biol.* 11:e1004240. doi: 10.1371/journal.pcbi.1004240

Jessen, K. R., and Mirsky, R. (2016). The repair Schwann cell and its function in regenerating nerves. *J. Physiol.* 594, 3521–3531. doi: 10.1113/JP270874

Kinney, H. C., Brody, B. A., Kloman, A. S., and Gilles, F. H. (1988). Sequence of central nervous system myelination in human infancy. *J. Neuropathol. Exp. Neurol.* 47, 217–234. doi: 10.1097/00005072-198805000-00003

Knight, M. J., Damion, R. A., and Kauppinen, R. A. (2018). Observation of angular dependence of T1 in the human white matter at 3T. *Biomed. Spectrosc. Imaging* 7, 125–133. doi: 10.3233/BSI-180183

Koenig, S. H. (1991). Cholesterol of myelin is the determinant of gray-white contrast in MRI of brain. *Magn. Reson. Med.* 20, 285–291. doi: 10.1002/mrm.1910200210

Kucharczyk, W., Macdonald, P. M., Stanisz, G. J., and Henkelman, R. M. (1994). Relaxivity and magnetization transfer of white matter lipids at MR imaging: importance of cerebrosides and pH. *Radiology* 192, 521–529. doi: 10.1148/radiology.192.2.8029426

Kwon, D., Pfefferbaum, A., Sullivan, E. V., and Pohl, K. M. (2018). Regional growth trajectories of cortical myelination in adolescents and young adults: longitudinal validation and functional correlates. *Brain Imaging Behav.* doi: 10.1007/s11682-018-9980-3 [Epub ahead of print].

Lam, Y. W., and Sherman, S. M. (2018). Convergent synaptic inputs to layer 1 cells of mouse cortex. *Eur. J. Neurosci.* doi: 10.1111/ejn.14324 [Epub ahead of print].

Larkum, M. E., Petro, L. S., Sachdev, R. N. S., and Muckli, L. (2018). A perspective on cortical layering and layer-spanning neuronal elements. *Front. Neuroanat.* 12:56. doi: 10.3389/fnana.2018.00056

Lebenberg, J., Mangin, J. F., Thirion, B., Poupon, C., Hertz-Pannier, L., Leroy, F., et al. (2019). Mapping the asynchrony of cortical maturation in the infant brain: a MRI multi-parametric clustering approach. *Neuroimage* 185, 641–653. doi: 10.1016/j.neuroimage.2018.07.022

Leuze, C., Aswendt, M., Ferenczi, E., Liu, C. W., Hsueh, B., Goubran, M., et al. (2017). The separate effects of lipids and proteins on brain MRI contrast

revealed through tissue clearing. *Neuroimage* 156, 412–422. doi: 10.1016/j.neuroimage.2017.04.021

Leuze, C. W., Anwander, A., Bazin, P. L., Dhital, B., Stüber, C., Reimann, K., et al. (2014). Layer-specific intracortical connectivity revealed with diffusion MRI. *Cereb. Cortex* 24, 328–339. doi: 10.1093/cercor/bhs311

Loewenstein, Y., Yanover, U., and Rumpel, S. (2015). Predicting the dynamics of network connectivity in the neocortex. *J Neurosci.* 35, 12535–12544. doi: 10.1523/JNEUROSCI.2917-14.2015

Logothetis, N. K., Augath, M., Murayama, Y., Rauch, A., Sultan, F., Goense, J., et al. (2010). The effects of electrical microstimulation on cortical signal propagation. *Nat. Neurosci.* 13, 1283–1291. doi: 10.1038/nn.2631

Lozano, A. M., Schmidt, M., and Roach, A. (1995). A convenient *in vitro* assay for the inhibition of neurite outgrowth by adult mammalian CNS myelin using immortalized neuronal cells. *J. Neurosci. Methods* 63, 23–28. doi: 10.1016/0165-0270(95)00081-x

Lutti, A., Dick, F., Sereno, M. I., and Weiskopf, N. (2014). Using high-resolution quantitative mapping of R1 as an index of cortical myelination. *Neuroimage* 93, 176–188. doi: 10.1016/j.neuroimage.2013.06.005

Marques, J. P., Kober, T., Krueger, G., van der Zwaag, W., van de Moortele, P. F., and Gruetter, R. (2010). MP2RAGE, a self bias-field corrected sequence for improved segmentation and T1-mapping at high field. *Neuroimage* 49, 1271–1281. doi: 10.1016/j.neuroimage.2009.10.002

McKenzie, I. A., Ohayon, D., Li, H., de Faria, J. P., Emery, B., Tohyama, K., et al. (2014). Motor skill learning requires active central myelination. *Science* 346, 318–322. doi: 10.1126/science.1254960

Micheva, K. D., Chang, E. F., Nana, A. L., Seeley, W. W., Ting, J. T., Cobbs, C., et al. (2018). Distinctive structural and molecular features of myelinated inhibitory axons in human neocortex. *eNeuro* 5:ENEURO.0297-18.2018. doi: 10.1523/ENEURO.0297-18.2018

Micheva, K. D., Wolman, D., Mensh, B. D., Pax, E., Buchanan, J., Smith, S. J., et al. (2016). A large fraction of neocortical myelin ensheathes axons of local inhibitory neurons. *Elife* 5:e15784. doi: 10.7554/eLife.15784

Morawski, M., Kirilina, E., Scherf, N., Jäger, C., Reimann, K., Trampel, R., et al. (2018). Developing 3D microscopy with CLARITY on human brain tissue: towards a tool for informing and validating MRI-based histology. *Neuroimage* 182, 417–428. doi: 10.1016/j.neuroimage.2017.11.060

Naselaris, T., Kay, K. N., Nishimoto, S., and Gallant, J. L. (2011). Encoding and decoding in fMRI. *Neuroimage* 56, 400–410. doi: 10.1016/j.neuroimage.2010.07.073

Nave, K. A., and Werner, H. B. (2014). Myelination of the nervous system: mechanisms and functions. *Annu. Rev. Cell Dev. Biol.* 30, 503–533. doi: 10.1146/annurev-cellbio-100913-013101

Nieuwenhuys, R. (2013). The myeloarchitectonic studies on the human cerebral cortex of the Vogt-Vogt school and their significance for the interpretation of functional neuroimaging data. *Brain Struct. Funct.* 218, 303–352. doi: 10.1007/s00429-012-0460-z

Nieuwenhuys, R., and Broere, C. A. (2017). A map of the human neocortex showing the estimated overall myelin content of the individual architectonic areas based on the studies of adolf hopf. *Brain Struct. Funct.* 222, 465–480. doi: 10.1007/s00429-016-1228-7

Nieuwenhuys, R., Broere, C. A., and Cerliani, L. (2015). A new myeloarchitectonic map of the human neocortex based on data from the Vogt-Vogt school. *Brain Struct. Funct.* 220, 2551–2573. doi: 10.1007/s00429-014-0806-9

O'Muircheartaigh, J., Vavasour, I., Ljungberg, E., Li, D. K. B., Rauscher, A., Levesque, V., et al. (2019). Quantitative neuroimaging measures of myelin in the healthy brain and in multiple sclerosis. *Hum. Brain Mapp.* 40, 2104–3116. doi: 10.1002/hbm.24510

Palomero-Gallagher, N., and Zilles, K. (2018). Cyto- and receptor architectonic mapping of the human brain. *Handb. Clin. Neurol.* 150, 355–387. doi: 10.1016/b978-0-444-63639-3.00024-4

Potjans, T. C., and Diesmann, M. (2014). The cell-type specific cortical microcircuit: relating structure and activity in a full-scale spiking network model. *Cereb. Cortex* 24, 785–806. doi: 10.1093/cercor/bhs358

Rowley, C. D., Bazin, P. L., Tardif, C. L., Sehmbi, M., Hashim, E., Zaharieva, N., et al. (2015). Assessing intracortical myelin in the living human brain using myelinated cortical thickness. *Front. Neurosci.* 9:396. doi: 10.3389/fnins.2015.00396

Rushton, W. A. (1951). A theory of the effects of fibre size in medullated nerve. *J. Physiol.* 115, 101–122. doi: 10.1113/jphysiol.1951.sp004655

Sanchez Panchuelo, R. M., Turner, R., Mougin, O., and Francis, S. (2018). "A 2D multi-shot inversion recovery EPI (MS-IR-EPI) sequence for high spatial resolution T1-mapping at 7T," in *26th Annual Meeting, Paris, Proc. Int. Soc. Magn. Reson. Med.* 60.

Sanides, F. (1964). The cyto-myeloarchitecture of the human frontal lobe and its relation to phylogenetic differentiation of the cerebral cortex. *J. Hirnforsch.* 7, 269–282.

Schulz, J., Siegert, T., Reimer, E., Labadie, C., Maclaren, J., Herbst, M., et al. (2012). An embedded optical tracking system for motion-corrected magnetic resonance imaging at 7T. *MAGMA* 25, 443–453. doi: 10.1007/s10334-012-0320-0

Schuman, B., Machold, R. P., Hashikawa, Y., Fuzik, J., Fishell, G. J., and Rudy, B. (2019). Four unique interneuron populations reside in neocortical layer 1. *J. Neurosci.* 39, 125–139. doi: 10.1523/JNEUROSCI.1613-18.2018

Sereno, M. I., Lutti, A., Weiskopf, N., and Dick, F. (2013). Mapping the human cortical surface by combining quantitative T_1 with retinotopy. *Cereb. Cortex* 23, 2261–2268. doi: 10.1093/cercor/bhs213

Shipp, S. (2007). Structure and function of the cerebral cortex. *Curr. Biol.* 17, R443–R449. doi: 10.1016/j.cub.2007.03.044

Shmuel, A., Augath, M., Oeltermann, A., and Logothetis, N. K. (2006). Negative functional MRI response correlates with decreases in neuronal activity in monkey visual area V1. *Nat. Neurosci.* 9, 569–577. doi: 10.1038/nn1675

Smith, G. E. (1907). A new topographical survey of the human cerebral cortex, being an account of the distribution of the anatomically distinct cortical areas and their relationship to the cerebral sulci. *J. Anat. Physiol.* 41, s237–s254.

Snaidero, N., Möbius, W., Czopka, T., Hekking, L. H., Mathisen, C., Verkleij, D., et al. (2014). Myelin membrane wrapping of CNS axons by PI(3,4,5)P3-dependent polarized growth at the inner tongue. *Cell* 156, 277–290. doi: 10.1016/j.cell.2013.11.044

Staal, J. A., and Vickers, J. C. (2011). Selective vulnerability of non-myelinated axons to stretch injury in an *in vitro* co-culture system. *J. Neurotrauma* 28, 841–847. doi: 10.1089/neu.2010.1658

Stedehouder, J., Brizee, D., Shpak, G., and Kushner, S. A. (2018). Activity-dependent myelination of parvalbumin interneurons mediated by axonal morphological plasticity. *J. Neurosci.* 38, 3631–3642. doi: 10.1523/JNEUROSCI.0074-18.2018

Stedehouder, J., Couey, J. J., Brizee, D., Hosseini, B., Slotman, J. A., Dirven, C. M. F., et al. (2017). Fast-spiking parvalbumin interneurons are frequently myelinated in the cerebral cortex of mice and humans. *Cereb. Cortex* 27, 5001–5013. doi: 10.1093/cercor/bhx203

Stüber, C., Morawski, M., Schäfer, A., Labadie, C., Wähnert, M., Leuze, C., et al. (2014). Myelin and iron concentration in the human brain: a quantitative study of MRI contrast. *Neuroimage* 93, 95–106. doi: 10.1016/j.neuroimage.2014.02.026

Su, P., Kuan, C. C., Kaga, K., Sano, M., and Mima, K. (2008). Myelination progression in language-correlated regions in brain of normal children determined by quantitative MRI assessment. *Int. J. Pediatr. Otorhinolaryngol.* 72, 1751–1763. doi: 10.1016/j.ijporl.2008.05.017

Thallmair, M., Metz, G. A., Z'Graggen, W. J., Raineteau, O., Kartje, G. L., and Schwab, M. E. (1998). Neurite growth inhibitors restrict plasticity and functional recovery following corticospinal tract lesions. *Nat. Neurosci.* 1, 124–131. doi: 10.1038/373

Trampel, R., Bazin, P. L., Pine, K., and Weiskopf, N. (2017). *in vivo* magnetic resonance imaging (MRI) of laminae in the human cortex. *Neuroimage* doi: 10.1016/j.neuroimage.2017.09.037 [Epub ahead of print].

Trampel, R., Ott, D. V., and Turner, R. (2011). Do the congenitally blind have a stria of Gennari? First intracortical insights *in vivo*. *Cereb. Cortex* 21, 2075–2081. doi: 10.1093/cercor/bhq282

Turkheimer, F. E., Hellyer, P., Kehagia, A. A., Expert, P., Lord, L. D., Vohryzek, J., et al. (2019). Conflicting emergences. Weak vs. strong emergence for the modelling of brain function. *Neurosci. Biobehav. Rev.* 99, 3–10. doi: 10.1016/j.neubiorev.2019.01.023

Turner, R. (2016). Uses, misuses, new uses and fundamental limitations of magnetic resonance imaging in cognitive science. *Philos. Trans. R. Soc. Lond. B Biol. Sci.* 371:20150349. doi: 10.1098/rstb.2015.0349

Turner, R., and Geyer, S. (2014). Comparing like with like: the power of knowing where you are. *Brain Connect.* 4, 547–557. doi: 10.1089/brain.2014.0261

Vogt, C., and Vogt, O. (1919). Allgemeinere ergebnisse unserer hirnforschung. *J. Psychol. Neurol.* 25, 279–468.

Waxman, S. G. (1975). Electron-microscopic observations on preterminal fibers in the oculomotor nucleus of the cat. *J. Neurol. Sci.* 26, 395–400. doi: 10.1016/0022-510x(75)90210-5

Wen, J., Goyal, M. S., Astafiev, S. V., Raichle, M. E., and Yablonskiy, D. A. (2018). Genetically defined cellular correlates of the baseline brain MRI signal. *Proc. Natl. Acad. Sci. U S A* 115, E9727–E9736. doi: 10.1073/pnas.1808121115

Xiao, L., Ohayon, D., McKenzie, I. A., Sinclair-Wilson, A., Wright, J. L., Fudge, A. D., et al. (2016). Rapid production of new oligodendrocytes is required in the earliest stages of motor-skill learning. *Nat. Neurosci.* 19, 1210–1217. doi: 10.1038/nn.4351

Yeatman, J. D., Wandell, B. A., and Mezer, A. A. (2014). Lifespan maturation and degeneration of human brain white matter. *Nat. Commun.* 5:4932. doi: 10.1038/ncomms5932

Yeung, M. S., Zdunek, S., Bergmann, O., Bernard, S., Salehpour, M., Alkass, K., et al. (2014). Dynamics of oligodendrocyte generation and myelination in the human brain. *Cell* 159, 766–774. doi: 10.3410/f.725245304.793502077

Conflict of Interest Statement: The author declares that the research was conducted in the absence of any commercial or financial relationships that could be construed as a potential conflict of interest.

frontiers in Neuroscience

ORIGINAL RESEARCH
published: 07 August 2019
doi: 10.3389/fnins.2019.00764

In vivo Probabilistic Structural Atlas of the Inferior and Superior Colliculi, Medial and Lateral Geniculate Nuclei and Superior Olivary Complex in Humans Based on 7 Tesla MRI

María G. García-Gomar[1]†, Christian Strong[2†], Nicola Toschi[1,3], Kavita Singh[1], Bruce R. Rosen[1], Lawrence L. Wald[1] and Marta Bianciardi[1]**

[1] Department of Radiology, Athinoula A. Martinos Center for Biomedical Imaging, MGH and Harvard Medical School, Boston, MA, United States, [2] Department of Neurosurgery, Brigham and Women's Hospital, Harvard Medical School, Boston, MA, United States, [3] Medical Physics Section, Department of Biomedicine and Prevention, Faculty of Medicine, Tor Vergata University of Rome, Rome, Italy

OPEN ACCESS

Edited by:
John Ashburner, University College London, United Kingdom

Reviewed by:
Anneke Alkemade, University of Amsterdam, Netherlands
Li-Wei Kuo, National Health Research Institutes, Taiwan

***Correspondence:**
María G. García-Gomar
mgarciagomar@mgh.harvard.edu
Marta Bianciardi
martab@mgh.harvard.edu

† These authors have contributed equally to this work as first authors

Specialty section:
This article was submitted to Brain Imaging Methods, a section of the journal Frontiers in Neuroscience

Received: *26 April 2019*
Accepted: *09 July 2019*
Published: *07 August 2019*

Citation:
García-Gomar MG, Strong C, Toschi N, Singh K, Rosen BR, Wald LL and Bianciardi M (2019) In vivo Probabilistic Structural Atlas of the Inferior and Superior Colliculi, Medial and Lateral Geniculate Nuclei and Superior Olivary Complex in Humans Based on 7 Tesla MRI. Front. Neurosci. 13:764. doi: 10.3389/fnins.2019.00764

Despite extensive neuroimaging research of primary sensory cortices involved in auditory and visual functions, subcortical structures within these domains, such as the inferior and superior colliculi, the medial and lateral geniculate nuclei and the superior olivary complex, are currently understudied with magnetic resonance imaging (MRI) in living humans. This is because a precise localization of these nuclei is hampered by the limited contrast and sensitivity of conventional neuroimaging methods for deep brain nuclei. In this work, we used 7 Tesla multi-modal (T_2-weighted and diffusion fractional anisotropy) 1.1 mm isotropic resolution MRI to achieve high sensitivity and contrast for single-subject brainstem and thalamic nuclei delineation. After precise coregistration to stereotactic space, we generated an *in vivo* human probabilistic atlas of auditory (medial geniculate nucleus, inferior colliculus, and superior olivary complex) and visual (lateral geniculate nucleus and superior colliculus) subcortical nuclei. We foresee the use of this atlas as a tool to precisely identify the location and shape of auditory/visual deep nuclei in research as well as clinical human studies.

Keywords: inferior/superior colliculi, medial/lateral geniculate nuclei, superior olivary complex, *in vivo* neuroimaging-based human atlas, multi-contrast 7 Tesla MRI, visual/oculo-motor and auditory/auditory-motor functions

INTRODUCTION

Brainstem nuclei such as the inferior colliculus (IC), superior colliculus (SC) and the superior olivary complex (SOC), as well as thalamic nuclei such as the medial geniculate nucleus (MG) and lateral geniculate nucleus (LG) modulate auditory/auditory-motor (IC, SOC and MG) and visual/oculo-motor (SC and LG) functions. These nuclei are also involved in the pathogenesis of

disorders such as auditory agnosia, pure-word deafness, eye-movement and visual-field deficits, hallucinations in Parkinson's disease, and glaucoma (Joswig et al., 2015; Pasu et al., 2015; Wang et al., 2015; Biotti et al., 2016; Lee et al., 2016). Nevertheless, a stereotaxic probabilistic structural atlas of these nuclei in living humans does not exist. This limits research and clinical (diagnostic, prognostic, pharmaceutical, surgical) studies of their structure, function and connectivity in health and disease.

We briefly review the localization and the anatomical connectivity of the aforementioned structures. The IC, an oval shaped region located in the caudal half of the mesencephalic tectum, receives inputs from several brainstem auditory pathway nuclei such as the cochlear nuclei, nuclei of the lateral lemniscus, lateral and medial superior olive as well as from the auditory cortex. One of the efferent pathways from IC projects to the deeper layers of the SC (thus coordinating eye and head orientation in response to visual/auditory stimuli) while another ascends in the brachium of the IC targeting the MG in the thalamus (Olszewski and Baxter, 2014). The SC is a gray matter nucleus located in the rostral half of the mesencephalic tectum. Its primary function is the orientation of the head toward objects of interest. The optical tract is a major afferent of this nucleus. The SC also receives projections from the parabigeminal nucleus, substantia nigra pars reticulata, zona incerta and corticotectal projections from visual cortical areas and the medial temporal cortex (Olszewski and Baxter, 2014; May, 2006). The SC plays a key role for generation of saccadic eye movements, as it projects to the paramedian pontine reticular formation through the descending predorsal bundle; meanwhile its ascending branch projects toward the interstitial nucleus of Cajal, a vertical saccade generator in the midbrain, and to the mediodorsal thalamic nucleus and the intralaminar thalamic nuclei. The major output of the SC projects toward the LG in its way to the visual cortex (Olszewski and Baxter, 2014; May, 2006). The SOC contains two principal nuclei: the medial superior olivary nucleus and the lateral superior olivary nucleus. The SOC is located in the ventrolateral border of the caudal pontine tegmentum. The function of this nucleus is to process the binaural input converging from the cochlear nuclei from the two ears. The SOC projects to the IC via the lateral lemniscus (Kulesza, 2007). The MG is the thalamic relay of the auditory pathway. It is located in the ventromedial thalamus, it receives input from the IC and projects toward the auditory cortex. Finally, the LG is the thalamic relay of the visual pathway and is located in the ventrolateral thalamus. The LG receives input form the SC and projects toward the visual cortex.

As opposed to previous work performing indirect localization of the MG and LG based on fMRI and DTI connectivity analyses (Chen et al., 1999; Bestmann et al., 2004; Kastner et al., 2004; Schneider et al., 2004; Barnes et al., 2010; Javad et al., 2014; Keifer et al., 2015), we aimed at directly localizing these and the other aforementioned nuclei from *in vivo* structural magnetic resonance images (MRI). Previous structural MRI work reports the automatic/semi-automatic segmentation of some thalamic nuclei at 1.5 Tesla with 3 mm resolution (Wiegell et al., 2003), including the MG and LG. Additionally, previous studies performed automatic segmentation of the LG in an attempt to compare human healthy controls to glaucoma patients using T_1-weighted images acquired with 3 Tesla and 1.5 Tesla MRI with 1.30 and 1.20 mm resolution respectively (Wang et al., 2015), as well as semi-automated segmentation of the LG to characterize its morphometry at 3 Tesla and 1.5 Tesla MRI with a voxel size of 1 mm (Hernowo et al., 2011; Cecchetti et al., 2016). Nevertheless, these studies mainly focused on single-subject nuclei segmentations rather than creating *in vivo* human probabilistic (i.e., representative of a population) atlases of the visual and auditory thalamic/brainstem nuclei.

Both auditory and visual pathways demonstrated lower gray matter volumes in disease states relative to healthy controls (specifically, lower volume of the right IC and left hippocampus in tinnitus patients (Landgrebe et al., 2009) or lower LG volume in blind patients relative to sighted individuals (Aguirre et al., 2016)). Similarly, other studies suggest that visual deficits can be predicted by delineation of the optic tract (de Blank et al., 2018), while other studies report being able to track the optic neuritis recovery by measuring functional activation in the LG (Korsholm et al., 2007). An improved understanding of the anatomical boundaries of these nuclei may better elucidate such prognostic frameworks. Further, acoustic pathway delineation is limited by current MRI techniques (Maffei et al., 2018). In this context, an improved localization of auditory nuclei such as the MG, IC and SOC might help better characterize this pathway. Finally, LG is relevant in psychiatric diseases like schizophrenia (Mai et al., 1993; Selemon and Begovic, 2007; Dorph-Petersen et al., 2009; Buchmann et al., 2014).

The primary objective of our work was to create an *in vivo* probabilistic neuroimaging-based atlas of the right and left IC, SC, MG, LG and SOC using: (1) cutting-edge technology (7 Tesla MRI scanner, 32-channel receive coil-array) to maximize MRI detection sensitivity; (2) a high-resolution (1.1 mm isotropic) multi-contrast [T_2-weighted and diffusion fractional anisotropy (FA)] echo-planar-imaging (EPI) approach, which provided complementary contrasts for brainstem anatomy with precisely matched geometric distortions and resolution.

MATERIALS AND METHODS

MRI Data Acquisition

Data were obtained in a prior study (Bianciardi et al., 2015). While the acquisition and analysis are summarized below, full details can be found in Bianciardi et al., 2015. Twelve healthy subjects (6m/6f, age 28 $\pm$ 1 years) provided informed and written consent for 7 Tesla MRI (Magnetom, Siemens Healthineers, Germany) per Massachusetts General Hospital Institutional Review Board approval in accordance with the Declaration of Helsinki. A custom-built 32-channel receive coil and volume transmit coil was employed in data acquisition (Keil et al., 2010), providing improved sensitivity for the brainstem compared to commercial coils with a similar number of channels. The improved sensitivity of this coil was due to: (i) a more posterior arrangement of the coil elements; (ii) its shape curving around the back of the head enabling a closer proximity to the cerebellum and brainstem as opposed to commercial coils that

typically extend straight down along the lower parts of the head; (iii) a more efficient flip angle calibration for lower parts of the brain because the coil extends more inferiorly than traditional coils. We utilized a common single-shot 2D echo-planar imaging scheme for 1.1 mm isotropic sagittal diffusion-tensor images (DTI), and T_2-weighted images, with matrix size/GRAPPA factor/nominal echo-spacing = 180 × 240/3/0.82 ms. This provided T_2-weighted anatomical images with resolution and geometric distortions perfectly matched to the DTI dataset. With the echo-planar-imaging scheme, we were also able to mitigate specific-absorption-rate limits of spin-warp T_2-weighted MRI at 7 Tesla. Other specifications of DTI and T_2-weighted images included: spin-echo EPI, 61 slices, echo-time/repetition-time = 60.8 ms/5.6 s, partial Fourier: 6/8, unipolar diffusion-weighting gradients (for DTI), 60 diffusion directions (for DTI, *b*-value ∼ 1000 s/mm^2), 7 interspersed "b0" images (non-diffusion weighted, *b*-value ∼ 0 s/mm^2, which were also utilized as T_2-weighted MRI), 4 repetitions, acquisition time/repetition 6'43". The total acquisition time for DTI and T_2-weighted MRI was ∼27'. Importantly, use of unipolar (Stejskal and Tanner, 1965) rather than bipolar (Reese et al., 2003) diffusion gradients allowed shortening of the echo-time by ∼30 ms and hence provided significantly improved sensitivity of high-resolution DTI.

MRI Data Pre-processing and Alignment to MNI Space

On an individual subject basis, the diffusion FA map was calculated from the DTI acquisition concatenated across 4 repetitions and preprocessed (distortion and motion-corrected) with the Diffusion Toolbox of the FMRIB Software Library (FSL, Oxford, United Kingdom) as in Bianciardi et al. (2015). After motion correction, the 28 "b0" T_2-weighted images were averaged and co-registered to DTI data via affine transformation.

Co-registration to MNI space was performed on a single-subject basis for both FA and T_2-weighted images as in Bianciardi et al. (2015). Each subject's FA image was aligned to an MNI space-based diffusion FA template (coined "IIT space") (IIT human brain atlas, v.3, Chicago, IL, United States) (Varentsova et al., 2014). This template was utilized because it encompasses the entirety of the brainstem, is compatible with diffusion-based tractography, and provides high contrast detail in the brainstem. Specifically, we utilized the Advanced Normalization Tool (ANTs, Philadelphia, PA, United States) (Avants et al., 2011) by concatenating a generic affine and a high-dimensional non-linear warp transformation computed for images having the same modality (FA maps). The generic affine transformation was computed by concatenating center-of mass alignment (degrees of freedom, dof = 3), rigid (dof = 6), similarity (dof = 7) and fully affine (dof = 12) transformations with smoothing sigmas: 4, 2, 1, 0 voxels – fixed image space. The high-dimensional non-linear warp transformation employed a symmetric diffeomorphic normalization transformation model with smoothing sigmas: 3, 2, 1, 0 voxels – fixed image space –, and histogram image matching prior to registration. It also employed a cross correlation metric, regular sampling, gradient step size: 0.2; four multi-resolution levels: shrink factors 6, 4, 2, 1 voxels – fixed image space; data winsorization – quantiles: 0.005, 0.995; convergence criterion: slope of the normalized energy profile over the last 10 iterations $<10^{-8}$. The combined transformation was then applied to both single-subject FA and T_2-weighted images, using a single-interpolation step (interpolation method: linear). Single-subject FA and T_2-weighted images were also aligned to MNI152 standard (non-linear 6th generation MNI152_T1_1mm available for instance in FSL) space (coined "MNI152_1mm space"), which is frequently utilized space for fMRI analysis. While the MNI152_1mm space and the IIT space are well aligned elsewhere, there is slight misalignment in the brainstem, particularly in the pons and medulla. Therefore, single-subject FA and T_2-weighted images were aligned to MNI152_1mm space by applying two concatenated transformations, using a single-interpolation step (interpolation method: linear): first, the single-subject to IIT space transformation computed above; and second, the IIT to MNI152_1mm non-linear transformation computed in Bianciardi et al. (2015), using the same parameters as above.

Single-Subject Labeling and Probabilistic Atlas Generation

On a single-subject basis, two raters (C.S. and M.B. for IC, SC, and MG; M.G. and M.B for LG and SOC) independently performed a manual segmentation (fslview, FSL, Oxford, United Kingdom) of multi-contrast (FA maps and T_2-weighted) images in IIT space to yield single-subject labels (i.e., masks) of the regions of interest (ICl/r, SCl/r, MGl/r, LGl/r, SOCl/r). Each rater inspected both imaging modalities simultaneously. For each nucleus in each subject, we defined a "*final label*" including only voxels marked by both raters (i.e., the intersection of the labels of the two raters). The manual segmentation was performed by utilizing image contrast and anatomical landmarks (Paxinos et al., 2012) as follows.

The IC was delineated based on a hypointense region in T_2-weighted images located in the tectum of the midbrain, caudal to the SC on the dorsal aspect of the mesencephalon, lateral – in its dorsal aspect- to the periaqueductal gray (hyperintense in T_2-weighted images), and –ventrally– to the cuneiform nucleus (hypointense in the FA map). The IC was bounded laterally by the cerebrospinal fluid. The SC was visible in the midbrain as a hypointense region on T_2-weighted images, rostral to the IC, lateral to the periaqueductal gray and bounded laterally by the cerebrospinal fluid. The MG was identified as a small rounded/oval shaped eminence hypointense in T_2-weighted images, adjacent to the corticospinal tract (hyperintense in the FA map), pulvinar nucleus (hypointense in T_2-weighted images), LG (hypointense in FA maps), and substantia nigra (hypointense in T_2-weighted images). The LG was identified as a "rainbow-shaped" ovoid structure hypointense in FA maps in the posteroinferior thalamus, located lateral to the corticospinal tract (hyperintense in the FA map), and anterolateral to the MG (hypointense in T_2-weighted images). The SOC, comprising the lateral and medial superior olive, the lateroventral and

medioventral periolivary nucleus, and the superior paraolivary nucleus, was identified on FA maps as a hypointense oval region dorsolateral to the central tegmental tract, and with its most caudal part posterior to the superior border of the inferior olive.

Note that, to delineate each nucleus, we mainly used the image modality (either FA or T_2-weighted MRI – for instance T_2-weighted MRI for IC, SC and MGN; FA for LG and SOC) that displayed the nucleus boundaries with good contrast, and employed the other modality (which had poor contrast for that nucleus – e.g., FA for IC, SC and MGN; T_2-weighted MRI for LG and SOC) to identify neighboring nuclei or landmarks.

A probabilistic neuroimaging atlas in IIT space was formulated for each nucleus as an average probability map of the nucleus label encompassing all subjects (highest probability = 100% overlap of nuclei labels across subjects, n = 12). After registering the individual subject labels to MNI152_1mm space (by applying the IIT to MNI152 transformations described above, interpolation method: nearest neighbor in order to preserve label intensities), a probabilistic neuroimaging atlas in MNI152_1mm spaces of these nuclei was also formulated. The atlas was developed in both IIT and MNI152 spaces to facilitate extrapolation to structural, diffusion and functional MRI modalities.

For each subject and each final label (coregistered to single-subject native space via the inverse of the transformations described in 2.2) we also calculated the label volume in native space. We then computed the mean (s.e.) label volume across all subjects.

Atlas Validation

The probabilistic nuclei atlas was validated by computing for each nucleus and subject: (i) the inter-rater agreement, as the modified Hausdorff distance between labels delineated by the two raters; (ii) the internal consistency across subjects of the final label, as the modified Hausdorff distance between each final label and the probabilistic atlas label (thresholded at 35%) generated by averaging the labels across the other 11 subjects (leave-one-out cross validation). For both (i) and (ii), the modified Hausdorff distance (Dubuisson and Jain, 1994), a measure of spatial overlap frequently used in neuroimaging (Fischl et al., 2008; Ghosh et al., 2010; Klein et al., 2010; Yendiki et al., 2011; Augustinack et al., 2013), was calculated as follows: the minimum distance of each point within one label from the other label was averaged across all points for each label, resulting in two distance values; the maximum value of these 2 values was calculated. We also evaluated the inter-rater agreement and the internal consistency of labels with a metric more commonly used in the literature (especially for larger brain structures), the Dice similarity coefficient (Dice, 1945). The Dice similarity coefficient of two labels X and Y (e.g., of the two raters for the inter-rater agreement) is defined as $(2^*|X \cap Y|)/(|X| + |Y|)$, where $|X| + |Y|$ are the volumes of each label and $|X \cap Y|$ is the volume of the union of the two labels. Finally, for each nucleus, the modified Hausdorff distance as well as the Dice similarity coefficient in both cases (i) and (ii) was averaged across subjects.

RESULTS

The probabilistic neuroimaging-based structural labels in MNI space of ICl/r are shown in **Figure 1**. The left and right IC nuclei appeared as hypointensities compared to neighboring regions on T_2-weighted MRI. The probabilistic neuroimaging-based structural labels in MNI space of SCl/r are shown in **Figure 2**. Again, the left and right nuclei appeared as hypointensities on T_2-weighted MRI, possibly indicating a higher iron concentration compared to neighboring areas (Drayer et al., 1986). In **Figure 3**, we show the probabilistic atlas label in MNI space of the MGl/r. The MG was also hypointense in T_2-weighted MRI. In **Figure 4**, we show the probabilistic atlas label in MNI space of the LGl/r, which was hypointense in the FA map. In **Figure 5**, we show the probabilistic atlas label in MNI space of the SOCl/r, which was an oval hypointense structure in the FA map. All the nuclei (ICl/r, SCl/r, MGl/r, LGl/r and SOCl/r) demonstrated good spatial (i.e., up to 100%) agreement of labels across subjects indicating the feasibility of delineating the probabilistic label of these nuclei in standard space.

The inter-rater label agreement and the internal consistency of each label (computed for validation) are both shown in **Figure 6**. For each nucleus, the average modified Hausdorff distance assessing the inter-rater agreement and the internal consistency of nuclei atlas labels (**Figure 6**, upper row) was below the linear spatial imaging resolution (1.1 mm) ($p < 0.05$, unpaired t-test), thus confirming the accuracy of the delineations of two independent raters. In addition, the Dice similarity coefficient for the inter-rater agreement and the internal consistency (**Figure 6**, bottom row) was always above 0.63, thus showing a good performance of both metrics.

In **Table 1**, for each nucleus we report the mean ($\pm$ s.e.) volume (as well as volume range) across 12 subjects obtained in the present study. Furthermore, in **Table 1** we also report an extensive literature review of volumes of IC, SC, MG, LG and SOC obtained in postmortem histological studies, as well as in structural and functional MRI. We mostly included studies performed in younger human adults [age between 19 and 47 years, except for two studies on older subjects (Nara et al., 1996; Sitek et al., 2019)] because it is known that the brain displays morphological changes with aging (Keuken et al., 2013). Except for the SC, the nuclei volumes obtained in this study fell ($p < 0.05$, t-test) within the range of literature values.

DISCUSSION

Compared to a large body of research focused on primary auditory/visual cortical areas (Ress et al., 2000; Morosan et al., 2001; Rademacher et al., 2001; Abdul-Kareem and Sluming, 2008; Hinds et al., 2009; Hoffmann et al., 2009; Bridge, 2011; Sánchez-Panchuelo et al., 2012; Augustinack et al., 2014; Saenz and Langers, 2014; Wasserthal et al., 2014; Cheng, 2016; Moerel et al., 2019), the structure, function and connectivity of subcortical brainstem and thalamic auditory/visual nuclei are currently understudied. New tools are

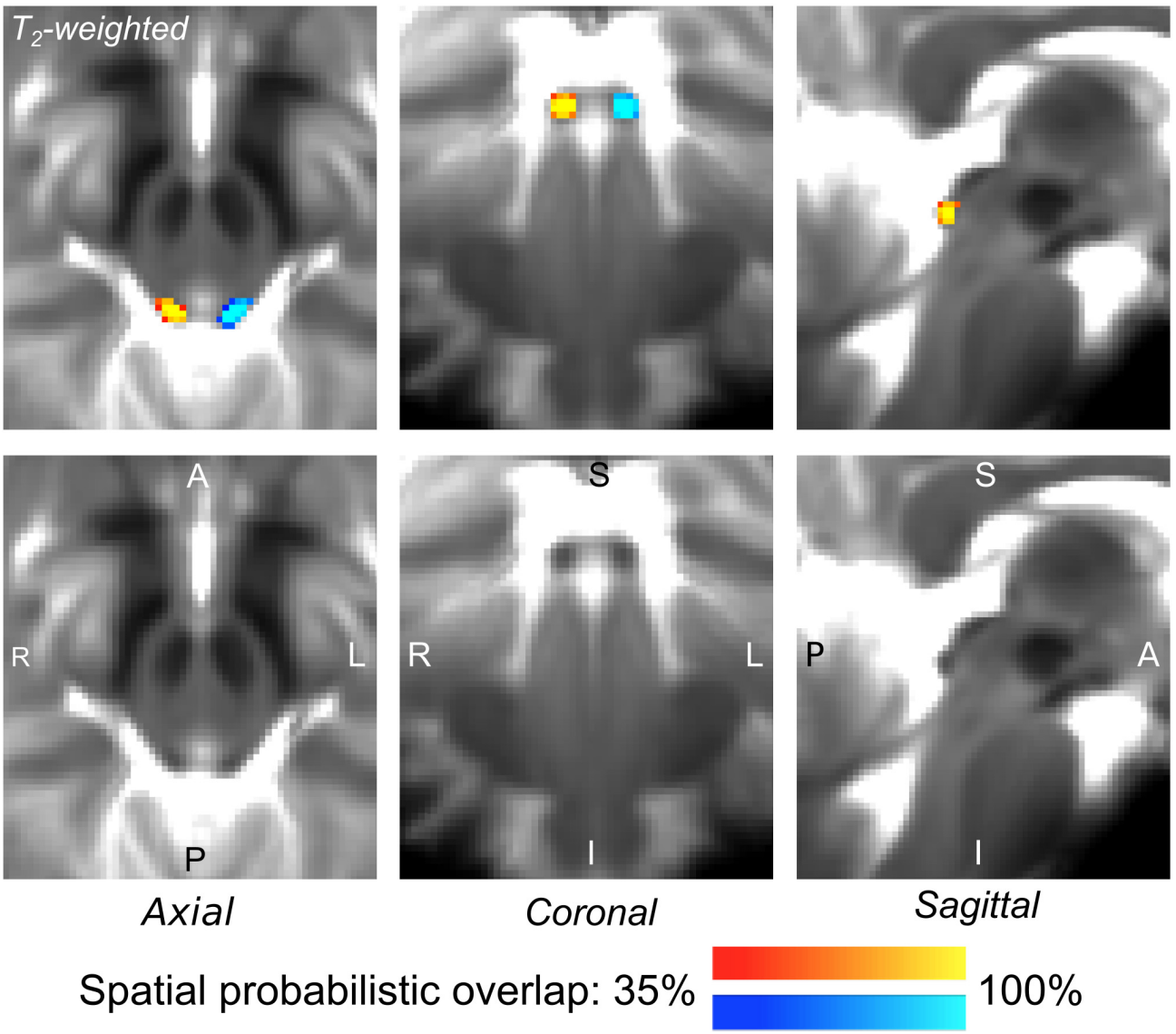

FIGURE 1 | Probabilistic atlas label in MNI space of the IC (**left:** blue-to-cyan; **right:** red-to-yellow). The IC was hypointense in T_2-weighted MRI; its label is overlaid on the group average T_2-weighted image. Very good (i.e., up to 100%) spatial agreement of labels across subjects was observed indicating the feasibility of delineating the probabilistic label of this nucleus involved in auditory and auditory-motor functions.

needed to fill this gap and enable accurate structural delineations of the underlying deep brain nuclei in future clinical and research studies.

We first review the technological and methodological advances of this study that overcame conventional imaging limitations and enabled the generation of a new tool, namely a structural probabilistic atlas of subcortical auditory/visual nuclei. Then, for each nucleus, we discuss the segmentation process, in relation to the MRI contrast used for the nucleus delineation, the identification of specific nuclei borders, and the obtained volumes in comparison to literature values. Further, we discuss the possible impact of the atlas for clinical and research studies. Finally, we acknowledge the limitations of this work and propose possible future extensions.

Technological and Methodological Advances

In this work we showed that the use of advanced ultra-high-field MRI sequences allowed *in vivo* structural imaging of tiny brainstem and thalamic nuclei with high contrast, sensitivity and good spatial resolution with respect to conventional (e.g., 3

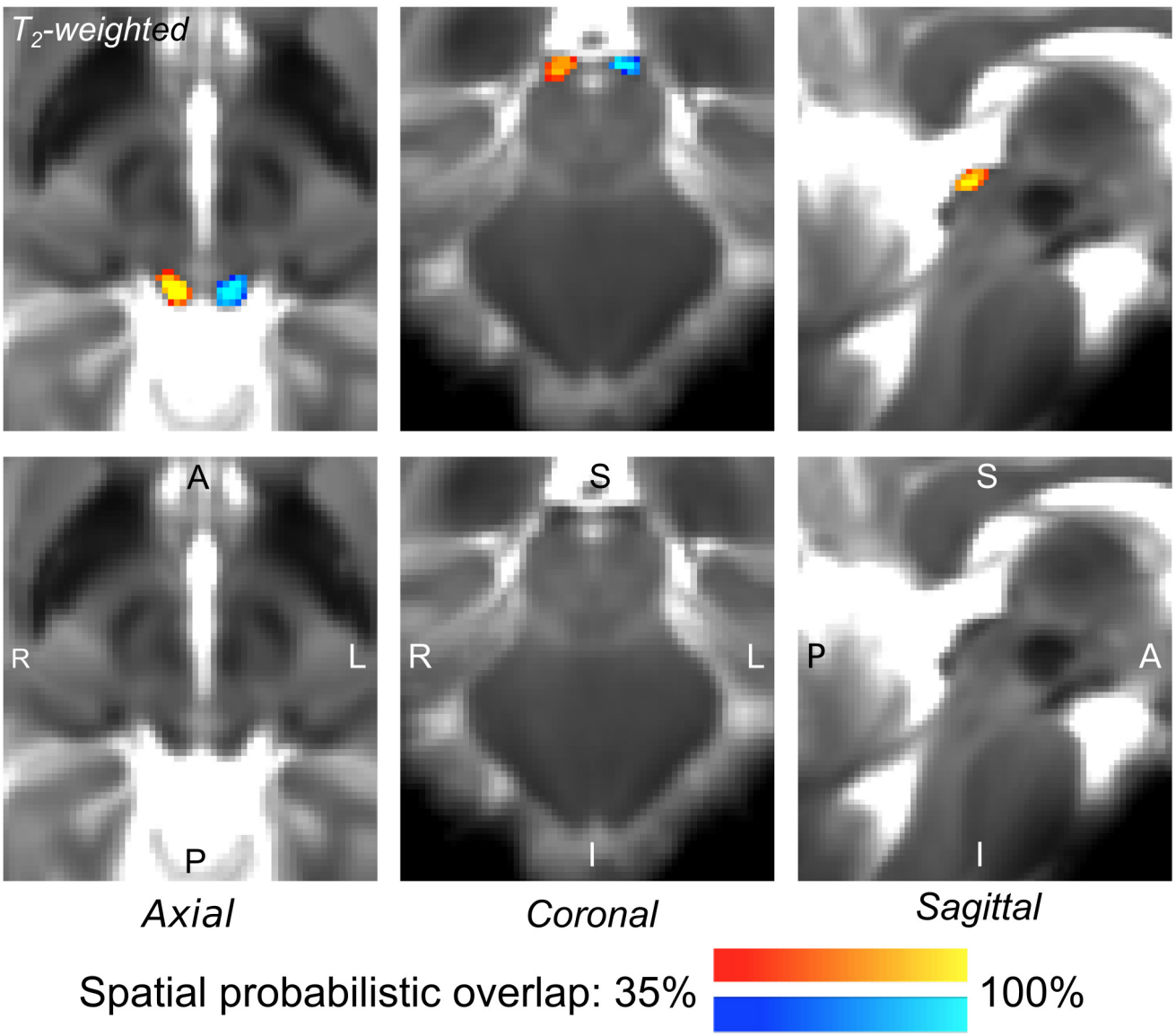

FIGURE 2 | Probabilistic atlas label in MNI space of the SC (**left:** blue-to-cyan; **right:** red-to-yellow). The SC was hypointense in T_2-weighted MRI; its label is overlaid on the group average T_2-weighted image. Very good (i.e., up to 100%) spatial agreement of labels across subjects was observed indicating the feasibility of delineating the probabilistic label of this nucleus involved in visual and oculo-motor functions.

Tesla) MRI. For instance, a 7 Tesla diffusion MRI is expected to yield a ∼2.2 increase in sensitivity with respect to 3 Tesla MRI, and gains in contrast related to decreased partial volume effects due to increased spatial resolution. Notably, the 7 Tesla sequence was optimized to: (i) achieve minimum echo time (e.g., by the use of a monopolar scheme) given the lower gray and white matter T_2 values at 7 Tesla compared to 3 Tesla; (ii) refine the RF transmit gain in the brainstem (to compensate for strong RF in-homogeneities at 7 Tesla), by tuning the RF voltage with an actual flip-angle imaging pulse sequence (Yarnykh, 2007); (iii) perform several iterations of semi-automatic B_0 shimming. Specifically, these 7 Tesla structural MRI (T_2-weighted and FA maps) techniques enabled the single-subject segmentation of subcortical auditory and visual subcortical nuclei based on their contrast with respect to neighboring areas. An important consideration regards the multi-contrast, resolution- and distortion-matched structural image acquisition used in this work. The latter allowed us to discriminate the structural boundaries of some nuclei due to the improved visualization of multiple contrasts in a common

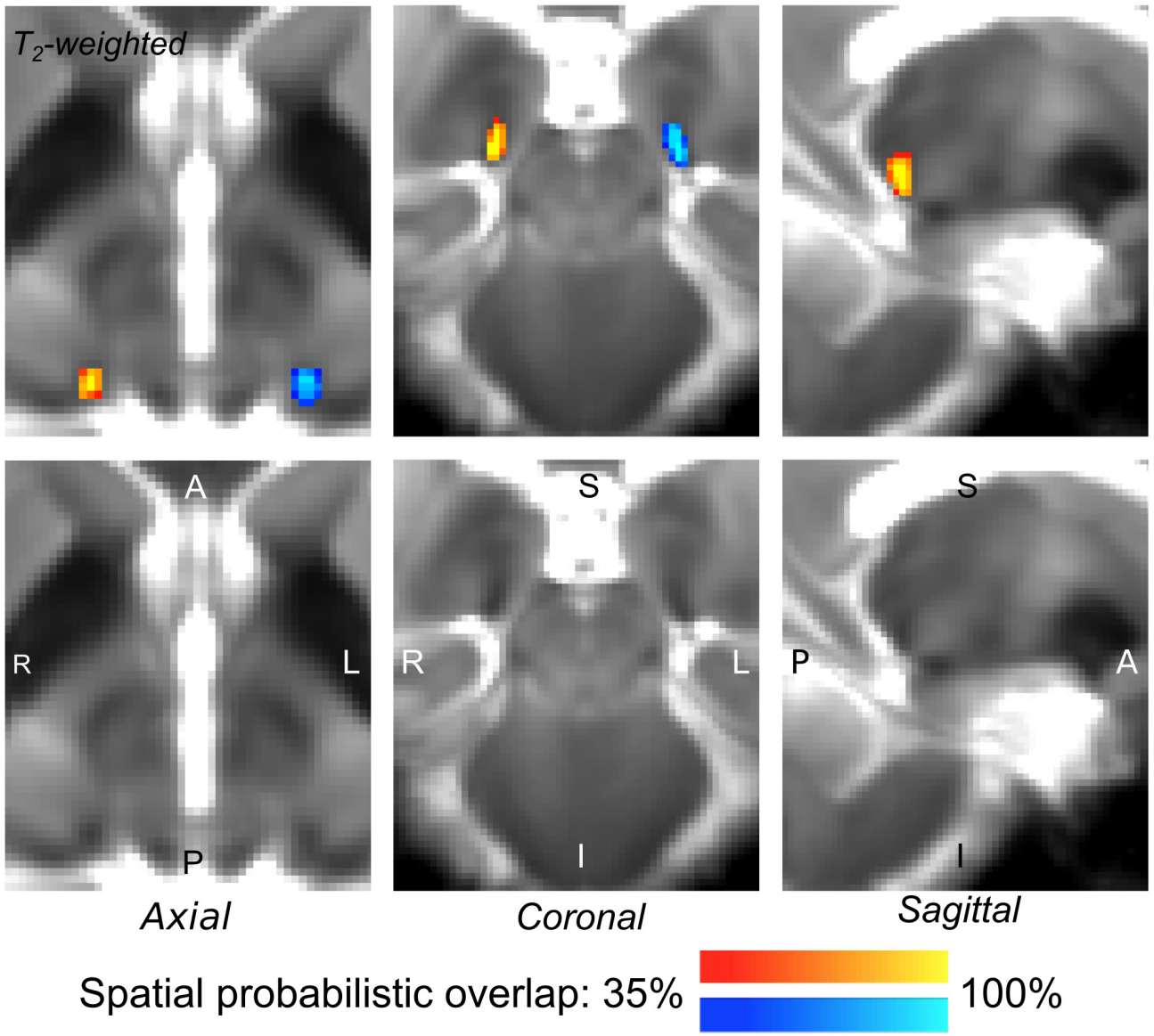

FIGURE 3 | Probabilistic atlas label in MNI space of the MG (**left:** blue-to-cyan; **right:** red-to-yellow). The MG was hypointense in T_2-weighted MRI; its label is overlaid on the group average T_2-weighted image. Very good (i.e., up to 100%) spatial agreement of labels across subjects was observed indicating the feasibility of delineating the probabilistic label of this nucleus, which is a thalamic relay between the IC and the auditory cortex, and thus it is crucially involved in auditory and auditory-motor functions.

space, and to the use of complementary information derived from different image contrasts.

On the Atlas Creation

Our findings demonstrate the feasibility of delineating auditory/visual brainstem and thalamic nuclei by segmentation of single-subject high-contrast and high-sensitivity MRI images at 7 Tesla. This extends previous reports (Li et al., 2012) of manual single-subject localization of LG using neuroimaging in living humans based on the identification of anatomical landmarks. Crucially, our work also demonstrated the feasibility of generating a validated *in vivo* stereotaxic probabilistic atlas of these structures after precise coregistration to MNI (or another stereotactic) space. This atlas complements existing *in vivo* neuroimaging atlases of other brain structures (Tzourio-Mazoyer et al., 2002; Desikan et al., 2006; Destrieux et al., 2010).

We generated labels for two (bilateral) mescencephalic tegmental nuclei ICl/r and SCl/r. They were hypointense oval shaped structures easily identifiable on a T_2-weighted MRI. The periaqueductal gray and the cuneiform nucleus were located at

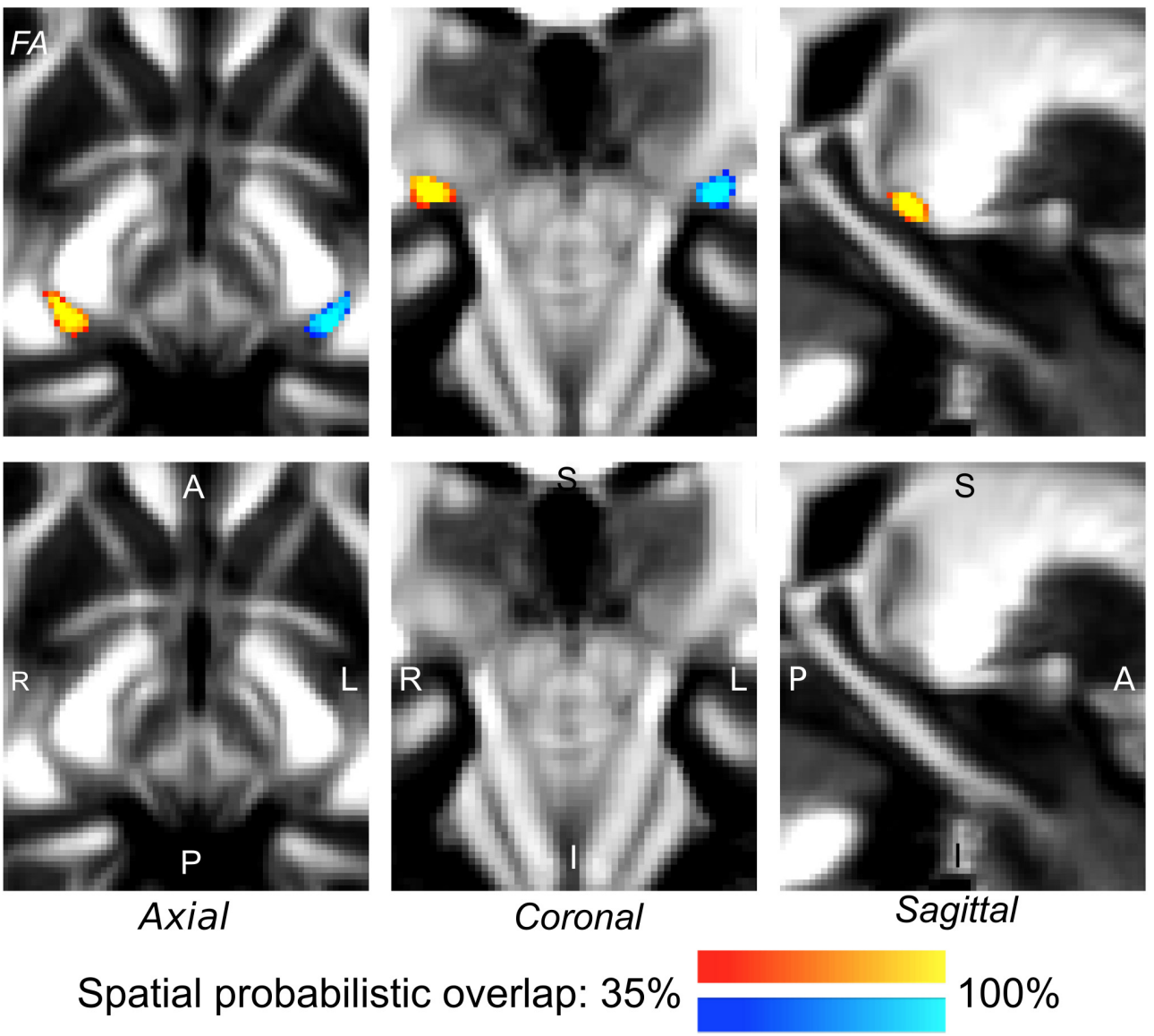

FIGURE 4 | Probabilistic atlas label in MNI space of the LG (**left:** blue-to-cyan; **right:** red-to-yellow). The LG was hypointense in diffusion FA MRI; its label is overlaid on the group average FA map. Very good spatial (i.e., up to 100%) agreement of labels across subjects was observed indicating the feasibility of delineating the probabilistic label of this nucleus, which is a thalamic relay for visual and oculo-motor pathways.

the anteromedial border of the IC (with good contrast in FA maps) and the cerebrospinal fluid limited its lateral edge. For the SC, its inferior edge was clearly located near the most rostral part of the IC, yet its rostro-ventral edge —in proximity to the thalamus— was less clearly defined due to the absence of an abrupt change in contrast in that area. The periaqueductal gray neighbored the medial border of the SC, while the cerebrospinal fluid delimited the posterolateral border of this structure. As visible in **Table 1**, our IC volumes were within literature values (specifically, closer to the inferior range of the latter), mainly derived from histology and structural MRI studies. Instead, the volume of the SC was slightly lower than reported literature values. Further validation work with MRI and histology might better elucidate the relationship between the achieved contrast in *in vivo* T_2-weighted images and the distribution of iron (or of other microstructural properties) within different layers of this nucleus (Drayer et al., 1986).

For the manual delineation of the thalamic auditory MG nucleus we mainly used the T_2-weighted image contrast. The MG was visible as a hypointense area neighboring (at its upper edge) the posteroventral thalamic nuclei, bounded inferiorly by the cerebrospinal fluid and limited by the pulvinar on its

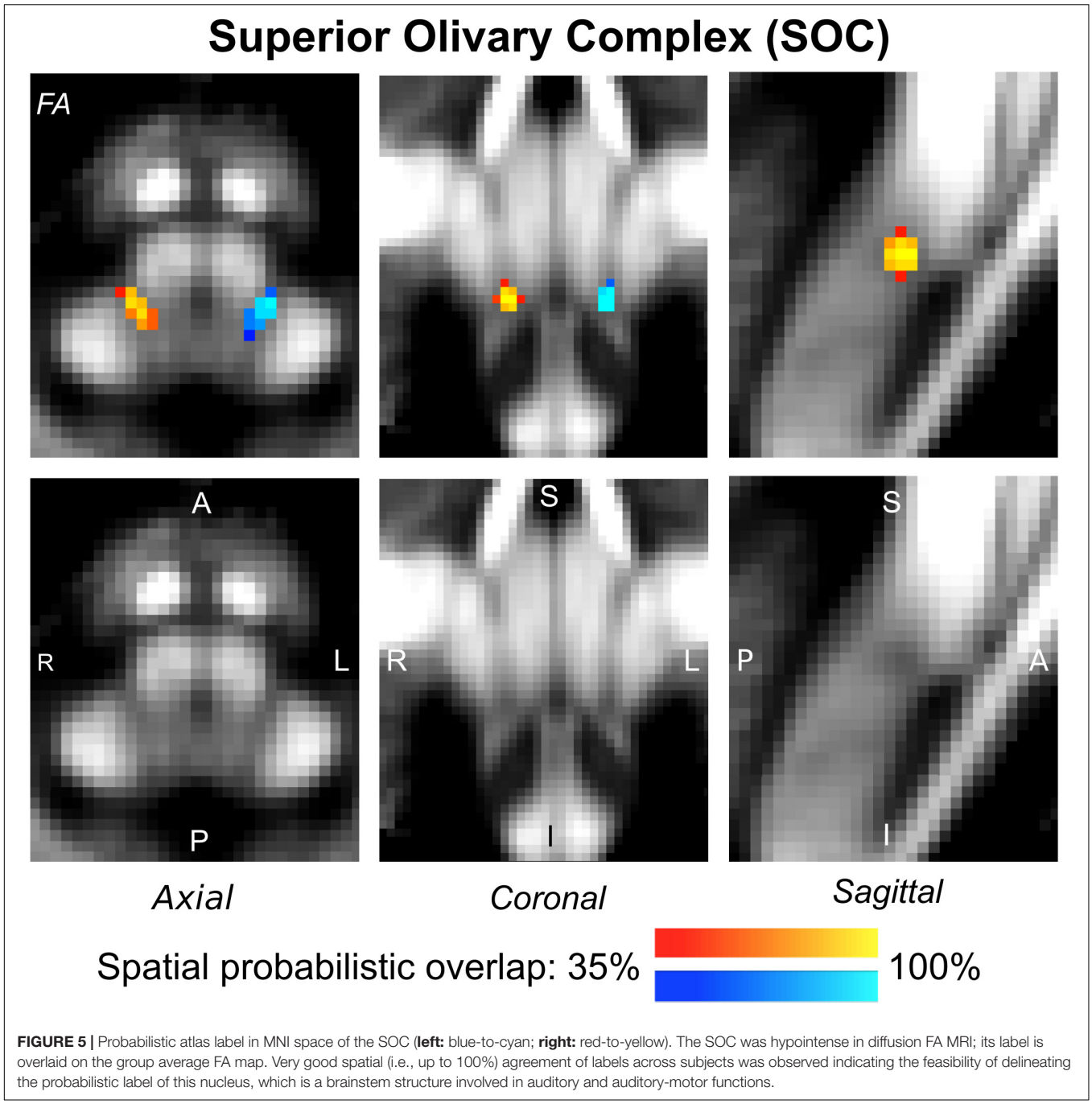

FIGURE 5 | Probabilistic atlas label in MNI space of the SOC (**left:** blue-to-cyan; **right:** red-to-yellow). The SOC was hypointense in diffusion FA MRI; its label is overlaid on the group average FA map. Very good spatial (i.e., up to 100%) agreement of labels across subjects was observed indicating the feasibility of delineating the probabilistic label of this nucleus, which is a brainstem structure involved in auditory and auditory-motor functions.

posterolateral border. Its medial border was clearly visible in FA maps, due to the high contrast with neighboring white matter bundles, such as the medial lemniscus and the spinothalamic tract. It is interesting to note the high variability in the MG volume values reported in the literature (see **Table 1**) for this structure. For instance, fMRI studies reported larger MG volumes compared to histology and structural MRI studies, possibly due to partial volume effects and artifacts due to draining veins in this region (Sitek et al., 2019). The MG volumes obtained in this study were within the range of previous literature reports (see **Table 1**).

The MG label was useful to delimitate the posteromedial border of the LG, yet for the other borders of the LG we also used the contrast available in the FA maps. Notably, we used the FA maps to identify white matter bundles neighboring the LG, such as the optic tract anterior to LG and, in its medial aspect, the mesencephalic peduncles. The LG has an array of six cell layers currently not visible in our MRIs. Interestingly, recent *in vivo* studies report changes in the volume and shape of LG compatible with the location of the magnocellular layer in dyslexia according to previous hypothesis for this disease

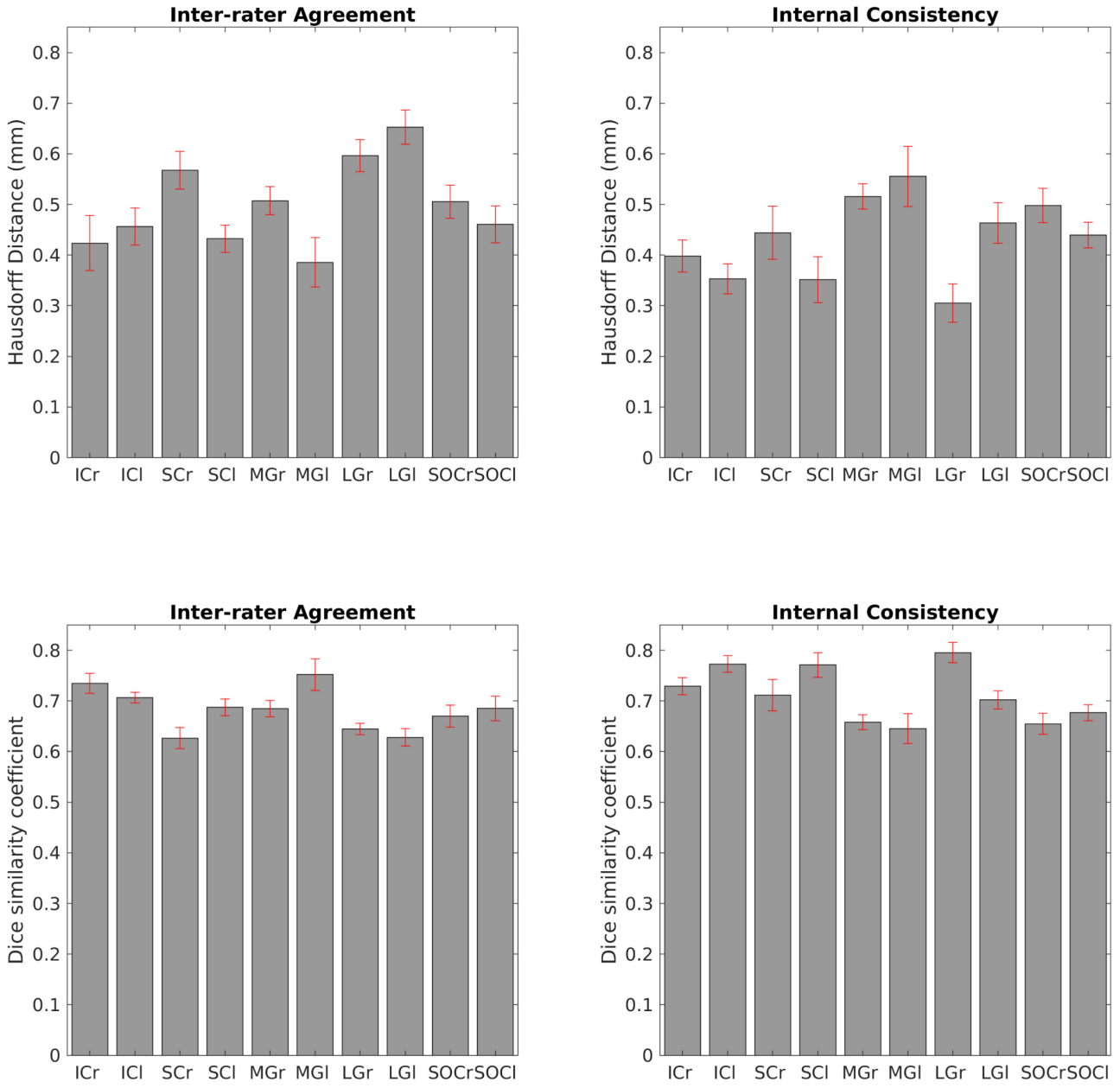

FIGURE 6 | Atlas validation. **Upper left:** inter-rater agreement of nuclei labels (bar/error bar = mean/s.e. modified Hausdorff distance across 12 subjects). **Upper right:** internal consistency of nuclei labels across subjects (bar/errorbar = mean/s.e. modified Hausdorff distance across 12 subjects). **Lower left:** Dice similarity coefficient (range: 0–1) of the inter-rater agreement (bar/error bar = mean/s.e. Dice similarity coefficient across 12 subjects) **Lower right:** Dice similarity coefficient (range: 0–1) of the internal consistency (bar/error bar = mean/s.e. Dice similarity coefficient across 12 subjects). The labels of the IC, SC, MG, LG and SOC displayed good spatial overlap across raters and subjects (i.e., modified Hausdorff distance smaller than the imaging resolution and Dice similarity coefficient higher than 0.63), thus validating the probabilistic nuclei atlas.

(Giraldo-Chica et al., 2015; Giraldo-Chica and Schneider, 2018). Previous reports of the LG volume show high degree of variability (up to two-fold) between individuals even when using the same techniques (Andrews et al., 1997; Selemon and Begovic, 2007; Kitajima et al., 2015; Wang et al., 2015). The LG volumes obtained in the present study were within the range of literature values (see **Table 1**). In the current study we found that the right LG was slightly larger compared to the left LG, in agreement with previous reports (Li et al., 2012; Lee et al., 2014).

The SOC was a round-oval hypointense area in FA maps with well-defined borders, yet at its most postero-lateral aspects its boundaries were more difficult to delineate due to its close proximity with other structures (e.g., the facial nucleus) (Kulesza, 2007). Our probabilistic SOC label is compatible with

TABLE 1 | Volumes of the IC, SC, MG, LG, and SOC.

NUCLEUS name (acronym)	Prior studies									Cross-modal* Volume range (mm^3)	Current study	
	Histology			Structural MRI			fMRI					
	Volume (mm^3) (range)	Age (years)	References	Volume (mm*) (range)	Age (years) (range or mean ± s.e)	References	Volume (mm*) (range)	Age (years) (range or mean ± s.e)	References		Right nucleus Volume (mm^3) mean ± s.e (range)	Left nucleus Volume (mm^3) mean ± s.e. (range)
Inferior Colliculus (IC)	63	65	Sitek et al., 2019	73	65	Sitek et al., 2019	200	25–30	Sitek et al., 2019	20.7–200	60 ± 3 (40–77)	55 ± 3 (41–69)
	20.7	63	Nara et al., 1996	119–165	28	Bestmann et al., 2004	193–194	20	Amaral et al., 2016			
	65. 2	–	Glendenning and Masterton, 1998				111–118	32 ± 9	Cecchetti et al., 2016			
							124–135	27 ± 6	Kang et al., 2008			
Superior Colliculus (SC)	–	–	–	90–110	20–35	Schneider and Kastner, 2009	171–176	20	Amaral et al., 2016	86–180	71 ± 5 (44–95)	75 ± 4 (44–95)
				86	22–35	Schneider and Kastner, 2005	170–190	32 ± 9	Cecchetti et al., 2016			
							158- 165	27 ± 6	Kang et al., 2008			
Medial Geniculate Nucleus (MGN)	75	65	Sitek et al., 2019	134	65	Sitek et al., 2019	285	25–30	Sitek et al., 2019	46.6–285	57 ± 6 (28–101)	66 ± 8 (35–126)
	58	–	Glendenning and Masterton, 1998	115–116	*20*	Amaral et al., 2016	185	28	Bestmann et al., 2004			
	46.6–71.2	28, 32	Armstrong, 1979	129	37 ± 7	Kitajima et al., 2015						
	105	–	Hopf, 1965									
Lateral Geniculate Nucleus (LGN)	104	–	Dorph-Petersen et al., 2009	87.7–88.8	47 ± 9	Schmidt et al., 2018	579	30 ± 4	Barnes et al., 2010	66–579	101 ± 5 (83–126)	93 ± 6 (73–129)
	66–152	–	Zvorykin, 1981	133–135	32 ± 9	Cecchetti et al., 2016	121–129	20–35	Schneider and Kastner, 2009			
	416	–	Stephan et al., 1981	117–144	37 ± 12	Wang et al., 2016	215	22–35	Schneider and Kastner, 2005			
	91–157	32	Andrews et al., 1997	250–274	20	Amaral et al., 2016	234–244	21–38	Kastner et al., 2004			
	69–78	28, 32	Armstrong, 1979	135	37 ± 7	Kitajima et al., 2015	440	22–30	Schneider et al., 2004			
	77–115	–	Putnam, 1926	70–170	51 ± 15	Wang et al., 2015						
				112–120	22–26	Giraldo-Chica et al., 2015	239–258	22–38	O'Connor et al., 2002			
				159	30 ± 12	Kelly et al., 2014	270	19–29	Chen et al., 1999			
				110	37	Hernowo et al., 2014						
				93–106	45 ± 11	Lee et al., 2014						
				90–177	35	Chen et al., 2013						
				158–165	32 ± 3	Mcketton et al., 2014						
				52–105	38 ± 14	Li et al., 2012						
				129.6–143.5	35	Dai et al., 2011						
				267	32	Korsholm et al., 2007						
				270	20–37	Horton et al., 1990						
Superior Olivary Complex (SOC)	6	65	Sitek et al., 2019	4	65	Sitek et al., 2019	124	25–30	Sitek et al., 2019	4–124	16 ± 1 (11–21)	20 ± 1 (12–27)
	5.76	54–76	Hilbig et al., 2009†									
	5.82	–	Glendenning and Masterton, 1998†									

**Cross-modal across prior histological, structural MRI and fMRI studies.*

†The reported values only include the volume of the lateral and medial olivary complex.

a complex comprising five nuclei described in the Paxinos atlas: the medial and lateral superior olive, the lateroventral and medioventral periolivary nucleus and the superior paraolivary nucleus (Paxinos et al., 2012). Previous histological and structural MRI studies report smaller SOC volumes (less than 6 mm^3) than in the current work, most probably because they constrain their investigation to the small medial and lateral superior olivary nuclei (Glendenning and Masterton, 1998; Hilbig et al., 2009), and exclude the larger periolivary nuclei as well as the superior paraolivary nucleus. Yet, fMRI results report a larger volume (124 mm^3) of the SOC, and our findings are within the range of literature values.

The atlas was validated with measures of inter-rater agreement and internal consistency of label delineations evaluated with the modified Hausdorff distance, a metric mostly unbiased by the size of the nucleus. We also evaluated the inter-rater agreement and the internal consistency using the Dice similarity coefficient, a more commonly used index in the neuroimaging literature for larger cortical and subcortical structures (Kaur et al., 2014; Iglesias et al., 2016; Tona et al., 2017). However, its sensitivity (similarly, to the Jaccard index) is biased toward larger structures with poorer performance in smaller structures such as tiny brainstem nuclei.

Potential Impact of the Atlas

The current work presents a human *in vivo* probabilistic atlas of auditory and visual subcortical nuclei in stereotactic (e.g., MNI) space.

Upon its release on public repositories of neuroimaging data and tools, this atlas might be used as a tool to better identify the IC, SC, MG, LG, SOC nuclei location in conventional (e.g., 3 Tesla) MRI, and enable more accurate characterizations of auditory and visual connectivity pathways in fMRI and diffusion tractography studies. The current work provides a detailed description of the location, shape and anatomy of these nuclei that could be useful in research as well as in future clinical studies to aid treatment delivery and tuning of strategies such as repetitive transcranial magnetic stimulation, neurosurgical planning or focused ultrasound therapies i.e., in tinnitus treatment (Smit et al., 2016; Yilmaz and Yilmaz, 2018) or advanced stages of Parkinson's disease with catalepsy symptoms (Engelhardt et al., 2018). This atlas could also be used to evaluate microstructural changes in the brainstem, such as the location of microbleeds/lesions/tumors.

We foresee that this atlas might improve the reconstruction of three dimensional auditory/visual tracts by providing more precise seeding information in diffusion tractography using MRI. Further, this tool might be applied to improve diagnosis, prognosis and therapeutic decisions for different pathologies, such as glaucoma, amblyopia, optic neuritis, hemianopsia, congenital or genetic abnormalities that involve alterations in auditory or visual pathways (i.e., congenital blindness or congenital deafness), macular degeneration, cognitive (i.e., dyslexia) and psychiatric disorders (i.e., schizophrenia) among other applications (Brown et al., 2016; Prins et al., 2016).

Limitations and Future Perspectives

In the delimitation of LG and SOC we mainly used the contrast of FA maps, assuming that the observed low FA values within these nuclei were due to low myelin content (e.g., as expected in a gray matter region). To further corroborate our findings future human postmortem brain imaging with histological validation is needed to rule out possible confounds (such as low diffusion anisotropy due to crossing fibers). High angular resolution diffusion imaging (HARDI) acquisitions (preferentially with b-values $>$ 2000 s/mm^2) coupled with inspection of fiber orientation distributions and the application of tractography methods (Tournier et al., 2004; Zhang et al., 2012; Dell'Acqua and Tournier, 2019) could also provide useful information for brainstem nuclei delineation (such as a more accurate identification of neighboring fibers and of fibers traversing a nucleus, yet with higher uncertainty at the level of crossing fibers). At ultra-high magnetic fields, shorter T_2 values might reduce the signal to noise ratio of high b-value diffusion images; yet, this effect is expected to be counterbalanced by gains in sensitivity due to the increased field strength.

We created an atlas based on images of healthy young adults, yet future work needs to be done in order to acknowledge possible differences across the lifespan. Future work should also investigate gender differences in nuclei shape and location.

Despite these limitations, our subcortical atlas is a unique non-invasive *in vivo* morphological tool to study the anatomy of deep brainstem and thalamic nuclei in healthy subjects, and its possible changes in different clinical populations.

CONCLUSION

We foresee the use of the generated probabilistic atlas of the IC, SC, MG, LG and SOC to aid the localization of these nuclei in conventional (e.g., 3 Tesla) images in future research studies of auditory and visual functions. Further, this atlas, upon coregistration to clinical MRI, might improve the evaluation of lesions and the assessment of connectivity pathways underlying auditory and visual mechanisms in a broad set of disease populations (e.g., auditory agnosia, pure-word deafness, eye movement and visual field deficits, Parkinson's hallucinations, and glaucoma).

DATA AVAILABILITY

The datasets for this manuscript are not publicly available because we are using this data-set to currently expand our atlas and connectome of brainstem nuclei, as promised to a federal funding agency. The data-set, atlas and connectome will be released upon termination of this work. Requests to access the datasets should be directed to MB, martab@mgh.harvard.edu.

ETHICS STATEMENT

Twelve healthy subjects (6m/6f, age 28 $\pm$ 1 years) provided informed and written consent for 7 Tesla MRI (Magnetom,

Siemens Healthineers, Germany) per Massachusetts General Hospital Institutional Review Board approval in accordance with the Declaration of Helsinki.

AUTHOR CONTRIBUTIONS

NT and MB preprocessed and analyzed the data. MG-G, CS, and MB manually labeled the ROIs. MG-G, CS, KS, and MB wrote the manuscript. MB designed the research, performed the experiments, and secured the funding. BR and LW gave feedback along the process.

FUNDING

This work was supported by the following sources of funding: National Institutes of Health (NIH) National Institute for Biomedical Imaging and Bioengineering, K01 EB019474 and P41 EB015896, National Institute on Deafness and other Communication Disorders R21 DC015888, National Cancer Institute U01 CA193632, and the Massachusetts General Hospital Claflin Distinguished Scholar Award. This work was also in part made possible by the resources provided by Shared Instrumentation Grants 1S10RR023401, 1S10RR019307, and 1S10RR023043.

REFERENCES

Abdul-Kareem, I. A., and Sluming, V. (2008). Heschl gyrus and its included primary auditory cortex: structural MRI studies in healthy and diseased subjects. *J. Magnet. Reson. Imaging* 28, 287–299. doi: 10.1002/jmri.21445

Aguirre, G. K., Datta, R., Benson, N. C., Prasad, S., Jacobson, S. G., Cideciyan, A. V., et al. (2016). Patterns of individual variation in visual pathway structure and function in the sighted and blind. *PLoS One* 11:e0164677. doi: 10.1371/journal.pone.0164677

Amaral, L., Ganho-Ávila, A., Osório, A., Soaresm, M. J., He, D., Chen, Q., et al. (2016). Hemispheric asymmetries in subcortical visual and auditory relay structures in congenital deafness. *Eur. J. Neurosci.* 44, 2334–2339. doi: 10.1111/ejn.13340

Andrews, T. J., Halpern, S. D., and Purves D. (1997). Correlated size variations in human visual cortex, lateral geniculate nucleus, and optic tract. *J. Neurosci.* 17, 2859–2868. doi: 10.1523/JNEUROSCI.17-08-02859.1997

Armstrong, E. (1979). Quantitative comparison of the hominoid thalamus. I. Specific sensory relay nuclei. *Am. J. Phys. Anthropol.* 51, 365–382. doi: 10.1002/ajpa.1330510308

Augustinack, J. C., Huber, K. E., Stevens, A. A., Roy, M., Frosch, M. P., van der Kouwe, A. J., et al. (2013). Predicting the location of human perirhinal cortex, Brodmann's Area 35, from MRI. *Neuroimage* 64, 32–42. doi: 10.1016/j.neuroimage.2012.08.071

Augustinack, J. C., Magnain, C., Reuter, M., van der Kouwe, A. J., Boas, D., and Fischl, B. (2014). MRI parcellation of ex vivo medial temporal lobe. *Neuroimage* 93(Pt 2), 252–259. doi: 10.1016/j.neuroimage.2013.05.053

Avants, B. B., Tustison, N. J., Song, G., Cook, P. A., Klein, A., and Gee, J. C. (2011). A reproducible evaluation of ANTs similarity metric performance in brain image registration. *Neuroimage* 54, 2033–2044. doi: 10.1016/j.neuroimage.2010.09.025

Barnes, G. R., Li, X., Thompson, B., Singh, K. D., Dumoulin, S. O., and Hess, R. F. (2010). Decreased gray matter concentration in the lateral geniculate nuclei in human amblyopes. *Investig. Ophthalmol. Vis. Sci.* 51, 1432–1438. doi: 10.1167/iovs.09-3931

Bestmann, S., Baudewig, J., Siebner, H. R., Rothwell, J. C., and Frahm, J. (2004). Functional MRI of the immediate impact of transcranial magnetic stimulation on cortical and subcortical motor circuits. *Eur. J. Neurosci.* 19, 1950–1962. doi: 10.1111/j.1460-9568.2004.03277.x

Bianciardi, M., Toschi, N., Edlow, B. L., Eichner, C., Setsompop, K., Polimeni, J. R., et al. (2015). Toward an *In Vivo* neuroimaging template of human brainstem nuclei of the ascending arousal, autonomic, and motor systems. *Brain Connectivity* 5, 597–607. doi: 10.1089/brain.2015.0347

Biotti, D., Barbieux, M., and Brassat, D. (2016). Teaching video neuro images?: alternating skew deviation with abducting hypertropia following superior colliculus infarction. *Neurology* 86, e93–e94. doi: 10.1212/WNL.0000000000002425

Bridge, H. (2011). Mapping the visual brain: how and why. *Eye* 25, 291–296. doi: 10.1038/eye.2010.166

Brown, H. D., Woodall, R. L., Kitching, R. E., Baseler, H. A., and Morland, A. B. (2016). Using magnetic resonance imaging to assess visual deficits: a review. *Ophthalmic Physiol. Opt.* 36, 240–265. doi: 10.1111/opo.12293

Buchmann, A., Dentico, D., Peterson, M. J., Riedner, B. A., Sarasso, S., Massimini, M., et al. (2014). Reduced mediodorsal thalamic volume and prefrontal cortical spindle activity in schizophrenia. *Neuroimage* 102(Pt 2), 540–547. doi: 10.1016/j.neuroimage.2014.08.017

Cecchetti, L., Ricciardi, E., Handjaras, G., Kupers, R., Ptito, M., and Pietrini, P. (2016). Congenital blindness affects diencephalic but not mesencephalic structures in the human brain. *Brain Struct. Funct.* 221, 1465–1480. doi: 10.1007/s00429-014-0984-985

Chen, W., Zhu, X. H., Thulborn, K. R., and Ugurbil, K. (1999). Retinotopic mapping of lateral geniculate nucleus in humans using functional magnetic resonance imaging. *Proc. Natl. Acad. Sci. U.S.A.* 96, 2430–2434. doi: 10.1073/pnas.96.5.2430

Chen, Z., Wang, J., Lin, F., Dai, H., Mu, K., and Zhang, H. (2013). Correlation between lateral geniculate nucleus atrophy and damage to the optic disc in glaucoma. *J. Neuroradiol.* 40, 281–287. doi: 10.1016/j.neurad.2012.10.004

Cheng, K. (2016). What we have learned about human primary visual cortex from high resolution functional magnetic resonance imaging. *Magnet. Reson. Med. Sci.* 15, 1–10. doi: 10.2463/mrms.2015-2018

Dai, H., Mu, K. T., Qi, J. P., Wang, C. Y., Zhu, W. Z., Xia, L. M., et al. (2011). Assessment of lateral geniculate nucleus atrophy with 3T MR imaging and correlation with clinical stage of glaucoma. *Am. J. Neuroradiol.* 32, 1347–1353. doi: 10.3174/ajnr.A2486

de Blank, P., Fisher, M. J., Gittleman, H., Barnholtz-Sloan, J. S., Badve, C., and Berman, J. I. (2018). Validation of an automated tractography method for the optic radiations as a biomarker of visual acuity in neurofibromatosis-associated optic pathway glioma. *Exp. Neurol.* 299, 308–316. doi: 10.1016/j.expneurol.2017.06.004

Dell'Acqua, F., and Tournier, J. D. (2019). Modelling white matter with spherical deconvolution: how and why?. *NMR Biomed.* 32:e3945. doi: 10.1002/nbm.3945

Desikan, R. S., Ségonne, R., Fischl, B., Quinn, B. T., Dickerson, B. C., Blacker, D., et al. (2006). An automated labeling system for subdividing the human cerebral cortex on MRI scans into gyral based regions of interest. *Neuroimage* 31, 968–980. doi: 10.1016/j.neuroimage.2006.01.021

Destrieux, C., Fischl, B., Dale, A., and Halgren, E. (2010). Automatic parcellation of human cortical gyri and sulci using standard anatomical nomenclature. *Neuroimage* 53, 1–15. doi: 10.1016/j.neuroimage.2010.06.010

Dice, L. R. (1945). Measures of the amount of ecologic association between species. *Ecology* 26, 297–302. doi: 10.2307/1932409

Dorph-Petersen, K. A., Caric, D., Saghafi, R., Zhang, W., Sampson, A. R., and Lewis, D. A. (2009). Volume and neuron number of the lateral geniculate nucleus in schizophrenia and mood disorders. *Acta Neuropathol.* 117, 369–384. doi: 10.1007/s00401-008-0410-412

Drayer, B., Burger, P., Darwin, R., Riederer, S., Herfkens, R., and Johnson, G. A. (1986). Magnetic resonance imaging of brain iron. *Am. J. Neuroradiol.* 7, 373–380.

Dubuisson, M., and Jain, A. K. (1994). "A Modified Hausdorff Distance for Object Matching," in *Proceedings of 12th International Conference on Pattern Recognition*, Jerusalem. doi: 10.1109/ICPR.1994.576361

Engelhardt, K. A., Marchetta, P., Schwarting, R. K. W., and Melo-Thomas, L. (2018). Haloperidol–Induced catalepsy is ameliorated by deep brain stimulation of the inferior colliculus. *Sci. Rep.* 8:2216. doi: 10.1038/s41598-018-19990-y

Fischl, B., Rajendran, N., Busa, E., Augustinack, J., Hinds, O., Thomas Yeo, B. T., et al. (2008). Cortical folding patterns and predicting cytoarchitecture. *Cereb. Cortex* 18, 1973–1980. doi: 10.1093/cercor/bhm225

Ghosh, S. S., Kakunoori, S., Augustinack, J., Nieto-Castanon, A., Kovelman, I., Gaab, N., et al. (2010). Evaluating the validity of volume-based and surface-based brain image registration for developmental cognitive neuroscience studies in children 4 to 11years of age. *Neuroimage* 53, 85–93. doi: 10.1016/j.neuroimage.2010.05.075

Giraldo-Chica, M., Hegarty, J. P., and Schneider, K. A. (2015). Morphological differences in the lateral geniculate nucleus associated with dyslexia. *Neuroimage Clin.* 7, 830–836. doi: 10.1016/j.nicl.2015.03.011

Giraldo-Chica, M., and Schneider, K. A. (2018). Hemispheric asymmetries in the orientation and location of the lateral geniculate nucleus in dyslexia. *Dyslexia* 24, 197–203. doi: 10.1002/dys.1580

Glendenning, K. K., and Masterton, R. B. (1998). Comparative morphometry of mammalian central auditory systems: variation in nuclei and form of the ascending system. *Brain Behav. Evol.* 51, 59–89. doi: 10.1159/000006530

Hernowo, A. T., Boucard, C. C., Jansonius, N. M., Hooymans, J. M. M., and Cornelissen, F. W. (2011). Automated morphometry of the visual pathway in primary open-angle glaucoma. *Investig. Ophthalmol. Vis. Sci.* 52, 2758–2766. doi: 10.1167/iovs.10-5682

Hernowo, A. T., Prins, D., Baseler, H. A., Plank, T., Gouws, A. D., Hooymans, J. M. M., et al. (2014). Morphometric analyses of the visual pathways in macular degeneration. *Cortex* 56, 99–110. doi: 10.1016/j.cortex.2013.01.003

Hilbig, H., Beil, B., Hilbig, H., Call, J., and Bidmon, H. J. (2009). Superior olivary complex organization and cytoarchitecture may be correlated with function and catarrhine primate phylogeny. *Brain Struct. Funct.* 213, 489–497. doi: 10.1007/s00429-008-0201-205

Hinds, O., Polimeni, J. R., Rajendran, N., Balasubramanian, M., Amunts, K., Zilles, K., et al. (2009). Locating the functional and anatomical boundaries of human primary visual cortex. *Neuroimage* 46, 915–922. doi: 10.1016/j.neuroimage.2009.03.036

Hoffmann, M. B., Stadler, J., Kanowski, M., and Speck, O. (2009). Retinotopic mapping of the human visual cortex at a magnetic field strength of 7T. *Clin. Neurophysiol.* 120, 108–116. doi: 10.1016/j.clinph.2008.10.153

Hopf, A. (1965). Volumetrische untersuchunger zur ver- gleichenden anatomie des thalamus. *J. F. Hirnforschung.* 8, 25–38.

Horton, J. C., Landau, K., Maeder, P., and Hoyt, W. F. (1990). Magnetic resonance imaging of the human lateral geniculate body. *Arch. Neurol.* 47, 1201–1206. doi: 10.1001/archneur.1990.00530110059017

Iglesias, J. E., Van Leemput, K., Augustinack, J., Insausti, R., Fischl, B., and Reuter M. (2016). Bayesian longitudinal segmentation of hippocampal substructures in brain MRI using subject-specific atlases. *Neuroimage* 141, 542–555. doi: 10.1016/j.neuroimage.2016.07.020

Javad, F., Warren, J. D., Micallef, C., Thornton, J. S., Golay, X., Yousry, T., et al. (2014). Auditory tracts identified with combined fMRI and diffusion tractography. *Neuroimage* 84, 562–574. doi: 10.1016/j.neuroimage.2013.09.007

Joswig, H., Schönenberger, U., Brügge, D., Richter, H., and Surbeck, W. (2015). Reversible pure word deafness due to inferior colliculi compression by a pineal germinoma in a young adult. *Clin. Neurol. Neurosurg.* 139, 62–65. doi: 10.1016/j.clineuro.2015.08.034

Kang, D. H., Kwon, K. W., Gu, B. M., Choi, J. S., Jang, J. H., and Kwon, J. S. (2008). Structural abnormalities of the right inferior colliculus in schizophrenia. *Psychiatry Res.* 164, 160–165. doi: 10.1016/j.pscychresns.2007.12.023

Kastner, S., O'Connor, D. H., Fukui, M. M., Fehd, H. M., Herwig, U., and Pinsk, M. A. (2004). Functional imaging of the human lateral geniculate nucleus and pulvinar. *J. Neurophysiol.* 91, 438–448. doi: 10.1152/jn.00553.2003

Kaur, S., Powell, S., He, L., Pierson, C. R., and Parikh, N. A. (2014). Reliability and repeatability of quantitative tractography methods for mapping structural white matter connectivity in preterm and term infants at term-equivalent age. *PLoS One* 9:e85807. doi: 10.1371/journal.pone.0085807

Keifer, O. P., Gutman, D. A., Hecht, E. E., Keilholz, S. D., and Ressler, K. J. (2015). A comparative analysis of mouse and human medial geniculate nucleus connectivity: a DTI and anterograde tracing study. *Neuroimage* 105, 53–66. doi: 10.1016/j.neuroimage.2014.10.047

Keil, B., Triantafyllou, C., Hamm, M., and Wald, L. L. (2010). "Design Optimization of a 32- Channel Head Coil at 7 T," in *Proceedings of the Annual Meeting of the International Society for Magnetic Resonance in Medicine*, Stockholm, 1493.

Kelly, K. R., McKetton, L., Schneider, K. A., Gallie, B. L., and Steeves, J. K. E. (2014). Altered anterior visual system development following early monocular enucleation. *Neuroimage Clin.* 4, 72–81. doi: 10.1016/j.nicl.2013.10.014

Keuken, M. C., Bazin, P. L., Schäfer, A., Neumann, J., Turner, R., and Forstmann, B. U. (2013). Ultra-High 7T MRI of structural age-related changes of the subthalamic nucleus. *J. Neurosci.* 33, 4896–4900. doi: 10.1523/JNEUROSCI.3241-12.2013

Kitajima, M., Hirai, T., Yoneda, T., Iryo, Y., Azuma, M., Tateishi, M., et al. (2015). Visualization of the medial and lateral geniculate nucleus on phase difference enhanced imaging. *Am. J. Neuroradiol.* 36, 1669–1674. doi: 10.3174/ajnr.A4356

Klein, A., Ghosh, S. S., Avants, B., Yeo, B. T. T., Fischl, B., Ardekani, B., et al. (2010). Evaluation of volume-based and surface-based brain image registration methods. *Neuroimage* 51, 214–220. doi: 10.1016/j.neuroimage.2010.01.091

Korsholm, K., Madsen, K. H., Frederiksen, J. L., Skimminge, A., and Lund, T. E. (2007). Recovery from optic neuritis: an ROI-Based analysis of LGN and visual cortical areas. *Brain* 130, 1244–1253. doi: 10.1093/brain/awm045

Kulesza, R. J. (2007). Cytoarchitecture of the human superior olivary complex: medial and lateral superior olive. *Hear. Res.* 225, 80–90. doi: 10.1016/j.heares.2006.12.006

Landgrebe, M., Langguth, B., Rosengarth, K., Braun, S., Koch, A., Kleinjung, T., et al. (2009). Structural brain changes in tinnitus: grey matter decrease in auditory and non-auditory brain areas. *Neuroimage* 46, 213–218. doi: 10.1016/j.neuroimage.2009.01.069

Lee, J. Y., Jeong, H. J., Lee, J. H., Kim, Y. J., Kim, E. Y., Kim, Y. Y., et al. (2014). An investigation of lateral geniculate nucleus volume in patients with primary open-angle glaucoma using 7 tesla magnetic resonance imaging. *Investig. Ophthalmol. Vis. Sci.* 55, 3468–3476. doi: 10.1167/iovs.14-13902

Lee, J. Y., Yoon, E. J., Lee, W. W., Kim, Y. K., Lee, J. Y., and Jeon, B. (2016). Lateral geniculate atrophy in parkinson's with visual hallucination: a trans-synaptic degeneration? *Mov. Disord.* 31, 547–554. doi: 10.1002/mds.26533

Li, M., He, H. G., Shi, W., Li, J., Lv, B., Wang, C. H., et al. (2012). Quantification of the human lateral geniculate nucleus in vivo using MR imaging based on morphometry: volume loss with age. *Am. J. Neuroradiol.* 33, 915–921. doi: 10.3174/ajnr.A2884

Maffei, C., Jovicich, J., De Benedictis, A., Corsini, F., Barbareschi, M., Chioffi, F., et al. (2018). Topography of the human acoustic radiation as revealed by Ex Vivo fibers micro-dissection and in vivo diffusion-based tractography. *Brain Struct. Funct.* 223, 449–459. doi: 10.1007/s00429-017-1471-1476

Mai, J. K., Berger, K., and Sofroniew, M. V. (1993). Morphometric evaluation of neurophysin-immunoreactivity in the human brain: pronounced inter-individual variability and evidence for altered staining patterns in schizophrenia. *J. Fur Hirnforschung* 34, 133–154.

May, P. J. (2006). The mammalian superior colliculus: laminar structure and connections. *Prog. Brain Res.* 151, 321–378. doi: 10.1016/S0079-6123(05)51011-51012

Mcketton, L., Kelly, K. R., and Schneider, K. A. (2014). Abnormal lateral geniculate nucleus and optic chiasm in human albinism. *J. Comp. Neurol.* 522, 2680–2687. doi: 10.1002/cne.23565

Moerel, M., De Martino, F., Uðurbil, K., Yacoub, E., and Formisano, E. (2019). Processing complexity increases in superficial layers of human primary auditory cortex. *Sci. Rep.* 9:5502. doi: 10.1038/s41598-019-41965-w

Morosan, P., Rademacher, J., Schleicher, A., Amunts, K., Schormann, T., and Zilles, K. (2001). Human primary auditory cortex: cytoarchitectonic subdivisions and mapping into a spatial reference system. *Neuroimage* 13, 684–701. doi: 10.1006/nimg.2000.0715

Nara, T., Goto, N., Hamano, S., and Okada, A. (1996). Morphometric development of the human fetal auditory system: inferior collicular nucleus. *Brain Dev.* 18, 35–39. doi: 10.1016/0387-7604(95)00089-5

O'Connor, D. H., Fukui, M. M., Pinsk, M. A., and Kastner, S. (2002). Attention modulates responses in the human lateral geniculate nucleus. *Nat. Neurosci.* 5, 1203–1209. doi: 10.1038/nn957

Olszewski, J., and Baxter, D. (2014). *Cytoarchitecture of the Human Brain Stem*, 3rd Edn. Karger (Philadelphia, PA: Lippincott), 104–119.

Pasu, S., Ridha, B. H., Wagh, V., Jindahra, P., Siddiqui, A., Plant, G., et al. (2015). Homonymous sectoranopia: asymptomatic presentation of a lateral geniculate

nucleus lesion. *Neuro Ophthalmol.* 39, 289–294. doi: 10.3109/01658107.2015.1079221

Paxinos, G., Xu-Feng, H., Sengul, G., and Watson, C. (2012). *Organization of Brainstem Nuclei. The Human Nervous System*. Amsterdam: Elsevier Academic Press.

Prins, D., Hanekamp, S., and Cornelissen, F. W. (2016). Structural brain MRI studies in eye diseases: are they clinically relevant? A review of current findings. *Acta Ophthalmol.* 94, 113–121. doi: 10.1111/aos.12825

Putnam, T. J. (1926). Studies on the central visual system: IV. The details of the organization of the geniculostriate system in man. *Arch. Neurol. Psychiatry* 16, 683–707. doi: 10.1001/archneurpsyc.1926.02200300003001

Rademacher, J., Morosan, P., Schormann, T., Schleicher, A., Werner, C., Freund, H. J., et al. (2001). Probabilistic mapping and volume measurement of human primary auditory cortex. *Neuroimage* 13, 669–683. doi: 10.1006/nimg.2000.0714

Reese, T. G., Heid, O., Weisskoff, R. M., and Wedeen, V. J. (2003). Reduction of eddy-current-induced distortion in diffusion MRI using a twice-refocused spin echo. *Magnet. Reson. Med.* 49, 177–182. doi: 10.1002/mrm.10308

Ress, D., Backus, B. T., and Heeger, D. J. (2000). Activity in primary visual cortex predicts performance in a visual detection task. *Nat. Neurosci.* 3, 940–945. doi: 10.1038/78856

Saenz, M., and Langers, D. R. M. (2014). Tonotopic mapping of human auditory cortex. *Hear. Res. Hum. Aud. Neuroimaging* 307, 42–52. doi: 10.1016/j.heares.2013.07.016

Sánchez-Panchuelo, R. M., Francis, S. T., Schluppeck, D., and Bowtell, R. W. (2012). Correspondence of human visual areas identified using functional and anatomical MRI in Vivo at 7 T. *J. Magnet. Reson. Imaging* 35, 287–299. doi: 10.1002/jmri.22822

Schmidt, M. A., Knott, M., Heidemann, R., Michelson, G., Kober, T., Dörfler, A., et al. (2018). Investigation of lateral geniculate nucleus volume and diffusion tensor imaging in patients with normal tension glaucoma using 7 tesla magnetic resonance imaging. *PLoS One* 13:e0198830. doi: 10.1371/journal.pone.0198830

Schneider, K. A., and Kastner, S. (2005). Visual responses of the human superior colliculus: a high-resolution functional magnetic resonance imaging study. *J. Neurophysiol.* 94, 2491–2503. doi: 10.1152/jn.00288.2005

Schneider, K. A., and Kastner, S. (2009). Effects of sustained spatial attention in the human lateral geniculate nucleus and superior colliculus. *J. Neurosci.* 29, 1784–1795. doi: 10.1523/JNEUROSCI.4452-08.2009

Schneider, K. A., Richter, M. C., and Kastner, S. (2004). Retinotopic organization and functional subdivisions of the human lateral geniculate nucleus: a high-resolution functional magnetic resonance imaging study. *J. Neurosci.* 24, 8975–8985. doi: 10.1523/JNEUROSCI.2413-04.2004

Selemon, L. D., and Begovic, A. (2007). Stereologic analysis of the lateral geniculate nucleus of the thalamus in normal and schizophrenic subjects. *Psychiatry Res.* 151, 1–10. doi: 10.1016/j.psychres.2006.11.003

Sitek, K. R., Gulban, O. F., Calabrese, E., Johnson, G. A., Lage-Castellanos, A., Moerel, M., et al. (2019). Mapping the human subcortical auditory system using histology, post mortem MRI and *in vivo* MRI at 7T. *eLife* 8, 1–44. doi: 10.7554/eLife.48932

Smit, J. V., Janssen, M. L. F., van Zwieten, G., Jahanshahi, A., Temel, Y., and Stokroos, R. J. (2016). Deep brain stimulation of the inferior colliculus in the rodent suppresses tinnitus. *Brain Res.* 1650, 118–124. doi: 10.1016/j.brainres.2016.08.046

Stejskal, E. O., and Tanner, J. E. (1965). Spin diffusion measurements: spin echoes in the presence of a time-dependent field gradient. *J. Chem. Phys.* 42, 288–292. doi: 10.1063/1.1695690

Stephan, H., Frahm, H., and Baron, G. (1981). New and revised data on volumes of brain structures in insectivores and primates. *Folia Primatol.* 35, 1–29. doi: 10.1159/000155963

Tona, K. D., Keuken, M. C., de Rover, M., Lakke, E., Forstmann, B. U., Nieuwenhuis, S., et al. (2017). In Vivo visualization of the locus coeruleus in humans: quantifying the test–retest reliability. *Brain Struct. Funct.* 222, 4203–4217. doi: 10.1007/s00429-017-1464-5

Tournier, J. D., Calamante, F., Gadian, D. G., and Connelly, A. (2004). Direct estimation of the fiber orientation density function from diffusion-weighted MRI data using spherical deconvolution. *Neuroimage* 23, 1176–1185. doi: 10.1016/j.neuroimage.2004.07.037

Tzourio-Mazoyer, N., Landeau, B., Papathanassiou, D., Crivello, F., Etard, O., Delcroix, N., et al. (2002). Automated anatomical labeling of activations in SPM using a macroscopic anatomical parcellation of the MNI MRI single-subject brain. *Neuroimage* 15, 273–289. doi: 10.1006/nimg.2001.0978

Varentsova, A., Zhang, S., and Arfanakis, K. (2014). Development of a high angular resolution diffusion imaging human brain template. *Neuroimage* 91, 177–186. doi: 10.1016/j.neuroimage.2014.01.009

Wang, J., Li, T., Sabel, B. A., Chen, Z., Wen, H., Li, J., et al. (2016). Structural brain alterations in primary open angle glaucoma: a 3T MRI study. *Sci. Rep.* 6:18969. doi: 10.1038/srep18969

Wang, J., Miao, W., Li, J., Li, M., Zhen, Z., Sabel, B., et al. (2015). Automatic segmentation of the lateral geniculate nucleus: application to control and glaucoma patients. *J. Neurosci. Methods* 255, 104–114. doi: 10.1016/j.jneumeth.2015.08.006

Wasserthal, C., Brechmann, A., Stadler, J., Fischl, B., and Engel, K. (2014). Localizing the human primary auditory cortex in Vivo using structural MRI. *Neuroimage* 93(Pt 2), 237–251. doi: 10.1016/j.neuroimage.2013.07.046

Wiegell, M. R., Tuch, D. S., Larsson, H. B. W., and Wedeen, V. J. (2003). Automatic segmentation of thalamic nuclei from diffusion tensor magnetic resonance imaging. *Neuroimage* 19(2 Pt 1), 391–401. doi: 10.1016/s1053-8119(03)00044-2

Yarnykh, V. L. (2007). Actual flip-angle imaging in the pulsed steady state: a method for rapid three-dimensional mapping of the transmitted radiofrequency field. *Magnet. Reson. Med.* 57, 192–200. doi: 10.1002/mrm.21120

Yendiki, A., Panneck, P., Srinivasan, P., Stevens, A., Zöllei, L., Augustinack, J., et al. (2011). Automated probabilistic reconstruction of white-matter pathways in health and disease using an atlas of the underlying anatomy. *Front. Neuroinformatics* 5:23. doi: 10.3389/fninf.2011.00023

Yilmaz, Y. Z., and Yilmaz, M. (2018). "Transcranial Magnetic Stimulation in the Treatment of Tinnitus," in *En Transcranial Magnetic Stimulation in Neuropsychiatry* ed. L. Ustohal (Rijeka: InTech) doi: 10.5772/intechopen.73221

Zhang, H., Schneider, T., Wheeler-Kingshott, C. A., and Alexander, D. C. (2012). NODDI: practical *in Vivo* neurite orientation dispersion and density imaging of the human brain. *Neuroimage* 61, 1000–1016. doi: 10.1016/j.neuroimage.2012.03.072

Zvorykin, V. P. (1981). Neuromorphological evidence of individual differences in human vision. *Arkhiv Anatomii Gistologii I Embriologii* 81, 21–24.

Conflict of Interest Statement: The authors declare that the research was conducted in the absence of any commercial or financial relationships that could be construed as a potential conflict of interest.

frontiers in Neuroscience

REVIEW
published: 12 September 2019
doi: 10.3389/fnins.2019.00964

Brain Functional Connectivity Through Phase Coupling of Neuronal Oscillations: A Perspective From Magnetoencephalography

Laura Marzetti[1,2]*, *Alessio Basti*[1,2], *Federico Chella*[1,2], *Antea D'Andrea*[1,2], *Jaakko Syrjälä*[1,2] *and Vittorio Pizzella*[1,2]

[1] *Imaging and Clinical Sciences, Department of Neuroscience, University of Chieti-Pescara, Chieti, Italy,* [2] *Institute for Advanced Biomedical Technologies, University of Chieti-Pescara, Chieti, Italy*

Magnetoencephalography has gained an increasing importance in systems neuroscience thanks to the possibility it offers of unraveling brain networks at time-scales relevant to behavior, i.e., frequencies in the 1–100 Hz range, with sufficient spatial resolution. In the first part of this review, we describe, in a unified mathematical framework, a large set of metrics used to estimate MEG functional connectivity at the same or at different frequencies. The different metrics are presented according to their characteristics: same-frequency or cross-frequency, univariate or multivariate, directed or undirected. We focus on phase coupling metrics given that phase coupling of neuronal oscillations is a putative mechanism for inter-areal communication, and that MEG is an ideal tool to non-invasively detect such coupling. In the second part of this review, we present examples of the use of specific phase methods on real MEG data in the context of resting state, visuospatial attention and working memory. Overall, the results of the studies provide evidence for frequency specific and/or cross-frequency brain circuits which partially overlap with brain networks as identified by hemodynamic-based imaging techniques, such as functional Magnetic Resonance (fMRI). Additionally, the relation of these functional brain circuits to anatomy and to behavior highlights the usefulness of MEG phase coupling in systems neuroscience studies. In conclusion, we believe that the field of MEG functional connectivity has made substantial steps forward in the recent years and is now ready for bringing the study of brain networks to a more mechanistic understanding.

Keywords: magnetoencephalography, functional connectivity, brain networks, phase coupling, brain rhythms

OPEN ACCESS

Edited by:
Federico Giove, Centro Fermi—Museo Storico della Fisica e Centro Studi e Ricerche Enrico Fermi, Italy

Reviewed by:
Linda J. Larson-Prior, College of Medicine, University of Arkansas for Medical Sciences, United States
Arne Ewald, Philips Research Hamburg, Germany

***Correspondence:**
Laura Marzetti
laura.marzetti@unich.it

Specialty section:
This article was submitted to Brain Imaging Methods, a section of the journal Frontiers in Neuroscience

Received: *30 April 2019*
Accepted: *28 August 2019*
Published: *12 September 2019*

Citation:
Marzetti L, Basti A, Chella F, D'Andrea A, Syrjälä J and Pizzella V (2019) Brain Functional Connectivity Through Phase Coupling of Neuronal Oscillations: A Perspective From Magnetoencephalography. Front. Neurosci. 13:964. doi: 10.3389/fnins.2019.00964

INTRODUCTION

In the last decades, systems neuroscience has made it clear that brain functioning requires the cooperation of several spatially separated brain regions to allow for integrative functions (e.g., vision, audition), as well as for higher order functions (e.g., understanding of actions), for a review see e.g., Rizzolatti et al. (2018). The reliable estimation of this cooperation, i.e., of functional connectivity between brain areas, is thus of primary importance to disclose the physiological and pathological organization of the human brain. To this end, several non-invasive imaging techniques

and novel analysis methods have contributed to the examination of whole-brain functional connectivity patterns: functional Magnetic Resonance (fMRI) and functional Near Infrared Spectroscopy (fNIRS) have investigated the level of co-activation between brain regions as a proxy for functional communication (e.g., Smith et al., 2013; Wang et al., 2017), while electrophysiological techniques such as ElectroEncephaloGraphy (EEG) and MagnetoEncephaloGraphy (MEG), have characterized both the level of co-activation between brain regions and the coupling of their respective signals, i.e., the statistical relationship between time-series of neuronal signals. A recent review on the theory and algorithms of electrophysiological brain connectivity analysis can be found in He et al. (2019).

In this review we will focus on MEG, i.e., the measurement of the magnetic field generated by neural currents. Indeed, MEG has gained an increasing importance in systems neuroscience as testified by the impact of MEG related publications (Baillet, 2017). Magnetoencephalography, being able to track neuronal activity without the filtering effect of the neuro-vascular coupling (Singh, 2012) can provide direct information about neuronal activity and functional connectivity. In the last decade, MEG functional connectivity has contributed to reinforce the concept of Resting State Networks (RSNs) as defined by fMRI (Deco and Corbetta, 2011) by assessing the correlation between the Blood-Oxygen-Level-Dependent (BOLD) time-series of two brain regions. In MEG, initially Amplitude Envelope Correlation (AEC) has been used to assess the level of co-activation between MEG signals of different brain regions. Specifically, MEG AEC has been calculated as the correlation of the slow temporal fluctuations (envelope) of the orthogonalized MEG signals (for a review see O'Neill et al., 2015). Moreover, MEG is able to track neuronal activity at its characteristic time scale, i.e., milliseconds, and it is thus ideally suited to assess the faster dynamics of the different brain areas as well as of their functional connectivity. Indeed, this characteristic makes MEG also able to investigate, with high spectral resolution, neural oscillations which are known to subserve brain connectivity and to play important roles in cognitive processes (Varela et al., 2001; Engel et al., 2013). In more detail, it has been hypothesized that only coherently oscillating neuronal groups can interact effectively. This hypothesis, namely Communication Through Coherence (CTC; Fries, 2005), is grounded in the fact that neural oscillations are associated to neuronal excitability fluctuations: two neuronal groups can communicate only when they share the same excitability state, with a possible time lag between the two that takes into account the speed of traveling signals (Bastos et al., 2015; Fries, 2015). Thus, long range connectivity can be assessed through the characterization of phase-phase coupling (hereinafter simply referred to as phase coupling) between MEG signals which has also been related to the concept of RSNs (e.g., Marzetti et al., 2013).

This review aims at introducing the different methods used to assess connectivity in MEG, with emphasis on methods based on phase coupling. We will discuss the advantages of studying brain connectivity starting from neural sources, as estimated from MEG, over studying brain connectivity directly from the measured signals. MEG has been often considered similar to EEG since both are related to the electromagnetic field generated by the currents flowing within neurons and in the surrounding medium, i.e., the brain volume. Indeed, while sharing the same elementary neuronal phenomena, each of the two techniques has its own strengths as summarized in Lopes da Silva (2013), and the physics laws that describe how these currents translate into magnetic field and electric potential show the differences between the two techniques (Hämäläinen et al., 1993). Among others, the lower sensitiveness of MEG to the properties of the conducting medium (Vorwerk et al., 2014; Stenroos and Nummenmaa, 2016) and the need for a reference signal in EEG (Chella et al., 2016a, 2017; Van de Steen et al., 2019) imply an important advantage of MEG over EEG in the assessment of brain functional connectivity.

This review is organized as follows. Firstly, the principles of MEG, including the methods used to estimate brain activity and its relevance to neuronal oscillations, will be revised. Secondly, an extensive review of the methods commonly used to assess functional connectivity will be presented, in which the different methods are classified as undirected or directed according to their outputs, univariate or multivariate, and same-frequency or cross-frequency according to their inputs. Finally, the use of phase coupling methods on MEG data in the context of resting state, visuospatial attention and working memory will be presented. **Table 1** clarifies the terminology used throughout this review.

MAGNETOENCEPHALOGRAPHY

The aim of this paragraph is to briefly review the major characteristics of the MEG signal, including its origin, the identification of brain sources from the measured MEG signal, and the potential of MEG to detect neuronal oscillations and to investigate functional connectivity.

Beyond these aspects, we want to emphasize here that the unique features of MEG have made this technique more and more attractive to researchers in order to answer neuroscientific as well as clinical questions (Baillet, 2017). In parallel, the need for guidelines for the acquisition and analysis of MEG data has emerged. To instruct newcomers, as well as to standardize procedures across MEG laboratories, good practice papers have been recently published for both basic (Gross et al., 2013) and clinical neuroscience (Burgess et al., 2011; Hari et al., 2018). To facilitate the analysis, several open-source software packages are available to the user, the most widely used being: Brainstorm (Tadel et al., 2011), FieldTrip (Oostenveld et al., 2011), MNE (Gramfort et al., 2014), and SPM8 (Litvak et al., 2011). Additionally, a multimodal extension of the Brain Imaging Data Structure (BIDS), originally proposed to standardize MRI data formats (MRI-BIDS), has been proposed for MEG data (MEG-BIDS; Niso et al., 2018). This will allow a smoother data harmonization as well as to reduce sharing efforts across the MEG community.

Origin of MEG Signal

Nowadays, it is commonly agreed that MEG signals originate mostly from postsynaptic currents in the apical dendrites of

TABLE 1 | List of terms and definitions used.

Term	Definition
Magnetoencephalography (MEG)	MEG is a non-invasive neuroimaging technique that can be used to detect extremely weak magnetic fields generated by spatially aligned neurons that are simultaneously activated. The measured MEG signal originates from postsynaptic currents in the apical dendrites of pyramidal neurons.
Neural oscillations	Assemblies of neurons influence each other through excitatory and inhibitory synaptic connections which leads to rhythmic activation and inhibition of neurons in the network. The rhythmic activity is reflected in oscillating signals that can be measured outside of the scalp with EEG and MEG.
Phase	The phase of periodic oscillation, i.e., an oscillation which repeats itself exactly after one period (e.g., sinusoidal wave) indicates the fractional portion of the period that has been completed. The phase is typically expressed as an angle spanning a whole turn (2π) as the oscillation goes through a period. In the context of neural oscillations, the phase reflects the excitability state of the neurons and therefore the phase influences the discharge times of the neurons in the network.
Functional connectivity	Functional connectivity refers to statistical associations or temporal correlations between two or more anatomically distinct brain regions.
Phase coupling	The term phase coupling refers to the relationship between oscillation phases in different brain regions. More specifically, in this work, the term phase coupling is used to indicate the presence of peaks in the distribution of the phase difference across time or signal realizations (e.g., trials, or different segments into which continuous signals can be divided). Phase coupling is considered to be a fundamental neural mechanism that supports neural communication, neural plasticity and it is considered relevant for many cognitive processes. In the literature also the term *phase synchronization* is used as a synonym of phase coupling.
Communication through Coherence (CTC)	CTC refers to the concept that only coherently oscillating neuronal groups can interact efficiently. The concept is grounded in the fact that neural oscillations are associated to neuronal excitability fluctuations. Only when inputs from presynaptic group consistently arrive to the postsynaptic group at the time of high input gain (at appropriate phase) the two groups can effectively communicate. This requires coherence between the pre- and postsynaptic groups since otherwise the inputs arrive at random phases of excitability state and will have less impact on the postsynaptic neurons.

pyramidal neurons in the cortical mantle. Maxwell's equations in their quasi-static approximation describe how these currents translate into magnetic field (Hämäläinen et al., 1993). The MEG challenge lies into measuring such an extremely weak magnetic field, about one million times smaller than the Earth's magnetic field, in an often magnetically noisy environment due to nearby large metal objects or strong electric currents. Typically, the simultaneous activation of about tens of thousands of spatially aligned nearby neurons (i.e., a neuronal pool) is needed to generate a detectable MEG signal.

All of the currently operating MEG systems are based on superconducting magnetometers, namely SQUIDs (superconducting quantum interference device). These sensors feature an exquisite sensitivity to pick up the weak neuromagnetic fields the bandwidth of which spans from few kHz down to almost DC (Baillet, 2017). Moreover, all MEG systems operate in a magnetic shielded room to reduce environmental magnetic noise. Recently, the development of new sensors operating at room temperature, namely Optically Pumped Magnetometers (OPMs), have open new opportunities for the widening of MEG applications. These devices, although still suffering from higher noise and limited bandwidth with respect to SQUIDs, offer the possibility to record MEG using a wearable device in a more ecological setting (Boto et al., 2018; Iivanainen et al., 2019).

Source Space MEG

MEG sensor signals arise from the mixture of the activity of several neuronal pools. In fact, each MEG sensor measures, with different weights, the signal generated by all neuronal pools active at a given time. This results in the overlap, at sensor level, of the fields generated by each pool. Even if one would unrealistically assume that only one pool is active, and thus no actual brain connectivity is present, a fake connectivity profile between the sensors would be detected as the result of all sensors measuring the activity of the one brain source. Thus, assessing true brain connectivity directly from MEG signals at sensor level is challenging (Schoffelen and Gross, 2009).

A prerequisite to reliably assess functional connectivity is to rely on source space data, i.e., the activity of each neuronal pool. In fact, the estimation of functional connectivity from sensor space data, i.e., from the activities measured by the sensors outside the head, is not only prone to the above described fake connectivity profile but is also very difficult to be interpreted in terms of the underlying functional connectivity between brain regions given that the same connectivity profile can be generated by different configurations of interacting sources. Unfortunately, the estimation of the activities of brain regions requires the solution of an ill-posed electromagnetic inverse problem (Ilmoniemi and Sarvas, 2019). In practice, there exist reasonable approximations incorporating prior knowledge (e.g., from fMRI) and constraints (e.g., minimum norm) that make this issue less severe and allow the use of MEG in brain imaging and in the study of brain networks.

The solution to the MEG inverse problem requires a forward model, which gives the mathematical relationship between the brain currents (sources) and the measured magnetic field. The forward model includes models for the sources, the geometry of the conducting medium (i.e., the head), and the MEG sensors. Besides the intrinsic non-uniqueness of the electromagnetic inverse problem solution and the correctness of *a priori* assumptions and constraints used to make the

solution unique, the attainable accuracy in the solution highly depends on the accuracy of these models. The influence of the head model has been investigated in a number of studies (e.g., Güllmar et al., 2010; Stenroos et al., 2014; Vorwerk et al., 2014). The distinction between white and gray matter and the inclusion of the cerebrospinal fluid have been shown to considerably improve forward model accuracy (Vorwerk et al., 2014; Stenroos and Nummenmaa, 2016). To date, anatomically realistic and sufficiently detailed head models can be constructed from the segmentation of structural head images (usually MRI or computed tomography scans; for guidelines, see Vorwerk et al., 2014). Nonetheless, the forward model accuracy is still limited by approximations in geometry structures, uncertainty in conductivity values (Akhtari et al., 2002; Dannhauer et al., 2011), as well as errors in head-to-sensor co-registration (Adjamian et al., 2004; Troebinger et al., 2014; Chella et al., 2019).

The estimates of neural activity are usually obtained by either a localization approach or an imaging approach. The former assumes that brain activity at a given time point is generated by a limited number of neuronal pools, each represented by an equivalent current dipole (ECD), the location, orientation, and strength of which need to be estimated. Numerical approaches based on least-squares techniques are usually used to this purpose. The latter, i.e., the imaging approach, aims at estimating the overall distribution of neural activity by discretizing the brain, and thus is more suitable for whole brain functional connectivity estimation. Typically, a grid of elementary sources (dipoles), fixed in location and, possibly, in orientation, in the brain volume or limited to the cortical gray matter surface is used: the inverse problem solution for imaging approaches results in the estimation of the magnitude of all these elementary sources. Among imaging approaches, several strategies have been developed, including distributed source imaging methods (e.g., least-squares techniques such as minimum norm estimation approaches), scanning methods, and spatial filter methods. For reviews on the different imaging methods see Baillet et al. (2001), He et al. (2018), Ilmoniemi and Sarvas (2019).

The different source imaging methods are all characterized by a source-leakage effect, namely that the measured activity coming from a single elementary source is projected onto several nearby sources depending on the point spread function of the specific imaging method (Hauk et al., 2011). Source-leakage may induce a fake connectivity profile, usually referred to as "artificial connectivity" (Palva and Palva, 2012). This effect can be mitigated by using functional connectivity methods which exclude zero-phase correlations between source signals (see e.g., Marzetti et al., 2008; Nolte et al., 2009; Brookes et al., 2011a). Similarly, a priori selecting regions-of-interest as seeds for connectivity analysis, as opposed to performing whole-brain estimation, can provide misleading results in terms of "spurious connectivity" (Palva and Palva, 2012) as the activity of the sources not selected as seeds may leak into the estimated activity of the selected seeds (Hari and Parkkonen, 2015).

To show an example of this effect, 2-min of synthetic MEG recordings, sampled at 512 Hz, were simulated by using the head model and MEG sensor layout of one subject taken from the Human Connectome Project dataset (Larson-Prior et al., 2013). The time series for two interacting dipolar sources in the cortex, with orientation perpendicular to the local cortical surface, were generated as follows: the time series of source 1 was sampled from a Gaussian distribution; the time series of source 2 was set to a Finite-Impulse-Response (FIR) filtered version of the time series of the first source; the FIR filter coefficients were randomly drawn from a standard normal distribution and a filter order $P = 5$ was used. The location of source 1 was kept fixed (black dot in panel A of **Figure 1**), while the location of source 2 was varied across all the remaining cortical locations. The source time series were then projected to the sensor level by solving the MEG forward problem (Nolte, 2003). Uncorrelated sensor noise was added to sensor signals. From the synthetic recordings, source time series were reconstructed by using the eLORETA inverse approach (Pascual-Marqui et al., 2011). In **Figure 1A**, we show the cortical map for the absolute value of the eLORETA Point Spread Function (PSF) of source 1, a measure of the degree to which the activity originating from a single elementary source leaks into nearby sources.

Functional connectivity between reconstructed source time series was then estimated by using coherence (see section Methods to assess brain connectivity based on phase coupling for the mathematical description of the method). Artificially inflated coherence estimates can be observed in **Figure 1B** where the ratio between the estimated functional connectivity values and the true value (i.e., the one obtained directly from the generated source time sources) as a function of the distance between sources 1 and 2 is shown. Values larger than 1 indicate inflated functional connectivity values due to zero-lag correlations induced by source leakage. Such an effect is more relevant when the distance between the two interacting sources is small.

MEG, Neuronal Oscillations, and Functional Connectivity

The activity of neuronal pools features several oscillatory bands with frequencies ranging from about 0.05 Hz up to 500 Hz (Buzsáki and Draguhn, 2004). These frequencies are classified into several frequency bands. **Figure 2** below shows one typical classification scheme, although finer grained classifications are also possible (e.g., low alpha/high alpha as well as low gamma/high gamma).

The different frequencies are related to the different properties of the physical architecture of neuronal networks as well as to the speed of neuronal communication limited by axon conduction and synaptic delays. Indeed, higher frequency bands are characteristic of smaller spatial scales, while lower frequencies are distinctive of large-scale networks (von Stein et al., 2000; Florin and Baillet, 2015). Magnetoencephalography, thanks to its exquisite temporal resolution, excels in picking up this rhythmic brain activity and is thus an ideal tool to study local oscillatory activity.

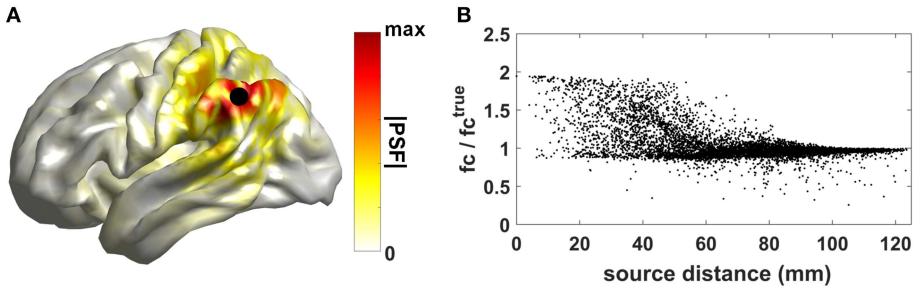

FIGURE 1 | Effects of source leakage on connectivity estimates. **(A)** Cortical map for the absolute value of the Point Spread Function (PSF) of source 1. **(B)** Ratio between the estimated functional connectivity values and the true value (i.e., the one obtained directly from the generated source time sources) as a function of the distance between sources 1 and 2.

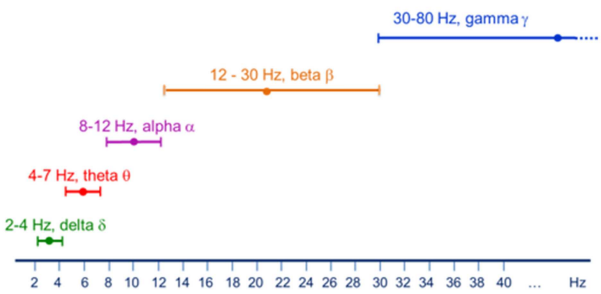

FIGURE 2 | Major brain rhythms as classified by their frequency span.

Modulations of local oscillatory activity can be observed as a consequence of task execution or stimulus presentation in a variety of conditions. One of the most prominent examples is provided by motor execution in which the oscillatory beta power in the primary motor cortex is reduced during the movement in comparison to the preceding period (ERD, Event Related Desynchronization) while it is enhanced after the movement (ERS, Event Related Synchronization, i.e., beta rebound), see Pfurtscheller and Lopes da Silva (1999) for details, or section "Magnetoencephalography as a tool for imaging brain activity" in Pizzella et al. (2014) and references therein. A modulation of local oscillatory activity shared by two brain regions is often considered as a marker of functional connectivity. In fact, Amplitude Envelope Correlation approaches have been extensively used to disclose brain functional connectivity during task (Brookes et al., 2011a) as well as at rest (de Pasquale et al., 2010; Brookes et al., 2011b). However, a more physiologically oriented probe on brain functional connectivity can be identified by phase-based metrics under the CTC hypothesis (Fries, 2005), that states that only coherently oscillating neuronal groups can interact effectively. Thus, MEG can be an ideal tool to assess functional connectivity by investigating the phase relationship between two (possibly) interacting areas. This approach will be discussed extensively in the following section.

METHODS TO ASSESS BRAIN CONNECTIVITY BASED ON PHASE COUPLING

This section provides an overview of the most widely used methods for assessing brain connectivity based on phase coupling between neural oscillations. The notion of phase is usually associated to a periodic oscillation, i.e., an oscillation which repeats itself exactly after one period (e.g., a sinusoidal wave). For a periodic oscillation, the phase indicates the fractional portion of the period that has been completed. It is typically expressed as an angle spanning a whole turn (2π) as the oscillation goes through a period. Of note, the value of the phase is meaningless if the origin of the oscillation has no physical meaning (e.g., a trigger or a stimulus). Nonetheless, the phase difference between two oscillations is always well-defined, since the dependence on the origin is implicitly canceled out in the computation of the difference. Indeed, the phase difference can be used to assess phase couplings between oscillations, as discussed below.

The concept of phase coupling has been widely discussed in the literature (e.g., Rosenblum et al., 1996; Pascual-Marqui, 2007a; Stam et al., 2007). In this work, the term "phase coupling" between two signals is meant as the presence of peaks in the distribution of the phase difference across time or signal realizations (e.g., trials, or different segments into which continuous signals can be divided), that reflect preferred values of the phase difference irrespective of the signal amplitudes (see **Figure 3**). To clarify this concept, we simulated two scenarios depicted in **Figure 3**. For scenario 1 (**Figure 3A**), we simulated one-thousand realizations, each of 1-s length and sampled at 512 Hz, of two phase-coupled signals i and j as described in the next sentences. The time series of a 5-Hz oscillator was generated by band-pass filtering white Gaussian noise around 5 Hz with 1 Hz bandwidth. The time series of the signal i, i.e., $x_i(t)$, was set to the time series of the 5 Hz oscillator while the time series of the signal j was set to a time-delayed copy of the time series of signal i, i.e., $x_j(t) = x_j(t-\tau)$, with a time delay $\tau = 75$ ms. Uncorrelated white Gaussian noise was finally added to both the generated signals. For each signal realization, the circular phase difference between signals i and j was calculated as the phase of their complex-valued coherency (see section Univariate

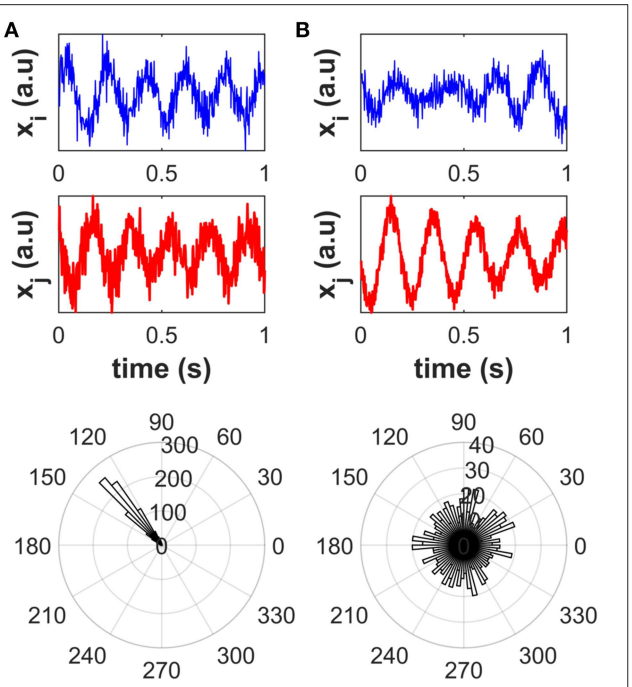

FIGURE 3 | Distribution of the circular phase difference across signal realizations for phase-coupled signals **(A)** and independent signals **(B)**. Top plots: an illustrative example of signal realization. Bottom plots: polar histogram for the distribution of the circular phase difference. A narrow peak in the circular phase difference distribution can be observed in the case of phase-coupled signals, as opposed to the case of independent signals.

methods for mathematical details). For scenario 2 (**Figure 3B**) the two signals i and j were independently generated as two 5-Hz oscillators. A narrow peak in the circular phase difference distribution can be observed in the case of phase-coupled signals (A), as opposed to the case of independent signals (B).

In the following paragraphs, the different connectivity methods will be classified as frequency-specific or cross-frequency phase-coupling methods, depending on whether they allow investigating the phase coupling at the same or different frequencies, respectively. Moreover, they will be divided into univariate and multivariate methods; the formers are designed to assess connectivity from two univariate (or scalar) time series, while the latter take as input multivariate (or vector) time series (see also **Table 2**).

Frequency-Specific Phase Coupling Methods

Univariate Methods

Let us denote by $x_i(t)$ and $x_j(t)$ the time series of the signals i and j, which can be, e.g., the estimated activities of two distinct elementary sources. The cross-spectrum between two signals i and j at a given frequency f is defined as

$$S_{ij}(f) := \left\langle X_i(f)\ X_j^*(f) \right\rangle,$$

where $X_i(f)$ and $X_j(f)$ are the Fourier transforms of $x_i(t)$ and $x_j(t)$, respectively, $(.)^*$ denotes the complex conjugate, and $\langle . \rangle$ denotes the expectation value. The latter is usually evaluated as the average across a sufficiently large number of signal realizations (or segments) under ergodicity assumption.

The *coherency* is a normalized version of the cross-spectrum (Brillinger, 1981; Rosenberg et al., 1989; Halliday et al., 1995), i.e.,

$$C_{ij}(f) := \frac{S_{ij}(f)}{\sqrt{S_{ii}(f)\ S_{jj}(f)}},$$

the absolute value of which, termed coherence, is a measure of the phase coupling between signals at a given frequency. This can be seen by representing the complex-valued Fourier transforms in terms of their amplitudes $A_i(f)$ and phases $\theta_i(f)$, i.e., $X_i(f) = A_i(f)\ e^{\iota\theta_i(f)}$ and $X_j(f) = A_j(f)\ e^{\iota\theta_j(f)}$, where ι denotes the imaginary unit. Using this notation, coherence has the following form:

$$|C_{ij}(f)| := \left| \frac{\left\langle A_i(f)\ A_j(f)\ e^{\iota\ \Delta\theta_{ij}(f)} \right\rangle}{\sqrt{\langle A_i^2(f)\rangle \left\langle A_j^2(f)\right\rangle}} \right|,$$

where the argument of the exponential function contains the phase difference between signals i and j, i.e., $\Delta\theta_{ij}(f) = \theta_i(f) - \theta_j(f) \in [-\pi, \pi]$. It turns out that coherence is the absolute value of the weighted average of $e^{\iota\ \Delta\theta_{ij}(f)}$ across signal realizations, where the weights are a function of the amplitudes. If the signals are independent, the phase difference varies randomly across realizations and the coherence vanishes. If the signals are phase-coupled, the phase difference fluctuates around some constant value, and the coherence is non-vanishing.

If the amplitude weights in the above equation are omitted, we get the mean resultant length of the phase difference (i.e., the absolute value of the average of $e^{\iota\ \Delta\theta_{ij}(f)}$ across signal realizations), which is called *phase-locking-value* (PLV; Lachaux et al., 1999), i.e.,

$$\mathrm{PLV}_{ij}(f) := \left| \left\langle e^{\iota\ \Delta\theta_{ij}(f)} \right\rangle \right|.$$

Alternative formulations for the PLV rely on the instantaneous phase difference between signals, which can be obtained from, e.g., a wavelet or Hilbert transform (Tass et al., 1998, Lachaux et al., 1999; Colclough et al., 2016).

A limitation on the use of the above measures for the assessment of phase coupling between reconstructed source signals is that they are affected by artificial zero-lag correlations, such as the ones induced by source leakage, which inflate the estimated values. In the last two decades, a number of measures have been proposed to mitigate this issue. Nolte et al. (2004) suggested the use of the *imaginary part of coherency* (ImCoh)

$$\mathrm{ImCoh}_{ij}(f) := \Im\left(C_{ij}(f)\right),$$

since it requires a phase difference between signals to be non-vanishing, and thus it does not lead to artificial phase

TABLE 2 | List of phase coupling measures.

Connectivity measure	Abbreviations	Phase coupling type	Class	Directionality	Artifactual detections due to zero-lag coupling	References	Software
Coherency	C	Same-frequency	Univariate	Undirected	Yes	Brillinger, 1981	Brainstorm; FieldTrip; MNE; METH
Phase locking value	PLV	Same-frequency	Univariate	Undirected	Yes	Lachaux et al., 1999	Brainstorm; FieldTrip; MNE; METH
Imaginary part of coherency	ImCoh	Same-frequency	Univariate	Undirected	No	Nolte et al., 2004	Brainstorm; FieldTrip; MNE; METH
Lagged coherence	ρ^2	Same-frequency	Univariate	Undirected	No	Pascual-Marqui, 2007a	Brainstorm; LORETA-KEY; METH
Imaginary part of phase locking value	iPLV	Same-frequency	Univariate	Undirected	No	Palva and Palva, 2012	
Phase lag index	PLI	Same-frequency	Univariate	Undirected	No	Stam et al., 2007	MNE; METH
Weighted phase lag index	wPLI	Same-frequency	Univariate	Undirected	No	Vinck et al., 2011	FieldTrip; MNE
Phase slope index	PSI	Same-frequency	Univariate	Directed	No	Nolte et al., 2008	FieldTrip; METH
Phase transfer entropy	pTE	Same-frequency	Univariate	Directed	No	Lobier et al., 2014	Brainstorm
Multivariate interaction measure	MIM	Same-frequency	Multivariate	Undirected	No	Ewald et al., 2012	METH
Multivariate lagged coherence	*P*	Same-frequency	Multivariate	Undirected	No	Pascual-Marqui, 2007b	LORETA-KEY
Multivariate phase slope index	MPSI	Same-frequency	Multivariate	Directed	No	Basti et al., 2018	
n:m phase locking value	$PLV^{n:m}$	Cross-frequency	Univariate	Undirected	Yes	Palva et al., 2005	
Bicoherency	Bic	Cross-frequency	Univariate	Undirected	Yes	Nikias and Petropulu, 1993	
Antisymmetric part of bicoherency	aBic	Cross-frequency	Univariate	Undirected	No	Chella et al., 2016b	

For each connectivity methods we indicate: (i) the abbreviation used in this paper; (ii) whether it investigates same- or cross-frequency phase coupling; (iii) whether it is either a univariate or a multivariate connectivity measure; (iv) whether it is directed or undirected connectivity methods; (v) whether or not the method handles the issue induced by the artificial zero-lag correlation; (vi) a reference publication for the method; (vii) main software toolbox in which the measure is implemented: Brainstorm Tadel et al., 2011; FieldTrip Oostenveld et al., 2011; LORETA-KEY (http://www.uzh.ch/keyinst/loreta.htm#_Toc391372607); METH (https://www.uke.de/english/departments-institutes/institutes/neurophysiology-and-pathophysiology/research/working-groups/); MNE Gramfort et al., 2014.

coupling detections due to zero-lag correlations due to e.g. source leakage. An alternative approach was proposed by Pascual-Marqui (2007a) with the *lagged coherence* (ρ^2), i.e.,

$$\rho_{ij}^2(f) := \frac{\left[\Im\left(S_{ij}(f)\right)\right]^2}{S_{ii}(f)\ S_{jj}(f) - \left[\Re\left(S_{ij}(f)\right)\right]^2},$$

where the instantaneous, i.e., zero lag, contributions are partialled out. This formulation is equivalent to the *"corrected" imaginary coherence* defined in Ewald et al. (2012).

Based on similar arguments, the *imaginary part of PLV* (iPLV; Palva and Palva, 2012), i.e.,

$$\mathrm{iPLV}_{\mathrm{ij}}(f) := \left|\left\langle \Im\left(e^{\imath\ \Delta\theta_{ij}(f)}\right)\right\rangle\right|$$

solely detects phase-lagged coupling.

Instead of averaging the imaginary part of $e^{\imath\ \Delta\theta_{ij}(f)}$, the *phase-lag-index* (PLI; Stam et al., 2007) quantifies the asymmetry in the distribution of the phase difference across realizations, when this distribution is centered around zero, as

$$\mathrm{PLI}_{\mathrm{ij}}(f) := \left|\left\langle sign\left(\Delta\theta_{ij}(f)\right)\right\rangle\right|.$$

To improve the robustness of PLI with respect to correlated and uncorrelated noise, as well as to increase the statistical power of the metric, Vinck et al. (2011) proposed the *weighted PLI* (wPLI) as a weighted average of the signs of the phase difference, i.e.

$$\mathrm{wPLI}_{\mathrm{ij}}(f) := \frac{\left|\left\langle\left|\Im\left(X_i(f)\ X_j^*(f)\right)\right| sign\left(\Delta\theta_{ij}(f)\right)\right\rangle\right|}{\left\langle\left|\Im\left(X_i(f)\ X_j^*(f)\right)\right|\right\rangle},$$

where the weights are equal to the imaginary part of the cross-spectra computed within realizations.

The effects of source leakage on these different connectivity measures is shown in **Figure 4**. Synthetic source time series were simulated as described in section Source space MEG. Functional connectivity between reconstructed source time courses was estimated by using either coherence (C; top left), or phase locking

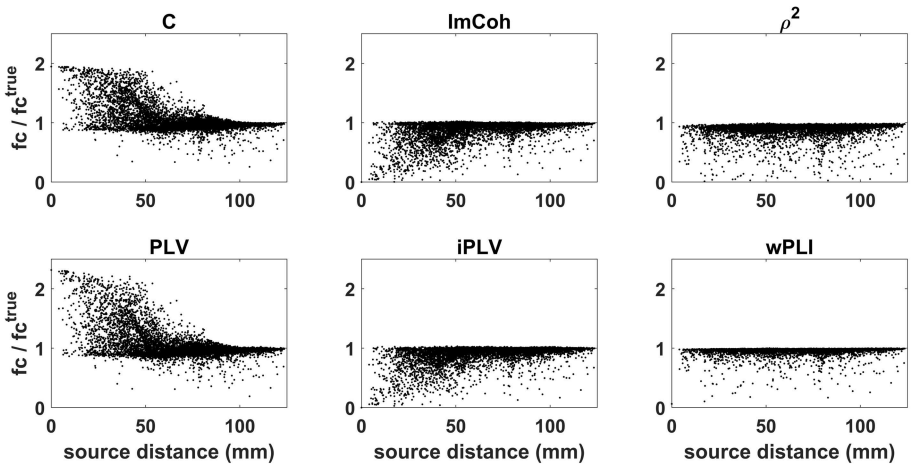

FIGURE 4 | Effects of source leakage on different connectivity measures. Functional connectivity was estimated by using: coherence (C; top left), phase locking value (PLV; bottom left), imaginary part of coherency (ImCoh; top center), imaginary part of phase locking value (iPLV; bottom center), lagged coherence (ρ^2; top right), weighted phase lag index (wPLI; bottom right). For each connectivity measure, the ratio between the estimated functional connectivity values and the true value is plotted as a function of the distance between sources 1 and 2. Artificially inflated connectivity estimates (ratio values larger than 1) can be observed for coherence and phase locking value, but not for other measures which were specifically designed to handle the effects of source leakage.

value (PLV; bottom left), or imaginary part of coherency (ImCoh; top center), or imaginary part of phase locking value (iPLV; bottom center), or lagged coherence (ρ^2; top right), or weighted phase lag index (wPLI; bottom right). For each connectivity measure, the ratio between the estimated functional connectivity values and the true value (i.e., the one obtained directly from the generated source time sources) is plotted as a function of the distance between sources 1 and 2. Artificially inflated connectivity estimates (ratio values larger than 1) can be observed for coherence and phase locking value as an effect of source leakage. Of note, this effect is not limited to close by sources but is present also when the sources are far apart (e.g., with distance of about 6 cm). Conversely, measures which were specifically designed to handle the effects of source leakage (e.g., ImCoh or iPLV) are rather conservative (ratio values smaller than 1) and tend to underestimate true connectivity values.

The following two methods are conceived to investigate the directionality of phase coupling. Specifically, Nolte et al. (2008) exploited the properties of the complex-valued coherency, and introduced the *phase slope index* (PSI) as

$$\mathrm{PSI}_{ij}(F) := \sum_{f\in F} \Im\left(C_{ij}(f+df)\left(C_{ij}(f)\right)^*\right)$$
$$= \sum_{f\in F} \left|C_{ij}(f+df)\ C_{ij}^*(f)\right| \sin\left(\Delta\theta_{\mathrm{ij}}(\mathrm{f}+\mathrm{df}) - \Delta\theta_{\mathrm{ij}}(\mathrm{f})\right),$$

where df is an incremental step in the frequency domain, and F denotes the frequency band of interest. PSI is essentially a weighted average of the slope of the phase difference $\Delta\theta_{ij}(f+df) - \Delta\theta_{ij}(f)$ across F, whose sign provides a measure of the directionality. In particular, a positive value indicates that the signal i precedes (thus leads) the signal j, while a negative value indicates the opposite (Basti et al., 2017). Similarly to ImCoh, PSI requires a phase slope between signals to be non-vanishing, and thus it does not lead to artifactual detection of directed connectivity due to artificial zero-lag correlations.

Lobier et al. (2014) applied the concept of transfer entropy (Schreiber, 2000), developed in the framework of information theory (Shannon, 1948), to the assessment of directed phase coupling, by introducing the *phase transfer entropy* (pTE). The pTE from a signal i to a signal j is defined as

$$pTE_{ij}(F,\tau) := H\left(\theta_j(F,t),\theta_j(F,t-\tau)\right) + H\left(\theta_j(F,t-\tau),\theta_i(F,t-\tau)\right) - H\left(\theta_j(F,t-\tau)\right)$$
$$-H\left(\theta_j(F,t),\ \theta_j(F,t-\tau),\theta_i(F,t-\tau)\right).$$

In the above notation, $\theta_j(F,t)$ denotes the instantaneous phase signal obtained from, e.g., Hilbert or wavelet transform of the bandpass filtered signal j; F denotes the frequency band of interest; τ denotes a given time delay; and $H(Z) := -\int p(Z)\ln\left(p(Z)\right)$ denotes the information entropy of the random variable Z, where $p(Z)$ is the probability density function (see Lobier et al., 2014, and references therein for more details). The direction of the phase coupling can be assessed through the comparison between the pTE from signal i to j and the one from j to i (Hillebrand et al., 2016). pTE has the advantage over the traditional transfer entropy measure of being able to handle the artificial zero-lag correlation effects (Lobier et al., 2014).

The above described methods are univariate methods since they are designed to assess connectivity between pairs of univariate signals, e.g., MEG signals at sensor level. When dealing with brain activity estimated from MEG signals, e.g., according to one of the strategies described in section Source space MEG, the most general situation results into three brain activity components (also termed dipole orientations or dipole moments) at each location of the discretized brain. To apply

univariate connectivity methods on these three-dimensional activity components, it is necessary to perform a dimensionality reduction to one-dimensional signals which might result in a loss of information and in a subsequent inaccuracy in the estimation of connectivity. Conversely, multivariate connectivity methods are specifically designed to take into account the whole information contained in the multidimensional nature of the input signals, i.e., they do not require a dimensionality reduction of the input signals. In the following subparagraph, a review of multivariate methods for MEG connectivity is provided.

Multivariate Methods

Let $\boldsymbol{x}_I(t) = \left(x_{i_1}(t), \ldots, x_{i_N}(t)\right)^{\mathrm{T}}$ and $x_J(t) = \left(x_{j_1}(t), \ldots, x_{j_M}(t)\right)^{\mathrm{T}}$ be the multivariate time series for the N-dimensional signals I and the M-dimensional signals J, where T denotes the transpose operator. For instance, these could represent the three-dimensional vector-source activities at two given brain locations, and thus they would have a dimension $N = M = 3$, or they could indicate two different multivariate time series consisting of the activities of all the sources within a region of interest, and thus they would have a dimension equal to the number of locations belonging to those parcels. Let also $X_I(f)$ and $X_J(f)$ be the corresponding vector Fourier transforms. The cross-spectral density matrix between $x_I(t)$ and $x_J(t)$ at a given frequency f is defined as

$$\mathbf{S}_{IJ}(f) \left\langle \boldsymbol{X}_I(f)\ \mathbf{X}_J^H(f) \right\rangle := \begin{bmatrix} \left\langle X_{i_1}(f)\ X_{j_1}^*(f) \right\rangle & \cdots & \left\langle X_{i_1}(f)\ X_{j_M}^*(f) \right\rangle \\ \vdots & \ddots & \vdots \\ \left\langle X_{i_N}(f)\ X_{j_1}^*(f) \right\rangle & \cdots & \left\langle X_{i_N}(f)\ X_{j_M}^*(f) \right\rangle \end{bmatrix},$$

where $(\cdot)^{\mathrm{H}}$ denotes the Hermitian conjugate of a matrix. The elements of $\mathbf{S}_{IJ}(f)$ are the cross-spectra between all the pairwise combinations of univariate time series of I and J.

The *multivariate interaction measure* (MIM, Ewald et al., 2012) is an index of the total phase coupling between vector-signals I and J, and it is defined as

$$\mathrm{MIM}_{IJ}(f) := Tr\left(\left(\boldsymbol{S}_{II}^{\Re}(f)\right)^{-1} \boldsymbol{S}_{IJ}^{\Im}(f) \left(\boldsymbol{S}_{JJ}^{\Re}(f)\right)^{-1} \left(\boldsymbol{S}_{IJ}^{\Im}(f)\right)^{\mathrm{T}} \right),$$

where the superscripts $\Re$ and $\Im$ denote the real and imaginary part of the complex-valued cross-spectral density matrices, $(\cdot)^{-1}$ and $Tr(\cdot)$ are the inverse and trace operators. MIM is the generalization of ImCoh to multivariate time series analysis and, in the case of two univariate time series, it coincides with the squared ImCoh. Similarly to ImCoh, MIM does not lead to artifactual phase coupling detections due to artificial zero-lag correlations. Furthermore, MIM is invariant under invertible and static linear transformations of $x_I(t)$ and $x_J(t)$ (Ewald et al., 2012), such as rotations of the physical coordinate system in which the MEG source space is defined.

The generalization of the lagged coherence to the multivariate case will be here referred to as the *multivariate lagged coherence* (P; Pascual-Marqui, 2007b), and it has the form

$$_{IJ}(f) := \ln \frac{\det\left(\Re\begin{bmatrix}\mathbf{S}_{JJ}(f) & \mathbf{S}_{JI}(f)\\ \mathbf{S}_{IJ}(f) & \mathbf{S}_{II}(f)\end{bmatrix}\right) \Big/ \det\left(\Re\begin{bmatrix}\mathbf{S}_{JJ}(f) & \mathbf{0}\\ \mathbf{0}^{\mathrm{T}} & \mathbf{S}_{II}(f)\end{bmatrix}\right)}{\det\left(\begin{bmatrix}\mathbf{S}_{JJ}(f) & \mathbf{S}_{JI}(f)\\ \mathbf{S}_{IJ}(f) & \mathbf{S}_{II}(f)\end{bmatrix}\right) \Big/ \det\left(\begin{bmatrix}\mathbf{S}_{JJ}(f) & \mathbf{0}\\ \mathbf{0}^{\mathrm{T}} & \mathbf{S}_{II}(f)\end{bmatrix}\right)}$$

where $\det(\cdot)$ denotes the determinant of a matrix, and $\mathbf{0}$ is a $M \times N$ matrix of zeros. In the particular case of univariate time series, the following identity holds: $P_{ij}(f) = -\ln\left(1 - \rho_{ij}^2(f)\right)$. Similarly to MIM, the multivariate lagged coherence is invariant under invertible and static linear transformations of input signals.

To assess the directionality from pairs of vector-signals, Basti et al. (2018) generalized the definition of PSI to multivariate time series, called *multivariate phase slope index* (MPSI). MPSI is defined as

$$\begin{aligned}\mathrm{MPSI}_{\mathrm{IJ}}(\mathrm{F}) := 4\sum_{f\in F} \mathrm{Tr}\Big(&\left(\mathbf{S}_{II}^{\Re}(\mathrm{d}f+f) + \mathbf{S}_{II}^{\Re}(f)\right)^{-1} \\ &\mathbf{S}_{IJ}^{\Im}(\mathrm{d}f+f)\ \left(\mathbf{S}_{JJ}^{\Re}(\mathrm{d}f+f) + \mathbf{S}_{JJ}^{\Re}(f)\right)^{-1} \mathbf{S}_{JI}^{\Re}(f) \\ &+ \left(\mathbf{S}_{II}^{\Re}(\mathrm{d}f+f) + \mathbf{S}_{II}^{\Re}(f)\right)^{-1} \mathbf{S}_{IJ}^{\Re}(\mathrm{d}f+f) \\ &\left(\mathbf{S}_{JJ}^{\Re}(\mathrm{d}f+f) + \mathbf{S}_{JJ}^{\Re}(f)\right)^{-1} \mathbf{S}_{JI}^{\Im}(f)\Big)\end{aligned}$$

where df and F denote an incremental step in the frequency domain and the frequency band of interest, respectively. MPSI solely detects the directionality of phase-lagged coupling; a positive value of MPSI indicates that the vector-signal I leads the vector-signal J, while a negative value indicates the opposite. Moreover, similarly to MIM, MPSI is invariant under invertible and static linear transformations, and thus it is independent on rotations of the physical coordinate system of MEG source space (Basti et al., 2018). In the case of two univariate time series, MPSI coincides with PSI, apart from a normalization factor.

Cross-Frequency Phase Coupling Methods

In section Frequency-specific phase coupling methods, we introduced a large set of connectivity methods based on phase coupling of oscillatory signals at the same frequency, which has been hypothesized as a mechanism for communication, at large scale for slower rhythms and at small scale for higher frequencies. Additionally, neuronal oscillations at different frequencies can also couple according to different possible relations between their phases, their amplitudes or in a phase-to-amplitude mode (Jensen and Colgin, 2007). This cross-frequency coupling has been hypothesized as a mechanism for information integration across different spatial scales characteristic of the faster and slower oscillations.

In this review, consistently with what already presented for coupling at the same frequency, we focus on methods to detect phase to phase cross-frequency coupling.

A popular cross-frequency measure in this framework is the *n:m synchronization index* (Rosenblum et al., 1996; Tass et al.,

1998). This measure relies on the estimation of the generalized phase difference $\Phi_{ij}^{n:m}$ between two signals i and j, i.e.,

$$\Phi_{ij}^{n:m}(f_1, f_2, t) := n\,\theta_i(f_1, t) - m\,\theta_j(f_2, t),$$

where f_1 and f_2 are two frequencies whose ratio is given by the integers n and m, i.e., $n f_1 = m f_2$, and $\theta_i(f, t)$ denotes the instantaneous phase signal. A $n:m$ coupling between two signals occurs when the mean resultant length of $\Phi_{ij}^{n,m}$ is non-vanishing (Tass et al., 1998). This can be evaluated, e.g., through the *$n:m$ phase-locking-value* ($\mathrm{PLV}^{n:m}$) which is defined as

$$\mathrm{PLV}_{i,j}^{n:m}(f_1, f_2) := \left| \left\langle e^{\iota\, \Phi_{ij}^{n,m}(f_1, f_2, t)} \right\rangle \right|.$$

where $\langle . \rangle$ denotes the average over signal realizations and time (Palva et al., 2005; Siebenhühner et al., 2016).

A different class of cross-frequency phase-coupling measures relies on the estimation of the third order spectrum, or cross-bispectrum, between signals (Nikias and Petropulu, 1993). The most general expression for the cross-bispectrum involves three signals, i, j and k, and three frequencies, f_1, f_2 and $f_3 = f_1 + f_2$, and it has the form

$$B_{ijk}(f_1, f_2) := \left\langle X_i(f_1)\; X_j(f_2)\; X_k^*(f_1 + f_2) \right\rangle.$$

The frequency f_3 is set to $f_1 + f_2$ because all other choices lead to vanishing cross-bispectra under stationarity assumption (Chella et al., 2016b; Shahbazi Avarvand et al., 2018). A pairwise bispectral analysis between two signals can be accomplished by setting two out of the three signal indices equal to each other, e.g., $i = j$ which yields $B_{ik}(f_1, f_2)\; B_{iik}(f_1, f_2)$.

The *bicoherency* (Nikias and Petropulu, 1993) is the normalized version of the cross-bispectrum, which is the analogous of the coherency for the cross-spectrum. The absolute value of bicoherency, i.e., the bicoherence, is a measure of the coupling between the phases in signals i and j at two possibly different frequencies, $\theta_i(f_1)$ and $\theta_j(f_2)$, with respect to the phase in signal k at a third frequency which is the sum of the other two, $\theta_k(f_1 + f_2)$, such that the mean resultant length of the phase difference $\Phi_{ij}^{q}(f_1, f_2)\,\theta_i(f_1) + \theta_j(f_2) - \theta_k(f_1 + f_2)$ is non-vanishing. Such a phenomenon is called quadratic phase coupling, and it conceptually different from the *n:m* coupling described above. There is one case in which the two phenomena coincide, that is the case of $f_1 = f_2 =: f$ and $f_3 = 2f$, in which the quadratic phase coupling involves only two frequency components, i.e., one frequency and its double, thus matching the 1:2 phase locking.

Similarly to coherence, bicoherence estimates are inflated by artificial zero-lag correlations. To face this issue, Chella et al. (2014, 2016b) proposed to use the *antisymmetric part of bicoherency*,

$$\mathrm{aBic}_{ijk}(f_1, f_2) := \frac{B_{ijk}(f_1, f_2) - B_{kji}(f_1, f_2)}{Q_i(f_1)\; Q_j(f_2)\; Q_k(f_1 + f_2) + Q_k(f_1)\; Q_j(f_2)\; Q_i(f_1 + f_2)}$$

where $Q_i(f) = \sqrt[3]{\left\langle |X_i(f)|^3 \right\rangle}$ (Shahbazi et al., 2014). The aBic is the difference between two bicoherencies where two signal indices have been switched, i.e., i and k in the above equation.

EXEMPLARY APPLICATIONS OF PHASE COUPLING TO ASSESS BRAIN CONNECTIVITY

In the following, exemplary applications of phase coupling estimated from MEG data to neuroscience are recalled. To this end, we will focus on three widely studied domains in which phase coupling methods have contributed in disclosing the putative mechanisms underlying brain operations: resting state, visuospatial attention, and working memory. The aim of this chapter is not to give an exhaustive review of respective literature but rather to give the reader an idea of how phase coupling methods from MEG data has contributed in the study of the covered fields. It is worth noting that the same domains that we recall here, have been studied also with EEG and the contribution of these studies to our knowledge in the respective domains cannot be underestimated (e.g., Crespo-Garcia et al., 2013, Sauseng et al., 2004, 2005a,b). However, in line with the perspective of this review we will focus on the studies that have used phase coupling methods on source-space MEG data. Finally, it needs to be highlighted that applications of the phase coupling methods are not limited to the covered examples. Specifically, the value of neurophysiological signals as potential biomarkers has been recognized. Recent literature have identified the potential in using neurophysiological signals for diagnostic purposes in schizophrenia (Bowyer et al., 2015), autism spectrum disorders (Port et al., 2015), post-traumatic stress disorder, mild traumatic brain injury (Huang et al., 2016), Alzheimer's disease (Maestú et al., 2019) and epilepsy (Soriano et al., 2017). Furthermore, the use of MEG-based markers is not limited to diagnostics but shows promise also in probing cognitive decline in multiple sclerosis (Schoonhoven et al., 2018) and even in treatment response monitoring (Light and Swerdlow, 2015) and drug development (Javitt et al., 2008).

MEG Resting State Connectivity

Resting state is defined as an intrinsic state in which the subject is not engaged in a specific task or acting in response to a given stimulus. More specifically, according to Snyder and Raichle (2012), "… *rest* is an operational definition referring to a constant condition without imposed stimuli or other behaviorally salient events." The definition of resting state encompasses eyes closed or eyes open conditions, the latter with or without visual fixation.

In the first decade of the 2000s, the study of the functional architecture of the resting brain has become an emerging line of research in neuroscience, although it poses some challenges (e.g., signal-to-noise ratio and lack of temporal reference) due to rest being a quite uncontrolled experimental paradigm compared to task-based experiments. Specifically, a growing number of fMRI studies have investigated functional topographies in the resting brain, as well as the relation of these topographies to evoked-response patterns and to anatomy (for a review see Fox

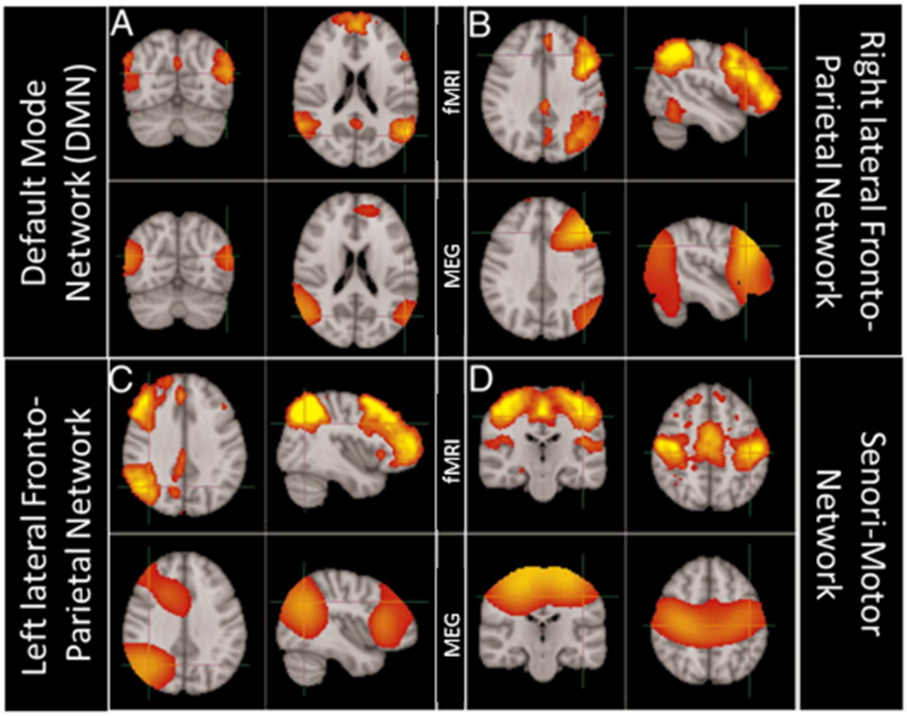

FIGURE 5 | Comparison of brain networks obtained using ICA independently on MEG and fMRI data. Modified from Brookes et al. (2011b) (CCBY license). **(A)** Top row: fMRI derived Default Mode Network (DMN); bottom row MEG derived DMN. **(B)** Top row: fMRI derived Right lateral FrontoParietal Network; bottom row MEG derived Right lateral FrontoParietal Network. **(C)** Top row: fMRI derived Left lateral FrontoParietal Network; bottom row MEG derived Left lateral FrontoParietal Network. **(D)** Top row: fMRI derived Sensori-Motor Network; bottom row MEG derived Sensori-Motor Network.

and Raichle, 2007). Taken together, these studies have shown that the resting brain is characterized by distributed large-scale cortical networks of coherent activity, namely RSNs, which cover at least the 66% of the human brain (Deco and Corbetta, 2011) and account for the largest part of brain energy consumption (Raichle, 2006). The RSNs most commonly identified by fMRI include (Yeo et al., 2011): The Default Mode Network (DMN), the Dorsal Attention Network (DAN), the Ventral Attention Network (VAN), the Sensori-Motor Network (SMN), the Visual Network (VN), the Fronto-Parietal Control Network (FPN), the Language Network (LN).

Nevertheless, given that fMRI BOLD activity is not a direct measure of neuronal activity, neuroscientists have become more and more interested in using electrophysiological techniques, as a stand alone or in combination with fMRI, to unravel the electrophysiological correlates of RSNs and their potential relation to brain oscillations (see e.g., Mantini et al., 2007). In the last decade, advancements in MEG data analysis have made it possible to rely on source space MEG connectivity to study RSNs. The richness of the MEG signal has offered several perspectives to look at RSNs (Larson-Prior et al., 2013) and, from that, to enhance the understanding of the putative mechanisms underlying their formation. The first studies (de Pasquale et al., 2010, 2012) used a signal analysis strategy aimed at extracting slow fluctuations of the MEG signal and investigating their temporal correlation, closely resembling the signal analysis strategy used for resting state fMRI data. Additionally, spatial Independent Component Analysis (ICA) has been used on resting state MEG (rsMEG) data to extract networks of coherent fluctuations, showing that MEG RSNs feature significant similarity in their spatial structure compared with fMRI RSNs as evidenced in **Figure 5** (Brookes et al., 2011b).

In addition, rsMEG has shown its potential to move beyond fMRI RSNs by relying on connectivity metrics which can exploit the rich frequency content of the MEG signal (typically 1–80 Hz; Baillet, 2017) by assessing phase locking between oscillatory activities. Metrics based on phase coupling have thus been used to assess frequency specific patterns of coupled activity. By using Multivariate Interaction Measure (Ewald et al., 2012), our group has shown that coupling within and between RSNs features frequency specific signatures (Marzetti et al., 2013). Specifically, by seeding parietal and frontal node of the Dorsal Attention Network in the left hemisphere (namely left inferior parietal sulcus and frontal eye field) we observed coupling with the contralateral regions specific to the delta and the alpha frequency bands (**Figure 6** for the alpha band). Concurrently, we observed that the same DAN nodes are coupled to nodes belonging to other networks in different specific frequencies: DAN and SMN couple in the beta band while DAN and visual network couple in the alpha band. Overall, our work demonstrated that brain networks that can be observed with resting state MEG show frequency specificity and that the involved frequencies overlap to those

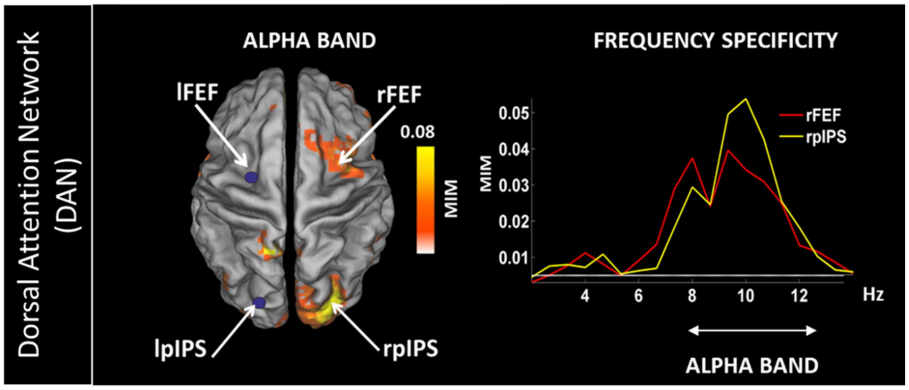

FIGURE 6 | (Left) Topography of the phase synchronization between the major nodes of the Dorsal Attention Network (DAN) in the left hemisphere, i.e., left Frontal Eye Field (lFEF), left posterior Inferior Parietal Sulcus (lpIPS) and the homologous DAN nodes in the alpha band (right FEF and right pIPS). **(Right)** Frequency specificity of the coupling shown on the left. Modified from Marzetti et al. (2013).

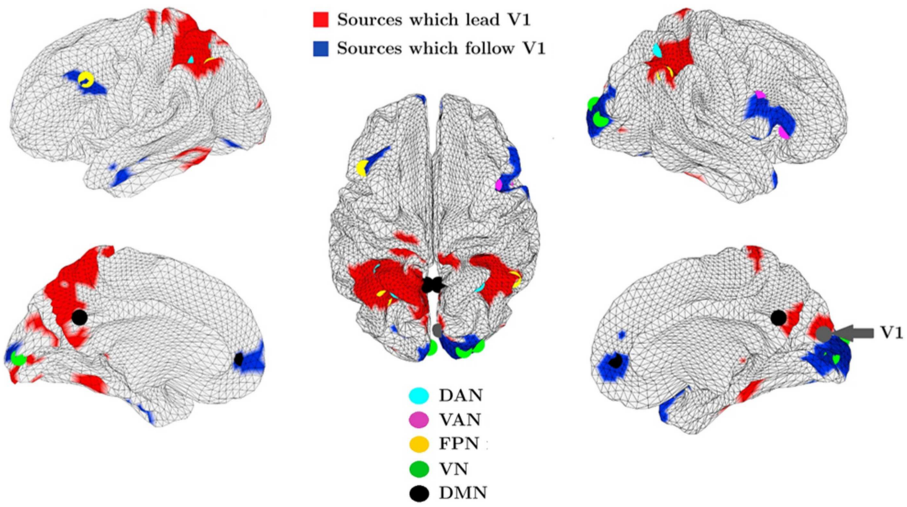

FIGURE 7 | Group averaged map in the alpha band between the primary visual cortex (V1) and all other locations over the cortex obtained by MPSI. The cortical locations in red exert an influence on V1 while V1 exerts an influence on the regions in blue. The dots, in color according to the legend, represent resting state network nodes which overlap areas which lead or follow V1. Modified from Basti et al. (2018) (CCBY license).

observed during tasks which are known to recruit regions in these networks.

More recently, our group introduced a novel phase coherence metric, namely the Multivariate Phase Slope Index, to investigate the directionality of functional coupling in MEG and EEG data (Basti et al., 2018). This novel metric has been used to investigate the directionality of functional coupling in the alpha frequency band between the visual network and the whole brain in resting state MEG data from a large cohort of healthy subjects from the Human Connectome Project (Larson-Prior et al., 2013). With this approach, we observed sets of regions belonging to various RSNs which either lead or follow the primary visual cortex (Basti et al., 2018) as shown in **Figure 7**. For example, we observed coupling between the primary visual cortex (V1) and the Dorsal Attention Network. Parietal areas of the latter lead V1, in line with the notion of a feedback mechanism, while no clear evidence of follower or leader relationship was observed between V1 and the frontal regions in the DAN, suggesting that coupling of V1 to frontal DAN areas observed in Marzetti et al. (2013) can possibly exhibit both feed-forward and feedback characteristics which might lead to the absence of a clear directionality observed in Basti et al. (2018).

Additionally, with mPSI we observed a consistent relationship in the alpha band between V1 and the dorsolateral pre-frontal cortex (dlPFC) with the latter following V1 in accordance with the putative role of dlPFC in action preparation in response to the visual stimulus (Heekeren et al., 2006). For the interested reader, we refer to the original paper for details on the method and on the coupling of V1 to the other RSNs shown in **Figure 7**.

While literature on resting state frequency specific coupling by MEG is relatively abundant, less has been investigated about cross-frequency coupled networks. To date, few studies have investigated the coupling between the local phase of a low frequency oscillation and the local amplitude of a high frequency

oscillation, i.e., Phase-Amplitude Coupling (PAC). In their interesting paper, Roux et al. (2013) showed that in resting-state MEG, local gamma-band activity is coupled with the phase of the alpha band rhythm in the visual cortex. Furthermore, Florin and Baillet (2015) showed that resting-state networks derived from signal model based on the PAC, substantially overlapped with DMN, DAN/SMN, VN, and right FPN, indicating that the PAC is an important component of the network generation in the resting-state. More recently, an effort to disclose n:m-cross-frequency phase coupling RSNs and to disentangle these networks from phase-amplitude coupling networks has been made by Siebenhühner et al. (2019). Nevertheless, the topic still needs further investigation.

Visuospatial Attention

As the selection of information relevant to behave in the environment is a fundamental process, the human brain is endowed with selective attention mechanisms necessary to route information in order to perform different tasks while ignoring distracting input. MEG and EEG evidence show that long range coupling of neuronal oscillations through phase coherence in a large-scale functional connectivity network, identified through the synchronization of neuronal oscillations, subserve this attentional selection process (Siegel et al., 2008; Doesburg et al., 2009; Sauseng et al., 2005b; Lobier et al., 2018; D'Andrea et al., 2019).

The study from Siegel et al. (2008) provided one of the first evidence for a modulation of phase coherence induced by attention with different spectral signatures and stimulus dependence between cortical areas. Indeed, Siegel et al. recorded MEG data in eight subjects performing a motion discrimination task, in which they had to discriminate the motion direction of a cloud of dots in the cued hemifield ignoring the uncued hemifield. Coupling between five regions specifically implicated in the attention mechanisms and visual motion processing (see **Figure 8** for details on the regions) was estimated through phase coherence, either in the stimulus or in the delay interval. A relative enhancement of phase coherence was found at high frequencies (35–100 Hz) and a relative decrease was found at low frequencies (5–35 Hz) in the hemisphere contralateral to the attended hemifield (**Figure 8**). Specifically, in the delay interval a reduction of gamma band connectivity was observed in the hemisphere ipsilateral to the cued hemifield between the posterior Intra Parietal Sulcus (pIPS) and middle Temporal (MT+), sustained also during the stimulus presentation, and between FEF and MT+. This reduction was paired to an enhancement of alpha phase coherence between pIPS and MT+ in the all intervals (Delay and Stimulus) as well as to an enhancement of phase coherence in the beta band between FEF and MT+ specific to the Stimulus Interval. By using coherence it was shown that attentional modulations of synchronization between ROIs is spatially selective, across all bands and intervals, representing a long range synchronization that does not depend on power effects.

More recently, another study (Lobier et al., 2018) investigated the role of long-range phase coupling in visuospatial attention

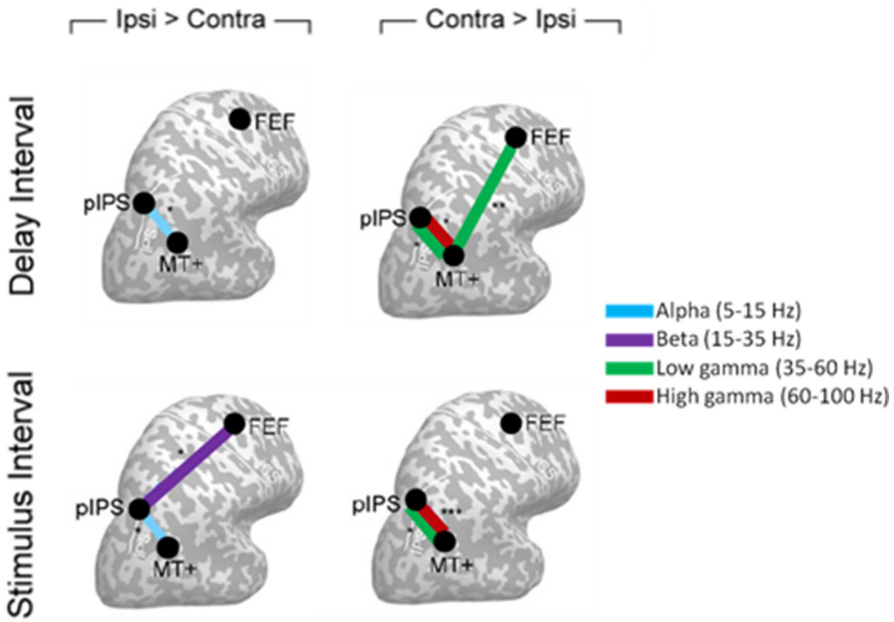

FIGURE 8 | Cartoon of the interregional phase coherence modulated by attention in Siegel et al. (2008), displayed on a flattened cortex. Circles indicate cortical areas in which phase coupling was observed to be modulated, namely: posterior intraparietal sulcus (pIPS), middle temporal (MT+), and frontal eye field (FEF). Panels on the left show the cortical areas between which attention significantly reduced phase coherence in the hemisphere ipsilateral as compared to contralateral to the attended hemifield. Panels on the right highlight the corresponding attentional enhancement of phase coherence. The different frequency bands (alpha, beta, low gamma, and high gamma) involved are indicated by different colors.

processes, without a priori selection of frequency-bands or regions of interest. This study is particularly relevant from a methodological point of view since here phase coupling was assessed both using the weighted Phase Lag Index and the Phase Locking Value, the former to minimize the contribution of source leakage and the latter to exclude changes in phase lags without a change in coupling strength. Cortical activity was recorded with MEG from fourteen healthy participants performing a cued stimulus discrimination task. After a rightward or leftward cue presentation, subjects had to discriminate between two geometrical shapes with two different contrast conditions. The shapes were presented in the attended or non-attended hemifield. The results showed an increased inter-areal phase coupling in the high-alpha frequency band between visual, parietal, and frontal cortices. Interestingly, no major difference was observed between phase coupling assessed through wPLI or through PLV indicating that the observed findings cannot be attributed merely to source leakage nor to "systematic changes in phase lags without a change in coupling strength" (Lobier et al., 2018). No other frequency bands such as gamma and beta were found to be involved in this task.

A recent study from our group, D'Andrea et al. (2019), further investigated, through MIM, PSI and aBic, the frequency specificity of the inter-areal phase coupling induced by attention, and, at the same time, the relationship between this inter-areal phase coupling and anatomical connections. Magnetoencephalographic data from 28 participants performing a visuospatial attention task and high angular resolution diffusion imaging (HARDI) magnetic resonance (MR) data, in the same subjects, were used. From MEG data seed-based MIM in the alpha and beta frequency bands, and cross-frequency aBic coupling between these two frequency ranges were quantified. From MR data, the Superior Longitudinal Fasciculus branches were reconstructed and asymmetry for each branch was calculated as the difference between the volume of the left branch and that of the right branch (for details see D'Andrea et al., 2019).

The MIM and the PSI highlighted an increase of functional connectivity in the alpha band from parietal areas to the occipital cortex (**Figure 9**) always larger in the hemisphere ipsilateral to the hemifield to which attention is directed.

This interaction, reflecting a top down mechanism exerted by parietal areas for the inhibition of visual cortices, was found to be related to behavioral performance and to indices of anatomical connectivity. Specifically, the hemispheric asymmetry of this occipito-parietal modulation of connectivity was predicted by the asymmetry in the volume of the first and the second tracts of the Superior Longitudinal Fasciculus and was positively correlated to the accuracy in performing the task. Additionally, the antisymmetric part of bicoherency revealed an increase in alpha-beta coupling, induced by the cue presentation, between the right FEF and parietal areas in both hemifields (**Figure 10**). No other frequency band was observed.

Overall, these results highlight that neuronal oscillations and functional connectivity at low frequencies are strongly implicated in attentional mechanisms and are possibly related to functional inhibition through feedback mechanisms (Jensen and Mazaheri, 2010). Nevertheless, further investigation is needed to clarify the specific role of the different frequency (sub-)bands observed in long-range phase coupling. Indeed, while it is conceivable that gamma frequencies are implicated in bottom-up information processing, still poor evidence demonstrate the involvement of long-range gamma-band coherence in top-down processing (Siegel et al., 2008; Gregoriou et al., 2009) and further investigation are needed to associate different frequency bands with specific mechanism of feedback and feed-forward interactions (Siegel et al., 2012).

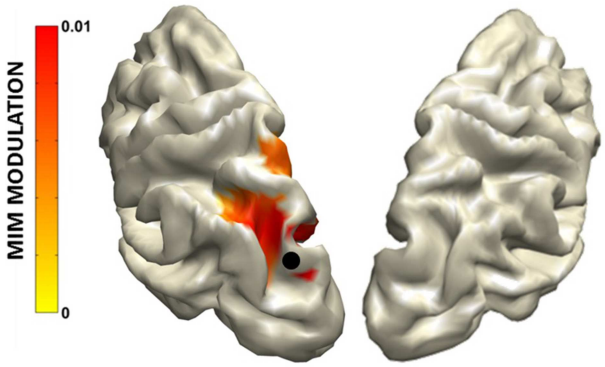

FIGURE 9 | Grand average MIM functional connectivity modulation (mMIM) with respect to the left superior occipital cortex (indicated by the black dot) for the "Attend Left" condition vs. Baseline in the alpha band. Modified from D'Andrea et al. (2019) (CCBY license).

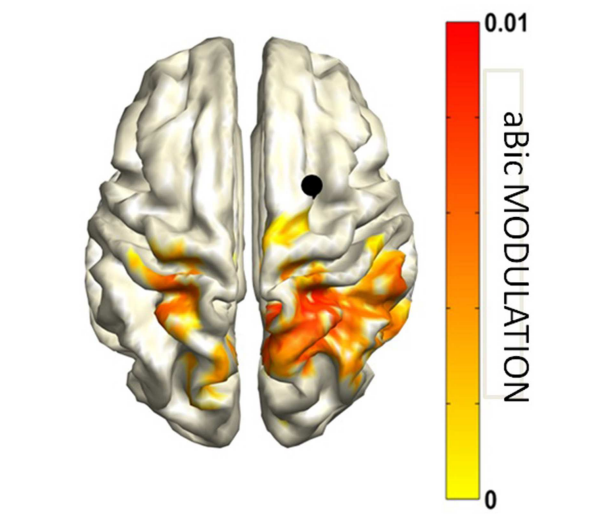

FIGURE 10 | Attend Left and Attend Right conjunction map of aBic modulation vs. Baseline in the alpha-beta band with respect to the right frontal cortex seed (indicated by the black dot). Modified from D'Andrea et al. (2019) (CCBY license).

Working Memory

Complex cognitive tasks such as language comprehension, reasoning and learning rely on our brains' ability to temporary maintain and manipulate information, that is, working memory

(WM) (Baddeley, 1992). The phase coupling is fundamental neural mechanism that supports neural communication and it is therefore an apparent prospect for the underlying neural mechanism of the WM. Indeed, the role of phase coupling in memory processes has been studied extensively and the literature supports the relevance of phase coupling in memory processes (see Fell and Axmacher, 2011 for review). The majority of the studies examining the phase coupling in WM have relied on EEG data. Moreover, most of the studies have evaluated the phase coupling in sensor space, which, as discussed earlier in this review, is problematic. Here we focus on those WM studies that have examined the role of phase coupling in source space using MEG data, with the benefit of being more specific about the involved brain areas.

Palva et al. (2010) used combined recordings of MEG and EEG to characterize phase coupled networks underlying the maintenance phase of delayed match to sample task (DMS). The inter-areal phase coupling was assessed by PLV, and statistically significant couplings were represented as undirected graphs in which vertices were the cortical areas and edges the significant couplings. Network hubs were identified by using vertex degree and betweenness centrality (graph theoretical indices). The phase coupling in alpha, beta, and gamma bands was shown to be sustained and stable throughout the visual working memory (VWM) retention period. Increasing memory load strengthened interareal coupling among the frontoparietal regions particularly strongly in the alpha band, while beta and gamma bands underlay coupling in visual regions. These observations, combined with the trend of alpha band hubs being located more frontally compared to beta and gamma band hubs, led to the suggestion that alpha band network underlies higher level attentional functions. Conversely, coupling in the beta and gamma bands were suggested to be involved in binding neuronal representations. The analysis of the most important hubs revealed that the intraparietal sulcus (IPS) was the most central hub predicting individual WM capacity and it also connected the visual and frontoparietal networks (beta and gamma). Therefore, it was concluded that IPS might control the information flow between visual representation and frontoparietal attention network (Palva et al., 2010).

Another study examined phase coupling (wPLI) networks underlying the maintenance phase of DMS task in 6-year old children (Sato et al., 2018). The results showed that, compared to baseline, whole brain connectivity in the alpha band was increased during the retention period. Sato et al. (2018) associated the alpha band connectivity to attentional functions similarly to Palva et al. (2010). The whole brain connectivity was significantly greater in correct trials compared to incorrect trials. The authors speculated that the decreased connectivity associated with incorrect trials might be due to children's inability to dedicate enough attentional resources to trials which were incorrectly answered. The children also showed more fronto-temporal coupling rather than the more common fronto-parietal coupling. Furthermore, key network hubs were located to the left inferior frontal triangularis, left hippocampus, left middle temporal gyrus, and the left superior temporal gyrus. It was stated that these results might indicate that the children used rehearsal strategies and recognition processes to perform the task. Further evidence of fronto-temporal coupling during the maintenance phase of WM task was presented in a study by Daume et al. (2017). They combined directional and non-directional metrics to show that phase coupling in theta/alpha range (ImCoh) was significantly greater in memory condition compared to control and the direction of this coupling (PSI) was from frontopolar cortex to inferior temporal cortex, possibly indicating that the frontopolar cortex to temporal area coupling is involved in coordinating the maintenance of visual object representations in a top down manner (Daume et al., 2017).

Alpha band phase coupling has also been related to inhibitory process in the context of WM. Overall alpha band connectivity (wPLI) was found to be stronger during the retention period of a variant of Sternberg task compared to baseline (Wianda and Ross, 2019). The most prominent connections involved occipital, frontal, and mid-brain sources. Long-range connectivity was observed between visual cortices and the retrosplenial cingulate cortex and thalamic sources. Furthermore, pre-frontal cortices were connected to midbrain sources and temporal cortices. The authors proposed that alpha coupling between frontotemporal and occipital areas is involved in inhibiting distractors. This interpretation is in accordance with some results reported in attention studies (see Working Memory) highlighting the close relationship between WM and attention.

The studies presented above have all focused on the maintenance phase of the WM. Kaplan et al. (2014) focused on the retrieval phase of spatial memory. The phase coupling was assessed by calculating PLV between a seed voxel in the medial Pre-frontal Cortex (mPFC) and all the other voxels in the brain. Significant increase (compared to baseline) in theta coupling was found between right anterior medial temporal lobe (aMTL) and the seed voxel and this theta coupling was argued to play a role in mnemonic functions. The phase coupling was also analyzed with PLI and this analysis confirmed that the increase in theta coupling was not an artifact of volume conduction. The PLI analysis also showed increased theta coupling between the seed and nearby anterior cingulate cortex. However, the authors acknowledged that the phase coupling between so nearby regions should be interpreted with caution (Kaplan et al., 2014). The evidence indicates that phase coupling within different frequency bands plays a role in WM processes. Siebenhühner et al. (2016) expanded the perspective by showing that during the maintenance period of DMS task, cross-frequency coupling (assessed by $PLV^{n:m}$) was enhanced above baseline between high-alpha and beta and gamma band oscillations. Similarly, cross-frequency coupling between high-theta and alpha, beta and gamma band oscillations were enhanced in contrast to baseline. The strength of the cross-frequency coupling of theta and high-alpha with their corresponding higher frequencies was also positively correlated with the VWM load and predicted inter-individual variability in VWM capacity. The hubs characterized by low-frequency oscillation were located predominantly in the frontoparietal and to a lesser extent in dorsal attention areas. The low frequency oscillations exhibited by these hubs were coupled with faster oscillations in the visual system and dorsal attention

areas. In contrast, the higher frequency oscillations had hubs pre-dominantly in dorsal attention areas and in the visual cortex (gamma band). Moreover, the most central hubs involved in the cross-frequency coupling were co-localized with the most central hubs involved in the slow and fast within frequency coupling. These results suggest that cross-frequency coupling connects the visual system and attentional networks and therefore integrates the representational and central executive functions of VWM (Siebenhühner et al., 2016).

Taken together, various MEG studies have shown that phase coupling within different frequency bands plays a role in WM memory processes. Phase coupling in alpha band is the most frequently reported observation and it is linked to inhibiting distractors (Wianda and Ross, 2019) and attentional functions (Palva et al., 2010; Sato et al., 2018). Phase coupling in beta and gamma bands on the other hand is linked to binding neuronal representations, a process in which IPS could be the key hub between the visual and frontoparietal networks (Palva et al., 2010). Furthermore, cross-frequency coupling could be the mechanism which integrates different functional systems together (Siebenhühner et al., 2016).

Interestingly, all the WM studies referred made contrast only between one working memory state and baseline/control. This approach can lead to an illusion that observed phase coupling networks are dedicated solely to the WM state that has been studied. This combined with a-priori selection of seed regions or frequency bands can lead to a conclusion where single or few functional interactions are dedicated to the function of interest. An fMRI study (Soreq et al., 2019) recently showed, by contrasting a broad range of behavioral conditions, that different aspects of WM were characterized by heavily overlapping multivariate activation and connectivity patterns.

CONCLUSIONS

In the last decade, the increasing body of work dealing with MEG functional connectivity analysis and with method development has demonstrated the efficacy of this technique in assessing the coupling between brain regions and in characterizing brain networks.

In this review, we focused on data-driven methods to estimate functional connectivity based on phase coupling by MEG. All of these methods are here formulated for static connectivity analysis, which requires averages over a theoretically infinite number of data segments. In practice, data length is always finite, and the reliability of these methods is impacted by the overall number of available data time points. This issue has been discussed in simulated data for linear coupling methods (e.g., Sommariva et al., 2017), while for cross-frequency coupling methods this is still to be explicitly investigated. Moreover, to date several evidences have been provided concerning the changes of functional connectivity patterns across different time-scales (Breakspears et al., 2004). The extension of the above described methods to the study of dynamical phase coupling is straightforwardly achievable through the use of the Time-Frequency resolved versions of these metrics, at least for task-induced connectivity.

Besides the above reviewed methods, there is a wide family of connectivity methods which could be used to assess functional or effective couplings between neuronal oscillations, both at the same or at different frequencies. These include, but are not limited to: phase-amplitude coupling methods, which assess the coupling between the phase of a low-frequency oscillation and the amplitude of a high-frequency oscillation (Canolty et al., 2006; Cohen, 2008; Tort et al., 2010; Özkurt and Schnitzler, 2011); amplitude-amplitude coupling methods, which investigate the covariation of aperiodic fluctuations such as the amplitudes of brain oscillations at a specific frequency (Brookes et al., 2011b; Hipp et al., 2012); model-based approaches, such as the dynamic causal models (Friston et al., 2003), which infer the causal structure of brain connections by relying on Bayesian inference; methods to assess the directionality of interactions based on the concept of Granger causality (Geweke, 1982; Kaminski and Blinowska, 1991; Sameshima and Baccalá, 1999; Marinazzo et al., 2008). In addition, methods to identify brain states can provide further insight into brain networks and especially into their dynamics. In this framework, microstate analysis identifies sensor level topographies that remain stable for a certain period of time before transitioning to a different topography. Changes in the topography are assumed to indicate a reorganization in the global coordination of neuronal activity over time. This approach has a long lasting tradition in EEG, but it has seen a new flourishing in the recent years due to close link to brain network analysis. For timely reviews see Michel and König (2018) and He et al. (201. Similarly, Hidden Markov Model (HMM) approaches reveal the transition of brain networks between states that recur at different points in time. This approach has been used in MEG source space data in Baker et al. (2014) for network identification through amplitude based correlation, and in Vidaurre et al. (2018) to identify phase coherence based networks. A more detailed description of all these methods for assessing brain connectivity and brain networks would require a dedicated review paper and it is thus beyond the scope of this work.

There are a number of methodological issues and open questions concerning connectivity estimation which need to be addressed. For instance, the question of whether increases in connectivity might be merely driven by increases in the amplitude of oscillatory activity, or whether the connectivity itself might induce increases in local amplitudes is still debated (Daffertshofer and van Wijk, 2011; Moon et al., 2015; Tewarie et al., 2019). Another methodological issue is that all connectivity methods, including those which have been designed to specifically handle artificial connectivity detections due to zero-lag correlations, are not safe from spurious connections caused by source leakage in the proximity of true interactions, i.e., the so-called "ghost interactions" (Palva et al., 2018). Finally, the relationship between some coupling measures and the underlying physiological mechanisms is not well-understood. For instance, cross-frequency coupling measures might be influenced by features in the signal that do not relate to interactions, such as the

non-sinusoidal waveform of brain oscillations which generate the coupling between harmonically related frequencies (Aru et al., 2015; Lozano-Soldevilla et al., 2016; Deco et al., 2017).

In this review, we also show examples of applications of phase coupling methods to MEG data from different cognitive domains. Of note, in these studies, connectivity results were disentangled from power results proving evidence for a genuine phase coupling between brain areas. Moreover, in the resting state and in the visuospatial attention examples, the MEG connectivity results have been supported by MRI functional or anatomical connectivity. While the benefits of integrating different modalities in the study of functional connectivity by MEG is self-evident, still actual multimodal connectivity analysis tools are lacking. Along the same line, a comprehensive characterization of the benefits and/or limitations in the integration procedures is missing. One example of integrating MEG functional connectivity with MRI information is the recent characterization of the impact of MEG-MRI coregistration errors in functional connectivity estimated through different metrics (Chella et al., 2019).

In conclusion, we believe that the field has made substantial steps forward in the recent years and is now ready for bringing the study of functional connectivity toward a more mechanistic understanding of the role of brain rhythms, also aided by high-level modality integration tools for connectivity.

AUTHOR CONTRIBUTIONS

LM and VP contributed to the conception and design of the review and wrote the first draft of the manuscript. AB, FC, AD'A, and JS wrote the sections of the manuscript. All authors contributed to manuscript revision, read, and approved the submitted version.

FUNDING

This work was partially supported by the University of Chieti-Pescara Faculty Resources Grant 2018 of author LM, entitled Methods and models for the estimation of functional and effective connectivity with MEG and EEG. Moreover, JS has received support from the European Union's Horizon 2020 research and innovation programme under the Marie Skłodowska-Curie grant agreement no. 713645.

ACKNOWLEDGMENTS

This work was conducted under the framework of the Departments of Excellence 2018-2022 initiative of the Italian Ministry of Education, University and Research for the Department of Neuroscience, Imaging and Clinical Sciences (DNISC) of the University of Chieti-Pescara.

REFERENCES

Adjamian, P., Barnes, G. R., Hillebrand, A., Holliday, I. E., Singh, K. D., Furlong, P. L., et al. (2004). Co-registration of magnetoencephalography with magnetic resonance imaging using bite-bar-based fiducials and surface-matching. *Clin. Neurophysiol.* 115, 691–698. doi: 10.1016/j.clinph.2003.10.023

Akhtari, M., Bryant, H. C., Mamelak, A. N., Flynn, E. R., Heller, L., Shih, J. J., et al. (2002). Conductivities of three-layer live human skull. *Brain Topogr.* 14, 151–167. doi: 10.1023/A:1014590923185

Aru, J., Aru, J., Priesemann, V., Wibral, M., Lana, L., Pipa, G., et al. (2015). Untangling cross-frequency coupling in neuroscience. *Curr. Opin. Neurol.* 31, 51–61. doi: 10.1016/j.conb.2014.08.002

Baddeley, A. (1992). Working memory. *Science* 255, 556–559. doi: 10.1126/science.1736359

Baillet, S. (2017). Magnetoencephalography for brain electrophysiology and imaging. *Nat. Neurosci.* 20, 327–339. doi: 10.1038/nn.4504

Baillet, S., Mosher, J. C., and Leahy, R. M. (2001). Electromagnetic brain mapping. *IEEE Signal Process. Magaz.* 18, 14–30. doi: 10.1109/79.962275

Baker, A. P., Brookes, M. J., Rezek, I. A., Smith, S. M., Behrens, T., Probert Smith, P. J., et al. (2014). Fast transient networks in spontaneous human brain activity. *Elife* 3:e01867. doi: 10.7554/eLife.01867

Basti, A., Pizzella, V., Chella, F., Romani, G. L., Nolte, G., and Marzetti, L. (2018). Disclosing large-scale directed functional connections in MEG with the multivariate phase slope index. *Neuroimage* 175, 161–175. doi: 10.1016/j.neuroimage.2018.03.004

Basti, A., Pizzella, V., Nolte, G., Chella, F., and Marzetti, L. (2017). Disclosing brain functional connectivity from electrophysiological signals with phase slope based metrics. *J. Serbian Soc. Comput. Mech.* 11, 50–62. doi: 10.24874/jsscm.2017.11.02.05

Bastos, A. M., Vezoli, J., and Fries, P. (2015). Communication through coherence with inter-areal delays. *Curr. Opin. Neurobiol.* 31, 173–180. doi: 10.1016/j.conb.2014.11.001

Boto, E., Holmes, N., Leggett, J., Roberts, G., Shah, V., Meyer, S. S., et al. (2018). Moving magnetoencephalography towards real-world applications with a wearable system. *Nature* 555, 657–661. doi: 10.1038/nature26147

Bowyer, S. M., Gjini, K., Zhu, X., Kim, L., Moran, J. E., Rizvi, S. U., et al. (2015). Potential biomarkers of schizophrenia from MEG resting-state functional connectivity networks : preliminary data. *J. Behav. Brain Sci.* 5, 1–11. doi: 10.4236/jbbs.2015.51001

Breakspears, M., Williams, L. M., and Stam, C. J. (2004). A novel method for the topographic analysis of neural activity reveals formation and dissolution of 'Dynamic Cell Assemblies' *J. Comp. Neurosci.* 16, 49–68. doi: 10.1023/B:JCNS.0000004841.66897.7d

Brillinger, D. R. (1981). *Time Series-Data Analysis and Theory, 2nd Edn*. San Francisco, CA: Holden Day. doi: 10.2307/2530198

Brookes, M. J., Wood, J. R., Stevenson, C. M., Zumer, J. M., White, T. P., Liddle, P. F., et al. (2011a). Changes in brain network activity during working memory tasks: a magnetoencephalography study. *Neuroimage* 55, 1804–1815. doi: 10.1016/j.neuroimage.2010.10.074

Brookes, M. J., Woolrich, M., Luckhoo, H., Price, D., Hale, J. R., Stephenson, M. C., et al. (2011b). Investigating the electrophysiological basis of resting state networks using magnetoencephalography. *Proc. Natl. Acad. Sci. U.S.A.* 08, 16783–16788. doi: 10.1073/pnas.1112685108

Burgess, R. C., Barkley, G. L., and Bagić, A. I. (2011). Turning a new page in clinical magnetoencephalography: practicing according to the first clinical practice guidelines. *J. Clin. Neurophysiol.* 28, 336–340. doi: 10.1097/WNO.0b013e3181cde47b

Buzsáki, G., and Draguhn, A. (2004). Neuronal oscillations in cortical networks. *Science* 304, 1926–1929. doi: 10.1126/science.1099745

Canolty, R. T., Edwards, E., Dalal, S. S., Soltani, M., Nagarajan, S. S., Kirsch, H. E., et al. (2006). High gamma power is phase-locked to theta oscillations in human neocortex. *Science* 313, 1626–1628. doi: 10.1126/science.1128115

Chella, F., D'Andrea, A., Basti, A., Pizzella, V., and Marzetti, L. (2017). Non-linear analysis of scalp EEG by using bispectra: the effect of the reference choice. *Front. Neurosci.* 11:262. doi: 10.3389/fnins.2017.00262

Chella, F., Marzetti, L., Pizzella, V., Zappasodi, F., and Nolte, G. (2014). Third order spectral analysis robust to mixing artifacts for mapping

cross-frequency interactions in EEG/MEG. *Neuroimage* 91, 146–161. doi: 10.1016/j.neuroimage.2013.12.064

Chella, F., Marzetti, L., Stenroos, M., Parkkonen, L., Ilmoniemi, R. J., Romani, G. L., et al. (2019). The impact of improved MEG–MRI co-registration on MEG connectivity analysis. *Neuroimage* 197, 354–367. doi: 10.1016/j.neuroimage.2019.04.061

Chella, F., Pizzella, V., Zappasodi, F., and Marzetti, L. (2016a). Impact of the reference choice on scalp EEG connectivity estimation. *J. Neural Eng.* 13:036016. doi: 10.1088/1741-2560/13/3/036016

Chella, F., Pizzella, V., Zappasodi, F., Nolte, G., and Marzetti, L. (2016b). Bispectral pairwise interacting source analysis for identifying systems of cross-frequency interacting brain sources from electroencephalographic or magnetoencephalographic signals. *Phys. Rev. E* 93:052420. doi: 10.1103/PhysRevE.93.052420

Cohen, M. X. (2008). Assessing transient cross-frequency coupling in EEG data. *J. Neurosci. Methods* 168, 494–499. doi: 10.1016/j.jneumeth.2007.10.012

Colclough, G. L., Woolrich, M. W., Tewarie, P. K., Brookes, M. J., Quinn, A. J., and Smith, S. M. (2016). How reliable are MEG resting-state connectivity metrics? *Neuroimage* 138, 284–293. doi: 10.1016/j.neuroimage.2016.05.070

Crespo-Garcia, M., Pinal, D., Cantero, J. L., Díaz, F., Zurrón, M., and Atienza, M. (2013). Working memory processes are mediated by local and long-range synchronization of alpha oscillations. *J. Cogn. Neurosci.* 25, 1343–1357. doi: 10.1162/jocn_a_00379

Daffertshofer, A., and van Wijk, B. (2011). On the influence of amplitude on the connectivity between phases. *Front. Neuroinform.* 5:6. doi: 10.3389/fninf.2011.00006

D'Andrea, A., Chella, F., Marshall, T. R., Pizzella, V., Romani, G. L., Jensen, O., et al. (2019). Alpha and alpha-beta phase synchronization mediate the recruitment of the visuospatial attention network through the Superior Longitudinal Fasciculus. *Neuroimage* 188, 722–732. doi: 10.1016/j.neuroimage.2018.12.056

Dannhauer, M., Lanfer, B., Wolters, C. H., and Knösche, T. R. (2011). Modeling of the human skull in EEG source analysis. *Hum. Brain Mapp.* 32, 1383–1399. doi: 10.1002/hbm.21114

Daume, J., Gruber, T., Engel, A. K., and Friese, U. (2017). Phase-amplitude coupling and long-range phase synchronization reveal frontotemporal interactions during visual working memory. *J. Neurosci.* 37, 313–322. doi: 10.1523/JNEUROSCI.2130-16.2016

de Pasquale, F., Della Penna, S., Snyder, A. Z., Lewis, C., Mantini, D., Marzetti, L., et al. (2010). Temporal dynamics of spontaneous MEG activity in brain networks. *Proc. Natl. Acad. Sci. U.S.A.* 107, 6040–6045. doi: 10.1073/pnas.0913863107

de Pasquale, F., Della Penna, S., Snyder, A. Z., Marzetti, L., Pizzella, V., Romani, G. L., et al. (2012). A cortical core for dynamic integration of functional networks in the resting human brain. *Neuron* 74, 753–764. doi: 10.1016/j.neuron.2012.03.031

Deco, G., Cabral, J., Woolrich, M. W., Stevner, A. B., Van Hartevelt, T. J., and Kringelbach, M. L. (2017). Single or multiple frequency generators in on-going brain activity: a mechanistic whole-brain model of empirical MEG data. *Neuroimage* 152, 538–550. doi: 10.1016/j.neuroimage.2017.03.023

Deco, G., and Corbetta, M. (2011). The dynamical balance of the brain at rest. *Neuroscientist* 17, 107–123. doi: 10.1177/1073858409354384

Doesburg, S. M., Green, J. J., McDonald, J. J., and Ward, L. M. (2009). From local inhibition to long-range integration: a functional dissociation of alpha-band synchronization across cortical scales in visuospatial attention. *Brain Res.* 1303, 97–110. doi: 10.1016/j.brainres.2009.09.069

Engel, A. K., Gerloff, C., Hilgetag, C. C., and Nolte, G. (2013). Intrinsic coupling modes: multiscale interactions in ongoing brain activity. *Neuron* 80, 867–886. doi: 10.1016/j.neuron.2013.09.038

Ewald, A., Marzetti, L., Zappasodi, F., Meinecke, F. C., and Nolte, G. (2012). Estimating true brain connectivity from EEG/MEG data invariant to linear and static transformations in sensor space. *Neuroimage* 60, 476–488. doi: 10.1016/j.neuroimage.2011.11.084

Fell, J., and Axmacher, N. (2011). The role of phase synchronization in memory processes. *Nat. Rev. Neurosci.* 12, 105–118. doi: 10.1038/nrn2979

Florin, E., and Baillet, S. (2015). The brain's resting-state activity is shaped by synchronized cross-frequency coupling of neural oscillations. *Neuroimage* 111, 26–35. doi: 10.1016/j.neuroimage.2015.01.054

Fox, M. D., and Raichle, M. E. (2007). Spontaneous fluctuations in brain activity observed with functional magnetic resonance imaging. *Nat. Rev. Neurosci.* 8, 700–711. doi: 10.1038/nrn2201

Fries, P. (2005). A mechanism for cognitive dynamics: neuronal communication through neuronal coherence. *Trends Cogn. Sci.* 9, 474–480. doi: 10.1016/j.tics.2005.08.011

Fries, P. (2015). Rhythms for cognition: communication through coherence, *Neuron* 88, 220–235. doi: 10.1016/j.neuron.2015.09.034

Friston, K. J., Harrison, L., and Penny, W. (2003). Dynamic causal modelling. *Neuroimage* 19, 1273–1302. doi: 10.1016/S1053-8119(03)00202-7

Geweke, J. (1982). Measurement of linear dependence and feedback between multiple time series. *J. Am. Stat. Assoc.* 77, 304–313. doi: 10.1080/01621459.1982.10477803

Gramfort, A., Luessi, M., Larson, E., Engemann, D. A., Strohmeier, D., Brodbeck, C., et al. (2014). MNE software for processing MEG and EEG data. *Neuroimage* 86, 446–460. doi: 10.1016/j.neuroimage.2013.10.027

Gregoriou, G. G., Gotts, S. J., Zhou, H., and Desimone, R. (2009). High-frequency, long-range coupling between prefrontal and visual cortex during attention. *Science* 324, 1207–1210. doi: 10.1126/science.1171402

Gross, J., Baillet, S., Barnes, G. R., Henson, R. N., Hillebrand, A., Jensen, O., et al. (2013). Good practice for conducting and reporting MEG research. *Neuroimage* 65, 349–363. doi: 10.1016/j.neuroimage.2012.10.001

Güllmar, D., Haueisen, J., and Reichenbach, J. R. (2010). Influence of anisotropic electrical conductivity in white matter tissue on the EEG/MEG forward and inverse solution. A high-resolution whole head simulation study. *Neuroimage* 51, 145–163. doi: 10.1016/j.neuroimage.2010.02.014

Halliday, D. M., Rosenberg, J. R., Amjad, A. M., Breeze, P., Conway, B. A., and Farmer, S. F. (1995). A framework for the analysis of mixed time series/point process data—Theory and application to the study of physiological tremor, single motor unit discharges and electromyograms. *Prog. Biophys. Mol. Biol.* 64, 237–278. doi: 10.1016/S0079-6107(96)00009-0

Hämäläinen, M. S., Hari, R., Ilmoniemi, R. J., Knuutila, J., and Lounasma, O. V. (1993). Magnetoencephalography: theory, instrumentation, and applications to non-invasive studies of the working human brain. *Rev. Mod. Phys.* 65, 413–497. doi: 10.1103/RevModPhys.65.413

Hari, R., Baillet, S., Barnes, G., Burgess, R., Forss, N., Gross, J., et al. (2018). IFCN-endorsed practical guidelines for clinical magnetoencephalography (MEG). *Clin. Neurophysiol.* 129, 1720–1747. doi: 10.1016/j.clinph.2018.03.042

Hari, R., and Parkkonen, L. (2015). The brain timewise: how timing shapes and supports brain function. *Philos. Trans. R. Soc. Lond. B. Biol. Sci.* 370:20140170. doi: 10.1098/rstb.2014.0170

Hauk, O., Wakeman, D. G., and Henson, R. (2011). Comparison of noise-normalized minimum norm estimates for MEG analysis using multiple resolution metrics. *Neuroimage* 54, 1966–1974. doi: 10.1016/j.neuroimage.2010.09.053

He, B., Astolfi, L., Valdes-Sosa, P. A., Marinazzo, D., Palva, S. O., Benar, C. G., et al. (2019). Electrophysiological brain connectivity: theor y and implementation. *IEEE Trans. Biomed. Eng.* 66, 2115–2137. doi: 10.1109/TBME.2019.2913928

He, B., Sohrabpour, A., Brown, E., and Liu, Z. (2018). Electrophysiological source imaging: a noninvasive window to brain dynamics. *Ann. Rev. Biomed. Eng.* 20, 171–196. doi: 10.1146/annurev-bioeng-062117-120853

Heekeren, H. R., Marret, S., Ruff, D. A., Bandettini, P. A., and Ungerleider, L. G. (2006). Involvement of human left dorsolateral prefrontal cortex in perceptual decision making is independent of response modality. *Proc. Natl. Acad. Sci. U.S.A.* 103, 10023–10028. doi: 10.1073/pnas.0603949103

Hillebrand, A., Tewarie, P., van Dellen, E., Yu, M., Carbo, E. W. S., Douw, L., et al. (2016). Direction of information flow in large-scale resting-state networks is frequency-dependent. *Proc. Natl. Acad. Sci U.S.A.* 113, 3867–3872. doi: 10.1073/pnas.1515657113

Hipp, J. F., Hawellek, D. J., Corbetta, M., Siegel, M., and Engel, A. K. (2012). Large-scale cortical correlation structure of spontaneous oscillatory activity. *Nat. Neurosci.* 15, 884–90. doi: 10.1038/nn.3101

Huang, M., Risling, M., and Baker, D. G. (2016). The role of biomarkers and MEG-based imaging markers in the diagnosis of post-traumatic stress disorder

and blast-induced mild traumatic brain injury. *Psychoneuroendocrinology* 63, 398–409. doi: 10.1016/j.psyneuen.2015.02.008

Iivanainen, J., Zetter, R., Grön, M., Hakkarainen, K., and Parkkonen, L. (2019). On-scalp MEG system utilizing an actively shielded array of optically-pumped magnetometers. *Neuroimage* 194, 244–258. doi: 10.1016/j.neuroimage.2019.03.022

Ilmoniemi, R. J., and Sarvas, J. (2019). *Brain Signals. Physics and Mathematics of MEG and EEG*. London: The MIT press.

Javitt, D. C., Spencer, K. M., Thaker, G. K., Winterer, G., and Hajós, M. (2008). Neurophysiological biomarkers for drug development in schizophrenia. *Nat. Rev. Drug Discov.* 7, 68–83. doi: 10.1038/nrd2463

Jensen, O., and Colgin, L. L. (2007). Cross-frequency coupling between neuronal oscillations. *Trends Cogn. Sci.* 11, 267–269. doi: 10.1016/j.tics.2007.05.003

Jensen, O., and Mazaheri, A. (2010). Shaping functional architecture by oscillatory alpha activity: gating by inhibition. *Front. Hum. Neurosci.* 4:186. doi: 10.3389/fnhum.2010.00186

Kaminski, M. J., and Blinowska, K. J. (1991). A new method of the description of the information flow in the brain structures. *Biol. Cybern.* 65, 203–210. doi: 10.1007/BF00198091

Kaplan, R., Bush, D., Bonnefond, M., Bandettini, P. A., Barnes, G. R., Doeller, C. F., et al. (2014). Medial prefrontal theta phase coupling during spatial memory retrieval. *Hippocampus* 24, 656–665. doi: 10.1002/hipo.22255

Lachaux, J.-P., Rodriguez, E., Martinerie, J., and Varela, F. J. (1999). Measuring phase synchrony in brain signals. *Hum. Brain Mapp.* 8, 194–208. doi: 10.1002/(SICI)1097-0193(1999)8:4<194::AID-HBM4>3.0.CO;2-C

Larson-Prior, L. J., Oostenveld, R., Della Penna, S., Michalareas, G., Prior, F., Babajani-Feremi, A., et al. (2013). Adding dynamics to the Human Connectome Project with MEG. *Neuroimage* 80, 190–201. doi: 10.1016/j.neuroimage.2013.05.056

Light, G. A., and Swerdlow, N. R. (2015). Future clinical uses of neurophysiological biomarkers to predict and monitor treatment response for schizophrenia. *Ann. N. Y. Acad. Sci.* 1344, 105–119. doi: 10.1111/nyas.12730

Litvak, V., Mattout, J., Kiebel, S. J., Phillips, C., Henson, R. N. A., Kilner, J., et al. (2011). EEG and MEG data analysis in SPM8. *Comput. Intell. Neurosci.*, 2011:852961. doi: 10.1155/2011/852961

Lobier, M., Palva, J. M., and Palva, S. (2018). High-alpha band synchronization across frontal, parietal and visual cortex mediates behavioral and neuronal effects of visuospatial attention. *Neuroimage* 165, 222–237. doi: 10.1016/j.neuroimage.2017.10.044

Lobier, M., Siebenhühner, F., Palva, S., and Palva, J. M. (2014). Phase transfer entropy: a novel phase-based measure for directed connectivity in networks coupled by oscillatory interactions. *Neuroimage* 85, 853–872. doi: 10.1016/j.neuroimage.2013.08.056

Lopes da Silva, F. (2013). EEG and MEG: relevance to Neuroscience. *Neuron* 80, 1112–1128, doi: 10.1016/j.neuron.2013.10.017

Lozano-Soldevilla, D., ter Huurne, N., and Oostenveld, R. (2016). Neuronal oscillations with non-sinusoidal morphology produce spurious phase-to-amplitude coupling and directionality. *Front. Comput. Neurosci.* 10:87. doi: 10.3389/fncom.2016.00087

Maestú, F., Cuesta, P., Hasan, O., Fernandéz, A., Funke, M., and Schulz, P. E. (2019). The importance of the validation of M / EEG with current biomarkers in Alzheimer ' s disease. *Front. Hum. Neurosci.* 13, 1–10. doi: 10.3389/fnhum.2019.00081

Mantini, D., Perrucci, M. G., Del Gratta, C., Romani, G. L., and Corbetta, M. (2007). Electrophysiological signatures of resting state networks in the human brain. *Proc. Natl. Acad. Sci. U.S.A.* 104, 13170–13175. doi: 10.1073/pnas.0700668104

Marinazzo, D., Pellicoro, M., and Stramaglia, S. (2008). Kernel method for nonlinear Granger causality. *Phys. Rev. Lett.* 100:144103. doi: 10.1103/PhysRevLett.100.144103

Marzetti, L., Del Gratta, C., and Nolte, G. (2008). Understanding brain connectivity from EEG data by identifying systems composed of interacting sources. *Neuroimage* 42, 87–98. doi: 10.1016/j.neuroimage.2008.04.250

Marzetti, L., Della Penna, S., Snyder, A. Z., Pizzella, V., Nolte, G., de Pasquale, F., et al. (2013). Frequency specific interactions of MEG resting state activity within and across brain networks as revealed by the multivariate interaction measure. *Neuroimage* 79, 172–183. doi: 10.1016/j.neuroimage.2013.04.062

Michel, C. M., and König, T. (2018). EEG microstates as a tool for studying the temporal dynamics of whole-brain neuronal networks: a review. *Neuroimage* 180, 577–593. doi: 10.1016/j.neuroimage.2017.11.062

Moon, J. Y., Lee, U., Blain-Moraes, S., and Mashour, G. A. (2015). General relationship of global topology, local dynamics, and directionality in large-scale brain networks. *PLoS Comput. Biol.* 11:e1004225. doi: 10.1371/journal.pcbi.1004225

Nikias, C. L., and Petropulu, A. P. (1993). *Higher-Order Spectra Analysis: A Nonlinear Signal Processing Framework*. Englewood Cliffs, NJ: PTR Prentice Hall.

Niso, G., Gorgolewski, K. J., Bock, E., Brooks, T. L., Flandin, G., Gramfort, A., et al. (2018). MEG-BIDS, the brain imaging data structure extended to magnetoencephalography. *Sci. Data* 5:180110. doi: 10.1038/sdata.2018.110

Nolte, G. (2003). The magnetic lead field theorem in the quasi-static approximation and its use for magnetoencephalography forward calculation in realistic volume conductors. *Phys. Med. Biol.* 48, 3637–3652. doi: 10.1088/0031-9155/48/22/002

Nolte, G., Bai, O., Wheaton, L., Mari, Z., Vorbach, S., and Hallett, M. (2004). Identifying true brain interaction from EEG data using the imaginary part of coherency. *Clin. Neurophysiol.* 115, 2292–2307. doi: 10.1016/j.clinph.2004.04.029

Nolte, G., and Marzetti, L., Valdes-Sosa. (2009). Minimum Overlap Component Analysis (MOCA) of EEG/MEG data for more than two sources. *J. Neurosci. Meth.* 183, 72–76. doi: 10.1016/j.jneumeth.2009.07.006

Nolte, G., Ziehe, A., Nikulin, V. V., Schlögl, A., Krämer, N., Brismar, T., et al. (2008). Robustly estimating the flow direction of information in complex physical systems. *Phys. Rev. Lett.* 100:234101. doi: 10.1103/PhysRevLett.100.234101

O'Neill, G. C., Barratt, E. L., Hunt, B. A., Tewarie, P. K., and Brookes, M. J. (2015). Measuring electrophysiological connectivity by power envelope correlation: a technical review on MEG methods. *Phys. Med. Biol.* 60, R271–R295. doi: 10.1088/0031-9155/60/21/R271

Oostenveld, R., Fries, P., Maris, E., and Schoffelen, J. M. (2011). FieldTrip: open source software for advanced analysis of MEG, EEG, and invasive electrophysiological data. *Comput. Intell. Neurosci.*,2011:156869. doi: 10.1155/2011/156869

Özkurt, T. E., and Schnitzler, A. (2011). A critical note on the definition of phase–amplitude cross-frequency coupling. *J. Neurosci. Methods* 201, 438–443. doi: 10.1016/j.jneumeth.2011.08.014

Palva, J. M., Monto, S., Kulashekhar, S., and Palva, S. (2010). Neuronal synchrony reveals working memory networks and predicts individual memory capacity. *Proc. Natl. Acad. Sci. U.S.A.* 107, 7580–7585. doi: 10.1073/pnas.0913113107

Palva, J. M., Palva, S., and Kaila, K. (2005). Phase synchrony among neuronal oscillations in the human cortex. *J. Neurosci.* 25, 3962–3972. doi: 10.1523/JNEUROSCI.4250-04.2005

Palva, J. M., Wang, S. H., Palva, S., Zhigalov, A., Monto, S., Brookes, M. J., et al. (2018). Ghost interactions in MEG/EEG source space: a note of caution on inter-areal coupling measures. *Neuroimage* 173, 632–643. doi: 10.1016/j.neuroimage.2018.02.032

Palva, S., and Palva, J. M. (2012). Discovering oscillatory interaction networks with M/EEG: challenges and breakthroughs. *Trends Cogn. Sci.* 16, 219–230. doi: 10.1016/j.tics.2012.02.004

Pascual-Marqui, R. D. (2007a). Coherence and phase synchronization: generalization to pairs of multivariate time series, and removal of zero-lag contributions. *arXiv:0706.1776v3 [stat.ME]*. Available online at: http://arxiv.org/pdf/0706.1776

Pascual-Marqui, R. D. (2007b). Instantaneous and lagged measurements of linear and nonlinear dependence between groups of multivariate time series: frequency decomposition. *arXiv:0711.1455 [stat.ME]*. Available online at: http://arxiv.org/pdf/0711.1455

Pascual-Marqui, R. D., Lehmann, D., Koukkou, M., Kochi, K., Anderer, P., Saletu, B., et al. (2011). Assessing interactions in the brain with exact low-resolution electromagnetic tomography. *Philos. Trans. R. Soc. Math. Phys. Eng. Sci.* 369, 3768–3784. doi: 10.1098/rsta.2011.0081

Pfurtscheller, G., and Lopes da Silva, F. H. (1999). Event-related EEG/MEG synchronization and desynchronization: basic principles. *Clin. Neurophysiol.* 110, 1842–1857. doi: 10.1016/S1388-2457(99)00141-8

Pizzella, V., Marzetti, L., Della Penna, S., de Pasquale, F., Zappasodi, F., and Romani, G. L. (2014). Magnetoencephalography in the study of brain dynamics. *Funct. Neurol.* 29, 241–253.

Port, R. G., Anwar, A. R., Ku, M., Carlson, G. C., Siegel, S. J., and Roberts, T. P. (2015). Prospective MEG biomarkers in ASD : pre-clinical evidence and clinical promise of electrophysiological signatures. *Yale J. Biol. Med.* 88, 25–36.

Raichle, M. E. (2006). Neuroscience. The brain's dark energy. *Science* 314, 1249–1250. doi: 10.1126/science.1134921

Rizzolatti, G., Fabbri-Destro, M., Caruana, F., and Avanzini, P. (2018). System neuroscience: past, present, and future. *CNS Neurosci. Ther.* 24, 685–693. doi: 10.1111/cns.12997

Rosenberg, J. R., Amjad, A. M., Breeze, P., Brillinger, D. R., and Halliday, D. M. (1989). The Fourier approach to the identification of functional coupling between neuronal spike trains. *Prog. Biophys. Mol. Biol.* 53, 1–31. doi: 10.1016/0079-6107(89)90004-7

Rosenblum, M. G., Pikovsky, A. S., and Kurths, J. (1996). Phase synchronization of chaotic oscillators. *Phys. Rev. Lett.* 76, 1804–1807. doi: 10.1103/PhysRevLett.76.1804

Roux, F., Wibral, M., Singer, W., Aru, J., and Uhlhaas, P. J. (2013). The phase of thalamic alpha activity modulates cortical gamma-band activity: evidence from resting-state MEG recordings. *J. Neurosci.* 33, 17827–17835. doi: 10.1523/JNEUROSCI.5778-12.2013

Sameshima, K., and Baccalá, L. A. (1999). Using partial directed coherence to describe neuronal ensemble interactions. *J. Neurosci. Methods* 94, 93–103. doi: 10.1016/S0165-0270(99)00128-4

Sato, J., Mossad, S. I., Wong, S. M., Hunt, B. A. E., Dunkley, B. T., Smith, M. L., et al. (2018). Alpha keeps it together: alpha oscillatory synchrony underlies working memory maintenance in Young Children. *Dev. Cogn. Neurosci.* 34, 114–123. doi: 10.1016/j.dcn.2018.09.001

Sauseng, P., Klimesch, W., Doppelmayr, M., Hanslmayr, S., Schabus, M., and Gruber, W. R. (2004). Theta coupling in the human electroencephalogram during a working memory task. *Neurosci. Lett.* 354, 123–126. doi: 10.1016/j.neulet.2003.10.002

Sauseng, P., Klimesch, W., Doppelmayr, M., Pecherstorfer, T., Freunberger, R., and Hanslmayr, S. (2005a). EEG alpha synchronization and functional coupling during top-down processing in a working memory task. *Hum. Brain Mapp.* 26, 148–155. doi: 10.1002/hbm.20150

Sauseng, P., Klimesch, W., Stadler, W., Schabus, M., Doppelmayr, M., Hanslmayr, S., et al. (2005b). A shift of visual spatial attention is selectively associated with human EEG alpha activity. *Eur J Neurosci.* 22, 2917–2926. doi: 10.1111/j.1460-9568.2005.04482.x

Schoffelen, J. M., and Gross, J. (2009). Source connectivity analysis with MEG and EEG. *Hum. Brain Mapp.* 30, 1857–1865. doi: 10.1002/hbm.20745

Schoonhoven, D. N., Fraschini, M., Tewarie, P., Uitdehaag, B. M., Eijlers, A. J., Geurts, J. J., et al. (2018). Resting-state MEG measurement of functional activation as a biomarker for cognitive decline in MS. *Mult. Scler. J.* 1–11. doi: 10.1177/1352458518810260

Schreiber, T. (2000). Measuring information transfer. *Phys. Rev. Lett.* 85, 461–464. doi: 10.1103/PhysRevLett.85.461

Shahbazi Avarvand, F., Bartz, S., Andreou, C., Samek, W., Leicht, G., Mulert, C., et al. (2018). Localizing bicoherence from EEG and MEG. *Neuroimage* 174, 352–363. doi: 10.1016/j.neuroimage.2018.01.044

Shahbazi, F., Ewald, A., and Nolte, G. (2014). Univariate normalization of bispectrum using Hölder's inequality. *J. Neurosci. Methods* 233, 177–186. doi: 10.1016/j.jneumeth.2014.05.030

Shannon, C. E. (1948). A Mathematical theory of communication. *Bell Syst. Tech. J.* 27, 379–423. doi: 10.1002/j.1538-7305.1948.tb01338.x

Siebenhühner, F., Wang, S. H., Arnulfo, G., Nobili, L., Palva, J. M., and Palva, S. (2019). Resting-state cross-frequency coupling networks in human electrophysiological recordings. *bioRxiv* 547638. doi: 10.1101/547638

Siebenhühner, F., Wang, S. H., Palva, J. M., and Palva, S. (2016). Cross-frequency synchronization connects networks of fast and slow oscillations during visual working memory Maintenance. *Elife* 5:e13451. doi: 10.7554/eLife.13451

Siegel, M., Donner, T. H., and Engel, A. K. (2012). Spectral fingerprints of large-scale neuronal interactions. *Nat. Rev. Neurosci.* 13, 121–34. doi: 10.1038/nrn3137

Siegel, M., Donner, T. H., Oostenveld, R., Fries, P., and Engel, A. K. (2008). Neuronal synchronization along the dorsal visual pathway reflects the focus of spatial attention. *Neuron* 60, 709–19. doi: 10.1016/j.neuron.2008.09.010

Singh, K. D. (2012). Which "neural activity" do you mean? fMRI, MEG, oscillations and neurotransmitters. *Neuroimage* 62, 1121–1130. doi: 10.1016/j.neuroimage.2012.01.028

Smith, S. M., Vidaurre, D., Beckmann, C. F., Glasser, M. F., Jenkinson, M., Miller, K. L., et al. (2013). Functional connectomics from resting-state fMRI. *Trends Cogn. Sci.* 17, 666–682. doi: 10.1016/j.tics.2013.09.016

Snyder, A. Z., and Raichle, M. E. (2012). A brief history of the resting state: the Washington University Perspective. *Neuroimage* 62, 902–910. doi: 10.1016/j.neuroimage.2012.01.044

Sommariva, S., Sorrentino, A., Piana, M., Pizzella, V., and Marzetti, L. (2017). A comparative study of the robustness of frequency-domain connectivity measures to finite data length. *Brain Topogr.* 32, 675–695. doi: 10.1007/s10548-017-0609-4

Soreq, E., Leech, R., and Hampshire, A. (2019). Dynamic network coding of working-memory domains and working-memory processes. *Nat. Commun.* 10:936. doi: 10.1038/s41467-019-08840-8

Soriano, M. C., Niso, G., Clements, J., Ortín, S., Carrasco, S., Gudín, M., et al. (2017). Automated detection of epileptic biomarkers in resting-state interictal MEG data. *Front. Neuroinform.* 11, 1–12. doi: 10.3389/fninf.2017.00043

Stam, C. J., Nolte, G., and Daffertshofer, A. (2007). Phase lag index: assessment of functional connectivity from multichannel EEG and MEG with diminished bias from common sources. *Hum. Brain Mapp.* 28, 1178–1193. doi: 10.1002/hbm.20346

Stenroos, M., Hunold, A., and Haueisen, J. (2014). Comparison of three-shell and simplified volume conductor models in magnetoencephalography. *Neuroimage* 94, 337–348. doi: 10.1016/j.neuroimage.2014.01.006

Stenroos, M., and Nummenmaa, A. (2016). Incorporating and compensating cerebrospinal fluid in surface-based forward models of magneto-and electroencephalography. *PLoS ONE* 11:e0159595. doi: 10.1371/journal.pone.0159595

Tadel, F., Baillet, S., Mosher, J. C., Pantazis, D., and Leahy, R. M. (2011). Brainstorm: a user-friendly application for MEG/EEG analysis. *Comput. Intell. Neurosci.* 2011:879716. doi: 10.1155/2011/879716

Tass, P., Rosenblum, M. G., Weule, J., Kurths, J., Pikovsky, A., Volkmann, J., et al. (1998). Detection of *n:m* phase locking from noisy data: application to magnetoencephalography. *Phys. Rev. Lett.* 81, 3291–3294. doi: 10.1103/PhysRevLett.81.3291

Tewarie, P., Hunt, B. A., O'Neill, G. C., Byrne, A., Aquino, K., Bauer, M., et al. (2019). Relationships between neuronal oscillatory amplitude and dynamic functional connectivity. *Cereb. Cortex* 29, 2668–2681. doi: 10.1093/cercor/bhy136

Tort, A. B., Komorowski, R., Eichenbaum, H., and Kopell, N. (2010). Measuring phase-amplitude coupling between neuronal oscillations of different frequencies. *J. Neurophysiol.* 104, 1195–1210. doi: 10.1152/jn.00106.2010

Troebinger, L., López, J. D., Lutti, A., Bradbury, D., Bestmann, S., and Barnes, G. (2014). High precision anatomy for MEG. *Neuroimage* 86, 583–591. doi: 10.1016/j.neuroimage.2013.07.065

Van de Steen, F., Faes, L., Karahan, E., Songsiri, J., Valdes-Sosa, P. A., and Marinazzo, D. (2019). Critical comments on EEG sensor space dynamical connectivity analysis. *Brain Topogr.* 32, 643–654. doi: 10.1007/s10548-016-0538-7

Varela, F., Lachaux, J.-P., Rodriguez, E., and Martinerie, J. (2001). The brainweb: phase synchronization and large-scale integration. *Nat. Rev. Neurosci.* 2, 229–239. doi: 10.1038/35067550

Vidaurre, D., Hunt, L. T., Quinn, A. J., Hunt, B. A. E., Brookes, M. J., Nobre, A. C., et al. (2018). Spontaneous cortical activity transiently organises into frequency specific phase-coupling networks. *Nat. Commun.* 9:2987. doi: 10.1038/s41467-018-05316-z

Vinck, M., Oostenveld, R., van Wingerden, M., Battaglia, F., and Pennartz, C. M. A. (2011). An improved index of phase-synchronization for electrophysiological data in the presence of volume-conduction, noise and

sample-size bias. *Neuroimage* 55, 1548–1565. doi: 10.1016/j.neuroimage.2011.01.055

von Stein, A., Chiang, C., and König, P. (2000). Top-down processing mediated by interareal synchronization. *Proc. Natl. Acad. Sci. U.S.A.* 97, 14748–14753. doi: 10.1073/pnas.97.26.14748

Vorwerk, J., Cho, J. H., Rampp, S., Hamer, H., Knösche, T. R., and Wolters, C. H. (2014). A guideline for head volume conductor modeling in EEG and MEG. *Neuroimage* 100, 590–607. doi: 10.1016/j.neuroimage.2014.06.040

Wang, J., Dong, Q., and Niu, H. (2017). The minimum resting-state fNIRS imaging duration for accurate and stable mapping of brain connectivity network in children. *Sci. Rep.* 7:6461. doi: 10.1038/s41598-017-06340-7

Wianda, E., and Ross, B. (2019). The roles of alpha oscillation in working memory retention. *Brain Behav.* 9:e01263. doi: 10.1002/brb3.1263

Yeo, B. T., Krienen, F. M., Sepulcre, J., Sabuncu, M. R., Lashkari, D., Hollinshead, M., et al. (2011). The organization of the human cerebral cortex estimated by intrinsic functional connectivity. *J. Neurophysiol.* 106, 1125–1165. doi: 10.1152/jn.00338.2011

Conflict of Interest Statement: The authors declare that the research was conducted in the absence of any commercial or financial relationships that could be construed as a potential conflict of interest.

frontiers in Neuroscience

ORIGINAL RESEARCH
published: 18 September 2019
doi: 10.3389/fnins.2019.00965

Brain Networks Underlying Eye's Pupil Dynamics

Mauro DiNuzzo[1], Daniele Mascali[1,2], Marta Moraschi[1,2], Giorgia Bussu[3], Laura Maugeri[1], Fabio Mangini[1], Michela Fratini[1,4] and Federico Giove[1,2]*

[1] Fondazione Santa Lucia (IRCCS), Rome, Italy, [2] Centro Fermi – Museo Storico della Fisica e Centro Studi e Ricerche Enrico Fermi, Rome, Italy, [3] Donders Institute for Brain, Cognition and Behavior, Radboud University, Nijmegen, Netherlands, [4] CNR Nanotec, Rome, Italy

Phasic changes in eye's pupil diameter have been repeatedly observed during cognitive, emotional and behavioral activity in mammals. Although pupil diameter is known to be associated with noradrenergic firing in the pontine Locus Coeruleus (LC), thus far the causal chain coupling spontaneous pupil dynamics to specific cortical brain networks remains unknown. In the present study, we acquired steady-state blood oxygenation level-dependent (BOLD) functional magnetic resonance imaging (fMRI) data combined with eye-tracking pupillometry from fifteen healthy subjects that were trained to maintain a constant attentional load. Regression analysis revealed widespread visual and sensorimotor BOLD-fMRI deactivations correlated with pupil diameter. Furthermore, we found BOLD-fMRI activations correlated with pupil diameter change rate within a set of brain regions known to be implicated in selective attention, salience, error-detection and decision-making. These regions included LC, thalamus, posterior cingulate cortex (PCC), dorsal anterior cingulate and paracingulate cortex (dACC/PaCC), orbitofrontal cortex (OFC), and right anterior insular cortex (rAIC). Granger-causality analysis performed on these regions yielded a complex pattern of interdependence, wherein LC and pupil dynamics were far apart in the network and separated by several cortical stages. Functional connectivity (FC) analysis revealed the ubiquitous presence of the superior frontal gyrus (SFG) in the networks identified by the brain regions correlated to the pupil diameter change rate. No significant correlations were observed between pupil dynamics, regional activation and behavioral performance. Based on the involved brain regions, we speculate that pupil dynamics reflects brain processing implicated in changes between self- and environment-directed awareness.

Keywords: steady-state BOLD-fMRI, pupillometry, human brain, locus coeruleus, granger-causality, functional connectivity

OPEN ACCESS

Edited by:
Daniel Baumgarten, UMIT – Private Universität für Gesundheitswissenschaften, Medizinische Informatik und Technik, Austria

Reviewed by:
Merlin D. Larson, University of California, San Francisco, United States
Peter Herman, Yale University, United States

****Correspondence:***
Mauro DiNuzzo
mauro.dinuzzo@neuroenergetics.org

Specialty section:
This article was submitted to Brain Imaging Methods, a section of the journal Frontiers in Neuroscience

Received: *11 April 2019*
Accepted: *28 August 2019*
Published: *18 September 2019*

Citation:
DiNuzzo M, Mascali D, Moraschi M, Bussu G, Maugeri L, Mangini F, Fratini M and Giove F (2019) Brain Networks Underlying Eye's Pupil Dynamics. Front. Neurosci. 13:965. doi: 10.3389/fnins.2019.00965

INTRODUCTION

Consensual changes in eye's pupil size are strongly associated with neuromodulatory tone. Specifically, pupil size is controlled by sympathetic and parasympathetic systems (McDougal and Gamlin, 2015) and it is recognized as a peripheral index of arousal (Bradley et al., 2008; Gilzenrat et al., 2010; Jepma and Nieuwenhuis, 2011; Nassar et al., 2012; Wierda et al., 2012; Naber et al., 2013; Urai et al., 2017; Wang et al., 2018; Aminihajibashi et al., 2019;

van Kempen et al., 2019), in addition to the well-known regulation by ambient illumination (reviewed by Mathot and Van der Stigchel, 2015). In monkeys and rodents, light-independent pupil dilations have been found to be correlated with neuronal firing in the pontine locus coeruleus (LC), the major source of noradrenergic input to the cerebral cortex (Rajkowski et al., 1993; Joshi et al., 2016). Accordingly, pupil dilations are associated with desynchronized cortical electroencephalographic and electrophysiological signals and enhancement of sensory responses, i.e., attentive state (Reimer et al., 2014).

Although the results found in animal models might not directly translate to the human brain, the relationship between pupil dynamics and LC has been indirectly confirmed in humans using pupillometry and functional magnetic resonance imaging (fMRI) (Alnaes et al., 2014; Murphy et al., 2014; Yellin et al., 2015; Schneider et al., 2016; Elman et al., 2017). An important difference between animal and human studies is that the fMRI signal only indirectly reflects neuronal firing through the action of neurovascular coupling (Logothetis and Pfeuffer, 2004). However, recent experimental evidence in mice demonstrated that resting-state hemodynamics can be predicted from spontaneous neuronal activity using a convolution-based approach, indicating that hemodynamic fluctuations are indeed a low-pass filtered version of the underlying neuronal activity (Ma et al., 2016). Moreover, either electrode recordings within LC or aggregate neuronal calcium signaling in cortical axonal projections from LC (the latter having an intrinsically slow dynamics, e.g., several hundreds of ms), have been reported to be closely correlated to pupil size fluctuations (Joshi et al., 2016; Reimer et al., 2016). Accordingly, pupil dilations after activation of LC occur on a relatively slow time-scale (500–1000 ms) (Larsen and Waters, 2018). These findings strongly support the possibility to track pupil-related brain activity using neurovascular coupling through the fMRI blood oxygenation level-dependent (BOLD) signals, as evidenced by several experiments. In particular, LC activation was initially observed using the temporal derivatives of the canonical hemodynamic response function (HRF) (Murphy et al., 2014 and references therein). Subsequently, it was found that it is not pupil size *per se* but the change rate of pupil diameter to be correlated with the BOLD signals in LC and other subcortical and cortical areas during resting state (Schneider et al., 2016). This notion is consistent with electrophysiological measurements in mice showing that, during both quiet waking and locomotion, pupil size is correlated with the cholinergic system, while its time derivative is correlated with the noradrenergic LC (Reimer et al., 2016). It should be noted, however, that LC does not directly control pupil size, and the functional relevance of anatomical pathways between LC and oculomotor neurons such as preganglionic cells of the Edinger-Westphal midbrain nucleus is not definitely established (McDougal and Gamlin, 2015). Thus, it is important to remark that fMRI is not able to resolve these dependencies, especially the correlations between regional brain activity and the high-frequency components of pupil dynamics.

Remarkably, during stimulus-related protocols in humans, such as reward-anticipation (Schneider et al., 2018) or fear-learning (Leuchs et al., 2017), but also during mind-wandering resting-state (Schneider et al., 2016), pupil-related activations consistently implicated cortical areas of the salience-network, including anterior cingulate cortex (ACC) and anterior insular cortex (AIC) (Menon and Uddin, 2010). Furthermore, a large degree of overlap has been reported in pupil-related BOLD activation maps during either continuous rest-fixation or block-design visual-imagery experiments (Yellin et al., 2015). These observations raise the possibility that at least in part low-frequency pupil dynamics reflects task-independent fluctuations in cortical activity.

In the present study, we sought to characterize the pupil-related brain networks during a steady-state experimental protocol designed to achieve a continuous degree of attentional load. To this end, we recorded pupillometry and fMRI data along with response times from healthy human subjects exposed to a whole-field visual stimulation and either left or right hemifield-directed attention. We were particularly interested in the brain network comprising LC and thalamus (TH), two critical components of the ascending reticular activating system (ARAS). The ARAS is responsible for arousal and it is thought to subserve both self and environmental awareness (Yeo et al., 2013). The aims of this work were (i) to interrogate the pupil-related brain networks during a continuous attentive state, and (ii) to identify the underlying functional hierarchy between the involved brain areas by means of causality and connectivity analysis.

MATERIALS AND METHODS

Participants

Fifteen healthy volunteers (age: 26 ± 5 years, mean ± SD; age range: 18–44 years; 5 females) participated in the study. The protocol of the study was approved by the Ethics Committee of Santa Lucia Foundation. All subjects gave written informed consent in accordance with the Declaration of Helsinki and with the European Union regulations.

MR Acquisitions

MR data were acquired on a 3T scanner (Siemens, Magnetom Allegra, Erlangen, Germany) equipped with a standard birdcage coil. Functional images were collected with a multi-echo (Speck and Hennig, 1998) planar imaging sequence (TR = 3100 ms, TE1/TE2/TE3 = 16/39/63 ms, Flip Angle = 85°, voxel size = 3× 3 × 3.75 mm^3, FOV = 192 × 192 mm^2) lasting 12 min and 43 s for a total of 246 volumes (including 4 dummy scans). Two functional runs were acquired for each subject. Parallel imaging and partial k-space sampling were avoided by leveraging the high scanner gradient performances (rise time 100 μs to reach a maximum amplitude of 40 mT/m). Clinical scans were also acquired to comply with institutional guidelines and to exclude pathological conditions.

Steady-State Attentional Task

During the acquisition of functional images, subjects performed a continuous motion detection task with covert attention. The constant-luminance (21 cd/m^2) visual stimulation (**Figure 1A**) consisted of two circle-shaped (3° of radius) white-black rotating

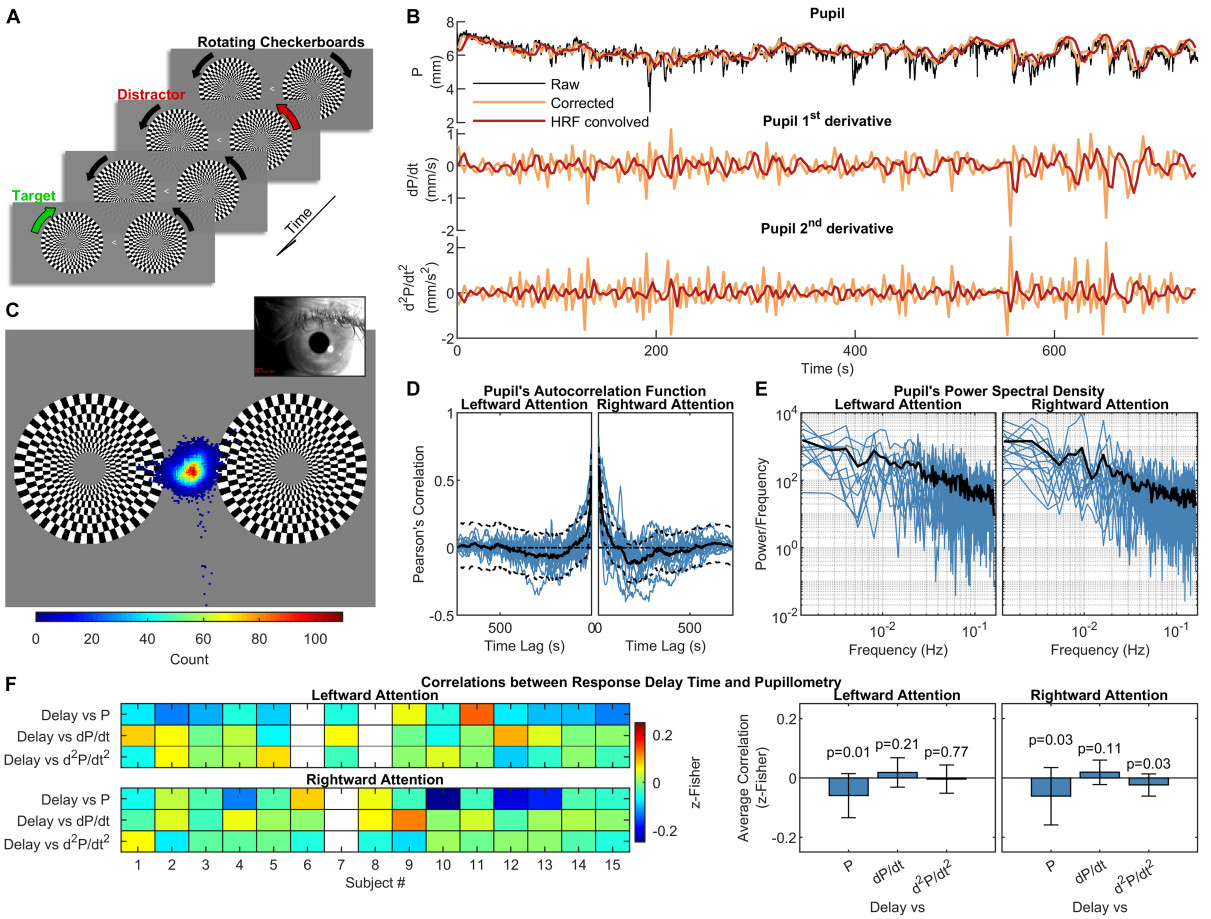

FIGURE 1 | Experimental design, pupillometry and relation to subject's performance. **(A)** Schematization of the visual stimulation with leftward attention presented during the functional scans. While maintaining the gaze on the central arrow, subjects had to pay attention to the change in the direction of rotation of the target checkerboard while ignoring the distracting checkerboard on the opposite hemifield. One run with leftward and one with rightward attention were acquired for each subject. **(B)** Pupil and pupil-derived time courses from one representative subject. **(C)** Eye-position heat map overlaid over the visual stimulation for one representative subject during the leftward attention run. The distribution is centered on the fixation point, demonstrating subject's compliance. **(D)** and **(E)** panels show the autocorrelation function and power spectral density of the corrected and resampled pupil data, respectively. The black lines represent the across-subject averages, which are displayed over single-subject data (blue lines). **(F)** Correlations between response delay times and pupillometry over time, displayed separately for each subject (left panel) and for the entire group (right panel). The white rectangles on the left panel indicate missing data. The error bars on the right panel represent the standard deviation, while the *p*-values are the results of one-sample *t*-tests on the distribution of correlations.

(2 cycles/s) checkerboards located in the left and right hemifield at 4° horizontal decentering and vertically centered. The two checkerboards inverted the direction of rotation independently of one another, with a random inversion period ranging uniformly from 1 to 3 s. A leftward or rightward white arrow located at the center of the screen identified the fixation point. Subjects were asked to keep the gaze on the central arrow while maintaining the attention to checkerboard pointed by the arrow, and to push an MRI compatible button whenever the target checkerboard inverted the direction of rotation. Two functional runs were acquired for each subject, with either leftward or rightward attention. The run ordering was randomized across subjects. The visual stimulation was generated with Cogent 2000 (Laboratory of Neurobiology, Wellcome Trust, London, United Kingdom) running on Matlab 7.1 (The Mathworks Inc., Natick, MA, United States). A single chip Digital Light Processing (DLP) projector model NP216G (NEC Display Solutions, Itasca, IL, United States), located outside the magnet room, projected the stimulation on a screen mounted on the magnet bore behind the subject, who viewed it via a mirror mounted on the head coil. The fixation distance between subjects' eyes and the screen was approximately 65 cm.

Preprocessing of Functional Images

Preprocessing of functional images was performed with AFNI (Cox, 1996). After discarding four dummy scans, correction for head motion was estimated from the second-echo series, using the first volume as reference (3dvolreg). Each echo series was slice-timing corrected (3dTshift) and then motion corrected by applying the previously estimated transformations (3dAllineate). Non-brain regions were removed by intersecting the realigned volumes with a mask obtained via 3dAutomask applied to a

provisional optimal combined time series. Then, the three-echo series were fed to "tedana.py" to perform multi-echo ICA denoising (ME-ICA) (Kundu et al., 2012; Kundu et al., 2013). ME-ICA removes nuisance sources of variance by performing ICA decomposition followed by component classification based on their TE dependency, with TE-independent components marked as non-BOLD components and hence removed from the data. Tedana yielded a single cleaned "optimal combined" series, obtained via a T2*-weighted average of the three echoes (Posse et al., 1999). The cleaned series was normalized to Montreal Neurological Institute (MNI) space ($3 \times 3 \times 3$ mm^3) using as source image the mean of the motion-corrected second-echo series. The transformation to MNI space was obtained combining an affine transformation (@auto_tlrc) with a non-linear warp (3dQwarp), and it was applied in a single interpolation step using 3dNwarpApply. Slow frequencies (<0.008 Hz), linear and quadratic trends, as well as motion-derived parameters were regressed out using 3dTproject. Finally, the resulting series was smoothed within the brain mask with an isotropic 4 mm FWHM Gaussian kernel (3dBlurInMask).

Pupillometry and Pupil Data Preprocessing

Eye-tracking data were acquired during complete darkness (ambient luminance measured inside the bore during the stimulation < 1 lux) in order to counter-balance the influence of the visual stimulation (at constant light intensity, see above) on pupil constriction, as addition of light facilitates the detection of spontaneous (i.e., light-independent) changes in pupil diameter (Behrends et al., 2019). Adaptation to the light conditions (ambient darkness plus visual stimulation) lasted ∼15 min while the acquisition of anatomical reference images and clinical scans took place. We did not test different light conditions, as eye-tracking measurements (e.g., number and duration of blink/eye closure) and fMRI-related variables (e.g., motion parameters and regional pupil-BOLD correlations) have been previously shown not to differ significantly in either light or dark conditions (Yellin et al., 2015; Schneider et al., 2016), although luminance might affect pupillary responses under cognitive load (Peysakhovich et al., 2017). During acquisitions, subject's gaze was recorded (60 Hz) through an eye-tracking system (Applied Science Laboratories, model 504) equipped with remote pan/tilt optic infrared module and a video camera that was custom-adapted for use in the scanner. After a 16-points calibration procedure, eye-position traces, linearly interpolated and smoothed (after an up-sampling to 1 kHz) by a boxcar filter (width ± 25 ms), were used to verify subject's compliance. Pupil diameter was directly computed by the eye-tracking software through automatic elliptical fitting and major axis determination (preferred over area to avoid partial pupil coverage by the eyelid). Peak-envelope of pupil diameter time course was determined based on its frequency-spectrum and downsampled to 1/TR to be used for regression analysis. Data underwent outliers-removal using Hampel Filter and detrending (only for linear trends), thus obtaining artifact-free pupil diameter time courses (**Figure 1B**). It is noted that the convolution approach used for pupil-BOLD regression carries the Nyquist frequency of 0.16 Hz, which means that our analysis of pupillary oscillations is correspondingly limited to low frequencies.

Identification of Brain Regions Correlated to Pupil Dynamics

We performed a regression analysis by convolving the canonical HRF with the pupil diameter time-course as well as its first-order (pupil diameter change rate) and second-order time derivatives. The analysis was performed with SPM12[1] running on Matlab 2018a (The Mathworks Inc., Natick, MA, United States). Statistical t-maps were thresholded at $p < 0.001$; Family-wise error (FWE) correction for multiple comparisons was performed at cluster level ($p_{FWE} < 0.05$). Each cluster identified a specific region of interest (ROI) used for further analysis (see below), with the following exceptions. Left and right orbitofrontal cortices, as well as anterior paracingulate cortex and cingulate cortex, were grouped together due to high homology and substantial temporal correlation between the corresponding time-series, thus reducing the eight clusters to six ROIs.

Granger Causality Analysis

Pairwise conditional GC was computed using the state-of-the-art Multivariate Granger Causality (MVGC) Matlab Toolbox (Barnett and Seth, 2014). In particular, the algorithm performs numerical computation and statistical inference of multivariate GC given an ensemble of fMRI data time series (variables are the ROIs defined above, observations are time points, and trials are subjects/sessions). Since we found no difference in activation maps for left and right hemifield-directed attention, we lumped together all sessions. Vector autoregressive model parameter estimation was performed using the Levinson-Durbin-Whittle-Wiggins-Robinson (LWR) method and model selection was done using the Bayesian information criterion (BIC). Significance level was set to $p < 0.05$ with Bonferroni correction for multiple comparisons. The binarized version of the matrix of suprathreshold elements was interpreted as adjacency matrix for directed graph determination and calculation of node centrality.

Seed-to-Voxel Functional Connectivity

With the aim of exploring the steady-state networks associated with the above-mentioned ROIs, we computed the seed-to-voxel functional connectivity (FC) maps (Biswal et al., 1995) as the Pearson's correlation coefficient between the ROI-averaged time course and every other voxel time course. Group-level maps were generated with SPM12 using one-sample t-tests on the z-Fisher-transformed maps. FWE correction for multiple comparisons was performed both at voxel ($p_{FWE} < 0.05$) and cluster ($p_{FWE} < 0.001$) level.

Data Availability

All data sets (fMRI-BOLD and pupil size time series) are available upon reasonable request to the corresponding author.

[1] http://www.fil.ion.ucl.ac.uk/spm

RESULTS

Pupillometry and steady-state fMRI data were successfully acquired from all subjects (two sessions from two different subjects were discarded due to low-quality of eye-tracking recordings and one session of a separate subject was discarded due to excessive in-scanner head motion). Overall task performance was high, with an average fraction of correct responses of 89 ± 10% (mean ± SD) and an average response delay time of 433 ± 42 ms (mean ± SD). All subjects kept their gaze consistently on the fixation point at the center of the screen (**Figure 1C**). As previously reported (Yellin et al., 2015), autocorrelation and frequency analysis revealed no periodic frequencies in the pupil data (**Figures 1D,E**). No significant correlation was found between mean performance and the average of either pupil diameter or its 1st- and 2nd-order time derivatives. A very small ($r = -0.06$) but significant ($p < 0.05$, one-sample, two-tailed t-test) negative correlation was observed using the response delay and the pupil diameter across time (**Figure 1F**).

To determine pupil-related cortical areas, we performed regression analysis using general linear model by employing HRF-convolved pupil diameter and its time derivatives. Widespread deactivation maps correlated to pupil diameter were observed in visual and sensory-motor cortices (**Figure 2A** and **Table 1**). Activation maps correlated to pupil diameter change rate were observed in several subcortical and cortical areas (**Figure 2B** and **Table 2**), including LC, TH, posterior cingulate cortex (PCC), dorsal anterior cingulate and paracingulate cortex (dACC/PaCC), orbitofrontal cortex (OFC) as well as right anterior insular cortex (rAIC). Notably, separate regression analysis for left and right hemifield-directed attention revealed no suprathreshold cluster for either left > right or right > left statistical tests ($p > 0.9$ uncorrected, data not shown).

In order to elucidate the ability of each ROI (see section "Materials and Methods" for ROI definition) in predicting the behavior of the others within the pupil-related network, we performed Granger causality (GC) analysis. We found a complex pattern of interdependence between the cortical areas correlated with pupil diameter change (**Figure 3**). Specifically, PCC and dACC/PaCC exhibited the largest pairwise conditional GC for outwardly and inwardly directed causal influences, respectively. Node centrality analysis accordingly revealed that dACC/PaCC is the main authority and PCC is the main hub of the cortical

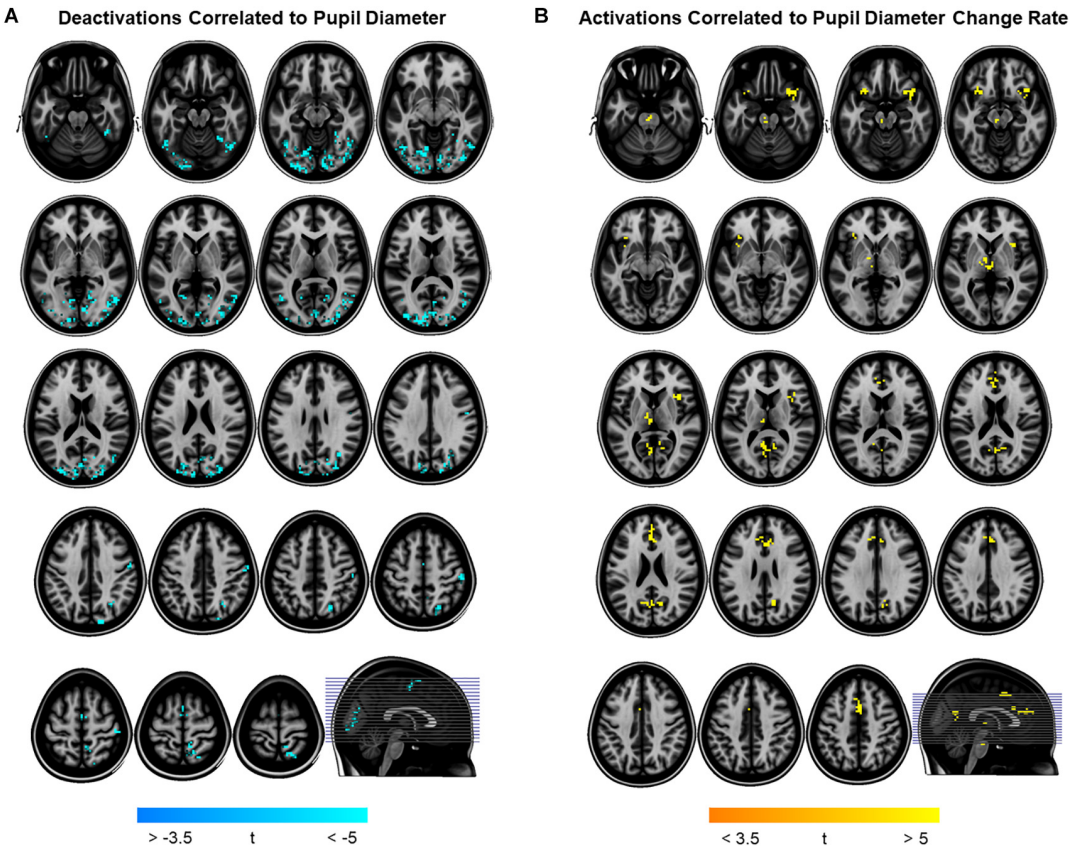

FIGURE 2 | Brain regions correlated to pupil dynamics. Regression analysis yielded clusters of brain regions significantly (cluster-level $p_{FWE} < 0.05$) related to pupil diameter **(A)** and to pupil diameter change rate **(B)**, while no significant cluster was found testing the effect of pupil second-order time derivative. **(A)** Deactivations (i.e., negative correlations) were found by testing the effect of pupil diameter (see **Table 1** for details). **(B)** Activations (i.e., positive correlations) were found by testing the effect of pupil diameter change rate (see **Table 2** for details). Images are presented in neurological convention.

TABLE 1 | Brain regions negatively correlated to pupil diameter.

Region	Cluster		Voxel			
	p_{FWE}	k	t_{PEAK}	x	y	z
Occipital fusiform/lingual gyrus (OF/LG) (R)	<0.001	38	7.94	15	−66	−6
Occipital fusiform/lingual gyrus (OF/LG) (L)	<0.001	114	6.46	−18	−72	−9
Lateral occipital cortex (LOC) (R)	<0.001	985	9.67	54	−66	−6
Postcentral/supramarginal gyrus (PC/SMG) (R)	<0.001	34	7.10	54	−27	54
Superior parietal lobule (SPL) (R)	<0.001	51	6.62	12	−48	63

Reported clusters survived cluster-level Family-Wise Error (FWE) correction for multiple comparisons ($p_{FWE} < 0.05$). Voxel-level significance level was set to $p < 0.001$. Cluster size (in voxels) is indicated by k, while t_{PEAK} stands for the t-value of the peak voxel. Coordinates (x, y, z) are expressed in mm in the MNI-space.

TABLE 2 | Brain regions positively correlated to pupil diameter change rate.

Region	Cluster		Voxel			
	p_{FWE}	k	t_{PEAK}	x	y	z
Locus coeruleus (LC)	<0.01	17	6.21	−6	−27	−18
Thalamus (TH)	<0.001	37	7.11	−6	−18	−3
Posterior cingulate cortex (PCC)	<0.001	79	6.47	−9	−63	21
Dorsal anterior cingulate cortex (dACC)	<0.001	76	5.50	0	30	21
Anterior paracingulate cortex (PaCC)	<0.001	26	6.94	0	9	45
Orbitofrontal Cortex (OFC) (L)	<0.001	37	5.64	−30	18	−18
Orbitofrontal Cortex (OFC) (R)	<0.001	45	9.59	36	18	−18
Anterior Insular Cortex (AIC) (R)	<0.003	21	6.20	36	12	6

Reported clusters survived cluster-level Family-Wise Error (FWE) correction for multiple comparisons ($p_{FWE} < 0.05$). Voxel-level significance level was set to $p < 0.001$. Cluster size (in voxels) is indicated by k, while t_{PEAK} stands for the t-value of the peak voxel. Coordinates (x, y, z) are expressed in mm in the MNI-space.

network (**Table 3**). No significant correlation was found between mean within ROI t-value and either pupil dynamics or average task performance ($q_{FDR} > 0.2$, data not shown).

To further characterize pupil-related networks, we determined seed-to-voxel FC maps with each ROI taken as seed (**Figure 4A** and **Table 4**). As expected, the PCC-seed FC yielded default mode network (DMN) areas including superior frontal gyrus (SFG). Subregions of the SFG were common members in all FC networks. The correlation between the different FC maps was globally very high, with PCC-seed versus rAIC-seed exhibiting the lowest correlation.

DISCUSSION

In this study, we investigated the brain networks related to temporal variations of the eye's pupil. We were mainly interested in examining the connection between pupil dynamics and LC in the pons, which together with TH and other subcortical structures (e.g., catecholaminergic nuclei) are linked to the arousal/ARAS system (Yeo et al., 2013). The regression analysis between steady-state fMRI signals and pupil diameter showed deactivations in a widespread cortical territory comprising visual and sensorimotor areas (**Figure 2A** and **Table 1**), in excellent agreement with previous studies (Murphy et al., 2014; Yellin et al., 2015; Schneider et al., 2016). Since the cholinergic system is thought to be correlated to pupil diameter (Reimer et al., 2016), the negative activations that we report here might be explained by a decreased cholinergic input to visual and sensorimotor areas. However, in humans the cholinergic nucleus basalis of Meynert innervates predominantly the limbic system (Mesulam, 2004) while the patterns of cholinergic innervation in the visual cortex varies considerably across mammalian species (Gu, 2003). Previous reports interpreted these deactivations as reflecting the suppression of interoceptive processes (including mental imagery) during alertness-induced pupil dilations, possibly mediated by the cholinergic branch of the ARAS (Yellin et al., 2015; Schneider et al., 2016). Further research is required to elucidate the significance of these results.

Positive activations were found using pupil diameter change rate (i.e., first-order time derivative of the pupil size) as regressor, which identified a set of subcortical and cortical regions including LC and TH as well as PCC, ACC, OFC and AIC (**Figure 2B** and **Table 2**). These areas largely overlap with previously published results (see **Table 5**). It should be noted that differences between findings unrelated to specific experimental design (e.g., rest-fixation resting-state, block-design or steady-state task, and so on) might result from a variety of sources, including but not limited to preprocessing of pupillometry and fMRI data, physiological noise (e.g., respiratory and cardiac rhythms) correction and statistical significance thresholds (e.g., voxel- and cluster-level correction for multiple comparisons).

The network of brain areas related to pupil diameter change rate was found to have PCC as its main cortical hub, as evidenced by GC analysis (**Figure 3**) and node centrality (**Table 3**). PCC appears to be the principal cortical region in initiating the

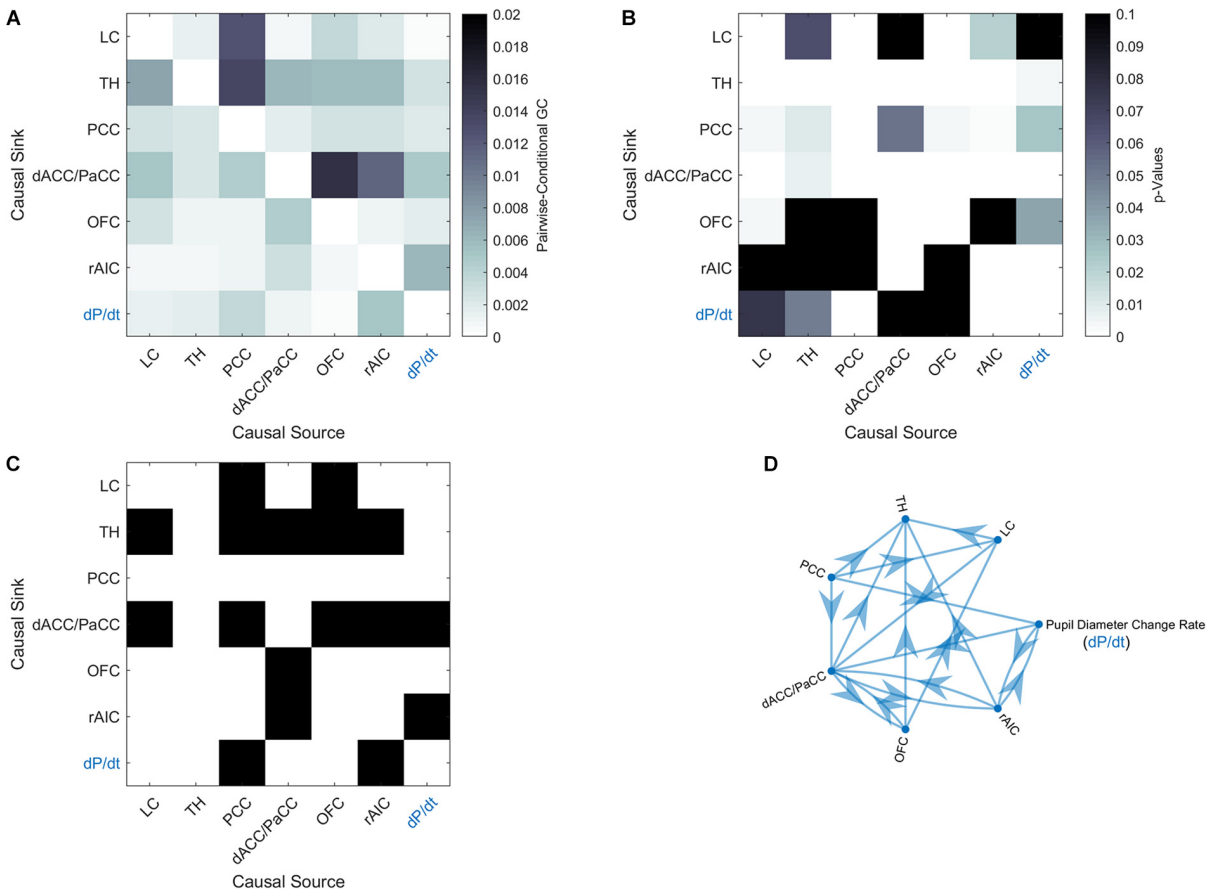

FIGURE 3 | Granger-causality analysis for the pupil-related network. **(A)** Estimated pairwise conditional GC between BOLD time courses within each ROI. **(B)** Corresponding *p*-values. **(C)** Statistically significant ($p < 0.05$, Granger's *F*-test, Bonferroni corrected) causal influences against the null hypothesis of no causality. **(D)** Directed graph of causal influences obtained using the result shown on panel C as adjacency matrix.

TABLE 3 | Node centrality of ROIs within the pupil-related brain network.

Name	Degree		Closeness		Betweenness	Pagerank	Hubs	Authorities
	in	out	in	out				
LC	2	2	0.069	0.077	0	0.0946	0.1597	0.1462
TH	5	0	0.143	0	0	0.2445	0	0.3028
PCC	0	4	0	0.125	0	0.0511	0.2373	0
dACC/PaCC	5	3	0.139	0.099	11.0	0.2261	0.1083	0.2992
OFC	1	3	0.078	0.087	3.0	0.1152	0.1985	0.0364
rAIC	2	3	0.087	0.087	3.5	0.1609	0.1985	0.0691

The different measures can be briefly described as follows. Degree: (in) number of incoming edges to each node, (out) number of outgoing edges from each node. Closeness: (in) normalized number of nodes reachable from it, (out) normalized number of nodes reaching it. Betweenness: regions most often found on the shortest path between two nodes. Pagerank: average time spent on each node during a random walk. Hubs: sum of the authorities scores of all its successors. Authorities: sum of the hubs scores of all its predecessors.

communication with both LC and pupil. In turn, the edges connecting LC to pupil diameter change rate always involve dACC/PaCC and rAIC, the latter mediating the sole mutual connection with pupil. These findings are consistent with the hypothesis that LC is "informed" by the cortex (here directly by OFC and PCC and indirectly by ACC), which largely support the Aston-Jones and Cohen (2005) model. It is noted that the edges between the nodes of the network do not necessarily entail the presence of a direct connection or the absence of an indirect connection, as in our GC analysis not all brain regions are incorporated and even those that are incorporated as ROIs might be subregions of the actual labeled area. As an illustration, the TH cluster resulting from our analysis only comprises parts of specific thalamic nuclei (i.e., medial dorsal nucleus, ventral

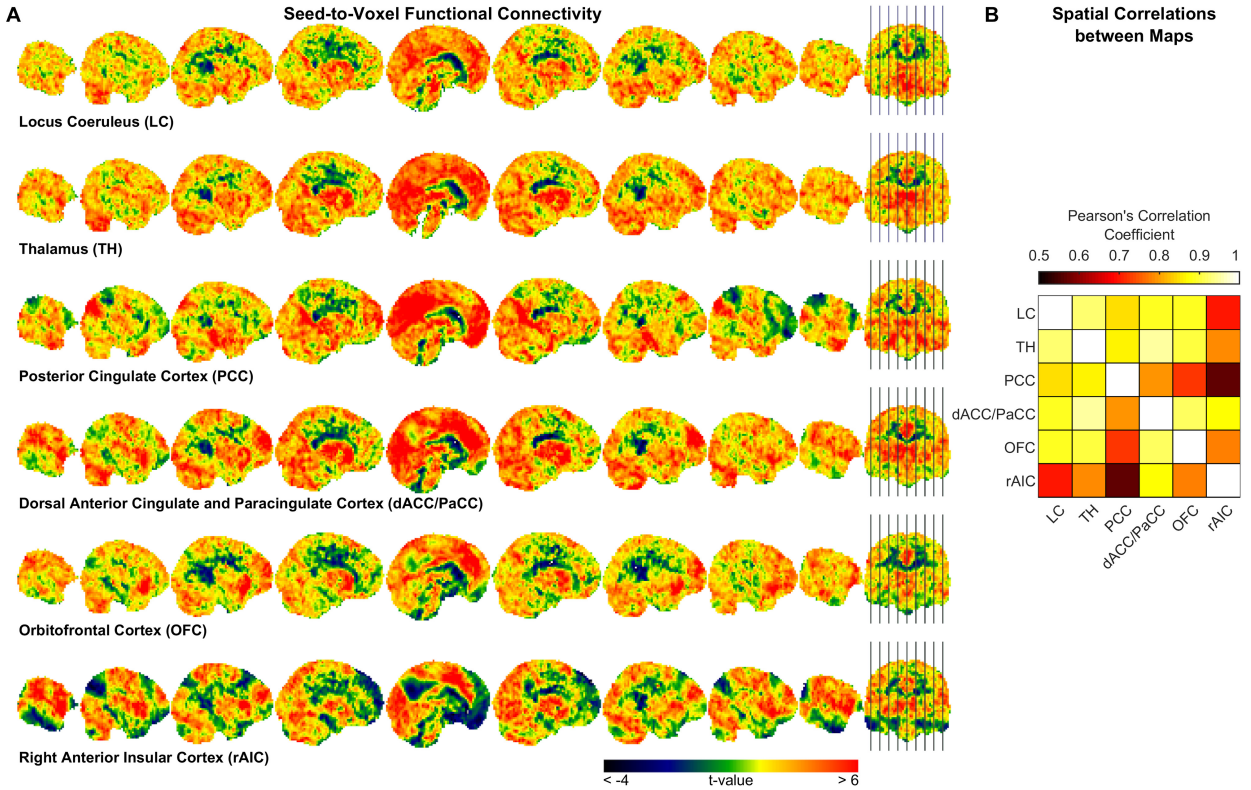

FIGURE 4 | Seed-to-voxel functional connectivity analysis. **(A)** Unthresholded t-maps showing the second-level effect of seed-to-voxel connectivity (see **Table 4** for the corrected statistics). The seed-ROI is indicated below each map. **(B)** Correlation matrix between each pair of ROI-seed FC maps.

anterior nucleus, central lateral nucleus, and lateral posterior nucleus) and the absence of outward edges from TH cannot be interpreted as lack of thalamocortical connections.

In order to somewhat reduce such limitation, we performed seed-to-voxel FC. Interestingly, all cortical regions that were correlated with the pupil diameter change rate had the SFG (orbital, medial, dorsolateral or posterior subregion) within the corresponding FC network (**Table 4**), consistently with the proposed parcellation and connectivity patterns of this area (Li et al., 2013). It is noted that the hub of the network related to the pupil diameter change rate, namely PCC, coincides with the main hub of the DMN. The DMN is the seat of internally generated and self-directed brain activity (Stawarczyk et al., 2011). SFG is part of the DMN (Buckner et al., 2008) and it has been linked to self-awareness (Goldberg et al., 2006).

Consistent with our expectation that pupil dynamics reflects spontaneous, task-independent fluctuations in cortical activity, we did not find any significant correlation between pupil diameter (or its time derivatives), pupil-related brain regions and task performance. This is particularly interesting considering that the task required a constant and relatively high degree of attention, which is known to implicate the ARAS and related cortical areas. While it is possible that the correlation between pupil and performance depend on specific kind of attentive processes (e.g., top-down attention versus decision-making, see van Kempen et al., 2019), our results are consistent with electroencephalography-pupillometry data showing no correlation between pupil and reaction time (Hong et al., 2014). Generally, understanding of the conditions where a correlation between pupil and performance exists is not straightforward (van den Brink et al., 2016; Trani and Verhaeghen, 2018). Notably, LC activity and pupil does not necessarily correlate with behavioral performance (Varazzani et al., 2015). We only report a very small correlation between instantaneous response delay time and pupil diameter time course, which might be explained by the known relation between pupil dilation and increase in attentional load (Lisi et al., 2015).

Virtually all regions of the pupil-related network are known to be implicated in arousal, selective attention, salience, error-detection, decision-making and perception (Schneider et al., 2016), i.e., more generally, in consciousness. Pupil dynamics has been proposed to reflect both conscious (Kang and Wheatley, 2015) and preconscious (Laeng et al., 2012) brain activity. In particular, pupillometry might be an index of spontaneous fluctuations in the arousal state that are characterized by a switch between internally directed (e.g., mind wandering) and environmentally directed (e.g., on-task) attentional resources (Unsworth and Robison, 2018). Pupil size has also been linked to the subjective passage of time (Suzuki et al., 2016). Notably, time-perception tasks implicate the AIC (see Gili et al., 2018). Timing has been related to the metastability of cortical networks, something that is hypothesized to be dynamically "adjusted" by

TABLE 4 | Brain regions functionally connected to the ROIs of the pupil-related network.

Region	Cluster		Voxel			
	p_{FWE}	k	t_{PEAK}	x	y	z
Locus coeruleus (LC)						
Locus coeruleus	<0.001	76	27.33	6	−27	−15
Thalamus	<0.001	6	9.90	−6	−18	−6
Superior frontal gyrus (medial)	<0.001	6	9.85	−3	42	36
Thalamus (TH)						
Thalamus	<0.001	141	16.64	6	−18	0
Median cingulate and paracingulate cortex	<0.001	7	10.97	0	−21	27
Superior frontal gyrus (medial)	<0.001	6	10.64	−6	33	33
Superior frontal gyrus (medial)	<0.001	6	9.86	6	42	39
Calcarine fissure and surrounding cortex	<0.001	5	9.54	0	−63	12
Posterior cingulate cortex (PCC)						
Posterior cingulate cortex	<0.001	758	22.81	−9	−63	21
Angular gyrus (L)	<0.001	73	19.21	−42	−75	33
Angular gyrus (R)	<0.001	15	11.53	57	−66	21
Ventromedial prefrontal cortex	<0.001	80	14.78	−6	39	−27
Superior frontal gyrus (medial)	<0.001	23	13.65	−3	60	36
Superior frontal gyrus (dorsolateral) (R)	<0.001	15	12.08	21	45	48
Superior frontal gyrus (orbital)	<0.001	13	12.60	−3	36	−6
Dorsal Anterior Cingulate and Paracingulate Cortex (dACC/PaCC)						
Anterior cingulate and paracingulate cortex	<0.001	217	15.05	9	30	30
Superior frontal gyrus (dorsolateral) (L)	<0.001	16	11.27	−30	54	21
Superior frontal gyrus (dorsolateral) (R)	<0.001	39	11.89	24	45	18
Superior frontal gyrus (posterior)	<0.001	21	10.61	0	9	48
Thalamus (L)	<0.001	15	11.11	−9	3	0
Thalamus (R)	<0.001	16	11.66	6	0	−3
Calcarine fissure and surrounding cortex	<0.001	15	10.31	0	−75	15
Caudate nucleus (L)	<0.001	13	11.26	−12	15	−12
Caudate nucleus (R)	<0.001	8	12.60	18	9	−15
Insula (L)	<0.001	24	11.09	−42	15	−9
Orbitofrontal cortex (OFC)						
Orbitofrontal cortex (L)	<0.001	93	15.74	−33	21	−15
Orbitofrontal cortex (R)	<0.001	79	13.90	30	24	−15
Anterior cingulate and paracingulate cortex	<0.001	64	13.80	−6	30	30
Superior frontal gyrus (dorsolateral) (R)	<0.001	12	9.87	30	57	18
Right anterior insular cortex (rAIC)						
Insula (L)	<0.001	42	11.89	−33	15	6
Insula (R)	<0.001	69	22.29	33	18	3
Superior frontal gyrus (posterior)	<0.001	20	10.65	3	15	51
Superior temporal gyrus (L)	<0.001	8	10.28	−63	3	−9
Superior temporal gyrus (R)	<0.001	9	10.22	63	6	−6
Temporal pole (L)	<0.001	12	10.11	−54	15	−12
Temporal pole (R)	<0.001	9	9.31	57	−9	6

Voxel-level significance threshold was set at $p_{FWE} < 0.05$ (Family-Wise Error correction for multiple comparisons). Only clusters with $p_{FWE} < 0.001$ are shown. Cluster size (in voxels) is indicated by k, while t_{PEAK} stands for the t-value of the peak voxel. Coordinates (x, y, z) are expressed in mm in the MNI-space. Seed regions are indicated in italics.

the PCC (Leech and Sharp, 2014). We found that the rAIC-seed FC network and the PCC-seed FC network exhibited the lowest between-map correlation (**Figure 4B**), although both rAIC and PCC were strongly correlated with the pupil diameter change rate (**Figure 2** and **Table 2**). Notably, the within-ROI BOLD time course of rAIC and PCC were anticorrelated ($p = 0.0029$, one-sample, two-tailed t-test). These regions may subserve complementary functions, as evidenced by the finding that activation of rAIC can cause deactivation of the PCC in response to unexpected salient events (Sridharan et al., 2008). It has been proposed that the anterior insula signals the need to direct attention externally, thereby leading the PCC to reduce

TABLE 5 | Summary of findings obtained in previous pupillometry-fMRI experiments.

Study Ref.	Sample	Protocol (*)	Regressor used	Anatomical locations (**)
Murphy et al., 2014	*n* = 14 Healthy subjects Age: 29 ±8 years (Mean ± SD) Age range: 21–48 years 6 Females	Rest-fixation or continuous attentive task	Pupil diameter + HRF derivatives	*Positive correlations*: Occipital gyrus (inferior, middle, superior) Fusiform gyrus Lingual gyrus Cuneus Supplementary Motor area[1] Anterior cingulate cortex Inferior frontal gyrus[2] Insular cortex Thalamus Midbrain Pons (LC) Medulla
Yellin et al., 2015	*n* = 20 Healthy subjects Age: 29 ± n.d. years (Mean ± SD) Age range: 26–48 years 13 Females	Rest-fixation or block-design visual imagery	Pupil diameter	*Positive correlations*: Inferior parietal lobule[3] Posterior cingulate cortex Precuneus medial prefrontal cortex *Negative correlations*: Early visual cortices[4] Central sulcus[5] Lateral sulcus[6]
Schneider et al., 2016	*n* = 32 Healthy subjects Age: 26 ± 4 years (Mean ± SD) Age range: 18–35 years 17 Females Subjects were asked to refrain from caffeine and underwent a 2 h mild sleep deprivation protocol on the day of the experiment	Rest-fixation (dark versus light condition)	Pupil diameter	*Positive correlations*: Cerebellum Thalamus Caudate Nucleus Putamen *Negative correlations*: Occipital gyrus (inferior, middle, superior) Fusiform gyrus Lingual gyrus Cuneus Precentral gyrus[7] Postcentral gyrus[8] Supplementary motor area[1] Superior temporal gyrus Temporal pole precuneus Insular cortex Parahippocampal gyrus Amygdala
			1st-order time derivative of pupil diameter	*Positive correlations*: Inferior frontal gyrus[2] Middle frontal gyrus Superior frontal gyrus Anterior cingulate cortex Middle Cingulate Cortex Inferior parietal lobule[3] Middle temporal gyrus Precuneus Insular cortex Thalamus Caudate Nucleus Putamen Brainstem Cerebellum *Negative correlations*: Occipital gyrus (inferior, middle, superior) Fusiform gyrus Lingual gyrus Cuneus Precentral gyrus[7] Postcentral gyrus[8] Paracentral gyrus Supplementary motor area[1] Precuneus Parahippocampal gyrus Amygdala
			2nd-order time derivative of pupil diameter	*Positive correlations*: Middle temporal gyrus Middle cingulate gyrus Supramarginal gyrus Precuneus Thalamus *Negative correlations*: Occipital gyrus (inferior, middle, superior) Fusiform gyrus Lingual gyrus Cuneus Precentral gyrus[7] Postcentral gyrus[8]

(*) All the listed experimental protocols within individual studies yielded almost identical results. (**) The original nomenclature used in the relevant study is retained (see numbered footnotes for details). [1]Posterior subregion of the superior frontal gyrus; [2]Includes orbitofrontal cortex; [3]Includes supramarginal gyrus and angular gyrus; [4]Includes occipital gyrus (inferior, middle, superior), fusiform gyrus and lingual gyrus; [5]Includes primary motor cortex and primary somatosensory cortex; [6]Includes inferior frontal gyrus, insular cortex and temporal pole; [7]Primary motor cortex; and [8]Primary somatosensory cortex.

whole-brain metastability in order to facilitate the activation of cortical areas/networks that are appropriate for the current behavioral state (Leech and Sharp, 2014). Based on our results, we speculate that the eye's pupil reflects continuous switches between self- (PCC) and environment- (OFC and rAIC) directed awareness (Sridharan et al., 2008; Scheibner et al., 2017).

It should be realized that cortical regions participate in the maintenance of conscious state through consciousness-entangled contributions that are region-specific. For example, OFC is implicated in metacognitive processes related to self-awareness (Lak et al., 2014; Xie et al., 2018), in synergy with the LC noradrenergic system (Sadacca et al., 2017). The right anterior insula is involved in interoceptive body representation (i.e., integration of autonomic, visceral and sensory information) and together with anterior cingulate and prefrontal cortex constitutes a task-independent network known to be linked to goal-directed behavior (Eckert et al., 2009 and references therein). Even the rAIC is related to the awareness of visceral and sensory information (Kotani et al., 2009). The PCC is part of a functional noradrenergic arousal circuitry (together with LC and TH, among others) and has been proposed as a cortical hub for consciousness (see section "Discussion" in Song et al., 2017).

CONCLUSION

In conclusion, we used steady-state fMRI to study the relation between pupil dynamics and brain networks. Our results advance a potential important link between changes in pupil and cortical state (Schwalm and Rosales Jubal, 2017). It would be interesting to study how the pupil-related network evolves during altered states of consciousness. For example, resting-state fMRI during pharmacological modulation of arousal established the brainstem (putatively LC) and TH as two main subcortical structures involved in consciousness (Gili et al., 2013; Song et al., 2017). In our analysis, LC and TH had the SFG as a functionally connected cortical region, in common with all pupil-related cortical areas. This result advances the possibility that FC with SFG might be used as an index of the pupillometry-fMRI relation. Finally, disruption of pupillary responses has been linked to neurodegeneration such as Parkinson's disease (Wang et al., 2016) and Alzheimer's disease (Granholm et al., 2017). For example, the identification of pupil-related network and the study of its integrity might be useful as an early marker of cognitive decline, e.g., in MCI patients (Elman et al., 2017). Although the interpretation of the data is made difficult by the complexity of the interplay between pupil size regulation and brain state, our results provide useful information that might help designing new experiments aiming at further investigating the pupil-BOLD relation in the human brain.

DATA AVAILABILITY

The datasets generated for this study are available on request to the corresponding author.

ETHICS STATEMENT

The protocol of the study was approved by the Ethics Committee of Santa Lucia Foundation. All subjects gave written informed consent in accordance with the Declaration of Helsinki and with the European Union regulations.

AUTHOR CONTRIBUTIONS

MD conceived the idea. FG designed and supervised the experiments. GB, DM, MM, and FG performed the experiments. MD and DM analyzed the data and prepared the figures. MD wrote the manuscript. All authors contributed to the interpretation of the results, critically reviewed the manuscript, and approved the content of the manuscript.

FUNDING

This work was partially funded by the Italian Ministry of Health Young Researcher Grant 2013 (GR-2013-02358177).

ACKNOWLEDGMENTS

The authors thank Maxim Zaitsev at the University Medical Center Freiburg for the implementation of Multi Echo EPI on Siemens platform.

REFERENCES

Alnaes, D., Sneve, M. H., Espeseth, T., Endestad, T., Van De Pavert, S. H., and Laeng, B. (2014). Pupil size signals mental effort deployed during multiple object tracking and predicts brain activity in the dorsal attention network and the locus coeruleus. *J. Vis.* 14:1. doi: 10.1167/14.4.1

Aminihajibashi, S., Hagen, T., Foldal, M. D., Laeng, B., and Espeseth, T. (2019). Individual differences in resting-state pupil size: evidence for association between working memory capacity and pupil size variability. *Int. J. Psychophysiol.* 140, 1–7. doi: 10.1016/j.ijpsycho.2019.03.007

Aston-Jones, G., and Cohen, J. D. (2005). Adaptive gain and the role of the locus coeruleus-norepinephrine system in optimal performance. *J. Comp. Neurol.* 493, 99–110. doi: 10.1002/cne.20723

Barnett, L., and Seth, A. K. (2014). The MVGC multivariate Granger causality toolbox: a new approach to Granger-causal inference. *J. Neurosci. Methods* 223, 50–68. doi: 10.1016/j.jneumeth.2013.10.018

Behrends, M., Larson, M. D., Neice, A. E., and Bokoch, M. P. (2019). Suppression of pupillary unrest by general anesthesia and propofol sedation. *J. Clin. Monit. Comput.* 33, 317–323. doi: 10.1007/s10877-018-0147-y

Biswal, B., Yetkin, F. Z., Haughton, V. M., and Hyde, J. S. (1995). Functional connectivity in the motor cortex of resting human brain using echo-planar MRI. *Magn. Reson. Med.* 34, 537–541. doi: 10.1002/mrm.1910340409

Bradley, M. M., Miccoli, L., Escrig, M. A., and Lang, P. J. (2008). The pupil as a measure of emotional arousal and autonomic activation. *Psychophysiology* 45, 602–607. doi: 10.1111/j.1469-8986.2008.00654.x

Buckner, R. L., Andrews-Hanna, J. R., and Schacter, D. L. (2008). The brain's default network: anatomy, function, and relevance to disease. *Ann. N. Y. Acad. Sci.* 1124, 1–38. doi: 10.1196/annals.1440.011

Cox, R. W. (1996). AFNI: software for analysis and visualization of functional magnetic resonance neuroimages. *Comput. Biomed. Res.* 29, 162–173. doi: 10.1006/cbmr.1996.0014

Eckert, M. A., Menon, V., Walczak, A., Ahlstrom, J., Denslow, S., Horwitz, A., et al. (2009). At the heart of the ventral attention system: the right anterior insula. *Hum. Brain Mapp.* 30, 2530–2541. doi: 10.1002/hbm.20688

Elman, J. A., Panizzon, M. S., Hagler, D. J., Eyler, L. T., Granholm, E. L., Fennema-Notestine, C., et al. (2017). Task-evoked pupil dilation and BOLD variance as indicators of locus coeruleus dysfunction. *Cortex* 97, 60–69. doi: 10.1016/j.cortex.2017.09.025

Gili, T., Ciullo, V., and Spalletta, G. (2018). Metastable states of multiscale brain networks are keys to crack the timing problem. *Front. Comput. Neurosci.* 12:75. doi: 10.3389/fncom.2018.00075

Gili, T., Saxena, N., Diukova, A., Murphy, K., Hall, J. E., and Wise, R. G. (2013). The thalamus and brainstem act as key hubs in alterations of human brain network connectivity induced by mild propofol sedation. *J. Neurosci.* 33, 4024–4031. doi: 10.1523/JNEUROSCI.3480-12.2013

Gilzenrat, M. S., Nieuwenhuis, S., Jepma, M., and Cohen, J. D. (2010). Pupil diameter tracks changes in control state predicted by the adaptive gain theory of locus coeruleus function. *Cogn. Affect. Behav. Neurosci.* 10, 252–269. doi: 10.3758/CABN.10.2.252

Goldberg, I. I., Harel, M., and Malach, R. (2006). When the brain loses its self: prefrontal inactivation during sensorimotor processing. *Neuron* 50, 329–339. doi: 10.1016/j.neuron.2006.03.015

Granholm, E. L., Panizzon, M. S., Elman, J. A., Jak, A. J., Hauger, R. L., Bondi, M. W., et al. (2017). Pupillary responses as a biomarker of early risk for alzheimer's disease. *J. Alzheimers Dis.* 56, 1419–1428. doi: 10.3233/JAD-161078

Gu, Q. (2003). Contribution of acetylcholine to visual cortex plasticity. *Neurobiol. Learn. Mem.* 80, 291–301. doi: 10.1016/s1074-7427(03)00073-x

Hong, L., Walz, J. M., and Sajda, P. (2014). Your eyes give you away: prestimulus changes in pupil diameter correlate with poststimulus task-related EEG dynamics. *PLoS One* 9:e91321. doi: 10.1371/journal.pone.0091321

Jepma, M., and Nieuwenhuis, S. (2011). Pupil diameter predicts changes in the exploration-exploitation trade-off: evidence for the adaptive gain theory. *J. Cogn. Neurosci.* 23, 1587–1596. doi: 10.1162/jocn.2010.21548

Joshi, S., Li, Y., Kalwani, R. M., and Gold, J. I. (2016). Relationships between pupil diameter and neuronal activity in the locus coeruleus, colliculi, and cingulate cortex. *Neuron* 89, 221–234. doi: 10.1016/j.neuron.2015.11.028

Kang, O., and Wheatley, T. (2015). Pupil dilation patterns reflect the contents of consciousness. *Conscious. Cogn.* 35, 128–135. doi: 10.1016/j.concog.2015.05.001

Kotani, Y., Ohgami, Y., Kuramoto, Y., Tsukamoto, T., Inoue, Y., and Aihara, Y. (2009). The role of the right anterior insular cortex in the right hemisphere preponderance of stimulus-preceding negativity (SPN): an fMRI study. *Neurosci. Lett.* 450, 75–79. doi: 10.1016/j.neulet.2008.11.032

Kundu, P., Brenowitz, N. D., Voon, V., Worbe, Y., Vertes, P. E., Inati, S. J., et al. (2013). Integrated strategy for improving functional connectivity mapping using multiecho fMRI. *Proc. Natl. Acad. Sci. U.S.A.* 110, 16187–16192. doi: 10.1073/pnas.1301725110

Kundu, P., Inati, S. J., Evans, J. W., Luh, W. M., and Bandettini, P. A. (2012). Differentiating BOLD and non-BOLD signals in fMRI time series using multi-echo EPI. *Neuroimage* 60, 1759–1770. doi: 10.1016/j.neuroimage.2011.12.028

Laeng, B., Sirois, S., and Gredeback, G. (2012). Pupillometry: a window to the preconscious? *Perspect. Psychol. Sci.* 7, 18–27. doi: 10.1177/1745691611427305

Lak, A., Costa, G. M., Romberg, E., Koulakov, A. A., Mainen, Z. F., and Kepecs, A. (2014). Orbitofrontal cortex is required for optimal waiting based on decision confidence. *Neuron* 84, 190–201. doi: 10.1016/j.neuron.2014.08.039

Larsen, R. S., and Waters, J. (2018). Neuromodulatory correlates of pupil dilation. *Front. Neural. Circuits* 12:21. doi: 10.3389/fncir.2018.00021

Leech, R., and Sharp, D. J. (2014). The role of the posterior cingulate cortex in cognition and disease. *Brain* 137, 12–32. doi: 10.1093/brain/awt162

Leuchs, L., Schneider, M., Czisch, M., and Spoormaker, V. I. (2017). Neural correlates of pupil dilation during human fear learning. *Neuroimage* 147, 186–197. doi: 10.1016/j.neuroimage.2016.11.072

Li, W., Qin, W., Liu, H., Fan, L., Wang, J., Jiang, T., et al. (2013). Subregions of the human superior frontal gyrus and their connections. *Neuroimage* 78, 46–58. doi: 10.1016/j.neuroimage.2013.04.011

Lisi, M., Bonato, M., and Zorzi, M. (2015). Pupil dilation reveals top-down attentional load during spatial monitoring. *Biol. Psychol.* 112, 39–45. doi: 10.1016/j.biopsycho.2015.10.002

Logothetis, N. K., and Pfeuffer, J. (2004). On the nature of the BOLD fMRI contrast mechanism. *Magn. Reson. Imaging* 22, 1517–1531. doi: 10.1016/j.mri.2004.10.018

Ma, Y., Shaik, M. A., Kozberg, M. G., Kim, S. H., Portes, J. P., Timerman, D., et al. (2016). Resting-state hemodynamics are spatiotemporally coupled to synchronized and symmetric neural activity in excitatory neurons. *Proc. Natl. Acad. Sci. U.S.A.* 113, E8463–E8471. doi: 10.1073/pnas.1525369113

Mathot, S., and Van der Stigchel, S. (2015). New light on the mind's eye: the pupillary light response as active vision. *Curr. Dir. Psychol. Sci.* 24, 374–378. doi: 10.1177/0963721415593725

McDougal, D. H., and Gamlin, P. D. (2015). Autonomic control of the eye. *Compr. Physiol.* 5, 439–473. doi: 10.1002/cphy.c140014

Menon, V., and Uddin, L. Q. (2010). Saliency, switching, attention and control: a network model of insula function. *Brain Struct. Funct.* 214, 655–667. doi: 10.1007/s00429-010-0262-0

Mesulam, M. M. (2004). The cholinergic innervation of the human cerebral cortex. *Prog. Brain Res.* 145, 67–78. doi: 10.1016/s0079-6123(03)45004-8

Murphy, P. R., O'connell, R. G., O'sullivan, M., Robertson, I. H., and Balsters, J. H. (2014). Pupil diameter covaries with BOLD activity in human locus coeruleus. *Hum. Brain Mapp.* 35, 4140–4154. doi: 10.1002/hbm.22466

Naber, M., Alvarez, G. A., and Nakayama, K. (2013). Tracking the allocation of attention using human pupillary oscillations. *Front. Psychol.* 4:919. doi: 10.3389/fpsyg.2013.00919

Nassar, M. R., Rumsey, K. M., Wilson, R. C., Parikh, K., Heasly, B., and Gold, J. I. (2012). Rational regulation of learning dynamics by pupil-linked arousal systems. *Nat. Neurosci.* 15, 1040–1046. doi: 10.1038/nn.3130

Peysakhovich, V., Vachon, F., and Dehais, F. (2017). The impact of luminance on tonic and phasic pupillary responses to sustained cognitive load. *Int. J. Psychophysiol.* 112, 40–45. doi: 10.1016/j.ijpsycho.2016.12.003

Posse, S., Wiese, S., Gembris, D., Mathiak, K., Kessler, C., Grosse-Ruyken, M. L., et al. (1999). Enhancement of BOLD-contrast sensitivity by single-shot multi-echo functional MR imaging. *Magn. Reson. Med.* 42, 87–97. doi: 10.1002/(sici)1522-2594(199907)42:1<87::aid-mrm13>3.0.co;2-o

Rajkowski, J., Kubiak, P., and Aston-Jones, G. (1993). Correlations between locus coeruleus (LC) neural activity, pupil diameter and behavior in monkey support a role of LC in attention. *Soc. Neurosci.* 19:974.

Reimer, J., Froudarakis, E., Cadwell, C. R., Yatsenko, D., Denfield, G. H., and Tolias, A. S. (2014). Pupil fluctuations track fast switching of cortical states during quiet wakefulness. *Neuron* 84, 355–362. doi: 10.1016/j.neuron.2014.09.033

Reimer, J., Mcginley, M. J., Liu, Y., Rodenkirch, C., Wang, Q., Mccormick, D. A., et al. (2016). Pupil fluctuations track rapid changes in adrenergic and cholinergic activity in cortex. *Nat. Commun.* 7:13289. doi: 10.1038/ncomms13289

Sadacca, B. F., Wikenheiser, A. M., and Schoenbaum, G. (2017). Toward a theoretical role for tonic norepinephrine in the orbitofrontal cortex in facilitating flexible learning. *Neuroscience* 345, 124–129. doi: 10.1016/j.neuroscience.2016.04.017

Scheibner, H. J., Bogler, C., Gleich, T., Haynes, J. D., and Bermpohl, F. (2017). Internal and external attention and the default mode network. *Neuroimage* 148, 381–389. doi: 10.1016/j.neuroimage.2017.01.044

Schneider, M., Hathway, P., Leuchs, L., Samann, P. G., Czisch, M., and Spoormaker, V. I. (2016). Spontaneous pupil dilations during the resting state are associated with activation of the salience network. *Neuroimage* 139, 189–201. doi: 10.1016/j.neuroimage.2016.06.011

Schneider, M., Leuchs, L., Czisch, M., Samann, P. G., and Spoormaker, V. I. (2018). Disentangling reward anticipation with simultaneous pupillometry/fMRI. *Neuroimage* 178, 11–22. doi: 10.1016/j.neuroimage.2018.04.078

Schwalm, M., and Rosales Jubal, E. (2017). Back to pupillometry: how cortical network state fluctuations tracked by pupil dynamics could explain neural signal variability in human cognitive neuroscience. *eNeuro* 4:ENEURO.293-16.2017. doi: 10.1523/ENEURO.0293-16.2017

Song, A. H., Kucyi, A., Napadow, V., Brown, E. N., Loggia, M. L., and Akeju, O. (2017). Pharmacological modulation of noradrenergic arousal circuitry disrupts functional connectivity of the locus ceruleus in humans. *J. Neurosci.* 37, 6938–6945. doi: 10.1523/JNEUROSCI.0446-17.2017

Speck, O., and Hennig, J. (1998). Functional imaging by I0- and T2*-parameter mapping using multi-image EPI. *Magn. Reson. Med.* 40, 243–248. doi: 10.1002/mrm.1910400210

Sridharan, D., Levitin, D. J., and Menon, V. (2008). A critical role for the right fronto-insular cortex in switching between central-executive and default-mode networks. *Proc. Natl. Acad. Sci. U.S.A.* 105, 12569–12574. doi: 10.1073/pnas.0800005105

Stawarczyk, D., Majerus, S., Maquet, P., and D'argembeau, A. (2011). Neural correlates of ongoing conscious experience: both task-unrelatedness and stimulus-independence are related to default network activity. *PLoS One* 6:e16997. doi: 10.1371/journal.pone.0016997

Suzuki, T. W., Kunimatsu, J., and Tanaka, M. (2016). Correlation between pupil size and subjective passage of time in non-human primates. *J. Neurosci.* 36, 11331–11337. doi: 10.1523/jneurosci.2533-16.2016

Trani, A., and Verhaeghen, P. (2018). Foggy windows: pupillary responses during task preparation. *Q. J. Exp. Psychol.* 71, 2235–2248. doi: 10.1177/1747021817740856

Unsworth, N., and Robison, M. K. (2018). Tracking arousal state and mind wandering with pupillometry. *Cogn. Affect. Behav. Neurosci.* 18, 638–664. doi: 10.3758/s13415-018-0594-4

Urai, A. E., Braun, A., and Donner, T. H. (2017). Pupil-linked arousal is driven by decision uncertainty and alters serial choice bias. *Nat. Commun.* 8:14637. doi: 10.1038/ncomms14637

van den Brink, R. L., Murphy, P. R., and Nieuwenhuis, S. (2016). Pupil diameter tracks lapses of attention. *PLoS One* 11:e0165274. doi: 10.1371/journal.pone.0165274

van Kempen, J., Loughnane, G. M., Newman, D. P., Kelly, S. P., Thiele, A., O'connell, R. G., et al. (2019). Behavioural and neural signatures of perceptual decision-making are modulated by pupil-linked arousal. *eLife* 8:e42541. doi: 10.7554/eLife.42541

Varazzani, C., San-Galli, A., Gilardeau, S., and Bouret, S. (2015). Noradrenaline and dopamine neurons in the reward/effort trade-off: a direct electrophysiological comparison in behaving monkeys. *J. Neurosci.* 35, 7866–7877. doi: 10.1523/JNEUROSCI.0454-15.2015

Wang, C. A., Baird, T., Huang, J., Coutinho, J. D., Brien, D. C., and Munoz, D. P. (2018). Arousal effects on pupil size, heart rate, and skin conductance in an emotional face task. *Front. Neurol.* 9:1029. doi: 10.3389/fneur.2018.01029

Wang, C. A., Mcinnis, H., Brien, D. C., Pari, G., and Munoz, D. P. (2016). Disruption of pupil size modulation correlates with voluntary motor preparation deficits in Parkinson's disease. *Neuropsychologia* 80, 176–184. doi: 10.1016/j.neuropsychologia.2015.11.019

Wierda, S. M., Van Rijn, H., Taatgen, N. A., and Martens, S. (2012). Pupil dilation deconvolution reveals the dynamics of attention at high temporal resolution. *Proc. Natl. Acad. Sci. U.S.A.* 109, 8456–8460. doi: 10.1073/pnas.1201858109

Xie, Y., Nie, C., and Yang, T. (2018). Covert shift of attention modulates the value encoding in the orbitofrontal cortex. *eLife* 7:e31507. doi: 10.7554/eLife.31507

Yellin, D., Berkovich-Ohana, A., and Malach, R. (2015). Coupling between pupil fluctuations and resting-state fMRI uncovers a slow build-up of antagonistic responses in the human cortex. *Neuroimage* 106, 414–427. doi: 10.1016/j.neuroimage.2014.11.034

Yeo, S. S., Chang, P. H., and Jang, S. H. (2013). The ascending reticular activating system from pontine reticular formation to the thalamus in the human brain. *Front. Hum. Neurosci.* 7:416. doi: 10.3389/fnhum.2013.00416

Conflict of Interest Statement: The authors declare that the research was conducted in the absence of any commercial or financial relationships that could be construed as a potential conflict of interest.

frontiers in Physics

ORIGINAL RESEARCH
published: 09 October 2019
doi: 10.3389/fphy.2019.00141

Myelin Water Imaging and Transcranial Magnetic Stimulation Suggest Structure-Function Relationships in Multiple Sclerosis

*Eric Y. Zhao[1], Irene M. Vavasour[2], Marjan Zakeri[3], Michael R. Borich[3], Cornelia Laule[2,4,5,6], Alexander Rauscher[2,6,7], Anthony Traboulsee[8], David K. B. Li[2,8], Lara A. Boyd[3] and Alex L. MacKay[2,6]**

[1] Department of Medicine, University of British Columbia, Vancouver, BC, Canada, [2] Department of Radiology, University of British Columbia, Vancouver, BC, Canada, [3] Brain Behaviour Lab, Department of Physical Therapy, University of British Columbia, Vancouver, BC, Canada, [4] Department of Pathology and Laboratory Medicine, University of British Columbia, Vancouver, BC, Canada, [5] International Collaboration on Repair Discoveries, University of British Columbia, Vancouver, BC, Canada, [6] Department of Physics and Astronomy, University of British Columbia, Vancouver, BC, Canada, [7] Department of Pediatrics, University of British Columbia, Vancouver, BC, Canada, [8] Division of Neurology, Department of Medicine, University of British Columbia, Vancouver, BC, Canada

OPEN ACCESS

Edited by:
Marta Bianciardi, Massachusetts General Hospital and Harvard Medical School, United States

Reviewed by:
Michelle Ploughman, Memorial University of Newfoundland, Canada
Jeffrey A. Stanley, Wayne State University, United States

***Correspondence:**
Alex L. MacKay
mackay@physics.ubc.ca

Specialty section:
This article was submitted to Medical Physics and Imaging, a section of the journal Frontiers in Physics

Received: *29 April 2019*
Accepted: *13 September 2019*
Published: *09 October 2019*

Citation:
Zhao EY, Vavasour IM, Zakeri M, Borich MR, Laule C, Rauscher A, Traboulsee A, Li DKB, Boyd LA and MacKay AL (2019) Myelin Water Imaging and Transcranial Magnetic Stimulation Suggest Structure-Function Relationships in Multiple Sclerosis. Front. Phys. 7:141. doi: 10.3389/fphy.2019.00141

Demyelination can be assessed structurally by magnetic resonance imaging (MRI) and functionally with transcranial magnetic stimulation (TMS). Here, we combined these techniques to investigate demyelination of the corpus callosum in multiple sclerosis (MS). Our objective was to determine if corpus callosal demyelination impacts transcallosal inhibition (TCI). TCI is a brief suppression of voluntary activity in the primary motor cortex elicited by stimulation of the homologous region of the contralateral hemisphere, which is assumed to be transmitted via the corpus callosum. MRI and TMS were performed in 26 participants with MS and 10 controls. Myelin water fraction (MWF) was measured in five regions of the corpus callosum and compared with the onset latency, duration, and depth of TCI as measured by electromyography at the forearm. Callosal MWF was greatest posteriorly compared to other regions of the corpus callosum. Lower MWF in MS compared to controls was more pronounced in the posterior corpus callosum. MS participants had a prolonged TCI duration ($p = 0.016$), which correlated with EDSS ($p = 0.020$) and disease duration ($p = 0.045$). In MS, TCI depth correlated negatively with the MWF of the posterior callosal midbody ($p = 0.039$), a region thought to mediate TCI transmission. In summary, TCI duration was increased in MS and demyelination of the posterior corpus callosum midbody was associated with measurable functional changes. This work demonstrates the potential for combining MRI and TMS with electromyography to draw insights about structure-function relationships in MS pathophysiology.

Keywords: myelin water imaging, transcranial magnetic stimulation, multiple sclerosis, demyelinating diseases, central nervous system, neurophysiology, corpus callosum

INTRODUCTION

Multiple sclerosis (MS) is a central nervous system (CNS) disease characterized by demyelination in focal lesions and normal appearing white matter (NAWM). *In vivo* assessment of myelin loss in MS can be ascertained with magnetic resonance imaging (MRI) by using myelin water imaging. The principles of myelin water imaging are based on the fact that in CNS tissue the MR signal decay due to T_2 relaxation follows a multi-exponential time course. Non-negative least squares methods can fit the T_2 decay curve to a sum of exponential components [1], which arise from water in different environments. The myelin water fraction (MWF) is the signal fraction with short T_2 times (10–40 ms) arising from water trapped between myelin bilayers and has been validated as a marker for myelin in CNS tissue [2–7]. MWF may be employed to quantitatively monitor demyelination in MS [8, 9]. Lesions demonstrate heterogeneously decreased MWF and NAWM MWF is ∼16% lower on average in individuals with MS than in controls [8].

An alternate approach for investigating CNS damage in MS employs transcranial magnetic stimulation (TMS). TMS has been utilized to non-invasively investigate cortical excitability, functional connectivity, and underlying white matter tract integrity in humans *in vivo* [10]. TMS applied over the motor cortex (M1) generates motor evoked potentials (MEPs) in contralateral musculature via the corticospinal tract. The magnitude of transcallosally-mediated inhibition between homologous M1 representations can also be interrogated with TMS. When TMS is applied over M1 during a volitional contraction of a muscle ipsilateral to the side of stimulation, a transient inhibition of muscle activity is observed due to transcallosally-mediated inhibition [11, 12]. The degree of inhibition is represented by the magnitude of suppression of activity in the electromyogram (EMG) of the ipsilateral muscle, termed the ipsilateral silent period (iSP) [13]. Longer durations of the iSP and/or greater EMG suppression during the iSP represent larger degrees of transcallosally-mediated inhibition measured with TMS. In previous work, individuals with MS displayed delayed onset and prolonged duration, but similar depth of inhibition on average, when compared with healthy controls [14, 15]. iSP onset and duration correlate with the total area of MS lesions in the CC [16], and an absence of an iSP has been observed in individuals with lesions in the CC arising from infarcts and other abnormalities [13, 17].

Used together, MWF imaging and TMS-evoked EMG responses have the potential to provide complementary information about the structure-function relationship in brain white matter. Other MRI techniques such as diffusion tensor imaging, in conjunction with TCI, have uncovered potential relationships between functional connectivity and white matter fibre microstructure in healthy adults [18]. However, DTI does not provide a specific measure of myelin content as it is influenced by crossing fibres (although, this may be less of an issue in the CC) and the presence of MS pathology such as oedema or inflammation [19, 20]. MWF, as a myelin-specific imaging marker, has the potential to enable demonstration of the impact of diffuse demyelination on the functional connectivity of transcallosal fibres as measured by TCI. We hypothesized that localized MWF changes in the corpus callosum would be correlated with TCI, especially onset latency and duration. In this exploratory study, we sought to characterize the relationship between CC MWF and TCI to examine whether the joint use of imaging and functional studies could help inform CC function.

MATERIALS AND METHODS

Study Participants

Twenty-six individuals with relapsing remitting MS (RRMS), ages 28–59 years (mean age 42.0 years, 5 males/21 females), were included in the study, as well as 10 healthy controls recruited from the university community (mean age 43.4 years, 2 males/8 females). The MS cohort had an Kurtzke Expanded Disability Status Scale (EDSS) [21] range of 0.0–6.0 (median: 2.0) and a disease duration of 0.5–28 years (mean: 7.54 years) (**Figure 1**). All MS participants were on glatiramer acetate (GA, Copaxone®) treatment at the time of testing, and had previously been prescribed GA treatment for 0–4.5 years (mean length of time on GA = 1.15 years). All study participants provided written informed consent and all study procedures were approved by the University of British Columbia Clinical Ethics Research Board (H09-01938).

Magnetic Resonance Imaging Protocol and Analysis

MRI Acquisition

MRI scans were performed on a Philips 3.0 T Achieva scanner with an 8 channel head coil to collect the following sequences: (1) axial $3DT_1$-weighted turbo field echo (TR: 1,638 ms, TE: 3.5 ms, TI: 850 ms, voxel: 1.00 × 1.00 × 1.00 mm), (2) sagittal 3D combined gradient echo and spin echo (GRASE) [22, 23] (TR: 1,000 ms, echo spacing: 10 ms, 32 spin echoes with a gradient echo immediately before and another immediately after, voxel acquired at 0.99 × 1.01 × 5.00 mm, reconstructed to 0.96 × 0.96 × 2.5 mm, sense factor 2), and (3) sagittal 3D turbo spin echo double inversion recovery [TR: 8,000 ms, TEeff: 156 ms, TI: 3,200/500 ms, voxel acquired at 1.00 × 1.00 × 2.00 mm, reconstructed to 1.00 × 1.00 × 1.00 mm, sense factor 2.5 (phase) and 2 (slice)].

Image Registration

Registration was performed using the software tools provided by The Oxford Centre for Functional Magnetic Resonance Imaging of the Brain (FMRIB), the FMRIB Software Library (FSL) [24, 25]. $3DT_1$ images of each subject were registered to T_2 GRASE images using FMRIB's Linear Image Registration Tool (FLIRT) to allow delineation of the CC for region of interest (ROI) selection.

Calculation and Mapping of Myelin Water Fraction

The T_2 decay curve obtained by the T_2 GRASE sequence was modelled by multiple exponential components and the T_2 distribution was estimated using non-negative least squares with the extended phase graph algorithm [22] applied in order to account for the effect of stimulated echo artefact on the decay curves. MWF in each image voxel was computed as the ratio of

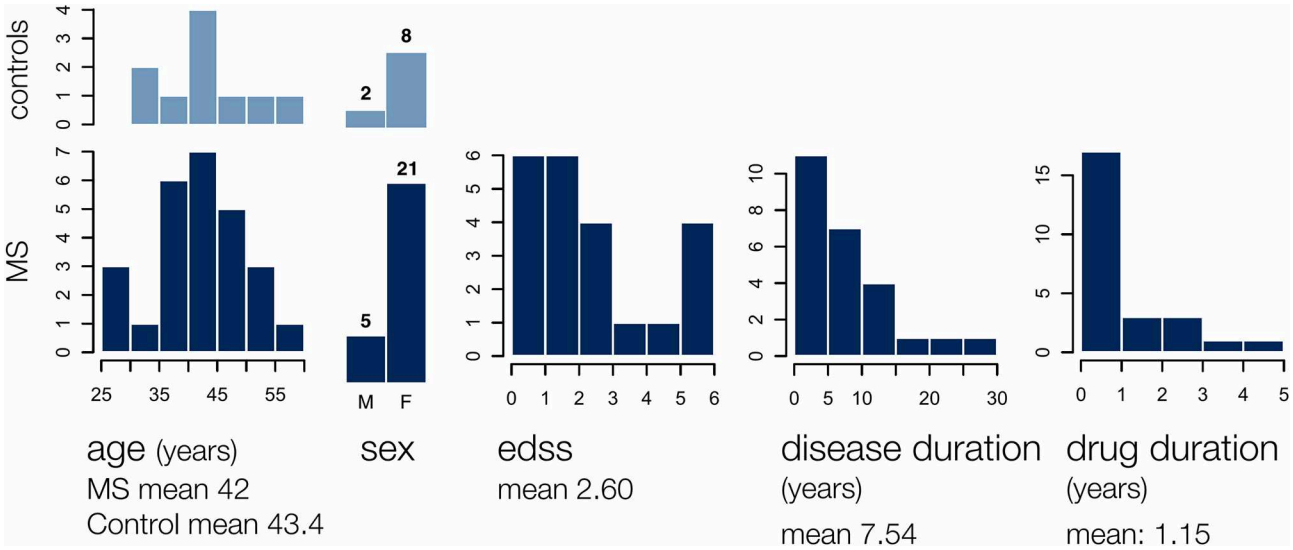

FIGURE 1 | The MS group participants included 5 males and 21 females of age 28–59 years, with an EDSS range of 0–6, a disease duration of 0.5–28 years, and a glatiramer acetate use duration of 0–5 years. Demographics for 10 age and gender matched controls are also shown.

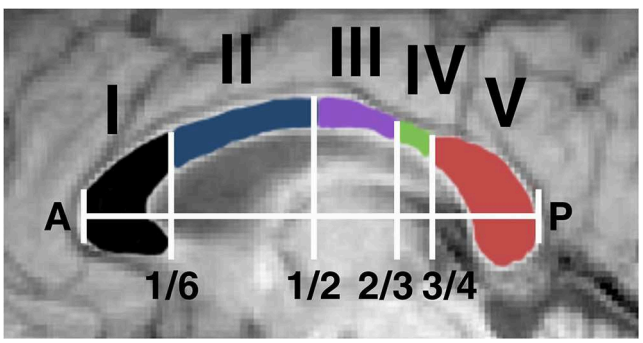

FIGURE 2 | The corpus callosum was segmented into structurally distinct regions for analysis of regional myelin water fraction. This was performed by an automated system which identified a maximum length anterior-posterior (AP) line and selected segments based on fractional AP position. The segments have been shown to contain fibres connecting (I) prefrontal, (II) premotor and supplementary motor, (III) motor, (IV) sensory, and (V) parietal, temporal, and occipital regions [26].

the area under the T_2 distribution between 10 and 40 ms to the total area under the distribution [1, 22].

Region of Interest Analysis

The CC was defined in the sagittal plane of registered images by manually selected ROIs with a minimum lateral width of 7 mm (central slice + 3 mm in each direction from the midline). MWF values were averaged over the whole CC, as well as in five anterior to posterior fractions defined slice-wise based on the scheme proposed by Hofer and Frahm [26] (**Figure 2**). This segmentation scheme provides regions roughly in agreement with more recent work [27] while unambiguously delineating segments along the maximum-length anterior-posterior (A-P). A single unblinded rater drew all ROIs. For quality assurance checks, automated segmentation was also undertaken and MWF values were compared to rule out significant discrepancies. This allowed us to ensure that MWF mean values would not change dramatically with slightly different ROIs and mitigated the risk of bias. Automated segmentation of the CC was performed by registration of the JHU ICBM atlas CC region in FSL [28–30]. T_2 GRASE images were registered onto $3DT_1$ images and masks obtained by automated segmentation were applied to MWF maps co-registered using the same registration matrix.

Obtaining an Anterior-to-Posterior CC MWF Distribution

Within the CC, MWF was averaged across all vertical voxel-thick strips in each sagittal slice and interpolated linearly to 100 values between the anterior and posterior ends. These 100 values per slice were averaged across slices, yielding an anterior-to-posterior MWF distribution for each individual. These distributions were then averaged across all participants with MS and controls separately and a 95% confidence interval was calculated for each point.

Transcranial Magnetic Stimulation Protocol and Analysis

Transcranial Magnetic Stimulation

TMS was performed using a figure-of-eight coil attached to a Magstim 200^2 stimulator targeting the motor cortex representation of the contra-lateral forearm extensor musculature. Recording electrodes for EMG were placed on the extensor carpi radialis (ECR) muscle bilaterally with the ground electrode on the olecranon process of the elbow. The optimal site for TMS activation of the ECR was determined using standard procedures [31]. The motor threshold was defined as the lowest stimulation intensity that elicited a motor response in

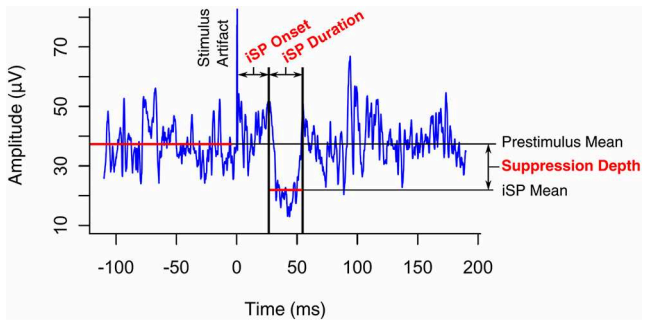

FIGURE 3 | Transcallosal inhibition (TCI) of voluntary hand contraction was elicited by transcranial magnetic stimulation of the ipsilateral motor representation of the hand. The ipsilateral silent period (iSP) was identified on the resulting electromyogram as a transient inhibition of voluntary activity and its onset, duration, and depth were quantified as shown.

ECR of ≥50 μV in 5 of 10 trials [32]. Participants were asked to perform a voluntary contraction to 20% of their maximal force using an isometric hand dynamometer. TMS stimulus intensity was adjusted to 1.5 times the threshold for evoking a motor response or to maximum output if the threshold exceeded 66% of the maximum stimulator output. Study participants performed an isometric grip contraction using the hand ipsilateral to the stimulated hemisphere. Transient inhibition in voluntary EMG activity was used to quantify the iSP. The stimulation protocol was performed bilaterally starting with a randomly selected side.

Ipsilateral Silent Period Identification

EMG data was averaged across 20 trials per participant per hemisphere to achieve a satisfactory signal-to-noise ratio. Automated detection located the minimum point in the EMG data between 15 and 90 ms after the TMS stimulus, within the physiological range of TCI times. It then located the onset (start) and offset (end) times of the iSP as the nearest points above the pre-stimulus mean on either side of the minimum (**Figure 3**). Where adjustment of the automated selection was required or the iSP was absent, traces were reviewed in detail by at least two researchers. iSP duration was calculated as the difference between offset and onset times. The inhibition depth was calculated by subtracting the mean iSP amplitude from the mean iSP pre-stimulus amplitude.

Analysis of Myelin Water and TCI Data

Treatment of Non-normally Distributed Data

Non-normality in data was identified visually by histograms and quantile-quantile (Q-Q) plots. Shapiro-Wilk tests with a Holm-Bonferroni [33] adjusted $p < 0.05$ were taken as further evidence of non-normality. All CC MWF and TCI measures (onset, duration, and depth) yielded normally distributed data with the exception of inhibition depth (**Supplemental Figure 1**). Thus, for subsequent parametric analyses, inhibition depth values were subject to a power transform. The Box-Cox method identified the value of the optimal power parameter, λ, to be zero [34]. Therefore, the transform $y_i = GM(y) \ln y_i$ was applied, where $GM(y) = (\prod_1^n y_i)^{\frac{1}{n}}$ is the geometric mean of the set of observations $\{y_1 ... y_n\}$. This resulted in normally distributed data and is referred to here as the transformed inhibition depth.

Independent MRI and TMS Analysis

Myelin water maps and TCI data were analysed independently to identify differences between stimulated hemisphere (left vs. right), study groups (MS vs. control), and CC regions (I–V).

MWF values obtained from manual CC selection were compared with values obtained by automated segmentation using a paired *t*-test. Paired *t*-tests were performed to assess differences in TCI between hemispheres. Two-tailed homoscedastic student's *t*-tests with a Holm-Bonferroni correction were performed to test for differences in MWF and TCI quantifiers between MS and controls. One-way ANOVA was employed to compare mean MWF among the CC regions and Tukey's range test was performed for pairwise comparisons with adjusted significance thresholds.

This analysis was visualized using standard boxplots displaying means, quartiles, and outliers. *p*-values were reported and values below 0.05 were taken to be statistically significant. All reported margins of error represent 95% confidence intervals.

Correlations

Scatterplots between MWF data (whole CC and regions I–V) and TCI quantifiers (onset, duration, and depth) were used to identify correlations in individuals with MS alone. Pearson product-moment correlations were performed and correlation test *p*-values were computed and adjusted for multiple comparisons using a Holm-Bonferroni correction.

RESULTS

Six MS participants and one control did not show quantifiable bilateral TCI. In addition, one MS participant had contraindications to TMS. These individuals were incorporated into the MRI-only analysis, but omitted from analyses where TMS data was required. One MS participant had MRI contraindications and was excluded from analyses requiring MRI data. Independent analyses of MRI and TMS data, as well as correlations between MRI and TMS data are reported here. Within our 26-participant cohort, no reported structural or functional measurements were observed to differ significantly between males and females (unadjusted $p > 0.1$ for all 28 measured variables assessed).

MWF Was Higher in the Posterior CC Than in the Anterior CC

We examined the association of MWF with both region and group (MS vs. control) using a generalized estimating equations (GEE) approach to account for repeated measures (within-sample error) and assuming independence between samples. MWF varied significantly by region, and was highest in the posterior CC (**Figure 4**). *Post-hoc* pairwise comparisons of neighbouring regions with a Bonferroni correction of *p*-values showed statistically significant differences between II and III (*p*

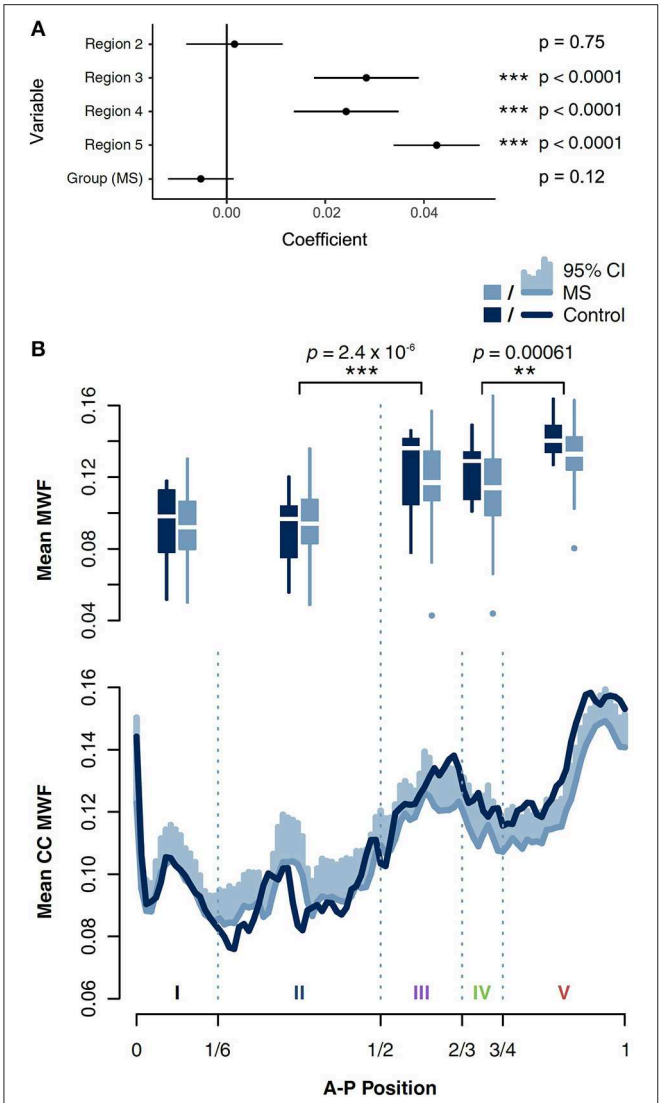

FIGURE 4 | (A) MWF was found to vary significantly by corpus callosal region using a multivariate generalized estimating equations (GEE) model. MWF was lower in MS than in controls, but this finding did not reach statistical significance. Likelihood ratios are shown relative to their difference from control group, region 1. **(B)** Boxplots of MWF in five regions of the CC in individuals with MS and controls. Significant differences based on Tukey's range test between adjacent regions are shown. MWF averaged in voxel-thick vertical strips in each sagittal slice were interpolated linearly to 100 values between anterior and posterior ends, and then averaged across slices to obtain a CC MWF distribution for each subject. These distributions were then averaged across individuals with MS and controls separately, with 95% confidence intervals shown.

$= 2.4 \times 10^{-6}$) and IV and V ($p = 0.00061$). This distribution of MWF was seen independently in both MS and control groups (**Supplemental Table 1**).

Although median MWF was consistently lower in MS across all regions, this trend did not independently achieve statistical significance ($p = 0.12$). In a separate model, we also examined the interaction of group and region as a regression term,

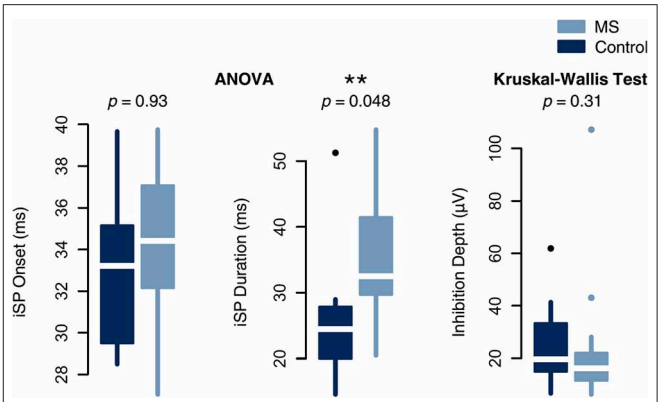

FIGURE 5 | Analysis of inter-group differences in normally distributed TCI measures by one-way ANOVA and non-normally distributed measures by the non-parametric Kruskal-Wallis test. iSP duration was significantly increased in MS whereas iSP onset and inhibition depth were not significantly different between groups.

which was also not a statistically significant predictor of MWF (**Supplementary Figure 2**).

iSP Duration Was Increased in Individuals With MS Compared With Controls

Paired *t*-tests on iSP onset, iSP duration, and transformed inhibition depth did not yield evidence of a significant difference between stimulation of left and right hemispheres (iSP onset $p = 0.995$, iSP duration $p = 0.995$, transformed inhibition depth $p = 0.358$; Holm-Bonferroni adjusted *p*-values). TCI values were averaged across the two hemispheres. A comparison between individuals with MS and controls demonstrated that average iSP duration was significantly prolonged in individuals with MS compared to controls (MS: 36.0 ± 5.2 ms; control: 25.6 ± 8.2 ms; adjusted $p = 0.048$). There was no significant difference in iSP onset and transformed inhibition depth between MS and control groups (**Figure 5**). However, median values and quantile-wise comparison suggested a possible subtle increase in iSP onset latency and decrease in inhibition depth in individuals with MS (**Supplemental Figure 1**). Considering this finding, *post-hoc* analysis of clinical measures found that iSP duration correlated with EDSS score ($r = 0.614$, $p = 0.020$) and disease duration ($r = 0.551$, $p = 0.045$), whereas iSP onset did not (**Figure 6**).

MWF in Regions III and IV Correlated Negatively With Inhibition Depth in MS

MWF in regions III and IV correlated negatively with transformed inhibition depth in the MS group (Pearson product-moment correlation: $r = -0.73$, adjusted $p = 0.0062$ in both regions). The same correlations were non-significant when MS and control data was combined ($r = -0.47$, adjusted $p = 0.17$ in region III; $r = -0.53$, adjusted $p = 0.059$ in region IV) (**Figure 7**). iSP onset and duration did not correlate with MWF in any region. No systematic artefacts were observed in the regression standardized residuals.

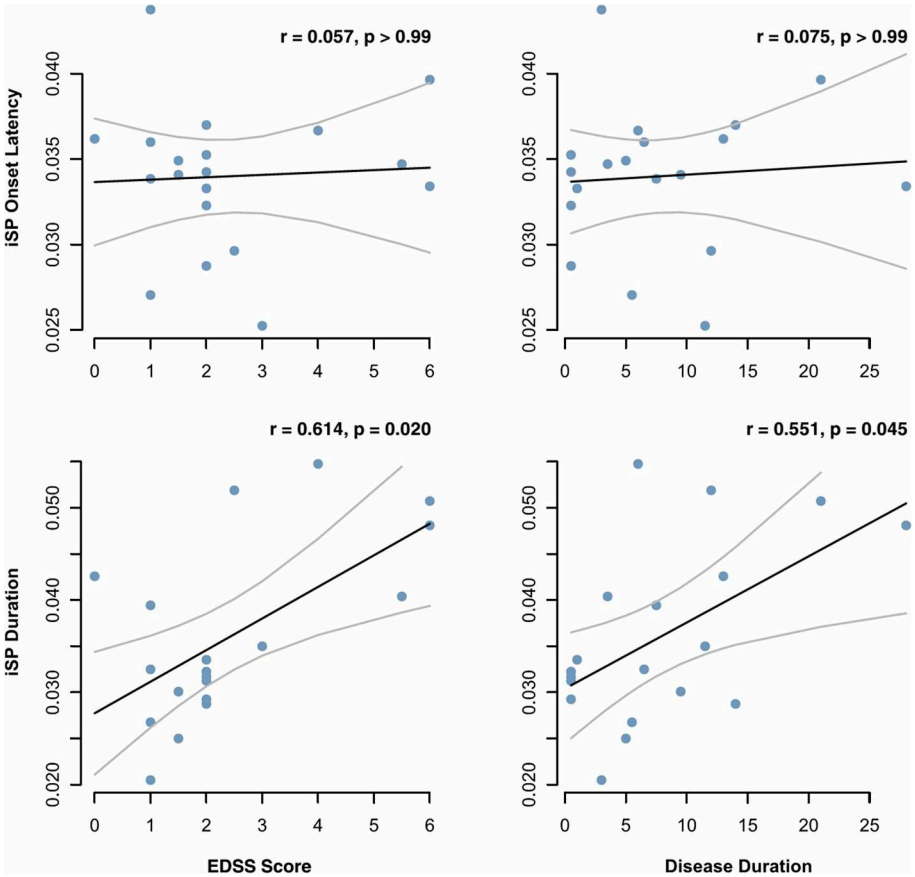

FIGURE 6 | Onset latency and duration of the ipsilateral silent period (iSP), as measured by transcranial magnetic stimulation, were correlated with MS clinical measures. Correlation coefficients and *p* values were calculated based on Pearson correlation and adjusted for multiple comparisons by the Holm-Bonferroni method.

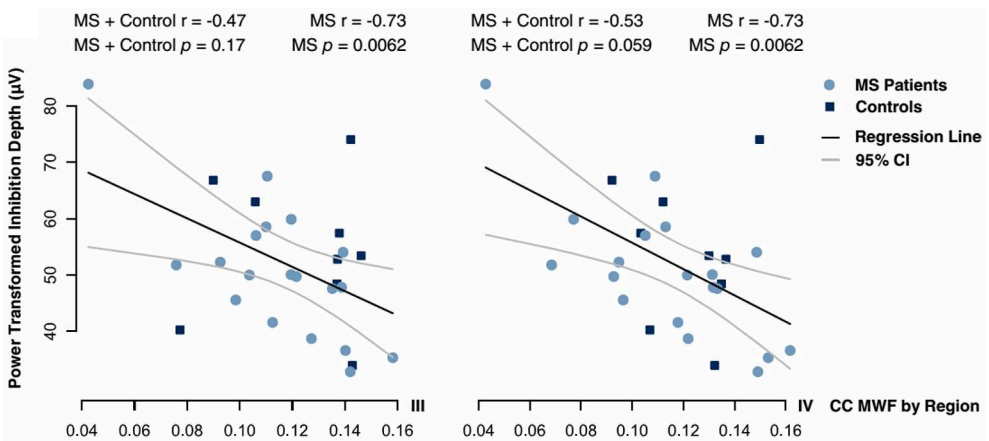

FIGURE 7 | Correlations between inhibition depth with Box-Cox power transform and MWF in regions III and IV of the CC. Data were fitted by Pearson regression. Product-moment correlation coefficients and *p*-values adjusted for multiple comparisons by a Holm-Bonferroni correction are given.

DISCUSSION

This study investigated relationships between MRI-based measures of CC myelination and TMS-based measures of transcallosal connectivity. TMS measures showed that iSP duration was significantly prolonged in MS compared to controls. We also found that the distribution of MWF across the corpus callosum was in agreement with previous studies

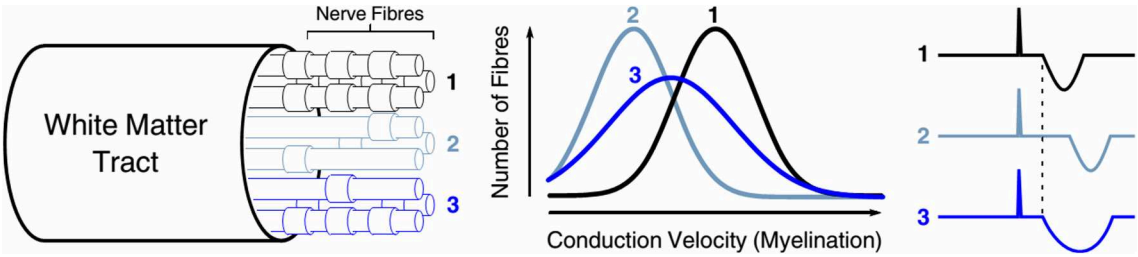

FIGURE 8 | Selective demyelination may play a role in prolonged iSP duration. When compared with (1) a healthy white matter tract, (2) uniformly demyelinated tracts in more advanced disease cause delayed iSP onset. However, (3) partially demyelinated tracts may lead to an increased iSP duration due to a wider distribution of conduction velocities among individual neurons.

[3, 35]. In addition, the MWF in CC regions III and IV (posterior midbody) correlated with the transformed depth of inhibition. MS participants showed reduced MWF along the length of the corpus callosum. Although, the present analysis was not sufficiently powered to confirm statistical significance, this finding agrees with that of previous study [8]. These findings allow us to draw conclusions both on the clinical utility of these techniques as well as the underlying neurobiology of CC demyelination.

iSP Duration May Be a More Sensitive Biomarker of MS Disability Than iSP Onset Latency

iSP duration was significantly longer in MS than in controls while iSP onset latency and inhibition depth were comparable between groups. Two previous studies observed both prolonged iSP duration and increased iSP onset latency in MS patients [14, 36]. In the first study [14], the MS subjects had greater EDSS scores (range 2–8, median 3.0). For the second study [36], the MS subjects had milder disability (EDSS 0–4.5, mean 1.5) Another study on 49 RRMS subjects EDSS 0.0–4.0 (mean 1.3) observed prolonged iSP duration but no change in iSP latency relative to healthy controls [37]. Based on EDSS, our participants also had less advanced disease (range 0–6, median 2.0). To assess the effect of disease severity on iSP onset latency and duration, we performed *post-hoc* analysis which demonstrated that, in our MS participants, iSP duration correlated with clinical measures of disability whereas iSP onset latency did not (**Figure 6**). Taken together, these findings provide evidence that iSP duration may be a more sensitive biomarker than delayed iSP onset in individuals with lower disability as measured by EDSS.

We propose that our observations may arise from incomplete demyelination, resulting in a "spreading" of TCI, thereby prolonging the iSP duration rather than delaying iSP onset (**Figure 8**). One proposed mechanism of selective neuronal damage is size-selective demyelination, with smaller axons demonstrating a greater susceptibility to damage [38]. When compared with a healthy white matter tract, uniformly demyelinated tracts in more advanced disease cause delayed iSP onset. However, partially demyelinated tracts may lead to an increased iSP duration due to a wider distribution of conduction velocities among individual neurons. Although iSP duration differed between MS and control groups, it did not correlate with CC MWF.

Interpretation of the Correlation Between Depth of TCI and CC Posterior Midbody MWF

Inhibition depth correlated negatively with MS MWF in regions III and IV of the CC, which make up the posterior midbody, a region containing axons associated with the motor and sensory cortices [26]. Lesion studies demonstrate that the posterior midbody carries the majority of fibres associated with transcallosal inhibition (TCI) [16, 39, 40]. In addition, we found that tracts in the posterior midbody possessed 27% higher MWF when compared with the anterior half of the CC trunk. The decrease in MWF in the MS group from control group was larger in the posterior regions than in the anterior regions of the CC. This agrees with previous findings which showed that the splenium of the CC has a higher MWF than the genu by 26% in MS and 32% in controls, and that the splenium has a significantly lower MWF in MS whereas the genu does not [8].

The negative correlation between MWF in regions III/IV and inhibition depth indicates that demyelination of these TCI-mediating regions is associated with greater inhibition depth. Callosal atrophy and axonal damage have been previously shown to weaken or eliminate TCI [36, 41]. Also, higher fractional anisotropy values correlate with greater inhibition depth during the iSP in healthy individuals [18]. Our data suggest the opposite relationship between TCI and demyelination. This finding suggests that demyelination within specific regions of the CC alters TCI in a manner that differs from axonal damage. Given that a polysynaptic circuit mediates TCI, the observed association could possibly reflect compensatory intracortical mechanisms that may explain this unexpected finding in MS. Future work should characterize intracortical excitability in conjunction with TCI assessments to better understand the relationships between demyelination and cortical circuit excitability.

Because the CC has been observed to continually mediate both inhibitory and excitatory processes [42], CC damage may dysregulate these processes and cause TCI to either increase or decrease in amplitude. For example, studies of CC damage and its effect on neuromuscular tone have found that while congenital

agenesis of the CC is linked with decrease muscle tone [43], CC injury has also been observed to cause hypertonia in some animal models [44].

Our findings demonstrate that the tracts of regions III and IV of the CC, previously shown to mediate TCI, are highly myelinated in healthy brains but undergo demyelination in MS that is more severe than other regions of the CC. Demyelination in this critical region, as assessed by MWF, correlates with increases in TCI in MS participants but not controls. This amounts to a localizable structure-function relationship within the CC characterized by MRI and TMS together.

LIMITATIONS OF THE STUDY

From rodent spinal cord studies, there is evidence that, due to movement of water between the myelin bilayers and the intra and extracellular spaces, the measured MWF is reduced in neurons which have thinner myelin sheaths [45]. Such effects have not been confirmed in the brain, but could lead to an underestimation of MWF in regions with thin myelin. Although the control cohort was matched for age and sex, coming from a university population, the controls likely had more years of education than the MS cohort which may affect the MWF [46]. The observation of fewer significant correlations between iSP parameters and MWF in the control group compared to the MS group may have been partly due to there being fewer control subjects. The ROIs were defined for a narrow slice of the CC to avoid anatomical ambiguity in more lateral slices, but it is possible that this would fail to capture demyelination occurring more laterally within transcallosal fibres. Both MWF and TCI are subject to noise and systematic artefacts. Time-averaging of TCI data across trials is necessary to obtain a sufficient signal to noise ratio, but may introduce artefacts or suppress subpopulations of trials with outlying onsets and/or durations. Finally, we did not look for the presence or absence of focal lesions in the corpus callosum for the MS cohort and we did not control for subject age, education, disease duration, or EDSS; our goal was a global characterisation of the corpus callosum and it's five segments for comparison with TMS. While we did not control for age in this study, previous work [47] has shown minimal change in MWF in the corpus callosum in healthy controls aged 25–55 years.

CONCLUSIONS

Our study investigated the process of TCI, the distribution of CC MWF, and the effects of CC demyelination on transcallosal connectivity in RRMS. Taken together with previous studies, our work further describes the diagnostic value of iSP onset and duration, demonstrating that iSP duration is a sensitive MS biomarker. The pairing of myelin water imaging and TMS has elucidated structure-function relationships of CC myelination. Correlations between MWF and inhibition depth provide evidence that demyelination in the posterior CC, particularly regions III and IV, can increase inhibition depth. This supports the notion that the posterior midbody of the CC mediates TCI and demonstrates that increases in TCI magnitude may be indicative of demyelination. It is our hope that these findings encourage further study in the combined use of MRI and TMS techniques for monitoring neurological disease. This study serves as a starting point for understanding how these non-invasive methods can enable *in vivo* characterization of the structure-function relationships of myelin.

DATA AVAILABILITY STATEMENT

The datasets for this study will not be made publicly available because public data availability was not part of the consent form signed by study participants. Requests to access the datasets should be directed to the corresponding author.

ETHICS STATEMENT

This study was carried out in accordance with the recommendations of the University of British Columbia Clinical Research Ethics Board with written informed consent from all subjects. All subjects gave written informed consent in accordance with the Declaration of Helsinki. The protocol was approved by the UBC Clinical Research Ethics Board—Approval Certificate (H09-01938).

AUTHOR CONTRIBUTIONS

IV, CL, AT, DL, LB, and AM: conception and design of study. IV, AT, and MZ: data collection. EZ, IV, and MB: data analysis. EZ, IV, MZ, MB, CL, AR, AT, DL, LB, and AM: data interpretation, edited, and revised manuscript. EZ: drafted manuscript.

FUNDING

Funding was provided by Teva Canada Innovation and an NSERC Discovery grant to AM.

ACKNOWLEDGMENTS

The authors would like to sincerely thank all of the study participants, as well as MRI technologists and support staff at the UBC MRI Research Centre. This study was supported by funding from Teva Canada Innovation. The decision to publish this article was solely the responsibility of the authors. All statements, opinions, and content presented in the published article are those of the authors and do not represent the opinions of Teva. Teva provided a medical accuracy review of the article. The UBC MRI Research Centre acknowledges the ongoing support of Philips Healthcare. We also thank Nolan Shelley, Praveena Manogaran, Yinshan Zhao, and Alex Ng for helpful discussion regarding analysis and statistics, and Chantal Roy-Hewitson for clinical support. EZ was supported by a UBC Dean of Science Undergraduate Summer Research Award. MB was supported by funding from the Heart and Stroke Foundation. CL was the recipient of the Women Against MS endMS Research and Training Network Transitional Career Development Award from the Multiple Sclerosis Society of Canada. AR was supported by a CIHR New Investigator Award and was supported by Canada Research Chairs, the Natural Sciences and Engineering

Research Council of Canada, and the National MS Society. LB was funded by the Canadian Research Chairs and the Michael Smith Foundation for Health Research. AM was supported by grants from the Natural Sciences and Engineering Research Council of Canada and the MS Society of Canada.

SUPPLEMENTARY MATERIAL

The Supplementary Material for this article can be found online at: https://www.frontiersin.org/articles/10.3389/fphy.2019.00141/full#supplementary-material

REFERENCES

1. Whittall KP, Mackay AL. Quantitative interpretation of nmr relaxation data. *J Magn Reson.* (1989) **84**:134–52. doi: 10.1016/0022-2364(89)90011-5
2. Mackay A, Whittall K, Adler J, Li D, Paty D, Graeb D. *In vivo* visualization of myelin water in brain by magnetic resonance. *Magn Reson Med.* (1994) **31**:673–7. doi: 10.1002/mrm.1910310614
3. Whittall KP, Mackay AL, Graeb DA, Nugent RA, Li DK, Paty DW. *In vivo* measurement of T2 distributions and water contents in normal human brain. *Magn Reson Med.* (1997) **37**:34–43. doi: 10.1002/mrm.1910370107
4. Moore GRW, Leung E, Mackay AL, Vavasour IM, Whittall KP, Cover KS, et al. A pathology-MRI study of the short-T2 component in formalin-fixed multiple sclerosis brain. *Neurology.* (2000) **55**:1506–10. doi: 10.1212/WNL.55.10.1506
5. Webb S, Munro CA, Midha R, Stanisz GJ. Is multicomponent T2 a good measure of myelin content in peripheral nerve? *Magn Reson Med.* (2003) **49**:638–45. doi: 10.1002/mrm.10411
6. Laule C, Leung E, Lis DK, Traboulsee AL, Paty DW, Mackay AL, et al. Myelin water imaging in multiple sclerosis: quantitative correlations with histopathology. *Mult Scler.* (2006) **12**:747–53. doi: 10.1177/1352458506070928
7. Laule C, Kozlowski P, Leung E, Li DK, Mackay AL, Moore GR. Myelin water imaging of multiple sclerosis at 7 T: correlations with histopathology. *Neuroimage.* (2008) **40**:1575–80. doi: 10.1016/j.neuroimage.2007.12.008
8. Laule C, Vavasour IM, Moore GRW, Oger J, Li DKB, Paty DW, et al. Water content and myelin water fraction in multiple sclerosis: a T2 relaxation study. *J Neurol.* (2004) **251**:284–93. doi: 10.1007/s00415-004-0306-6
9. Vargas WS, Monohan E, Pandya S, Raj A, Vartanian T, Nguyen TD, et al. Measuring longitudinal myelin water fraction in new multiple sclerosis lesions. *Neuroimage Clin.* (2015) **9**:369–75. doi: 10.1016/j.nicl.2015.09.003
10. Barker AT, Jalinous R, Freeston IL. Non-invasive magnetic stimulation of human motor cortex. *Lancet.* (1985) **1**:1106–7. doi: 10.1016/S0140-6736(85)92413-4
11. Wassermann EM, Fuhr P, Cohen LG, Hallett M. Effects of transcranial magnetic stimulation on ipsilateral muscles. *Neurology.* (1991) **41**:1795–9. doi: 10.1212/WNL.41.11.1795
12. Ferbert A, Priori A, Rothwell JC, Day BL, Colebatch JG, Marsden CD. Interhemispheric inhibition of the human motor cortex. *J Physiol.* (1992) **453**:525–46. doi: 10.1113/jphysiol.1992.sp019243
13. Meyer BU, Roricht S, Grafin Von Einsiedel H, Kruggel F, Weindl A. Inhibitory and excitatory interhemispheric transfers between motor cortical areas in normal humans and patients with abnormalities of the corpus callosum. *Brain.* (1995) **118**:429–40. doi: 10.1093/brain/118.2.429
14. Boroojerdi B, Hungs M, Mull M, Topper R, Noth J. Interhemispheric inhibition in patients with multiple sclerosis. *Electroencephalogr Clin Neurophysiol.* (1998) **109**:230–7. doi: 10.1016/S0924-980X(98)00013-7
15. Neva JL, Lakhani B, Brown KE, Wadden KP, Mang CS, Ledwell NH, et al. Multiple measures of corticospinal excitability are associated with clinical features of multiple sclerosis. *Behav Brain Res.* (2016) **297**:187–95. doi: 10.1016/j.bbr.2015.10.015
16. Hoppner J, Kunesch E, Buchmann J, Hess A, Grossmann A, Benecke R. Demyelination and axonal degeneration in corpus callosum assessed by analysis of transcallosally mediated inhibition in multiple sclerosis. *Clin Neurophysiol.* (1999) **110**:748–56. doi: 10.1016/S1388-2457(98)00075-3
17. Li JY, Lai PH, Chen R. Transcallosal inhibition in patients with callosal infarction. *J Neurophysiol.* (2013) **109**:659–65. doi: 10.1152/jn.01044.2011
18. Fling BW, Benson BL, Seidler RD. Transcallosal sensorimotor fiber tract structure-function relationships. *Hum Brain Mapp.* (2013) **34**:384–95. doi: 10.1002/hbm.21437
19. Mädler B, Drabycz SA, Kolind SH, Whittall KP, Mackay AL. Is diffusion anisotropy an accurate monitor of myelination? Correlation of multicomponent T2 relaxation and diffusion tensor anisotropy in human brain. *Magn Reson Imaging.* (2008) **26**:874–888. doi: 10.1016/j.mri.2008.01.047
20. Jones DK, Knosche TR, Turner R. White matter integrity, fiber count, and other fallacies: the do's and don'ts of diffusion MRI. *Neuroimage.* (2013) **73**:239–54. doi: 10.1016/j.neuroimage.2012.06.081
21. Kurtzke JF. Rating neurologic impairment in multiple sclerosis: an expanded disability status scale (EDSS). *Neurology.* (1983) **33**:1444–52. doi: 10.1212/WNL.33.11.1444
22. Prasloski T, Madler B, Xiang QS, Mackay A, Jones C. Applications of stimulated echo correction to multicomponent T2 analysis. *Magn Reson Med.* (2012) **67**:1803–14. doi: 10.1002/mrm.23157
23. Prasloski T, Rauscher A, Mackay AL, Hodgson M, Vavasour IM, Laule C, et al. Rapid whole cerebrum myelin water imaging using a 3D GRASE sequence. *Neuroimage.* (2012) **63**:533–9. doi: 10.1016/j.neuroimage.2012.06.064
24. Smith SM, Jenkinson M, Woolrich MW, Beckmann CF, Behrens TE, Johansen-Berg H, et al. Advances in functional and structural MR image analysis and implementation as FSL. *Neuroimage.* (2004) **23** (Suppl 1):S208–219. doi: 10.1016/j.neuroimage.2004.07.051
25. Jenkinson M, Beckmann CF, Behrens TE, Woolrich MW, Smith SM. FSL. *Neuroimage.* (2012) **62**:782–90. doi: 10.1016/j.neuroimage.2011.09.015
26. Hofer S, Frahm J. Topography of the human corpus callosum revisited–comprehensive fiber tractography using diffusion tensor magnetic resonance imaging. *Neuroimage.* (2006) **32**:989–94. doi: 10.1016/j.neuroimage.2006.05.044
27. Caminiti R, Carducci F, Piervincenzi C, Battaglia-Mayer A, Confalone G, Visco-Comandini F, et al. Diameter, length, speed, and conduction delay of callosal axons in macaque monkeys and humans: comparing data from histology and magnetic resonance imaging diffusion tractography. *J Neurosci.* (2013) **33**:14501–11. doi: 10.1523/JNEUROSCI.0761-13.2013
28. Mori S, Wakana S, van Zijl PCM. *MRI Atlas of Human White Matter*. Amsterdam: Elsevier (2005).
29. Wakana S, Caprihan A, Panzenboeck MM, Fallon JH, Perry M, Gollub RL, et al. Reproducibility of quantitative tractography methods applied to cerebral white matter. *Neuroimage.* (2007) **36**:630–44. doi: 10.1016/j.neuroimage.2007.02.049
30. Hua K, Zhang J, Wakana S, Jiang H, Li X, Reich DS, et al. Tract probability maps in stereotaxic spaces: analyses of white matter anatomy and tract-specific quantification. *Neuroimage.* (2008) **39**:336–47. doi: 10.1016/j.neuroimage.2007.07.053
31. Devanne H, Lavoie BA, Capaday C. Input-output properties and gain changes in the human corticospinal pathway. *Exp Brain Res.* (1997) **114**:329–38. doi: 10.1007/PL00005641
32. Rossi S, Hallett M, Rossini PM, Pascual-Leone A. Safety, ethical considerations, and application guidelines for the use of transcranial magnetic stimulation in clinical practice and research. *Clin Neurophysiol.* (2009) **120**:2008–39. doi: 10.1016/j.clinph.2009.08.016
33. Holm S. A simple sequentially rejective multiple test procedure. *Scand J Stat.* (1979) **6**:65–70.
34. Box G, Cox D. An analysis of transformations. *J R Stat Soc Ser B.* (1964) **26**:211–52. doi: 10.1111/j.2517-6161.1964.tb00553.x
35. Bjornholm L, Nikkinen J, Kiviniemi V, Nordstrom T, Niemela S, Drakesmith M, et al. Structural properties of the human corpus callosum: multimodal assessment and sex differences. *Neuroimage.* (2017) **152**:108–18. doi: 10.1016/j.neuroimage.2017.02.056
36. Lenzi D, Conte A, Mainero C, Frasca V, Fubelli F, Totaro P, et al. Effect of corpus callosum damage on ipsilateral motor activation in patients with multiple sclerosis: a functional and anatomical study. *Hum Brain Mapp.* (2007) **28**:636–44. doi: 10.1002/hbm.20305

37. Jung P, Beyerle A, Humpich M, Neumann-Haefelin T, Lanfermann H, Ziemann U. Ipsilateral silent period: a marker of callosal conduction abnormality in early relapsing-remitting multiple sclerosis? *J Neurol Sci.* (2006) **250**:133–9. doi: 10.1016/j.jns.2006.08.008
38. Evangelou N, Konz D, Esiri MM, Smith S, Palace J, Matthews PM. Size-selective neuronal changes in the anterior optic pathways suggest a differential susceptibility to injury in multiple sclerosis. *Brain.* (2001) **124**:1813–20. doi: 10.1093/brain/124.9.1813
39. Meyer BU, Roricht S, Woiciechowsky C. Topography of fibers in the human corpus callosum mediating interhemispheric inhibition between the motor cortices. *Ann Neurol.* (1998) **43**:360–9. doi: 10.1002/ana.410430314
40. Wahl M, Lauterbach-Soon B, Hattingen E, Jung P, Singer O, Volz S, et al. Human motor corpus callosum: topography, somatotopy, and link between microstructure and function. *J Neurosci.* (2007) **27**:12132–8. doi: 10.1523/JNEUROSCI.2320-07.2007
41. Manson SC, Palace J, Frank JA, Matthews PM. Loss of interhemispheric inhibition in patients with multiple sclerosis is related to corpus callosum atrophy. *Exp Brain Res.* (2006) **174**:728–33. doi: 10.1007/s00221-006-0517-4
42. Bloom JS, Hynd GW. The role of the corpus callosum in interhemispheric transfer of information: excitation or inhibition? *Neuropsychol Rev.* (2005) **15**:59–71. doi: 10.1007/s11065-005-6252-y
43. Moes P, Schilmoeller K, Schilmoeller G. Physical, motor, sensory and developmental features associated with agenesis of the corpus callosum. *Child Care Health Dev.* (2009) **35**:656–72. doi: 10.1111/j.1365-2214.2009.00942.x
44. Drobyshevsky A, Derrick M, Wyrwicz AM, Ji X, Englof I, Ullman LM, et al. White matter injury correlates with hypertonia in an animal model of cerebral palsy. *J Cereb Blood Flow Metab.* (2007) **27**:270–81. doi: 10.1038/sj.jcbfm.9600333
45. Harkins KD, Dula AN, Does MD. Effect of intercompartmental water exchange on the apparent myelin water fraction in multiexponential T2 measurements of rat spinal cord. *Magn Reson Med.* (2012) **67**:793–800. doi: 10.1002/mrm.23053
46. Flynn SW, Lang DJ, Mackay AL, Goghari V, Vavasour IM, Whittall KP, et al. Abnormalities of myelination in schizophrenia detected *in vivo* with MRI, and post-mortem with analysis of oligodendrocyte proteins. *Mol Psychiatry.* (2003) **8**:811–20. doi: 10.1038/sj.mp.4001337
47. Arshad M, Stanley JA, Raz N. Adult age differences in subcortical myelin content are consistent with protracted myelination and unrelated to diffusion tensor imaging indices. *Neuroimage.* (2016) **143**:26–39. doi: 10.1016/j.neuroimage.2016.08.047

Conflict of Interest: AT has received research grants from the MS Society of Canada and honoraria from Biogen, Chugai, Sanofi Genzyme, Roche, Teva Neurosciences, and EMD Serono not related to this analysis. DL has received research funding from the Canadian Institute of Health Research and Multiple Sclerosis Society of Canada. He is the Emeritus Director of the UBC MS/MRI Research Group which has been contracted to perform central analysis of MRI scans for therapeutic trials with Novartis, Perceptives, Roche and Sanofi-Aventis. The UBC MS/MRI Research Group has also received grant support for investigator-initiated independent studies from Genzyme, Merck-Serono, Novartis and Roche. He has acted as a consultant to Vertex Pharmaceuticals and served on the Data and Safety Advisory Board for Opexa Therapeutics and Scientific Advisory Boards for Adelphi Group, Novartis and Roche. He has also given lectures which have been supported by non-restricted education grants from Novartis and Biogen.

The remaining authors declare that the research was conducted in the absence of any commercial or financial relationships that could be construed as a potential conflict of interest.

frontiers in Physics

ORIGINAL RESEARCH
published: 17 October 2019
doi: 10.3389/fphy.2019.00160

Apparent Diffusion Coefficient Assessment of Brain Development in Normal Fetuses and Ventriculomegaly

Maria Giovanna Di Trani[1,2], Lucia Manganaro[3], Amanda Antonelli[3], Michele Guerreri[4], Riccardo De Feo[1,2], Carlo Catalano[3] and Silvia Capuani[4]*

[1] Centro Fermi—Museo Storico della Fisica e Centro Studi e Ricerche Enrico Fermi, Rome, Italy, [2] SAIMLAL Department, Sapienza University of Rome, Rome, Italy, [3] Department of Radiological Sciences, Oncology and Anatomo-Pathology, Faculty of Medicine and Dentistry, Sapienza University of Rome, Rome, Italy, [4] Nuclear Magnetic Resonance and Medical Physics Laboratory, Physics Department, CNR-Institute for Complex Systems, Sapienza University of Rome, Rome, Italy

Diffusion neuro-MRI has benefited significantly from sophisticated pre-processing procedures aimed at improving image quality and diagnostic. In this work, diffusion-weighted imaging (DWI) was used with artifact correction and the apparent diffusion coefficient (ADC) was quantified to investigate fetal brain development. The DWI protocol was designed in order to limit the acquisition time and to estimate ADC without perfusion bias. The ADC in normal fetal brains was compared to cases with isolated ventriculomegaly (VM), a common fetal disease whose DWI studies are still scarce. DWI was performed in 58 singleton fetuses (Gestational age (GA) range: 19–38w) at 1.5T. In 31 cases, VM was diagnosed on ultrasound. DW-Spin Echo EPI with b-values = 50, 200, 700 s/mm^2 along three orthogonal axes was used. All images were corrected for noise, Gibbs-ringing, and motion artifacts. The signal-to-noise ratio (SNR) was calculated and the ADC was measured with a linear least-squared algorithm. A multi-way ANOVA was used to evaluate differences in ADC between normal and VM cases and between second and third trimester in different brain regions. Correlation between ADC and GA was assessed with linear and quadratic regression analysis. Noise and artifact correction considerably increased SNR and the goodness-of-fit. ADC measurements were significantly different between second and third trimester in centrum semiovale, frontal white matter, thalamus, cerebellum and pons of both normal and VM brains ($p \leq 0.03$). ADC values were significantly different between normal and VM in centrum semiovale and frontal white matter ($p \leq 0.02$). ADC values in centrum semiovale, thalamus, cerebellum and pons linearly decreased with GA both in normal and VM brains, while a quadratic relation with GA was found in basal ganglia and occipital white matter of normal brains and in frontal white matter of VM ($p \leq 0.02$). ADC values in all fetal brain regions were lower than those reported in literature where DWI with b = 0 was performed. Conversely, they were in agreement with the results of other authors who measured perfusion and diffusion contributions separately. By optimizing our DWI protocol we achieved an unbiased quantification of brain ADC in reasonable scan time. Our findings suggested that ADC can be a useful biomarker of brain abnormalities associated with VM.

Keywords: fetal MRI, brain development, DWI, ADC, ventriculomegaly

OPEN ACCESS

Edited by:
Marta Bianciardi, Massachusetts General Hospital, Harvard Medical School, United States

Reviewed by:
Robert Mulkern, Boston Children's Hospital, Harvard Medical School, United States
Andrea Duggento, University of Rome Tor Vergata, Italy

****Correspondence:***
Maria Giovanna Di Trani
mgiovanna.ditrani@gmail.com

Specialty section:
This article was submitted to Medical Physics and Imaging, a section of the journal Frontiers in Physics

Received: *30 April 2019*
Accepted: *30 September 2019*
Published: *17 October 2019*

Citation:
Di Trani MG, Manganaro L, Antonelli A, Guerreri M, De Feo R, Catalano C and Capuani S (2019) Apparent Diffusion Coefficient Assessment of Brain Development in Normal Fetuses and Ventriculomegaly. Front. Phys. 7:160. doi: 10.3389/fphy.2019.00160

1. INTRODUCTION

The fascinating process of brain development involves a highly organized mechanism of cell proliferation, histogenesis and myelination leading to the formation of 100 billion neurons in neonatal brains [1].

During gestation, the fetal brain experiences its most vulnerable and important phase of maturation; hence, non-invasive prenatal imaging could be an extremely helpful tool to monitor brain development.

The sensitivity of diffusion-weighted imaging (DWI) techniques in detecting micro-structural changes of cerebral tissues enables the investigation of fetal brain maturation, helping to identify cases of abnormal brain development earlier. Furthermore, the measurement of the apparent diffusion coefficient (ADC) in different fetal brain regions can help to better understand the etiology and the evolution of certain neurological pathologies that develop in fetal age.

One of the most common diseases in fetuses is ventriculomegaly (VM), being diagnosed in approximately 1 out of every 1,000 live births [2], at any gestational age (GA), with a 36.7% probability of survival without disability [3]. Moreover, VM has been associated with numerous neurological conditions, such as autism [4], epilepsy [5], and schizophrenia [6]; however, DWI studies in fetal brain during gestation are scarce.

An important prognostic factor is whether VM is associated with other abnormalities, since fetuses manifest normal neurological development in the majority of isolated mild VM cases [7]. So far, it is not understood why mild VM can cause motor and cognitive disturbances to the newborn, unlike some cases of severe VMs. For this reason, it is necessary to develop new diagnostic markers to better understand this type of pathology.

The superiority of MRI in identifying fetal brain anomalies, with respect to the sonography [8–10], suggests further investigations on prenatal imaging and DWI is one of the best candidates, given its sensitivity for micro-structural changes.

Prenatal MRI is mainly performed at 1.5T to reduce heating effects and potential risks of the radio-frequency exposure [11], which limits image resolution and signal-to-noise ratio (SNR). Another limitation for fetal imaging is artifact due to motion of both the fetus and mother. In small brains, particularly in the second trimester of gestation, low resolution prevents a correct selection of brain regions and therefore the accuracy of measurements, causing ADC values to be biased by partial volume effects.

Studies in fetuses are limited and usually lack an appropriate pre-processing of raw data to improve the quality and reliability of the results [12–15]. In this work, we investigated the potential ability of DWI denoising methods [16] and artifact corrections [17, 18] to assess unbiased ADC values for characterizing normal and VM fetal brain development.

Toward this goal, we used a rapid DWI protocol to measure ADC in fetal brains at different gestational ages, in the second and third trimester of gestation. With the aim to establish normative ADC measurements, which will be useful to compare and identify cases with anomalies, this study analyzed variations in ADC during gestation of healthy fetuses, compared to cases of fetuses with mild, moderate, and severe VM.

Abbreviations: DWI, diffusion-weighted imaging; ADC, apparent diffusion coefficient; VM, ventriculomegaly; GA, gestational age; SNR, signal-to-noise ratio; VD, ventricular dilatation; TR, repetition time; TE, echo time; NSA, number of signal averages; IVIM, intra-voxel incoherent motion; WM, white matter; GM, gray matter; ROI, region of interest; CSO, centrum semiovale; FWM, frontal white matter; OWM, occipital white matter; TH, thalamus; BG, basal ganglia; CH, cerebellar hemispheres; SD, standard deviation; RMSE, root mean squared error.

MATERIALS AND METHODS

DWI was performed in 58 singleton fetuses during the second and third gestational trimester at 1.5T (Siemens Avanto, Erlangen, Germany), without mother-fetal sedation.

Thirty-one fetuses presenting ventricular dilatation (VD) on ultrasound investigation were referred to the Radiological Sciences Department of Sapienza University (Rome, Italy) for MRI scans to further assess brain pathologies. Atrial diameter was measured on ultrasound and MRI according to the International Society of Ultrasound in Obstetrics and Gynecology (ISUOG) guidelines [19] and ventriculomegaly (VM) was defined when the atrial diameter of one or both ventricles was $\geq$ 10 mm. The final cohort consisted of 31 fetuses with isolated VM and 27 normal fetuses, that is, with atrial diameter $<$ 10 mm. In 12 cases, VM was diagnosed as mild (VD $<$ 12 mm), in 8 as moderate (VD between 12–14 mm) and in 10 as severe (VD $\geq$ 15 mm). None of the fetuses showed cerebral anomalies observable with conventional MRI examination, consisting of T2-weighted and FLAIR images.

The study was conducted with the approval of the local Ethics Committee after obtaining a written informed consent from all the mothers. Pregnant women were examined in supine position with a phased-array coil placed over the pelvis. Before performing MRI, a multi-planar scanogram was obtained to localize the fetus.

The Diffusion MRI protocol included a DW-Spin Echo EPI with repetition time (TR) = 4,000 ms, echo time (TE) = 79 ms, bandwidth = 1,628 Hz/px, matrix dimension = 192 × 192, field of view (FOV) = 379 mm^2, in-plane resolution = 2 × 2 mm^2, slice-thickness = 4 mm, number of signal averages (NSA) = 2.

Preliminary tests were performed on three fetuses to carefully choose the diffusion directions and weightings, i.e., *b*-values, of the Diffusion MRI protocol. *B*-values were selected to reduce perfusion effects on ADC estimation and minimize the scanning time to obviate fetal motion. These tests were performed with *b*-values = 0, 10, 30, 50, 100, 200, 400, 700 s/mm^2, according to a typical Intra-voxel Incoherent Motion (IVIM) protocol [20, 21]. We evaluated ADC in a region of white matter (WM) and a region of gray mater (GM) using an IVIM model, mono-exponential model with *b*-values = 0, 50, 200, 700 s/mm^2 and mono-exponential model with *b*-values = 50, 200, 700 s/mm^2. As shown in **Figure 1C**, the fast decay of the diffusion-weighted signal, mainly due to perfusion, is strongly reduced at *b*-value = 50 s/mm^2. Therefore, from the comparison between diffusion parameters estimated using IVIM and mono-exponential

models, we selected b-values $= 50, 200, 700$ s/mm^2 for the diffusion protocol used to acquire data from all subjects of the healthy and VM cohorts. The total scan time was approximately 2 min.

PRE-PROCESSING AND DATA ANALYSIS

After a first inspection, 2 normal and 11 VM cases (2 mild, 2 moderate, 7 severe) showed motion artifacts impossible to correct or severe ventricle dilatation that prevented correct ROI selection; thus 13 subjects were discarded from the following analysis.

The pipeline for image correction (**Figure 1**) started with noise removal by using *dwidenoise* tool [16]; then, *unring* [17] was used to correct *denoised* DWI for Gibbs-ringing artifacts. Eventually, images were corrected for fetal/mother motion artifacts by using FLIRT [18]: each volume was registered to the image at b-value $= 50$ s/mm^2 through a rigid-body transformation, using a tri-linear interpolation method.

Seven regions of interest (ROI) were manually placed in the centrum semiovale (CSO), frontal white matter (FWM), occipital white matter (OWM), thalamus (TH), basal ganglia (BG), cerebellar hemispheres (CH) and pons, as reported in **Figure 1B**. In some VM cases, ROIs could not be placed in CSO (3 cases), FWM (3), BG (3), TH (3), OWM (3), CH (1) because VM was severe or the brain was too small.

SNR of raw and corrected DWI at each b-value was calculated to evaluate the reliability of estimated ADC values. SNR was calculated in each volume as the ratio between DWI signal averaged over all brain ROIs and the standard deviation (SD) of noise, as follows:

$$SNR = 0.655 \frac{mean(signal)}{SD(noise)} \quad (1)$$

where noise was estimated in the background and the factor 0.655 was used to account for Rayleigh distribution of background noise [22].

ADC values were measured through a fitting procedure developed in MATLAB, with a linear least-squares algorithm, and the goodness-of-fit was evaluated with the root mean squared error (RMSE). The fitting procedure was carried out voxel-by-voxel, making inter-volume motion correction a mandatory step for voxel alignment.

A multi-way ANOVA with Bonferroni correction was used to evaluate differences in ADC between normal and VM cases and between the second and third TR.

The relationship between ADC measurements and GA was assessed with linear and quadratic regression analysis by calculating the adjusted coefficient of determination R^2 and the b-value for the Fisher-test to evaluate the statistical significance of the model. Initially, linear regression was performed in each ROI. However, we observed that some brain regions (FWM, OWM and BG) showed an evident non-linear dependence on GA, thus we performed a quadratic regression in those regions. Outliers, that is values bigger than three median absolute deviations away from median, were not considered in the regression analysis.

RESULTS

The preliminary tests, performed to choose the optimal b-values of the Diffusion MRI protocol for reducing perfusion effects on ADC measurements, showed a fast decay of the DWI signal due to perfusion at low b-values ($b \leq 50$ s/mm^2). However, the fast signal decay was strongly reduced at b-values $= 50$ s/mm^2 (**Figure 1C**). Therefore we performed the study using b-values equal to $50, 200, 700$ s/mm^2. Moreover, the ADC estimated by the mono-exponential function with three b-values did not differ more than the SD the from the diffusion coefficient derived by the only diffusion component of the IVIM model, estimated with eight b-values.

SNR and the quality of DW-images considerably increased after noise and artifact correction ($SNR_{corr} = 19.5 \pm 7.8$, $SNR_{raw} = 7.8 \pm 3.1$; both calculated at b-value $= 700$ s/mm^2), as shown in **Figure 2A**. Also the goodness-of-fit significantly increased after correction ($RMSE_{raw} = 0.07$, $RMSE_{corr} = 0.06$, $p = 0.0001$, **Figure 2B**).

Mean ADC values in normal and VM fetuses, obtained in the second and third trimester of gestation and in different cerebral regions, are shown in **Figure 3**. Significant differences were found between second and third trimester in CSO, FWM, TH, CH and pons of both normal and VM brains ($p \leq 0.03$). ADC values in normal and VM ROIs were not significantly different, except for CSO and FWM ($p \leq 0.02$).

Linear regression analysis showed ADC values in CSO, TH, CH and pons to significantly decrease with GA both in normal ($p \leq 0.001$; **Figures 4A,B,D,E** and **Table 2**) and VM brains ($p \leq 0.001$; **Figures 4G,H,J,K** and **Table 2**). A significant quadratic relationship with GA was found in BG and OWM of normal brains ($p \leq 0.02$; **Figures 4C,F** and **Table 2**) and FWM of VM cases ($p \leq 0.02$; **Figure 4I** and **Table 2**).

In the entire data set, 6 outliers were found in TH (1.68×10^{-3} mm^2/s), BG ($1.77, 1.69 \times 10^{-3}$ mm^2/s), OWM (2.68×10^{-3} mm^2/s) and CH (1.74×10^{-3} mm^2/s) for normal brains and in pons (1.49×10^{-3} mm^2/s) for VM brains; these values were discarded from both linear and quadratic regression analysis.

DISCUSSIONS AND CONCLUSIONS

In this work, prenatal DWI was performed at 1.5T and the ADC was measured in fetal brains during the second and third trimester of gestation, both in normal and VM cases.

Prenatal imaging could be strongly affected by uncontrollable fetal/mother movement, especially when performed without sedation. In order to limit motion-derived artifacts, we designed our DWI protocol with limited number of signal averages (NSA $= 2$) to be as fast as possible, causing poor SNR ($SNR_{raw} = 7.8 \pm 3.1$ at b $= 700$ s/mm^2) in our data. To overcome image quality limitations, raw data were denoised and corrected for motion and Gibbs' ringing artifacts. Results, reported in **Figure 2A**, showed that image pre-processing significantly improved SNR and goodness-of-fit, guaranteeing a better ROI selection of different fetal brain regions and a reliable estimation of the ADC. Moreover, volume registration was fundamental to

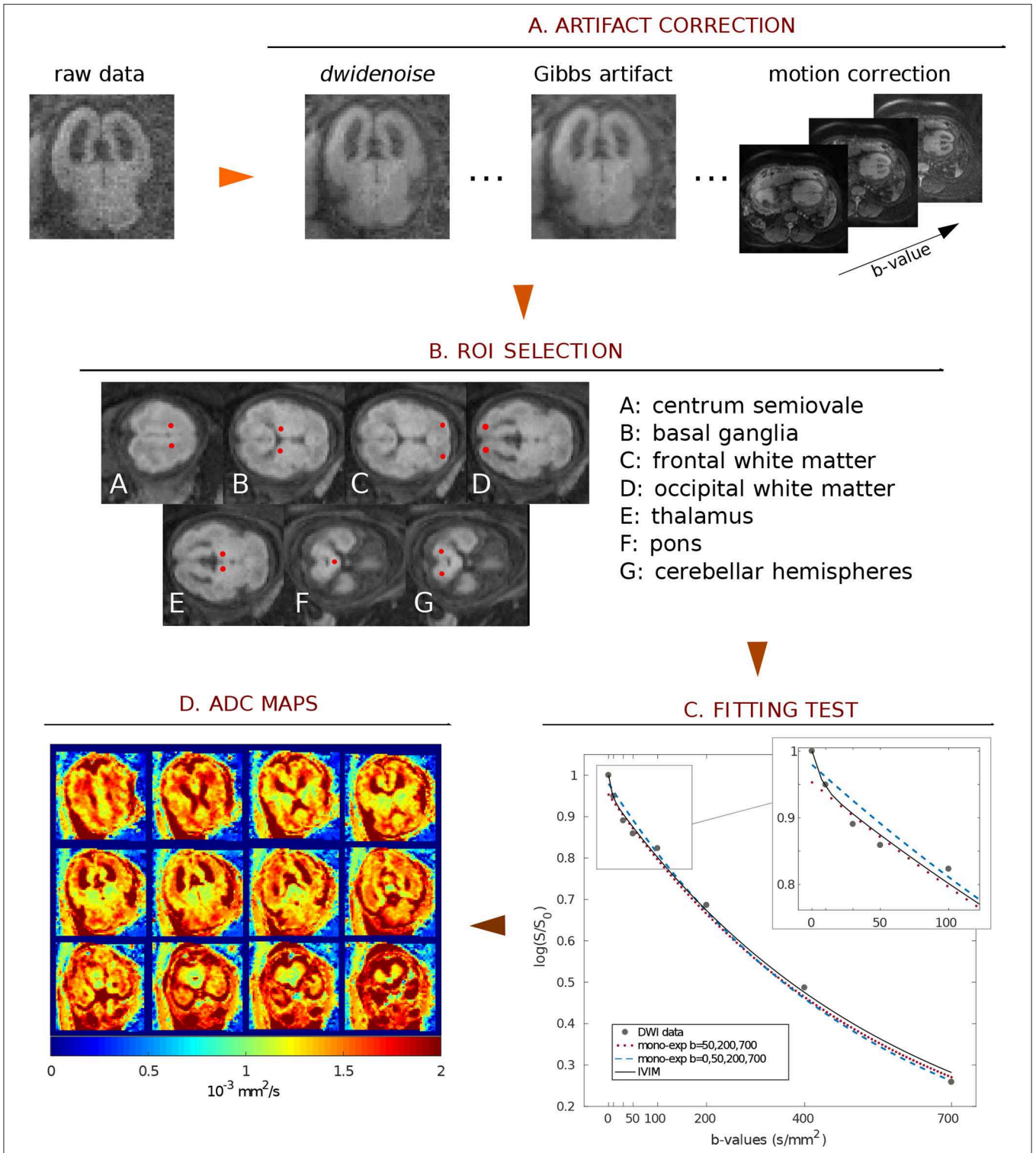

FIGURE 1 | Scheme of image analysis. **(A)** Raw images were first corrected for noise, Gibbs, and motion artifacts. **(B)** Seven ROIs were manually drawn. **(C)** In preliminary tests on 3 subjects we compared 3 fitting procedures to evaluate perfusion effects of DWI signal: 2 mono-exponential fit (with *b*-values = 50, 200, 700 s/mm^2 and *b*-values = 0, 50, 200, 700 s/mm^2) and an IVIM fit (with *b*-values = 0, 10, 30, 50, 100, 200, 400, 700 s/mm^2). The magnification highlights the greater slope of the mono-exponential fit with b = 0 caused by perfusion. **(D)** Finally, ADC maps were calculated by mono-exponential fit with *b*-values = 50, 200, 700 s/mm^2.

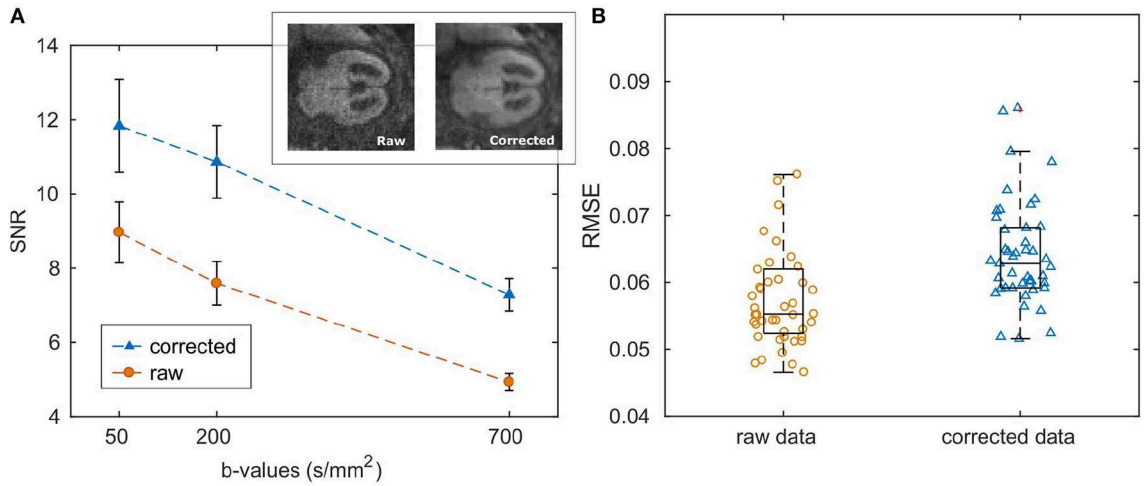

FIGURE 2 | (A) Mean and standard error of SNR calculated over the entire patient cohort. An example of raw and corrected DWI at *b*-value = 700 s/mm^2 is reported in the top right corner of the plot. **(B)** Boxplots of the root mean squared error of ADC fit; dots represent RMSE for each subject averaged over the ROI.

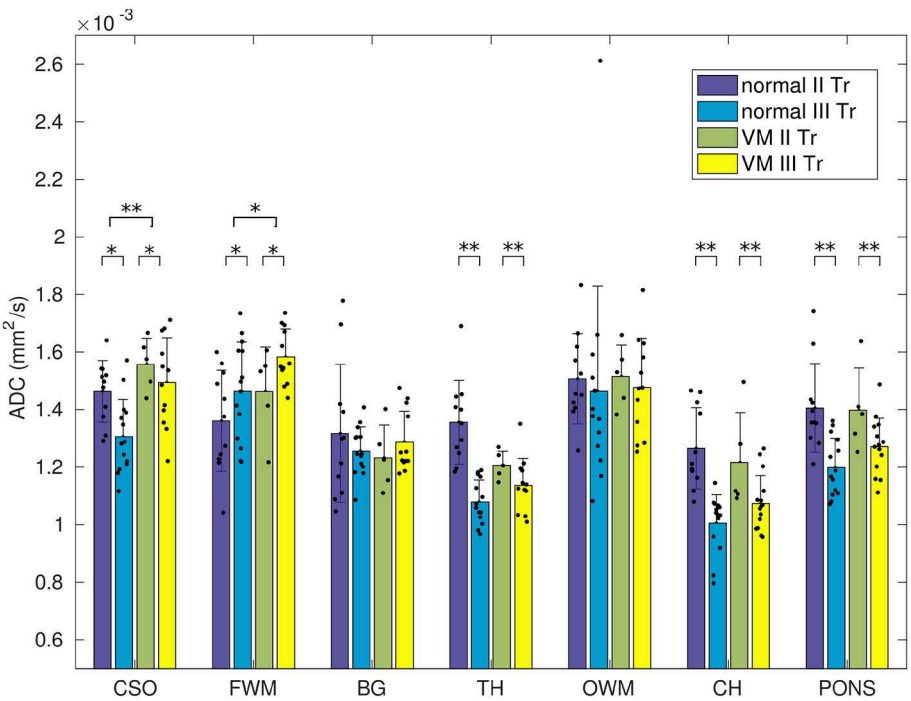

FIGURE 3 | ADC measurements in normal and VM brains of fetuses in the second and third trimester of gestation. Dots represent the ADC calculated for each subject and asterisks represent the *p*-value of multi-way ANOVA (*$p < 0.02$; **$p < 10^{-3}$).

minimize voxel misalignment, since the fitting procedure was carried-out voxel-by-voxel.

Since ADC estimation is strongly influenced by the diffusion weighting, in this study *b*-values were carefully chosen in order to minimize perfusion contamination of ADC measurements; therefore, DWI with *b*-value = 50 s/mm^2 was acquired as first volume and used to normalize data prior to fit. It is well known that DWI with low diffusion weighting is sensitive to perfusion motion, resulting from blood micro-circulation in capillaries [20], which contributes to increased ADC values. By normalizing diffusion data with the volume at *b*-value = 50 s/mm^2, we reduced the contribution of perfusion in our measurements, finding, in normal fetuses, lower ADC values compared to other studies that used b = 0 [12–15].

In a recent study [21], an IVIM technique was carried out to separately measure the contribution of perfusion and diffusion,

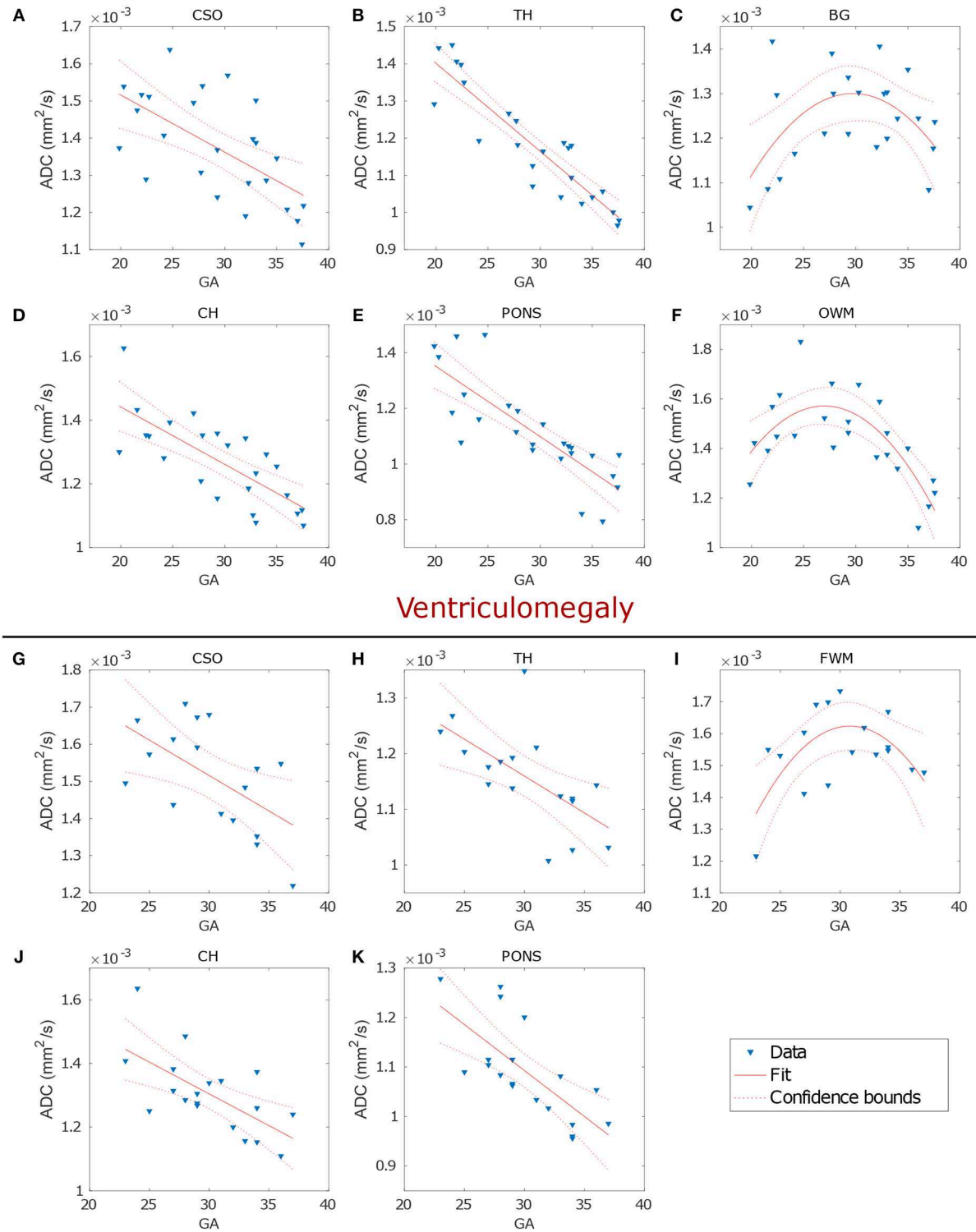

FIGURE 4 | Regression analysis of the ADC in normal (upper panel) and VM (lower panel) fetal brains showed the changes of biological water diffusion as a function of the gestational age (GA). Each plot, showing data fit and 95% confidence interval, refers to a particular ROI: CSO, TH, BG, CH, pons and OWM of normal brains (**A–F**, respectively) and CSO, TH, FWM, CH, and pons of VM cases (**G–K**, respectively).

in developing fetal brain. The authors [21] measured lower ADC values in CSO, FWM, OWM, CH and pons compared to those reported in literature [12–15], demonstrating that perfusion motion can affect ADC measurements in fetal brains. Our ADC values were in good accordance with the measurements derived from the contribution of solely diffusion in the IVIM study [21], suggesting that our acquisition strategy effectively minimized perfusion effects.

However, authors [21] acquired DWI with nine *b*-values (from 0 to 800 s/mm^2) in order to fit the IVIM model, using a total acquisition time of about 5 min. As a result of a longer acquisition time, compared to that used in this work (2 min), the IVIM study [21] discarded 56% of subjects due to fetal movements, while in this study only 22% of subjects was rejected for motion artifacts.

Analogously to other works in normal fetuses [13–15, 21, 23], we found that during brain development, ADC linearly decreased in CSO, TH, CH and pons, as well as in VM cases, reflecting the morphological changes of brain maturation that involves increasing cellularity, histogenesis and myelination [24]. The latter starts in the spinal cord (12 GA), followed by pons, cerebellar peduncles, and thalamic axons (14–20 GA), in the frontal, parietal and occipital lobes (30 GA) and finally in the cortex (35 GA), lasting for decades in the human brain [25–28]. The process of myelination begins with the accumulation of lipids and proteins [29] and the proliferation of oligodendrocyte precursors [30], causing a reduction of extracellular space, with a consequent decrease in ADC values. According to previous results [13–15, 21, 23], the ADC was found to be significantly higher in the fetal white matter than in the deep brain nuclei (BG, TH, and pons), suggesting an immature status of fiber myelination during fetal development.

Consistently with the timeline of myelination, we found the decrease of diffusivity in OWM (normal cases) and FWM (VM cases) to start from 28-30 GA, later than CSO, TH, CH and pons. An initial increase in ADC values was measured in cortical WM, from 23 to 30 GA, followed by a decline after 30 GA, as reported in other studies [31–33]. These results are in agreement with the normal progression of myelination that occurs from central to peripheral brain.

Although in VM fetuses no other alteration was reported by ultrasound exam, we found significantly higher diffusivity (**Figure 3** and **Table 1**) in CSO and FMW compared to normal fetal brain. This result may reveal delayed or abnormal maturation of white matter, as reported in other studies in neonates with isolated mild VM [34–36], suggesting that the ADC in CSO and FWM could be a marker of altered development and disorders associated with VM.

Furthermore, regression analysis in TH showed that ADC values were more strongly correlated with GA in normal than in VM cases (**Table 2** and **Figure 4B**), while no significant correlation was found in OWM of VM cases, suggesting the possibility of a delayed white matter maturation in VM brains, especially during the third trimester of gestation.

In contrast to a recent work [12], we did not find significantly higher ADC values in BG of VM compared to normal fetuses. Anatomically, BG is the nearest structure to the lateral ventricles, hence it is more prone to be affected by signal contamination from ventricles due to volume misalignment. This could have caused the disagreement with the work of Yaniv et al. [12], since they did not use any method to realign DWI.

TABLE 1 | Multi-way ANOVA to investigate the effects of brain maturation and VM disease on ADC measurements.

	II vs. III TR	Normal vs. VM
CSO	0.005	$<10^{-3}$
FWM	0.03	0.02
BG	ns	ns
TH	$<10^{-4}$	ns
OWM	ns	ns
PONS	$<10^{-4}$	ns
CH	$<10^{-4}$	ns

TABLE 2 | Regression analysis between ADC and gestational age.

	Normal				VM			
	Linear		Quadratic		Linear		Quadratic	
	R^2	p	R^2	p	R^2	p	R^2	p
CSO	0.36	0.001	–	–	0.28	0.02	–	–
FWM	–	ns	–	ns	–	ns	0.34	0.02
BG	–	ns	0.19	0.04	–	ns	–	–
TH	0.82	$<10^{-5}$	–	–	0.36	0.006	–	–
OWM	0.17	0.02	0.54	0.0001	–	ns	–	ns
PONS	0.54	$<10^{-3}$	–	–	0.48	$<10^{-2}$	–	–
CH	0.65	$<10^{-4}$	–	–	0.38	0.003	–	–

Moreover, the same authors [12] found lower ADC in FWM of VM fetuses compared to normal fetal brain, whereas we obtained the opposite result (**Figure 3**). FWM and OWM regions are supplied by the carotid system with large vessels, so perfusion is relatively high, as shown in reference [21]. We suspect that ADC measured by Yaniv et al. [12] was partially affected by perfusion, since they acquired data using *b*-values = 0 and 700 s/mm^2, leading to the discrepancies with our results.

To the best of our knowledge, no other works have investigated the ADC in brain development of VM fetuses (**Figures 4G–K**). Although our study was limited by a small statistical sample, it could help to establish criteria for recognizing abnormal brain development that is important for early diagnosis of diseases.

In addition to the small number of subjects, our study was also limited by the slice thickness, which should be reduced to minimize partial volume effects and to enable more accurate identification of brain tissues.

Our study on VM brains revealed the sensitivity of DWI in brain diseases, making this technique suitable also to patient follow-up. Moreover, our routine image correction had proven to be a reasonable and fast method for improving the quality of diffusion-weighted images and for providing a reliable identification of ROIs.

Perfusion motion might affect DWI signal, causing ADC to be artificially higher; in this work we showed that, using *b*-value =

50 s/mm^2 as first acquired diffusion-weighted volume, the ADC was quantified without significant perfusion contamination, since our measurements were comparable to those obtained by the IVIM model [21].

Although our work is limited by the use of 1.5T magnetic field, our rapid acquisition protocol combined with artifact correction allowed a reliable estimation of the ADC in a very short time and the identification of anomalies in fetal brain development.

This work suggested that regional differences in fetal ADC values and their variations with GA reflect micro-structural and physiological changes due to brain maturation. These preliminary data can contribute to delineate a reference standard to assess the normal progress of sulcation and myelination as well as the normative biometry of the fetal brain, contributing to improve knowledge of brain maturation.

DATA AVAILABILITY STATEMENT

The datasets generated for this study are available on request to the corresponding author.

ETHICS STATEMENT

This study was carried out in accordance with the recommendations of the International Society of Ultrasound in Obstetrics and Gynecology (ISUOG) guidelines with written informed consent from all subjects. All subjects gave written informed consent in accordance with the Declaration of Helsinki. The protocol was approved by the Policlinico Umberto I of Sapienza University Ethics Committee.

AUTHOR CONTRIBUTIONS

MD, SC, and LM conceived the original idea and planned the experiments. AA, LM, and SC carried out the experiment. MD elaborated all data and performed statistical analysis with contribution of MG and RD. MD and SC wrote the manuscript with contribution of LM. AA, CC, LM, and SC supervise the project. All authors contributed to the interpretation of the results, read, and approved the final manuscript.

REFERENCES

1. Ackerman S. (1992). *Discovering the Brain*. Washington, DC: National Academies Press.
2. Pilu G, Perolo A, Falco P, Visentin A, Gabrielli S, Bovicelli L. Ultrasound of the fetal central nervous system. *Curr Opin Obstet Gynecol*. (2000) **12**:93–103. doi: 10.1097/00001703-200004000-00007
3. Carta S, Kaelin Agten A, Belcaro C, Bhide A. Outcome of fetuses with prenatal diagnosis of isolated severe bilateral ventriculomegaly: systematic review and meta-analysis. *Ultrasound Obstet Gynecol*. (2018) **52**:165–73. doi: 10.1002/uog.19038
4. Palmen SJ, Hulshoff Pol HE, Kemner C, Schnack HG, Durston S, Lahuis BE, et al. Increased gray-matter volume in medication-naive high-functioning children with autism spectrum disorder. *Psychol Med*. (2005) **35**:561–70. doi: 10.1017/S0033291704003496
5. Jackson DC, Irwin W, Dabbs K, Lin JJ, Jones JE, Hsu DA, et al. Ventricular enlargement in new-onset pediatric epilepsies. *Epilepsia*. (2011) **52**:2225–32. doi: 10.1111/j.1528-1167.2011.03323.x
6. Wright IC, Sham P, Murray RM, Weinberger DR, Bullmore ET. Genetic contributions to regional variability in human brain structure: methods and preliminary results. *Neuroimage*. (2002) **17**:256–71. doi: 10.1006/nimg.2002.1163
7. Huisman TA. Fetal magnetic resonance imaging of the brain: is ventriculomegaly the tip of the syndromal iceberg? *Semin Ultrasound CT MR*. (2011) **32**:491–509. doi: 10.1053/j.sult.2011.08.002
8. Girard NJ. Magnetic resonance imaging of fetal developmental anomalies. *Top Magn Reson Imaging*. (2011) **22**:11–23. doi: 10.1097/RMR.0b013e3182425bb2
9. Manganaro L, Bernardo S, La Barbera L, Noia G, Masini L, Tomei A, et al. Role of foetal MRI in the evaluation of ischaemic-haemorrhagic lesions of the foetal brain. *J Perinat Med*. (2012) **40**:419–26. doi: 10.1515/jpm-2011-0182
10. Yin S, Na Q, Chen J, Li-Ling J, Liu C. Contribution of MRI to detect further anomalies in fetal ventriculomegaly. *Fetal Diagn Ther*. (2010). **27**:20–4. doi: 10.1159/000260389
11. Weisstanner C, Gruber GM, Brugger PC, Mitter C, Diogo MC, Kasprian G, et al. Fetal MRI at 3T-ready for routine use? *Br J Radiol*. (2016) **90**:20160362. doi: 10.1259/bjr.20160362
12. Yaniv G, Katorza E, Bercovitz R, Bergman D, Greenberg G, Biegon A, et al. Region-specific changes in brain diffusivity in fetal isolated mild ventriculomegaly. *Eur Radiol*. (2016) **26**:840–8. doi: 10.1007/s00330-015-3893-y
13. Hoffmann C, Weisz B, Lipitz S, Yaniv G, Katorza E, Bergman D, et al. Regional apparent diffusion coefficient values in 3rd trimester fetal brain. *Neuroradiology*. (2014) **56**:561–7. doi: 10.1007/s00234-014-1359-6
14. Schneider MM, Berman JI, Baumer FM, Glass HC, Jeng S, Jeremy RJ, et al. Normative apparent diffusion coefficient values in the developing fetal brain. *AJNR Am J Neuroradiol*. (2009) **30**:1799–803. doi: 10.3174/ajnr.A1661
15. Han R, Huang L, Sun Z, Zhang D, Chen X, Yang X, et al. Assessment of apparent diffusion coefficient of normal foetal brain development from gestational age week up to term age: a preliminary study. *Foetal Diagn Ther*. (2014) **37**:102–7. doi: 10.1159/000363650
16. Veraart J, Novikov DS, Christiaens D, Ades-aron B, Sijbers J, Fieremans E. Denoising of diffusion MRI using random matrix theory. *NeuroImage*. (2016) **142**:394–406. doi: 10.1016/j.neuroimage.2016.08.016
17. Kellner E, Dhital B, Kiselev VG, Reisert M. Gibbs-ringing artifact removal based on local subvoxel-shifts. *Magnet Res Med*. (2016) **76**:1574–81. doi: 10.1002/mrm.26054
18. Jenkinson M, Beckmann CF, Behrens TE, Woolrich MW, Smith SM. FSL. *NeuroImage*. (2012) **62**:782–90. doi: 10.1016/j.neuroimage.2011.09.015
19. International Society of Ultrasound in Obstetrics and Gynecology (ISUOG). Sonographic examination of the fetal central nervous system for performing the 'basic examination' and the 'fetal neurosonogram'. *Ultrasound Obstet Gynecol*. (2007) **29**:109–16. doi: 10.1002/uog.3909
20. Le Bihan D, Breton E, Lallemand D, Aubin ML, Vignaud J, Laval-Jeantet M. Separation of diffusion and perfusion in intravoxel incoherent motion MR imaging. *Radiology*. (1988) **168**:497–505.
21. Yuan X, Yue C, Yu M, Chen P, Du P, Shao CH, et al. Fetal brain development at 25-39 weeks gestational age: a preliminary study using intravoxel incoherent motion diffusion-weighted imaging. *J Magn Reson Imaging*. (2019) **50**:899–909. doi: 10.1002/jmri.26667
22. Dietrich O, Raya JG, Reeder SB, Reiser MF, Schoenberg SO. Measurement of signal-to-noise ratios in MR images: influence of multichannel coils, parallel imaging, and reconstruction filters. *J Magn Reson Imaging*. (2007) **26**:375–85. doi: 10.1002/jmri.20969
23. Brouwer MJ, van Kooij BJ, van Haastert IC, Koopman-Esseboom C, Groenendaal F, de Vries LS, et al. Sequential cranial ultrasound and cerebellar diffusion weighted imaging contribute to the early prognosis of neurodevelopmental outcome in preterm infants. *PLoS ONE*. (2014) **9**:e109556. doi: 10.1371/journal.pone.0109556
24. Langworthy OR. Development of behavior patterns and myelinization of the nervous system in the human fetus and infant. *Contrib Embryol*. (1993) **139**:1–57.

25. Miller JH, McKinstry RC, Philip JV, Mukherjee P, Neil JJ. Diffusion-tensor MR imaging of normal brain maturation: a guide to structural development and myelination. *Am J Roentgenol.* (2003) **180**:851–9. doi: 10.2214/ajr.180.3.1800851
26. Bird CR, Hedberg M, Drayer BP, Keller PJ, Flom RA, Hodak JA. MR assessment of myelination in infants and children: Usefulness of marker sites. *AJNR Am J Neuroradiol.* (1989) **10**:731–40.
27. Barkovich AJ, Kjos BO, Jackson DE Jr, Norman D. Normal maturation of the neonatal and infant brain: MR imaging at 1.5T. *Radiology.* (1988) **166**:173–80.
28. Hayakawa K., Konishi Y, Kuriyama M, Konishi K, Matsuda T. Normal brain maturation in MRI. *Eur J Radiol.* (1990) **12**:208–15.
29. Gilles FH, Shankle W, Dooling EC. Myelinated tracts: growth patterns. In: Gilles FH, Leviton A, Dooling EC, eds. *The Developing Human Brain-Growth and Epidemiologic Neuropathology*. Boston: John Wright PSG Inc. (1983). p. 117–83.
30. Back SA, Luo NL, Borenstein NS, Volpe JJ, Kinney HC. Arrested oligodendrocyte lineage progression during human cerebral white matter development: dissociation between the timing of progenitor differentiation and myelinogenesis. *J Neuropathol Exp Neurol.* (2002) **61**:197–211. doi: 10.1093/jnen/61.2.197
31. Schneider JF, Confort-Gouny S, Le Fur Y, Viout P, Bennathan M, Chapon F, et al. Diffusion-weighted imaging in normal fetal brain maturation. *Eur Radiol.* (2007) **17**:2422–9. doi: 10.1007/s00330-007-0634-x
32. Chau V, Synnes A, Grunau RE, Poskitt KJ, Brant R, Miller SP. Abnormal brain maturation in preterm neonates associated with adverse developmental outcomes. *Neurology.* (2013) **81**:2082–9. doi: 10.1212/01.wnl.0000437298.43688.b9
33. Hagmann P, Sporns O, Madan N, Cammoun L, Pienaar R, Wedeen VJ, et al. White matter maturation reshapes structural connectivity in the late developing human brain. *Proc Natl Acad Sci USA.* (2010) **107**:19067–72. doi: 10.1073/pnas.1009073107
34. Gilmore JH, Smith LC, Wolfe HM, Hertzberg BS, Smith JK, Chescheir NC, et al. Prenatal mild ventriculomegaly predicts abnormal development of the neonatal brain. *Biol Psychiatry.* (2008) **64**:1069–76. doi: 10.1016/j.biopsych.2008.07.031
35. Goodlett CB, Fletcher PT, Gilmore JH, Gerig G. Group analysis of DTI fiber tract statistics with application to neurodevelopment. *Neuroimage.* (2009) **45**:133–42. doi: 10.1016/j.neuroimage.2008.10.06
36. Lockwood Estrin G, Kyriakopoulou V, Makropoulos A, Ball G, Kuhendran L, Chew A, et al. Altered white matter and cortical structure in neonates with antenatally diagnosed isolated ventriculomegaly. *Neuroimage Clin.* (2016) **11**:139–48. doi: 10.1016/j.nicl.2016.01.012

Conflict of Interest: The authors declare that the research was conducted in the absence of any commercial or financial relationships that could be construed as a potential conflict of interest.

frontiers in Neuroscience

ORIGINAL RESEARCH
published: 27 November 2019
doi: 10.3389/fnins.2019.01260

Influence of Repetitive Transcranial Magnetic Stimulation on Human Neurochemistry and Functional Connectivity: A Pilot MRI/MRS Study at 7 T

*Heidi Gröhn[1,2†], Bernadette T. Gillick[3†], Ivan Tkáč[1], Petr Bednařík[1,4], Daniele Mascali[5], Dinesh K. Deelchand[1], Shalom Michaeli[1], Gregg D. Meekins[6], Michael J. Leffler-McCabe[6], Colum D. MacKinnon[6], Lynn E. Eberly[7] and Silvia Mangia[1]**

[1] Department of Radiology, Center for Magnetic Resonance Research, University of Minnesota, Minneapolis, MN, United States, [2] Diagnostic Imaging Center, Kuopio University Hospital, Kuopio, Finland, [3] Department of Rehabilitation Medicine, University of Minnesota, Minneapolis, MN, United States, [4] Department of Biomedical Imaging and Image-guided Therapy, High Field MR Centre, Medical University of Vienna, Vienna, Austria, [5] Museo Storico della Fisica e Centro Studi e Ricerche "Enrico Fermi", Rome, Italy, [6] Department of Neurology, University of Minnesota, Minneapolis, MN, United States, [7] Division of Biostatistics, School of Public Health, University of Minnesota, Minneapolis, MN, United States

OPEN ACCESS

Edited by:
Itamar Ronen,
Leiden University, Netherlands

Reviewed by:
Anouk Schrantee,
VU University Medical Center Amsterdam, Netherlands
Paul Gerald Mullins,
Bangor University, United Kingdom
Uzay Emir,
Purdue University, United States

***Correspondence:**
Silvia Mangia
mangia@umn.edu

† These authors have contributed equally to this work and share first authorship

Specialty section:
This article was submitted to Brain Imaging Methods, a section of the journal Frontiers in Neuroscience

Received: *05 June 2019*
Accepted: *06 November 2019*
Published: *27 November 2019*

Citation:
Gröhn H, Gillick BT, Tkáč I, Bednařík P, Mascali D, Deelchand DK, Michaeli S, Meekins GD, Leffler-McCabe MJ, MacKinnon CD, Eberly LE and Mangia S (2019) Influence of Repetitive Transcranial Magnetic Stimulation on Human Neurochemistry and Functional Connectivity: A Pilot MRI/MRS Study at 7 T. Front. Neurosci. 13:1260. doi: 10.3389/fnins.2019.01260

Repetitive transcranial magnetic stimulation (rTMS) is a non-invasive brain stimulation method commonly used in the disciplines of neuroscience, neurology, and neuropsychiatry to examine or modulate brain function. Low frequency rTMS (e.g., 1 Hz) is associated with a net suppression of cortical excitability, whereas higher frequencies (e.g., 5 Hz) purportedly increase excitability. Magnetic resonance spectroscopy (MRS) and resting-state functional MRI (rsfMRI) allow investigation of neurochemistry and functional connectivity, respectively, and can assess the influence of rTMS in these domains. This pilot study investigated the effects of rTMS on the primary motor cortex using pre and post MRS and rsfMRI assessments at 7 T. Seven right-handed males (age 27 ± 7 y.o.) underwent single-voxel MRS and rsfMRI before and about 30-min after rTMS was administered outside the scanner for 20-min over the primary motor cortex of the left (dominant) hemisphere. All participants received 1-Hz rTMS; one participant additionally received 5-Hz rTMS in a separate session. Concentrations of 17 neurochemicals were quantified in left and right motor cortices. Connectivity metrics included fractional amplitude of low-frequency fluctuations (fALFF) and regional homogeneity (ReHo) of both motor cortices, strength of related brain networks, and inter-hemispheric connectivity. The group-analysis revealed few trends (i.e., uncorrected for multiple comparisons), including a mean increase in the concentration of the inhibitory neurotransmitter γ-aminobutyric acid (GABA) after the inhibitory rTMS protocol as compared to baseline in the stimulated (left) motor cortex (+8%, p = 0.043), along with a slight increase of total creatine (+2%, p = 0.018), and decrease of aspartate (−18%, p = 0.016). Additionally, GABA tended to decrease in the contralateral hemisphere (−6%, p = 0.033). No other changes of metabolite concentrations were

found. Whereas functional connectivity outcomes did not exhibit trends of significant changes induced by rTMS, the percent changes of few connectivity metrics in both hemispheres were negatively correlated with GABA changes in the contralateral hemisphere. While studies in larger cohorts are needed to confirm these preliminary findings, our results indicate the safety and feasibility of detecting changes in key metabolites associated with neurotransmission after a single 1-Hz rTMS session, establishing the construct for future exploration of the neurochemical, and connectivity mechanisms of cortical responses to neuromodulation.

Keywords: GABA, repetitive transcranial magnetic stimulation, magnetic resonance spectroscopy, resting-state functional MRI, motor cortex, inhibition, non-invasive brain stimulation, functional connectivity

INTRODUCTION

Repetitive transcranial magnetic stimulation (rTMS) is a non-invasive brain stimulation method commonly used in the disciplines of neuroscience, neurology, and neuropsychiatry to examine or modulate brain function. The effects of rTMS are transient, and critically dependent upon the location, frequency and intensity of stimulation. Low frequency rTMS (e.g., 1 Hz) is associated with a net suppression of the excitability of cortical structures beneath the site of stimulation while higher frequency stimulation (e.g., 5 Hz) has been shown to increase net cortical excitability. rTMS has been shown to have potential efficacy for treating both psychiatric and non-psychiatric disorders (Machado et al., 2008), such as posttraumatic stress disorder, obsessive compulsive disorder, auditory hallucinations in schizophrenia, pain syndromes, and for improving motor function in neurodegenerative diseases or following stroke. rTMS is currently FDA approved for the symptomatic relief of treatment-resistant depression. Despite the increasing development and use of rTMS in research and clinical applications, its mechanisms of action are still relatively poorly understood. Studies in animals and humans have provided evidence that rTMS protocols can influence the excitability and function of neurons (neuromodulation), both near to, and distant from, the site of stimulation (Dayan et al., 2013; Liew et al., 2014; Huang et al., 2017). While it is still unclear how local and distant changes in function induced by specific rTMS protocols are mediated, changes in the levels of excitatory and inhibitory neurotransmitters, glutamate and γ-aminobutyric acid (GABA), respectively, most likely play a critical role in neuromodulation effects.

Recent advancements in functional MRI (fMRI) (Van Essen et al., 2012; Smith et al., 2013; Glasser et al., 2016) and functional magnetic resonance spectroscopy (fMRS) (recently reviewed in Jelen et al., 2018; Stanley and Raz, 2018) have allowed monitoring functional connectivity and neurochemistry in the human brain with exceptional sensitivity and robustness. We showed that an extensive number of brain metabolites can be measured non-invasively in the human brain at ultra-high magnetic field of 7 T (Tkáč et al., 2001). We subsequently demonstrated that changes in neural activity are associated with relatively small changes in several metabolite concentrations which could be reliably detected at 7 T (Mangia et al., 2007a,b; Bednařík et al., 2015, 2018), as confirmed by other labs (Lin et al., 2012; Schaller et al., 2013, 2014; Boillat et al., 2019). The capability to measure these functional changes provides unique insights into how brain metabolism is associated with neural activity (Mangia et al., 2009). Importantly, extensive efforts are currently focused on optimizing methodologies of edited MRS at 7 T for further enhancing the reliability of detection of the inhibitory neurotransmitter GABA (Chen et al., 2017; Hendriks et al., 2018).

The majority of studies exploring the effect of rTMS on neurochemical concentrations have been performed after multiple sessions of rTMS on prefrontal cortex for applications mostly in depressive disorders, and also in schizophrenia and addiction (Zheng et al., 2010; Croarkin et al., 2016; Dubin et al., 2016; Qiao et al., 2016; Dlabac-de Lange et al., 2017; Hone-Blanchet et al., 2017; Bridges et al., 2018). High frequency (10–20 Hz) stimulation resulted in significant metabolic changes, however, findings showed large variability likely due to different stimulation protocols, patient populations and brain areas from which MR spectra were acquired. In healthy volunteers, an increase in the glutamate plus glutamine (Glx) level was observed both near the stimulation site and in remote brain regions after single and series of consecutive rTMS sessions (Michael et al., 2003). In another study, 5 weeks of 10-Hz rTMS induced increase in GABA in medial prefrontal cortex with no significant effect on Glx in depressive disorder patients (Dubin et al., 2016). However, 3 weeks of 10-Hz rTMS was found in another study induced an increase of Glx levels in the left dorsolateral prefrontal cortex of treatment responders (Yang et al., 2014). Notably, only two previous studies have investigated the acute effects of a single session of rTMS, applied to the motor cortex, on neurochemical concentrations. A local decrease of NAA in the stimulated motor cortex was found in healthy adult control volunteers as well as in adults with dystonia after 8 min of 5-Hz rTMS, while GABA slightly increased in the controls and slightly decreased in the adults with dystonia (Marjanska et al., 2013). Similarly, Stagg et al. (2009b) showed an increase in GABA levels of the stimulated site up to 20 min after a short 40-s period of continuous theta burst stimulation applied to healthy controls, without significant change in Glx.

Considering this variability, and the gaps in understanding of the mechanisms of action of rTMS, the primary aim of this pilot study was to assess the feasibility of detecting

rTMS-induced effects on high-resolution functional connectivity metrics and neurochemicals measured at 7 T with state-of-art methodologies. In particular, we chose to acquire the MRS data with semi-LASER sequence for robust, simultaneous measurement of the full neurochemical profile, including excitatory (glutamate) and inhibitory (GABA) neurotransmitters. Our main focus was the investigation of a 1-Hz inhibitory rTMS intervention applied outside the scanner for 20 min over the primary motor cortex of the presumed dominant hemisphere. We hypothesized that rTMS would induce changes in the neurochemical profiles and functional outcomes, and that trends of such changes could be detected at 7 T. Specifically, we expected that a low-frequency rTMS protocol (1-Hz rTMS) that typically suppresses motor cortical excitability for 15 to 60 min (Chen et al., 1997; Hoogendam et al., 2010) would be associated with increased GABA concentration in the ipsilateral hemisphere. Since 1-Hz rTMS also induces a lasting suppression of GABAergic interhemispheric inhibition (Pal et al., 2005), we also hypothesized that low frequency rTMS would be associated with decreased GABA and increased glutamate in the contralateral motor cortex.

An additional objective of this study was to assess the safety of the study design which combines two 7 T MRI sessions acquired immediately before and after, respectively, a prolonged rTMS intervention. In fact, similar pre- and post- assessment designs have been used safely at 3 T with rTMS of shorter duration (Stagg et al., 2009b; Marjanska et al., 2013). Ultra-high field MRI has been also used in combination with TMS assessment of cortical excitability (Dyke et al., 2017). However, in that study no post-assessment MRI was performed, and only single and paired-pulse TMS was applied which, unlike rTMS, do not evoke lasting changes in corticomotor excitability. For this reason, we could not exclude the possibility of potential interaction effects between the two 7T MRI sessions and the rTMS intervention.

MATERIALS AND METHODS

Subject Characteristics and Consent

Seven adult (21 – 40 y.o.), healthy, right-handed males were recruited for the study. They all received 1-Hz rTMS, and one additionally received 5-Hz rTMS in a separate session, 3 weeks after the 1-Hz protocol. Exclusion criteria included females (to avoid unknown risks on the unborn fetus of multiple 7 T MRI sessions and a prolonged rTMS intervention combined in one study visit), contraindications to MRI, diagnosis of a psychiatric disorder, substance abuse, epilepsy, neurological and/or cardiovascular disease, head trauma that may have caused traumatic brain injury, brain tumor or stroke, sleep apnea, history of anxiety, syncope, panic attacks and/or claustrophobia, being currently on any medication. The study protocol was approved by the Institutional Review Board: Human Subjects Committee of the University of Minnesota in accordance with the recommendations of The Code of Federal Regulations and the Declaration of Helsinki. A written informed consent was provided by each subject right before the beginning of the study. The study was registered on ClinicalTrials.gov (NCT02677740).

Experimental Design

The study consisted of one study visit during which resting state fMRI and MRS data were collected at 7 T before and after the rTMS intervention. The study started with the pre-rTMS MRI session, during which metabolite concentrations and functional connectivity outcomes were first measured at baseline. ^{1}H MRS data were acquired from the volumes of interest (VOIs) located in the left and right motor cortices based on anatomical landmarks of high-resolution MRI. After the pre-rTMS imaging session finished, the participant was transferred from the magnet to a room with the equipment for rTMS. The subject rested for about half an hour to 1 hour, which was deemed sufficient for minimizing possible effects of the exposure to the high magnetic field on cortical excitability (Schlamann et al., 2010). First, motor evoked potentials (MEP) were measured by delivering TMS, then the 20-min rTMS intervention was administered, and then the MEP were measured again. At the end of the rTMS session, the subject was directly returned to the MR scanner room for the post-rTMS MRI/MRS session, where great care was applied to ensure that the MRS VOIs were selected as close as possible to those of the pre-rTMS session. For both pre- and post-rTMS sessions, data were acquired in the following order: anatomical MRI, MRS from left then from right motor cortex and finally rsfMRI. Given the transitory nature of neuromodulatory effects, we did not randomize the MRI acquisition order to minimize the uncertainty of the post-assessment timings. Participants were instructed to remain awake during both rsfMRI and MRS acquisitions, and to keep their eyes closed during the rsfMRI acquisitions. Operator-participant verbal contact was maintained during the MRI sessions using the intercom system to verify compliance, wakefulness and comfort level.

Safety Assessments and Feasibility Metrics

Recruitment status (i.e., number of drop-outs and incomplete datasets), safety issues, symptoms questionnaires, and protocol timings (i.e., post-assessment delays from the rTMS intervention) were recorded. Blood pressure and heart rates were also measured within 5 min before and after the rTMS intervention. Blood oxygenation and pulse rate were additionally measured with an MRI-compatible oximeter during the MRI sessions to monitor vital signs. Each participant was evaluated for any adverse event throughout the study. A medical director was present throughout the rTMS session and the second imaging session. The medical director reviewed all participant outcomes including responses to report of symptoms questionnaires after the MRI and rTMS sessions, along with the vital signs (blood pressure and heart rate before rTMS, blood oxygenation, and heart rate during the MRI scan), and approved continuation of the study after each session. A designated medical monitor was assigned to review any adverse event that occurred.

TMS, rTMS, and Neurophysiological Outcomes

TMS was delivered using a 70-mm figure-eight TMS coil connected to a Magstim 200 machine. The coil was positioned

over the hand region of the left motor cortex (approximately 5 cm lateral to each individual vertex of the head), contralateral to the dominant hand in all studied participants. The coil was oriented to a position tangential to the scalp and with the handle pointing posterolaterally at an approximately 45-degree angle to the sagittal line. TMS-induced MEPs were recorded by placing surface EMG electrodes over the first dorsal interosseous muscle of the participant's dominant hand, contralateral to the side of TMS. Stimulation was set to an initial intensity to evoke a discernable MEP amplitude. The position of the coil was moved systematically to find the location that evoked the largest and most reliable MEP ("hotspot").

The resting motor threshold (RMT) was the primary neurophysiologic outcome, and was defined as the minimum TMS intensity required to produce a 50 μV MEP while the participant was at rest. RMT was determined by progressively lowering the intensity until MEPs $\geq$ 50 μV peak-to-peak were evoked in at least 5 of 10 successive stimuli.

Immediately after completion of the RMT assessment, the rTMS intervention began. Participants received either 1-Hz (7 subjects) or 5-Hz (1 subject) rTMS, applied over the motor cortex hotspot contralateral to the dominant arm for 20–22 minutes at an intensity of 90% RMT (1-Hz rTMS: train of 10 pulses, 1 s wait time between trains, 120 trains, total pulses = 1200; 5-Hz rTMS: train of 25 pulses, 45 s wait time between trains, 24 trains, total pulses = 600). This number of stimuli were well within the published safety guidelines for use of rTMS (Wassermann, 1998). Corticospinal excitability was finally re-tested within no more than 10 min after the rTMS session using the same protocol as the pre-test.

MRI/MRS Acquisitions

The imaging sessions were performed using a 7-T/90-cm magnet (Agilent/Magnex Scientific, United Kingdom) equipped with a powerful gradient/shim coil (SC72, Siemens, Germany; maximum gradient strength of 70 mT/m; maximum second-order shim strength of 4.5 mT/m^2 except for Z^2 which was about 9 mT/m^2) and interfaced to a Siemens Syngo console. A single channel transmit/32-channel receive head (NOVA Medical, Wilmington, MA, United States) was used in combination with dielectric pads (Teeuwisse et al., 2012; Schaller et al., 2014). High permittivity water/titanate-based (30–50% v/v) dielectric pads (5–8 mm thick) were carefully placed on the participant's head above the central sulcus, so that each pad covered the primary motor cortex on one hemisphere. This approach enabled to generate B_1 over 25 μT within the VOI in the motor cortex. Head motion was minimized using a molded foam head cushion and padding placed snugly around the participant's head.

High-resolution 3D-MPRAGE images (TR = 2.5 s, TE = 2.42 ms, TI = 1.5 s, flip angle = 5^o, isotropic resolution = 1 × 1 × 1 mm^3, acquisition time of 5 min) were first obtained to visualize the anatomical structure of the motor cortices. Proton density images (TR = 1.42 s, TE = 2.42 ms, flip angle = 5^o, isotropic resolution = 1 × 1 × 1 mm^3, acquisition time of approximately 1.5 min) were also acquired as reference to allow normalization of the T_1-weighted signal intensities of MPRAGE images across the field of view (Van de Moortele et al., 2009). Then automatic B_0 field mapping and adjustment of 1st- and 2nd-order shims were achieved by FASTMAP with EPI readout (Gruetter and Tkáč, 2000). Spectroscopy VOIs (24 × 22 × 17 mm^3) were selected in left and right motor cortices based on anatomical landmarks (**Figure 1**). ^{1}H-MRS data were acquired using the semi-LASER localization sequence optimized for 7 T (Oz and Tkáč, 2011; Bednařík et al., 2015) with the gradient-modulated FOCI pulses for reducing the demands on maximum B_1 (TE = 28 ms, TR = 9 s, 64 scans, spectral width 6 kHz). The localization sequence included VAPOR water suppression interleaved with the outer-volume saturation (Tkáč and Gruetter, 2005). Unsuppressed water signal was also acquired from each VOI, which has been used for eddy current correction (Klose, 1990) and as an internal reference for metabolite quantification.

At the end of the MRS acquisitions, the dielectric pads were removed, T_1-weighted anatomical scans acquired again, and resting state fMRI performed with a 2D single-shot gradient echo EPI sequence to collect blood oxygenation level dependent (BOLD) data. Acquisition parameters were as follows: FOV = 208 × 208 mm^2, matrix = 104 × 104, 72 slices, slice thickness = 2 mm (resolution 2.0 × 2.0 × 2.0 mm^3), TR/TE = 1200/20 ms, flip angle = 45°, BW = 2003 Hz/pixel, iPat = 2, multiband factor = 3. A total of 280 volumes were acquired, corresponding to an acquisition time of approximately 6 min. Spin Echo based field maps were also collected for correction of image distortions (Smith et al., 2013; Sotiropoulos et al., 2013).

MRI/MRS Data Processing

Single-scan MRS data were corrected for small frequency and phase variations, summed and finally corrected for the residual eddy current effects using unsuppressed water signal (Klose, 1990). Brain metabolites were quantified by LCModel (Provencher, 1993, 2001; Pfeuffer et al., 1999; Tkáč et al., 2009) using a basis set of nineteen brain metabolites simulated with a spin density matrix approach (Henry et al., 2006), which included: alanine (Ala), ascorbate (Asc), aspartate (Asp), creatine (Cr), γ-aminobutyric acid (GABA), glucose (Glc), glutamate (Glu), glutamine (Gln), glutathione (GSH), glycerophosphocholine (GPC), *myo*-inositol (Ins), *scyllo*-inositol (sIns), lactate (Lac), N-acetylaspartate (NAA), N-acetylaspartylglutamate (NAAG), phosphocholine (PC), phosphocreatine (PCr), phosphoethanolamine (PE), and taurine (Tau). In addition, a spectrum of fast-relaxing macromolecules (MM) was also included in the basis set. Intensities of singlet resonances (CH_3 groups) in the basis set spectra of NAA, NAAG, GPC, PC, Cr, and PCr were corrected for differences in T_2 signal attenuation at TE = 28 ms between CH_3 groups (T_2 = 95 – 152 ms) relative to CH and CH_2 groups within the same molecule (T_2 = 84 – 95 ms) (Marjanska et al., 2012). High-resolution MRI data were used for 3D whole brain segmentation. The probabilistic maps of the gray matter (GM), white matter (WM), and cerebrospinal fluid (CSF) were calculated with SPM12[1] (Ashburner and Friston, 2005) from the T_1-weighted MPRAGE

[1]https://www.fil.ion.ucl.ac.uk/spm/

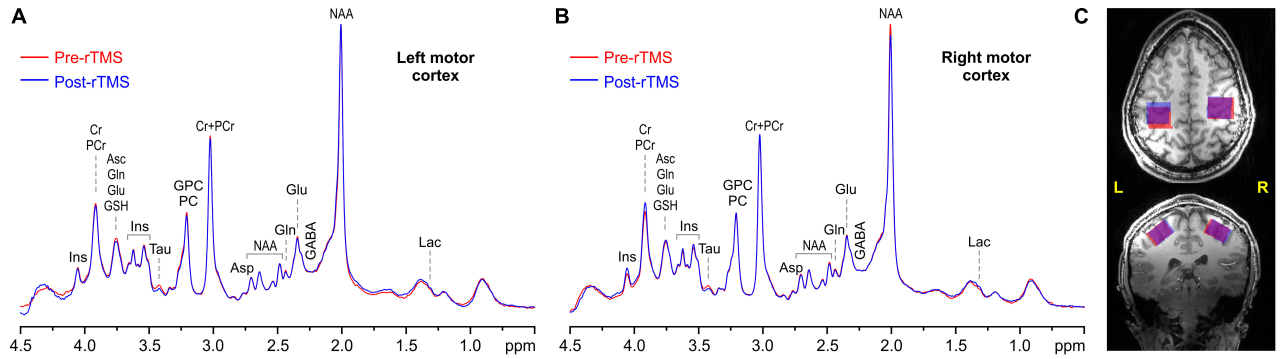

FIGURE 1 | Representative example spectra acquired pre (red) and post 1-Hz rTMS (blue) from the left **(A)** and right **(B)** VOIs, along with VOI placements **(C)** in the motor cortices in axial (top) and coronal (bottom) view (overlap is in purple). MRS acquisition parameters: 7 T, semi-LASER, 64 scans, TR = 9 s, and TE = 28 ms.

images that were normalized using the proton density reference (Van de Moortele et al., 2009). An in-house routine written in MATLAB R2009 was used to determine the volume fractions of GM, WM, and CSF in each VOI by adopting an iterative method of threshold selection (Ridler and Calvard, 1978). The CSF fraction was used to assess the brain tissue volume for each VOI selected for MRS. The tissue water content was calculated using GM and WM volume fractions in the VOIs and GM and WM water contents of 84% and 70%, respectively (Randall, 1938). Metabolite concentrations were additionally corrected for T_2-relaxation. Relaxation times of water (T_2 = 47 ms) and metabolites (T_2 = 90 ms, average value for CH and CH_2 groups) in occipital lobe (Marjanska et al., 2012) were multiplied by the factor 1.2 to correct for the CPMG effect of the semi-LASER RF pulse train. Only metabolite concentrations quantified with Cramèr-Rao lower bounds (CRLB) below 50% were included in further analysis. Finally, the overlap between pre- and post-rTMS VOI selection was evaluated, and quantification correlations among each metabolite as calculated in LCModel were extracted for all 4 spectra of one representative subject.

rsfMRI Data Processing

Resting-state data were preprocessed with the HCP "minimal-preprocessing pipeline" (Glasser et al., 2013), and denoised with the FMRIB's independent component analysis (ICA)-based X-noiseifier (FIX, Salimi-Khorshidi et al., 2014), which removes slow drifts (via a gentle high-pass filter with a 2000 s cutoff), motion-derived parameters (24 motion time series constructed from the 6-realignment parameters) and structured noise. We additionally regressed out the global signal (Burgess et al., 2016) and applied a low-pass filter (0.09 Hz cutoff) to remove non-structured and high frequency noise, respectively. Finally, the volume data were smoothed with an isotropic Gaussian kernel at 4 mm FWHM.

Resting-state activity (**Figure 2**) was quantified by examining various parameters, including the fractional amplitude of low-frequency fluctuations (fALFF, Zou et al., 2008), the regional homogeneity (ReHo, Zang et al., 2004), the global strength of the networks arising from the motor cortices, and the inter-hemispheric connectivity between the motor cortices. In particular, fALFF, which is thought to reflect the intensity of spontaneous brain activity, was calculated via AFNI function 3dRSFC (Cox, 1996) as the ratio of the power spectrum within the frequency range of interest ($0.008 < f < 0.09$ Hz) to that of the entire spectrum. ReHo, a measure of local synchronization, was calculated as the Kendall's coefficient of concordance among a given voxel time series and the time series of its 18 nearest neighbors (3dReHo, AFNI). fALFF and ReHo were computed for each voxel in the brain and were then averaged within the left and right motor cortices, separately. These two regions of interest (ROIs) were identified in the upper limb region of the precentral gyrus, as defined in the Brainnetome atlas (Fan et al., 2016). The

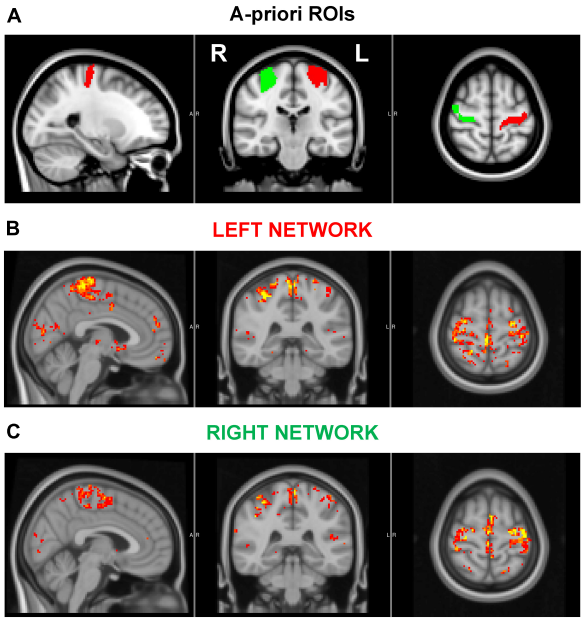

FIGURE 2 | (A) *A priori* regions of interest (ROIs). **(B–C)** Associated left **(B)** and right **(C)** motor cortex networks used in functional connectivity analyses. The ROIs encompassed the upper limb region of the precentral gyrus, as defined in the Brainnetome atlas. The displayed networks were calculated at a group level as described in the text.

strength of the network, arising from either the ipsilateral or contralateral motor cortices, was obtained by first computing the seed-based connectivity map as the Pearson's correlation between the average time series within the seed (either the left or right ROI) and the time series at each other voxel within the brain. Then, for each subject and seed, the network strength was defined as the average of the z-Fisher-transformed connectivity map within a group-level network, obtained via a one-sample, one-tail, *t*-test on the connectivity maps of the pre and post-intervention data ($p < 0.001$, minimum cluster size 20). The inter-hemispheric connectivity was calculated as the z-fisher-transformed Pearson's correlation between the average time-courses of right and left ROIs. Finally, the framewise displacement as defined in Power et al. (2012) was computed to assess head movements during functional acquisitions.

Statistical Analyses

VOI overlaps, VOI tissue compositions, signal-to-noise ratios (SNRs), and spectra linewidths were first subjected to comparisons with 2-sided paired *t*-test to ensure the absence of systematic biases in the datasets induced by VOI placements left vs. right, and pre- vs. post-rTMS where applicable (i.e., except VOI overlaps). Pre-rTMS metabolite concentrations were also compared between left and right motor cortices with 2-sided paired *t*-tests for further characterizing neurochemical profiles at baseline. Pre- vs. post-rTMS comparisons of metabolite concentrations and functional connectivity metrics were carried out with 2-sided paired *t*-test separately for left and right motor cortices where applicable (i.e., except inter-hemispheric connectivity). Given the nature of the study as a pilot investigation, multiple testing corrections to type I error were not applied. Finally, exploratory Pearson correlation analyses were performed between percent changes of connectivity metrics and MRS outcomes (namely glutamate and GABA concentrations). Since only one participant received the 5-Hz rTMS, analyses of rTMS-induced changes and their correlations were performed only on the 1-Hz rTMS dataset ($N = 7$). Results are presented as mean ± SD, and Pearson correlations are reported with 95% CI.

RESULTS

Safety, Feasibility, and Neurophysiological Outcomes

All recruited participants (ages 27 ± 7 y.o.) completed the study and provided a complete and usable dataset. Symptoms reported after each 7T MRI session were expected, occasional, and did not increase after the rTMS intervention. In particular, after the first MRI session, one participant reported metallic taste, one sleepiness and warmth, and one sleepiness and metallic taste. After the second MRI session, two participants reported sleepiness. The rTMS intervention did not increase symptoms reported prior to its administration. Indeed, one participant reported sleepiness, anxiety/worry/nervousness, headache, and tooth pain before and after the rTMS intervention. Two other participants reported either sleepiness, or sleepiness and anxiety/worry/nervousness, before but not after the rTMS intervention. Finally, one participant reported shoulder pain the day after the study. Vital signs were within physiological ranges during the entire study duration for all subjects.

There was no significant difference in the RMT before and after 1-Hz rTMS (mean change = 4.4 ± 13.4%; $p = 0.416$). Four participants showed an increase in RMT after receiving 1-Hz rTMS, which is consistent with a decrease in cortical excitability, but 3 participants showed an average decrease in motor threshold. In the participant that received 5-Hz rTMS, a 36% increase in motor threshold was observed. The delays of MRI/MRS post-assessments from the end of the rTMS intervention were (32 ± 3) min for MRS in left VOI, (59 ± 6) min for MRS in right VOI, and (84 ± 8) min for rsfMRI.

MRS Outcomes

Overlap between pre-rTMS and post-rTMS VOIs tended to be slightly higher in right (91 ± 4)% vs. left (85 ± 7)% motor cortex ($p = 0.035$). On the other hand, VOI compositions included on average (7 ± 3)% CSF, (48 ± 6)% GM, and (44 ± 7)% WM, with no significant difference between left and right VOIs, or pre- and post-rTMS. The combination of high magnetic field, sensitive RF coil, use of dielectric pads, highly efficient B_0 shimming, and full signal intensity semi-LASER localization sequence allowed obtaining artifact free spectra (**Figure 1**) with high signal-to-noise ratio (210 ± 27) and spectral resolution (FWHM = 10.2 ± 0.9 Hz, assessed from total Cr signal at 3 ppm) from all datasets, again with no significant differences between left and right VOIs, or pre- and post-rTMS.

Seventeen metabolites and the MM content were quantified (**Figure 3**) with average CRLB below 30%, among which Cr, PCr, GSH, Gln, Glu, *myo*-Ins, NAA, NAAG, PE, Tau and total choline (GPC + PC) and total creatine (Cr + PCr) had CRLBs below 10%. Macromolecules had 2% average CRLB. Only 4 out of 32 values of Glc and 5 out of 32 values of *s*Ins were excluded from the final analysis because of their CRLBs above 50%. The average CRLB of GABA and glutamate were 13% and 2%, respectively. In absolute terms, the values of CRLBs in concentration units were <0.2 μmol/g for most metabolites. In left motor cortex, the primary outcomes of interest, namely GABA and glutamate, had average concentrations of (1.70 ± 0.25) μmol/g (15% c.v.) and (8.89 ± 0.51) μmol/g (6% c.v.), respectively. Among the quantified metabolites, there was strong negative correlation between PCr and Cr, but both metabolites were consistently quantified in all subjects with very low CRLB (∼4%). Therefore, individual values could still be considered reliable. No negative correlations of GABA with any metabolite were observed. Correlation between GABA and MM was also negligible, ranging from −0.15 to −0.08.

At baseline (i.e., pre-rTMS), several metabolite concentrations had higher concentration in right vs. left motor cortex, including GABA (24%, $p = 0.002$), glutamate (8%, $p = 0.003$), glutamine (16%, $p = 0.001$), Cho (6%, $p = 0.019$), Ins (7%, $p = 0.003$), GSH (18%, $p = 0.041$), and NAA (6%, $p = 0.011$).

After the 1-Hz rTMS intervention (**Figure 4**), GABA concentration in the ipsilateral (left) motor cortex increased on average by 8% as compared to pre-rTMS ($p = 0.043$), while in the

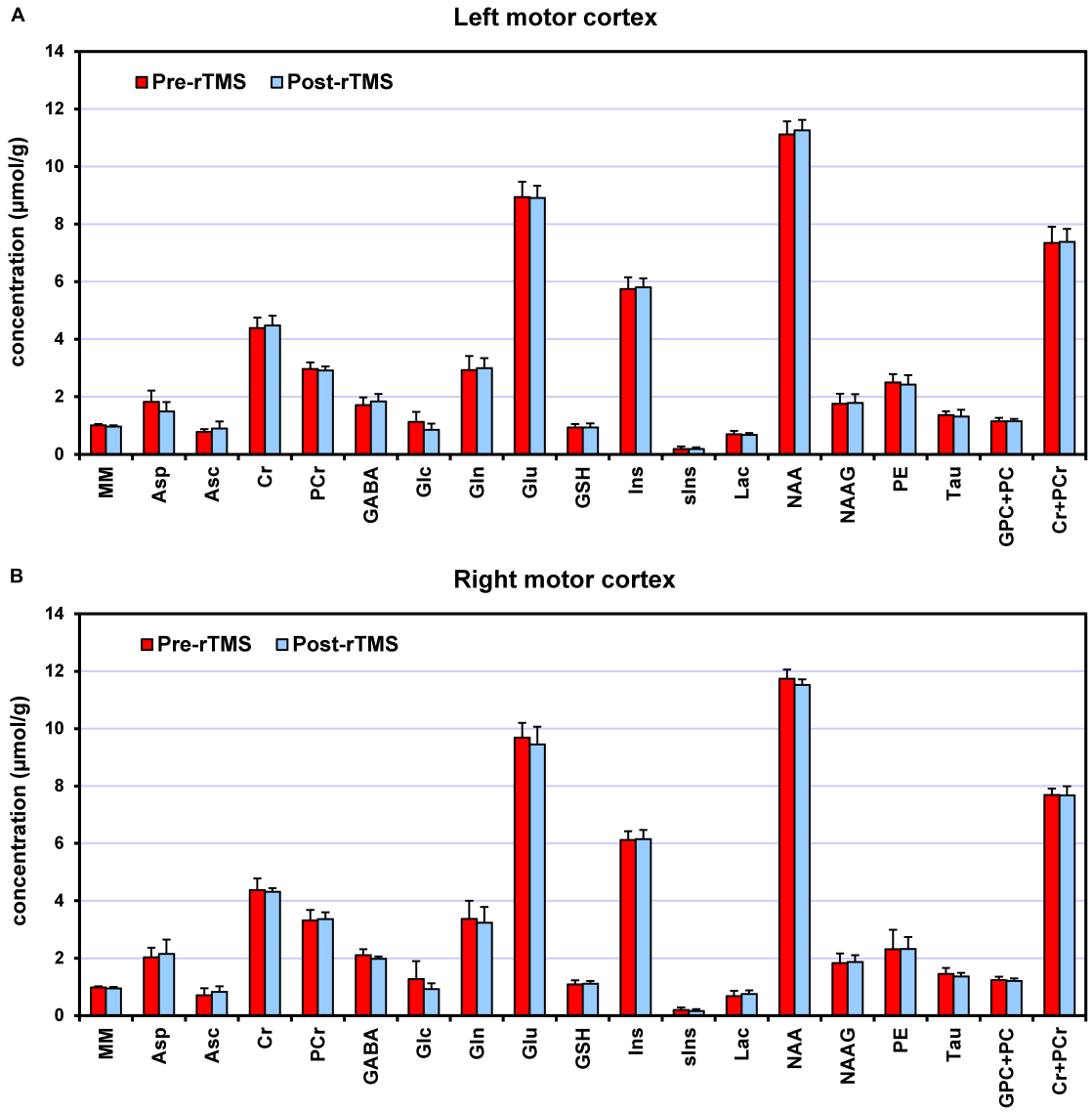

FIGURE 3 | Neurochemical profiles pre-rTMS (red) and post-rTMS (blue), from left **(A)** and right **(B)** motor cortices. Bar diagrams show mean ± SD across the subjects who underwent the 1-Hz rTMS (*N* = 7).

contralateral (right) motor cortex, decreased by 6% ($p = 0.033$). Opposite changes in GABA were seen in the only subject who underwent the 5-Hz rTMS. No significant changes in glutamate levels were detected in either left or right motor cortices.

No other metabolites exhibited significant concentration changes, except Cr (2%, $p = 0.016$) and Asp (−18%, $p = 0.018$) in the ipsilateral motor cortex. To check for robustness to parametric assumptions, paired comparisons were repeated with non-parametric Wilcoxon signed-rank tests; conclusions were no different and these results are not presented.

Functional Connectivity Outcomes

Head movements quantified by the framewise displacement were similar during pre-rTMS (0.17 ± 0.07 mm) and post-rTMS (0.16 ± 0.07 mm) rsfMRI acquisitions. None of the connectivity metrics showed significant rTMS-induced changes after the 1-Hz rTMS. However, as shown in **Figure 5**, percent changes in GABA concentration of the contralateral (right) motor cortex were negatively correlated with percent changes of fALFF in contralateral motor cortex ($r = -0.85$, $p = 0.013$, CI = −0.98; −0.26), as well as with percent changes of fALFF ($r = -0.99$, CI = −1; −0.92; $p < 0.0001$), and ReHo ($r = -0.98$, CI = −1; −0.88; $p < 0.0001$) in ipsilateral (left) motor cortex. No other significant correlations were observed.

DISCUSSION

In the present pilot investigation, we confirmed the feasible and safe integration of state-of-the-art MRS and rsfMRI at 7 T

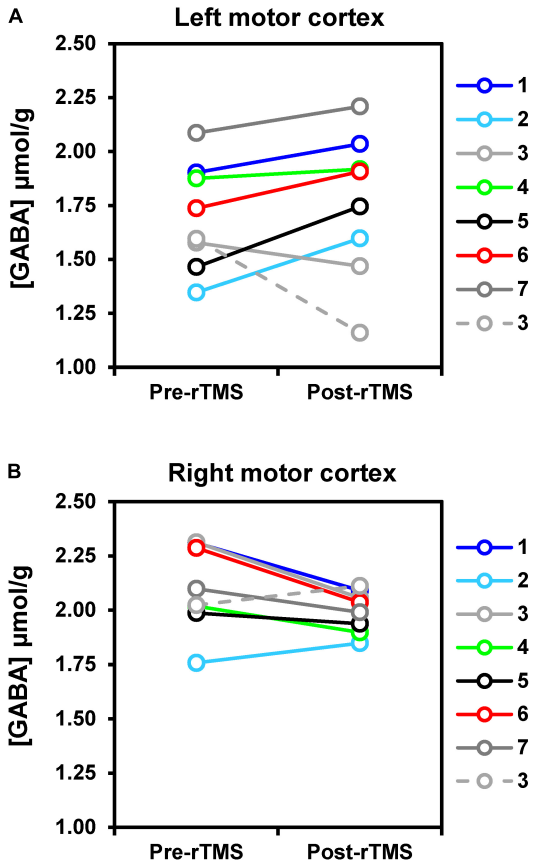

FIGURE 4 | rTMS-induced changes of GABA concentrations in left **(A)** and right **(B)** motor cortices. Solid lines represent data obtained with 1-Hz rTMS intervention ($N = 7$), while the dashed line refers to the one subject (namely subj. 3) who received 5-Hz rTMS in a separate study visit. Changes in GABA levels were small but detectable with statistical significance at uncorrected p-value. In particular, GABA increased by 8% on average after rTMS as compared to pre-rTMS in the motor cortex ipsilateral to the stimulation ($p = 0.043$), whereas it decreased by 6% on average in the right motor cortex ($p = 0.033$).

with rTMS interventions to measure changes in neurochemical profiles and functional connectivity metrics induced by rTMS. For this purpose we primarily focused on an inhibitory 1-Hz rTMS protocol applied over the primary motor cortex. The study was conducted on young, healthy males with the intent to minimize compounding the data with uncertain hormonal effects, as well as to avoid unknown risks to the unborn fetus of prolonged rTMS and multiple 7 T MRI sessions combined in one study visit.

1-Hz rTMS over the primary motor cortex had variable influence on RMT. While 4 participants showed the expected increase in threshold, 3 participants showed a decrease in threshold. This variability is expected given the known variability in response amplitude and polarity to rTMS across individuals (Lopez-Alonso et al., 2014; Huang et al., 2017).

On the other hand, the quality of acquired ^{1}H MR spectra resulted in neurochemical profiles of high inter-subject and intra-session reproducibility. High inter-session reproducibility of spectra acquired at 7 T with semi-LASER was demonstrated in previous studies by our group (Bednařík et al., 2018; Cheong et al., 2019). In order to minimize biases introduced by VOI compositions or by relaxation effects, the MRS post-processing pipelines included the different water content of GM, WM, and CSF fractions in each dataset (Gasparovic et al., 2006). For the first time, the pipelines also included the signal amplitude correction applied on metabolite basis spectra to account for differences in T_2-relaxation between CH_3 groups and other protons in the same molecule. Ultimately, the entire acquisition and processing strategy allowed the reliable quantification of an extensive set of neurochemicals. Of particular note is the quantification of GABA. The average CRLB (13%) and across-subjects coefficient of variation (15%) obtained with semi-LASER were similar to those observed with edited-MRS sequences at 7 T (Chen et al., 2017; Hendriks et al., 2018). A direct comparison of acquisition strategies in same subjects is still warranted to ultimately identify the most accurate and sensitive approach for GABA detection in functional MRS designs. Yet, the results of the present study indicate that semi-LASER can be suitable to detect small functional changes in GABA levels, despite the large overlaps of other resonances typical of non-edited MRS approaches. In fact, whereas handling of macromolecules can have major effects on metabolite quantification, especially GABA, the inclusion of MM spectrum in the LCModel basis set resulted in high precision of MM content assessments, and minimized the negative correlation between GABA and MM quantification. The absence of strong negative correlations between GABA and any other metabolite quantified in LCModel further supports a reliable estimate of GABA with short echo-time semi-LASER sequence. Trends of small rTMS-induced changes were ultimately detected in GABA levels of both ipsilateral and contralateral motor cortices. The increase in GABA concentration post-rTMS in the ipsilateral cortex, along with its decrease in the contralateral cortex, were in line with our initial hypothesis on GABA. However, the creatine and aspartate findings in the contralateral cortex were unexpected, and the explanation has not been resolved yet. In addition, the hypothesized decrease in glutamate levels in the contralateral motor cortex post-rTMS was not detected in this study despite the exceptional accuracy and reliability of glutamate quantification at 7 T as confirmed by an average CRLB of only 2%. Moreover, some unexpected differences in metabolite concentrations, including GABA and glutamate among others, were observed at baseline (i.e., pre-rTMS) between left and right motor cortices. The lack of randomization in the order of left and right MRS acquisitions unlikely explains such finding, as there are no conceivable dynamic events that may compound concentrations of selected metabolites in the absence of tasks or interventions. If corroborated by future research, the inter-hemispheric difference of neurochemical profiles would be interesting and informative, as it may uncover neurochemical imbalances that are potentially instrumental to support dominant and non-dominant hemisphere functions. However, further studies are necessary to specifically evaluate if and to what

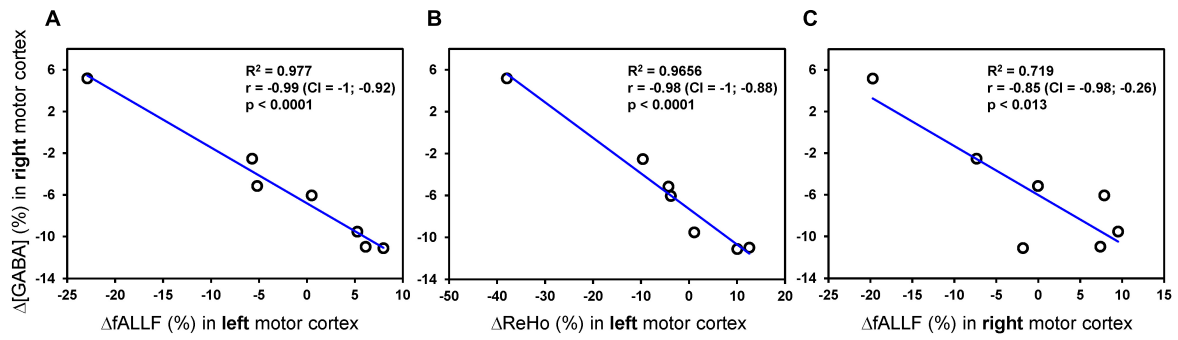

FIGURE 5 | Pearson correlations analyses between rTMS-induced percent changes of MRS and connectivity metrics. Only Pearson correlations with $p < 0.05$ (uncorrected) are displayed. The plots show a strong linear relationship between percent changes of GABA concentration [Δ(GABA)] in contralateral (right) motor cortex and both ΔfALLF **(A)** and ΔReHo **(B)** in ipsilateral (left) motor cortex. A similar relationship, but with more variance, was seen with the ΔfALLF in contralateral (right) motor cortex **(C)**.

degree was the data acquisition affected by the chemical shift displacement error in the same direction. Therefore, acquiring MRS data with opposite gradient polarity would be helpful to eliminate possible biases.

Our finding of increased GABA concentration after 20 min of inhibitory 1-Hz rTMS in the dominant motor cortex are similar to what reported by Marjanska et al. (2013), who also found a mild GABA increase after 8 min of excitatory 5-Hz rTMS in healthy volunteers by using edited MRS at 3 T for selective detection of NAA, Glx and GABA. The finding also resembled the GABA increase measured 20 minutes after 40-s of continuous theta burst stimulation (Stagg et al., 2009b). While there is a relative paucity of studies employing MRS and rTMS interventions applied to the motor cortex, metabolic changes in such brain areas have been more extensively studied in correspondence of transcranial direct current stimulation (tDCS), which is another form of neuromodulation that utilizes constant, low direct current delivered via electrodes to the head. Similar to high vs. low frequency rTMS protocols, the anodal and cathodal forms of tDCS increase or decrease neuronal excitability, respectively. In particular, anodal tDCS applied over the motor cortex using various protocols has been found to cause significant decrease in GABA concentration in the ipsilateral motor cortex (Stagg et al., 2009a; Kim et al., 2014; Bachtiar et al., 2015, 2018; Antonenko et al., 2019; Patel et al., 2019). Few tDCS MRS studies have been conducted at 7 T on the same premise of the present study that sensitivity and reliability of metabolic measurements largely benefit from ultra-high magnetic fields (Stagg et al., 2009a; Kim et al., 2014; Ryan et al., 2018). Yet the results of these tDCS 7 T investigations have been variable. No changes in Glu or GABA were observed in correspondence of bihemispheric tDCS (Ryan et al., 2018), while cathodal stimulation was reported to either induce a significant decrease in Glu/Cr (Stagg et al., 2009a) or no observable Glu change (Kim et al., 2014).

Functional changes in glutamate levels *during* sensory stimulation are generally ascribed to increased energetic demands, rather than to variations of the (small) synaptic pool due to increased neurotransmission (Mangia et al., 2009). However, the link to energetics likely does not apply for study designs investigating metabolite changes 20–30 min *after* a prolonged neuromodulatory interevention, at which point the energy balance has concivably gone back to baseline. In this case, it is rather plausible that changes in glutamate and/or GABA levels result from the sustained neuromodulatory effects of the intervention *per se*. Indeed, rTMS produce changes in ipsilateral corticomotor excitability lasting 15–60 min post-stimulation in healthy adults (Chen et al., 1997; Hoogendam et al., 2010). Thus, inhibitory (1 Hz) and excitatory (5 Hz) rTMS protocols would be expected to substantially increase the pools of GABA and glutamate concentrations, respectively. This timeframe may allow for a more reliable signal and the detection of changes within the synaptic pool. The fact that changes in neurotransmitter levels observed after neuromodulatory interventions are not related to energetics is consistent with the lack of concomitant changes in lactate and glucose that are typically observed during external stimuli.

Our data do not support changes in T2* 30–60 min after a 20-min long rTMS intervention, as the spectra line-widths of the post-assessments were not different from those of the pre-assessments. On the other hand, fMRI signal changes due to T2* alterations are commonly observed during or shortly after TMS of the motor cortex (Liew et al., 2014 and reference therein; Navarro de Lara et al., 2017), consistent with the acute effects of TMS on cortical excitability. The marked differences in acquisition protocols and assessment timings, along with the limitations of prolonged MRS acquisitions to detect T2* changes, may explain the differences in results. In fact, it should be emphasized that our study was not designed to quantify T2*, and spectra LW may be compounded by imperfect voxel re-positioning and changes in shimming during the acquisition.

No rTMS-induced changes were observed in any of the metrics measured to characterize local and distant connectivity of the motor cortices, possibly due to the prolonged delay of the post-assessment from the rTMS intervention. In a previous study by Watanabe et al. (Watanabe et al., 2014)

connectivity between bilateral primary motor cortices was found to be higher 10 minutes after 30-min of inhibitory 1-Hz rTMS as compared to the inter-hemispheric connectivity measured 1 week before the rTMS session, however, longer aftereffects were not investigated. Another study by Ji et al. (2017) found that, whereas 30 min of inhibitory 1-Hz rTMS increased connectivity in the left paracentral gyrus, the effect lasted only up to 10 min after the intervention. Despite the lack of statistically significant connectivity changes after rTMS, negative correlations were found between percent changes of few connectivity metrics in both hemispheres and GABA changes in contralateral motor cortex. The implications of these relationships should be validated and explored with future studies in larger cohorts. Interestingly, a negative correlation between GABA and functional connectivity was also previously noticed in motor cortex during tDCS (Stagg et al., 2014; Bachtiar et al., 2015).

Limitations

This pilot study was limited by the small number of participants, therefore no firm conclusions can be drawn until the findings are confirmed in larger cohorts. Yet our preliminary GABA findings are promising and consistent with common understanding of the mechanisms of rTMS as well with some previous literature. Calculations of sample sizes for future studies can be based on the findings of the present pilot investigation by carefully accounting for multiple comparison corrections according to the number of intended primary outcomes and general study design (e.g., number of regions of interest). Another limitation was the timing between the neuroimaging and neuromodulatory intervention. To avoid unforeseen problems related to the use of rTMS inside the 7 T magnetic field, we administered rTMS outside the scanner. The careful evaluation of the neurophysiology of the subject after rTMS, along with the optimization procedures needed for MRS acquisitions, led to 32, 59, and 84 min delays on average of the post-assessments MRS in left and right motor cortices, and rsfMRI, respectively. Despite this substantial delays, we could still detect rTMS-induced changes in GABA, although the delay was most likely too long for observing changes in functional connectivity. Simultaneous TMS/fMRI acquisitions at 3 T have been recently reported in the literature by implementing a dedicated multi-channel coil (Navarro de Lara et al., 2017), and such approach may be used for monitoring more efficiently the acute effects of rTMS on functional connectivity. However, the safety of TMS inside a 7 T scanner has not yet been shown, and would thus need to be established with future studies. The single-voxel MRS performance of a dedicated coil for simultaneous TMS/MRI would also need to be evaluated separately.

Conclusion

We conclude that single-voxel 7 T MRS with semi-LASER allows safe and reliable measurements of rTMS-induced changes in the full neurochemical profiles of motor cortices. GABA changes were detected with statistical significance after the rTMS despite the small sample size of 7 subjects and despite prolonged delays from the rTMS. On the other hand, post-assessment timing needs to be further optimized to allow detection of putative functional connectivity changes. Future investigations exploring the correlation between neuromodulation and neuroimaging are indicated, in concert with the influence on motor function and outcomes. Such investigations open tremendous opportunities for understanding the mechanism of actions of neuromodulation strategies by characterizing the mediation of key neurotransmitters such as GABA and glutamate. They also hold promise in discovering potential biomarkers for responders to neuromodulatory interventions, and optimizing functional outcomes.

DATA AVAILABILITY STATEMENT

The datasets generated for this study are available on request to the corresponding author.

ETHICS STATEMENT

The studies involving human participants were reviewed and approved by the Institutional Review Board: Human Subjects Committee of the University of Minnesota. The participants provided their written informed consent to participate in this study.

AUTHOR CONTRIBUTIONS

HG and BG participated in design of the work, acquisition, analysis and interpretation of the data, and preparing the manuscript. IT participated in analyses and interpretation of the data, and preparing the manuscript. PB participated in acquisition and analyses of the data, and editing the manuscript. DM and DD participated in analyses of data, and preparing the manuscript. SMi participated in design of the work, interpretation of the data, and editing the manuscript. GM and ML-M participated in acquisition of the data, interpretation of the data, and editing the manuscript. CM participated in design of the work, acquisition and analysis of the data, interpretation of the data, and editing the manuscript. LE participated in analysis of the data, interpretation of the data, and editing the manuscript. SMa participated in design of the work, analysis and interpretation of the data, and preparing the manuscript.

FUNDING

This research was supported by the University of Minnesota (Medical School Innovation Grant), the National Institutes of Health (P41 EB015894, P30 NS076408, and K01 HD078484), and the Instrumentarium Science Foundation, Finland. PB was partially supported by a NARSAD Young Investigator Grant

from the Brain and Behavior Research Foundation (Grant No. 27238) and the European Union's Horizon 2020 Research and Innovation Program under the Marie Skłodowska-Curie grant agreement no. 846793. The content is solely the responsibility of the authors and does not necessarily represent the official views of the funding bodies.

ACKNOWLEDGMENTS

We are grateful to the study coordinator and participants in the study who thereby made this research possible. We are also grateful to Dr. James Joers for preparing the dielectric pads, and to CMRR personnel for maintaining the 7 T scanner.

REFERENCES

Antonenko, D., Thielscher, A., Saturnino, G. B., Aydin, S., Ittermann, B., Grittner, U., et al. (2019). Towards precise brain stimulation: is electric field simulation related to neuromodulation? *Brain Stimul.* 12, 1159–1168. doi: 10.1016/j.brs.2019.03.072

Ashburner, J., and Friston, K. J. (2005). Unified segmentation. *Neuroimage* 26, 839–851. doi: 10.1016/j.neuroimage.2005.02.018

Bachtiar, V., Johnstone, A., Berrington, A., Lemke, C., Johansen-Berg, H., Emir, U., et al. (2018). Modulating regional motor cortical excitability with noninvasive brain stimulation results in neurochemical changes in bilateral motor cortices. *J. Neurosci.* 38, 7327–7336. doi: 10.1523/JNEUROSCI.2853-17.2018

Bachtiar, V., Near, J., Johansen-Berg, H., and Stagg, C. J. (2015). Modulation of GABA and resting state functional connectivity by transcranial direct current stimulation. *eLife* 4:e08789. doi: 10.7554/eLife.08789

Bednařík, P., Tkáč, I., Giove, F., DiNuzzo, M., Deelchand, D. K., Emir, U. E., et al. (2015). Neurochemical and BOLD responses during neuronal activation measured in the human visual cortex at 7 Tesla. *J. Cereb. Blood Flow Metab.* 35, 601–610. doi: 10.1038/jcbfm.2014.233

Bednařík, P., Tkáč, I., Giove, F., Eberly, L. E., Deelchand, D. K., Barreto, F. R., et al. (2018). Neurochemical responses to chromatic and achromatic stimuli in the human visual cortex. *J. Cereb. Blood Flow Metab.* 38, 347–359. doi: 10.1177/0271678X17695291

Boillat, Y., Xin, L., van der Zwaag, W., and Gruetter, R. (2019). Metabolite concentration changes associated with positive and negative BOLD responses in the human visual cortex: a functional MRS study at 7 Tesla. *J. Cereb. Blood Flow Metab.* doi: 10.1177/0271678X19831022 [Epub ahead of print].

Bridges, N. R., McKinley, R. A., Boeke, D., Sherwood, M. S., Parker, J. G., McIntire, L. K., et al. (2018). Single session low frequency left dorsolateral prefrontal transcranial magnetic stimulation changes neurometabolite relationships in healthy humans. *Front. Hum. Neurosci.* 12:77. doi: 10.3389/fnhum.2018.00077

Burgess, G. C., Kandala, S., Nolan, D., Laumann, T. O., Power, J. D., Adeyemo, B., et al. (2016). Evaluation of denoising strategies to address motion-correlated artifacts in resting-state functional magnetic resonance imaging data from the human connectome project. *Brain Connect.* 6, 669–680. doi: 10.1089/brain.2016.0435

Chen, C., Sigurdsson, H. P., Pepes, S. E., Auer, D. P., Morris, P. G., Morgan, P. S., et al. (2017). Activation induced changes in GABA: functional MRS at 7T with MEGA-sLASER. *Neuroimage* 156, 207–213. doi: 10.1016/j.neuroimage.2017.05.044

Chen, R., Classen, J., Gerloff, C., Celnik, P., Wassermann, E. M., Hallett, M., et al. (1997). Depression of motor cortex excitability by low-frequency transcranial magnetic stimulation. *Neurology* 48, 1398–1403. doi: 10.1212/wnl.48.5.1398

Cheong, I., Deelchand, D. K., Eberly, L. E., Marjanska, M., Manousakis, G., Guliani, G., et al. (2019). Neurochemical correlates of functional decline in amyotrophic lateral sclerosis. *J. Neurol. Neurosurg. Psychiatry* 90, 294–301. doi: 10.1136/jnnp-2018-318795

Cox, R. W. (1996). AFNI: software for analysis and visualization of functional magnetic resonance neuroimages. *Comput. Biomed. Res.* 29, 162–173. doi: 10.1006/cbmr.1996.0014

Croarkin, P. E., Nakonezny, P. A., Wall, C. A., Murphy, L. L., Sampson, S. M., Frye, M. A., et al. (2016). Transcranial magnetic stimulation potentiates glutamatergic neurotransmission in depressed adolescents. *Psychiatry Res. Neuroimaging* 247, 25–33. doi: 10.1016/j.pscychresns.2015.11.005

Dayan, E., Censor, N., Buch, E. R., Sandrini, M., and Cohen, L. G. (2013). Noninvasive brain stimulation: from physiology to network dynamics and back. *Nat. Neurosci.* 16, 838–844. doi: 10.1038/nn.3422

Dlabac-de Lange, J. J., Liemburg, E. J., Bais, L., van de Poel-Mustafayeva, A. T., de Lange-de Klerk, E. S. M., Knegtering, H., et al. (2017). Effect of bilateral prefrontal rTMS on left prefrontal NAA and Glx levels in schizophrenia patients with predominant negative symptoms: an exploratory study. *Brain Stimul.* 10, 59–64. doi: 10.1016/j.brs.2016.08.002

Dubin, M. J., Mao, X., Banerjee, S., Goodman, Z., Lapidus, K. A., Kang, G., et al. (2016). Elevated prefrontal cortex GABA in patients with major depressive disorder after TMS treatment measured with proton magnetic resonance spectroscopy. *J. Psychiatry Neurosci.* 41, E37–E45.

Dyke, K., Pepes, S. E., Chen, C., Kim, S., Sigurdsson, H. P., Draper, A., et al. (2017). Comparing GABA-dependent physiological measures of inhibition with proton magnetic resonance spectroscopy measurement of GABA using ultra-high-field MRI. *Neuroimage* 152, 360–370. doi: 10.1016/j.neuroimage.2017.03.011

Fan, L., Li, H., Zhuo, J., Zhang, Y., Wang, J., Chen, L., et al. (2016). The human brainnetome atlas: a new brain atlas based on connectional architecture. *Cereb. Cortex* 26, 3508–3526. doi: 10.1093/cercor/bhw157

Gasparovic, C., Song, T., Devier, D., Bockholt, H. J., Caprihan, A., Mullins, P. G., et al. (2006). Use of tissue water as a concentration reference for proton spectroscopic imaging. *Magn. Reson. Med.* 55, 1219–1226. doi: 10.1002/mrm.20901

Glasser, M. F., Smith, S. M., Marcus, D. S., Andersson, J. L., Auerbach, E. J., Behrens, T. E., et al. (2016). The Human Connectome Project's neuroimaging approach. *Nat. Neurosci.* 19, 1175–1187. doi: 10.1038/nn.4361

Glasser, M. F., Sotiropoulos, S. N., Wilson, J. A., Coalson, T. S., Fischl, B., Andersson, J. L., et al. (2013). The minimal preprocessing pipelines for the human connectome project. *Neuroimage* 80, 105–124. doi: 10.1016/j.neuroimage.2013.04.127

Gruetter, R., and Tkáč, I. (2000). Field mapping without reference scan using asymmetric echo-planar techniques. *Magn. Reson. Med.* 43, 319–323. doi: 10.1002/(sici)1522-2594(200002)43:2<319::aid-mrm22>3.0.co;2-1

Hendriks, A. D., Fracasso, A., Arteaga de Castro, C. S., Gosselink, M., Luijten, P. R., Petridou, N., et al. (2018). Maximizing sensitivity for fast GABA edited spectroscopy in the visual cortex at 7 T. *NMR Biomed.* 31:e3890. doi: 10.1002/nbm.3890

Henry, P. G., Marjanska, M., Walls, J. D., Valette, J., Gruetter, R., and Ugurbil, K. (2006). Proton-observed carbon-edited NMR spectroscopy in strongly coupled second-order spin systems. *Magn. Reson. Med.* 55, 250–257. doi: 10.1002/mrm.20764

Hone-Blanchet, A., Mondino, M., and Fecteau, S. (2017). Repetitive transcranial magnetic stimulation reduces anxiety symptoms, drug cravings, and elevates (1)H-MRS brain metabolites: a case report. *Brain Stimul.* 10, 856–858. doi: 10.1016/j.brs.2017.03.007

Hoogendam, J. M., Ramakers, G. M., and Di Lazzaro, V. (2010). Physiology of repetitive transcranial magnetic stimulation of the human brain. *Brain Stimul.* 3, 95–118. doi: 10.1016/j.brs.2009.10.005

Huang, Y. Z., Lu, M. K., Antal, A., Classen, J., Nitsche, M., Ziemann, U., et al. (2017). Plasticity induced by non-invasive transcranial brain stimulation: a position paper. *Clin. Neurophysiol.* 128, 2318–2329. doi: 10.1016/j.clinph.2017.09.007

Jelen, L. A., King, S., Mullins, P. G., and Stone, J. M. (2018). Beyond static measures: a review of functional magnetic resonance spectroscopy and its potential to investigate dynamic glutamatergic abnormalities in schizophrenia. *J. Psychopharmacol.* 32, 497–508. doi: 10.1177/0269881117747579

Ji, G. J., Yu, F., Liao, W., and Wang, K. (2017). Dynamic aftereffects in supplementary motor network following inhibitory transcranial magnetic stimulation protocols. *Neuroimage* 149, 285–294. doi: 10.1016/j.neuroimage.2017.01.035

Kim, S., Stephenson, M. C., Morris, P. G., and Jackson, S. R. (2014). tDCS-induced alterations in GABA concentration within primary motor cortex predict motor learning and motor memory: a 7 T magnetic resonance spectroscopy study. *Neuroimage* 99, 237–243. doi: 10.1016/j.neuroimage.2014.05.070

Klose, U. (1990). In vivo proton spectroscopy in presence of eddy currents. *Magn. Reson. Med.* 14, 26–30. doi: 10.1002/mrm.1910140104

Liew, S. L., Santarnecchi, E., Buch, E. R., and Cohen, L. G. (2014). Non-invasive brain stimulation in neurorehabilitation: local and distant effects for motor recovery. *Front. Hum. Neurosci.* 8:378. doi: 10.3389/fnhum.2014.00378

Lin, Y., Stephenson, M. C., Xin, L., Napolitano, A., and Morris, P. G. (2012). Investigating the metabolic changes due to visual stimulation using functional proton magnetic resonance spectroscopy at 7 T. *J. Cereb. Blood Flow Metab.* 32, 1484–1495. doi: 10.1038/jcbfm.2012.33

Lopez-Alonso, V., Cheeran, B., Rio-Rodriguez, D., and Fernandez-Del-Olmo, M. (2014). Inter-individual variability in response to non-invasive brain stimulation paradigms. *Brain Stimul.* 7, 372–380. doi: 10.1016/j.brs.2014.02.004

Machado, S., Bittencourt, J., Minc, D., Portella, C. E., Velasques, B., Cunha, M., et al. (2008). Therapeutic applications of repetitive transcranial magnetic stimulation in clinical neurorehabilitation. *Funct. Neurol.* 23, 113–122.

Mangia, S., Giove, F., Tkáč, I., Logothetis, N. K., Henry, P. G., Olman, C. A., et al. (2009). Metabolic and hemodynamic events after changes in neuronal activity: current hypotheses, theoretical predictions and in vivo NMR experimental findings. *J. Cereb. Blood Flow Metab.* 29, 441–463. doi: 10.1038/jcbfm.2008.134

Mangia, S., Tkáč, I., Gruetter, R., Van de Moortele, P. F., Maraviglia, B., and Ugurbil, K. (2007a). Sustained neuronal activation raises oxidative metabolism to a new steady-state level: evidence from 1H NMR spectroscopy in the human visual cortex. *J. Cereb. Blood Flow Metab.* 27, 1055–1063. doi: 10.1038/sj.jcbfm.9600401

Mangia, S., Tkáč, I., Logothetis, N. K., Gruetter, R., Van de Moortele, P. F., and Ugurbil, K. (2007b). Dynamics of lactate concentration and blood oxygen level-dependent effect in the human visual cortex during repeated identical stimuli. *J. Neurosci. Res.* 85, 3340–3346. doi: 10.1002/jnr.21371

Marjanska, M., Auerbach, E. J., Valabregue, R., Van de Moortele, P. F., Adriany, G., and Garwood, M. (2012). Localized 1H NMR spectroscopy in different regions of human brain in vivo at 7 T: T2 relaxation times and concentrations of cerebral metabolites. *NMR Biomed.* 25, 332–339. doi: 10.1002/nbm.1754

Marjanska, M., Lehericy, S., Valabregue, R., Popa, T., Worbe, Y., Russo, M., et al. (2013). Brain dynamic neurochemical changes in dystonic patients: a magnetic resonance spectroscopy study. *Mov. Disord.* 28, 201–209. doi: 10.1002/mds.25279

Michael, N., Gosling, M., Reutemann, M., Kersting, A., Heindel, W., Arolt, V., et al. (2003). Metabolic changes after repetitive transcranial magnetic stimulation (rTMS) of the left prefrontal cortex: a sham-controlled proton magnetic resonance spectroscopy (1H MRS) study of healthy brain. *Eur. J. Neurosci.* 17, 2462–2468. doi: 10.1046/j.1460-9568.2003.02683.x

Navarro de Lara, L. I., Tik, M., Woletz, M., Frass-Kriegl, R., Moser, E., Laistler, E., et al. (2017). High-sensitivity TMS/fMRI of the human motor cortex using a dedicated multichannel MR Coil. *Neuroimage* 150, 262–269. doi: 10.1016/j.neuroimage.2017.02.062

Oz, G., and Tkáč, I. (2011). Short-echo, single-shot, full-intensity proton magnetic resonance spectroscopy for neurochemical profiling at 4 T: validation in the cerebellum and brainstem. *Magn. Reson. Med.* 65, 901–910. doi: 10.1002/mrm.22708

Pal, P. K., Hanajima, R., Gunraj, C. A., Li, J. Y., Wagle-Shukla, A., Morgante, F., et al. (2005). Effect of low-frequency repetitive transcranial magnetic stimulation on interhemispheric inhibition. *J. Neurophysiol.* 94, 1668–1675. doi: 10.1152/jn.01306.2004

Patel, H. J., Romanzetti, S., Pellicano, A., Nitsche, M. A., Reetz, K., and Binkofski, F. (2019). Proton magnetic resonance spectroscopy of the motor cortex reveals long term GABA change following anodal transcranial direct current stimulation. *Sci. Rep.* 9:2807. doi: 10.1038/s41598-019-39262-7

Pfeuffer, J., Tkáč, I., Provencher, S. W., and Gruetter, R. (1999). Toward an in vivo neurochemical profile: quantification of 18 metabolites in short-echo-time (1)H NMR spectra of the rat brain. *J. Magn. Reson.* 141, 104–120. doi: 10.1006/jmre.1999.1895

Power, J. D., Barnes, K. A., Snyder, A. Z., Schlaggar, B. L., and Petersen, S. E. (2012). Spurious but systematic correlations in functional connectivity MRI networks arise from subject motion. *Neuroimage* 59, 2142–2154. doi: 10.1016/j.neuroimage.2011.10.018

Provencher, S. W. (1993). Estimation of metabolite concentrations from localized in vivo proton NMR spectra. *Magn. Reson. Med.* 30, 672–679. doi: 10.1002/mrm.1910300604

Provencher, S. W. (2001). Automatic quantitation of localized in vivo 1H spectra with LCModel. *NMR Biomed.* 14, 260–264. doi: 10.1002/nbm.698

Qiao, J., Jin, G., Lei, L., Wang, L., Du, Y., and Wang, X. (2016). The positive effects of high-frequency right dorsolateral prefrontal cortex repetitive transcranial magnetic stimulation on memory, correlated with increases in brain metabolites detected by proton magnetic resonance spectroscopy in recently detoxified alcohol-dependent patients. *Neuropsychiatr. Dis. Treat.* 12, 2273–2278. doi: 10.2147/NDT.S106266

Randall, L. O. (1938). Chemical topography of the brain. *J. Biol. Chem.* 124, 0481–0488.

Ridler, T. W., and Calvard, S. (1978). Picture Thresholding Using an Iterative Selection Method. *IEEE Trans. Syst. Man Cybern.* 8, 630–632. doi: 10.1109/tsmc.1978.4310039

Ryan, K., Wawrzyn, K., Gati, J. S., Chronik, B. A., Wong, D., Duggal, N., et al. (2018). 1H MR spectroscopy of the motor cortex immediately following transcranial direct current stimulation at 7 Tesla. *PLoS One* 13:e0198053. doi: 10.1371/journal.pone.0198053

Salimi-Khorshidi, G., Douaud, G., Beckmann, C. F., Glasser, M. F., Griffanti, L., and Smith, S. M. (2014). Automatic denoising of functional MRI data: combining independent component analysis and hierarchical fusion of classifiers. *Neuroimage* 90, 449–468. doi: 10.1016/j.neuroimage.2013.11.046

Schaller, B., Mekle, R., Xin, L., Kunz, N., and Gruetter, R. (2013). Net increase of lactate and glutamate concentration in activated human visual cortex detected with magnetic resonance spectroscopy at 7 tesla. *J. Neurosci. Res.* 91, 1076–1083. doi: 10.1002/jnr.23194

Schaller, B., Xin, L., O'Brien, K., Magill, A. W., and Gruetter, R. (2014). Are glutamate and lactate increases ubiquitous to physiological activation? A (1)H functional MR spectroscopy study during motor activation in human brain at 7Tesla. *Neuroimage* 93(Pt 1), 138–145. doi: 10.1016/j.neuroimage.2014.02.016

Schlamann, M., Yoon, M. S., Maderwald, S., Pietrzyk, T., Bitz, A. K., Gerwig, M., et al. (2010). Short term effects of magnetic resonance imaging on excitability of the motor cortex at 1.5T and 7T. *Acad. Radiol.* 17, 277–281. doi: 10.1016/j.acra.2009.10.004

Smith, S. M., Beckmann, C. F., Andersson, J., Auerbach, E. J., Bijsterbosch, J., Douaud, G., et al. (2013). Resting-state fMRI in the human connectome project. *Neuroimage* 80, 144–168. doi: 10.1016/j.neuroimage.2013.05.039

Sotiropoulos, S. N., Jbabdi, S., Xu, J., Andersson, J. L., Moeller, S., Auerbach, E. J., et al. (2013). Advances in diffusion MRI acquisition and processing in the human connectome project. *Neuroimage* 80, 125–143. doi: 10.1016/j.neuroimage.2013.05.057

Stagg, C. J., Bachtiar, V., Amadi, U., Gudberg, C. A., Ilie, A. S., Sampaio-Baptista, C., et al. (2014). Local GABA concentration is related to network-level resting functional connectivity. *eLife* 3:e01465. doi: 10.7554/eLife.01465

Stagg, C. J., Best, J. G., Stephenson, M. C., O'Shea, J., Wylezinska, M., Kincses, Z. T., et al. (2009a). Polarity-sensitive modulation of cortical neurotransmitters by transcranial stimulation. *J. Neurosci.* 29, 5202–5206. doi: 10.1523/JNEUROSCI.4432-08.2009

Stagg, C. J., Wylezinska, M., Matthews, P. M., Johansen-Berg, H., Jezzard, P., Rothwell, J. C., et al. (2009b). Neurochemical effects of theta burst stimulation as assessed by magnetic resonance spectroscopy. *J. Neurophysiol.* 101, 2872–2877. doi: 10.1152/jn.91060.2008

Stanley, J. A., and Raz, N. (2018). Functional magnetic resonance spectroscopy: the "New" mrs for cognitive neuroscience and psychiatry research. *Front. Psychiatry* 9:76. doi: 10.3389/fpsyt.2018.00076

Teeuwisse, W. M., Brink, W. M., Haines, K. N., and Webb, A. G. (2012). Simulations of high permittivity materials for 7 T neuroimaging and evaluation of a new barium titanate-based dielectric. *Magn. Reson. Med.* 67, 912–918. doi: 10.1002/mrm.24176

Tkáč, I., Andersen, P., Adriany, G., Merkle, H., Ugurbil, K., and Gruetter, R. (2001). In vivo 1H NMR spectroscopy of the human brain at 7 T. *Magn. Reson. Med.* 46, 451–456.

Tkáč, I., and Gruetter, R. (2005). Methodology of H NMR spectroscopy of the human brain at very high magnetic fields. *Appl. Magn. Reson.* 29, 139–157. doi: 10.1007/BF03166960

Tkáč, I., Oz, G., Adriany, G., Ugurbil, K., and Gruetter, R. (2009). In vivo 1H NMR spectroscopy of the human brain at high magnetic fields: metabolite quantification at 4T vs. 7T. *Magn. Reson. Med.* 62, 868–879. doi: 10.1002/mrm.22086

Van de Moortele, P. F., Auerbach, E. J., Olman, C., Yacoub, E., Ugurbil, K., and Moeller, S. (2009). T1 weighted brain images at 7 tesla unbiased for proton density, T2* contrast and RF coil receive B1 sensitivity with simultaneous vessel visualization. *Neuroimage* 46, 432–446. doi: 10.1016/j.neuroimage.2009.02.009

Van Essen, D. C., Ugurbil, K., Auerbach, E., Barch, D., Behrens, T. E., Bucholz, R., et al. (2012). The Human Connectome Project: a data acquisition perspective. *Neuroimage* 62, 2222–2231. doi: 10.1016/j.neuroimage.2012.02.018

Wassermann, E. M. (1998). Risk and safety of repetitive transcranial magnetic stimulation: report and suggested guidelines from the International Workshop on the Safety of Repetitive Transcranial Magnetic Stimulation, June 5-7, 1996. *Electroencephalogr. Clin. Neurophysiol.* 108, 1–16. doi: 10.1016/s0168-5597(97)00096-8

Watanabe, T., Hanajima, R., Shirota, Y., Ohminami, S., Tsutsumi, R., Terao, Y., et al. (2014). Bidirectional effects on interhemispheric resting-state functional connectivity induced by excitatory and inhibitory repetitive transcranial magnetic stimulation. *Hum. Brain Mapp.* 35, 1896–1905. doi: 10.1002/hbm.22300

Yang, X. R., Kirton, A., Wilkes, T. C., Pradhan, S., Liu, I., Jaworska, N., et al. (2014). Glutamate alterations associated with transcranial magnetic stimulation in youth depression: a case series. *J. ECT* 30, 242–247. doi: 10.1097/YCT.0000000000000094

Zang, Y., Jiang, T., Lu, Y., He, Y., and Tian, L. (2004). Regional homogeneity approach to fMRI data analysis. *Neuroimage* 22, 394–400. doi: 10.1016/j.neuroimage.2003.12.030

Zheng, H., Zhang, L., Li, L., Liu, P., Gao, J., Liu, X., et al. (2010). High-frequency rTMS treatment increases left prefrontal myo-inositol in young patients with treatment-resistant depression. *Prog. Neuropsychopharmacol. Biol. Psychiatry* 34, 1189–1195. doi: 10.1016/j.pnpbp.2010.06.009

Zou, Q. H., Zhu, C. Z., Yang, Y., Zuo, X. N., Long, X. Y., Cao, Q. J., et al. (2008). An improved approach to detection of amplitude of low-frequency fluctuation (ALFF) for resting-state fMRI: fractional ALFF. *J. Neurosci. Methods* 172, 137–141. doi: 10.1016/j.jneumeth.2008.04.012

Conflict of Interest: The authors declare that the research was conducted in the absence of any commercial or financial relationships that could be construed as a potential conflict of interest.

frontiers in Physiology

ORIGINAL RESEARCH
published: 18 December 2019
doi: 10.3389/fphys.2019.01541

Mild Propofol Sedation Reduces Frontal Lobe and Thalamic Cerebral Blood Flow: An Arterial Spin Labeling Study

*Neeraj Saxena[1,2], Tommaso Gili[1,3], Ana Diukova[1], Danielle Huckle[4], Judith E. Hall[5] and Richard G. Wise[1]**

[1]Cardiff University Brain Research Imaging Centre (CUBRIC), School of Psychology, Cardiff University, Cardiff, United Kingdom, [2]Department of Anaesthetics, Intensive Care and Pain Medicine, Cwm Taf Morgannwg University Health Board, Llantrisant, United Kingdom, [3]IMT School for Advanced Studies Lucca, Lucca, Italy, [4]Department of Anaesthetics, University Hospital of Wales, Cardiff, United Kingdom, [5]Department of Anaesthetics, Intensive Care and Pain Medicine, School of Medicine, Cardiff University, Cardiff, United Kingdom

OPEN ACCESS

Edited by:
Marta Bianciardi,
Harvard Medical School,
United States

Reviewed by:
Fernando Zelaya,
King's College London,
United Kingdom
Antonio Ferretti,
Università degli Studi G. d'Annunzio
Chieti e Pescara, Italy

***Correspondence:**
Richard G. Wise
wiserg@cardiff.ac.uk

Specialty section:
This article was submitted to Medical Physics and Imaging, a section of the journal Frontiers in Physiology

Received: 13 September 2019
Accepted: 05 December 2019
Published: 18 December 2019

Citation:
Saxena N, Gili T, Diukova A, Huckle D, Hall JE and Wise RG (2019) Mild Propofol Sedation Reduces Frontal Lobe and Thalamic Cerebral Blood Flow: An Arterial Spin Labeling Study. Front. Physiol. 10:1541. doi: 10.3389/fphys.2019.01541

Mechanisms of anesthetic drug-induced sedation and unconsciousness are still incompletely understood. Functional neuroimaging modalities provide a window to study brain function changes during anesthesia allowing us to explore the sequence of neurophysiological changes associated with anesthesia. Cerebral perfusion change under an assumption of intact neurovascular coupling is an indicator of change in large-scale neural activity. In this experiment, we have investigated resting state cerebral blood flow (CBF) changes in the human brain during mild sedation, with propofol. Arterial spin labeling (ASL) provides a non-invasive, reliable, and robust means of measuring cerebral blood flow (CBF) and can therefore be used to investigate central drug effects. Mild propofol sedation-related CBF changes were studied at rest (n = 15), in a 3 T MR scanner using a PICORE-QUIPSS II ASL technique. CBF was reduced in bilateral paracingulate cortex, premotor cortex, Broca's areas, right superior frontal gyrus and also the thalamus. This cerebral perfusion study demonstrates that propofol induces suppression of key cortical (frontal lobe) and subcortical (thalamus) regions during mild sedation.

Keywords: arterial spin labeling, functional magnetic resonance imaging, cerebral blood flow, propofol, sedation

INTRODUCTION

Mechanisms of anesthetic drug-induced sedation and unconsciousness are still incompletely understood. While neuroimaging studies suggest a reduction of activity in a number of cortical and subcortical areas along with breakdown of functional connectivity of thalamo-cortical, frontoparietal, or default mode networks (DMNs), the sequence and specificity of these changes remain disputed (Lee et al., 2009; Boveroux et al., 2010). Apart from revealing systems-level mechanisms of anesthesia, understanding brain perfusion and its alterations with sedation/anesthesia is thought to be helpful in exploiting the neuroprotective effects of these drugs in brain-injured (traumatic or stroke) patients receiving sedation or those undergoing neuro-anesthesia.

Techniques including Positron Emission Tomography and Blood Oxygen Level Dependent (BOLD) contrast-based Functional magnetic resonance imaging (fMRI) have been utilized to explore the neural correlates of anesthetic-related changes in consciousness and arousal. Recent improvements in arterial spin labeling (ASL) methodology, a measurement of tissue blood flow, render it practical to quantify pharmacological effects in the human brain. It is completely non-invasive, being based on an endogenous tracer (magnetically labeled arterial blood) and, since the perfusion signal is encoded in the difference between control and tagged images, it is minimally affected by baseline drift, making it suitable for long-term studies or those with low frequency changes. ASL-based techniques are, therefore, especially suited for physiological and pharmacological studies of brain activity.

Propofol, a GABA-ergic agonist compound, is an anesthetic drug widely used for sedation and anesthetic induction and maintenance. Recently, Qiu et al. (2017) have shown perfusion changes with deep sedation (a state characterized by unresponsiveness to verbal commands) induced with propofol, in the frontoparietal, DMN, visual networks, and thalamus.

In this experiment, we have used ASL to investigate resting state cerebral blood flow (CBF) changes in the human brain during mild sedation. We chose "mild" sedation as the earliest, objectively defined, step change in consciousness to evaluate the earliest changes in neural mechanisms associated with altered arousal. Based on previous observations from different imaging modalities, we hypothesized alteration of CBF in the frontal cortex, thalamus, brainstem, and regions of the default mode network (Byas-Smith et al., 2002; Gili et al., 2013).

METHODS

Cardiff University's School of Medicine Ethics Committee reviewed and approved the study. Fifteen right-handed, healthy, male volunteers (mean age 26 years; range 20–41 years) participated in this study after giving informed consent. They were recruited following a detailed screening procedure. Medical screening was performed to ensure that all subjects were in good physical and mental health and not on any medications (American Society of Anesthesiologists grade 1). Any volunteer with complaints of regular heartburn or hiatus hernia, known or suspected allergies to propofol (or its constituents), who was a regular smoker, or who snored frequently or excessively, or who had a potentially "difficult airway" was excluded. Volunteers were instructed to follow standard pre-anesthetic fasting guidelines. They avoided food for 6 h and any fluids for 2 h before the experiments. Following the experiments, they were monitored until they recovered from the effects of sedation and were discharged with safety advice after they fulfilled all day-case anesthesia discharge criteria. All participants underwent two fMRI scans within the same session, the first before and the second during intravenous propofol administration while remaining at rest. No behavioral task was presented apart from asking volunteers to remain still with their eyes closed and not to fall asleep.

Drug Administration

Propofol (Propofol-Lipuro 1%, Braun Ltd.) was administered using an Asena-PK infusion pump (Alaris Medical, CareFusion Ltd.) using a target-controlled infusion based on the Marsh pharmacokinetic model (Marsh et al., 1991). Infusion was started targeting an effect-site concentration of 0.6 μg ml^{-1}. Once the target was reached, 2 min were given for further equilibration. Drug infusion was increased in 0.2 μg ml^{-1} increments until the desired level of sedation was achieved. Sedation level was assessed by an anesthetist, blinded to the level of propofol being administered, using the modified Observer's assessment of alertness/sedation (OAA/S) (Chernik et al., 1990). The sedation endpoint was an OAA/S level of 4 (slurred speech with lethargic response to verbal commands). The average targeted propofol plasma concentration was 1.2 (SD 0.2) μg ml^{-1}. All subjects were monitored throughout the experiments by two qualified anesthetists (**Table 1**). Heart rate, non-invasive blood pressure, oxygen saturation, and concentrations of expired (end-tidal) carbon dioxide were monitored using aVeris MR Vital Signs monitoring system (MEDRAD Radiology).

Magnetic Resonance Imaging

MRI data were collected at three T (General Electric, HDx) using an eight-channel receive-only head coil. CBF was estimated using single-shot, proximal inversion with a control for off-resonance effects – quantitative imaging of perfusion using single subtraction II (PICORE-QUIPSS II) (Wong et al., 1998). Imaging parameters were: TR/TE = 2,200 ms/19.8 ms; TI = 1,500 ms; field of view, 24 cm × 24 cm; 12 slices, 7 mm thick, with a 1-mm gap between slices; matrix, 64 × 64. Each scan included 130 repetitions (65 pairs of tag-control images) over 4:46 min. With the same slice prescription, calibration scans were acquired to provide an estimate of M_0 (fully relaxed blood water magnetization). T1-weighted whole-brain structural scan was also acquired (1 mm × 1 mm × 1 mm voxels). Our previous work has demonstrated the robustness and repeatability of this sequence in a within-session design of experiment such as presented here (Murphy et al., 2011).

Preprocessing

ASL data were pre-processed as follows: correction for head motion and removal of non-brain voxels were performed using FSL: FMRIB's Software Library, www.fmrib.ox.ac.uk/fsl. Head motion correction was performed using MCFLIRT employing

TABLE 1 | Physiological data.

	HR (bpm)	SBP (mmHg)	DBP (mmHg)	MAP (mmHg)	SpO_2(%)
Awake	56 (7)	123 (10)	71 (8)	95 (8)	98 (1)
Sedated	55 (7)	119 (9)	70 (8)	92 (7)	98 (1)

Mean (SD) across subjects of physiological recordings measured before and during sedation. Paired t-tests revealed no significant differences between awake and sedated states; SD, standard deviation; HR, heart rate; SBP, systolic blood pressure; DBP, diastolic blood pressure; MAP, mean arterial pressure; SpO_2, oxygen saturation.

the same reference volume for both tag and control images. CBF data were processed using surround subtraction of the ASL tag and control images (Liu and Wong, 2005). CBF was calculated using a standard single-compartment model (Buxton et al., 1998). Data were then transformed first to individual subjects' structural space using FLIRT (FMRIB's Linear Registration Tool) and then to a standard space (Montreal Neurological Institute MNI152 standard map) using Advanced Normalization Tools (ANTS; Penn Image Computing & Science Lab, http://www.picsl.upenn.edu/ANTS/). The transformation was first applied to the individual subjects' T1 image, and then the resulting warp vectors were applied to the CBF images.

Analysis

To examine the influence of propofol sedation, permutation-based nonparametric within-subject paired *t*-tests (FSL randomize) were performed to identify areas where CBF varied significantly with the neurophysiological state (*awake* vs. *sedated*). The results were subject to threshold-free cluster enhancement and family-wise error (FWE) corrected for multiple comparisons by permutation testing using a significance level of $p < 0.05$.

RESULTS

There were no significant differences in systemic hemodynamics or oxygen saturation between the *awake* and *sedated* groups (**Table 1**). We compared head motion (relative volume to volume mean displacement) between awake and sedated groups, but there was no significant difference (two-tailed, paired *t*-test; $p = 0.39$).

Figure 1 shows CBF *awake* > *sedated* (paired *t* test), demonstrating frontal regions indicating a decrease in perfusion with sedation. Specifically, these areas were Paracingulate cortex [bilaterally (6, 34, 33) and (−4, 34, 33) MNI space coordinates], left and right Broca's areas [(−38, 10, 28) and (42, 10, 28) MNI space, respectively], left Insula [(−32, 24, 8), MNI space], Premotor cortex [bilaterally (−4, 20, 48) and (8, 16, 48) MNI space], and right Superior Frontal gyrus [(4, 48, 38) MNI space]. No significant changes were found in the opposite contrast *awake* < *sedated*.

To test our regional hypotheses concerning areas commonly reported in studies of arousal, we calculated the paired *t*-test with a small volume FWE correction ($p < 0.05$), within thalamus, brainstem, and a set of regions (ventromedial prefrontal cortex, posterior cingulate cortex, left and right inferior parietal lobule) included in the default mode network (DMN) (Buckner et al., 2008). Only the thalamus bilaterally [(−3, −13, 4) and (7, −13, 4) MNI space coordinates] showed a reduction of perfusion passing from the awake condition to the sedated one (**Figure 2**).

DISCUSSION

In this experiment, we have used ASL-fMRI to demonstrate that mild propofol sedation is associated with a reduction in CBF in some of the key cortical (frontal lobe) and subcortical (thalamus)

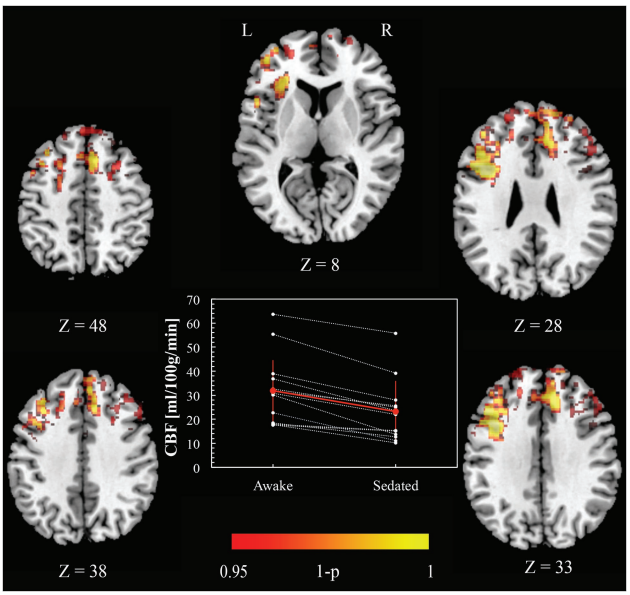

FIGURE 1 | Cerebral blood flow changes induced by propofol mild sedation. A paired *t*-test was calculated for the decrease (*awake* > *sedated*) of the cerebral blood flow. We report clusters that survived correction for multiple comparisons across space, *via* permutation testing, with FWE correction at $p < 0.05$. The axial coordinates are reported in MNI space (mm). The central plot shows quantitative cerebral blood flow calculated within the region resulting from the paired *t*-test contrast (*awake* > *sedated*, $p < 0.05$ FWE corr.) across subjects. The red values represent mean and standard deviation in the two conditions.

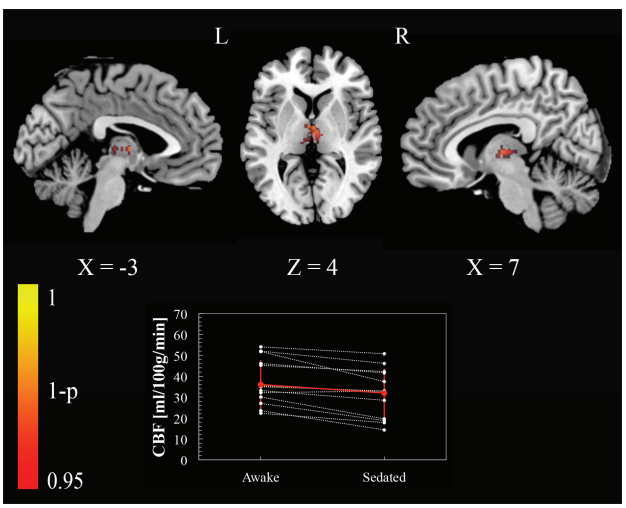

FIGURE 2 | Cerebral blood flow changes induced by propofol mild sedation. A paired *t*-test was calculated for the decrease (*awake* > *sedated*) of the cerebral blood flow. We report clusters that survived small volume correction for multiple comparisons across space, *via* permutation testing, with FWE correction at $p < 0.05$. Coordinates are reported in MNI space (mm). The central plot shows quantitative cerebral blood flow calculated within the portion of thalamus that showed significant decrease in the paired *t*-test across subjects. The red values represent mean and standard deviation in the two conditions.

areas involved in modulating consciousness while the blood flow in the brainstem and the DMN remains broadly unaffected.

Previous quantitative studies of CBF changes have focused on anesthetic-induced unconsciousness, with only a few looking at mild sedation. In this study, we anticipated diminished regional perfusion of the frontal brain regions and thalamus based on previous anesthetic literature and the established role of these regions in attention, cognition, working memory, and consciousness. Mild sedation is characterized by alterations in attention, cognition, and memory. PET-based studies have demonstrated reduction in CBF of the frontal brain regions during both pharmacological sedation and anesthesia. Veselis et al. (2004) found a reduction in CBF in the right sided anterior brain (inferior frontal gyrus, insula, and superior temporal gyrus) with propofol doses similar to those in our study. Sun et al. (2008) also reported a reduction in frontal lobe metabolism by about 10 ± 3% and temporal lobe metabolism by 13 ± 2% during light propofol sedation but, simultaneously, a greater reduction in activity of the occipital lobe, an effect not found in our study. Occipital lobe has a high density of GABA receptors (similar to the frontal lobe), but its deactivation with sedation has not been universally reported. In our study, the subjects were instructed to keep their eyes closed, which may have contributed to a reduced baseline activation of the occipital lobe to restrict further significant changes. Byas-Smith et al. (2002) using propofol sedation (at doses higher than those in our study) showed a reduction in CBF of the middle and inferior frontal gyrus and additionally in the parietal lobe, posterior cingulate cortex, and also the thalamus.

We found reduced CBF, bilaterally, in the premotor cortex, paracingulate cortex, and Broca's areas and right superior frontal gyrus. Prefrontal cortex plays an important role in attention and working memory. Dorsolateral prefrontal cortex is also functionally connected to parietal cortical regions forming the lateral frontoparietal attentional functional network, which becomes activated during executive tasks. Loss of frontoparietal feedback within these networks is associated with anesthetic-induced unconsciousness (Lee et al., 2009). Premotor cortex influences motor activity through its extensive connections with the primary motor cortex and also through the corticospinal and corticobulbar pathways. Anterior cingulate cortex plays an important role in cognitive processing, anticipation of incoming stimuli, attention and preparing and executing motor activity, both self-directed and in response to a verbal command. We have previously reported an increased connectivity of left premotor cortex and right ACC with the brainstem while their connectivity with thalamus was reduced with mild propofol sedation (Gili et al., 2013). Reduced perfusion of bilateral Broca's areas (inferior frontal regions) was another expected finding as these are involved in language processing and perception; "slurred speech" being the hallmark of mild sedation (differentiating "no sedation" with "mild sedation" on the objective assessment of alertness/sedation scale).

We had hypothesized a reduction in CBF of the thalamus, brainstem, and regions involved in the DMN. Although we did not find significant CBF changes in the whole brain analysis in those areas, a small volume FWE corrected analysis, driven by our *a priori* regional hypothesis, revealed a reduction of thalamic perfusion. Most neuroimaging experiments investigating anesthesia have pointed toward a thalamic suppression along with a disruption of thalamocortical functional connectivity. At sedative concentrations of propofol, Byas-Smith et al. (2002) showed a dose-related reduction in regional perfusion of thalamus. Bonhomme et al. (2001) also showed a dose-related reduction in BOLD response activity of the thalamus to a sensory stimulus with increasing doses of sedation. At deeper levels of propofol sedation, thalamic perfusion is reduced (Qiu et al., 2017). It is therefore likely that the small doses of propofol required to produce mild sedation in our study affected the activity of brain networks in two steps: first a substantial reduction of blood perfusion in frontal areas as a consequence of local reduced metabolism associated with a small reduction of perfusion in the thalamus, followed by a progressive metabolic decrease, with increasing doses that leads to a gradual functional suppression of key node areas and their mutual interaction, resulting in anesthetic-induced unconsciousness.

We did not find any changes in regions involved in the DMN (including posterior cingulate, bilateral inferior parietal and medial prefrontal cortices). DMN functional connectivity has previously been shown to be preserved or partially maintained during propofol sedation (Boveroux et al., 2010; Stamatakis et al., 2010). Changes in functional connectivity of a set of areas may occur without any change in their mean activity levels. Functional connectivity between two regions is mainly related to the synchrony of the BOLD signal slow oscillations, rather than its magnitude of change. Similar to thalamic perfusion, CBF in the DMN decreased with increasing doses of propofol (Qiu et al., 2017) suggesting a step-wise, dose-related effect. We had also predicted changes in brainstem perfusion based on the findings of our previous work (Gili et al., 2013). There were no changes in brainstem perfusion changes observed. The low spatial resolution and limited coverage of the brainstem could be a factor in this finding. Qiu et al. (2017) also did not find brainstem perfusion changes with deeper levels of propofol sedation, suggesting that brainstem perfusion changes probably occur closer to anesthetic doses.

One of the challenges in deducing neural effects from cerebral blood flow changes is the potential confounding effect due to alterations of neurovascular coupling induced by physiological changes in blood oxygenation, CO_2 concentration, and blood pressure, both as a consequence of drug effect on physiological variables and also the potential drug effect on neurovascular coupling *per se*. Propofol at sedative doses has been shown not to alter neurovascular coupling (Veselis et al., 2005).

The fixed order of awake state followed by the sedated state could be considered a limitation of the study design. However, within-session reproducibility of ASL measurements has previously been shown to be good, and better than between sessions, improving the power to detect drug effects with a within-session design (Murphy et al., 2011). Future study designs exploiting simultaneous BOLD and ASL to study coupling between changes in BOLD-CBF may also be useful

in studying effects of sedation through alterations in oxygen metabolism where drug effects on neurovascular coupling render difficult interpretations of BOLD or CBF signals alone (Merola et al., 2017; Chiacchiaretta et al., 2018).

To conclude, we report the use of ASL to investigate the hemodynamic changes induced by mild propofol sedation. We have shown that the level of propofol sedation considered is associated with a reduction of CBF in key frontal areas (including bilateral premotor cortex, bilateral paracingulate cortex, bilateral Broca's areas and right superior frontal gyrus) and in the thalamus, while the CBF in the brainstem and regions of the DMN was not significantly affected during mild sedation.

DATA AVAILABILITY STATEMENT

All datasets generated for this study are included in the article.

ETHICS STATEMENT

The studies involving human participants were reviewed and approved by School of Medicine Research Ethics Committee, Cardiff University. The patients/participants provided their written informed consent to participate in this study.

AUTHOR CONTRIBUTIONS

NS contributed to study design, data acquisition, data analysis, data interpretation, manuscript preparation, and final approval. TG and AD contributed to study design, data acquisition, data analysis, data interpretation, critical revision of manuscript, and final approval. DH contributed to data acquisition, critical revision of manuscript, and final approval. JH contributed to study design, data interpretation, critical revision of manuscript, and final approval. RW contributed to study design, data analysis, data interpretation, critical revision of manuscript, and final approval.

ACKNOWLEDGMENTS

RW and NS acknowledge the generous support of the Wellcome Strategic Award, "Multi-scale and multi-modal assessment of coupling in the healthy and diseased brain," grant reference 104943/Z/14/Z. NS and JH thank the European Society of Anesthesiologists for its support. TG thanks the European Commission for his Intra-European Fellowship. The Cardiff University Brain Research Imaging Centre was established with support from the United Kingdom Department of Trade and Industry, Cardiff University, and the Welsh Assembly Government.

REFERENCES

Bonhomme, V., Fiset, P., Meuret, P., Backman, S., Plourde, G., Paus, T., et al. (2001). Propofol anesthesia and cerebral blood flow changes elicited by vibrotactile stimulation: a positron emission tomography study. *J. Neurophysiol.* 85, 1299–1308. doi: 10.1152/jn.2001.85.3.1299

Boveroux, P., Vanhaudenhuyse, A., Bruno, M.-A., Noirhomme, Q., Lauwick, S., Luxen, A., et al. (2010). Breakdown of within- and between-network resting state functional magnetic resonance imaging connectivity during propofol-induced loss of consciousness. *Anesthesiology* 113, 1038–1053. doi: 10.1097/ALN.0b013e3181f697f5

Buckner, R. L., Andrews-Hanna, J. R., and Schacter, D. L. (2008). The brain's default network: anatomy, function, and relevance to disease. *Ann. N. Y. Acad. Sci.* 1124, 1–38. doi: 10.1196/annals.1440.011

Buxton, R. B., Frank, L. R., Wong, E. C., Siewert, B., Warach, S., and Edelman, R. R. (1998). A general kinetic model for quantitative perfusion imaging with arterial spin labeling. *Magn. Reson. Med.* 40, 383–396. doi: 10.1002/mrm.1910400308

Byas-Smith, M., Frolich, M. A., Votaw, J. R., Faber, T. L., and Hoffman, J. M. (2002). Cerebral blood flow during propofol induced sedation. *Mol. Imaging Biol.* 4, 139–146. doi: 10.1016/S1536-1632(01)00006-3

Chernik, D. A., Gillings, D., Laine, H., Hendler, J., Silver, J. M., Davidson, A. B., et al. (1990). Validity and reliability of the observer's assessment of alertness/sedation scale: study with intravenous midazolam. *J. Clin. Psychopharmacol.* 10, 244–251.

Chiacchiaretta, P., Cerritelli, F., Bubbico, G., Perrucci, M. G., and Ferretti, A. (2018). Reduced dynamic coupling between spontaneous BOLD-CBF fluctuations in older adults: a dual-Echo pCASL study. *Front. Aging Neurosci.* 10:115. doi: 10.3389/fnagi.2018.00115

Gili, T., Saxena, N., Diukova, A., Murphy, K., Hall, J. E., and Wise, R. G. (2013). The thalamus and brainstem act as key hubs in alterations of human brain network connectivity induced by mild propofol sedation. *J. Neurosci.* 33, 4024–4031. doi: 10.1523/JNEUROSCI.3480-12.2013

Lee, U., Kim, S., Noh, G.-J., Choi, B.-M., Hwang, E., and Mashour, G. A. (2009). The directionality and functional organization of frontoparietal connectivity during consciousness and anesthesia in humans. *Conscious. Cogn.* 18, 1069–1078. doi: 10.1016/j.concog.2009.04.004

Liu, T. T., and Wong, E. C. (2005). A signal processing model for arterial spin labeling functional MRI. *NeuroImage* 24, 207–215. doi: 10.1016/j.neuroimage.2004.09.047

Marsh, B., White, M., Morton, N., and Kenny, G. N. (1991). Pharmacokinetic model driven infusion of propofol in children. *Br. J. Anaesth.* 67, 41–48. doi: 10.1093/bja/67.1.41

Merola, A., Germuska, M. A., Warnert, E. A., Richmond, L., Helme, D., Khot, S., et al. (2017). Mapping the pharmacological modulation of brain oxygen metabolism: the effects of caffeine on absolute CMRO2 measured using dual calibrated fMRI. *NeuroImage* 155, 331–343. doi: 10.1016/j.neuroimage.2017.03.028

Murphy, K., Harris, A. D., Diukova, A., Evans, C. J., Lythgoe, D. J., Zelaya, F., et al. (2011). Pulsed arterial spin labeling perfusion imaging at 3 T: estimating the number of subjects required in common designs of clinical trials. *Magn. Reson. Imaging* 29, 1382–1389. doi: 10.1016/j.mri.2011.02.030

Qiu, M., Scheinost, D., Ramani, R., and Constable, R. T. (2017). Multi-modal analysis of functional connectivity and cerebral blood flow reveals shared and unique effects of propofol in large-scale brain networks. *Neuroimage* 148, 130–140. doi: 10.1016/j.neuroimage.2016.12.080

Stamatakis, E. A., Adapa, R. M., Absalom, A. R., and Menon, D. K. (2010). Changes in resting neural connectivity during propofol sedation. *PLoS One* 5:e14224. doi: 10.1371/journal.pone.0014224

Sun, X., Zhang, H., Gao, C., Zhang, G., Xu, L., Lv, M., et al. (2008). Imaging the effects of propofol on human cerebral glucose metabolism using positron emission tomography. *J. Int. Med. Res.* 36, 1305–1310. doi: 10.1177/147323000803600618

Veselis, R. A., Feshchenko, V. A., Reinsel, R. A., Beattie, B., and Akhurst, T. J. (2005). Propofol and thiopental do not interfere with regional cerebral blood flow response at sedative concentrations. *Anesthesiology* 102, 26–34. doi: 10.1097/00000542-200501000-00008

Veselis, R. A., Feshchenko, V. A., Reinsel, R. A., Dnistrian, A. M., Beattie, B., and Akhurst, T. J. (2004). Thiopental and propofol affect different regions of the brain at similar pharmacologic effects. *Anesth. Analg.* 99, 399–408. doi: 10.1213/01.ANE.0000131971.92180.DF

Wong, E. C., Buxton, R. B., and Frank, L. R. (1998). Quantitative imaging of perfusion using a single subtraction (QUIPSS and QUIPSS II). *Magn. Reson. Med.* 39, 702–708.

Conflict of Interest: The authors declare that the research was conducted in the absence of any commercial or financial relationships that could be construed as a potential conflict of interest.

frontiers in Physics

MINI REVIEW
published: 17 January 2020
doi: 10.3389/fphy.2019.00248

Mini Review on Anomalous Diffusion by MRI: Potential Advantages, Pitfalls, Limitations, Nomenclature, and Correct Interpretation of Literature

Silvia Capuani[1,2]* *and Marco Palombo*[3]

[1] NMR and Medical Physics Laboratory, CNR Institute for Complex Systems (ISC) c/o Department of Physics, Sapienza University of Rome, Rome, Italy, [2] Neuroimaging Laboratory, Santa Lucia Foundation, Rome, Italy, [3] Department of Computer Science and Centre for Medical Image Computing, University College of London, London, United Kingdom

OPEN ACCESS

Edited by:
Federico Giove, Centro Fermi - Museo Storico della Fisica e Centro Studi e Ricerche Enrico Fermi, Italy

Reviewed by:
Simon Auguste Lambert, Université Claude Bernard Lyon 1, France
Silvia De Santis, Institute of Neurosciences of Alicante (IN), Spain

***Correspondence:**
Silvia Capuani
silvia.capuani@isc.cnr.it

Specialty section:
This article was submitted to Medical Physics and Imaging, a section of the journal Frontiers in Physics

Received: *30 April 2019*
Accepted: *23 December 2019*
Published: *17 January 2020*

Citation:
Capuani S and Palombo M (2020) Mini Review on Anomalous Diffusion by MRI: Potential Advantages, Pitfalls, Limitations, Nomenclature, and Correct Interpretation of Literature. Front. Phys. 7:248. doi: 10.3389/fphy.2019.00248

In this mini-review, we addressed the transient-anomalous diffusion by MRI, starting from the assumption that transient-anomalous diffusion is ubiquitously observed in biological tissues, as demonstrated by different single-particle-tracking optical experiments. The purpose of this review is to identify the main pitfalls that can be encountered when venturing into the field of anomalous diffusion quantified by diffusion-MRI methods. Therefore, the theory of anomalous diffusion deriving from its mathematical definition was reported and connected with the consolidated description and the established procedures of conventional diffusion-MRI of tissues. We highlighted the two different modalities for quantifying subdiffusion and superdiffusion parameters of anomalous diffusion. Then we showed that most of the papers concerning anomalous diffusion, actually deal with pseudo-superdiffusion due to the use of a superdiffusion signal representation. Pseudo-superdiffusion depends on water diffusion multi-compartmentalization and local magnetic in-homogeneities that mimic the superdiffusion of spins. In addition to the relatively large production of pseudosuperdiffusion images, anomalous diffusion research is still in its early stages due to the limited flexibility of conventional clinical MRI scanners that currently prevent the acquisition of diffusion-weighted images by varying the diffusion time (the necessary acquisition modality to quantify transient-subdiffusion in human tissues). Moreover, the wide diffusion gradient pulses complicates the definition of a reliable function representative of anomalous diffusion signal behavior to fit data. Nevertheless, it is important and possible to address these limitations, as one of the potentialities of anomalous diffusion imaging is to increase the resolution, sensitivity, and specificity of MRI.

Keywords: diffusion NMR, anomalous diffusion, subdiffusion, superdiffusion, pseudo-superdiffusion, internal magnetic field gradients, magnetic susceptibility

INTRODUCTION

Diffusion magnetic resonance imaging (DMRI) is a consolidated radiation-free technology able to quantify *in vivo* features of water molecules' diffusion related to tissue microstructures [1]. The acquired diffusion-weighted images (DWI) are usually characterized by spatial resolution within the millimeter scale but are sensitized to the random motion of water molecules, providing an indirect measure of molecular displacement in the range of few tens micrometers (that is the intrinsic DMRI resolution). Conventional DMRI is based on normal (Brownian) diffusion, characterized by a Gaussian motion propagator (MP) for which the mean squared displacement (MSD) is linearly time dependent. Despite the great importance that DMRI has in medical diagnostics, being based on the Gaussian MP limits its potential in terms of intrinsic resolution, specificity, and sensitivity.

Indeed, biological tissues are structurally complex media with different length scales of intracellular and extracellular compartments, intricate microvasculature, submicroscopic traps, and barriers hindering water diffusion.

The normal diffusion of bulk water in tissues is not able to capture all these detailed microstructural features, providing non-local, diffusion measurement averaged on a length scale l_D approximately equal to the squared-root of the MSD of the diffusing particles.

However, all the aforementioned characteristics of biological tissues can be captured using an anomalous diffusion (AD) description of molecular diffusion in living systems that, unlike normal diffusion, has a non-Gaussian MP and its MSD is not linearly proportional to its diffusion time [2]. In particular, anomalous subdiffusion is the tendency of particles in a fluid to diffuse slower than normal diffusion due to random barriers and traps with heavy-tailed trap-time distribution, while anomalous superdiffusion is the behavior of particles that diffuse showing random walk with occasional very long steps in very short times [2].

AD is ubiquitously observed in biology: it can be due to macromolecular crowding in cytoplasmatic fluid of living cells [3], in cellular membranes [4–6] and extracellular space (ECS) [7], as shown by single-particle tracking (SPT) [8] and fluorescence-correlation spectroscopy (FCS) [9] techniques. Specifically, the cerebral ECS occupies ∼20% of the total brain volume and includes all the space outside of neurons, glial cells and the interstitial space between cells. ECS has a well-connected foam-like structure and it is rich in heterogeneous ions accumulation, obstructions due to macromolecules, extracellular matrix binding sites and dead space microdomains that transiently entrap diffusing molecules in a dead-end [7, 10–12]. All these ECS features affect the diffusion of molecules such as dextran, smaller proteins, or little fluorophores showing anomalous subdiffusion. Therefore, we could expect such structural features to have a similar impact also on water diffusion.

The quantification of DMRI parameters related to AD could then provide higher sensitivity, resolution, and complementary information for improving the detection of early changes due to pathological conditions, compared to conventional metrics. For these reasons, in the last 10 years, some theoretical and experimental approaches have been proposed to account for and quantify AD by MRI. However, the methodologies used, the results and their interpretation have often aroused doubts, even questioning the fact that biological water in tissues can effectively diffuse with AD [13, 14]. To confuse further this scenario, some authors have used in a phenomenological way the stretched-exponential function to fit experimental DWI data that de facto is the function type predicted by the AD theory to quantify the superdiffusion and subdiffusion parameters. Lastly, different authors have assigned different nomenclatures to indicate the same stretching exponent, fueling the confusion that characterizes the literature of AD methods in MRI.

This mini-review is organized as follows. In the next section, we briefly introduce AD and the principal approaches for AD by MRI while, in section Transient-Anomalous Diffusion in Biological Systems, we indicate how to reconcile the theory and the established procedures of conventional DMRI with the advanced modality of tissue analysis provided by the AD. In section The Pseudo-superdiffusion, we describe the origin of the peculiar image contrast mechanism named pseudo-superdiffusion through which we provide, in section Literature Examination in the Light of the Pseudo-superdiffusion Mechanism, a new interpretation to results published by different authors, making order and clarity in the AD MRI literature. In section Conclusion, we draw our conclusions.

AD BY MRI: MATHEMATICAL AND PHYSICAL EFFECTIVE APPROACHES

AD is mathematically defined as the asymptotic power-law increase of the mean-squared displacement (MSD) as a function of the lag time t of diffusing particles: $MSD = K_v t^v$ [15]. The sublinear increase with the exponent in the range $0 < v < 1$ defines subdiffusion whereas the exponent in the range $1 < v < 2$ regulates superdiffusion [15, 16]. Several theoretical models have been proposed to describe AD phenomenon, such as the continuous-time random walk (CTRW) model [15], the fractional motion (FM) model and others [3]. The adaptation of these models to DMRI experiments leads to fit experimental DW-data to functions containing stretched-exponentials. Two different approaches, based on CTRW framework, have emerged for quantifying parameters of AD by DMRI: a purely derived mathematical approach related to fractional derivatives [17, 18] and an effective approach mainly based on the physical phenomena [19, 20]. The mathematical approach, made use of stretched-exponential functions derived from fractional order differential operators in the Bloch-Torrey equation to quantify the subdiffusion and superdiffusion parameters, indicated as α and β, respectively. In particular, Magin et al. [17, 18] solved the fractional-derivative equations in space with the fractional-order time $\alpha = 1$ and the fractional-order in space $0.5 < \beta < 1$ and in time with $0 < \alpha < 1$ and $\beta = 1$. Successively, Mittag-Leffler type function [21], including both variable α and β were used [22, 23].

The effective physical approach takes into account AD by using two different functional forms to characterize subdiffusion and superdiffusion, quantified by two exponents α and $\mu = 2\gamma$, respectively [19]. In particular, to investigate subdiffusive processes it is possible to assume the following asymptotic behavior for the Fourier Transform of AD MP [19]:

$$W(k,t) \propto \exp(-K_\alpha k^2 t^\alpha) \qquad \text{when} \quad k^2 << 1/(K_\alpha t^\alpha) \qquad (1)$$

where $k = 1/(2\pi)g\delta\Upsilon$ with: g, the diffusion gradient strength, δ, the gradient-pulse width, Υ the nuclear gyromagnetic ratio and $0 < \alpha < 1$. Because the DW-signal is proportional to the Fourier-transform of the MP, AD parameters can be quantified by fitting the function W(k, t) to experimental DW-data. Clearly, to fit Equation (1) to the DW-signal, data must be collected by changing diffusion time $t = \Delta$ in a pulsed-field-gradient (PFG) acquisition sequence, as depicted in **Figure 1**. On the other hand, to quantify superdiffusive processes, it is possible to use the following function:

$$W(k,t) \propto \exp(-K^{2\gamma}|k|^{2\gamma} t) \qquad (2)$$

where $1 < 2\gamma < 2$. As k depends on g, the correct fit of Equation (2) to DW-signal requires data obtained by changing diffusion gradient strength g (**Figure 1**). It is very important to understand how to acquire the DW-signal (by changing g at fixed Δ or by changing Δ at fixed g) to disentangle and quantify subdiffusion or superdiffusion processes.

Indeed, clinical MRI scanners normally provide DW-images at varying g. Therefore, in principle, since there is no reason to find water superdiffusion in biological tissues, it would not be possible to quantify AD using conventional clinical scanners. However, in section The Pseudo-superdiffusion we report interesting results obtained by acquiring DW-signal at varying g and fitting Equation (2) to the data.

Some research groups have acquired DW-images at varying Δ, quantifying the subdiffusion in excised tissues [24, 25] and rat brain [26]. Other groups have collected data varying g while keeping Δ constant and varying Δ while keeping g constant to quantify subdiffusion and superdiffusion parameters by Mittag-Leffler type function [23, 27]. Since in a fractal-like system the subdiffusion is related to the fractal dimension d_f ($d_f = 2/\alpha$), Özarslan et al. [26] quantified d_f in rat cerebellum. Other authors [28] failed to quantify d_f in the human brain

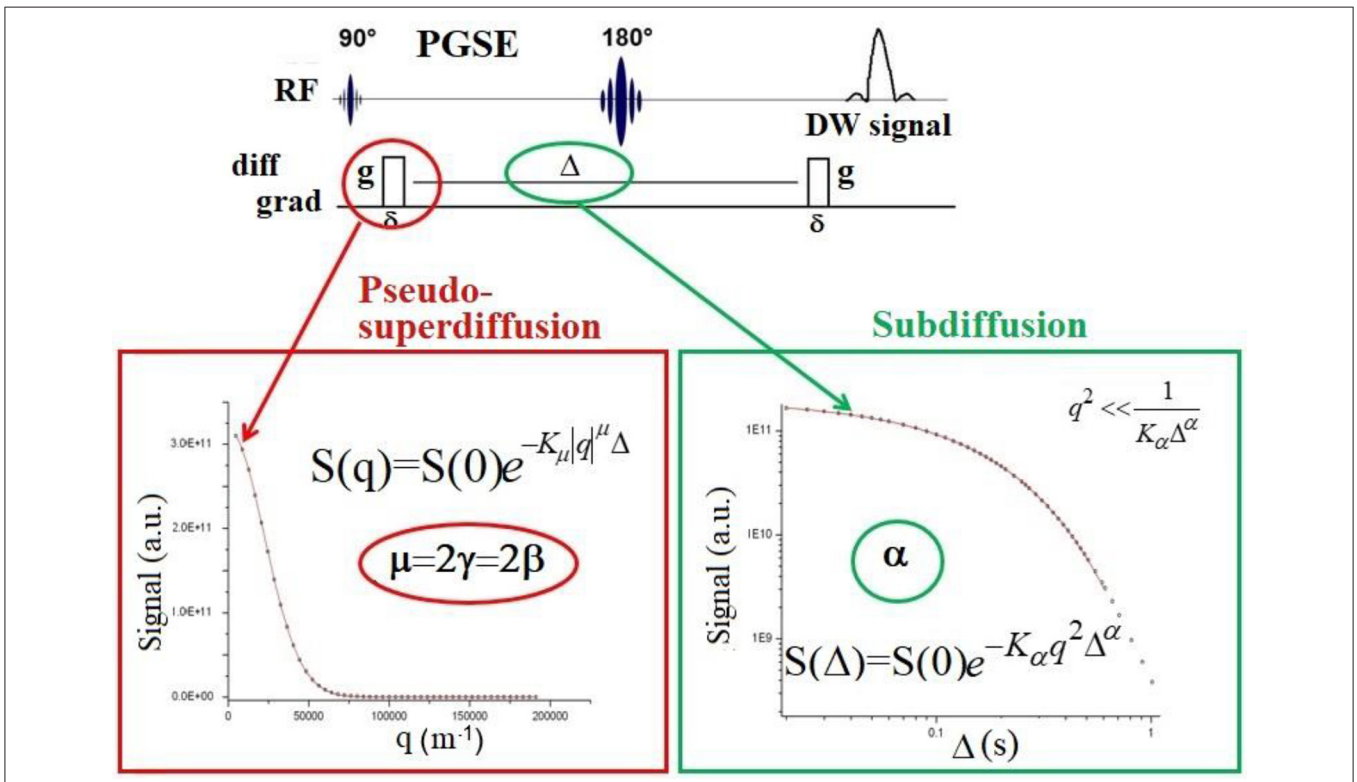

FIGURE 1 | Schematic representation of the PGSE sequence at a given b-value, where δ is the diffusion gradient pulse width. By changing the gradient strength g at a fixed value of diffusion time Δ, the DW-signal decay must be fitted to the function displayed in red box, which is the correct signal representation describing superdiffusion processes. Please note that this function depends on q^μ, where $q = (\gamma g\delta)1/2\pi$ and μ is the index that quantifies superdiffusion [15, 19] or the space derivative order. In literature, the μ index is also indicated as γ or β, where $\mu = 2\gamma = 2\beta$. Conversely, by changing Δ value at a fixed g, the DW-signal decay must be fitted to the function displayed in green box, which depends on Δ^α, where the index α quantifies subdiffusion phenomena, or the time derivative order. It is important to pay attention to PFG acquisition modality and to the corresponding signal representation to fit data. The vast majority of clinical MRI scanners allow to acquire the DW-signal by varying the gradient strength only.

because they acquired the DW-signal at varying g and fitted the stretched-exponential function reported in Equation (2) to the data. Therefore, they did not quantify subdiffusion, nor fractal dimension, although they obtained images of the human brain characterized by a new contrast compared to the conventional one provided by diffusion tensor imaging (DTI).

The incorrect use of the Mittag-Leffler function in AD MRI has generated questionable or unreliable results. Some authors have quantified both subdiffusion and superdiffusion parameters from data acquired at varying g fitted with the Mittag-Leffler function. In this way, the authors did not quantify the subdiffusion (because it is necessary to acquire DMRI by changing diffusion time) nor the correct value of the superdiffusion due to the simultaneous dependence of the Mittag-Leffler function on both α and β [29].

Another problem to deal with in AD MRI experiments using clinical scanners is related to the conditions of validity of the relations reported in Equations (1) and (2) and Magin et al. papers [17, 18], Ingo et al. papers [22, 23]. Equations (1) and (2) are valid when $\delta << \Delta$ (**Figure 1**), i.e., the diffusion-gradient pulse duration must be at least one order of magnitude shorter than the diffusion time. However, this condition is practically never satisfied in clinical scanners where the gradient pulse width of PFG is usually long. This scenario also influences the behavior of the DW-signal decay due to Gaussian diffusion, which is represented with a decreasing exponential function only when $\delta << \Delta$ [30, 31].

To overcome this drawback, Lin [32, 33] recently developed general expressions of PFG signal attenuation describing the AD NMR signal. Of particular interest is the general analytical expressions of PFG signal attenuation for AD that include the finite gradient pulse width effect, namely, the DW-signal attenuation during each gradient pulse application period [34, 35].

TRANSIENT-ANOMALOUS DIFFUSION IN BIOLOGICAL SYSTEMS

In physics literature, AD is defined to require the diffusion to be asymptotically anomalous. Considering the general AD relation: $MSD \propto K_v t^v$, where $MSD \propto D(t)^* t$ with the anomalous exponent $0 < v < 1$ that defines subdiffusion and $1 < v < 2$ defining superdiffusion, the time dependent diffusion coefficient D(t) can be written as:

$$D(t) \sim t^{v-1} \text{or}, \quad D(t) \sim 1/t^{1-v} \tag{3}$$

Using the above Equation (3) at long diffusion times, i.e., for $t \rightarrow \infty$ we obtain $D_\infty = 0$ and $D_\infty = \infty$ for subdiffusion and superdiffusion behavior, respectively. Therefore, when we use AD in living systems, we collide with one of the fixed points of the diffusion in biological tissues: the existence of a diffusion coefficient $D = D_\infty > 0$, related to the tortuosity limit $\tau = (D_0/D_\infty)^{1/2}$ that assumes finite no zero values at long diffusion times [7, 13, 31, 36–38]. In other words, because of the central limit theorem, the diffusion is Gaussian at long diffusion times, with a finite effective diffusivity $0 < D_\infty \leq D_0$ [14].

However, a suitable infinite hierarchical structure (such as fractals) leads to AD at all times, i.e., diffusion asymptotically anomalous. On the other hand, finite hierarchies (such as three or four orders of magnitude microstructures from 0.1 to 50 μm) lead to AD that becomes normal diffusion at long times [39, 40]. Realistically, we find "transient-AD" in biological tissue, where AD exists between two crossover times (cr) (**Figure 2**) as experimentally showed by several works [3–11, 41]. As shown in **Figure 2**, for $t <$ cr1, i.e., at very short diffusion times we find normal diffusion characterized by $D = D_0$, while for $t >$ cr2, i.e., at long diffusion times, we still find normal diffusion, defined by a finite value of $D = D_\infty \leq D_0$. Therefore, in the case of

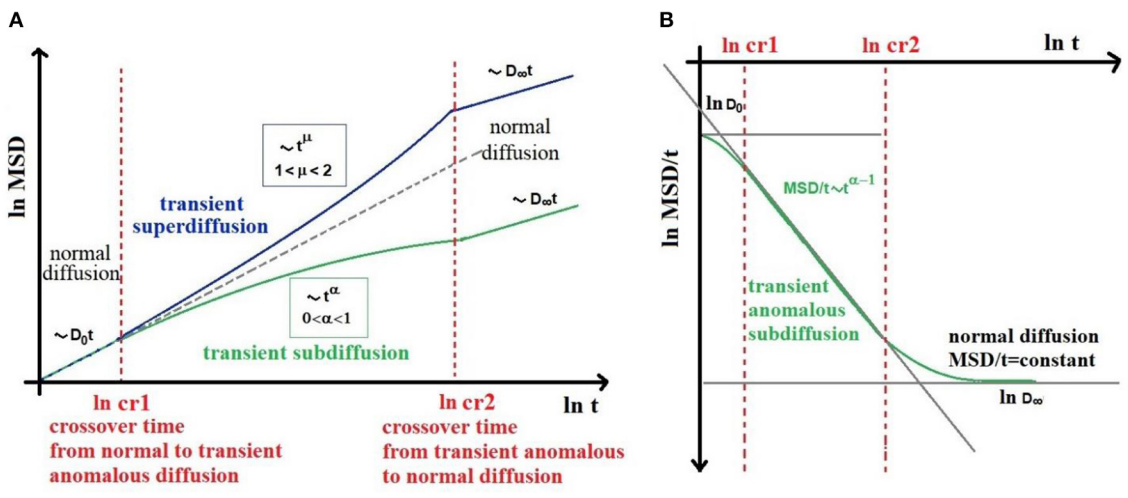

FIGURE 2 | Schematic representation of MSD **(A)** and D(t) **(B)** behavior in high heterogeneous complex biological tissues, showing transient anomalous diffusion (AD). AD exists between two crossover times (cr1 and cr2). For $t <$ cr1, i.e., at very short diffusion times we find normal diffusion characterized by $D = D_0$, while for $t >$ cr2, i.e., at long diffusion times, we still find normal diffusion, defined by a finite value of $D = D\infty$. The (cr1, cr2) time interval, must be long enough to include at least three orders of magnitude over time. As an example in AD MRI, the diffusion time Δ should run from 5 to 500 ms.

transient-subdiffusion, Equation (3) becomes [39]:

$$\begin{array}{l} D(t)\sim D_0/(1+t^{1-v}) \text{ with } 0<\nu<1 \text{ for } t\to 0 \\ D(t)\sim D\infty+1/t^{1-v} \text{ with } 0<v<1 \text{ for } t\to\infty \end{array} \quad (4)$$

And in case of transient-superdiffusion:

$$\begin{array}{l} D(t)\sim D_\infty/(1+t^{1-v}) \text{ with } 1<v<2 \text{ for } t\to\infty \\ D(t)\sim D_0+1/t^{1-v} \quad \text{with } 1<v<2 \text{ for } t\to 0 \end{array} \quad (5)$$

The (cr1, cr2) time interval, which depends on microstructure investigated, must be long enough to include at least three orders of magnitude over time for defining a power-low. Therefore, it is preferable to use echo-stimulated types sequences (i.e., pulse-gradient stimulated-echo, PGSTE) to acquire DW-signal, since PGSTE allows to select a wider range of Δ values (**Figure 1**) compared to a pulse-gradient spin-echo (PGSE) sequence [31].

Transient-AD described with Equations (4) and (5), reconciles the advanced modality of tissue analysis provided by the AD with the theory and the established procedures of conventional DMRI [13, 30].

THE PSEUDO-SUPERDIFFUSION

Since our first works concerning AD by MRI, we showed a strong connection between magnetic susceptibility and AD image contrast [19, 24, 42] when data obtained by changing g in a PFG sequence were fitted with Equation (2). In particular, we obtained more details at the interface between different substances in AD MRI [42] and a strong negative correlation between the $\mu = 2\gamma$ parameter quantifying superdiffusion and the internal magnetic-field-gradient variance (Gi) arisen from the magnetic susceptibilities differences ($\Delta\chi$) between water and polystyrene [19, 24]. Moreover, the dependence of γ on $\Delta\chi$ was stronger compared to that of the conventional apparent diffusion coefficient (ADC) on the same magnetic in-homogeneities. Building on our previous *in vitro* studies, we have recently demonstrated, using a clinical 3T MRI scanner, the utility of AD contrast in identifying key aspects of the composition (iron content, myelin density, and myelin distribution) and organization (tissue heterogeneity and tortuosity) in both cerebral white and gray matter [43]. Furthermore, we used this new AD image contrast based on γ maps, to obtain useful and complementary information (compared to that provided by DTI) about the early changing occurring in normal brain aging [44].

According to our experimental results, and considering the theory of AD, as well as the physical mechanisms underlying the MRI, we called the new AD image contrast "pseudo-superdiffusion," as water molecules do not experience a real superdiffusion. In fact, no superdiffusion dynamics were predicted in phantoms comprised of packed polystyrene micro-beads in water, nor in the biological tissues that may eventually express subdiffusion. In practice, the γ parameter obtained with an effective physical approach is equal to the β parameter quantified by Magin through a mathematical approach. Therefore, β or γ are fractional exponents associated with intravoxel spatial heterogeneity related to the heterogeneous diffusion jump length. Water molecules can produce a variable displacement in each move, because of water multi-compartmentalization and local magnetic in-homogeneities (due to $\Delta\chi$) at the interface between the different diffusion compartments. In particular, the coupling between diffusion gradients and Gi generated by $\Delta\chi$, causes an irreversible signal loss and an unexpected signal refocusing that can be modeled as a pseudo-superdiffusion process. More in deep, local magnetic gradients impart a phase shift to the spins within a spatial region strictly close to interfaces. This $\Delta\chi$-derived phase adds up to the phase shift given by the diffusion gradient pulse. When Gi and diffusion gradients are of the same order of magnitude, some spins contribute to increasing the DW signal attenuation; other spins (that can be very far from the first ones) acquire a phase shift that helps to increase the signal. Due to indistinguishable spins associated with water molecules, this scenario mimics a superdiffusion regime of water molecules, the signal of which disappears in one spot and appears in another one simulating long jumps of water molecules. This contrast mechanism increases the image sensitivity and resolution at the interfaces between different tissues [42, 43] and at sources of magnetic field inhomogeneities, such as iron accumulations in tissues [43, 44].

LITERATURE EXAMINATION IN THE LIGHT OF THE PSEUDO-SUPERDIFFUSION MECHANISM

Most of the papers concerning the measurement of AD parameters actually show the pseudo-superdiffusion measurement because the signal is acquired by changing g at a fixed value of Δ [43–49]. A careful examination of the maps shown in these papers reveals all the features of the pseudo-superdiffusion maps, namely: strong dependence on $\Delta\chi$ at the interfaces of different tissues; inverse correlation of voxels intensity with magnetic field in-homogeneities sources (iron and heavy metals deposits in the brain parenchyma), a better definition of density and orientation of the white matter tracts [47, 49].

Recently, a new elegant view of the formalism describing DMRI has been introduced [13, 30]. In particular, two complementary approaches have been highlighted for extracting information about the tissue microstructure from DW-signal: signal representations (or statistical model deriving from statistical quantum-mechanics) and tissue models [50]. Tissue models assume a priori picture of the underlying tissue while statistical models (such as DTI, diffusion kurtosis imaging, DKI, and AD imaging) aim at using mathematical representations of the empirical DW-signal without assumptions about the underlying tissue. Thus, they are applicable to any tissue type, but the estimated parameters lack specificity and therefore these methods need to be validated with complementary techniques such as SPT, FCS, and histology.

In the light of the considerations about the mechanism underpinning the pseudo-superdiffusion contrast, and taking into account DW-signal representation, it could be argued that most AD results (in particular those that seem most useful for

future clinical applications) [43, 44, 46, 47, 49, 51, 52], do not concern the quantification of the actual AD process but rather the estimation of a new parameter γ (or β) introduced by the use of DW-signal representation describing superdiffusion. The biophysical mechanism underpinning the pseudo-superdiffusion contrast resides in the interaction between diffusion in multi-compartments of different dimensions and the $\Delta\chi$ at the interfaces between the different compartments. The multi-compartmentalization, if related to compartments characterized by length scale that covers at least three orders of magnitude, can contribute to the behavior of transient-AD of water in the tissues, but the $\Delta\chi$ heavily contribute to varying the effective length scale simulating a more obvious AD behavior. The suspicion is that only the $\Delta\chi$ in a heterogeneous tissue could be enough to "modeling" the DW-signal as an AD signal representation.

CONCLUSION

In this brief review, we addressed the transient-AD by MRI, starting from the assumption that transient-AD can exist in biological tissues, as demonstrated by the SPT and FCS experiments in living systems. We highlighted the two different modalities for quantifying subdiffusion and superdiffusion parameters. In biological tissues, we expect subdiffusion, not superdiffusion. However, most of the results found in the literature actually concern quantification of superdiffusion. As explained in sections The Pseudo-superdiffusion and Literature Examination in the Light of the Pseudo-superdiffusion Mechanism, this is not real superdiffusion, rather pseudo-superdiffusion due to the use of a superdiffusion signal representation. The biophysical origin of pseudo-superdiffusion depends on the multi-compartmentalization of water diffusion and on the presence of local magnetic in-homogeneities. The recent development of DW-signal representation of AD [32–35] should be used in order to investigate the role of the interplay between internal (background) and diffusion gradients, and to consider the effect of finite width of the diffusion gradient pulses. In conclusion, AD MRI is still in its early stages due to the no-flexible conventional acquisition modality of the clinical MRI, the lack of validation experiments (for example by using optical imaging) and the difficulties in a reliable signal representation.

AUTHOR CONTRIBUTIONS

SC and MP conceived the original idea, planned the review, contributed to the interpretation of the literature, and read and approved the final manuscript. SC collected all the bibliography with the contribution of MP and wrote the manuscript.

FUNDING

This is part of ATTRACT that had received funding from the European Union's Horizon 2020 Research and Innovation Programme.

REFERENCES

1. Jones DK. *Diffusion MRI*. New York, NY: Oxford University Press (2011).
2. Klafter J, Sokolov IM. Anomalous diffusion spreads its wings. *Phys World*. (2005) **18**:29–32. doi: 10.1088/2058-7058/18/8/33
3. Hofling F, Franosch T. Anomalous transport in the crowded world of biological cells. *Rep Prog Phys*. (2013) **76**:046602. doi: 10.1088/0034-4885/76/4/046602
4. Saxton MJ, Jacobson K. Single-particle tracking: application to membrane dynamics. *Anu Rev Biophys Biomol Struct*. (1997) **26**:373–99. doi: 10.1146/annurev.biophys.26.1.373
5. Honigmann A, Muller V, Hell SW, Eggeling C. STED microscopy detects and quantifies liquid phase separation in lipid membranes using a new far-red emitting fluorescent phosphoglycerolipid analogue. *Faraday Disc*. (2013) **161**:77–89. doi: 10.1039/C2FD20107K
6. Weigel AV, Simon B, Tamkun MM, Krapf D. Ergodic and nonergodic processes coexist in the plasma membrane as observed by single-molecule tracking. *Proc Natl Acad Sci USA*. (2011) **108**:6438–43. doi: 10.1073/pnas.1016325108
7. Sykovà E, Nicholson C. Diffusion in brain extracellular space. *Physiol Rev*. (2008) **88**:1277–340. doi: 10.1152/physrev.00027.2007
8. Manzo C, Garcia-Parajo MF. A review of progress in single particle tracking: from methods to biophysical insights. *Rep Prog Phys*. (2015) **78**:124601. doi: 10.1088/0034-4885/78/12/124601
9. Elson EL. Fluorescence correlation spectroscopy: past, present, future. *Biophys J*. (2011) **101**:2855–70. doi: 10.1016/j.bpj.2011.11.012
10. Nicholson C. Anomalous diffusion inspires anatomical insights. *Biophys J*. (2015) **108**:2091–3. doi: 10.1016/j.bpj.2015.03.043
11. Xiao F, Hrabe J, Hrabetova S. Anomalous extracellular diffusion in rat cerebellum. *Biophys J*. (2015) **108**:2384–95. doi: 10.1016/j.bpj.2015.02.034
12. Sherpa AD, Van De Nes P, Fanrong X, Weedon J, Hrabetova S. Gliotoxin-induced swelling of astrocytes hinders diffusion in brain extracellular space via formation of dead-space microdomains. *Glia*. (2014) **62**:1053–65. doi: 10.1002/glia.22661
13. Novikov DS, Kiselev VG, Jespersen SN. On modeling. *Magn Reson Med*. (2018) **79**:3172–93. doi: 10.1002/mrm.27101
14. Novikov DS, Fieremans E, Jespersen SN, Kiselev VG. Quantifying brain microstructure with diffusion MRI: theory and parameter estimation. *NMR Biomed*. (2018) **32**:e3998. doi: 10.1002/nbm.3998
15. Metzler R, Klafter J. The random walk's guide to anomalous diffusion: a fractional dynamics approach. *Phys Rep*. (2000) **339**:1–77. doi: 10.1016/S0370-1573(00)00070-3
16. Metzler R, Jeon JH, Cherstvy AG, Barkai E. Anomalous diffusion models and their properties: non-stationarity, non-ergodicity, and ageing at the centenary of single particle tracking. *Phys Chem Chem Phys*. (2014) **16**:24128–64. doi: 10.1039/C4CP03465A
17. Magin RL, Abdullah O, Baleanu D, Zhou XJ. Anomalous diffusion expressed through fractional order differential operators in the Bloch-Torrey equation. *J Magn Reson*. (2008) **190**:255–70. doi: 10.1016/j.jmr.2007.11.007
18. Magin RL. Fractional calculus models of complex dynamics in biological tissues. *Comp Math Appl*. (2010) **59**:1586–93. doi: 10.1016/j.camwa.2009.08.039
19. Palombo M, Gabrielli A, De Santis S, Cametti C, Ruocco G, Capuani S. Spatio-temporal anomalous diffusion in heterogeneous media by nuclear magnetic resonance. *J Chem Phys*. (2011) **135**:034504. doi: 10.1063/1.3610367
20. Palombo M, Gabrielli A, Servedio VDP, Ruocco G, Capuani S. Structural disorder and anomalous diffusion in random packing of spheres. *Sci Rep*. (2013) **3**:2631. doi: 10.1038/srep02631
21. Yu X, Zhang Y, Sun H, Zheng C. Time fractional derivative model with Mittag-Leffler function kernel for describing anomalous diffusion: analytical solution in bounded-domain and model comparison. *Chaos Solitons Fractals*. (2018) **115**:306–12. doi: 10.1016/j.chaos.2018.08.026
22. Magin RL, Ingo C, Colon-Perez L, Triplett W, Mareci TH. Characterization of anomalous diffusion in porous biological tissues using fractional order

derivatives and entropy. *Microporous Mesoporous Mater*. (2013) **178**:39–43. doi: 10.1016/j.micromeso.2013.02.054
23. Ingo C, Magin RL, Colon-Perez L, Triplett W, Mareci TH. On random walks and entropy in diffusion-weighted magnetic resonance imaging studies of neural tissue. *Magn Reson Med*. (2014) **71**:617–27. doi: 10.1002/mrm.24706
24. Capuani S, Palombo M, Gabrielli A, Orlandi A, Maraviglia B, Pastore FS. Spatio-temporal anomalous diffusion imaging: results in controlled phantoms and in excised human meningiomas. *Magn Reson Imaging*. (2013) **31**:359–65. doi: 10.1016/j.mri.2012.08.012
25. Özarslan E, Basser PJ, Shepherd TM, Thelwall PE, Vemuri BC, Blackband SJ. Observation of anomalous diffusion in excised tissue by characterizing the diffusion-time dependence of the MR signal. *J Magn Reson*. (2006) **183**:315–23. doi: 10.1016/j.jmr.2006.08.009
26. Özarslan E, Shepherd TM, Koay CG, Blackband SJ, Basser PJ. Temporal scaling characteristics of diffusion as a new MRI contrast: findings in rat hippocampus. *NeuroImage*. (2012) **60**:1380–93. doi: 10.1016/j.neuroimage.2012.01.105
27. Fan Y, Gao JH. Fractional motion model for characterization of anomalous diffusion from NMR signals. *Phys Rev E*. (2015) **92**:012707. doi: 10.1103/PhysRevE.92.012707
28. Hall MG, Barrick TR. From diffusion-weighted MRI to anomalous diffusion imaging. *Magn Reson Med*. (2008) **59**:447–55. doi: 10.1002/mrm.21453
29. Karaman MM, Sui Y, Wang H, Magin RL, Li Y, Zhou XJ. Differentiating low- and high-grade pediatric brain tumors using a continuous-time random-walk diffusion model at high b-values. *Magn Reson Med*. (2016) **76**:1149–57. doi: 10.1002/mrm.26012
30. Kiselev VG. Fundamentals of diffusion MRI physics. *NMR Biomed*. (2017) **30**:e3602. doi: 10.1002/nbm.3602
31. Callaghan PT. *Principles of Nuclear Magnetic Resonance Microscopy*. New York, NY: Oxford University Press Inc. (1993).
32. Lin G. General pulsed-field gradient signal attenuation expression based on a fractional integral modified-Bloch equation. *Comm Nonl Sci Num Simul*. (2018) **63**:404–20. doi: 10.1016/j.cnsns.2018.04.008
33. Lin G. General PFG signal attenuation expressions for anisotropic anomalous diffusion by modified-Bloch equations. *Phys A Stat Mech Appl*. (2018) **497**:86–100. doi: 10.1016/j.physa.2018.01.008
34. Lin G. Analyzing signal attenuation in PFG anomalous diffusion via a modified Gaussian phase distribution approximation based on fractal derivative model. *Phys A Stat Mech Appl*. (2017) **467**:277–88. doi: 10.1016/j.physa.2016.10.036
35. Lin G. Analysis of PFG anomalous diffusion via real-space and phase-space approaches. *Mathematics*. (2018) **6**:17. doi: 10.3390/math6020017
36. Zecca M, Vogt SJ, Connolly PRJ, May EF, Johns ML. NMR measurements of tortuosity in partially saturated porous media. *Trans Porous Media*. (2018) **125**:271–88. doi: 10.1007/s11242-018-1118-y
37. Fieremans E, Burcaw LM, Lee HH, Lemberskiy G, Veraart J, Novikov DS. *In vivo* observation and biophysical interpretation of time-dependent diffusion in human white matter. *Neuroimage*. (2016) **129**:414–27. doi: 10.1016/j.neuroimage.2016.01.018
38. Novikov DS, Jensen JH, Helpern JA, Fieremans E. Revealing mesoscopic structural universality with diffusion. *Proc Natl Acad Sci USA*. (2014) **111**:5088–93. doi: 10.1073/pnas.1316944111
39. Saxton MJ. A biological interpretation of transient anomalous subdiffusion. I Qualitative model. *Biophys J*. (2007) **92**:1178–91. doi: 10.1529/biophysj.106.092619
40. Bouchaud JP, Georges A. Anomalous diffusion in disordered media. Statistical mechanisms, models and physical applications. *Phys Rep*. (1990) **195**:127–293. doi: 10.1016/0370-1573(90)90099-N
41. Platani MI, Goldberg I, Lamond AI, Swedlow JR. Cajal body dynamics and association with chromatin are ATP-dependent. *Nat Cell Biol*. (2002) **4**:502–8. doi: 10.1038/ncb809
42. Palombo M, Gabrielli A, De Santis A, Capuani S. The γ parameter of the stretched-exponential model is influenced by internal gradients: validation in phantoms. *J Magn Reson*. (2012) **216**:28–36. doi: 10.1016/j.jmr.2011.12.023
43. Caporale A, Palombo M, Macaluso E, Guerreri M, Bozzali M, Capuani S. The γ-parameter of anomalous diffusion quantified in human brain by MRI depends on local magnetic susceptibility differences. *Neuroimage*. (2017) **147**:619–31. doi: 10.1016/j.neuroimage.2016.12.051
44. Guerreri M, Palombo M, Caporale A, Fasano F, Macaluso E, Bozzali M, et al. Age-related microstructural and physiological changes in normal brain measured by MRI γ-metrics derived from anomalous diffusion signal representation. *Neuroimage*. (2019) **188**:654–67. doi: 10.1016/j.neuroimage.2018.12.044
45. De Santis S, Gabrielli A, Bozzali M, Maraviglia B, Macaluso E, Capuani S. Anisotropic anomalous diffusion assessed in the human brain by scalar invariant indice. *Magn Reson Med*. (2011) **65**:1043–52. doi: 10.1002/mrm.22689
46. Zhou XJ, Gao Q, Abdullah O, Magin RL. Studies of anomalous diffusion in the human brain using fractional order calculus. *Magn Reson Med*. (2010) **63**:562–9. doi: 10.1002/mrm.22285
47. Yu Q, Reutens D, Vegh V. Can anomalous diffusion models in magnetic resonance imaging be used to characterise white matter tissue microstructure? *Neuroimage*. (2018) **175**:122–37. doi: 10.1016/j.neuroimage.2018.03.052
48. Yu Q, Reutens D, O'Brien K, Vegh V. Tissue microstructure features derived from anomalous diffusion measurements in magnetic resonance imaging. *Hum Brain Mapp*. (2017) **38**:1068–81. doi: 10.1002/hbm.23441
49. Grinberg F, Farrher E, Ciobanu L, Geoffroy F, Le Bihan D, Shah NJ. (2014). Non-Gaussian diffusion imaging for enhanced contrast of brain tissue affected by ischemic stroke. *PLoS ONE*. (2014) **9**:e89225. doi: 10.1371/journal.pone.0089225
50. Jelescu IO, Budde MD. Design and validation of diffusion MRI models of white matter. *Front Phys*. (2017) **5**:61. doi: 10.3389/fphy.2017.00061
51. Xu B, Su L, Wang Z, Fan Y, Gong G, Zhu W, et al. Anomalous diffusion in cerebral glioma assessed using a fractional motion model. *Magn Reson Med*. (2017) **78**:1944–9. doi: 10.1002/mrm.26581
52. Sui Y, Wang H, Liu G, Damen FW, Wanamaker C, Li Y, et al. Differentiation of low-and high-grade pediatric brain tumors with high b-value diffusion-weighted MR imaging and a fractional order calculus model. *Radiology*. (2015) **277**:489–96. doi: 10.1148/radiol.2015142156

Conflict of Interest: The authors declare that the research was conducted in the absence of any commercial or financial relationships that could be construed as a potential conflict of interest.

frontiers in Neuroscience

ORIGINAL RESEARCH
published: 23 January 2020
doi: 10.3389/fnins.2019.01425

Probabilistic Template of the Lateral Parabrachial Nucleus, Medial Parabrachial Nucleus, Vestibular Nuclei Complex, and Medullary Viscero-Sensory-Motor Nuclei Complex in Living Humans From 7 Tesla MRI

Kavita Singh[1], Iole Indovina[2,3], Jean C. Augustinack[4], Kimberly Nestor[4], María G. García-Gomar[1], Jeffrey P. Staab[5,6] and Marta Bianciardi[1]*

[1] Brainstem Imaging Laboratory, Department of Radiology, Athinoula A. Martinos Center for Biomedical Imaging, Massachusetts General Hospital and Harvard Medical School, Boston, MA, United States, [2] Department of Medicine and Surgery, Saint Camillus International University of Health and Medical Sciences, Rome, Italy, [3] Laboratory of Neuromotor Physiology, IRCCS Santa Lucia Foundation, Rome, Italy, [4] Laboratory for Computational Neuroimaging, Department of Radiology, Athinoula A. Martinos Center for Biomedical Imaging, Massachusetts General Hospital and Harvard Medical School, Boston, MA, United States, [5] Department of Psychiatry and Psychology, Mayo Clinic, Rochester, MN, United States, [6] Department of Otorhinolaryngology – Head and Neck Surgery, Mayo Clinic, Rochester, MN, United States

OPEN ACCESS

Edited by:
Louis Lemieux, University College London, United Kingdom

Reviewed by:
Arash Kamali, University of Texas Health Science Center at Houston, United States
Gianfranco Bosco, University of Rome Tor Vergata, Italy

***Correspondence:**
Kavita Singh
ksingh0@mgh.harvard.edu

Specialty section:
This article was submitted to Brain Imaging Methods, a section of the journal Frontiers in Neuroscience

Received: *28 May 2019*
Accepted: *17 December 2019*
Published: *23 January 2020*

Citation:
Singh K, Indovina I, Augustinack JC, Nestor K, García-Gomar MG, Staab JP and Bianciardi M (2020) Probabilistic Template of the Lateral Parabrachial Nucleus, Medial Parabrachial Nucleus, Vestibular Nuclei Complex, and Medullary Viscero-Sensory-Motor Nuclei Complex in Living Humans From 7 Tesla MRI. Front. Neurosci. 13:1425. doi: 10.3389/fnins.2019.01425

The lateral parabrachial nucleus, medial parabrachial nucleus, vestibular nuclei complex, and medullary viscero-sensory-motor (VSM) nuclei complex (the latter including among others the solitary nucleus, vagus nerve nucleus, and hypoglossal nucleus) are anatomically and functionally connected brainstem gray matter structures that convey signals across multiple modalities between the brain and the spinal cord to regulate vital bodily functions. It is remarkably difficult to precisely extrapolate the location of these nuclei from *ex vivo* atlases to conventional 3 Tesla *in vivo* images; thus, a probabilistic brainstem template in stereotaxic neuroimaging space in living humans is needed. We delineated these nuclei using single-subject high contrast 1.1 mm isotropic resolution 7 Tesla MRI images. After precise coregistration of nuclei labels to stereotaxic space, we generated a probabilistic template of their anatomical locations. Finally, we validated the nuclei labels in the template by assessing their inter-rater agreement, consistency across subjects and volumes. We also performed a preliminary comparison of their location and microstructural properties to histologic sections of a postmortem human brainstem specimen. In future, the resulting probabilistic template of these brainstem nuclei in stereotaxic space may assist researchers and clinicians in evaluating autonomic, vestibular and VSM nuclei structure, function and connectivity in living humans using conventional 3 Tesla MRI scanners.

Keywords: lateral parabrachial nucleus, medial parabrachial nucleus, vestibular nuclei complex, solitary nucleus, vagus nerve nucleus, hypoglossal nucleus, *in vivo* neuroimaging-based human template, multi-contrast 7 Tesla MRI

INTRODUCTION

The lateral parabrachial (LPB) nucleus, medial parabrachial (MPB) nucleus, vestibular (Ve) nuclei complex and medullary viscero-sensory-motor (VSM) nuclei (i.e., solitary nucleus, vagus nerve nucleus, hypoglossal nucleus, prepositus, intercalated nucleus, and interpositus) complex are anatomically and functionally connected brainstem gray matter structures that convey signals across multiple modalities between the brain and the spinal cord to regulate vital bodily functions. Specifically, these structures, individually or synergistically, regulate arousal (e.g., LBP, MPB) (Kaur et al., 2013), gustatory processes (e.g., VSM) (Matsumoto, 2013), sensory-motor function (VSM) (Olszewski and Baxter, 1954), and autonomic functions like cardio-respiratory (e.g., LPB and MPB) (Damasceno et al., 2014) and gastrointestinal processes (e.g., VSM) (Bokiniec et al., 2017). Clinical conditions that alter the structure or function of these nuclei, including cerebrovascular events, autoimmune diseases, trauma, stroke (Choi and Kim, 2018) and neurodegenerative disorders may produce a wide variety of symptoms and signs including disruptions of sleep and alertness, autonomic dysregulation, vertigo, and impaired control of eye movements and gait.

To identify the location of arousal, vestibular and viscero-sensory-motor nuclei in living humans, neuroscientists and neurosurgeons currently rely on the work of neuroanatomists and pathologists, who created meticulous *postmortem* atlases of the human brainstem (Olszewski and Baxter, 1954; Paxinos and Huang, 1995; Naidich et al., 2009; Paxinos et al., 2012). Yet, it is remarkably difficult to precisely extrapolate the location of these nuclei from *ex vivo* atlases to conventional 3 Tesla *in vivo* images because these nuclei are not clearly visible in conventional imaging and display inter-subject and age-dependent variability. Moreover, *postmortem* atlases (Olszewski and Baxter, 1954; Paxinos and Huang, 1995; Naidich et al., 2009; Paxinos et al., 2012) are mostly *2D, non-probabilistic* (i.e., derived from a single or very few brainstem specimens —mostly of elderly subjects), and *non-deformable* (i.e., mostly static) representations of brainstem nuclei with inherent distortions due to tissue manipulation.

This indicates the need to expand current probabilistic neuroimaging brain atlases (Desikan et al., 2006; Destrieux et al., 2010; Bianciardi et al., 2015, 2018), to include these currently missing nuclei relevant for the aforementioned broad set of diseases.

The aim of this study was to create, in living humans, a stereotaxic probabilistic structural template of the right and left LPB (LPB-r and LPB-l), MPB (MPB-r and MPB-l), Ve (Ve-r and Ve-l), and VSM (VSM-r and VSM-l) using high-resolution (1.1-mm isotropic), multi-contrast diffusion fractional-anisotropy (FA) and T_2-weighted images at 7 Tesla. This tool may augment modern day research and clinical brainstem studies by enabling a more precise identification of the location of these nuclei in conventional 3 Tesla images of living humans.

MATERIALS AND METHODS

MRI Data Acquisition

To delineate LPB, MPB, Ve, and VSM nuclei we used data acquired in our previous study (Bianciardi et al., 2015), which is detailed below. After providing written informed consent in accordance with the Declaration of Helsinki, twelve healthy subjects (6m/6f, age 28 $\pm$ 1 years) underwent 7 Tesla MRI. The Massachusetts General Hospital Institutional Review Board approved the study protocol. Data were acquired using a custom-built 32-channel receive coil and volume transmit coil (Keil et al., 2010), which provided increased sensitivity for the brainstem compared to commercial coils. Common single-shot 2D echo-planar imaging (EPI) scheme was utilized to obtain 1.1 mm isotropic diffusion tensor images (DTI) in sagittal plane, and T_2-weighted images, with following parameters: matrix size/GRAPPA factor/nominal echo-spacing = 180 $\times$ 240/3/0.82 ms. The resulting T_2-weighted anatomical images and the DTI images had perfectly matched resolution and geometric distortions. The EPI scheme helped us overcome specific-absorption-rate limits of spin-warp T_2-weighted MRI at 7 Tesla. The additional parameters used for DTI and T_2-weighted image acquisition included: spin-echo EPI, echo-time/repetition-time = 60.8 ms/5.6 s, slices = 61, partial Fourier: 6/8, unipolar diffusion-weighting gradients (for DTI), number of diffusion directions = 60 (for DTI, *b*-value $\sim$ 1000 s/mm^2), 7 interspersed "b0" images (non-diffusion weighted, *b*-value $\sim$ 0 s/mm^2, also used as T_2-weighted MRI), 4 repetitions, acquisition time per repetition 6′43″. The entire acquisition time for T_2-weighted MRI and DTI was $\sim$ 27′. Importantly, for DTI acquisition at 7 Tesla, where tissue has shorter T_2 values, we used unipolar (Stejskal and Tanner, 1965) instead of bipolar (Reese et al., 2003) diffusion gradients. This led to shortened echo-time (less by $\sim$30 ms) and significantly improved sensitivity of high-resolution DTI.

MRI Data Pre-processing and Alignment to MNI Space

On a single-subject basis, after concatenation of four DTI repetitions, the data were preprocessed for distortion and motion artifacts using the Diffusion Toolbox in the FMRIB Software Library (FSL, Oxford, United Kingdom). The diffusion tensor at each voxel was estimated (using FRIMB's Diffusion toolbox) to compute diffusion tensor FA from tensor eigenvalues. After motion correction, affine transformation was performed to coregister the averaged 28 "b0" T_2-weighted images to DTI data (Bianciardi et al., 2015).

On a single-subject basis, precise coregistration of both T_2-weighted images and FA to MNI space was performed as in Bianciardi et al. (2015). Specifically, the brainstem of each subject was aligned to an MNI space based FA template (termed "IIT space"; Illinois Institute of Technology human brain atlas, v.3, Chicago, IL, United States) (Varentsova et al., 2014) using the Advanced Normalization Tool (ANTs, Philadelphia, PA, United States) (Avants et al., 2011). This template was used since it has high contrast, is compatible with

diffusion-based tractography and covers the whole brainstem (encompassing medulla as well). Particularly, we computed and concatenated a generic affine and a high-dimensional non-linear warp transformation of images with the same modality (FA maps). The generic affine transformation was calculated by concatenating center-of mass alignment (degrees of freedom-dof = 3), rigid (dof = 6), similarity (dof = 7), and fully affine (dof = 12) transformations with smoothing sigmas: 4, 2, 1, 0 voxels – fixed image space. The high-dimensional non-linear warp transformation employed histogram image matching prior to registration and a symmetric diffeomorphic normalization transformation model with smoothing sigmas: 3, 2, 1, 0 voxels – fixed image space. We also performed a cross correlation metric, gradient step size: 0.2; regular sampling, data winsorization – quantiles: 0.005, 0.995; four multi-resolution levels: shrink factors 6, 4, 2, 1 voxels – fixed image space; convergence criterion: slope of the normalized energy profile over the last 10 iterations $< 10^{-8}$. The resulting combined transformation (using a single-interpolation step method: linear), was then applied to both single-subject T_2-weighted and FA images. Further, for each subject, T_2-weighted and FA images were also aligned to MNI152 standard space (non-linear 6th generation MNI152_T1_1mm available for instance in FSL; coined "MNI152_1mm space"), which is a frequently utilized space for fMRI analysis. While the MNI152_1mm space and the IIT space show satisfactory alignment elsewhere, there is slight misalignment in the brainstem, particularly in the pons and medulla. As such, single-subject FA and T_2-weighted images were aligned to MNI152_1mm space. This was done by using a single-interpolation step (interpolation method: linear) and applying two concatenated transformations, namely single-subject to IIT space transformation (described above); and IIT to MNI152_1mm non-linear transformation, with parameters described above.

Single-Subject Labeling and Probabilistic Template Generation

On a single-subject basis, two raters (KS and MB) independently performed manual delineations (fslview, FSL, Oxford, United Kingdom) using multi-contrast FA maps and T_2-weighted images in IIT space to yield single-subject labels (i.e., masks) of the regions of interest (LPB-r/l, MPB-r/l, Ve-r/l, and VSM-r/l). The intersection of the labels of the two raters was used as the final label. Manual delineations were aided by the use of anatomical landmarks and neighborhood rules described in a literature postmortem brainstem atlas (Paxinos et al., 2012). Of note, to delineate each nucleus, we mainly used the image modality that displayed the nucleus boundaries with good contrast (FA MRI for LPB, MPB, Ve, VSM), and employed the other modality (T_2-weighted), which had poor contrast for that nucleus, to identify cerebrospinal fluid (CSF) boundaries (as for LPB and Ve nuclei).

A probabilistic neuroimaging template in IIT space was formulated for each nucleus as an average probability map of the nucleus label encompassing all subjects (100% overlap of nuclei labels across subjects, $n = 12$ was considered highest probability). After registering the individual subject labels to MNI152_1mm space, by applying the IIT to MNI152 transformations described above (nearest neighbors interpolation), a similar template was derived in MNI152_1mm. We developed the resulting template (in both IIT and MNI152 spaces), to facilitate extrapolation to diffusion and functional MRI modalities.

For each subject and label (coregistered to single-subject native space via an inverse of the method described in section "MRI Data Pre-processing and Alignment to MNI Space") we also calculated the label volume in native space, yielding the mean standard error (SE) volume for all subjects and compared these values to literature (Paxinos et al., 2012) volumes as described in section "Template Validation."

Template Validation

The probabilistic nuclei template was validated by computing for each nucleus and subject: (i) the inter-rater agreement, as the modified Hausdorff distance between labels delineated by the two raters; (ii) the internal consistency across subjects of the final label, as the modified Hausdorff distance between each final label and the probabilistic template label (thresholded at 35%) generated by averaging the labels across the other 11 subjects (leave-one-out cross validation). For both the inter-rater agreement and the internal consistency, we calculated the modified Hausdorff distance (Dubuisson and Jain, 1994) which is a measure of spatial overlap frequently used in neuroimaging (Fischl et al., 2008; Klein et al., 2009, 2010; Augustinack et al., 2013). For each label, the minimum distance of every point on one label from the other label was averaged across all points, resulting in two distance values. The maximum value of these two values was calculated and used as modified Hausdorff distance. For each nucleus, the modified Hausdorff distance of (i) and (ii) was then averaged across subjects.

For further (iii) probabilistic template validation, we computed the volume of the delineated nuclei (i.e., of the final labels, intersection of the labels generated by each rater) and compared them to precisely computed literature nuclei volumes from the Paxinos atlas (Paxinos et al., 2012). For nuclei volume calculation based on the Paxinos atlas, we acquired snapshots of brainstem plates ranging from −5 to +32 mm (Figures 8.12–8.49 of Paxinos et al., 2012) using Adobe Acrobat Reader. Later each snapshot was converted to single-slice nifti images with a slice thickness of 1 mm and proper spatial resolution using Matlab. To determine the in-plane isotropic spatial resolution of each slice, the number of pixels between adjacent coordinates was computed manually based on coordinate system provided for each plate (Paxinos et al., 2012). This varied between 0.0222 and 0.0417 mm in the examined plates. Based on Paxinos nomenclature (Paxinos et al., 2012), we manually delineated using ITK-Snap (Yushkevich et al., 2006) sub-regions of LPB, MPB, Ve and VSM and combined them to obtain final nuclei. For MPB, based on Paxinos terminology, we combined MPB and MPB external part (MPBE). For LPB, based on Paxinos atlas, we combined sub-nuclei of LPB external (LPBE), LPB central (LPBC), LPB dorsal (LPBD), LPB, LPB-superior (LPBS), and LPB unlabeled (i.e., a very small neighboring region compatible with LPB, yet missing the LPB label in the Paxinos atlas).

We delineated and combined to final Ve nuclei complex the following Paxinos sub-nuclei: the nucleus of origin of vestibular efferents of the vestibular nerve (EVe), lateral vestibular nucleus (LVe), medial vestibular nucleus magnocellular part (MVeMC), medial vestibular nucleus (MVe), medial vestibular nucleus parvicellular part (MVePC), paravestibular nucleus (PaVe), spinal (i.e., inferior) vestibular nucleus (SpVe), and superior vestibular nucleus (SuVe). Similarly for VSM, we delineated and combined labels of: solitary nucleus commissural part (SolC), solitary nucleus dorsolateral part (SolDL), solitary nucleus dorsal part (SolD), solitary nucleus gelatinous part (SolG), solitary nucleus intermediate part (SolIM), solitary nucleus interstitial part (SolI), solitary nucleus medial part (SolM), solitary nucleus paracommissural part (SolPaC), solitary nucleus ventrolateral part (SolVL), solitary nucleus ventral part (SolV), vagus nerve nucleus (10N), hypoglossal nucleus (12N), prepositus (Pr), intercalated nucleus (In), and interpositus nucleus (IPo). To get a literature nucleus/sub-nucleus volume, we multiplied the number of delineated voxels in each nucleus/sub-nucleus by the voxel volume for each slice and added the resulting number across slices for each nucleus/subnucleus.

For additional (iv) validation of LPB and MPB probabilistic template labels, we performed preliminary histological evaluation of these nuclei in a postmortem human brainstem specimen. A brainstem specimen from a 65-year-old adult male without neurologic disease was obtained from MGH Autopsy Suite and studied. Five mesopontine transverse vibratome sections (50 μm thick) were Nissl (cell body) stained, and five adjacent sections were Gallyas (myelin) stained. Each section was mounted onto a gelatin dipped glass slide and dried overnight. *Nissl thionin-based staining:* After defatting with chloroform-alcohol, and undergoing pre-treatment with acetic acid, sections were stained with 1% thionin for 3 min, differentiated in 70% with a few drops of glacial acetic acid, and dehydrated in ascending series (70, 70, 95, 95, 95, 100, and 100%) of alcohol. *Gallyas staining:* Sections were post-fixed with 10% formol for 10 days. Then, they underwent the following steps: (1) *acetylation* with 2:1 mixture of pyridine and acetic anhydride (30 min); (2) *wash* with distilled water; (3) *impregnation* with ammoniacal silver nitrate (pH 7.3, 30 min); (4) *wash* with distilled water; (5) *development* with stock ABC solutions of ammonium nitrate, sliver nitrate and tungstosilicic acid (10 min); (6) *development stop* with 1% acetic acid; (7) *bleaching* with 0.2% potassium ferricyanide (10 min); (8) *stop* with 0.5% acetic acid; (9) *stop* with 0.5% sodium thiosulfate; (10) *wash* with distilled water; and (11) *dehydration* with ascending series (50, 70, 95, and 100%) of alcohol. *Cover-slipping and digitization:* After Nissl or Gallyas staining, sections were cover-slipped from xylene using Permount. The Nissl and Gallyas stained sections were digitized using an 80i Nikon Microscope (Microvideo Instruments, Avon, MA, United States) with a 4× objective (i.e., 40× total magnification), which resulted in images with a 1.85 μm pixel size. We automatically acquired the images using the virtual tissue workflow provided from Stereo Investigator (MBF Bioscience, Burlington, VT, United States). Later we subtracted the background using GIMP[1], an open-source drawing and annotation software.

RESULTS

The probabilistic neuroimaging structural labels in MNI space of LPB-r/l, MPB-r/l, Ve-r//l, and VSM-r/l are shown in **Figures 1–4**. We briefly describe the nuclei delineations on the basis of the MRI contrast that guided them, as well as on the basis of neighborhood relationships with other visible structures. LPB (**Figure 1**) appeared as a thin hypointense region on FA maps at the mesopontine junction, bounded medially and ventro-medially by the superior cerebellar peduncle (SCP; a hyperintense region on FA maps), rostrally by the pedunculotegmental nucleus (a hypointense region on FA maps described in Bianciardi et al., 2018), and dorsally/dorsolaterally by the CSF (visible on T_2-weighted MRI). On FA maps, the MPB (**Figure 2**) was visible as a thin hypointense stripe lying along the medial surface of the SCP caudal to its decussation in the lateral part of the oral pontine tegmentum, and extending down to the level of oral pole of superior vestibular nucleus (described below). The superior, medial, lateral and spinal vestibular nuclei were not visible as individual nuclei, yet they appeared as a single hypointense oblong-shaped region on FA maps, which was labeled as Ve nuclei complex (**Figure 3**). This complex extended from the caudal tip of the MPB at the ponto-medullary junction, to the medulla at the level of the mid inferior olivary nucleus (a hypointense region in FA, delineated in our previous study (Bianciardi et al., 2015). On axial T_2-weighted images, this complex was bounded dorso-laterally by the CSF of the fourth ventricle (visible on T_2-weighted MRI). Finally, we delineated solitary along with nuclei 12N, 10N and smaller nuclei Pr, In, IPo within the VSM nuclei complex (**Figure 4**), an area of diffusion FA brighter than the adjacent medullary reticular formation and darker than neighboring white matter fiber bundles (e.g., medial longitudinal fasciculus). The VSM nuclei complex lay inferiorly to the ponto-medullary junction extending caudally throughout the medulla along the whole extent of the inferior olivary nucleus (hypointense region on FA images delineated in Bianciardi et al., 2015). On a coronal view, both VSM bilateral nuclei appeared as an inverted V-shape dorsally at their apex (**Figure 4**). Further, VSM assumed a lateral position in the floor of fourth ventricle in the periventricular medullary region. Orally, it lay next to Ve as a hypointense region, as seen in axial views of FA maps.

For each nucleus, the average modified Hausdorff distance assessing the inter-rater agreement and the internal consistency of nuclei template labels are shown in **Figure 5**. The modified Hausdorff distance and the internal consistency were found to be below ($p < 10^{-7}$ in unpaired one-tailed t-test) the linear spatial imaging resolution (1.1 mm), thus validating the generated probabilistic nuclei labels. Interestingly, we showed better values of inter-rater agreement (and the internal consistency, to a lesser extent) for Ve then LBP/MPB/VSM. This might be due to much bigger volume of Ve as opposed

[1]https://www.gimp.org

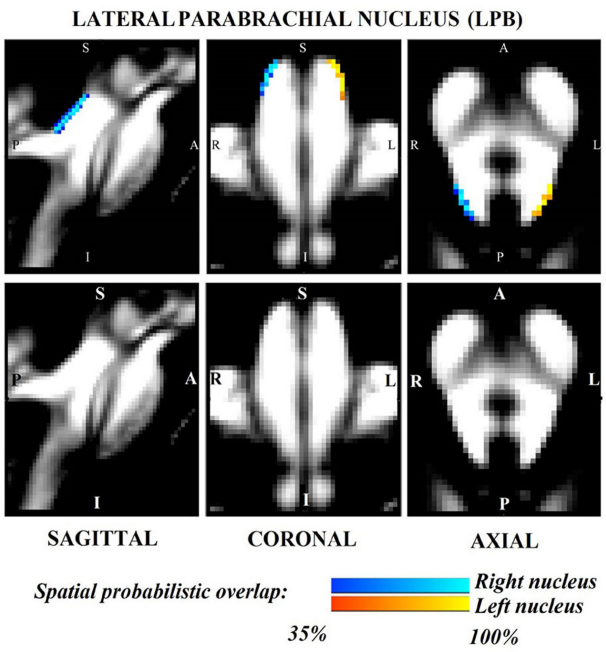

FIGURE 1 | Probabilistic (n = 12) template label in MNI space of the lateral parabrachial nucleus (right nucleus: blue-to-cyan; left nucleus: red-to-yellow). Very good (i.e., up to 100%) spatial agreement of labels across subjects was observed indicating the feasibility of delineating the probabilistic label of these nuclei involved in arousal and autonomic functions.

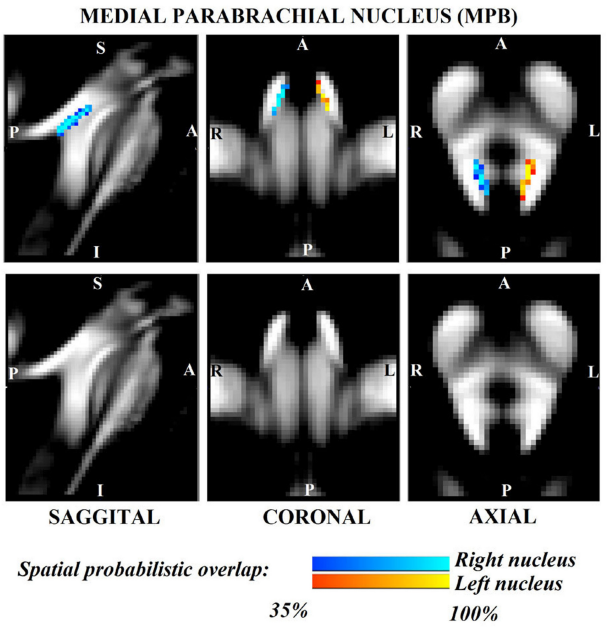

FIGURE 2 | Probabilistic (n = 12) template label in MNI space of the medial parabrachial nucleus (right nucleus: blue-to-cyan; left nucleus: red-to-yellow). Very good (i.e., up to 100%) spatial agreement of labels across subjects was observed indicating the feasibility of delineating the probabilistic label of these nuclei involved in arousal and autonomic functions.

to thin/smaller regions of LPB/MPB/VSM and very good contrast with respect to neighboring regions (e.g., white matter inferior cerebellar peduncle, ventricular CSF); however, nuclei volume should not be considered a limiting factor, and we found statistically significant values of inter-rater agreement and internal consistency in all nuclei.

The volume (mean ± SE across subjects) of each final label in native space and nuclei volumes from the literature (Paxinos et al., 2012) are shown in **Table 1**. The volume of MPB, Ve and VSM labels did not differ from Paxinos' volumes (p-value < 0.05), whereas the volumes of LPB were larger than volumes computed from the Paxinos atlas (Paxinos et al., 2012). In **Table 1**, we report details of volume computation of LPB, MPB, Ve, VSM nuclei and of nuclei sub-regions, as obtained from the Paxinos atlas and current study.

In **Figure 6**, we show a preliminary validation of the LPB and MPB *in vivo* nuclei label location and of their microstructural properties by the use of histology of a postmortem human brainstem specimen. Specifically, the FA map of MRI showed the hypointense region (as expected for gray matter nuclei) of LPB and MPB lining the hyperintense region of the SCP. Voxels of intermediate intensity in between SCP and parabrachial nuclei could be observed and could be attributed to partial volume effects. Nissl stain showed obvious difference between sparsely stained white matter of SCP and more densely stained gray matter of LPB and MPB displaying the distribution of neuronal cell bodies within these nuclei, further validating our nuclei localization. In the Gallyas staining, we found similar results where white matter of SCP could be demarcated from parabrachial nuclei based on their argyrophilic properties (**Figure 6**). These initial findings appear promising and need to be further extended for validation of Ve and VSM.

DISCUSSION

In the present work, we demonstrated the feasibility of single-subject delineations of LPB, MPB, Ve, and VSM nuclei in living humans using 7 Tesla MRI. Further, we created a probabilistic template of these nuclei after precise coregistration to stereotaxic neuroimaging space. Finally, we validated the generated template by assessing the inter-rater agreement, the consistency across subjects, and the volumes of the delineated labels. Our findings of most nuclei volumes match previously reported studies in literature (Paxinos et al., 2012), further strengthening our nuclei delineation. As a preliminary *ex vivo* validation, we performed histological staining of a few nuclei (LPB and MPB), which showed remarkable consistency to *in vivo* MRI. Here, we first discuss the strengths and limitations of nuclei delineations, then the nuclei function and the potential impact of the generated template.

Strengths and Limitations of Nuclei Delineations

We delineated LPB, MPB, Ve, and VSM nuclei based on high contrast FA maps and T_2–weighted images obtained at 7 Tesla. MRI acquisition at 7 Tesla as compared to 3 Tesla specifically

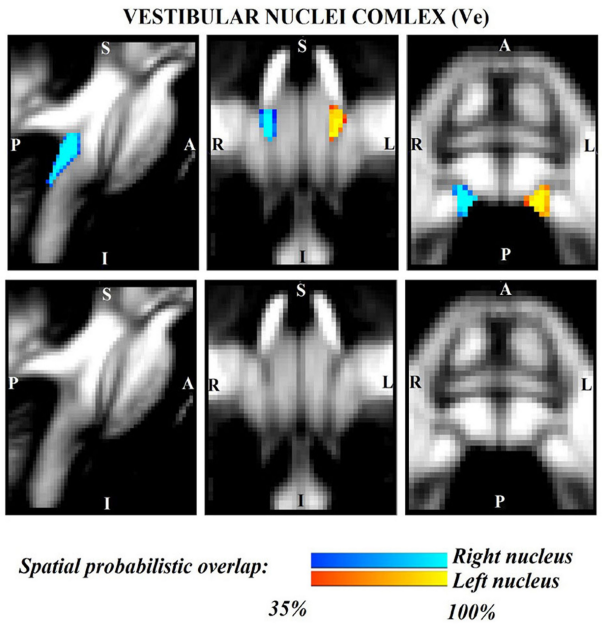

FIGURE 3 | Probabilistic (n = 12) template label in MNI space of the vestibular nuclei complex (right nuclei complex: blue-to-cyan; left nuclei complex: red-to-yellow). Very good (i.e., up to 100%) spatial agreement of labels across subjects was observed indicating the feasibility of delineating the probabilistic label of this complex of nuclei involved in vestibular functions (e.g., postural, oculo-motor control). Note that we did not have enough resolution/contrast to easily discriminate between *individual* (e.g., superior, lateral, medial, inferior) vestibular nuclei within this complex.

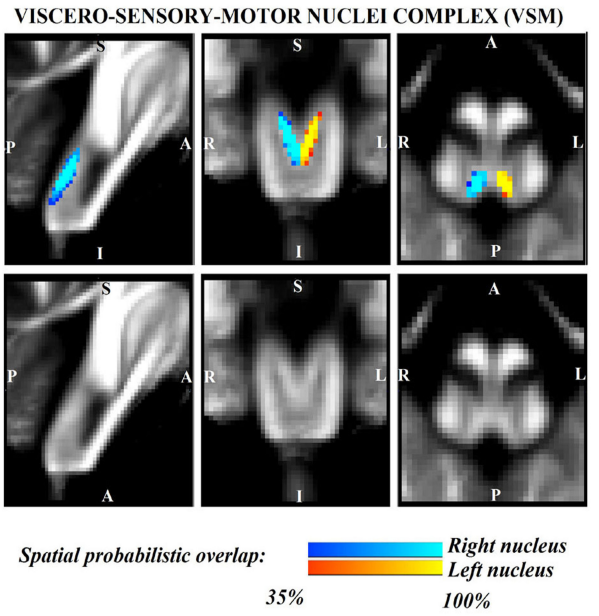

FIGURE 4 | Probabilistic (n = 12) template label in MNI space of the viscero-sensory-motor-nuclei complex (right nuclei complex: blue-to-cyan; left nuclei complex: red-to-yellow). Very good (i.e., up to 100%) spatial agreement of labels across subjects was observed indicating the feasibility of delineating the probabilistic label of this complex of nuclei. Note that we did find good contrast showing V-shaped nuclei in the coronal section, which matched the exact description of nuclei from literature (Olszewski and Baxter, 1954); yet, we did not have enough resolution/contrast to easily discriminate between *individual* nuclei within this complex (i.e., solitary nucleus, vagus nerve nucleus, hypoglossal nucleus, prepositus, intercalated nucleus, and interpositus).

provided better image sensitivity and resolution for nuclei delineations. The ∼2.2 fold increase in sensitivity due to the higher field strength was further augmented by the use of a custom-built volume transmit coil and 32-channel receive coil (Keil et al., 2010). The latter provided improved sensitivity for the brainstem compared to commercial coils with the same number of channels due to: (a) customized arrangement of the coil elements, also enabling a more efficient flip angle calibration

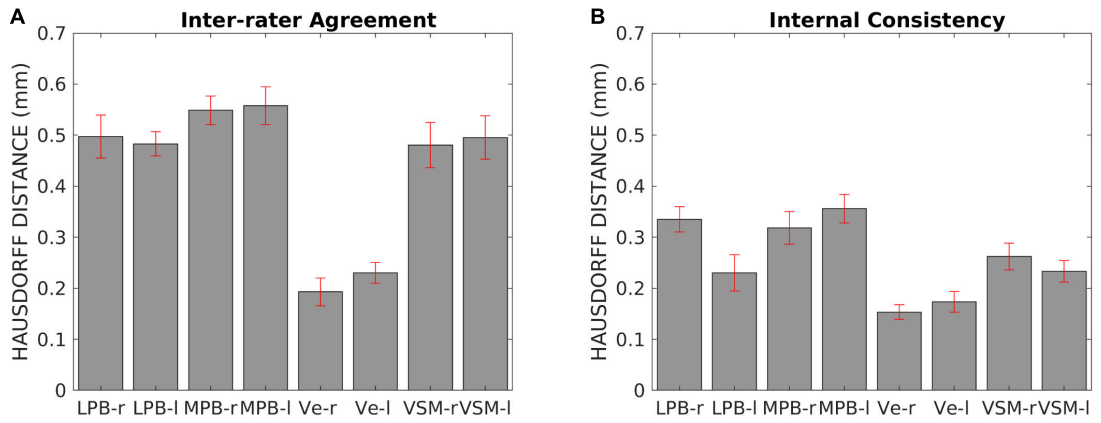

FIGURE 5 | Template validation. We show: **(A)** the inter-rater agreement of nuclei segmentations (bar/errorbar = mean/SE modified Hausdorff distance across 12 subjects); **(B)** the internal consistency of nuclei labels across subjects (bar/errorbar = mean/SE modified Hausdorff distance across 12 subjects). The labels of the LPB-r/l, MPB-r/l, Ve-r/l, and VSM-r/l displayed good spatial overlap across raters and subjects (the modified Hausdorff distance was smaller than the spatial imaging resolution), thus validating the probabilistic nuclei template.

TABLE 1 | Detailed computation of nuclei volumes from previous histology atlas (Paxinos et al., 2012) and from current study.

	Prior study (Paxinos et al., 2012)			Current study	
Nucleus name (acronym)	**Sub-nucleus name (acronym)**	**Volume (mm^3)**	**Total volume (mm^3)**	**Right nucleus volume (mm^3)**	**Left nucleus volume (mm^3)**
				Mean ± SE	**Mean ± SE**
Lateral parabrachial nucleus (LPB)	LPB	8.4	34.3	53.9 ± 2.6	54.7 ± 4.8
	LPB, central part (LPBC)	5.1			
	LPB, dorsal part (LPBD)	12.2			
	LPB, external part (LPBE)	2.5			
	LPB, unlabeled	6.1			
Medial parabrachial nucleus (MPB)	MPB	37.1	40.4	47.6 ± 3.8	46.3 ± 3.6
	MPB, external part (MPBE)	3.3			
Vestibular nuclei complex (Ve)	Nucleus of vestibular efferents (EVe)	0.5	136.4	135.5 ± 3.8	129.9 ± 4.0
	Lateral vestibular nucleus (LVe)	8.2			
	Medial vestibular nucleus (MVe)	35.9			
	MVe, magnocellular part (MVeMC)	6.2			
	MVe, parvicellular part (MVePC)	17			
	Paravestibular nucleus (PaVe)	3.7			
	Spinal vestibular nucleus (SpVe)	41.7			
	Superior vestibular nucleus (SuVe)	23.3			
Viscero-sensory-motor nuclei complex (VSM)	Solitary nucleus, commissural part (SolC)	1.8	90.6	84.9 ± 3.3	87.7 ± 3.2
	Sol, dorsolateral part (SolDL)	2.9			
	Sol, dorsal part (SolD)	0.2			
	Sol, gelatinous part (SolG)	4.4			
	Sol, intermediate part (SolIM)	6.6			
	Sol, interstitial part (SolI)	4.1			
	Sol, medial part (SolM)	5.9			
	Sol, paracommissural part (SolPaC)	1.4			
	Sol, ventrolateral part (SolVL)	1.7			
	Sol, ventral part (SolV)	1.7			
	Vagus nerve nucleus (10N)	11.8			
	Hypoglossal nucleus (12N)	19.1			
	Prepositus (Pr)	16.3			
	Intercalated nucleus (In)	6.4			
	Interpositus (IPo)	6.2			

for inferior areas of the brain; (b) sharp curvature posteriorly resembling human head and enabling better signal reception from the cerebellum and brainstem. To achieve optimized brainstem images at 7 Tesla it was also crucial to adopt: (i) minimum echo-time using monopolar scheme (given the lower gray and white matter T_2 values at higher magnetic field); (ii) optimized RF transmit gain in our region of interest (the brainstem), which was otherwise hindered by strong RF inhomogeneities at 7 Tesla, using actual flip angle imaging pulse sequence (Yarnykh, 2007); and (iii) semi-automatic B_0 shimming.

As expected from postmortem atlases, LPB bounded laterally and superiorly (in its most caudal aspect) the SCP, medially the CSF and inferiorly the pedunculotegmental nucleus. The MPB lay medial to the SCP, superior to vestibular nuclei and lateral to a gray matter area containing the locus coeruleus, the laterodorsal tegmental nucleus and the central gray of the rhombencephalon. The superior, medial, lateral and spinal vestibular nuclei were not clearly visible as individual nuclei, yet as a complex with homogeneous FA. The Ve nuclei complex, in line with Paxinos atlas, extended from the caudal tip of the MPB at the ponto-medullary junction, to the medulla at the level of the mid inferior olivary nucleus; it was medial to the inferior cerebellar peduncle and ventral to the forth ventricle. Similarly, Sol, 12N, 10N and smaller nuclei Pr, In, IPo were delineated within the VSM nuclei complex, not individually. We observed a peculiar diffusion FA contrast of the VSM, which displayed intermediate FA values between neighboring gray matter, such as the medullary reticular formation, and white matter, such as the medial longitudinal fasciculus. We speculate that the partial volume effect of the VSM with the

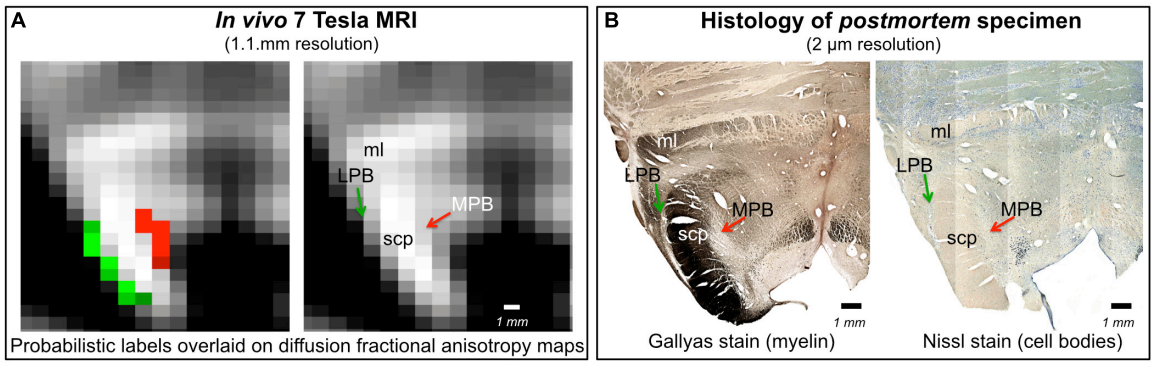

FIGURE 6 | *In vivo* nuclei template validation by preliminary histology of postmortem brainstem specimens. We provide further validation for the LPB and MPB brainstem nuclei delineations. As expected for gray matter regions, LPB and MPB were areas of: **(A)** hypointensity in *in vivo* 7 Tesla FA MRI maps; **(B)** hypointensity in myelin stains (left) and hyperintensity in cell body stains (right) of a postmortem brainstem specimen. In each panel, the LPB and MPB bounded, respectively, laterally and medially the white matter superior cerebellar peduncle (SCP; anterior to the SCP the medial lemniscus is labeled as ml).

solitary tract, nerves 10 and 12 might be at the origin of this contrast. In line with the Paxinos atlas (Paxinos et al., 2012), the VSM nuclei complex extended from the ponto-medullary junction, next to the Ve to the inferior medulla at a level of the lower tip of the inferior olivary nucleus, and was bounded dorsally by the CSF. Interestingly, on a coronal view, both VSM bilateral nuclei appeared as an inverted V-shape as described in other studies (Olszewski and Baxter, 1954; Naidich et al., 2009; Paxinos et al., 2012). These findings corroborated well with our histological evaluation (**Figure 6**), where we found similar anatomical landmarks for LPB and MPB as seen in our *in vivo* template. This postmortem evaluation was done in a cognitively healthy volunteer donor, who unfortunately did not undergo prior MRI evaluation. Thus, our validation was limited to a qualitative comparison for nuclei position, rather than a quantitative correlation of histology with *in vivo* MRI findings in the same subject. Note that, *in vivo* and *ex vivo* examination in same cognitively healthy adult volunteer are difficult to perform, especially in younger adults.

The quantitative validation using the inter-rater agreement and internal consistency of *in vivo* probabilistic labels provided positive results for all nuclei. The number of subjects in this study was limited; nevertheless, a sample size of 10–12 subjects was enough to achieve significant results in the current as well as previous brain/brainstem template work (Bianciardi et al., 2015, 2018; Croxson et al., 2018; García-Gomar et al., 2019). Comparison of the probabilistic label volume with the volume derived from the Paxinos histology-based atlas drawings (Olszewski and Baxter, 1954) was quite good for MPB, Ve, and VSM, yet there was some mismatch for LPB. We ascribe this discrepancy most probably to partial volume effects, because our LPB labels delineated using 1.1 mm isotropic resolution voxels might contain CSF and a stripe of the SCP adjacent to the LPB. The LPB is indeed a very thin stripe of gray matter with a width ranging between approximately 0.5 to 1 mm.

For proper applicability of this template, note that a precise coregistration to conventional MRI is needed. Nonetheless, coregistration of subcortical structure is less trivial than coregistration of cortical foldings (Fischl et al., 2008; Greve and Fischl, 2009). Moreover, with the development of new registration tools (Klein et al., 2009; Avants et al., 2011) and of multi-modal atlases in MNI space (Varentsova et al., 2014) including diffusion-based contrast and T_2-weighted contrast, beyond the original MNI T_1-weighted contrast, we predict better accuracy of brainstem coregistration, for example from native single-subject space to MNI space. Same modality coregistration of single-subject images to target stereotaxic images has provided promising outcomes for single-subject FA maps to the IIT FA map, as used here. Recent work by our group has demonstrated the feasibility of generating a template in MNI space and functional connectome of tiny brainstem structures, thus proving the feasibility of accurately coregistering these small nuclei across subjects to a common template.

On the Nuclei Function and the Potential Impact of the Generated Template

We delineated LPB and MPB nuclei located at the mesopontine junction and involved in chemoreception, nociception, stress, autonomic control, aversive behaviors and arousal functions (Spector, 1995; Bester et al., 1997; Reilly and Trifunovic, 2001; Gauriau and Bernard, 2002; Chamberlin, 2004; Pattinson et al., 2009; Fuller et al., 2011; Kaur et al., 2013; Davern, 2014; Myers et al., 2017). For instance, functional studies (Pattinson et al., 2009; Zuperku et al., 2017) show the involvement of LPB and MPB nuclei in respiratory control; however, their roles could not be segregated due to unavailability of *in vivo* human atlas specifically delineating these labels at high-resolution (Pattinson et al., 2009). MPB relays information from the taste area of the solitary nucleus to the ventral posteromedial nucleus of the thalamus and forebrain (Sclafani et al., 2001; Naidich et al., 2009), while the LPB relays viscero-sensory information. Owing to multi-functional involvement of sub-nuclei of LPB and its overlapping role with MPB, we speculate our template might help in

refining definite roles for these nuclei in functional imaging in human subjects.

Brainstem vestibular and autonomic nuclei display an intricate wiring diagram with other brainstem nuclei and with the rest of the brain, as shown by animal and *ex vivo* work (Balaban, 2002; Balaban et al., 2011; Staab et al., 2013). Alteration in the connectivity of these nuclei is the hallmark of several brain disorders (Millan, 2002; Niblock et al., 2004; Brown et al., 2010; Linnman et al., 2012; Mello-Carpes and Izquierdo, 2013; Satpute et al., 2013), including vestibular disorders and anxiety (Balaban and Thayer, 2001; Balaban, 2004; Bächinger et al., 2019). According to the National Institutes of Health National Institute on Deafness and other Communication Disorders (NIDCD) (NIDCD, 2015), chronic vestibular disorders (including chronic imbalance and dizziness) affect about 5% of the American adult population, their mechanisms are not fully understood (Kitahara et al., 1997; Ris et al., 1997; Godemann et al., 2005; Heinrichs et al., 2007; Best et al., 2009; Dutia, 2010; Mahoney et al., 2013; Cousins et al., 2014) and treatment with serotonergic antidepressants and vestibular habituation are only partially successful (Staab et al., 2013). Adverse vestibular-autonomic interactions (Fischl et al., 2008; Indovina et al., 2014, 2015; Staab et al., 2014; Riccelli et al., 2017a,b; Nigro et al., 2018; Passamonti et al., 2018) appear to precipitate and perpetuate chronic vestibular disorders, crucially underlying the pathophysiologic process of these disorders. Our findings offer potential benefits to investigate the connectivity pathways of Ve and autonomic nuclei in living humans on widely available 3 Tesla scanners, and expand our knowledge of successful compensation for acute vestibular events versus development of chronic vestibular disorders.

Solitary nuclei integrate interoceptive and viscero-sensory input with descending affective and cognitive information from the limbic forebrain (Rinaman and Dzmura, 2007). Early studies showed solitary nuclei role in autonomic control, however recent literature indicates their involvement in plethora of behavioral and neuroendocrine processes (Rinaman, 2010), thereby further providing impetus for precise delineations of these nuclei in living humans. Solitary nuclei have been involved in behaviors relating to fear memory, anxiety and depression (Miyashita and Williams, 2002; Ghosal et al., 2014) along with modulating behavioral responses to stress, which is also governed by parabrachial nuclei. Based on these growing evidences of overlapping functions and differential response of these nuclei to stimuli and their mode of action, we advocate that the present study might help with nuclei localization and their future functional assessment, as well as facilitate the study of various neurological disorders and neurosurgical planning.

Summary, Conclusion, and Future Directions

In summary, we foresee that the generated probabilistic template of LPB, MPB, Ve, and VSM in stereotaxic space —representative of younger human adults— might be a useful tool for improving localization of brainstem nuclei involved in autonomic, vestibular and VSM functions. Researchers and clinicians will be able to shift from the difficult and imprecise task of extrapolating locations from *ex vivo* atlases to this new, user-friendly 3D, probabilistic, and deformable tool to identify the location of brainstem nuclei more precisely in *in vivo* images derived from conventional 3 Tesla MRI scanners. After its release on public repositories of neuroimaging data and tools, users will be able to precisely coregister the template onto single-subject 3 Tesla MRI, just as existing atlases [e.g., AAL, Harvard Oxford (Desikan et al., 2006; Destrieux et al., 2010)] are now used. This will make the template accessible to researchers and clinicians who use widely available 3 Tesla scanners, and study brainstem mechanisms in health, vestibular and balance disorders, impairment in autonomic and VSM function, sleep and anxiety disorders, as well as neurodegenerative disease.

DATA AVAILABILITY STATEMENT

The datasets analyzed in this article are not publicly available. Requests to access the datasets should be directed to martab@mgh.harvard.edu.

ETHICS STATEMENT

The studies involving human participants were reviewed and approved by MGH Institutional Review Board, Massachusetts General Hospital, Boston, MA, United States. The patients/participants provided their written informed consent to participate in this study.

AUTHOR CONTRIBUTIONS

MB designed the research, performed the experiments, and secured the funding in collaboration with II and JS. MB preprocessed and analyzed the *in vivo* data. KS and MB manually labeled the ROIs. MB, JA, and KN performed the histology. KS, II, KN, MG-G, JS, and MB wrote the manuscript. All authors gave feedback along the process.

FUNDING

This work was supported by the following sources of funding: National Institute on Deafness and other Communication Disorders R21 DC015888, National Institutes of Health (NIH) National Institute of Biomedical Imaging and Bioengineering K01 EB019474 and P41 EB015896, National Cancer Institute U01 CA193632, the Massachusetts General Hospital Claflin Distinguished Scholar Award, and Harvard University Mind/Brain/Behavior Faculty Award. This work was also in part made possible by the resources provided by Shared Instrumentation Grants 1S10RR023401, 1S10RR019307, and 1S10RR023043, Italian Ministry of Health (PE-2013-02355372).

REFERENCES

Augustinack, J. C., Huber, K. E., Stevens, A. A., Roy, M., Frosch, M. P., van der Kouwe, A. J. W., et al. (2013). Predicting the location of human perirhinal cortex, Brodmann's area 35, from MRI. *NeuroImage* 64, 32–42. doi: 10.1016/j.neuroimage.2012.08.071

Avants, B. B., Tustison, N. J., Song, G., Cook, P. A., Klein, A., and Gee, J. C. (2011). A reproducible evaluation of ANTs similarity metric performance in brain image registration. *NeuroImage* 54, 2033–2044. doi: 10.1016/j.neuroimage.2010.09.025

Bächinger, D., Luu, N.-N., Kempfle, J. S., Barber, S., Zürrer, D., Lee, D. J., et al. (2019). Vestibular aqueduct morphology correlates with endolymphatic sac pathologies in menière's disease-A correlative histology and computed tomography study. *Otol. Neurotol.* 40, e548–e555. doi: 10.1097/MAO.0000000000002198

Balaban, C. D. (2002). Neural substrates linking balance control and anxiety. *Physiol. Behav.* 77, 469–475. doi: 10.1016/s0031-9384(02)00935-6

Balaban, C. D. (2004). Projections from the parabrachial nucleus to the vestibular nuclei: potential substrates for autonomic and limbic influences on vestibular responses. *Brain Res.* 996, 126–137. doi: 10.1016/j.brainres.2003.10.026

Balaban, C. D., Jacob, R. G., and Furman, J. M. (2011). Neurologic bases for comorbidity of balance disorders, anxiety disorders and migraine: neurotherapeutic implications. *Expert Rev. Neurother.* 11, 379–394. doi: 10.1586/ern.11.19

Balaban, C. D., and Thayer, J. F. (2001). Neurological bases for balance-anxiety links. *J. Anxiety Disord.* 15, 53–79. doi: 10.1016/s0887-6185(00)00042-6

Best, C., Eckhardt-Henn, A., Tschan, R., and Dieterich, M. (2009). Psychiatric morbidity and comorbidity in different vestibular vertigo syndromes. Results of a prospective longitudinal study over one year. *J. Neurol.* 256, 58–65. doi: 10.1007/s00415-009-0038-8

Bester, H., Matsumoto, N., Besson, J. M., and Bernard, J. F. (1997). Further evidence for the involvement of the spinoparabrachial pathway in nociceptive processes: a c-Fos study in the rat. *J. Comp. Neurol.* 383, 439–458. doi: 10.1002/(sici)1096-9861(19970714)383:4<439::aid-cne4>3.3.co;2-n

Bianciardi, M., Strong, C., Toschi, N., Edlow, B. L., Fischl, B., Brown, E. N., et al. (2018). A probabilistic template of human mesopontine tegmental nuclei from in vivo 7T MRI. *NeuroImage* 170, 222–230. doi: 10.1016/j.neuroimage.2017.04.070

Bianciardi, M., Toschi, N., Edlow, B. L., Eichner, C., Setsompop, K., Polimeni, J. R., et al. (2015). Toward an in vivo neuroimaging template of human brainstem nuclei of the ascending arousal, autonomic, and motor systems. *Brain Connect.* 5, 597–607. doi: 10.1089/brain.2015.0347

Bokiniec, P., Shahbazian, S., McDougall, S. J., Berning, B. A., Cheng, D., Llewellyn-Smith, I. J., et al. (2017). Polysialic acid regulates sympathetic outflow by facilitating information transfer within the nucleus of the solitary tract. *J. Neurosci.* 37, 6558–6574. doi: 10.1523/JNEUROSCI.0200-17.2017

Brown, E. N., Lydic, R., and Schiff, N. D. (2010). General anesthesia, sleep, and coma. *N. Engl. J. Med.* 363, 2638–2650. doi: 10.1056/NEJMra0808281

Chamberlin, N. L. (2004). Functional organization of the parabrachial complex and intertrigeminal region in the control of breathing. *Respir. Physiol. Neurobiol.* 143, 115–125. doi: 10.1016/j.resp.2004.03.015

Choi, K.-D., and Kim, J.-S. (2018). Vascular vertigo: updates. *J. Neurol.* 266, 1835–1843. doi: 10.1007/s00415-018-9040-3

Cousins, S., Cutfield, N. J., Kaski, D., Palla, A., Seemungal, B. M., Golding, J. F., et al. (2014). Visual dependency and dizziness after vestibular neuritis. *PLoS One* 9:e105426. doi: 10.1371/journal.pone.0105426

Croxson, P. L., Forkel, S. J., Cerliani, L., and Thiebaut de Schotten, M. (2018). Structural variability across the primate brain: a cross-species comparison. *Cereb. Cortex* 28, 3829–3841. doi: 10.1093/cercor/bhx244

Damasceno, R. S., Takakura, A. C., and Moreira, T. S. (2014). Regulation of the chemosensory control of breathing by Kölliker-Fuse neurons. *Am. J. Physiol. Regul. Integr. Comp. Physiol.* 307, R57–R67. doi: 10.1152/ajpregu.00024.2014

Davern, P. J. (2014). A role for the lateral parabrachial nucleus in cardiovascular function and fluid homeostasis. *Front. Physiol.* 5:436. doi: 10.3389/fphys.2014.00436

Desikan, R. S., Ségonne, F., Fischl, B., Quinn, B. T., Dickerson, B. C., Blacker, D., et al. (2006). An automated labeling system for subdividing the human cerebral cortex on MRI scans into gyral based regions of interest. *NeuroImage* 31, 968–980. doi: 10.1016/j.neuroimage.2006.01.021

Destrieux, C., Fischl, B., Dale, A., and Halgren, E. (2010). Automatic parcellation of human cortical gyri and sulci using standard anatomical nomenclature. *NeuroImage* 53, 1–15. doi: 10.1016/j.neuroimage.2010.06.010

Dubuisson, M. P., and Jain, A. K. (1994). "A modified Hausdorff distance for object matching," in *Proceedings of 12th International Conference on Pattern Recognition*, Jerusalem, 566–568.

Dutia, M. B. (2010). Mechanisms of vestibular compensation: recent advances. *Curr. Opin. Otolaryngol. Head Neck Surg.* 18, 420–424. doi: 10.1097/MOO.0b013e32833de71f

Mahoney, A. E. J., Edelman, S., and D Cremer, P. (2013). Cognitive behavior therapy for chronic subjective dizziness: longer-term gains and predictors of disability. *Am. J. Otolaryngol.* 34, 115–120. doi: 10.1016/j.amjoto.2012.09.013

Fischl, B., Rajendran, N., Busa, E., Augustinack, J., Hinds, O., Yeo, B. T. T., et al. (2008). Cortical folding patterns and predicting cytoarchitecture. *Cereb. Cortex* 18, 1973–1980. doi: 10.1093/cercor/bhm225

Fuller, P., Sherman, D., Pedersen, N. P., Saper, C. B., and Lu, J. (2011). Reassessment of the structural basis of the ascending arousal system. *J. Comp. Neurol.* 519, 933–956. doi: 10.1002/cne.22559

García-Gomar, M. G., Strong, C., Toschi, N., Singh, K., Rosen, B. R., Wald, L. L., et al. (2019). *In vivo* probabilistic structural atlas of the inferior and superior colliculi, medial and lateral geniculate nuclei and superior olivary complex in humans based on 7 tesla MRI. *Front. Neurosci.* 13:764. doi: 10.3389/fnins.2019.00764

Gauriau, C., and Bernard, J.-F. (2002). Pain pathways and parabrachial circuits in the rat. *Exp. Physiol.* 87, 251–258. doi: 10.1113/eph8702357

Ghosal, S., Bundzikova-Osacka, J., Dolgas, C. M., Myers, B., and Herman, J. P. (2014). Glucocorticoid receptors in the nucleus of the solitary tract (NTS) decrease endocrine and behavioral stress responses. *Psychoneuroendocrinology* 45, 142–153. doi: 10.1016/j.psyneuen.2014.03.018

Godemann, F., Siefert, K., Hantschke-Brüggemann, M., Neu, P., Seidl, R., and Ströhle, A. (2005). What accounts for vertigo one year after neuritis vestibularis - anxiety or a dysfunctional vestibular organ? *J. Psychiatr. Res.* 39, 529–534. doi: 10.1016/j.jpsychires.2004.12.006

Greve, D. N., and Fischl, B. (2009). Accurate and robust brain image alignment using boundary-based registration. *NeuroImage* 48, 63–72. doi: 10.1016/j.neuroimage.2009.06.060

Heinrichs, N., Edler, C., Eskens, S., Mielczarek, M. M., and Moschner, C. (2007). Predicting continued dizziness after an acute peripheral vestibular disorder. *Psychosom. Med.* 69, 700–707. doi: 10.1097/PSY.0b013e318151a4dd

Indovina, I., Riccelli, R., Chiarella, G., Petrolo, C., Augimeri, A., Giofrè, L., et al. (2015). Role of the insula and vestibular system in patients with chronic subjective dizziness: an fMRI study using sound-evoked vestibular stimulation. *Front. Behav. Neurosci.* 9:334. doi: 10.3389/fnbeh.2015.00334

Indovina, I., Riccelli, R., Staab, J. P., Lacquaniti, F., and Passamonti, L. (2014). Personality traits modulate subcortical and cortical vestibular and anxiety responses to sound-evoked otolithic receptor stimulation. *J. Psychosom. Res.* 77, 391–400. doi: 10.1016/j.jpsychores.2014.09.005

Kaur, S., Pedersen, N. P., Yokota, S., Hur, E. E., Fuller, P. M., Lazarus, M., et al. (2013). Glutamatergic signaling from the parabrachial nucleus plays a critical role in hypercapnic arousal. *J. Neurosci.* 33, 7627–7640. doi: 10.1523/JNEUROSCI.0173-13.2013

Keil, B., Triantafyllou, C., Hamm, M., and Wald, L. (2010). "Design optimization of a 32-channel head coil at 7 T," in *Proceedings of the Annual Meeting of the International Society for Magnetic Resonance in Medicine*, Stockholm, 1493.

Kitahara, T., Takeda, N., Saika, T., Kubo, T., and Kiyama, H. (1997). Role of the flocculus in the development of vestibular compensation: immunohistochemical studies with retrograde tracing and flocculectomy using Fos expression as a marker in the rat brainstem. *Neuroscience* 76, 571–580. doi: 10.1016/s0306-4522(96)00374-0

Klein, A., Andersson, J., Ardekani, B. A., Ashburner, J., Avants, B., Chiang, M.-C., et al. (2009). Evaluation of 14 nonlinear deformation algorithms applied to human brain MRI registration. *NeuroImage* 46, 786–802. doi: 10.1016/j.neuroimage.2008.12.037

Klein, A., Ghosh, S. S., Avants, B., Yeo, B. T. T., Fischl, B., Ardekani, B., et al. (2010). Evaluation of volume-based and surface-based brain image registration methods. *NeuroImage* 51, 214–220. doi: 10.1016/j.neuroimage.2010.01.091

Linnman, C., Moulton, E. A., Barmettler, G., Becerra, L., and Borsook, D. (2012). Neuroimaging of the periaqueductal gray: state of the field. *NeuroImage* 60, 505–522. doi: 10.1016/j.neuroimage.2011.11.095

Matsumoto, I. (2013). Gustatory neural pathways revealed by genetic tracing from taste receptor cells. *Biosci. Biotechnol. Biochem.* 77, 1359–1362. doi: 10.1271/bbb.130117

Mello-Carpes, P. B., and Izquierdo, I. (2013). The Nucleus of the Solitary Tract → Nucleus Paragigantocellularis → *Locus Coeruleus* → CA1 region of dorsal hippocampus pathway is important for consolidation of object recognition memory. *Neurobiol. Learn. Mem.* 100, 56–63. doi: 10.1016/j.nlm.2012.12.002

Millan, M. J. (2002). Descending control of pain. *Prog. Neurobiol.* 66, 355–474.

Miyashita, T., and Williams, C. L. (2002). Glutamatergic transmission in the nucleus of the solitary tract modulates memory through influences on amygdala noradrenergic systems. *Behav. Neurosci.* 116, 13–21. doi: 10.1037/0735-7044.116.1.13

Myers, B., Scheimann, J. R., Franco-Villanueva, A., and Herman, J. P. (2017). Ascending mechanisms of stress integration: implications for brainstem regulation of neuroendocrine and behavioral stress responses. *Neurosci. Biobehav. Rev.* 74, 366–375. doi: 10.1016/j.neubiorev.2016.05.011

Naidich, T. P., Duvernoy, H. M., Delman, B. N., Sorensen, A. G., Kollias, S. S., and Haacke, E. M. (2009). *Duvernoy's Atlas of the Human Brain Stem and Cerebellum: High-Field MRI, Surface Anatomy, Internal Structure, Vascularization and 3 D Sectional Anatomy*. Berlin: Springer Science & Business Media.

Niblock, M. M., Kinney, H. C., Luce, C. J., Belliveau, R. A., and Filiano, J. J. (2004). The development of the medullary serotonergic system in the piglet. *Auton. Neurosci. Basic Clin.* 110, 65–80. doi: 10.1016/j.autneu.2003.10.004

NIDCD (2015). *2012-2016 NIDCD Strategic Plan*. Available at: https://www.nidcd.nih.gov/about/strategic-plan/2012-2016/2012-2016-nidcd-strategic-plan (accessed April 19, 2019)

Nigro, S., Indovina, I., Riccelli, R., Chiarella, G., Petrolo, C., Lacquaniti, F., et al. (2018). Reduced cortical folding in multi-modal vestibular regions in persistent postural perceptual dizziness. *Brain Imaging Behav.* 13, 798–809. doi: 10.1007/s11682-018-9900-6

Olszewski, J., and Baxter, D. (1954). *Cytoarchitecture of the Human Brain Stem*. Basel: Karger.

Passamonti, L., Riccelli, R., Lacquaniti, F., Staab, J. P., and Indovina, I. (2018). Brain responses to virtual reality visual motion stimulation are affected by neurotic personality traits in patients with persistent postural-perceptual dizziness. *J. Vestib. Res. Equilib. Orientat.* 28, 369–378. doi: 10.3233/VES-190653

Pattinson, K. T. S., Mitsis, G. D., Harvey, A. K., Jbabdi, S., Dirckx, S., Mayhew, S. D., et al. (2009). Determination of the human brainstem respiratory control network and its cortical connections in vivo using functional and structural imaging. *NeuroImage* 44, 295–305. doi: 10.1016/j.neuroimage.2008.09.007

Paxinos, G., and Huang, X. (1995). *Atlas of Human Brainstem*. Amsterdam: Elsevier.

Paxinos, G., Xu-Feng, H., Sengul, G., and Watson, C. (2012). "Chapter 8 - Organization of brainstem nuclei," in *The Human Nervous System (Third Edition)*, eds J. K. Mai, and G. Paxinos (San Diego, CA: Academic Press), 260–327. doi: 10.1016/B978-0-12-374236-0.10008-2

Reese, T. G., Heid, O., Weisskoff, R. M., and Wedeen, V. J. (2003). Reduction of eddy-current-induced distortion in diffusion MRI using a twice-refocused spin echo. *Magn. Reson. Med.* 49, 177–182. doi: 10.1002/mrm.10308

Reilly, S., and Trifunovic, R. (2001). Lateral parabrachial nucleus lesions in the rat: neophobia and conditioned taste aversion. *Brain Res. Bull.* 55, 359–366. doi: 10.1016/s0361-9230(01)00517-2

Riccelli, R., Indovina, I., Staab, J. P., Nigro, S., Augimeri, A., Lacquaniti, F., et al. (2017a). Neuroticism modulates brain visuo-vestibular and anxiety systems during a virtual rollercoaster task. *Hum. Brain Mapp.* 38, 715–726. doi: 10.1002/hbm.23411

Riccelli, R., Passamonti, L., Toschi, N., Nigro, S., Chiarella, G., Petrolo, C., et al. (2017b). Altered insular and occipital responses to simulated vertical self-motion in patients with persistent postural-perceptual dizziness. *Front. Neurol.* 8:529. doi: 10.3389/fneur.2017.00529

Rinaman, L. (2010). Ascending projections from the caudal visceral nucleus of the solitary tract to brain regions involved in food intake and energy expenditure. *Brain Res.* 1350, 18–34. doi: 10.1016/j.brainres.2010.03.059

Rinaman, L., and Dzmura, V. (2007). Experimental dissociation of neural circuits underlying conditioned avoidance and hypophagic responses to lithium chloride. *Am. J. Physiol. Regul. Integr. Comp. Physiol.* 293, R1495–R1503. doi: 10.1152/ajpregu.00393.2007

Ris, L., Capron, B., de Waele, C., Vidal, P. P., and Godaux, E. (1997). Dissociations between behavioural recovery and restoration of vestibular activity in the unilabyrinthectomized guinea-pig. *J. Physiol.* 500(Pt 2), 509–522. doi: 10.1113/jphysiol.1997.sp022037

Satpute, A. B., Wager, T. D., Cohen-Adad, J., Bianciardi, M., Choi, J.-K., Buhle, J. T., et al. (2013). Identification of discrete functional subregions of the human periaqueductal gray. *Proc. Natl. Acad. Sci. U.S.A.* 110, 17101–17106. doi: 10.1073/pnas.1306095110

Sclafani, A., Azzara, A. V., Touzani, K., Grigson, P. S., and Norgren, R. (2001). Parabrachial nucleus lesions block taste and attenuate flavor preference and aversion conditioning in rats. *Behav. Neurosci.* 115, 920–933. doi: 10.1037//0735-7044.115.4.920

Spector, A. C. (1995). Gustatory function in the parabrachial nuclei: implications from lesion studies in rats. *Rev. Neurosci.* 6, 143–175.

Staab, J. P., Balaban, C. D., and Furman, J. M. (2013). Threat assessment and locomotion: clinical applications of an integrated model of anxiety and postural control. *Semin. Neurol.* 33, 297–306. doi: 10.1055/s-0033-1356462

Staab, J. P., Rohe, D. E., Eggers, S. D. Z., and Shepard, N. T. (2014). Anxious, introverted personality traits in patients with chronic subjective dizziness. *J. Psychosom. Res.* 76, 80–83. doi: 10.1016/j.jpsychores.2013.11.008

Stejskal, E. O., and Tanner, J. E. (1965). Spin diffusion measurements: spin echoes in the presence of a time-dependent field gradient. *J. Chem. Phys.* 42, 288–292. doi: 10.1063/1.1695690

Varentsova, A., Zhang, S., and Arfanakis, K. (2014). Development of a high angular resolution diffusion imaging human brain template. *NeuroImage* 91, 177–186. doi: 10.1016/j.neuroimage.2014.01.009

Yarnykh, V. L. (2007). Actual flip-angle imaging in the pulsed steady state: a method for rapid three-dimensional mapping of the transmitted radiofrequency field. *Magn. Reson. Med.* 57, 192–200. doi: 10.1002/mrm.21120

Yushkevich, P. A., Piven, J., Hazlett, H. C., Smith, R. G., Ho, S., Gee, J. C., et al. (2006). User-guided 3D active contour segmentation of anatomical structures: significantly improved efficiency and reliability. *NeuroImage* 31, 1116–1128. doi: 10.1016/j.neuroimage.2006.01.015

Zuperku, E. J., Stucke, A. G., Hopp, F. A., and Stuth, E. A. E. (2017). Characteristics of breathing rate control mediated by a subregion within the pontine parabrachial complex. *J. Neurophysiol.* 117, 1030–1042. doi: 10.1152/jn.00591.2016

Conflict of Interest: The authors declare that the research was conducted in the absence of any commercial or financial relationships that could be construed as a potential conflict of interest.

The reviewer GB declared a past co-authorship with one of the authors II.

frontiers in Neuroscience

PERSPECTIVE
published: 07 February 2020
doi: 10.3389/fnins.2020.00072

Multiscale Imaging Approach for Studying the Central Nervous System: Methodology and Perspective

Michela Fratini[1,2], Ali Abdollahzadeh[3], Mauro DiNuzzo[1], Raimo A. Salo[3], Laura Maugeri[1], Alessia Cedola[2], Federico Giove[1,4], Olli Gröhn[3], Jussi Tohka[3] and Alejandra Sierra[3]*

[1] IRCCS Fondazione Santa Lucia, Rome, Italy, [2] Institute of Nanotechnology-CNR c/o Physics Department, Sapienza University of Rome, Rome, Italy, [3] A. I. Virtanen Institute for Molecular Sciences, University of Eastern Finland, Kuopio, Finland, [4] Museo Storico della Fisica e Centro Studi e Ricerche Enrico Fermi, Rome, Italy

OPEN ACCESS

Edited by:
Ofer Pasternak, Harvard Medical School, United States

Reviewed by:
Diana Cash, King's College London, United Kingdom
Ayal Ben-Zvi, The Hebrew University of Jerusalem, Israel

***Correspondence:**
Michela Fratini
michela.fratini@gmail.com

Specialty section:
This article was submitted to Brain Imaging Methods, a section of the journal Frontiers in Neuroscience

Received: *09 September 2019*
Accepted: *20 January 2020*
Published: *07 February 2020*

Citation:
Fratini M, Abdollahzadeh A, DiNuzzo M, Salo RA, Maugeri L, Cedola A, Giove F, Gröhn O, Tohka J and Sierra A (2020) Multiscale Imaging Approach for Studying the Central Nervous System: Methodology and Perspective. Front. Neurosci. 14:72. doi: 10.3389/fnins.2020.00072

Non-invasive imaging methods have become essential tools for understanding the central nervous system (CNS) in health and disease. In particular, magnetic resonance imaging (MRI) techniques provide information about the anatomy, microstructure, and function of the brain and spinal cord *in vivo* non-invasively. However, MRI is limited by its spatial resolution and signal specificity. In order to mitigate these shortcomings, it is crucial to validate MRI with an array of ancillary *ex vivo* imaging techniques. These techniques include histological methods, such as light and electron microscopy (EM), which can provide specific information on the tissue structure in healthy and diseased brain and spinal cord, at cellular and subcellular level. However, these conventional histological techniques are intrinsically two-dimensional (2D) and, as a result of sectioning, lack volumetric information of the tissue. This limitation can be overcome with genuine three-dimensional (3D) imaging approaches of the tissue. 3D highly resolved information of the CNS achievable by means of other imaging techniques can complement and improve the interpretation of MRI measurements. In this article, we provide an overview of different 3D imaging techniques that can be used to validate MRI. As an example, we introduce an approach of how to combine diffusion MRI and synchrotron X-ray phase contrast tomography (SXRPCT) data. Our approach paves the way for a new multiscale assessment of the CNS allowing to validate and to improve our understanding of *in vivo* imaging (such as MRI).

Keywords: multimodal image coregistration, magnetic resonance image, X-ray phase contrast microtomography, multiscale imaging, brain, spinal cord, image coregistration

Abbreviations: 2D, two-dimensional; 3D, three-dimensional; ANTs, advanced normalization tools; CNS, central nervous system; dMRI, diffusion magnetic resonance imaging; DTI, diffusion tensor imaging; EM, electron microscopy; ESRF, european synchrotron radiation facility; FA, fractional anisotropy; LM, light microscopy; MRI, magnetic resonance imaging; SCT, spinal cord toolbox; SXRPCT, synchrotron X-ray phase contrast tomography.

INTRODUCTION

Diagnosis, monitoring, surgical interventions, and treatment planning strategies of diseases in the central nervous system (CNS) strongly benefit from non-invasive imaging methods. Among all imaging techniques, magnetic resonance imaging (MRI) has become the most valuable approach in both clinical and experimental settings because of its non-invasive nature and high image quality. Conventional MRI sequences, such as T1- or T2-weighted, are extensively used to detect tissue alterations and damage during neurodegeneration, tumor growth or after injury. However, conventional MRI methods have low sensitivity for distinct early pathological processes. Other MRI methodologies, such as magnetization transfer (Filippi and Rocca, 2004, 2007; Sled, 2018), proton density (Mezer et al., 2016), susceptibility weighted imaging (Liu et al., 2015; Vargas et al., 2018), and diffusion MRI (dMRI) (Andre and Bammer, 2010; Cohen et al., 2017) are increasingly used in the imaging of the CNS. Diffusion MRI methods, such as diffusion tensor imaging (DTI) (Basser et al., 1994), can obtain tissue microstructural information and unveil tissue changes often not detectable by conventional MRI methods. Even though DTI is already an established and widely used tool, dMRI continues to develop, generating new acquisition approaches such as high-angular resolution diffusion imaging (Tuch et al., 2002), q-space imaging (Cohen and Assaf, 2002; Jensen et al., 2005) or multidimensional dMRI (Westin et al., 2016; Topgaard, 2017), and more elaborate models for data analysis (Wedeen et al., 2008; Panagiotaki et al., 2012; Zhang et al., 2012). These advanced dMRI methods have a great potential to extract intravoxel microstructural information in the CNS beyond DTI.

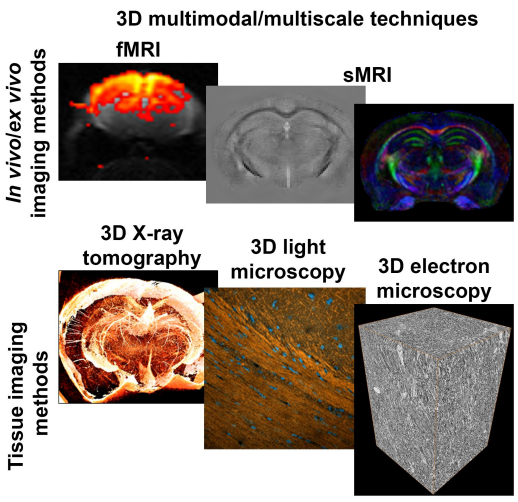

FIGURE 1 | 3D imaging methods. Functional and structural MRI techniques unveil tissue microstructural properties and function in health and during pathology *in vivo*. 3D multiscale tissue imaging methods offer characterization and validation of the MRI contrast *ex vivo*. DTI, diffusion tensor imaging; EM, electron microscopy; fMRI, functional MRI; LM, light microscopy; QSM, quantitative susceptibility mapping; XRPCT, X-ray phase contrast microtomography.

Other emerging MRI methods, such as quantitative susceptibility mapping (Schweser et al., 2011), can detect and discriminate between diamagnetic and paramagnetic materials, which is useful in conditions such as demyelination, calcifications or iron accumulation (Wang and Liu, 2015; Li et al., 2016; Aggarwal et al., 2018).

Despite the inherent value of structural and microstructural MRI techniques to detect abnormal tissue in the CNS, there is a lack of understanding of the origin of imaging contrast. The interpretation of MRI is a challenge because of the limited resolution, and leads us to question: *What information does a single voxel of MRI contain?* To answer this question, it is necessary to understand which tissue components dictate the MRI signal in each voxel. This level of understanding can be reached by correlating MRI contrast with underlying cellular components and characterizing the potential changes altering MRI signal. Therefore, the validation of MRI requires multimodal and multiscale imaging studies, from macro- to nanometer scale, with techniques able to show high-specificity and high-resolution tissue properties, such as cell somas, neurites, vessels, among others, and also in three-dimensional (3D) (**Figure 1**).

HIGH RESOLUTION IMAGING METHODS TO VALIDATE THE MRI CONTRAST

Traditionally, the validation of the MRI contrast has been done with *ex vivo* tissue preparations, e.g., employing histochemistry and immunohistochemistry, which are essentially two-dimensional (2D) approaches. Recent technological advances allow to image the tissue in high-resolution and in 3D with the possibility to image large tissue volumes (**Figure 1**). In particular, technological advances in light microscopy (LM) can image the tissue by optical sectioning of thick tissue sections (Helmstaedter et al., 2008). Confocal microscopes can image a tissue section up to 100 μm-thick (Stelzer, 2006). Tissue sections thicker than 100 μm can be imaged with more advanced techniques, such as light sheet microscopy (Weber and Huisken, 2011) or two-photon microscopy (Denk et al., 1990). Also, the resolution of LM methods have been improved in novel super-resolution techniques, such as stimulated-emission-depletion microscope reaching 40 nm planar resolution *ex vivo* (Hell and Wichmann, 1994)or structured illumination microscopy up to 100 nm resolution *in vivo* (Gustafsson, 2000). Additionally, tissue clearing techniques (Du et al., 2018), such as CLARITY (Chung et al., 2013), 3DCISCO (Ertürk and Bradke, 2013) or ScaleS (Hama et al., 2015), which make the tissue transparent and minimize light-scattering, have opened new avenues in the optical 3D imaging of large tissue coverage, e.g., whole brain.

Imaging of tissue ultrastructure can be achieved with electron microscopy (EM). Advanced EM techniques have expanded the applicability of EM by offering 3D imaging of large field-of-view of tissue (Briggman and Bock, 2012). Serial sectioning transmission EM methods can achieve nanometer in-plane resolution of large tissue sample by combining transmission EM with physical serial sectioning of the samples (Kreshuk et al., 2014). Automatic section-collection methods, such as

automated tape-collection ultramicrotome (Schalek et al., 2011), avoid laborious manual cutting of thousands of sections, image alignment, and missing/distorted sections. Other serial sectioning methods, such as serial block-face scanning electron microscopy (SBEM) can reduce tissue distortions by imaging the slice prior to sectioning (Denk and Horstmann, 2004). SBEM provides 3D high-resolution images collected at the mesoscopic scale in the order of a few hundred micrometers. Focused ion beam scanning electron microscopy (Heymann et al., 2006) is another 3D block-face EM technique (Heymann et al., 2006), which can achieve 4 nm resolution in-plane.

Conventional 3D X-ray imaging techniques, such as classical radiography and tomography (the most widely used tools for imaging objects with hard X-rays), are based on absorption contrast (i.e., on the imaginary part of the refraction index) and are obtained by measuring the attenuation of X-rays through the object. Conversely, high-resolution synchrotron X-ray phase contrast tomography (SXRPCT) (Fratini, 2018) achieves the contrast by imaging the phase modulation induced by an object in a coherent beam, exploiting the real part of the complex refractive index (Fratini et al., 2015). In particular, SXRPCT enables the simultaneous 3D visualization of both dense (e.g., bone) and soft objects (e.g., soft tissue) at length scales ranging from millimeters down to hundreds of nanometers, without the use of contrast agent, sectioning or destructive preparation of the samples (Fitzgerald, 2000; Stefanutti et al., 2018). Samples for XRPCT are typically prepared by perfusing with saline solution containing heparin (50 U/ml) followed by dissection, fixation in 4% paraformaldehyde, and storage in alcohol [for more details about the sample preparation see Fitzgerald (2000) and Stefanutti et al. (2018)].

Phase contrast makes SXRPCT attractive for studies of weakly absorbing samples, both in materials and life sciences. In particular, the highest sensitivity of SXRPCT to electron density with respect to conventional CT has allowed evaluating the morphological alterations in the vascular and the neuronal networks in animal models of neurodegenerative diseases such as multiple sclerosis and Alzheimer's disease (Bravin et al., 2012; Russo, 2017).

In the last decades, many X-ray phase contrast techniques have been developed and successfully applied. Such techniques permit to convert the phase variations of an X-ray beam, due to its interactions with the sample, in measurable intensity modulations.

A simple yet effective phase contrast method for hard X-rays is based on in-line imaging after free-space propagation, which does not require any additional optics, leading to source-limited rather than optics-limited resolution (Paganin et al., 2002). When X-rays illuminate the sample, variations in optical-path length produce slight local deviations (refraction) of the X-ray beam from its original path. When a free-space propagation distance is allowed between sample and detector, the recorded image contains the refraction information in the form of interference fringes, whose detectability depends on the coherence of the X-ray beam. Synchrotron-radiation X-ray sources provide high-photon flux X-ray beams, with a high degree of spatial coherence and allow for the possibility of providing monochromatic beams (Weitkamp et al., 2011). The high quality of the images helps optimize the algorithms used for image analysis and the 3D reconstruction. For the reconstruction of the SXRPCT volume, the first step is the phase retrieval which is applied to all projections of the tomographic measurements, using the code ANKAphase (Cedola et al., 2017; Massimi et al., 2019). The algorithm produces the projected thickness of the object, which is proportional to the refractive index decrement if the object is homogeneous. When applied to all tomographic projections, the retrieved phase maps can be fed to a standard filtered back-projection algorithm to obtain phase tomogram.

In summary, 3D high-resolution imaging methods can provide the necessary tissue information to validate the MRI contrast. LM, EM and X-ray imaging techniques offer 2D/3D high-resolution images, tissue specificity and sample coverage needed to understand the MRI signal in the healthy and diseased brain and spinal cord. Information regarding cell density or which type of cells are present in a particular area, density and orientation of axons forming fiber bundles, vascular density, shape and tortuosity, or any alteration in those tissue metrics during pathological processes can seed light into the interpretation of MRI parameters. Still, the challenge is to combine multidisciplinary and multiscale information into the same reference frame, which is the first step for analyses and quantification of areas of interest in the brain and spinal cord.

Therefore, more sophisticated co-registration tools are required to combine the MRI and tissue data into the same reference frame.

These microscopic techniques (nominal resolution of the order of one micron) could help providing a better interpretation of the images obtained with *in vivo* techniques, using higher-resolution images as a reference atlas.

Thus, from the co-registration between MRI, which has a nominal resolution of the order of 100 μm, and microscopic images, with a nominal resolution of the order of 1 μm, we can achieve information on the underlying microstructure influencing MRI contrast, such as vessels and neurons.

3D dMRI/SXRPCT CO-REGISTRATION METHOD OF THE MOUSE CNS

Here, we briefly describe a pipeline to co-register dMRI and SXRPCT data from the C57BL/6J mouse brain and spinal cord acquired from the same animal (**Figure 2**). *Ex vivo* DTI was acquired with a 9.4 T scanner using segmented spin-echo EPI (TE = 32 ms, TR = 1 s, *b*-value = 3000 s/mm (Filippi and Rocca, 2004), 42 diffusion directions, and 125 μm-isotropic resolution). We generated fractional anisotropy (FA) and directionally encoded colored maps. SXRPCT data was acquired at ID17 beamline at the European Synchrotron Radiation Facility (ESRF) in Grenoble, France. Free-space propagation method, beam energy = 34 keV, CCD pixel size = 3 μm, detector-sample distance ≈ 2.3 m, and samples loaded in a cell filled with agar-agar were used. As the different 3D imaging techniques require different holders, the curvature of the images may differ from each other to an unknown degree. We propose two potential solutions to the

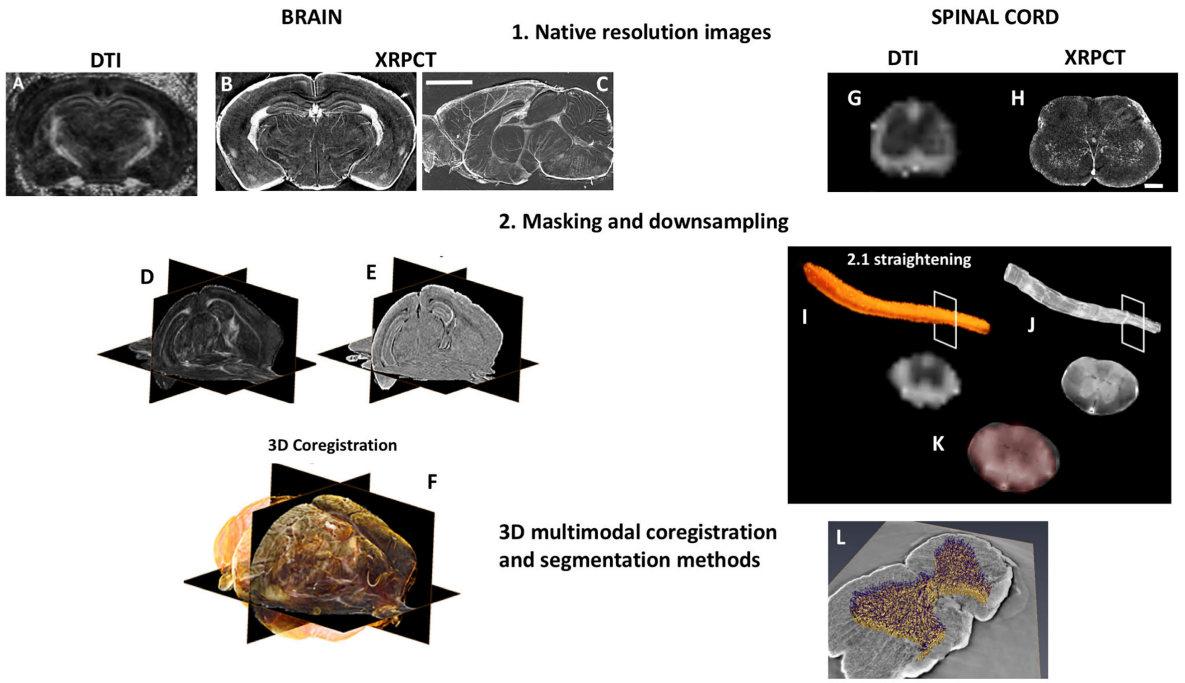

FIGURE 2 | 3D dMRI/XRPCT co-registration of the mouse brain and spinal cord. From the same subject, 3D dMRI and XRPCT image datasets were obtained. The native resolution of dMRI was 125 μm^3 isotropic resolution **(A,G)**, where XRPCT image spatial resolution was 6 μm **(B,C,H)**. The scale bar is 500 μm in the brain and 200 μm in the spinal cord. To facilitate the co-registration, masking of both FA and XRPCT images **(D,I)** and down-sampling of XRPCT images to the image resolution of dMRI maps **(E,J)** were performed. In the case of the spinal cord, we performed the straightening of the whole spinal cord. In the background of panels **(F,K)**, grayscale images represent FA map of the mouse brain, and yellow rendering in the brain and red in spinal cord show the XRPCT data. **(L)** Vascular segmentation of the co-registered spinal cord.

co-registration problem. In the first approach, we segmented 3D images acquired with both techniques, co-registered the images to each other, and fine-tuned using non-linear co-registration tools such as SyN (Avants et al., 2008). This approach works as long as the curvature of the images acquired by MRI and SXRPCT is reasonably similar. While this assumption is generally true with brain samples, this is typically not the case for the spinal cord. This required the development of a second approach, wherein, first of all, we skeletonized both of the segmented images. The resulting skeletons were then straightened, and the image planes perpendicular to the skeletons were moved using the translations and rotations derived from the straightening process.

3D dMRI/SXRPCT Co-registration Method of the Mouse Brain

First, SXRPCT images were low pass filtered to avoid aliasing, and we down-sampled the images to roughly match the dMRI resolution [125 μm (Sled, 2018)]. Then, dMRI images were brain-masked using FSL's BET (Smith, 2002) on the B0 image (**Figure 2D**). Since no suitable tools for automatically masking SXRPCT images are presently available, we used a combination of custom-made MATLAB routines for intensity thresholding, morphological operations, and manual fine-tuning for this task. The brain boundaries showed marginal ring artifacts due to different material density at the interface. An initial brain outline mask was produced using intensity thresholding and including low and high intensities into the mask to reduce the artifact. The mask was then dilated with a 3D circle-shaped structuring element (MATLAB imdilate; radius = 2 voxels) to close the borders and hole-filled using 2D operations (MATLAB-imfill) on the single slices. This was followed by erosions (MATLAB-imerode) with the 3D ball-shaped structuring element until parts of the mask outside of the brain disappeared. The mask was finally dilated to reach the edges of the brain volume (**Figure 2E**). Since FA contrast resembled the contrast in SXRPCT images in some regions, such as the corpus callosum, hippocampus proper and ventricles, we were able to co-register the FA images to the corresponding SXRPCT using advanced normalization tools (ANTs) (Avants et al., 2009). In addition to affine co-registration, we used non-linear diffeomorphic registration SyN (Avants et al., 2008) with Mattes metric (**Figure 2F**) to compensate for possible small sample alterations due to different preparations and susceptibility-induced distortions in the dMRI imaging.

Our analysis yielded a good anatomical agreement between dMRI and SXRPCT images after co-registration. After the 3D co-registration, the native resolution of SXRPCT images can be restored allowing a more advanced analysis and validation of the dMRI maps.

Therefore, a 3D high-resolution micro-imaging technique is required in order to delineate simultaneously the complex vascular organization, down to the smallest capillaries, and the

neuronal and axonal morphology in a large volume of tissue (i.e., the same volume of the MRI scanning) This is a fundamental step toward a better understanding of the neuro-vascular coupling.

3D dMRI/SXRPCT Co-registration of the Mouse Spinal Cord

While existing co-registration tools could be used forthe brain, they do not work for the spinal cord and different template and toolbox have been proposed (De Leener et al., 2017; Cohen-Adad, 2018). The geometry of spinal cord requires more sophisticated tools to co-register datasets into the same reference frame, and in particular the coarse invariance for axial translations is a significant challenge for proper co-registration. Therefore, we devised a potential strategy, as described below, based on a combination of MATLAB routines to obtain a good quality co-registration between dMRI and SXRPCT images of the spinal cord. Since the bones, i.e., vertebrae, were removed prior to the imaging, the location of the intervertebral discs based on image intensity was not possible. Therefore, both the SXRPCT and dMRI data were manually labeled at two consensus reference coordinates, e.g., close to the sample's extremities. These reference points were necessary to insert the images of the two different modalities in the same space, regardless of the image resolution. We use the spinal cord toolbox (SCT) (De Leener et al., 2017) for spinal cord straightening (**Figures 2I,J**).

Synchrotron X-ray phase contrast tomography images were first intensity-adjusted saturating top and bottom 0.3% and down-sampled using volumetric nearest-neighbor interpolation (**Figure 2**). The scaling value for down-sampling was chosen to maximize the image gradient at the sample-medium interface on selected slices in the xy-plane. Then, the contours of the spinal cord were determined in the volume using the "*approximate Canny* method" for 3D-edge-detection (Canny, 1987) (the approximate Canny method uses two thresholds to detect strong and weak edges). Image intensity threshold was calculated using Otsu's method (Otsu, 1979). Two different approaches were used to determine the spinal cord position on the SXRPCT images. The first was based on the center of mass of contour images determined on slices in the xy-plane, which yielded spinal cord centerlines. The second was based on filling of edge images using three-dimensional seeded region growing, which yielded spinal cord binary masks. The original SXRPCT stack and either the spinal cord centerline or the binary mask were then fed to the SCT straightening algorithm (De Leener et al., 2017). The SXRPCT binary mask and DTI images were finally then co-registered using ANTs (**Figures 2K,L**). This approach can be especially useful with parametric maps derived in the original image reference frames that could be transformed into the straightened form. This approach is also robust with respect to different curvatures in the images and, most importantly, it allows us to place all the spinal cord images from different individuals into the same reference frame. In addition, with XRPCT it is also possible to extract information simultaneously about the neuronal and vascular networks.

The potential outcomes of advancing these methods are great, enhancing our basic understanding of healthy human CNS function, and improving our ability to accurately diagnose and treat injury and disease and predict treatment outcomes.

The co-registration methods presented here open new possibilities to obtain complementary information to validate MRI. Future directions are to include other histological modalities, as 3D LM or EM data as well as other MRI modalities, into the pipeline. Also, new analysis methods, such as segmentation and quantification of individual cellular components (Abdollahzadeh et al., 2019a,b; **Figure 2L**), allow to extract more specific morphological information for the evaluation of areas under investigation. A multiscale and multidisciplinary approach as proposed in this article paves new ways to study the brain and spinal cord, and more importantly, to better understand the non-invasive information given by *in vivo* MRI.

DISCUSSION

Magnetic resonance imaging has become one of the most powerful tools in neuroscience research, with a wide range of applications in both clinical practice and research settings. However, the interpretation of highly complex MRI contrasts remains a daunting task, which would benefit tremendously from the progress of multimodal and multiscale imaging approaches.

Synchrotron X-ray phase contrast tomography, LM, or EM can perform 3D imaging of post-mortem CNS tissue displaying, e.g., from the architecture of the neuronal and vascular network up to a single neuronal soma. These methods can be useful to validate *in vivo* imaging techniques using the high-resolution images as a reference (Schulz et al., 2012; Gangolli et al., 2017; Cohen-Adad, 2018). In particular, LM and EM offer high-resolution and specificity to visualize different cellular substrates, which have already exploited for the microstructural MRI validation (Mac Donald et al., 2007; Budde et al., 2011; Salo et al., 2017; Cohen-Adad, 2018; Duval et al., 2019). In the recent years, LM and EM have been developed into 3D imaging techniques generating new ways for the MRI validation (Khan et al., 2015; Schilling et al., 2016, 2018; Salo et al., 2018; Lee et al., 2019). On the other hand, SXRPCT offers the possibility to study the tissue in 3D without sample sectioning and specific sample preparation (Fitzgerald, 2000). SXRPCT allows both the assessment of the overall 3D morphology of the sample and fine computing sectioning, as thin as 130 nm. SXRPCT has been applied in the imaging of the 3D distribution of vasculature and the single elements of the neuronal network in healthy and pathological CNS (Bravin et al., 2012; Stefanutti et al., 2018). The combination of the MRI with high-resolution SXRPCT can, in principle, allow the assessment of the tissue morphology and the segmentation of different anatomical structures (Schulz et al., 2012) thus permitting to shed light on pathological alterations.

Co-registration methods, as the one presented here, allow to gather information from complementary imaging methods at different length scales spanning from the macroscopic to the nanometric level. The application of these techniques to *ex vivo* brain and spinal cord, for example, allows quantifying microstructural alterations in diseased subjects, and it has the

potential to lead to a better understanding of the relationship between structure and function in the CNS. One of the major limitations of the co-registration using different imaging modalities on the same sample is the tissue preparation (Fitzgerald, 2000). In this work, the tissue was fixed with paraformaldehyde, which only induces a minor tissue shrinkage. Other methods, such as LM or EM, require that the tissue be stained, resulting in a more significant shrinkage that can complicate the co-registration process. Prospectively, the added value of a multimodal and multiscale imaging can be greatly increased by further improvements in co-registration approaches such as those outlined here.

DATA AVAILABILITY STATEMENT

The raw data supporting the conclusions of this article will be made available by the authors, without undue reservation, to any qualified researcher.

ETHICS STATEMENT

All animal procedures were carried out under licenses that have been approved by the Animal Ethics Committee of the Provincial Government of Southern Finland and in accordance with the guidelines of the European Community Council Directives 86/609/EREC.

AUTHOR CONTRIBUTIONS

MF and AS contributed to the concept and study design. AA, MD, RS, and LM performed the analyses. All authors have contributed to the interpretation the data, wrote the main manuscript text, and reviewed the manuscript.

ACKNOWLEDGMENTS

We thank Academy of Finland (AS #284544, #275453; OG #298007; JT #316258), COST Action CA15124 (NEUBIAS) (RS), and the Italian Ministry of Health under the Young Researcher Grant 2013 (GR-2013-02358177) for the financial support. In addition, part of the project was founded by the Progetto FISR – C.N.R. Tecnopolo di Nanotecnologia e Fotonica per la Medicina di Precisione and by the European Union Horizon 2020 Research and Innovation Program under the Marie Skłodowska-Curie grant agreement no. 691110 (MICROBRADAM).

REFERENCES

Abdollahzadeh, A., Belevich, I., Jokitalo, E., Sierra, A., and Tohka, J. (2019a). DeepACSON: automated segmentation of white matter in 3D electron microscopy. *bioRxiv [Preprint]* doi: 10.1101/828541

Abdollahzadeh, A., Belevich, I., Jokitalo, E., Tohka, J., and Sierra, A. (2019b). Automated 3D axonal morphometry of white matter. *Sci. Rep.* 9:6084. doi: 10.1038/s41598-019-42648-2

Aggarwal, M., Li, X., Gröhn, O., and Sierra, A. (2018). Nuclei-specific deposits of iron and calcium in the rat thalamus after status epilepticus revealed with quantitative susceptibility mapping (QSM). *J. Magn. Reson. Imaging* 47, 554–564. doi: 10.1002/jmri.25777

Andre, J. B., and Bammer, R. (2010). Advanced diffusion-weighted magnetic resonance imaging techniques of the human spinal cord. *Top. Magn. Reson. Imaging* 21, 367–378. doi: 10.1097/rmr.0b013e31823e65a1

Avants, B. B., Epstein, C. L., Grossman, M., and Gee, J. C. (2008). Symmetric diffeomorphic image registration with cross-correlation: evaluating automated labeling of elderly and neurodegenerative brain. *Med. Image Analysis* 12, 26–41. doi: 10.1016/j.media.2007.06.004

Avants, B. B., Tustison, N., and Song, G. (2009). Advanced normalization tools (ANTS). *Insight J.* 2, 1–35.

Basser, P. J., Mattiello, J., and LeBihan, D. (1994). MR diffusion tensor spectroscopy and imaging. *Biophys. J.* 66, 259–267. doi: 10.1016/s0006-3495(94)80775-1

Bravin, A., Coan, P., and Suortti, P. (2012). X-ray phase-contrast imaging: from pre-clinical applications towards clinics. *Phys. Med. Biol.* 58:R1. doi: 10.1088/0031-9155/58/1/R1

Briggman, K. L., and Bock, D. D. (2012). Volume electron microscopy for neuronal circuit reconstruction. *Curr. Opin. Neurobiol.* 22, 154–161. doi: 10.1016/j.conb.2011.10.022

Budde, M. D., Janes, L., Gold, E., Turtzo, L. C., and Frank, J. A. (2011). The contribution of gliosis to diffusion tensor anisotropy and tractography following traumatic brain injury: validation in the rat using Fourier analysis of stained tissue sections. *Brain* 134, 2248–2260. doi: 10.1093/brain/awr161

Canny, J. (1987). *A Computational Approach to Edge Detection. Readings in Computer Vision*. Amsterdam: Elsevier, 184–203.

Cedola, A., Bravin, A., Bukreeva, I., Fratini, M., Pacureanu, A., Mittone, A., et al. (2017). X-ray phase contrast tomography reveals early vascular alterations and neuronal loss in a multiple sclerosis model. *Sci. Rep.* 7:5890. doi: 10.1038/s41598-017-06251-7

Chung, K., Wallace, J., Kim, S.-Y., Kalyanasundaram, S., Andalman, A. S., Davidson, T. J., et al. (2013). Structural and molecular interrogation of intact biological systems. *Nature* 497, 332–337. doi: 10.1038/nature12107

Cohen, Y., Anaby, D., and Morozov, D. (2017). Diffusion MRI of the spinal cord: from structural studies to pathology. *NMR Biomed.* 30:e3592. doi: 10.1002/nbm.3592

Cohen, Y., and Assaf, Y. (2002). High b-value q-space analyzed diffusion-weighted MRS and MRI in neuronal tissues–a technical review. *NMR Biomed.* 15, 516–542. doi: 10.1002/nbm.778

Cohen-Adad, J. (2018). Microstructural imaging in the spinal cord and validation strategies. *Neuroimage* 182, 169–183. doi: 10.1016/j.neuroimage.2018.04.009

De Leener, B., Lévy, S., Dupont, S. M., Fonov, V. S., Stikov, N., Collins, D. L., et al. (2017). SCT: spinal cord toolbox, an open-source software for processing spinal cord MRI data. *Neuroimage* 145, 24–43. doi: 10.1016/j.neuroimage.2016.10.009

Denk, W., and Horstmann, H. (2004). Serial block-face scanning electron microscopy to reconstruct three-dimensional tissue nanostructure. *PLoS Biol.* 2:e329. doi: 10.1371/journal.pbio.0020329

Denk, W., Strickler, J. H., and Webb, W. W. (1990). Two-photon laser scanning fluorescence microscopy. *Science* 248, 73–76. doi: 10.1126/science.2321027

Du, H., Hou, P., Zhang, W., and Li, Q. (2018). Advances in CLARITY-based tissue clearing and imaging. *Exp. Ther. Med.* 16, 1567–1576.

Duval, T., Saliani, A., Nami, H., Nanci, A., Stikov, N., Leblond, H., et al. (2019). Axons morphometry in the human spinal cord. *Neuroimage* 185, 119–128. doi: 10.1016/j.neuroimage.2018.10.033

Ertürk, A., and Bradke, F. (2013). High-resolution imaging of entire organs by 3-dimensional imaging of solvent cleared organs (3DISCO). *Exp. Neurol.* 242, 57–64. doi: 10.1016/j.expneurol.2012.10.018

Filippi, M., and Rocca, M. A. (2004). Magnetization transfer magnetic resonance imaging in the assessment of neurological diseases. *J. Neuroimaging* 14, 303–313. doi: 10.1111/j.1552-6569.2004.tb00255.x

Filippi, M., and Rocca, M. A. (2007). Magnetization transfer magnetic resonance imaging of the brain, spinal cord, and optic nerve. *Neurotherapeutics* 4, 401–413. doi: 10.1016/j.nurt.2007.03.002

Fitzgerald, R. (2000). Phase-sensitive x-ray imaging. *Phys. Today* 53, 23–26. doi: 10.1063/1.1292471

Fratini, M. (2018). "The challenge of the vascularization of regenerated tissues," in *Advanced High-Resolution Tomography in Regenerative Medicine: Three-Dimensional Exploration into the Interactions between Tissues, Cells, and Biomaterials*, eds A. Giuliani, and A. Cedola, (Cham: Springer), 139. doi: 10.1007/978-3-030-00368-5_9

Fratini, M., Bukreeva, I., Campi, G., Brun, F., Tromba, G., Modregger, P., et al. (2015). Simultaneous submicrometric 3D imaging of the micro-vascular network and the neuronal system in a mouse spinal cord. *Sci. Rep.* 5:8514.

Gangolli, M., Holleran, L., Kim, J. H., Stein, T. D., Alvarez, V., McKee, A. C., et al. (2017). Quantitative validation of a nonlinear histology-MRI coregistration method using generalized Q-sampling imaging in complex human cortical white matter. *Neuroimage* 153, 152–167. doi: 10.1016/j.neuroimage.2017.03.059

Gustafsson, M. G. (2000). Surpassing the lateral resolution limit by a factor of two using structured illumination microscopy. *J. Microsc.* 198, 82–87. doi: 10.1046/j.1365-2818.2000.00710.x

Hama, H., Hioki, H., Namiki, K., Hoshida, T., Kurokawa, H., Ishidate, F., et al. (2015). ScaleS: an optical clearing palette for biological imaging. *Nat. Neurosci.* 18, 1518–1529. doi: 10.1038/nn.4107

Hell, S. W., and Wichmann, J. (1994). Breaking the diffraction resolution limit by stimulated emission: stimulated-emission-depletion fluorescence microscopy. *Opt. Lett.* 19, 780–782.

Helmstaedter, M., Briggman, K. L., and Denk, W. (2008). 3D structural imaging of the brain with photons and electrons. *Curr. Opin. Neurobiol.* 18, 633–641. doi: 10.1016/j.conb.2009.03.005

Heymann, J. A., Hayles, M., Gestmann, I., Giannuzzi, L. A., Lich, B., and Subramaniam, S. (2006). Site-specific 3D imaging of cells and tissues with a dual beam microscope. *J. Struct. Biol.* 155, 63–73. doi: 10.1016/j.jsb.2006.03.006

Jensen, J. H., Helpern, J. A., Ramani, A., Lu, H., and Kaczynski, K. (2005). Diffusional kurtosis imaging: the quantification of non-gaussian water diffusion by means of magnetic resonance imaging. *Magn. Reson. Med.* 53, 1432–1440. doi: 10.1002/mrm.20508

Khan, A. R., Cornea, A., Leigland, L. A., Kohama, S. G., Jespersen, S. N., and Kroenke, C. D. (2015). 3D structure tensor analysis of light microscopy data for validating diffusion MRI. *Neuroimage* 111, 192–203. doi: 10.1016/j.neuroimage.2015.01.061

Kreshuk, A., Koethe, U., Pax, E., Bock, D. D., and Hamprecht, F. A. (2014). Automated detection of synapses in serial section transmission electron microscopy image stacks. *PLoS One* 9:e87351. doi: 10.1371/journal.pone.0087351

Lee, H.-H., Yaros, K., Veraart, J., Pathan, J. L., Liang, F.-X., Kim, S. G., et al. (2019). Along-axon diameter variation and axonal orientation dispersion revealed with 3D electron microscopy: implications for quantifying brain white matter microstructure with histology and diffusion MRI. *Brain Struct. Funct.* 224, 1469–1488. doi: 10.1007/s00429-019-01844-6

Li, X., Harrison, D. M., Liu, H., Jones, C. K., Oh, J., Calabresi, P. A., et al. (2016). Magnetic susceptibility contrast variations in multiple sclerosis lesions. *J. Magn. Reson. Imaging* 43, 463–473. doi: 10.1002/jmri.24976

Liu, C., Li, W., Tong, K. A., Yeom, K. W., and Kuzminski, S. (2015). Susceptibility-weighted imaging and quantitative susceptibility mapping in the brain. *J. Magn. Reson. Imaging* 42, 23–41. doi: 10.1002/jmri.24768

Mac Donald, C., Dikranian, K., Song, S., Bayly, P., Holtzman, D., and Brody, D. (2007). Detection of traumatic axonal injury with diffusion tensor imaging in a mouse model of traumatic brain injury. *Exp. Neurol.* 205, 116–131. doi: 10.1016/j.expneurol.2007.01.035

Massimi, L., Bukreeva, I., Santamaria, G., Fratini, M., Corbelli, A., Brun, F., et al. (2019). Exploring Alzheimer's disease mouse brain through X-ray phase contrast tomography: from the cell to the organ. *Neuroimage* 184, 490–495. doi: 10.1016/j.neuroimage.2018.09.044

Mezer, A., Rokem, A., Berman, S., Hastie, T., and Wandell, B. A. (2016). Evaluating quantitative proton-density-mapping methods. *Hum. Brain Mapp.* 37, 3623–3635. doi: 10.1002/hbm.23264

Otsu, N. (1979). A threshold selection method from gray-level histograms. *IEEE Trans. Syst. Man Cybern.* 9, 62–66. doi: 10.1109/tsmc.1979.4310076

Paganin, D., Mayo, S., Gureyev, T. E., Miller, P. R., and Wilkins, S. W. (2002). Simultaneous phase and amplitude extraction from a single defocused image of a homogeneous object. *J. Microsc.* 206, 33–40. doi: 10.1046/j.1365-2818.2002.01010.x

Panagiotaki, E., Schneider, T., Siow, B., Hall, M. G., Lythgoe, M. F., and Alexander, D. C. (2012). Compartment models of the diffusion MR signal in brain white matter: a taxonomy and comparison. *Neuroimage* 59, 2241–2254. doi: 10.1016/j.neuroimage.2011.09.081

Russo, P. (2017). *Handbook of X-ray Imaging: Physics and Technology*. Boca Raton, FL: CRC Press.

Salo, R. A., Belevich, I., Manninen, E., Jokitalo, E., Gröhn, O., and Sierra, A. (2018). Quantification of anisotropy and orientation in 3D electron microscopy and diffusion tensor imaging in injured rat brain. *Neuroimage* 172, 404–414. doi: 10.1016/j.neuroimage.2018.01.087

Salo, R. A., Miettinen, T., Laitinen, T., Gröhn, O., and Sierra, A. (2017). Diffusion tensor MRI shows progressive changes in the hippocampus and dentate gyrus after status epilepticus in rat–histological validation with Fourier-based analysis. *Neuroimage* 152, 221–236. doi: 10.1016/j.neuroimage.2017.03.003

Schalek, R., Kasthuri, N., Hayworth, K., Berger, D., Tapia, J., Morgan, J., et al. (2011). Development of high-throughput, high-resolution 3D reconstruction of large-volume biological tissue using automated tape collection ultramicrotomy and scanning electron microscopy. *Microsc. Microanal.* 17, 966–967. doi: 10.1017/s1431927611005708

Schilling, K., Janve, V., Gao, Y., Stepniewska, I., Landman, B. A., and Anderson, A. W. (2016). Comparison of 3D orientation distribution functions measured with confocal microscopy and diffusion MRI. *Neuroimage* 129, 185–197. doi: 10.1016/j.neuroimage.2016.01.022

Schilling, K. G., Janve, V., Gao, Y., Stepniewska, I., Landman, B. A., and Anderson, A. W. (2018). Histological validation of diffusion MRI fiber orientation distributions and dispersion. *Neuroimage* 165, 200–221. doi: 10.1016/j.neuroimage.2017.10.046

Schulz, G., Waschkies, C., Pfeiffer, F., Zanette, I., Weitkamp, T., David, C., et al. (2012). Multimodal imaging of human cerebellum-merging X-ray phase microtomography, magnetic resonance microscopy and histology. *Sci. Rep.* 2:826. doi: 10.1038/srep00826

Schweser, F., Deistung, A., Lehr, B. W., and Reichenbach, J. R. (2011). Quantitative imaging of intrinsic magnetic tissue properties using MRI signal phase: an approach to in vivo brain iron metabolism? *Neuroimage* 54, 2789–2807. doi: 10.1016/j.neuroimage.2010.10.070

Sled, J. G. (2018). Modelling and interpretation of magnetization transfer imaging in the brain. *Neuroimage* 182, 128–135. doi: 10.1016/j.neuroimage.2017.11.065

Smith, S. M. (2002). Fast robust automated brain extraction. *Hum. Brain Mapp.* 17, 143–155. doi: 10.1002/hbm.10062

Stefanutti, E., Sierra, A., Miocchi, P., Massimi, L., Brun, F., Maugeri, L., et al. (2018). Assessment of the effects of different sample perfusion procedures on phase-contrast tomographic images of mouse spinal cord. *J. Instrum.* 13:C03027.

Stelzer, E. H. (2006). "The intermediate optical system of laser-scanning confocal microscopes," in *Handbook of Biological Confocal Microscopy*, ed. J. B. Pawley, (Berlin: Springer), 207–220. doi: 10.1007/978-0-387-45524-2_9

Topgaard, D. (2017). Multidimensional diffusion MRI. *J. Magn. Reson.* 275, 98–113. doi: 10.1016/j.jmr.2016.12.007

Tuch, D. S., Reese, T. G., Wiegell, M. R., Makris, N., Belliveau, J. W., and Wedeen, V. J. (2002). High angular resolution diffusion imaging reveals intravoxel white matter fiber heterogeneity. *Magn. Reson. Med.* 48, 577–582. doi: 10.1002/mrm.10268

Vargas, M., Delattre, B., Boto, J., Gariani, J., Dhouib, A., Fitsiori, A., et al. (2018). Advanced magnetic resonance imaging (MRI) techniques of the spine and spinal cord in children and adults. *Insights Imaging* 9, 549–557. doi: 10.1007/s13244-018-0626-1

Wang, Y., and Liu, T. (2015). Quantitative susceptibility mapping (QSM): decoding MRI data for a tissue magnetic biomarker. *Magn. Reson. Med.* 73, 82–101. doi: 10.1002/mrm.25358

Weber, M., and Huisken, J. (2011). Light sheet microscopy for real-time developmental biology. *Curr. Opin. Genet. Dev.* 21, 566–572. doi: 10.1016/j.gde.2011.09.009

Wedeen, V. J., Wang, R., Schmahmann, J. D., Benner, T., Tseng, W.-Y. I., Dai, G., et al. (2008). Diffusion spectrum magnetic resonance imaging (DSI) tractography of crossing fibers. *Neuroimage* 41, 1267–1277. doi: 10.1016/j.neuroimage.2008.03.036

Weitkamp, T., Haas, D., Wegrzynek, D., and Rack, A. (2011). ANKAphase: software for single-distance phase retrieval from inline X-ray phase-contrast radiographs. *J. Synchrotron Radiat.* 18, 617–629. doi: 10.1107/S0909049511002895

Westin, C.-F., Knutsson, H., Pasternak, O., Szczepankiewicz, F., Özarslan, E., van Westen, D., et al. (2016). Q-space trajectory imaging for multidimensional diffusion MRI of the human brain. *Neuroimage* 135, 345–362. doi: 10.1016/j.neuroimage.2016.02.039

Zhang, H., Schneider, T., Wheeler-Kingshott, C. A., and Alexander, D. C. (2012). NODDI: practical in vivo neurite orientation dispersion and density imaging of the human brain. *Neuroimage* 61, 1000–1016. doi: 10.1016/j.neuroimage.2012.03.072

Conflict of Interest: The authors declare that the research was conducted in the absence of any commercial or financial relationships that could be construed as a potential conflict of interest.

frontiers in Physiology

ORIGINAL RESEARCH
published: 21 April 2020
doi: 10.3389/fphys.2020.00360

Assessment of the Effects of Aerobic Fitness on Cerebrovascular Function in Young Adults Using Multiple Inversion Time Arterial Spin Labeling MRI

*Catherine Foster[1], Jessica J. Steventon[2,3], Daniel Helme[4], Valentina Tomassini[1,5,6,7] and Richard G. Wise[1,6,7]**

[1] Cardiff University Brain Research Imaging Centre (CUBRIC), School of Psychology, Cardiff University, Cardiff, United Kingdom, [2] Cardiff University Brain Research Imaging Centre (CUBRIC), School of Physics and Astronomy, Cardiff University, Cardiff, United Kingdom, [3] Neuroscience and Mental Health Research Institute (NMHRI), School of Medicine, Cardiff University, Cardiff, United Kingdom, [4] Department of Anaesthetics and Intensive Care Medicine, Cardiff University School of Medicine, Cardiff, United Kingdom, [5] Division of Psychological Medicine and Clinical Neurosciences, School of Medicine, Cardiff University, Cardiff, United Kingdom, [6] Department of Neuroscience, Imaging and Clinical Sciences, "G. D'Annunzio University" of Chieti-Pescara, Chieti, Italy, [7] Institute for Advanced Biomedical Technologies (ITAB), "G. D'Annunzio University" of Chieti-Pescara, Chieti, Italy

OPEN ACCESS

Edited by:
Marta Bianciardi, Massachusetts General Hospital, Harvard Medical School, United States

Reviewed by:
Paul Cumming, University of Bern, Switzerland
Ilaria Boscolo Galazzo, University of Verona, Italy

***Correspondence:**
Richard G. Wise
wiserg@cardiff.ac.uk

Specialty section:
This article was submitted to Medical Physics and Imaging, a section of the journal Frontiers in Physiology

Received: *12 September 2019*
Accepted: *27 March 2020*
Published: *21 April 2020*

Citation:
Foster C, Steventon JJ, Helme D, Tomassini V and Wise RG (2020) Assessment of the Effects of Aerobic Fitness on Cerebrovascular Function in Young Adults Using Multiple Inversion Time Arterial Spin Labeling MRI. Front. Physiol. 11:360. doi: 10.3389/fphys.2020.00360

This cross-sectional study investigated the effects of aerobic fitness on cerebrovascular function in the healthy brain. Gray matter cerebral blood flow (CBF) and cerebrovascular reactivity (CVR) were quantified in a sample of young adults within a normal fitness range. Based on existing Transcranial Doppler ultrasound and fMRI evidence, we predicted a positive relationship between fitness and resting gray matter CBF and CVR. Exploratory hypotheses that higher $\dot{V}O_2$peak would be associated with higher GM volume and cognitive performance were also investigated. 20 adults underwent a $\dot{V}O_2$peak test and a battery of cognitive tests. All subjects also underwent an MRI scan where multiple inversion time (MTI) pulsed arterial spin labeling (PASL) was used to quantify resting CBF and CVR to 5% CO_2. Region of interest analysis showed a non-significant inverse correlation between whole-brain gray matter CBF and $\dot{V}O_2$peak; $r = -0.4$, $p = 0.08$, corrected p (p') = 0.16 and a significant positive correlation between $\dot{V}O_2$peak and whole-brain averaged gray matter CVR; $r = 0.62$, $p = 0.003$, $p' = 0.006$. Voxel-wise analysis revealed a significant inverse association between $\dot{V}O_2$peak and resting CBF in the left and right thalamus, brainstem, right lateral occipital cortex, left intra-calcarine cortex and cerebellum. The results of this study suggest that aerobic fitness is associated with lower baseline CBF and greater CVR in young adults.

Keywords: arterial spin labeling, cerebral blood flow, cerebral hemodynamics, cerebrovascular reactivity, exercise

INTRODUCTION

Aerobic fitness has emerged as a modifiable lifestyle factor which reduces the risk of all-cause mortality (Kodama et al., 2009; Lee et al., 2010), cardiovascular events (Haskell et al., 2007; Lee et al., 2010; Roque et al., 2013) and protects the brain against age and disease-related decline (Hillman et al., 2008; Hayes et al., 2014a; Nishijima et al., 2016). In addition, brain structure and function

are closely linked; to maintain healthy brain tissue, adequate energy must be supplied. Many studies have investigated the link between aerobic fitness and brain structure (Voss et al., 2015) but the relationship between aerobic fitness and cerebrovascular function has not been extensively studied in humans. The present study focuses on how aerobic fitness may affect the cerebrovascular processes which maintain delivery of brain nutrients.

Neuroimaging studies have provided evidence of a neuroprotective effect of aerobic fitness in older adults, linking higher aerobic fitness with greater brain volume (Erickson et al., 2011) and cerebral blood flow (CBF) (Thomas et al., 2013). Aerobic fitness has also been associated with greater cerebrovascular reactivity (CVR), which reflects the ability of the cerebral vessels to dilate, or the vascular reserve, assessed using transcranial Doppler (TCD) ultrasound (Bailey et al., 2013) in both older and younger adults. However, Barnes et al. (2013), using the same technique, did not find a relationship between CVR and $\dot{V}O2_{max}$ in younger adults despite observing the same trend as Bailey et al. (2013) in older adults. Further, the findings of Bailey et al. (2013) and Barnes et al. (2013) in older adults, do not agree with the MRI results of Thomas et al. (2013) who reported a lower BOLD-based CVR in masters athletes vs. sedentary young and age-matched controls. Finally, Gauthier et al. (2015) found that in older adults, BOLD CVR was negatively correlated with $\dot{V}O_2$max in frontal regions but positively correlated in periventricular white matter and portions of the somatosensory cortex. These conflicting CVR data represent an issue of inconsistent findings regarding aerobic fitness and its effects on cerebrovascular function across the lifespan.

Recent findings from Hwang et al. (2017) using TCD, also suggest that young adults with higher levels of aerobic fitness have a greater cerebrovascular response to hypercapnia in the middle cerebral artery (MCA), during exercise, but found no differences at rest. The fitter group also scored better on tests of fluid reasoning, but not on any other tasks included in the cognitive battery. However, as we are interested in how aerobic fitness may lead to general improvements in cerebrovascular health rather than vascular regulation during exercise, the current cross-sectional study focused on the relationship between aerobic fitness and cerebrovascular function in the resting brain of young, healthy adults. As the TCD literature suggests a positive relationship between fitness and CVR in young people, it is important to establish whether functional MRI reports the same effects, as TCD reflects the velocity of arterial blood rather than perfusion of gray matter.

The objective of this study was to quantify using pulsed arterial spin labeling (PASL) MRI at multiple post-labeling delay times, variations in resting CBF and CVR, two widely used indices of cerebrovascular function, in a sample of young, healthy adults within a normal range of fitness levels (i.e., sedentary and active, but not athletes in structured training). Based on the extant TCD and fMRI evidence, we predicted a positive relationship between fitness and resting gray matter CBF. We also expected to see a positive correlation between CVR to CO_2 and $\dot{V}O_2$peak, a measure of aerobic fitness, in line with previous findings (Bailey et al., 2013; Hwang et al., 2017). Tests chosen to measure a number of cognitive domains were included to examine the exploratory hypotheses that higher $\dot{V}O_2$peak would be associated with better cognitive performance and higher gray matter volume. If CBF and CVR differences due to fitness were evident, then demonstrating additional cognitive benefits would provide evidence for functionally relevant effects of neurobiological differences.

MATERIALS AND METHODS

Participants

Twenty healthy adults (11 females, mean age 25 ± 4.6) were recruited from Cardiff University. The study was approved by the Cardiff University School of Psychology Research Ethics Committee and performed in accordance with the guidelines stated in the Cardiff University Research Framework (version 4.0, 2010). All participants were non-smokers and educated to university level. Informed written consent was obtained from all subjects.

Study Procedures

The study consisted of 3 lab visits. In Visit 1, eligibility screening for MRI, respiratory modulations (see **Supplementary Figure S1**) and intensive exercise was carried out. Contraindications to exercise were assessed using the Physical Activity Readiness Questionnaire (PARQ). Sociodemographic information was recorded and estimations of weekly activity level were established using the International Physical Activity Questionnaire (IPAQ) Short Form (Craig et al., 2003). Elevated CO_2 inhalation can cause sensations of breathlessness, light headedness and anxiety in some individuals. For this reason, all volunteers took part in a gas modulation session in a MR scanner simulator. A stepwise protocol was employed to allow participants time to become accustomed to CO_2 inhalation (see **Supplementary Figure S1**).

In Visit 2, volunteers completed 7 cognitive tests, administered by the same researcher for all participants, prior to the fitness test. The tests, covering a range of cognitive domains, were chosen as they are validated for use in patient and control samples (see **Table 1**).

Fitness Test

The fitness test was also performed in Visit 2. The PAR-Q was conducted a second time to identify potential risk factors associated with exercise in the unlikely case of circumstance changes from Visit 1. The $\dot{V}O_2$peak test protocol used has previously been described by Collett et al. (2011) and Cooney et al. (2013). The test began with a 2 min unloaded warm up at 50 revolutions per minute (rpm) on a Lode cycle ergometer (Lode, Groningen, Netherlands). During the test, participants maintained a constant 50 rpm and work rate was increased from 50 watts by 25 watts every 2 min. The test was terminated if any of the following criteria were reached; work rate fell below 45 rpm for >10 s, volitional exhaustion occurred, or maximal predicted heart rate exceeded 100%. At the end of each 2 min step Borg ratings of perceived exertion, on the CR10 scale

TABLE 1 | List of cognitive tests used in this study and domains they are intended to assess.

Test	Domain measured
Speed and capacity of language processing (SCOLP) (Baddeley et al., 1992)	Information processing, speed, and language comprehension
Forward digit span	Working memory
Letter fluency (categories)	Verbal fluency
Conners continuous performance test (Conners, 2000)	Sustained attention and response inhibition
Trail making test (part B)	Processing speed and executive function
Symbol digit modalities test	Information processing speed

(Borg and Kaijser, 2006) were used to record perceived heaviness of legs and breathing.

Blood lactate concentration was sampled from the earlobe using Unistik 3 1.8 mm lancets (Williams Medical, Caerphilly, United Kingdom) and tested using the Lactate Plus system (Nova Biomedical, Waltam, MA, United States) at baseline, 2 min intervals and at exhaustion. Blood pressure (BP) was recorded at baseline, HR at baseline and 2 min intervals during the test. Respiratory gas exchanges were continuously monitored using breath by breath analysis with the Cortex Metalyser 3b (Cortex Biophysik Metalyzer, Germany). $\dot{V}O_2$peak was taken as the highest value over a 30 s block average at the maximum recorded work rate. Heart rate (HR) and work rate were also recorded at baseline and at 2 min intervals and electrocardiography (ECG) was monitored for the duration of the test. Following termination of the $\dot{V}O_2$peak test participants were monitored for 10 min. In this 10 min recovery period blood pressure, HR and blood lactate were sampled every 2 min before subjects left the lab.

MRI Acquisition

In Visit 3, volunteers underwent the MR scan. Images were acquired on a 3T whole body MRI system (GE Excite HDx, Milwaukee, WI, United States) using an eight-channel receive-only head coil. Heart rate was recorded using a pulse oximeter and a respiratory bellows monitored breathing. A sampling line connected to the face mask of the breathing circuit (Tancredi et al., 2014) was used to monitor the partial pressure of end-tidal CO_2 ($P_{ET}CO_2$) and O_2 ($P_{ET}O_2$) via the Biopac® system (Biopac, Worcestershire, United Kingdom). The MEDRAD system (MEDRAD, Pittsburgh, PA, United States) was used to monitor O_2 saturation throughout the experiment.

PASL data were acquired using a single subtraction PICORE QUIPSS II (Wong et al., 1998) with a dual-echo gradient-echo readout (Liu et al., 2002) and spiral k-space acquisition (Glover and Lai, 1998) the first echo being used for CBF quantification. Data were acquired at 8 inversion times; 400, 500, 600, 700, 1100, 1400, 1700, and 2000 ms. QUIPSS II cut-off at 700 ms meant that short and long inversion times were acquired in separate runs. 16 and 8 tag-control pairs were acquired for each of the short and long inversion time respectively. A variable TR was used for efficiency, 1200–1500 ms for short TI data (400–700 ms) and 1700–2600 ms for long TIs (1100–2000 ms). Other acquisition parameters were; TE = 2.7 ms, voxel size = 3.1 × 3.1 × 7 mm^3, matrix size 64 × 64 mm, FOV = 19.8 cm, flip angle = 90°, inter-slice time 55 ms, 15 slices, slice gap 1.5 mm for maximum brain coverage. Label thickness was 200 mm with 10 mm gap between the end of the label and the most proximal imaging slice.

A calibration image without any labeling was acquired before the perfusion mages using the same acquisition parameters, except a long TR; this was used to obtain the equilibrium magnetization of cerebrospinal fluid (M_0, CSF), needed for the quantification of CBF. The acquisition parameters for this CSF were identical to the PASL acquisition, except that no labeling was applied so that the image was acquired with fully relaxed magnetization. A minimal contrast image was also acquired to correct for coil inhomogeneities with TE = 11 ms, TR = 2 s. The PASL acquisition was performed twice, first during rest, then while volunteers were hypercapnic. The hypercapnic modulation was carried out using the prospective control method described by Tancredi and Hoge (2013). A gas mixing chamber constructed in-house had three feeding lines coming in for the delivery of medical air, 5% CO_2, and medical oxygen, the latter incorporated as a safety backup but not used during experimentation, the circuit is described in detail by Tancredi et al. (2014). $P_{ET}CO_2$ elevation of 7mmHg was targeted using 5% CO_2 (balance air) and the scan commenced once participants reached the target CO_2 level. ASL data acquisition lasted ∼6 min during rest, followed by a delay to allow the onset of hypercapnia. Once a $P_{ET}CO_2$ elevation of approximately 7mmHg was achieved, the ∼6 min ASL acquisition was repeated.

A T1-weighted 3D structural fast spoiled gradient echo (FSPGR) scan was also acquired for registration of functional data and voxel-based morphometry (VBM) analysis; TR/TE = 7.8/2.9 ms, resolution = 1 mm isotropic.

Data Analysis

$\dot{V}O_2$peak Calculation

$\dot{V}O_2$peak was calculated from the respiratory gas exchanges which were continuously monitored using breath-by-breath analysis and averaged over 10 s blocks. $\dot{V}O_2$peak was defined as the 30 s averaged value at maximum recorded work rate. HR, respiratory exchange ratio (RER) and blood lactate were recorded every 2 min and at termination of the fitness test to validate $\dot{V}O_2$peak criteria being reached. The test result was considered valid if heart rate exceeded 90% of age predicted maximum, RER > 1 and blood lactate concentration was greater than 8 mM at the end of the test (Milani et al., 2006; Poole et al., 2008; Horton et al., 2011).

Cognitive Data Scoring

Cognitive data were scored by hand by the same researcher, the Conners Continuous Performance test is computer based and scored automatically. Demeaned scores were calculated for correlation analysis with $\dot{V}O_2$peak and MR data.

Image Analysis

Physiological noise correction was carried out using a modified RETROICOR (Glover et al., 2000) to remove cardiac and respiratory noise components from the data. ASL data were motion corrected using MCFLIRT within FSL (FMRIB's Software

Library;[1] Jenkinson et al., 2002, RRID:SCR_002823). The CBF timeseries for the normocapnia and hypercapnia scans were corrected for coil sensitivity inhomogeneities using the minimal contrast images (Wang et al., 2005). Average difference images were obtained for each inversion time from tag-control subtraction of the CBF time series (Lu et al., 2006) and a perfusion map was created from all inversion times using a two-compartment CBF kinetic model implemented using the BASIL toolkit of FSL (Chappell et al., 2010). Within this framework, perfusion maps were converted to ml/100 g/min using the CSF signal as a reference to estimate the fully relaxed magnetization of water in blood (Chalela et al., 2000). The mean resting CBF for each subject was calculated by averaging the CBF time series over all voxels within the masked gray matter image (see below). CVR was calculated by dividing the percentage change in CBF from rest during hypercapnia by the mmHg change in $P_{ET}CO_2$ increase during hypercapnia.

Gray Matter Volume

T1-weighted structural data were analyzed with FSL-VBM (Good et al., 2001; Douaud et al., 2007).[2] Structural images were brain extracted and segmented into gray matter, white matter and CSF before being registered to the MNI 152 standard space template using non-linear registration (Andersson et al., 2007). The resulting images were averaged and flipped along the x-axis to create a left-right symmetric, group-specific GM template. Second, all native GM images were non-linearly registered to this study-specific template and modulated to correct for local expansion (or contraction) due to the non-linear component of the spatial transformation. The modulated GM images were then smoothed with an isotropic Gaussian kernel with a sigma of 3 mm. Finally, voxel-wise GLM was applied using permutation-based non-parametric testing, correcting for multiple comparisons across space to investigate whether GM volume and $\dot{V}O_2$peak were correlated.

ROI Analysis of Whole Gray Matter CBF and CVR

Individual subject gray matter masks were created using FMRIB's Automated Segmentation Tool (FAST) and thresholded to include voxels with >50% gray matter probability. ROI analysis of the relationship between gray matter CBF at rest, CVR and $\dot{V}O_2$peak was carried out using correlation analysis and permutation testing (100,000 permutations per comparison) in Matlab (Mathworks Inc., MA, United States). Permutation testing was used as an alternative to Bonferroni correction for multiple comparisons which is too conservative when potentially related variables are tested. This approach was also applied to examine the associations between gray matter CBF and CVR, and cognitive test scores.

Voxelwise Analysis of Gray Matter CBF and CVR

Follow up voxelwise analysis was conducted using FSL's Randomize tool[3] (Winkler et al., 2014) to examine the voxelwise correlation between (i) CBF and $\dot{V}O_2$peak and (ii) CVR and $\dot{V}O_2$peak. The individual subject masks described in the ROI Analysis section were used to confine this analysis to global gray matter only. Randomize is a permutation testing method that uses threshold free cluster enhancement (TFCE) (Smith and Nichols, 2009) to correct for multiple comparisons across voxels. Significance was set at $p < 0.05$ (FWE corrected).

[1] www.fmrib.ox.ac.uk/fsl

[2] http://fsl.fmrib.ox.ac.uk/fsl/fslwiki/FSLVBM

[3] http://www.fmrib.ox.ac.uk/fsl/randomise/index.html

RESULTS

All subjects completed the fitness test. Out of the 20 subjects 17 achieved an RER > 1.1 and 3 achieved RER > 1. 17 subjects exceeded the 90% HR maximum threshold and achieved a lactate peak >9, the remaining 3 exceeded 80% of HR maximum and achieved a lactate peak > 6. As this was a $\dot{V}O_2$peak test all subjects satisfied test criteria by working to volitional exhaustion. Based on typical $\dot{V}O_2$max criteria, 17 subjects fulfilled criteria for a maximal exercise test (Wilkinson et al., 2009; Dupuy et al., 2015). No adverse effects due to elevated CO_2 inhalation during the MRI scans were reported in this sample. See **Table 2** for group demographic and physiological data.

Correlations Between CBF, CVR, and $\dot{V}O_2$peak

ROI Analysis

There was a non-significant inverse association between $\dot{V}O_2$peak and resting CBF in gray matter; $r = -0.4$, $p = 0.08$, $p' = 0.16$ (**Figure 1**) and a significant positive correlation between $\dot{V}O_2$peak and CVR; $r = 0.62$, $p = 0.003$, $p' = 0.006$ (**Figure 2**).

TABLE 2 | Group characteristics and fitness test outcomes including $\dot{V}O_2$peak and secondary validation criteria.

Characteristics	Mean (sd)
Sex (11 female, 9 male)	–
Age (years)	25 (4.6)
Weight (kg)	69.1 (8.8)
Height (cm)	173 (7)
BMI	23 (2.1)
$\dot{V}O_2$peak (L/min)	2.9 (0.6)
$\dot{V}O_2$peak (L/kg/min)	41.2 (8)
Baseline lactate mmol/L	0.96 (0.3)
Post-exercise lactate	9.5 (2)
Baseline HR	79.2 (18.8)
Peak HR	185.4 (9.8)
Baseline BP (pre- $\dot{V}O_2$peak)	119/68
Peak RER	1.1 (0.04)
Maximum Work Rate (watts)	205 (40)
Baseline Borg (legs)	0.08 (0.2)
Peak Borg (legs)	8.5 (1.7)
Baseline Borg (breathing)	0.08 (0.3)
Peak Borg (breathing)	7.55 (2)
Baseline $ETCO_2$	36.6 (3)
Hypercapnia $ETCO_2$	44.2 (3.8)
$ETCO_2$ Increase during hypercapnia	7.8 (1.4)

$ETCO_2$ values represent values recorded during the ASL scan.

Follow-up exploratory analysis showed that baseline $P_{ET}CO_2$ was not associated with $\dot{V}O_2$peak; $r = -0.05$, $p = 0.8$ (**Supplementary Figure S2**), nor was the $P_{ET}CO_2$ change during hypercapnia associated with $\dot{V}O_2$peak; $r = 0.26$, $p = 0.27$.

A supplementary power analysis to aid in the design of future studies in presented as **Supplementary Table S3**.

Group average gray matter CBF maps during rest and hypercapnia are shown in **Supplementary Figure S5** for reference to demonstrate the CBF increase during hypercapnia.

Voxel-Wise Analysis

Voxel-wise analysis revealed a significant inverse association between $\dot{V}O_2$peak and resting CBF in the left and right thalamus, brainstem, right lateral occipital cortex, left intra-calcarine cortex and cerebellum (**Figure 3**). No regions were significantly positively correlated with $\dot{V}O_2$peak. Voxel-wise CVR did not correlate with $\dot{V}O_2$peak.

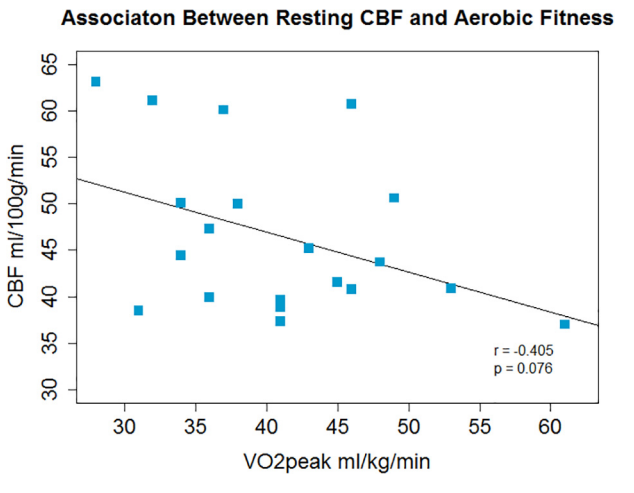

FIGURE 1 | A non-significant inverse association between aerobic fitness and whole brain gray matter CBF was observed.

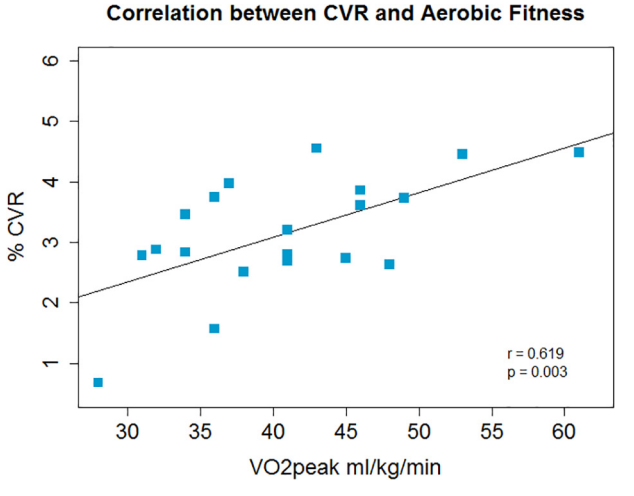

FIGURE 2 | Across the group whole brain gray matter CVR and aerobic fitness were positively correlated.

Cognitive Performance, Gray Matter Volume, and $\dot{V}O_2$peak

Finally, correlation analysis did not reveal any significant associations between $\dot{V}O_2$peak and cognitive performance, or cognitive performance and cerebrovascular measures. Mean scores and correlations are shown in **Supplementary Tables S1, S2**. VBM analysis of gray matter volume did not show a trend or association with $\dot{V}O_2$peak.

DISCUSSION

In this study, we examined the association between aerobic fitness and resting CBF and CVR using multiple inversion time PASL. This is the first study to report associations between aerobic fitness, CBF-based CVR, as opposed to BOLD-based CVR, and whole-brain gray matter CBF in young adults using ASL. Across the group, higher $\dot{V}O_2$peak was associated with lower regional resting CBF and greater global gray matter CVR to CO_2. $\dot{V}O_2$peak was not associated with cognitive task performance or gray matter volume in this cohort.

$\dot{V}O_2$peak, CBF and CVR

The inverse correlation between CBF and $\dot{V}O_2$peak was not expected, as the opposite has been found in children (Chaddock-Heyman et al., 2016), young adults (Bailey et al., 2013) and older adults (Ainslie et al., 2008; Brown et al., 2010; Bailey et al., 2013; Thomas et al., 2013; Zimmerman et al., 2014). However, with the exception of Thomas et al. (2013); Zimmerman et al. (2014), and Chaddock-Heyman et al. (2016), previous studies have used TCD ultrasound. TCD measures blood flow velocity, not flow, as TCD does not measure vessel diameter which would be required to calculate flow using this method. In contrast, ASL measures CBF directly through the labeling of inflowing water to tissue. Therefore, results may differ as they are measuring different vascular parameters. Recent efforts to characterize differences between MRI and TCD measures of CVR are valuable and will allow the methods to be used as complementary techniques given that TCD can be conducted under conditions not suited to MRI. For example, Burley et al. (2017) reported a positive correlation between VO_2max and CVR using both BOLD fMRI and TCD suggesting that the methods are not necessarily contradictory (Bailey et al., 2013; Thomas et al., 2013) and could be used to investigate brain function within groups at rest and during exercise. The main limitations of TCD are that it lacks the spatial resolution and the ability to measure tissue perfusion that is afforded by quantitative ASL MRI.

Most existing MRI studies investigated groups undergoing neurodevelopment (Chaddock-Heyman et al., 2016) or older adults (Thomas et al., 2014; Zimmerman et al., 2014) where the mechanistic relationships with aerobic fitness may be different to adults not in stages of either development or decline which may explain why results are not consistent across studies with different age groups. Further evidence for differential effects of

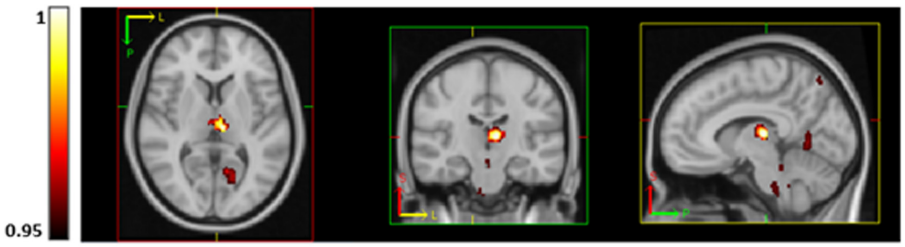

FIGURE 3 | Regions of significantly lower CBF (using TFCE thresholding and FWE corrected) in subjects with higher aerobic fitness at rest in the thalamus, brainstem, precuneus, visual cortex (V1) and lingual gyrus. *P*-values are displayed as 1-p where a value of 1 is most significant.

aerobic fitness with age comes from a recent structural MRI study by Williams et al. (2017) which reported a positive correlation between cortical thickness and $\dot{V}O_2$peak in older adults but an inverse correlation between these measures in young adults. CBF quantification in older adults must also be interpreted with caution where partial volume effects have not been controlled for. Coarse spatial resolution of ASL combined with cortical atrophy and a lack of correction for partial volume errors, plus delayed bolus arrival times may mean that perfusion is mis-estimated in the aging brain.

In the present study, $\dot{V}O_2$peak showed a non-significant inverse correlation with CBF averaged across the whole of gray matter. Statistical significance of an inverse correlation between CBF and $\dot{V}O_2$peak was localized to regions of the thalamus, brainstem, visual cortex, cerebellum and precuneus. Regional variation in contrast-to-noise may explain why CBF in these specific regions correlated with fitness in this sample. Even though the same direction of effect was observed in both the ROI and voxel-wise analyses, the results should be interpreted with caution given the small sample size of the present study. Although the direction of the relationship between $\dot{V}O_2$peak and baseline CBF was the opposite to that predicted at the outset of the study, the result is plausible in the light of a recent corroborative finding from our group in an independent cohort of young healthy volunteers. The study by Furby et al. (2019) was conducted using similar ASL MRI methods and demonstrated an inverse correlation between fitness and whole-brain averaged gray matter CBF. The interpretation of regional inverse correlations of baseline CBF with $\dot{V}O_2$peak remains speculative in the present study. It is possible that sensory gating in relation to fitness, in association with physical training, may affect the tonic level of activity in the thalamus as there is evidence of altered sensorimotor gating in athletes (Hormigo et al., 2019). However, it must be noted that participants in the present study were not selected for their high level of athletic performance.

A study by Robertson et al. (2015) in stroke survivors, using single inversion time PCASL, similarly found an inverse correlation between precuneus CBF and aerobic fitness, but a positive correlation between thalamic and posterior cingulate CBF and aerobic fitness. Gauthier et al. (2015) found both positive and inverse correlations between CVR and aerobic fitness in older adults, and this, along with the Robertson et al. (2015) study adds to the evidence that aerobic fitness may have complex, regionally varying and age dependent effects on the brain. Although the direction of the correlation in stroke survivors in the thalamus and posterior cingulate cortex contradicts the current results, the current study and those of Robertson et al. (2015) and Gauthier et al. (2015) further suggest that aerobic fitness may exert localized effects on CBF (Thomas et al., 2013; Chaddock-Heyman et al., 2016). Given that participants in each of these cited studies have differed in age and health status, the fact that consistent findings have not been reported is unsurprising. The variance in the effects of aerobic fitness on brain function with age needs further investigation through interventions in young and older groups as there may be a cross-over effect whereby higher CBF in youth and older adulthood has different functional importance. The current study consists of a normal sample of young adults who varied in fitness level, but not to the extent that a cross-sectional sample comprised of athletes and sedentary individuals would. However, our sample had a mean $\dot{V}O_2$peak of 41 ml/kg/min, standard deviation 8, similar to Hwang et al. (2017) who reported an average $\dot{V}O_2$max of 37.8, standard deviation 9.6 in a sample of 87 participants and also found a positive correlation between aerobic fitness and CVR in the MCA. The range of fitness levels within the study sample is likely to dictate the degree of observed fitness-related brain effects, especially in healthy groups. In fact, as well as differences in study design, the spread of fitness levels within studies may also explain the differences in the results of Barnes et al. (2013) and Bailey et al. (2013). Bailey et al. (2013) compared CVR between two groups, sedentary vs. trained, whereas Barnes et al. (2013) used a single group with a range of fitness levels who did not participate in a structured training regime.

We offer a neurobiological interpretation which potentially explains the negative correlation between CBF and $\dot{V}O_2$peak in this study. However, we stress that we do not have further data to support this mechanistic interpretation instead it forms a hypothesis that requires further investigation. Regular exercise training which increases $\dot{V}O_2$max, can result in increased tissue capacity to extract oxygen from blood in muscle (Kalliokoski et al., 2001; Ookawara et al., 2002), potentially as a result of greater blood vessel density which facilitates oxygen diffusion throughout the tissue. Similarly young animals subjected to wheel running for several weeks have shown increased angiogenesis, and therefore capillary density, in the brain compared with

sedentary animals (Swain et al., 2003; Pereira et al., 2007). Should this also be the case in humans, greater capillary density would be associated with enhanced oxygen diffusivity into tissue (Germuska et al., 2019), and higher oxygen extraction fraction (OEF), implying that a lower CBF is needed to sustain a given cerebral rate of oxygen metabolism. In terms of oxygen metabolism, future studies examining the relationship between aerobic fitness, CBF and OEF are needed.

Animal models can shed light on the mechanisms underpinning the effects of fitness on the brain at the microscopic and biochemical level. In particular, such work has demonstrated increased mitochondrial biogenesis following exercise training, in regions including the brainstem, cerebellum and hippocampus (Steiner et al., 2011). Mitochondrial dysfunction plays a role in many diseases for which aerobic fitness has been shown to reduce the incidence, such as cardiovascular disease and neurodegenerative diseases such as dementia (Navarro et al., 2009; Bertram et al., 2016). Similarly, exercise may influence angiogenesis (Black et al., 1990) as discussed above, and synaptogenesis in the form of region-specific increases in presynaptic density in the dentate gyrus and CA3 region of the hippocampus as demonstrated in aged rats (Siette et al., 2013). Changes at the synaptic level could drive metabolic demand and it is important to understand these changes in humans to fully interpret functional MRI data. Recent advances in PET imaging now allow potential biomarkers of synaptic density to be measured, for example, synaptic vesicle glycoprotein 2A (SV2A) (Nabulsi et al., 2016) can be targeted with an SV2A radiotracer to quantify this index of synaptic density to be compared between individuals with different levels of aerobic fitness.

Upon neuronal activation, there is an increase in demand for energy; in the healthy brain this is met with an increase in CBF. The lower resting CBF observed in higher fitness individuals, although initially counterintuitive, is not problematic if there is an adequate vascular reserve to meet changes in energy demand. The data support this argument as a greater gray matter CVR to CO_2 was observed in subjects with a higher $\dot{V}O_2$peak. If aerobic fitness maintains CBF and oxygenation, both of which are affected by aging (Aanerud et al., 2012), then an increase in CBF, and potentially CVR, in the trained group, would be expected when comparing trained vs. sedentary older adults. However, if aerobic fitness also enhances oxygen extraction efficiency, in young people this so-called efficiency may be observed as a lower resting CBF if aerobic fitness does indeed increase the number of blood vessels and therefore CBV as outlined above. Greater vessel density would increase the capacity for oxygenation and oxygen diffusion gradient across the tissue. In addition, CVR and $\dot{V}O_2$peak may then be positively correlated due to a higher vascular reserve, leading to a greater CBF response to CO_2 as CBF increases well above what is required to respond to a stimulus (Fox and Raichle, 1986). Future work which quantifies OEF, CBF, and CVR in similar populations could provide the additional necessary information to understand cerebral vascular and metabolic function at different levels of aerobic fitness.

The ROI analysis showed a positive correlation between CVR and $\dot{V}O_2$peak in global gray matter, however, no specific regions emerged in a follow-up voxel-wise analysis. CVR declines with age (De Vis et al., 2015; Peng et al., 2018) but in the literature, there are contradictory reports on the association between CVR and aerobic fitness (Bailey et al., 2013; Barnes et al., 2013; Thomas et al., 2013; Gauthier et al., 2015), as discussed in the introduction. The positive association between $\dot{V}O_2$peak and CVR reported here is in line with the TCD findings by Bailey et al. (2013), whereby trained young adults had greater CVR than a sedentary comparison group. However, few studies have investigated the relationship between CVR and aerobic fitness in healthy young adults, therefore more work is needed to adequately understand this relationship. Overall results across studies using MRI and TCD to study CBF, flow velocity and CVR suggest that exercise training and aerobic fitness has complex and varying effects on brain regions with potential mechanistic differences across the lifespan. This complexity presents an important area of future research in different age groups, and a need to comprehensively map cerebrovascular function across the brain. Future studies using both TCD and ASL would also add important information on the central and vascular effects of aerobic fitness on CBF and the source of any differences between the two methods.

Finally, it should be noted that De Vis et al. (2015) showed that resting $P_{ET}CO_2$ accounted for age-related CBF differences almost entirely. In this study, there was a non-significant positive trend ($r = 0.4$, $p = 0.06$) between baseline $P_{ET}CO_2$ and CBF, but no strong associations between $\dot{V}O_2$peak and baseline $P_{ET}CO_2$ ($r = 0.05$, $p = 0.8$) or the $\Delta P_{ET}CO_2$ during hypercapnia ($r = 0.26$, $p = 0.27$, see **Supplementary Figures S2–S4**). This suggests a cerebrovascular effect of fitness on CVR rather than an effect driven by $P_{ET}CO_2$ differences.

Cognitive Performance and Gray Matter Volume

Cognitive performance scores were similar across the group and there were no strong associations with $\dot{V}O_2$peak nor with CBF or CVR (see **Supplementary Tables S1, S2**). It is possible that cognitive differences in young adults may only be visible at more extreme ends of the fitness spectrum than sampled in this study. It is also possible that more sensitive cognitive tests are required to detect differences among high functioning groups separated only by fitness level.

The cognitive reserve hypothesis (Chodzko-Zajko and Moore, 1994) states that higher fitness in older age offsets age-related decline in cerebral circulation, enhancing oxygen delivery to support neural demand. More recently, Etnier et al. (2006) conducted a meta-regression on studies examining the effects of fitness on cognitive function. In summary, the authors did not find strong support for a beneficial effect of fitness in any age group once moderator variables were considered, and in fact found a negative association between fitness and cognition in studies using a pre-post design. Only a very small number of studies report a beneficial effect of fitness or physical activity on select cognitive domains in young people (Themanson et al., 2009;

Baym et al., 2011; Stroth et al., 2016) and other studies report significant effects in older but not young adults (Hayes et al., 2014b). In summary, more work is needed in young adults to determine neurophysiological effects of aerobic fitness and their functional relevance in terms of health and cognition.

Aerobic fitness is believed to reduce age-related atrophy, mainly in the hippocampus (Erickson et al., 2011; Firth et al., 2018). In this study the focus was on cerebrovascular function, not brain structure, however, if structural differences were present, this would affect CBF and CVR. The VBM analysis showed that gray matter global volume differences due to fitness were not present. As this group was young and healthy, this finding is not wholly surprising, and suggests that volumetric differences only become apparent in later life, adding to our knowledge of the lifelong effects of aerobic fitness.

Limitations

Hemoglobin (Hb) levels were not measured. Hb is responsible for transport of O_2 to tissue. The concentration of Hb in blood affects exercise performance; lower Hb means that blood can carry less oxygen (Calbet et al., 2006) and therefore muscle function is impaired. In addition, Hb affects perfusion estimates as there is an inverse relationship between [Hb] and the longitudinal relaxation time (T_1) of blood. Brain capillary [Hb] cannot be measured directly *in vivo*, however, peripheral capillary samples may provide an indication of Hb differences between subjects or groups which could help to explain biological mechanisms driving CBF differences.

Second, investigations were restricted to gray matter. Due to the limited SNR of ASL, reliable quantification of CBF and CVR in white matter is difficult as CBF is much lower than in gray matter. However, adequate blood supply and energy metabolism is necessary for all round brain health, and aging is associated with damage to white matter microstructure and reductions in myelination (Gunning-Dixon et al., 2009). Therefore, improvement of methods to study the WM vasculature are also needed to understand the global effects of fitness.

The voxelwise and ROI analyses did not show the same statistical significances. While the voxelwise analysis of CBF revealed regions of significantly lower CBF with fitness, the ROI analysis showed a non-significant trend in the same direction for global gray matter. The ROI analysis of CVR, however, showed a moderate (0.6) significant correlation with fitness while the voxelwise analysis did not reach statistical significance. ASL is an intrinsically low SNR technique compared to BOLD fMRI. Although ASL offers significant benefits in terms of quantification of physiological parameters, the SNR may have prevented detection of greater voxelwise associations with $\dot{V}O_2$peak. An alternative possibility is that CBF is more heterogeneous throughout the brain than CVR which is more affected by low SNR; therefore greater averaging of data in the ROI analysis allowed CVR differences to be detected.

Lastly, there are known hormonal effects on exercise test performance (de Jonge, 2003) and CBF (Brackley et al., 1999; Duckles and Krause, 2007). In the present study, the resting CBF difference was not significant between males and females; $t(18) = -0.119$, $p = 0.734$ but controlling for menstrual cycle phase, which was not done here, could reduce variability within cohorts. This is a preferable option to limiting studies to males only as hormonal differences may play a role in the acute response to exercise and possibly in mediating the effects of fitness on brain health.

Summary and Future Directions

The results of this study suggest that aerobic fitness is associated with lower CBF and greater CVR in young, healthy adults, however, the modest effects observed need replication in larger samples. We currently know very little about the functional relevance of CBF or CVR differences in young adults, and how the observed neurophysiological effects of physical training differ from those observed in older adults. With recent advances in quantitative MRI techniques, non-invasive mapping of multiple indices of cerebrovascular function, e.g., CBF, CVR, CBV OEF and the cerebral metabolic rate of oxygen consumption is possible within a single scan session (Bulte et al., 2012; Gauthier et al., 2012; Gauthier and Hoge, 2013; Wise et al., 2013). Notably, regional CBV quantification would bring us a step closer to comparisons with experimental data on angiogenesis and capillary density following exercise.

Application of these techniques to study brain function in both young and older trained and sedentary adults will provide information necessary to move forward in developing exercise training protocols to increase the adoption of fitness training as a preventative health tool.

Research over the next decade should also work to establish whether regular exercise regardless of intensity level delivers brain benefits, or whether there is an aerobic fitness threshold, above which benefits such as maintained CBF with aging, are observed. Answering this question will guide optimal exercise dose recommendations and interventional studies.

AUTHOR'S NOTE

This manuscript can be found as a preprint on BioRxiv (Foster et al., 2019) at: https://www.biorxiv.org/content/10.1101/539072v1. This work first appeared in the lead author's thesis (Foster, 2017; Chapter 4) which can be accessed here: http://orca.cf.ac.uk/109647/.

DATA AVAILABILITY STATEMENT

The datasets generated for this study are available on request to the corresponding author.

ETHICS STATEMENT

The study was approved by the Cardiff University School of Psychology Research Ethics Committee and performed in accordance with the guidelines stated in the Cardiff University Research Framework (version 4.0, 2010). Informed written consent was obtained from all subjects.

AUTHOR CONTRIBUTIONS

CF conceived and designed the study with input from RW. CF and JS coordinated the project and collected the data with assistance from DH. CF and RW analyzed the data. CF prepared the manuscript with RW providing input and interpretation of results as well as reviewing and editing the final manuscript. VT supervised CF throughout the project. All authors approved the manuscript before submission.

FUNDING

This work was supported by the Wellcome Trust (Grant Nos. 506285 and 200804/Z/16/Z) and The Waterloo Foundation.

SUPPLEMENTARY MATERIAL

The Supplementary Material for this article can be found online at: https://www.frontiersin.org/articles/10.3389/fphys.2020.00360/full#supplementary-material

REFERENCES

Aanerud, J., Borghammer, P., Chakravarty, M. M., Vang, K., Rodell, A. B., Møller, A., et al. (2012). Brain energy metabolism and blood flow differences in healthy aging. *J. Cereb. Blood Flow Metab.* 2, 1177–1187. doi: 10.1038/jcbfm.2012.18

Ainslie, P. N., Cotter, J. D., George, K. P., Lucas, S., Murrell, C., Shave, R., et al. (2008). Elevation in cerebral blood flow velocity with aerobic fitness throughout healthy human ageing. *J. Physiol.* 16, 4005–4010. doi: 10.1113/jphysiol.2008.158279

Andersson, J. L., Jenkinson, M., and Smith, S. (2007). *Non-linear Registration Aka Spatial Normalisation FMRIB Technial Report TR07JA2*. Oxford, United Kingdom: FMRIB Analysis Group of the University of Oxford.

Baddeley, A. D., Emslie, H., and Nimmo-Smith, I. (1992). *The Speed and Capacity of Language-Processing Test (SCOLP)*. Bury St Edmunds: Thames Valley Test Company.

Bailey, D. M., Marley, C. J., Brugniaux, J. V., Hodson, D., New, K. J., Ogoh, S., et al. (2013). Elevated aerobic fitness sustained throughout the adult lifespan is associated with improved cerebral hemodynamics. *Stroke* 44, 3235–3238. doi: 10.1161/STROKEAHA.113.002589

Barnes, J. N., Taylor, J. L., Kluck, B. N., Johnson, C. P., and Joyner, M. J. (2013). Cerebrovascular reactivity is associated with maximal aerobic capacity in healthy older adults. *J. Appl. Physiol.* 114, 1383–1387. doi: 10.1152/japplphysiol.01258.2012

Baym, C. L., Khan, N. A., Pence, A., Raine, L. B., Hillman, C. H., and Cohen, N. J. (2011). Aerobic fitness predicts relational memory but not item memory performance in healthy young adults. *J. Cogn. Neurosci.* 26, 2645–2652. doi: 10.1162/jocn

Bertram, S., Brixius, K., and Brinkmann, C. (2016). Exercise for the diabetic brain: how physical training may help prevent dementia and Alzheimer's disease in T2DM patients. *Endocrine* 53, 350–363. doi: 10.1007/s12020-016-0976-8

Black, J. E., Isaacs, K. R., Anderson, B. J., Alcantara, A. A., and Greenough, W. T. (1990). Learning causes synaptogenesis, whereas motor activity causes angiogenesis, in cerebellar cortex of adult rats. *Proc. Natl. Acad. Sci. U.S.A.* 87, 5568–5572. doi: 10.1073/pnas.87.14.5568

Borg, E., and Kaijser, L. (2006). A comparison between three rating scales for perceived exertion and two different work tests. *Scand. J. Med. Sci. Sports* 16, 57–69. doi: 10.1111/j.1600-0838.2005.00448.x

Brackley, K. J., Ramsay, M. M., Broughton Pipkin, F., and Rubin, P. C. (1999). The effect of the menstrual cycle on human cerebral blood flow: studies using Doppler ultrasound. *Ultrasound Obstetr. Gynecol.* 14, 52–57. doi: 10.1046/j.1469-0705.1999.14010052.x

Brown, A. D., McMorris, C. A., Longman, R. S., Leigh, R., Hill, M. D., Friedenreich, C. M., et al. (2010). Effects of cardiorespiratory fitness and cerebral blood flow on cognitive outcomes in older women. *Neurobiol. Aging* 31, 2047–2057. doi: 10.1016/j.neurobiolaging.2008.11.002

Bulte, D. P., Kelly, M., Germuska, M., Xie, J., Chappell, M. A., Okell, T. W., et al. (2012). Quantitative measurement of cerebral physiology using respiratory-calibrated MRI. *Neuroimage* 60, 582–591. doi: 10.1016/j.neuroimage.2011.12.017

Burley, C. V., Mullinger, K. J., Francis, S. T., Phillips, A. C., and Lucas, S. J. (2017). Assessing cerebrovascular responsiveness: comparing functional magnetic resonance imaging with Doppler Ultrasound. *Med. Sci. Sports Exerc.* 49, 825–825. doi: 10.1249/01.mss.0000519215.31383.62

Calbet, J. A., Lundby, C., Koskolou, M., and Boushel, R. (2006). Importance of hemoglobin concentration to exercise: acute manipulations. *Respir. Physiol. Neurobiol.* 151, 132–140. doi: 10.1016/j.resp.2006.01.014

Chaddock-Heyman, L., Erickson, K. I., Chappell, M. A., Johnson, C. L., Kienzler, C., Knecht, A., et al. (2016). Aerobic fitness is associated with greater hippocampal cerebral blood flow in children. *Dev. Cogn. Neurosci.* 20, 52–58. doi: 10.1016/j.dcn.2016.07.001

Chalela, J. A., Alsop, D. C., Gonzalez-Atavales, J. B., Maldjian, J. A., Kasner, S. E., and Detre, J. A. (2000). Magnetic resonance perfusion imaging in acute ischemic stroke using continuous arterial spin labeling. *Stroke* 31, 680–687. doi: 10.1161/01.str.31.3.680

Chappell, M. A., MacIntosh, B. J., Donahue, M. J., Gonther, M., Jezzard, P., and Woolrich, M. W. (2010). Separation of macrovascular signal in multi-inversion time arterial spin labelling MRI. *Magn. Reson. Med.* 63, 1357–1365. doi: 10.1002/mrm.22320

Chodzko-Zajko, W. J., and Moore, K. A. (1994). Physical fitness and cognitive functioning in aging. *Exerc. Sport Sci. Rev.* 22, 195–220. doi: 10.1097/JES.0b013e3182553430

Collett, J., Dawes, H., Meaney, A., Sackley, C., Barker, K., Wade, D., et al. (2011). Exercise for multiple sclerosis: a single-blind randomized trial comparing three exercise intensities. *Multiple Scler. J.* 17, 594–603. doi: 10.1177/1352458510391836

Conners, C. K. (2000). *Continuous Performance Test II Technical Guide and Software Manual*. Toronto, ON: Multi-Health Systems.

Cooney, J. K., Moore, J. P., Ahmad, Y. A., Jones, J. G., Lemmey, A. B., Casanova, F., et al. (2013). A simple step test to estimate cardio-respiratory fitness levels of rheumatoid arthritis patients in a clinical setting. *Int. J. Rheumatol.* 2013:174541. doi: 10.1155/2013/174541

Craig, C. L., Marshall, A. L., Sstrm, M., Bauman, A. E., Booth, M. L., Ainsworth, B. E., et al. (2003). International physical activity questionnaire: 12-Country reliability and validity. *Med. Sci. Sports Exerc.* 35, 1381–1395. doi: 10.1249/01.MSS.0000078924.61453.FB

de Jonge, X. A. J. (2003). Effects of the menstrual cycle on exercise performance. *Sports Med.* 33, 833–851. doi: 10.2165/00007256-200333110-00004

De Vis, J. B., Hendrikse, J., Bhogal, A., Adams, A., Kappelle, L. J., and Petersen, E. T. (2015). Age-related changes in brain hemodynamics; a calibrated MRI study. *Hum. Brain Mapping* 36, 3973–3987. doi: 10.1002/hbm.22891

Douaud, G., Smith, S., Jenkinson, M., Behrens, T., Johansen-Berg, H., Vickers, J., et al. (2007). Anatomically related grey and white matter abnormalities in adolescent-onset schizophrenia. *Brain* 130, 2375–2386. doi: 10.1093/brain/awm184

Duckles, S. P., and Krause, D. N. (2007). Cerebrovascular effects of oestrogen: multiplicity of action. *Clin. Exp. Pharmacol. Physiol.* 34, 801–808. doi: 10.1111/j.1440-1681.2007.04683.x

Dupuy, O., Gauthier, C. J., Fraser, S. A., Desjardins-Crèpeau, L., Desjardins, M., Mekary, S., et al. (2015). Higher levels of cardiovascular fitness are associated with better executive function and prefrontal oxygenation in younger and older women. *Front. Hum. Neurosci.* 9:66. doi: 10.3389/fnhum.2015.00066

Erickson, K. I., Voss, M. W., Prakash, R. S., Basak, C., Szabo, A., Chaddock, L., et al. (2011). Exercise training increases size of hippocampus and improves memory. *Proc. Natl. Acad. Sci. U.S.A.* 108, 3017–3022. doi: 10.1073/pnas.1015950108

Etnier, J. L., Nowell, P. M., Landers, D. M., and Sibley, B. A. (2006). A meta-regression to examine the relationship between aerobic fitness and cognitive performance. *Brain Res. Rev.* 52, 119–130. doi: 10.1016/j.brainresrev.2006.01.002

Firth, J., Stubbs, B., Vancampfort, D., Schuch, F., Lagopoulos, J., Rosenbaum, S., et al. (2018). NeuroImage Effect of aerobic exercise on hippocampal volume in humans: a systematic review and meta-analysis. *Neuroimage* 166, 230–238. doi: 10.1016/j.neuroimage.2017.11.007

Foster, C. (2017). *Investigating Cerebrovascular Health and Functional Plasticity Using Quantitative FMRI*. Doctoral dissertation, Cardiff University, Cardiff.

Foster, C., Steventon, J., Helme, D., Tomassini, V., and Wise, R. G. (2019). Assessment of the effects of aerobic fitness on cerebrovascular function in young adults using multiple inversion time arterial spin labelling MRI. *bioRxiv* [Preprint]. doi: 10.1101/539072

Fox, P. T., and Raichle, M. E. (1986). Focal physiological uncoupling of cerebral blood flow and oxidative metabolism during somatosensory stimulation in human subjects. *Proc. Natl. Acad. Sci. U.S.A.* 83, 1140–1144. doi: 10.1073/pnas.83.4.1140

Furby, H. V., Warnert, E. A., Marley, C. J., Bailey, D. M., and Wise, R. G. (2019). Cardiorespiratory fitness is associated with increased middle cerebral arterial compliance and decreased cerebral blood flow in young healthy adults: a pulsed ASL MRI study. *J. Cereb. Blood Flow Metab.* [Epub ahead of print].

Gauthier, C. J., Desjardins-crépeau, L., Madjar, C., Bherer, L., and Hoge, R. D. (2012). NeuroImage Absolute quanti fi cation of resting oxygen metabolism and metabolic reactivity during functional activation using QUO2 MRI. *Neuroimage* 63, 1353–1363. doi: 10.1016/j.neuroimage.2012.07.065

Gauthier, C. J., and Hoge, R. D. (2013). A generalized procedure for calibrated MRI incorporating hyperoxia and hypercapnia. *Hum. Brain Mapp.* 34, 1053–1069. doi: 10.1002/hbm.21495

Gauthier, C. J., Lefort, M., Mekary, S., Desjardins-Crépeau, L., Skimminge, A., Iversen, P., et al. (2015). Hearts and minds: linking vascular rigidity and aerobic fitness with cognitive aging. *Neurobiol. Aging* 36, 304–314. doi: 10.1016/j.neurobiolaging.2014.08.018

Germuska, M., Chandler, H. L., Stickland, R. C., Foster, C., Fasano, F., Okell, T. W., et al. (2019). Dual-calibrated fMRI measurement of absolute cerebral metabolic rate of oxygen consumption and effective oxygen diffusivity. *Neuroimage* 184, 717–728. doi: 10.1016/j.neuroimage.2018.09.035

Glover, G. H., and Lai, S. (1998). Self-navigated spiral fMRI: interleaved versus single-shot. *Magn. Reson. Med. Sci.* 39, 361–368. doi: 10.1002/mrm.1910390305

Glover, G. H., Li, T. Q., and Ress, D. (2000). Image-based method for retrospective correction of physiological motion effects in fMRI: RETROICOR. *Magn. Reson. Med.* 44, 162–167. doi: 10.1002/1522-2594(200007)44:1<162::aid-mrm23>3.0.co;2-e

Good, C. D., Johnsrude, I., Ashburner, J., Henson, R. N., Friston, K. J., and Frackowiak, R. S. (2001). Cerebral asymmetry and the effects of sex and handedness on brain structure: a voxel-based morphometric analysis of 465 normal adult human brains. *Neuroimage* 14, 685–700. doi: 10.1006/nimg.2001.0857

Gunning-Dixon, F. M., Brickman, A. M., Cheng, J. C., and Alexopoulos, G. S. (2009). Aging of cerebral white matter: a review of MRI findings. *Int. J. Geriatr. Psychiatry* 24, 109–117. doi: 10.1002/gps.2087

Haskell, W. L., Lee, I., Pate, R. R., Powell, K. E., and Blair, S. N. (2007). Physical activity and public health: updated recommendation for adults from the american college of sports medicine and the american heart association. *Med. Sci. Sports Exerc.* 39, 1423–1434. doi: 10.1249/mss.0b013e3180616b27

Hayes, S. M., Alosco, M. L., and Forman, D. E. (2014a). The effects of aerobic exercise on cognitive and neural decline in aging and cardiovascular disease. *Curr. Geriatr. Rep.* 3, 282–290. doi: 10.1007/s13670-014-0101-x

Hayes, S. M., Forman, D. E., and Verfaellie, M. (2014b). Cardiorespiratory fitness is associated with cognitive performance in older but not younger adults. *J. Gerontol. B Psychol. Sci. Soc. Sci.* 71, 1–8. doi: 10.1093/geronb/gbu167

Hillman, C. H., Erickson, K. I., and Kramer, A. F. (2008). Be smart, exercise your heart: exercise effects on brain, and cognition. *Nat. Rev. Neurosci.* 9:58. doi: 10.1038/nrn2298

Hormigo, S., Cardoso, A., Sancho, C., López, D. E., and Moreno, C. (2019). Associations between sensorimotor gating mechanisms, and athletic performance in a variety of physical conditioning tests. *Eur. J. Appl. Physiol.* 119, 921–932. doi: 10.1007/s00421-019-04081-1

Horton, T. J., Grunwald, G. K., Lavely, J., Donahoo, W. T., Horton, T. J., Dow, S., et al. (2011). Glucose kinetics differ between women and men, during and after exercise Glucose kinetics differ between women and men, during and after exercise. *J. Appl. Physiol.* 100, 1883–1894. doi: 10.1152/japplphysiol.01431.2005

Hwang, J., Castelli, D. M., and Gonzalez-lima, F. (2017). Physiology & Behavior The positive cognitive impact of aerobic fi tness is associated with peripheral in fl ammatory and brain-derived neurotrophic biomarkers in young adults. *Physiol. Behav.* 179, 75–89. doi: 10.1016/j.physbeh.2017.05.011

Jenkinson, M., Bannister, P., Brady, M., and Smith, S. (2002). Improved optimization for the robust and accurate linear registration and motion correction of brain images. *Neuroimage* 17, 825–841. doi: 10.1016/S1053-8119(02)91132-8

Kalliokoski, K. K., Oikonen, V., Takala, T. O., Kari, K., Oikonen, V., Teemu, O., et al. (2001). Enhanced oxygen extraction and reduced flow heterogeneity in exercising muscle in endurance-trained men. *Am. J. Physiol. Endocrinol. Metab.* 280, 1015–1021.

Kodama, S., Saito, K., Tanaka, S., Maki, M., Yachi, Y., Asumi, M., et al. (2009). Cardiorespiratory fitness as a quantitative predictor of all-cause mortality and cardiovascular events in healthy men and women: a meta-analysis. *JAMA* 301, 2024–2035.

Lee, D., Artero, E. G., Sui, X., and Blair, S. N. (2010). Mortality trends in the general population: the importance of cardiorespiratory fitness. *J. Psychopharmacol.* 4(Suppl.), 27–35. doi: 10.1177/1359786810382057

Liu, J. Z., Dai, T. H., Sahgal, V., Brown, R. W., and Yue, G. H. (2002). Nonlinear cortical modulation of muscle fatigue: a functional MRI study. *Brain Res.* 957, 320–329. doi: 10.1016/S0006-8993(02)03665-X

Lu, H., Donahue, M. J., and Van Zijl, P. C. M. (2006). Detrimental effects of BOLD signal in arterial spin labeling fMRI at high field strength. *Magn. Reson. Med.* 56, 546–552. doi: 10.1002/mrm.20976

Milani, R. V., Lavie, C. J., Mehra, M. R., and Ventura, H. O. (2006). Understanding the basics of cardiopulmonary exercise testing. *Mayo Clin. Proc.* 81, 1603–1611. doi: 10.4065/81.12.1603

Nabulsi, N. B., Mercier, J., Holden, D., Carré, S., Najafzadeh, S., Vandergeten, M. C., et al. (2016). Synthesis and preclinical evaluation of 11C-UCB-J as a PET tracer for imaging the synaptic vesicle glycoprotein 2A in the brain. *J. Nucl. Med.* 57, 777–784. doi: 10.2967/jnumed.115.168179

Navarro, A., Boveris, A., Bández, M. J., Sánchez-Pino, M. J., Gómez, C., Muntané, G., et al. (2009). Human brain cortex: mitochondrial oxidative damage and adaptive response in Parkinson disease and in dementia with Lewy bodies. *Free Radic. Biol. Med.* 46, 1574–1580. doi: 10.1016/j.freeradbiomed.2009.03.007

Nishijima, T., Torres-Aleman, I., and Soya, H. (2016). Exercise and cerebrovascular plasticity. *Prog. Brain Res.* 225, 243–268. doi: 10.1016/bs.pbr.2016.03.010

Ookawara, T., Suzuk, K., Haga, S., Ha, S., Chung, K. S., Toshinai, K., et al. (2002). Transcription regulation of gene expression in human skeletal muscle in response to endurance training. *Res. Commun. Mol. Pathol. Pharmacol.* 111, 41–54.

Peng, S., Chen, X., Li, Y., Rodrigue, K. M., Park, D. C., and Lu, H. (2018). Age-related changes in cerebrovascular reactivity and their relationship to cognition: a four-year longitudinal study. *Neuroimage* 174, 257–262. doi: 10.1016/j.neuroimage.2018.03.033

Pereira, A. C., Huddleston, D. E., Brickman, A. M., Sosunov, A. A., Hen, R., McKhann, G. M., et al. (2007). An in vivo correlate of exercise-induced neurogenesis in the adult dentate gyrus. *Proc. Natl. Acad. Sci. U.S.A.* 104, 5638–5643. doi: 10.1073/pnas.0611721104

Poole, D. C., Wilkerson, Æ. D. P., and Jones, A. M. (2008). Validity of criteria for establishing maximal O 2 uptake during ramp exercise tests. *Eur. J. Appl. Physiol.* 102, 403–410. doi: 10.1007/s00421-007-0596-3

Robertson, A. D., Crane, D. E., Rajab, A. S., Swardfager, W., Marzolini, S., and Shirzadi, Z. (2015). Exercise intensity modulates the change in cerebral blood flow following aerobic exercise in chronic stroke. *Exp. Brain Res.* 233, 2467–2475. doi: 10.1007/s00221-015-4317-6

Roque, F. R., Hernanz, R., Salaices, M., and Briones, A. M. (2013). Exercise training and cardiometabolic diseases: focus on the vascular system. *Curr. Hypertens. Rep.* 15, 204–214. doi: 10.1007/s11906-013-0336-5

Siette, J., Westbrook, R. F., Cotman, C., Sidhu, K., Zhu, W., Sachdev, P., et al. (2013). Age-specific effects of voluntary exercise on memory and the older brain. *Biol. Psychiatry* 73, 435–442. doi: 10.1016/j.biopsych.2012.05.034

Smith, S. M., and Nichols, T. E. (2009). Threshold-free cluster enhancement: addressing problems of smoothing, threshold dependence and localisation in cluster inference. *Neuroimage* 44, 83–98. doi: 10.1016/j.neuroimage.2008.03.061

Steiner, J. L., Murphy, E. A., McClellan, J. L., Carmichael, M. D., and Davis, J. M. (2011). Exercise training increases mitochondrial biogenesis in the brain. *J. Appl. Physiol.* 111, 1066–1071. doi: 10.1152/japplphysiol.00343.2011

Stroth, S., Hille, K., Spitzer, M., and Reinhardt, R. (2016). Aerobic endurance exercise benefits memory and affect in young adults. *Neuropsychol. Rehabil.* 19, 223–243. doi: 10.1080/09602010802091183

Swain, R., Harris, A., Wiener, E., Dutka, M., Morris, H., Theien, B., et al. (2003). Prolonged exercise induces angiogenesis and increases cerebral blood volume in primary motor cortex of the rat. *Neuroscience* 117, 1037–1046. doi: 10.1016/S0306-4522(02)00664-4

Tancredi, F. B., and Hoge, R. D. (2013). Comparison of cerebral vascular reactivity measures obtained using breath-holding and CO2 inhalation. *J. Cereb. Blood Flow Metab.* 33, 1066–1074. doi: 10.1038/jcbfm.2013.48

Tancredi, F. B., Lajoie, I., and Hoge, R. D. (2014). A simple breathing circuit allowing precise control of inspiratory gases for experimental respiratory manipulations. *BMC Res. Notes* 7:235. doi: 10.1186/1756-0500-7-235

Themanson, J. R., Pontifex, M. B., and Hillman, C. H. (2009). Fitness and action monitoring: evidence for improved cognitive flexibility in young adults. *Neuroscience* 157, 319–328. doi: 10.1016/j.neuroscience.2008.09.014

Thomas, B. P., Liu, P., Park, D. C., van Osch, M. J., and Lu, H. (2014). Cerebrovascular reactivity in the brain white matter: magnitude, temporal characteristics, and age effects. *J. Cereb. Blood Flow Metab.* 34, 242–247. doi: 10.1038/jcbfm.2013.194

Thomas, B. P., Yezhuvath, U. S., Tseng, B. Y., Liu, P., Levine, B. D., Zhang, R., et al. (2013). Life-long aerobic exercise preserved baseline cerebral blood flow but reduced vascular reactivity to CO2. *J. Magn. Reson. Imaging JMRI* 38, 1177–1183. doi: 10.1002/jmri.24090

Voss, M. W., Nagamatsu, L. S., Liu-ambrose, T., Arthur, F., Fedewa, A. L., Ahn, S., et al. (2015). Exercise, brain, and cognition across the life span adults. *J. Appl. Physiol.* 111, 1505–1513. doi: 10.1152/japplphysiol.00210.2011

Wang, J., Qiu, M., and Constable, R. T. (2005). In vivo method for correcting transmit/receive nonuniformities with phased array coils. *Magn. Reson. Med.* 53, 666–674. doi: 10.1002/mrm.20377

Wilkinson, M., Leedale-brown, D., and Winter, E. M. (2009). Validity of a Squash-Specific Fitness Test. *Int. J. Sports Physiol. Perform.* 4, 29–40. doi: 10.1123/ijspp.4.1.29

Williams, V. J., Hayes, J. P., Forman, D. E., Salat, D. H., Sperling, R. A., Verfaellie, M., et al. (2017). Cardiorespiratory fi tness is di ff erentially associated with cortical thickness in young and older adults. *Neuroimage* 146, 1084–1092. doi: 10.1016/j.neuroimage.2016.10.033

Winkler, A. M., Ridgway, G. R., Webster, M. A., Smith, S. M., and Nichols, T. E. (2014). NeuroImage Permutation inference for the general linear model. *Neuroimage* 92, 381–397. doi: 10.1016/j.neuroimage.2014.01.060

Wise, R. G., Harris, A. D., Stone, A. J., and Murphy, K. (2013). Measurement of OEF and absolute CMRO2: MRI-based methods using interleaved and combined hypercapnia and hyperoxia. *Neuroimage* 83, 135–147. doi: 10.1016/j.neuroimage.2013.06.008

Wong, E. C., Buxton, R. B., and Frank, L. R. (1998). Quantitative imaging of perfusion using a single subtraction (QUIPSS and QUIPSS II). *Magn. Reson. Med.* 39, 702–708. doi: 10.1002/mrm.1910390506

Zimmerman, B., Bradley, P., Low, K. A., Fletcher, M. A., Tan, C. H., Schneider-Garces, N., et al. (2014). Cardiorespiratory fitness mediates the effects of aging on cerebral blood flow. *Front. Aging Neurosci.* 6:59. doi: 10.3389/fnagi.2014.00059

Conflict of Interest: The authors declare that the research was conducted in the absence of any commercial or financial relationships that could be construed as a potential conflict of interest.

frontiers in Physiology

ORIGINAL RESEARCH
published: 08 May 2020
doi: 10.3389/fphys.2020.00428

Cerebral Metabolic Changes During Visuomotor Adaptation Assessed Using Quantitative fMRI

*Catherine Foster[1], Jessica J. Steventon[2,3], Daniel Helme[4], Valentina Tomassini[1,5,6,7] and Richard G. Wise[1,6,7]**

[1] Cardiff University Brain Research Imaging Centre (CUBRIC), School of Psychology, Cardiff University, Cardiff, United Kingdom, [2] Cardiff University Brain Research Imaging Centre (CUBRIC), School of Physics and Astronomy, Cardiff University, Cardiff, United Kingdom, [3] Neuroscience and Mental Health Research Institute (NMHRI), School of Medicine, Cardiff University, Cardiff, United Kingdom, [4] Department of Anaesthetics and Intensive Care Medicine, Cardiff University School of Medicine, Cardiff, United Kingdom, [5] Division of Psychological Medicine and Clinical Neurosciences, School of Medicine, Cardiff University, Cardiff, United Kingdom, [6] Department of Neuroscience, Imaging and Clinical Sciences, "G. D'Annunzio University" of Chieti-Pescara, Chieti, Italy, [7] Institute for Advanced Biomedical Technologies (ITAB), "G. D'Annunzio University" of Chieti-Pescara, Chieti, Italy

OPEN ACCESS

Edited by:
Marta Bianciardi, Harvard Medical School, United States

Reviewed by:
Alessandra Caporale, University of Pennsylvania Perelman School of Medicine, United States
Hannes Michel Wiesner, University of Minnesota, United States

***Correspondence:**
Richard G. Wise
wiserg@cardiff.ac.uk

Specialty section:
This article was submitted to Medical Physics and Imaging, a section of the journal Frontiers in Physiology

Received: *12 September 2019*
Accepted: *08 April 2020*
Published: *08 May 2020*

Citation:
Foster C, Steventon JJ, Helme D, Tomassini V and Wise RG (2020) Cerebral Metabolic Changes During Visuomotor Adaptation Assessed Using Quantitative fMRI. Front. Physiol. 11:428. doi: 10.3389/fphys.2020.00428

The brain retains a lifelong ability to adapt through learning and in response to injury or disease-related damage, a process known as functional neuroplasticity. The neural energetics underlying functional brain plasticity have not been thoroughly investigated experimentally in the healthy human brain. A better understanding of the blood flow and metabolic changes that accompany motor skill acquisition, and which facilitate plasticity, is needed before subsequent translation to treatment interventions for recovery of function in disease. The aim of the current study was to characterize cerebral blood flow (CBF) and oxygen consumption (relative $CMRO_2$) responses, using calibrated fMRI conducted in 20 healthy participants, during performance of a serial reaction time task which induces rapid motor adaptation. Regions of interest (ROIs) were defined from areas showing task-induced BOLD and CBF responses that decreased over time. BOLD, CBF and relative $CMRO_2$ responses were calculated for each block of the task. Motor and somatosensory cortices and the cerebellum showed statistically significant positive responses to the task compared to baseline, but with decreasing amplitudes of BOLD, CBF, and $CMRO_2$ response as the task progressed. In the cerebellum, there was a sustained positive BOLD response in the absence of a significant $CMRO_2$ increase from baseline, for all but the first task blocks. This suggests that the brain may continue to elevate the supply energy even after $CMRO_2$ has returned to near baseline levels. Relying on BOLD fMRI data alone in studies of plasticity may not reveal the nature of underlying metabolic responses and their changes over time. Calibrated fMRI approaches may offer a more complete picture of the energetic changes supporting plasticity and learning.

Keywords: calibrated fMRI, cerebral blood flow, functional MRI, motor adaptation, oxygen metabolism

INTRODUCTION

The brain retains a lifelong ability to adapt through learning and in response to injury or disease-related damage, a process known as functional neuroplasticity. Residual neuroplasticity in chronic diseases such as Multiple Sclerosis (MS), or following stroke, can be harnessed in rehabilitation strategies to promote recovery of function. However, the neuronal and vascular mechanisms underlying plasticity are not fully understood. Adequate energy delivery in the form of cerebral blood flow (CBF), which carries oxygen, glucose and other nutrients to tissue, is essential for healthy neuronal function, as is the capacity to metabolize these substrates. In MS for example, there is evidence of both CBF (D'haeseleer et al., 2011; Ota et al., 2013) and metabolic dysfunction (Kidd et al., 1999; Ge et al., 2012; Fan et al., 2015) which may play a central role in limiting plasticity. The neural energetics underlying functional brain plasticity have not been thoroughly investigated experimentally in the healthy human brain. A better understanding of the blood flow and metabolism changes which occur during motor skill acquisition, and which facilitate plasticity, is needed before characterization in disease, and subsequent translation to inform treatment interventions to maintain or recover function.

Calibrated fMRI enables measurement of regional CBF and relative changes in the rate of cerebral metabolic rate of oxygen consumption ($CMRO_2$) through the addition of hypercapnic calibration (Davis et al., 1998; Hoge et al., 1999) during dual-acquisition of BOLD and CBF weighted images. The technique has potential applications in identifying clinically relevant abnormalities in vascular and metabolic function which may not be evident using BOLD fMRI alone. CBF and $CMRO_2$ provide additional information which aids interpretation of fMRI studies of aging and disease where neurovascular coupling (NVC) is likely to be altered (Restom et al., 2008). For example, greater BOLD responses with increasing age during a Stroop task have been reported, alongside a reduced $CMRO_2$ increase in response to the task (Mohtasib et al., 2012). This suggests that as CBF was unaffected by age in this cohort, the greater BOLD signal changes were due to a reduction in the $CMRO_2$ response. As $CMRO_2$ and neuronal firing are closely coupled (Mathiesen et al., 1998; Martindale et al., 2003), a decreased neural response with age is a possible explanation for these results. Such changes in vascular reserve and NVC would not have been revealed by BOLD fMRI alone, and the results demonstrate the value of calibrated fMRI in studies where cerebral energetics may be altered by experimental conditions or over time.

The aim of the current study was to measure BOLD, CBF and $CMRO_2$ responses during performance of a serial reaction time (SRT) task (Nissen and Bullemer, 1987) using calibrated fMRI. In the SRT task, participants respond to a sequence of stimuli that appear one-by-one at various locations on a screen. Participants respond by indicating the current stimulus location which follows a repeating pattern (see **Figure 1** which depicts the first three presentations in the sequence) allowing participants to identify this sequence with practice, improving the accuracy and speed of responses. Visuomotor task performance can be improved over short periods of time, accompanied by hemodynamic changes in task-relevant regions, which are thought to reflect short-term plasticity in the adult brain (Olson et al., 2006; Fernández-Seara et al., 2009; Shannon et al., 2016). Previous work has demonstrated BOLD and CBF task responses in motor and visual cortex as well as prefrontal regions and the cerebellum during task performance (Ungerleider et al., 2002). BOLD signal reductions over time, due to task adaptation have also been observed within a single MRI session (Floyer-Lea and Matthews, 2004; Shannon et al., 2016). Therefore, we expected to observe reduced BOLD signal responses in task-relevant areas as motor adaptation occurred. CBF and $CMRO_2$ may change dynamically with adaptation to the task in ways that are not visible by looking solely at the BOLD response, as it is the result of changes in vascular and metabolic processes. For example, although BOLD and CBF responses have been reported during motor skill learning task (Olson et al., 2006), it is not clearly established whether their changes over time follow similar patterns or whether there are also alterations in the $CMRO_2$ response, as previous works have reported both no changes (Madsen et al., 1995) and reductions in $CMRO_2$ response (Shannon et al., 2016) during skill learning.

To examine motor task adaptation, BOLD, CBF, and $CMRO_2$ responses were calculated for each block of an SRT task in regions which showed reducing BOLD and CBF responses across the task. Changes in each parameter from baseline were investigated along with differences between brain regions and task blocks. Lastly, regression analysis was conducted to determine whether CBF, $CMRO_2$ or BOLD predicted task performance.

MATERIALS AND METHODS

Participants

A total of 20 right-handed, healthy participants (10 females, mean age 25 $\pm$ 4.6) took part in this study. All participants were non-smokers and educated to university level. The study was approved by the Cardiff University School of Psychology Research Ethics Committee and performed in accordance with the guidelines stated in the Cardiff University Research Framework (version 4.0, 2010). Informed written consent was obtained for all subjects.

Imaging

Imaging was performed on a whole body 3T MRI (GE Excite HDx, Milwaukee WI, United States) system using an 8-channel receive-only head coil. Simultaneous perfusion and BOLD weighted data were acquired with a PICORE QUIPSS II (Wong et al., 1998) pulsed arterial spin labelling (PASL) sequence (non-commercial) with a dual-echo gradient-echo readout (Liu et al., 2002) and spiral k-space acquisition (Glover, 1999).

Imaging parameters for functional scans (task and hypercapnic calibration) were: TR = 2.4 s, TE1 = 2.7 ms, TE2 = 29 ms, TI1 = 700 ms, TI2 = 1.5 s (most proximal slice), FOV = 19.8 cm, flip angle = 90° matrix size = 64 $\times$ 64, slice thickness 7 mm, 1.5 mm gap, 3.1 mm in plane resolution with 15 slices. Label thickness was 200 mm with a 10 mm gap between the end of the label and the most proximal imaging slice. A separate single volume M_0 scan was acquired using the same

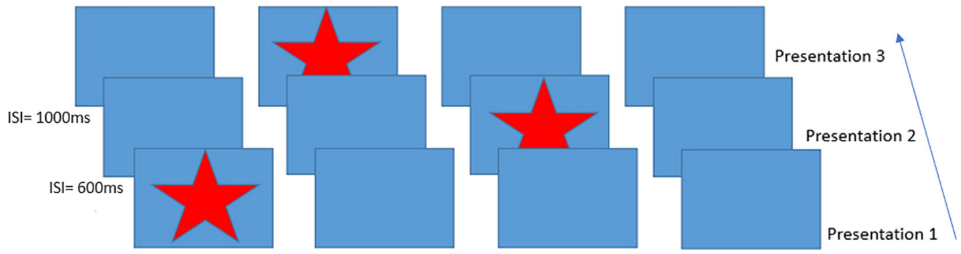

FIGURE 1 | Schematic of the Serial Reaction Time task presentation, inter-stimulus intervals on the left indicate example times between trials. This figure shows an example of the presentation of the first three items of the 12-item sequence. Participants responded to each star position using a handheld 4-button response box.

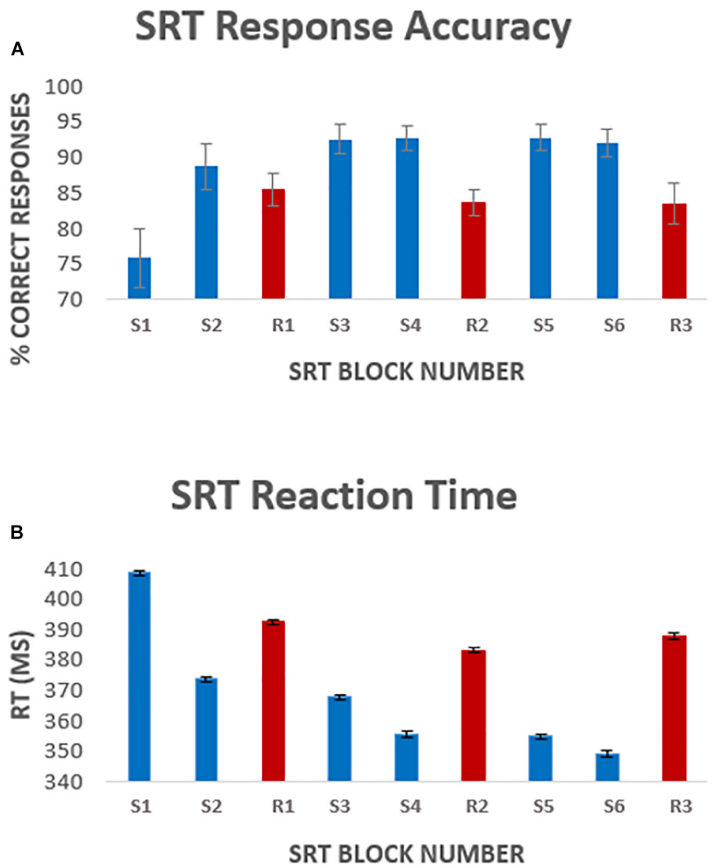

FIGURE 2 | Average [mean ± standard error of the mean (SEM)] response accuracy per block **(A)**, and average response latency **(B)** per task block. Error bars represent the standard error of the mean across participants. Blocks S1–S6 represent the 6 sequence blocks, responses to these blocks were the focus of the analysis. Blocks R1, R2, and R3 (shown in red) represent pseudorandom sequence blocks.

parameters, except TR = 4 s, to measure the equilibrium brain tissue magnetization of cerebrospinal fluid (CSF) for absolute CBF estimation. For registration, a 3D T1-weighted fast spoiled gradient echo sequence was acquired; TR = 7.9 ms, TE = 3 ms, 256 × 256, slice thickness = 1 mm, giving a resolution of 1 mm^3.

Physiological monitoring was performed using a respiratory belt placed just below the ribs to monitor ventilation and a pulse oximeter to obtain cardiac traces. A sampling line connected to a tightly fitted face mask (Quadralite Intersurgical, Wokingham, Berkshire, United Kingdom) was used to record expired $P_{ET}CO_2$ and $P_{ET}O_2$ concentrations using the Biopac system (Biopac®, Worcestershire, United Kingdom). The face mask was connected to a breathing circuit used to deliver gas mixtures and followed the design of Tancredi et al. (2014). The MEDRAD system (MEDRAD, Pittsburgh, PA, United States) was used to monitor blood arterial O_2 saturation during hypercapnia.

Visuomotor Task

The SRT (Nissen and Bullemer, 1987) is a visuomotor task which has been used previously in fMRI studies in healthy subjects

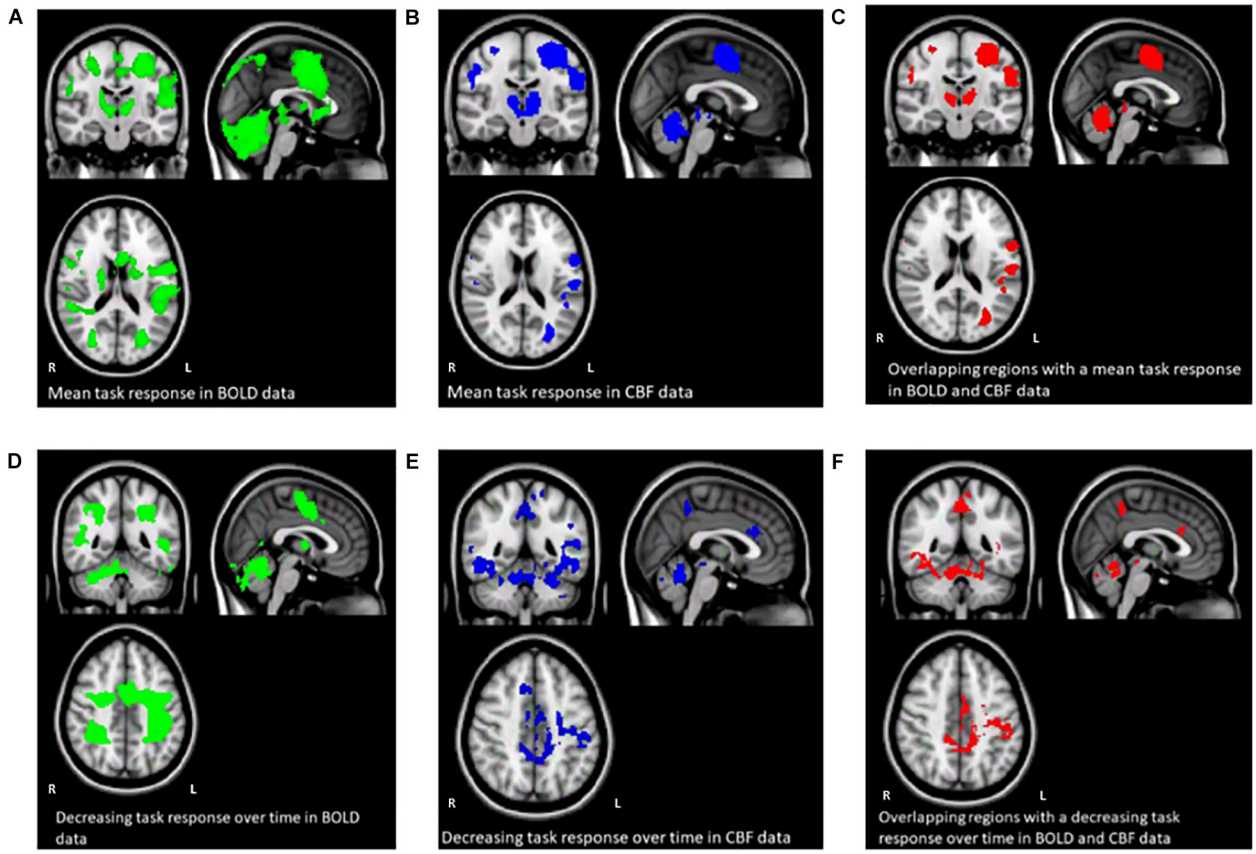

FIGURE 3 | Maps **(A–C)** show the mean BOLD signal response to the task across all subjects and sequence blocks (green), the CBF response (blue), and regions with overlapping BOLD and CBF task-related signal increases from rest (red). Maps **(D–F)** show areas of BOLD signal decrease over time during the SRT task (green), decreasing CBF responses (blue) and overlapping BOLD and CBF signal decreases across the task. Random blocks were not included in this analysis.

as well as in patient groups such as MS, chronic stroke and Huntington's Disease (HD) (Knopman and Nissen, 1991; Boyd and Winstein, 2001; Bonzano et al., 2011).

A modified version of the SRT developed by Nissen and Bullemer (1987) was used as the visuo-motor learning task during imaging acquisition. The task was projected via a screen inside the scanner at a frame rate of 60 Hz and a resolution of 1024 × 768. A star appeared on the screen in a sequence of four boxes (**Figure 1**), participants responded by pressing the corresponding button on a button box in their right hand. The 12-minute task consisted of 6 blocks of a 12-item sequence repeated 6 times with variable inter-stimulus interval (600–1000 ms) interspersed with a pseudorandom sequence on every third block to assess response latency decreases related to task familiarization rather than sequence learning. Participants were not informed that there was a repeating sequence during task instructions. Sequence blocks are referred to as blocks S1–S6 throughout the text, and random blocks are referred to as blocks R1–R3.

Hypercapnic Calibration

The SRT task was followed by hypercapnic calibration to obtain a measure of cerebrovascular reactivity (CVR) to CO_2 for estimation of $CMRO_2$, using the fixed-inspired gas method. Participants breathed through a tight-fitting facemask as described above, gases were administered from gas cylinders connected to an in-house built manually controlled flow meter system. Gases were piped through a mixing chamber with three feeding lines coming in for the delivery of medical air, 5% CO_2, and medical oxygen. Medical oxygen was not administered but was connected in case of emergency. The scan began with a 2-minute normocapnia period during which participants breathed medical air (20.9% O_2 balance N_2) with a flow rate of 30 L/min. This was followed by a rapid switch to 2 min of hypercapnia where an increase in $P_{ET}CO_2$ of +7 mmHg was targeted. In total, the scan consisted of three 2-minute blocks of normocapnia and two 2-minute blocks of hypercapnia.

Data Analysis

Image Preprocessing

Perfusion and BOLD weighted images were created from the first and second echo data respectively. Physiological noise correction was carried out using a modified RETROICOR technique (Glover et al., 2000) to remove cardiac and respiratory noise components from the BOLD and CBF task data. First and second harmonics

TABLE 1 | Mean (SEM) CVR. *M* and flow-metabolism coupling ratio (*n*) values for each ROI shown in **Figures 4–7**.

ROI	BOLD CVR%/mmHg	CBF CVR%/mmHg	M%	Flow-Metabolism Coupling Ratio (n)	Number of outliers removed from imaging data
Global	0.17 (0.09)	2.4 (1)	8 (0.5)	1.45 (0.95)	1
Cerebellum	0.23 (0.04)	2.5 (0.3)	8 (1.7)	1.58 (1.02)	2
M1	0.2 (0.02)	2.3 (0.3)	13 (3.6)	1.2 (0.5)	1
S1	0.2 (0.03)	2.2 (0.3)	17 (5.6)	1.4 (0.8)	3

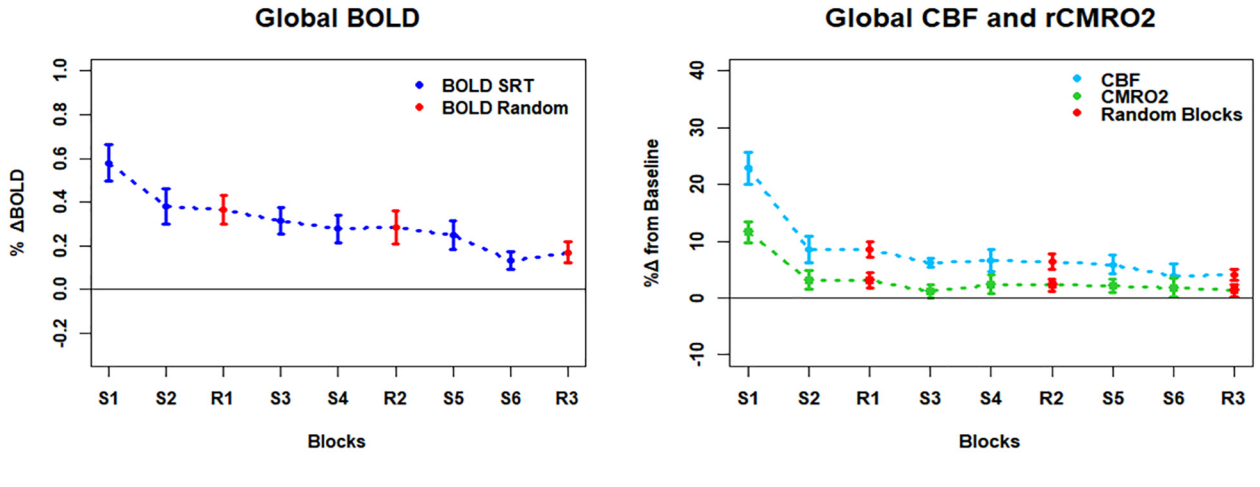

Changes from Baseline and between Blocks

	S1	S2	R1	S3	S4	R2	S5	S6	R3	S1 vs S2	S1 vs S6
BOLD	Y	Y	Y	Y	Y	Y	Y	-	Y	Y	Y
CBF	Y	Y	Y	Y	Y	Y	Y	-	Y	Y	Y
CMRO2	Y	-	-	-	-	-	-	-	-	Y	Y

FIGURE 4 | Plots showing the mean ± SEM responses for each task block in the global mean reduction ROI shown in **Figure 3F**. S1 = SRT sequence block 1, R1 = pseudorandom block 1. Y = Yes to indicate statistically significant ($p < 0.05$), signal changes from baseline and between first and second and first and last SRT blocks. BOLD and CBF showed significant increases from baseline across all blocks except the final sequence block S6. $CMRO_2$ was significantly higher than baseline in the first sequence block only. For BOLD, CBF, and $CMRO_2$, there were significant reductions in the responses between the first and second and first and last sequence blocks.

of the respiratory and cardiac cycle along with the interaction term were regressed from the raw CBF signal (before tag and control subtraction) in a general linear model (GLM) framework. In addition, variability related to CO_2, O_2, respiration and heart rate were removed from the SRT task run (Birn et al., 2009). Surround averaging was applied to the BOLD weighted images to remove contamination from perfusion weighting (Liu and Wong, 2005). Perfusion signal modeling was carried out within FEAT (FMRI Expert Analysis Tool, FMRIB's Software Library, RRID:SCR_002823)[1] to model the difference between control and tag images in the timeseries.

Task Response Modeling

One subject was excluded from the analysis due to a low task response rate. The remaining 19 subjects' BOLD and CBF task responses were analyzed using a GLM within FEAT with high pass filtering (cut off 80s). The voxelwise GLM was used to identify statistically significant BOLD and CBF responses across all sequence blocks. Further contrasts modeled linear response changes over time, using the task timing regressor to model the average change across the experiment as opposed to a block by block change. Cluster based thresholding was applied to define significant BOLD and CBF task responses which were threshold-adjusted using a standard voxel-level z score >2.3, $p < 0.05$, family-wise error corrected. A second FEAT GLM was carried out with contrasts set to calculate BOLD and CBF responses for each individual task block.

Individual subject's functional data were registered to the high resolution T1-weighted structural image using FLIRT, FMRIB's linear image registration tool (Jenkinson and Smith, 2001), with six degrees of freedom. The high-resolution images were then

[1] www.fmrib.ox.ac.uk/fsl

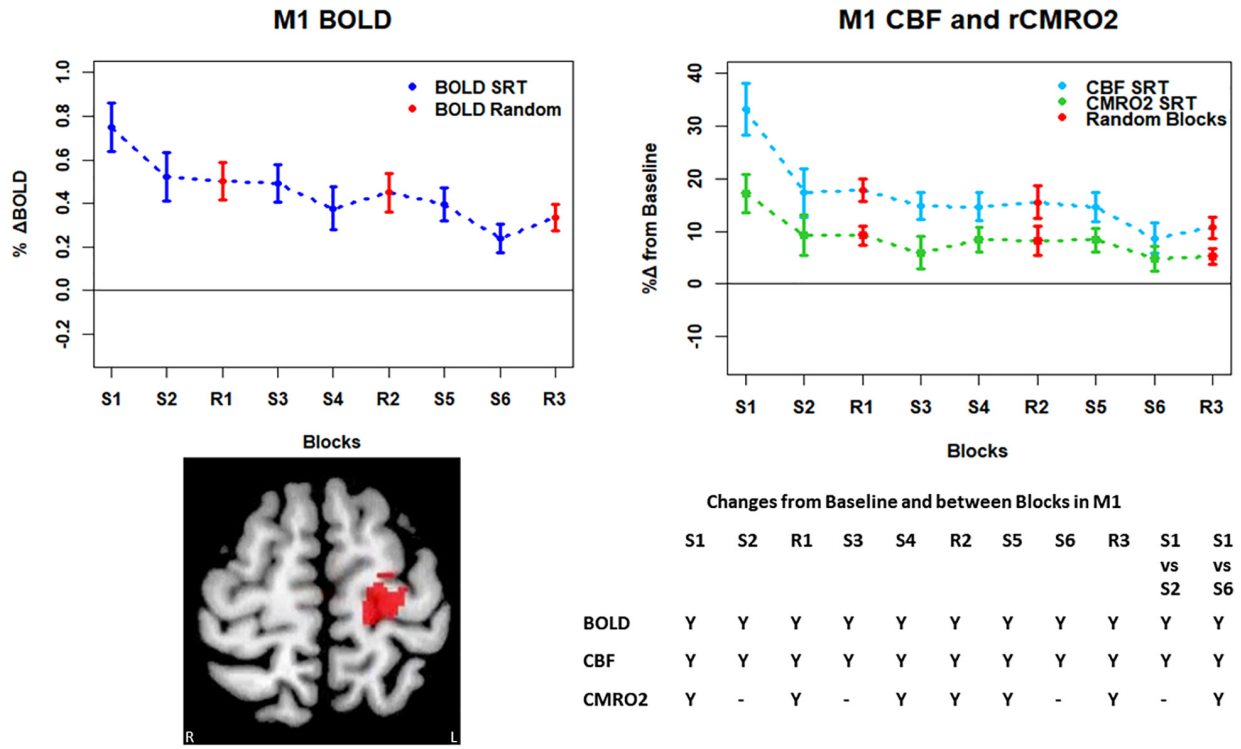

Changes from Baseline and between Blocks in M1

	S1	S2	R1	S3	S4	R2	S5	S6	R3	S1 vs S2	S1 vs S6
BOLD	Y	Y	Y	Y	Y	Y	Y	Y	Y	Y	Y
CBF	Y	Y	Y	Y	Y	Y	Y	Y	Y	Y	Y
CMRO2	Y	-	Y	-	Y	Y	Y	-	Y	-	Y

FIGURE 5 | Mean ± SEM SRT task responses in M1. Plots show a mean reduction in BOLD and CBF across task blocks. S1 = SRT block 1, R1 = random block 1. Y = Yes to indicate statistically significant ($p < 0.05$), signal changes from baseline and between first and second and first and last SRT blocks. BOLD and CBF showed significant increases from baseline across all sequence and pseudorandom task blocks. There were also significant reductions in BOLD and CBF between sequence blocks S1 and S2 and S1 and S6. The $CMRO_2$ was significantly elevated from baseline across all blocks except squence blocks S2 and S6. There was also a significant reduction in $CMRO_2$ between S1 and S6.

registered to the Montreal Neurological Institute (MNI) standard space with 12 degrees of freedom. FEAT contrasts were set up to investigate positive and negative task vs. rest activity. All subjects' data were then entered into a higher-level FEAT analysis to define functional regions of interest (ROIs) for further analysis.

Definition of ROIs

Regions of interest were created from regions where there was a linearly decreasing component to the task-induced-signal (in both BOLD and CBF data) over sequence blocks, to investigate training related adaptation. All reported ROIs were created from the intersection between BOLD and CBF task responses unless otherwise stated. Random blocks were not included in ROI creation. These areas were then separated into anatomical regions using the Harvard-Oxford cortical and subcortical atlases within FSL. For each ROI, the parameter estimate (PE) for each stimulus block was used to calculate the percentage CBF change or BOLD response for each stimulus block.

Calculation of CVR and $CMRO_2$

Cerebrovascular reactivity to CO_2 was calculated according to the method described previously (Bright and Murphy, 2013), where the beta weight calculated for the CO_2 regressor reflects the percentage BOLD or CBF signal change caused by hypercapnia and is normalized by the change in in end-tidal CO_2 (mmHg). CVR was calculated using the voxel-averaged timeseries in each ROI. As the timing of the hemodynamic response is not uniform across the brain and there are delays in the physiological response to CO_2, the end-tidal CO_2 regressors were selected based on which of the 97 time shifts applied produced the best fit to the data. The delay was optimized using cross correlation between the regressor and the ROI timeseries shifted in steps of 0.1 s (Bright and Murphy, 2013). Ninety-seven time shifts were used as this was the maximum number possible given the length of the physiological recordings.

The Davis model (Davis et al., 1998) was used to calculate $CMRO_2$ from normalized BOLD and CBF data in each ROI. The hypercapnia measurement was performed to estimate the scaling parameter M (see eq.1) which represents the estimated maximum BOLD signal response upon washout of all deoxyhaemoglobin according to the calibrated fMRI equation (Davis et al., 1998) (eq. 2). This model assumes that the targeted level of hypercapnia does not change $CMRO_2$. The values for α and β must also be assumed. In the model, α represents the change in CBV as a function of CBF, the original value of this exponent as proposed by Grubb et al. (1974) was 0.38 to describe arterio-venous blood volume. More recently it has been established that the volume of the deoxyhaemoglobin compartment, venous CBV, is what is required to calculate M. Chen and Pike (2010) used steady-state flow and volume changes to estimate the power–law relationship

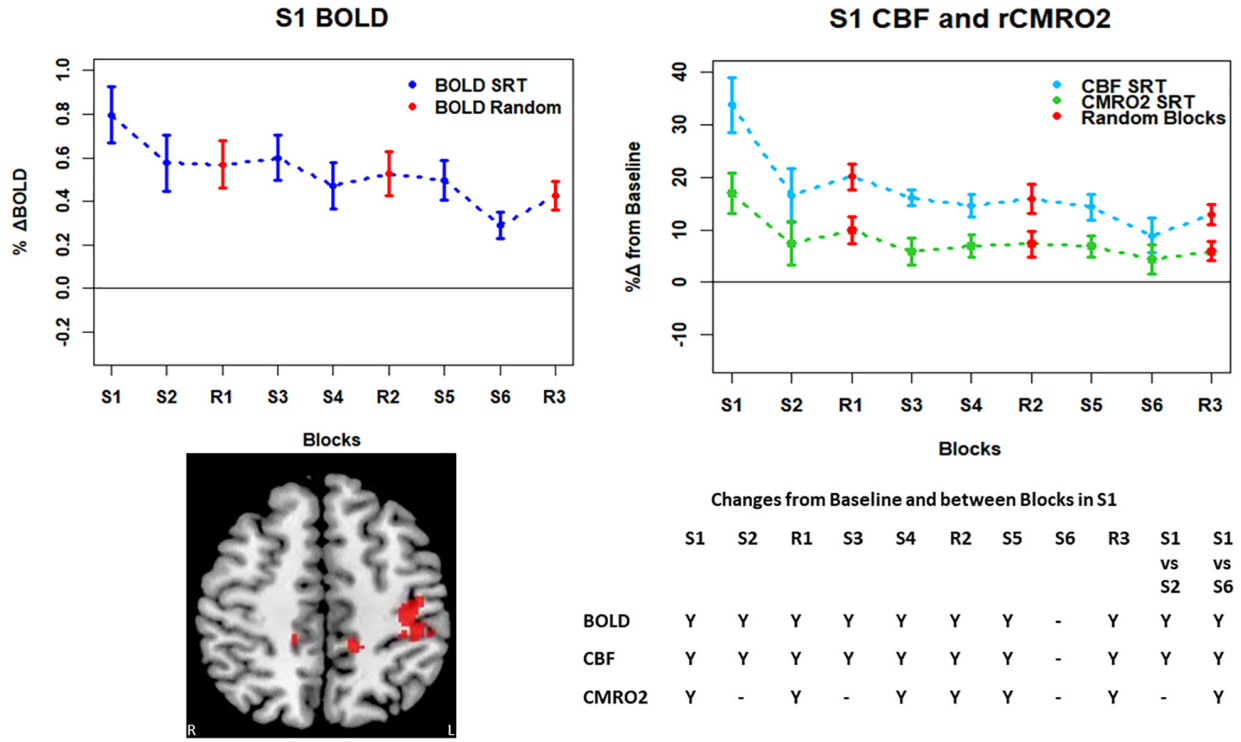

FIGURE 6 | Mean ± SEM SRT task responses in S1. Plots show a mean reduction in BOLD and CBF across task blocks. S1 = SRT block 1, R1 = random block 1. Y = Yes to indicate statistically significant ($p < 0.05$), signal changes from baseline and between first and second and first and last SRT blocks. BOLD and CBF showed significant increases from baseline across all sequence and pseudorandom task blocks, except S6. There were also significant reductions in BOLD and CBF between sequence blocks S1 and S2 and S1 and S6. There was a sustained $CMRO_2$ increase across all random blocks and the first, fourth and fifth sequence blocks but $CMRO_2$ was not different from baseline in the second, third or final sequence blocks. As in M1, there was only a significant difference between S1 and S6 in $CMRO_2$.

between CBV and CBF and the model fit produced a coefficient of 0.18 which is comparable to simulation work (Griffeth and Buxton, 2011) and values between 0.18 and 0.23 and are more commonly used at 3T. However, being a biological parameter, actual α values are likely to vary with age, health status and under different experimental conditions.

The parameter β which equals 1.5 in the original equation is a constant representing the relationship between blood oxygenation and the BOLD signal. As relaxivity is field dependent an optimized value of 1.3 tends to be used at 3T (Mark et al., 2011; Bulte et al., 2012). Values of α = 0.20, β = 1.3 were used in this study (Bulte et al., 2012).

$$M = \frac{B_H - 1}{1 - F_H^{-(\beta-\alpha)}} \quad (1)$$

$$rCMRO_2(t) = F(t)^{1-\alpha/\beta}\left(1 - \frac{B(t) - 1}{M}\right)^{1/\beta} \quad (2)$$

Equations for the calculation of M (Eq. 1) and relative $CMRO_2$ ($rCMRO_2$) (Davis et al., 1998) (Eq. 2). B_H represents the fractional BOLD signal change during CO_2 breathing F_H represents the change in CBF from baseline, α is the estimated ratio of fractional change in CBF to CBV and β which represents the field strength dependent relationship between blood oxygenation and the BOLD signal, $F(t)$ = CBF at time (t), $B(t)$ = BOLD at time (t).

Statistical Analysis

Statistical analyses were carried out using R (RRID:SCR_001905)[2] and SPSS version 20.0 (IBM Corp., Armonk, NY, United States, RRID:SCR_002865). The false discovery rate was used correct for multiple corrections where such corrections were necessary; a corrected p-value of <0.05 was considered significant in all cases. To derive an overview of block-by-block responses, repeated measures ANOVAs with tests for sphericity were used to compare each block to a zero baseline, and to compare responses in sequence blocks 1, 2, and 6 against each other, as this is where we expected the greatest differences in task responses. Paired t-tests were carried out to identify significant changes between the first and second, and first and last blocks.

Repeated measures ANOVAs were used to investigate changes in the flow-metabolism coupling ratio n, the ratio of the fractional change in CBF relative to the fractional change in $CMRO_2$ (Buxton et al., 2004), in each ROI and between blocks 1, 2, and 6.

Repeated measures ANOVAs were again conducted for behavioral data to identify significant reaction time changes

[2]https://www.R-project.org

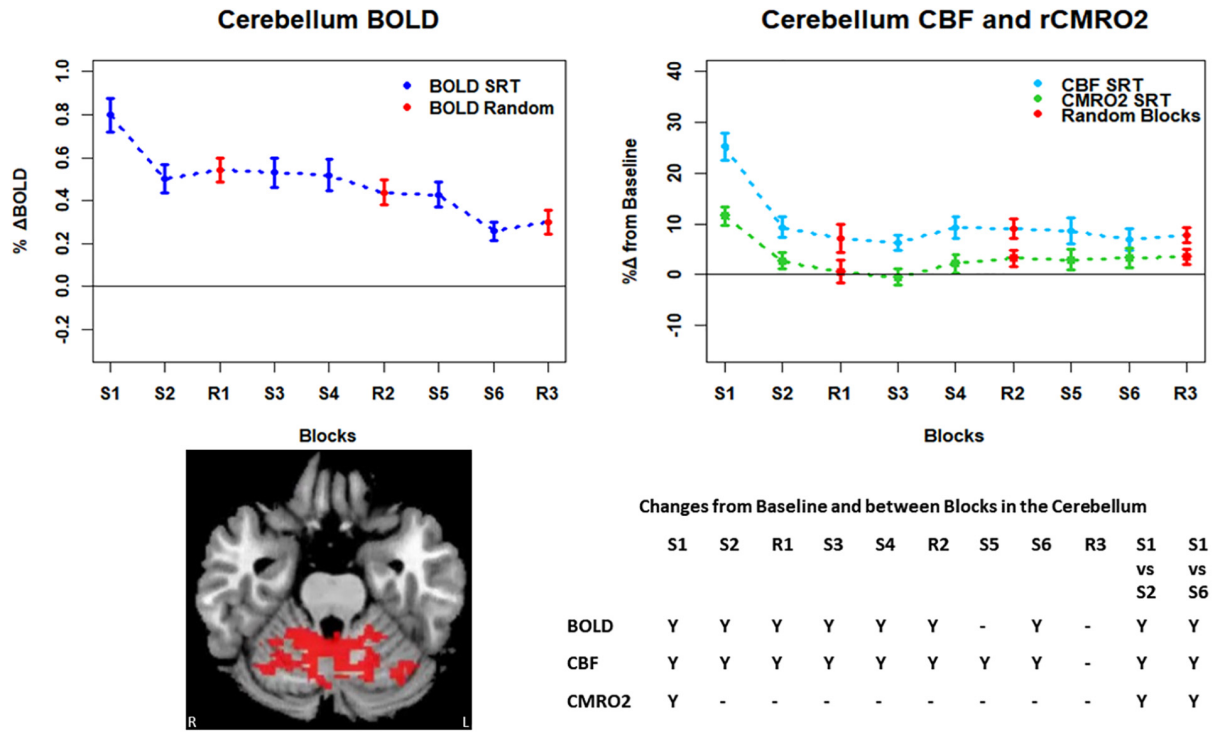

Changes from Baseline and between Blocks in the Cerebellum

	S1	S2	R1	S3	S4	R2	S5	S6	R3	S1 vs S2	S1 vs S6
BOLD	Y	Y	Y	Y	Y	Y	-	Y	-	Y	Y
CBF	Y	Y	Y	Y	Y	Y	Y	Y	-	Y	Y
CMRO2	Y	-	-	-	-	-	-	-	-	Y	Y

FIGURE 7 | Mean ± SEM SRT task responses in the cerebellum. Plots show a mean reduction in BOLD and CBF across task blocks. S1 = SRT block 1, R1 = random block 1. Y = Yes to indicate statistically significant ($p < 0.05$), signal changes from baseline and between first and second and first and last SRT blocks. BOLD and CBF showed significant increases from baseline across all sequence and pseudorandom task blocks, except S5 and R3 for BOLD, and R3 for CBF. There were also significant reductions in BOLD and CBF between sequence blocks S1 and S2 and S1 and S6. $CMRO_2$ increases from baseline were only detected in the first sequence blocks and there were significant reductions from S1 in S2, and S6.

from sequence block 1 vs. all subsequent sequence and random blocks. Reaction time was then used to investigate relationships between behavior and neurophysiological data. Finally, multiple linear regression analysis was used to investigate the relationships between reaction time and imaging-based responses.

Outliers in the BOLD, CBF and $CMRO_2$ data were identified using Tukey's method (Tukey, 1977) where the interquartile range is multiplied by 1.5 to define a reasonable range.

RESULTS

Behavioral Responses: Performance Accuracy Across Sequence Blocks

A one-way repeated measures ANOVA was carried out to compare performance across sequence blocks. Mauchley's test for sphericity was significant with $p < 0.001$ therefore degrees of freedom were corrected using Greenhouse-Geisser estimates of sphericity, $\varepsilon = 0.441$. The results showed that there was a significant effect of time on performance; response accuracy improved over time; $F(2.2, 38.3) = 12.47$, $p < 0.001$. Follow up comparisons indicated that all subsequent blocks had a significantly higher accuracy rate than block one. There was a 16.9 ± 9% accuracy improvement from sequence block S1 to sequence block S6, $p < 0.001$. Accuracy was higher in sequence blocks than random blocks, except for sequence block S1 which had the lowest performance of all blocks (**Figure 2A**). Random blocks R1 and R2 had significantly lower accuracy than sequence blocks 3–6. However, random block R3 scores were only significantly lower than sequence blocks S3, S4, and S6, all $p < 0.05$.

There was a significant effect of time on reaction speed; $F(5, 85) = 298$, $p < 0.001$. Follow up comparisons showed that reaction time decreased by 5.1 ± 11% from block S1 to block S6, $p < 0.001$. Random blocks had a greater response latency, again except compared to sequence block S1 (**Figure 2B**). Reaction time was significantly longer in random block R1 than sequence blocks S2–S6 and random block R2. Reaction time in random blocks R2 and R3 was longer than sequence blocks S3–S6, all $p < 0.05$.

Imaging Data

Figures 3A–F shows the mean BOLD and CBF task positive responses, and regions where task-induced signal responses decreased on average across all subjects and task blocks as well as the conjunction between BOLD and CBF responses in each case. There were no areas of statistically significant CBF, or BOLD response increases across the task blocks; there were only decreases. **Table 1** shows the group mean CVR, M and flow-metabolism coupling ratio values for each ROI shown in **Figures 4–7**. Several subjects were rejected from each

ROI following the outlier removal process described in section "Definition od ROIs."

BOLD, CBF, and $CMRO_2$ Responses in Each Task Block

Regions of interest for further analysis were defined from the intersection between all areas showing both BOLD and CBF task response reductions (global reduction ROI, shown in **Figure 3F**) and subdivided using the Harvard-Oxford atlas (50% tissue probability threshold) into anatomical regions hypothesized to be central to the motor task: the pre-central gyrus (M1), the post-central gyrus (S1) and cerebellum. **Figure 4** shows the group mean BOLD, CBF and $CMRO_2$ responses for each task block across the global reduction ROI and **Figures 5–7** show the same data for M1, S1 and the cerebellum.

Significant $CMRO_2$ changes between blocks were observed in the global reduction ROI, the cerebellum and between the first and last blocks in M1 and S1. Relative $CMRO_2$ significantly above baseline was observed in the first sequence block only for the global ROI (**Figure 4**) and the cerebellum (**Figure 7**). Increases from baseline were also observed in M1 and S1 (**Figures 5**, **6**) for the first sequence block, but in addition to this, positive $CMRO_2$ responses were also detected in all random blocks (R1–R3) as well as sequence blocks S4 and S5. Statistically significant BOLD and CBF increases from baseline were detected in almost all blocks in all regions, as well as reductions between the first and second and first and last blocks being observed in all regions. However, only M1 and the cerebellum showed significant BOLD and CBF responses for the final sequence block (S6).

FMRI and Task Reaction Time

Regression analysis was conducted to determine whether reaction time was predicted by BOLD, CBF or $CMRO_2$ task-related responses. For this, we focused on the first and last SRT task blocks. Multiple linear regression was carried out across subjects for each ROI with reaction time as the dependent variable, and BOLD, CBF, and $CMRO_2$ as independent variables. Neither BOLD, CBF nor $CMRO_2$ task responses were predictors of reaction time at the beginning or end of the task (data not shown).

DISCUSSION

In this study we have shown reductions in the sizes of BOLD, CBF, and $CMRO_2$ responses with time in multiple brain regions recruited during performance of an SRT task. The pattern of changes was heterogeneous across regions, but the largest response amplitudes occurred in the first task block for all brain regions considered. BOLD and CBF responses were sustained (significantly raised above baseline) across nearly all blocks in the regions investigated. In the amalgamated group of regions defined by task related reductions in BOLD and CBF over time and in the cerebellum, a subset of these regions, a sustained positive CBF response was also observed in the absence of a significant positive $CMRO_2$ response after the first sequence block.

The greater reaction time for random task blocks, compared to the sequence blocks, was not reflected by greater BOLD or CBF responses, and reaction time in SRT blocks did not correlate significantly with the imaging data, despite fMRI responses and reaction time both decreasing in a similar fashion across blocks. Therefore, the BOLD, CBF or $CMRO_2$ responses cannot be assumed to reflect sequence specific learning directly. What we are demonstrating, is the flow and oxygenation changes occurring with repeated execution of a motor sequence, and therefore this study has important implications for the study of plasticity and higher cognitive processes such as learning. With appropriate tasks for examining the function of interest in future studies, $CMRO_2$ could be calculated during early and late phases of learning as well as before and after behavioral or drug interventions to study energetic changes during learning and memory processes, and to evaluate the neural changes brought out by interventions.

Energetic Adaptations During the SRT

Task responses and response reductions over time were identified in regions typical of a visuomotor learning task, namely M1, S1, and the cerebellum, key areas involved in motor performance. The cerebellum is critically involved in motor learning and coordination of voluntary movement. The observed decreases in the $CMRO_2$ response in this area across blocks may therefore represent a shift toward automated performance of the motor task, given the sustained CBF response and $CMRO_2$ near baseline levels. The sustained CBF response in the absence of significant $CMRO_2$ response may suggest a preparatory or anticipatory component to energy supply. Further, the $CMRO_2$ data suggests that motor adaptation occurred quickly, with greater effort required for the first sequence block and random blocks. The sustained BOLD and CBF data, in all but the final blocks may be a result of the preparatory motor response (Gjedde et al., 2004) with a smaller, or in some blocks negligible, subsequent metabolic increase.

The $CMRO_2$ responses observed in M1 and S1 may be explained by ongoing recruitment of these regions for motor execution, rather than adaptation or learning. As shown in **Figures 4–7**, the greatest responses in BOLD, CBF, and $CMRO_2$ are always observed in the first SRT block. This is likely to be a result of the initial demands of the task, focusing visual attention on the task and selecting the correct motor responses, as well as processing task information to identify the repeating sequence. In this task, subjects quickly adapted to the task demands, as evidenced by the rapid improvement in accuracy and reduction in response time. This fast adaptation may explain the sharp reduction in BOLD and CBF responses, as well as the small, and sometimes non-statistically significant $CMRO_2$ increases from baseline in later blocks, as this adaptation led to a reduced neuronal demand.

While the neurobiological phenomena discussed above may explain the data, it must also be kept in mind that the $CMRO_2$ measurements obtained using calibrated fMRI are prone to noise and therefore lower power than individual optimized measurements of each parameter. $CMRO_2$ measured using calibrated fMRI being derived from BOLD and PASL CBF

signals suffers from a lower CNR ratio than BOLD, limiting the detectability of small $CMRO_2$ changes. As a result, changes from baseline may not have been detected in some instances, whereas BOLD and CBF changes, more robust over short timescales, were detected.

Signal reductions over task blocks observed in this study have been reported previously for BOLD and PET (Honda et al., 1998; Floyer-Lea and Matthews, 2004) with the largest reduction also occurring between the first and second task blocks. Fernández-Seara et al. (2009) used pulsed continuous ASL (PCASL) to investigate CBF changes during two separate 6-minute explicit learning tasks where a different pattern of sequential finger movements was trained in each task. To investigate learning-related changes, three learning phases were defined representing early to intermediate learning. CBF decreases relative to CBF measured during a control block were reported bilaterally for regions recruited during task performance, and perfusion reached levels comparable to baseline by the final task block in agreement with many ROIs in the current study. However, in contrast to the current study, where no perfusion increases over time were found, Fernández-Seara et al. (2009) found perfusion increases with task practice in somatosensory cortex, the posterior insula and putamen, cingulate cortex and left hippocampus which may be due to differences in the task design or PCASL sequence, which provides increased perfusion signal over PASL.

Although significant changes in CBF and $CMRO_2$ without accompanying BOLD changes were not observed, acquiring CBF and $CMRO_2$ data is still valuable as it can provide an insight into the main processes contributing to the measured BOLD signal. This is evident where BOLD and CBF remain elevated from baseline across the task despite $CMRO_2$ being close to, or reduced from, baseline, as observed in the global task ROI and cerebellum, and a number of mid-task blocks in M1 and S1. In agreement with Buxton et al. (2014), the $CMRO_2$ response suggests more rapid adaptation to the task than the BOLD or CBF data; it is possible that neural adaptation occurs faster than the hemodynamic response adaptation. Changes in later blocks became more variable across ROIs, but overall $CMRO_2$ responses were close to baseline, in contrast to the larger responses seen in the first SRT block. This pattern may be similar to previously reported rapid adaptation followed by slower, more gradual adaptations which are likely to continue beyond the short task duration (Doyon and Benali, 2005).

Behavioral Responses to the SRT

Brain measures did not correlate significantly with gains in performance in the form of accuracy and reaction time. Contributing to this observation may the low level of task difficulty such that ceiling effects were observed in the performance data, alongside very low variability in performance across subjects. Coupled with the high variability of the brain data, this may explain why no correlations were observed. Therefore, although motor adaptations were observed in the form of performance improvements and signal reductions, the signal changes cannot be directly interpreted as sequence specific motor learning. In the pseudorandom task blocks performance was lower, however, there was no significant difference in BOLD or CBF in these blocks compared to the SRT tasks before and after (data not shown). This suggests that the changes in BOLD, CBF and $CMRO_2$ were not due to sequence specific motor learning but more to adaptation to repeated finger movements. Also, performance improvements over time can largely be attributed to sequence familiarization rather than more general motor skill improvements.

Limitations

The principal limitation is the low CNR ratio of $CMRO_2$ estimates, largely arising from the low CNR of the ASL CBF measurement. Previous work studying cerebrovascular changes during cognitive tasks has generally used much longer paradigms than the 12-minute task used here, with some exceptions (Fernández-Seara et al., 2009). Only 6 sequence blocks were included here in order to limit the duration of the scan session, meaning that SNR was relatively low for the purposes of looking at individual 45 s block activity. Additional blocks would allow "chunking" of the data into early, intermediate and late blocks to examine differences between stages of motor adaptation with increased SNR. For example, Olson et al. (2006) incorporated three 20-minute SRT blocks in their protocol which served to dilute the effects of transient anomalies in activity and build a more reliable picture of average group responses. While the 12-minute task is useful for measuring short term adaptation differences between patients and controls and to limit head motion and fatigue effects, to quantitatively assess motor adaptation or learning, longer paradigms should be used along with larger sample sizes to establish whether the variability observed in this study is due to real individual differences or simply the low CNR inherent in ASL data.

We decided to restrict our analysis to the larger regions of interest that are central to motor skills due to limited contrast-to-noise (CNR) ratio inherent in ASL, and thus $CMRO_2$ estimation. The low CNR may also have affected our estimations of M. There is also the possibility that baseline physiology differences between brain regions and individual contributed to M variability, which in turn affected $CMRO_2$ estimations. Future studies investigating similar processes could include more detailed measurements of baseline physiology to inform differences in $CMRO_2$ responses that may not be strictly driven by the task. Recently published voxelwise M maps acquired using hyperoxic and hypercapnic calibration (Englund et al., 2019) found that gray matter M values ranged from 8.5 to 11.7%, depending on the calibration method used, in data from 10 subjects. Our estimates in the global ROI and cerebellum are in line with this, however, M1 and S1 estimates were higher at 13 and 17% respectively. However, the values of M were consistent across subjects and as the main function of interest is the change in task responses across blocks, the M constant was deemed unlikely to result in unreliable results. The limited CNR prevented more detailed investigation of flow-metabolism coupling ratio n and whether this changes across blocks during tasks such as the SRT. Establishing regional

flow-metabolism coupling values in the healthy brain would also be useful for comparison with metabolic changes in disease.

CONCLUSION

This study demonstrates the use of calibrated fMRI to detect regional BOLD, CBF, and $CMRO_2$ responses to a short motor adaptation task, and the changes in the amplitude of these responses over time in a sample of healthy adults. The most interesting result of this study is the finding that in the cerebellum there was a sustained BOLD hemodynamic response in the absence of a significant $CMRO_2$ increase from baseline. This suggests that the brain may continue to elevate the supply energy even after actual utilization ($CMRO_2$) has reduced to near baseline levels. Therefore, relying on BOLD data alone in behavioral studies can mask the nature of underlying metabolic responses and their changes over time with repeated task performance. With refinements to the task and MR acquisition, calibrated fMRI could be used to study energetic changes during learning in the healthy brain and to investigate the vascular and metabolic changes underlying reduced cognitive and motor function and limited plasticity in aging and disease.

DATA AVAILABILITY STATEMENT

The raw data can be made available by the authors upon request.

ETHICS STATEMENT

The study was reviewed and approved by the Cardiff University School of Psychology Research Ethics Committee and performed in accordance with the guidelines stated in the Cardiff University Research Framework (version 4.0, 2010).

AUTHOR CONTRIBUTIONS

CF conceived and designed the study with input from RW and VT. CF and JS coordinated the project and collected data with assistance from DH. CF analyzed the data. CF prepared the manuscript. RW provided the input and interpretation of results as well as reviewing and editing the final manuscript. All authors approved the manuscript before submission.

FUNDING

This work was supported by the Wellcome Trust (grant numbers: 506285 and 200804/Z/16/Z) and The Waterloo Foundation.

ACKNOWLEDGMENTS

The authors would like to thank Dr. Claudine Gauthier and Dr. Christopher Steele for helpful discussions on data analysis and interpretation and Dr. Ilona Lipp for assistance with analysis pipelines and task development. RW and VT are supported by the Higher Education Funding Council for Wales. This manuscript can be found as a preprint on BioRxiv (Foster et al., 2019) at: https://www.biorxiv.org/content/10.1101/539130v1. This work first appeared in the lead author's thesis (Foster, 2017, Chapter 7) which can be accessed here: http://orca.cf.ac.uk/109647/.

REFERENCES

Birn, R. M., Murphy, K., Handwerker, D. A., and Bandettini, P. A. (2009). fMRI in the presence of task-correlated breathing variations. *Neuroimage* 47, 1092–1104. doi: 10.1016/j.neuroimage.2009.05.030

Bonzano, L., Tacchino, A., Roccatagliata, L., Sormani, M. P., Mancardi, G. L., and Bove, M. (2011). Impairment in explicit visuomotor sequence learning is related to loss of microstructural integrity of the corpus callosum in multiple sclerosis patients with minimal disability. *Neuroimage* 57, 495–501.

Boyd, L. A., and Winstein, C. J. (2001). Implicit motor-sequence learning in humans following unilateral stroke: the impact of practice and explicit knowledge. *Neurosci. Lett.* 298, 65–69.

Bright, M. G., and Murphy, K. (2013). Reliable quantification of BOLD fMRI cerebrovascular reactivity despite poor breath-hold performance. *Neuroimage* 83, 559–568. doi: 10.1016/j.neuroimage.2013.07.007

Bulte, D. P., Kelly, M., Germuska, M., Xie, J., Chappell, M. A., Okell, T. W., et al. (2012). Quantitative measurement of cerebral physiology using respiratory-calibrated MRI. *Neuroimage* 60, 582–591. doi: 10.1016/j.neuroimage.2011.12.017

Buxton, R. B., Griffeth, V. E. M., Simon, A. B., and Moradi, F. (2014). Variability of the coupling of blood flow and oxygen metabolism responses in the brain: a problem for interpreting BOLD studies but potentially a new window on the underlying neural activity. *Front. Neurosci.* 8:139. doi: 10.3389/fnins.2014.00139

Buxton, R. B., Uludağ, K., Dubowitz, D. J., and Liu, T. T. (2004). Modeling the hemodynamic response to brain activation. *Neuroimage* 23(Suppl. 1), S220–S233. doi: 10.1016/j.neuroimage.2004.07.013

Chen, J. J., and Pike, G. B. (2010). MRI measurement of the BOLD-specific flow- volume relationship during hypercapnia and hypocapnia in humans. *Neuroimage* 53, 383–391. doi: 10.1016/j.neuroimage.2010.07.003

Davis, T. L., Kwong, K. K., Weisskoff, R. M., and Rosen, B. R. (1998). Calibrated functional MRI: mapping the dynamics of oxidative metabolism. *Proc. Natl. Acad. Sci. U.S.A.* 95, 1834–1839. doi: 10.1073/pnas.95.4.1834

D'haeseleer, M., Cambron, M., Vanopdenbosch, L., and De Keyser, J. (2011). Vascular aspects of multiple sclerosis. *Lancet Neurol.* 10, 657–666. doi: 10.1016/S1474-4422(11)70105-3

Doyon, J., and Benali, H. (2005). Reorganization and plasticity in the adult brain during learning of motor skills. *Curr. Opin. Neurobiol.* 15, 161–167. doi: 10.1016/j.conb.2005.03.004

Englund, E. K., Fernández-Seara, M. A., Rodríguez-Soto, A. E., Lee, H., Rodgers, Z. B., Vidorreta, M., et al. (2019). Calibrated fMRI for dynamic mapping of CMRO2 responses using MR-based measurements of whole-brain venous oxygen saturation. *J. Cereb. Blood Flow Metab.* 271678X19867276.

Fan, A. P., Evans, K. C., Stout, J. N., Rosen, B. R., and Adalsteinsson, E. (2015). NeuroImage Regional quanti fi cation of cerebral venous oxygenation from MRI susceptibility during hypercapnia. *Neuroimage* 104, 146–155. doi: 10.1016/j.neuroimage.2014.09.068

Fernández-Seara, M. A., Aznárez-Sanado, M., Mengual, E., Loayza, F. R., and Pastor, M. A. (2009). NeuroImage continuous performance of a novel

motor sequence leads to highly correlated striatal and hippocampal perfusion increases. *Neuroimage* 47, 1797–1808. doi: 10.1016/j.neuroimage.2009.05.061

Floyer-Lea, A., and Matthews, P. M. (2004). Changing brain networks for visuomotor control with increased movement automaticity. *J. Neurophysiol.* 92, 2405–2412. doi: 10.1152/jn.01092.2003

Foster, C. (2017). *Investigating Cerebrovascular Health and Functional Plasticity Using Quantitative FMRI*. Doctoral dissertation, Cardiff University, Cardiff.

Foster, C., Steventon, J., Helme, D., Tomassini, V., and Wise, R. G. (2019). Cerebral metabolic changes during visuomotor adaptation assessed using quantitative FMRI. *bioRxiv* [Preprint], doi: 10.1101/539130

Ge, Y., Zhang, Z., Lu, H., Tang, L., Jaggi, H., Herbert, J., et al. (2012). Characterizing brain oxygen metabolism in patients with multiple sclerosis with T2-relaxation-under-spin-tagging MRI. *J. Cereb. Blood Flow Metab.* 32, 403–412. doi: 10.1038/jcbfm.2011.191

Gjedde, A., Vafaee, M. S., Gjedde, A., Vafaee, M. S., and Gjedde, A. (2004). Spatially dissociated flow-metabolism coupling in brain activation. *Neuroimage* 21, 507–515. doi: 10.1016/j.neuroimage.2003.10.003

Glover, G. H. (1999). Simple analytic spiral k-space algorithm. *Magnet. Reson. Med.* 42, 412–415.

Glover, G. H., Li, T., and Ress, D. (2000). Image based retrospective correction of noise. *Magn. Res. Med.* 167, 162–167.

Griffeth, V., and Buxton, R. B. (2011). "Modeling the effect of changes in hematocrit, O2 extraction fraction, and blood volume distribution on the BOLD signal and estimates of CMRO2 change with a calibrated BOLD method," in *Proceedings of the 18th Annual Meeting of the ISMRM*, Piscataway, NJ.

Grubb, R. L. Jr., Raichle, M. E., Eichling, J. O., and Ter-Pogossian, M. M. (1974). The effects of changes in $PaCO_2$ cerebral blood volume, blood flow, and vascular mean transit time. *Stroke* 5, 630–639. doi: 10.1161/01.str.5.5.630

Hoge, R. D., Atkinson, J., Gill, B., Crelier, G. R., Marrett, S., and Pike, G. B. (1999). Investigation of BOLD signal dependence on cerebral blood flow and oxygen consumption: the deoxyhemoglobin dilution model. *Magnet. Reson. Med.* 42, 849–863.

Honda, M., Deiber, M. P., Ibánez, V., Pascual-Leone, A., Zhuang, P., and Hallett, M. (1998). Dynamic cortical involvement in implicit and explicit motor sequence learning. A PET study. Brain 121, 2159–2173. doi: 10.1093/brain/121.11.2159

Jenkinson, M., and Smith, S. M. (2001). A global optimization method for robust affine registration of brain images. *Med. Imaging Analy.* 5, 143–156.

Kidd, D., Barkhof, F., Mcconnell, R., Algra, P. R., Allen, I. V., and Revesz, T. (1999). Cortical lesions in multiple sclerosis. *Nat. Rev. Neurol.* 6, 17–26.

Knopman, D., and Nissen, M. J. (1991). Procedural learning is impaired in Huntington's disease: evidence from the serial reaction time task. *Neuropsychologia* 29, 245–254.

Liu, T. T., and Wong, E. C. (2005). A signal processing model for arterial spin labeling functional MRI. *Neuroimage* 24, 207–215. doi: 10.1016/j.neuroimage.2004.09.047

Liu, T. T., Wong, E. C., Frank, L. R., and Buxton, R. B. (2002). Analysis and design of perfusion-based event-related fMRI experiments. *Neuroimage* 16, 269–282. doi: 10.1006/nimg.2001.1038

Madsen, P. L., Hasselbalch, S. G., Hagemann, L. P., Olsen, K. S., Bülow, J., Holm, S., et al. (1995). Persistent resetting of the cerebral Oxygen/Glucose uptake ratio by brain activation: evidence obtained with the Kety—schmidt technique. *J. Cereb. Blood Flow Metab.* 15, 485–491. doi: 10.1038/jcbfm.1995.60

Mark, C. I., Fisher, J. A., and Pike, G. B. (2011). Neuroimage improved fMRI calibration: precisely controlled hyperoxic versus *Hypercapnic stimuli*. *Neuroimage* 54, 1102–1111. doi: 10.1016/j.neuroimage.2010.08.070

Martindale, J., Mayhew, J., Berwick, J., Jones, M., Martin, C., Johnston, D., et al. (2003). The hemodynamic impulse response to a single neural event. *J. Cereb. Blood Flow Metab.* 23, 546–555.

Mathiesen, C., Caesar, K., Akgören, N., and Lauritzen, M. (1998). Modification of activity-dependent increases of cerebral blood flow by excitatory synaptic activity and spikes in rat cerebellar cortex. *J. Physiol.* 512, 555–566.

Mohtasib, R. S., Lumley, G., Goodwin, J. A., Emsley, H. C. A., Sluming, V., and Parkes, L. M. (2012). Neuroimage calibrated fMRI during a cognitive stroop task reveals reduced metabolic response with increasing age. *Neuroimage* 59, 1143–1151. doi: 10.1016/j.neuroimage.2011.07.092

Nissen, M. J., and Bullemer, P. (1987). Attentional requirements of learning: evidence from performance measures. *Cognit. Psychol.* 19, 1–32. doi: 10.1016/0010-0285(87)90002-8

Olson, I. R., Rao, H., Moore, K. S., Wang, J., Detre, J. A., and Aguirre, G. K. (2006). Using perfusion fMRI to measure continuous changes in neural activity with learning. *Brain Cogn.* 60, 262–271. doi: 10.1016/j.bandc.2005.11.010

Ota, M., Sato, N., Nakata, Y., Ito, K., Kamiya, K., Maikusa, N., et al. (2013). Abnormalities of cerebral blood flow in multiple sclerosis: a pseudocontinuous arterial spin labeling MRI study. *Magn. Reson. Imaging* 31, 990–995. doi: 10.1016/j.mri.2013.03.016

Restom, K., Perthen, J. E., and Liu, T. T. (2008). Calibrated fMRI in the medial temporal lobe during a memory-encoding task. *Neuroimage* 40, 1495–1502. doi: 10.1016/j.neuroimage.2008.01.038

Shannon, B. J., Neil, S., Vlassenko, A. G., Shimony, J. S., and Rutlin, J. (2016). Brain aerobic glycolysis and motor adaptation learning. *Proc. Natl. Acad. Sci.* 1–10. doi: 10.1073/pnas.1604977113

Tancredi, F. B., Lajoie, I., and Hoge, R. D. (2014). A simple breathing circuit allowing precise control of inspiratory gases for experimental respiratory manipulations. *BMC Res. Notes* 7:235. doi: 10.1186/1756-0500-7-235

Tukey, J. W. (1977). Exploratory data analysis. *Analysis* 2:688. doi: 10.1007/978-1-4419-7976-6

Ungerleider, L., Doyon, J., and Karni, A. (2002). Imaging brain plasticity during motor skill learning. *Neurobiol. Learn. Mem.* 78, 553–564. doi: 10.1006/nlme.2002.4091

Wong, E. C., Buxton, R. B., and Frank, L. R. (1998). Quantitative imaging of perfusion using a single subtraction (QUIPSS and QUIPSS II). *Magn. Reson. Med.* 39, 702–708. doi: 10.1002/mrm.1910390506

Conflict of Interest: The authors declare that the research was conducted in the absence of any commercial or financial relationships that could be construed as a potential conflict of interest.

frontiers in Physiology

ORIGINAL RESEARCH
published: 08 May 2020
doi: 10.3389/fphys.2020.00422

Brain Network Modularity During a Sustained Working-Memory Task

Marta Moraschi[1,2†], Daniele Mascali[1,2†], Silvia Tommasin[3], Tommaso Gili[1,2], Ibrahim Eid Hassan[4,5], Michela Fratini[2,6], Mauro DiNuzzo[7], Richard G. Wise[8,9], Silvia Mangia[10], Emiliano Macaluso[11] and Federico Giove[1,2]*

[1] Centro Fermi–Museo Storico della Fisica e Centro di Studi e Ricerche Enrico Fermi, Rome, Italy, [2] Fondazione Santa Lucia IRCCS, Rome, Italy, [3] Dipartimento di Neuroscienze Umane, Sapienza Univeristà di Roma, Rome, Italy, [4] Dipartimento di Fisica, Sapienza Università di Roma, Rome, Italy, [5] Department of Physics, Helwan University, Cairo, Egypt, [6] Istituto di Nanotecnologia, Consiglio Nazionale delle Ricerche, Rome, Italy, [7] Independent Researcher, Rome, Italy, [8] Institute for Advanced Biomedical Technologies, University of Chieti, Chieti, Italy, [9] Cardiff University Brain Research Imaging Centre, School of Psychology, Cardiff University, Cardiff, United Kingdom, [10] Center for Magnetic Resonance Research, Department of Radiology, University of Minnesota, Minneapolis, MN, United States, [11] ImpAct Team, Lyon Neuroscience Research Center, Université de Lyon, Lyon, France

Spontaneous oscillations of the blood oxygenation level-dependent (BOLD) signal are spatially synchronized within specific brain networks and are thought to reflect synchronized brain activity. Networks are modulated by the performance of a task, even if the exact features and degree of such modulations are still elusive. The presence of networks showing anticorrelated fluctuations lend initially to suppose that a competitive relationship between the default mode network (DMN) and task positive networks (TPNs) supports the efficiency of brain processing. However, more recent results indicate that cooperative and competitive dynamics between networks coexist during task performance. In this study, we used graph analysis to assess the functional relevance of the topological reorganization of brain networks ensuing the execution of a steady state working-memory (WM) task. Our results indicate that the performance of an auditory WM task is associated with a switching between different topological configurations of several regions of specific networks, including frontoparietal, ventral attention, and dorsal attention areas, suggesting segregation of ventral attention regions in the presence of increased overall integration. However, the correct execution of the task requires integration between components belonging to all the involved networks.

Keywords: functional connectivity, modularity, topology, working memory, connectivity dynamics, brain segregation

OPEN ACCESS

Edited by:
Ewald Moser,
Medical University of Vienna, Austria

Reviewed by:
Andreas Hess,
University of Erlangen-Nuremberg, Germany
Xiaoyun Liang,
Australian Catholic University, Australia

***Correspondence:**
Federico Giove
federico.giove@uniroma1.it

† These authors have contributed equally to this work

Specialty section:
This article was submitted to Medical Physics and Imaging, a section of the journal Frontiers in Physiology

Received: *30 September 2019*
Accepted: *07 April 2020*
Published: *08 May 2020*

Citation:
Moraschi M, Mascali D, Tommasin S, Gili T, Hassan IE, Fratini M, DiNuzzo M, Wise RG, Mangia S, Macaluso E and Giove F (2020) Brain Network Modularity During a Sustained Working-Memory Task. Front. Physiol. 11:422. doi: 10.3389/fphys.2020.00422

INTRODUCTION

Brain activity is associated, both at rest and during cognitive engagement, with spatial patterns of synchronized, slow (<0.1 Hz) blood oxygenation level-dependent (BOLD) fluctuations which identify different brain networks, namely, neural systems which are coupled together (Rogers et al., 2007). Functional connectivity (FC) can be characterized exploiting various analytical methods and metrics, but it is commonly defined as the temporal correlation between signals from anatomically distinct regions (Friston, 1994; Horwitz, 2003). Consistency of resting-state functional magnetic resonance imaging (fMRI) networks in healthy human adults is well established (Damoiseaux et al., 2006; van den Heuvel and Hulshoff Pol, 2010) and the pathophysiological relevance of network

connectivity changes induced by several diseases and aging has been reported (Sala-Llonch et al., 2014; Zhao et al., 2014; Mascali et al., 2015; Brueggen et al., 2016).

However, the current knowledge of modulation properties of networks and function in response to experimental challenges is still incomplete. In particular, little is known about the changes of functional interaction between networks during the execution of a task.

Several studies (Fox et al., 2005; Fransson, 2006; Golland et al., 2008) roughly identified two distinct large-scale systems, based on their observed functional response to stimuli requiring external attention, including working-memory (WM) tasks. One large system is implicated in cognitive functions entailing attentional demand, in particular top-down or goal-directed attention (Corbetta and Shulman, 2002; Fox et al., 2005; Corbetta et al., 2008). This system, usually named task-positive network (TPN) (Fox et al., 2005), includes the dorsal attention network (DAN) and ventral attention network (VAN), the frontoparietal network (FPN), as well as somatosensory and visual areas. The second system, identified as the default mode network (DMN) (Buckner et al., 2008), responds to attention-demanding tasks with a decreased BOLD signal, thus indicating deactivation (Harrison et al., 2008), while being preferentially activated during unconstrained thoughts, introspection, memory retrieval, and self-evaluation of future perspective (Greicius and Menon, 2004; Greicius et al., 2004; Fransson, 2006; Buckner et al., 2008; Fornito et al., 2012).

Spontaneous BOLD fluctuations in TPN and DMN were found to be reciprocally anticorrelated (Fox et al., 2005), and the internal coherency fluctuations were found differently modulated during cognitive functions, often in opposite directions (Lowe et al., 2000; Hampson et al., 2002, 2006; Newton et al., 2007; Gordon et al., 2014; Liang et al., 2016). At first, this competitive nature was thought to foster the switching between internal thought and reaction to external stimuli, to support the efficiency of brain processing (Fox et al., 2005; Fransson, 2006; Golland et al., 2008). Indeed, the degree of anticorrelation between DMN and TPN regions has been associated with faster reaction times during cognitively demanding tasks (Kelly et al., 2008) and better performance in WM n-back tasks (Hampson et al., 2006).

However, other studies supported task-specific cooperation rather than competition between DMN and TPN areas (Newton et al., 2007; Spreng et al., 2010; Bluhm et al., 2011; Leech et al., 2011; Fornito et al., 2012; Bray et al., 2015; Piccoli et al., 2015; Zuo et al., 2018). Cooperative dynamics was found to entail reallocation of flexible areas inside each network, implying a topological reorganization of networks themselves (Bullmore and Sporns, 2009; Braun et al., 2015; Liang et al., 2016). Flexible modules are thought to operate as functionally independent entities in response to specific environmental demands (Newton et al., 2007; Spreng et al., 2010; Leech et al., 2011; Fornito et al., 2012; Bray et al., 2015; Piccoli et al., 2015; Vatansever et al., 2015), and modular reorganization has been shown to be associated with behavior (Leech et al., 2011; Fornito et al., 2012; Braun et al., 2015; Vatansever et al., 2015) and modified by pathology (Crossley et al., 2013; Lerman-Sinkoff and Barch, 2016; Bordier et al., 2018).

In a recent study investigating FC adaptations to a sustained n-back WM task, we have shown that connectivity changes associated with task execution include a widespread modulation of synchronization patterns both within and between brain networks (Tommasin et al., 2018). This widespread change preserved the gross topology of whole-brain connectivity, with the exception of specific areas within some networks, including DMN, FPN, DAN, and VAN. These findings raise the issue of identifying the topological relations between flexible areas that showed adaptation to the task. In the present work, we applied to the same data of our previous study the graph analysis developed by Fornito et al. (2012) to identify the relevance and the behavioral role of the topological reorganization of a set of brain networks during a steady-state working-memory task.

MATERIALS AND METHODS

Subjects

Twenty right-handed Italian-speaking subjects (eight females, age 33 ± 6 years), with no history of neurological or psychiatric disease, participated in the study. All subjects gave written informed consent in accordance with the Declaration of Helsinki and European Union regulations and the Ethics Committee of Santa Lucia Foundation in Rome approved the study. Subjects and data included in this study are the same involved in our previous study (Tommasin et al., 2018).

Image Acquisition

Data were collected on a head-only 3 T MRI Scanner (Magnetom Allegra, Siemens Healthineers, Erlangen, Germany) equipped with a standard quadrature birdcage coil, used for both transmission and detection. Functional images were acquired via a gradient-echo planar imaging (GE-EPI) sequence (TR = 2100 ms, TE = 30 ms, FA = 70°, voxel size $3 \times 3 \times 2.5$ mm^3) lasting 24 min and 38 s for a total of 704 volumes (four dummy scans included). The slices were positioned starting from the vertex and covered the whole cerebrum. High resolution T1-weighted images were acquired for anatomic reference and tissue segmentation purpose using a Magnetization Prepared Rapid Acquisition Gradient Echo (MPRAGE, TE = 4.38 ms, TR = 2000 ms, FA = 8°, voxel size $1.33 \times 1.33 \times 1$ mm^3).

Stimulation Paradigm and Task Performance

The experimental setup and stimulation paradigm are fully described in Tommasin et al. (2018). Briefly, BOLD data were acquired within a block-design paradigm, composed of alternated epochs of open-eyes resting state and sustained auditory WM task (4 min and 54 s each, starting with a resting-state epoch). The auditory WM task involved continuous n-back trials at "high" load (two-back) or "low" load (one-back). Each trial was composed of a 500-ms window, in which subjects were aurally presented with a pseudorandom vowel, and a subsequent 1600-ms response window, during which subjects had to report whether the current vowel was the same as the one presented

one stimulus prior (one-back) or two stimuli prior (two-back). Subjects responded via an MRI compatible two-button keyboard, with one button reserved for positive responses (matching trial) and one button reserved for negative responses (not matching trial). During the entire functional run, subjects were asked to maintain the gaze on the center, marked by a 1° circle over a uniform black background.

Each subject underwent two functional runs during the same experimental session, with epoch ordering: rest/one-back/rest/two-back/rest or rest/two-back/rest/one-back/rest.

Subjects responses to the WM task were monitored at runtime and recorded for subsequent correlation analyses with modularity metrics (see below). For each subject, performance during each task epoch was evaluated in terms of accuracy computed as the percentage of valid responses on the number of trials (response was considered as valid, if it was both correct and given during the 1600-ms response window).

Image Preprocessing and Processing

Functional and structural MRI data were pre-processed using FC toolbox (CONN 17.c) (Whitfield-Gabrieli and Nieto-Castanon, 2012) and analyzed with dedicated in-house routines based on Matlab R2013a (The Mathworks Inc., Natick, MA, United States) and AFNI (Cox, 1996). Detailed descriptions of preprocessing steps are reported in Tommasin et al. (2018). Briefly, functional images underwent motion and slice-timing correction, and were normalized to the Montreal Neurological Institute (MNI) space (voxel size $2 \times 2 \times 2$ mm^3). Spurious variance was further removed by regressing out motion-derived parameters and aCompCor signals (Behzadi et al., 2007), by applying a bandpass filter (0.008–0.09 Hz) and by censoring motion-contaminated volumes (Jo et al., 2013). Finally, spatial smoothing was applied with an $8 \times 8 \times 8$ mm^3 FWHM Gaussian kernel. An unsmoothed version of the data was retained for FC computation.

Each functional run was split in five epochs. The first resting-state epoch was discarded from analyses and was used only for cortical parcelation. Specifically, using the smoothed data of the first epochs (resting epochs), the cortex was parcelated in 350 regions of interest (ROIs) by means of group level ROIs based on the similarity among voxel time courses (Craddock et al., 2012). ROIs were then classified into seven large-scale networks using the atlas from Yeo et al. (2011). We retained ROIs belonging to four networks of interest (205 ROIs) which included the DAN, DMN, the FPN, and the VAN networks. These four networks showed the most conspicuous traces of reorganization in spite of the overall preserved topology that we had reported on the same dataset (Tommasin et al., 2018), and are thought to respond during the execution of a WM task, as described in Section "Introduction."

The remaining four epochs, i.e., one-back, two-back, and two resting states, were used to extract epoch-related FC. For each ROI and epoch, an average time-course was extracted from unsmoothed data and correlated to each other ROI time-course, leading to an ROI-to-ROI (205×205 sized) correlation matrix. Fisher's Z transformation was applied to the correlation matrix to improve normality. Then, correlation matrices computed from homologous epochs, as well as from task epochs with different load levels, were averaged for each subject in order to obtain two single resting-state and task-related matrices for each subject. These connectivity matrices were fed into the graph analysis procedure described below. The common treatment of both task levels conforms to choices adopted in our previous study, justified by the observation that the network behavior was indistinguishable between the levels; in particular we did not observe reproducible FC effects of task load (for details, see Tommasin et al., 2018).

Graph Analysis

We used the modularity analysis proposed by Fornito et al. (2012) to characterize networks reconfiguration during rest and task conditions. Modules are defined as clusters of nodes showing greater FC within the clusters than with the rest of the brain.

For each subject and condition (i.e., rest and task), we modeled interactions between networks as a graph of 205 nodes, representing regions of parcelation constituting each network. We identified the optimal modular decomposition, maximizing a quality function (Q) (Rubinov and Sporns, 2011) reflecting the goodness of partition, using the Louvain method (Blondel et al., 2008), implemented in Brain connectivity Toolbox[1], with resolution parameter set to unity. We defined the *optimal modular decomposition* as the partition with the maximum Q over 10,000 iterations of the algorithm.

The modularity, as expressed by Q, gives an index of degree of modular segregation in the graph (Lebedev et al., 2018). Q is close to one when there are few edges between modules and high density inside modules, while Q is close to zero when the number of connections between modules is comparable to those of a random graph. We compared Q between conditions by means of a two-sample paired t-test.

For each subject and each node in the graph, from the optimal modular decomposition, we computed the within-module strength, z, and the diversity coefficient, h, for rest (named z_R and h_R) and task (named z_T and h_T) condition, respectively. The within-module strength quantifies the node's intramodular connectivity and it was calculated as the z-score-transformed degree of centrality within the module. Formally, for each node i, z_i is defined as

$$z_i = \frac{s_i(m_i) - \bar{s}(m_i)}{\sigma_{\bar{s}(m_i)}}$$

where m_i is the module containing node i, $s_i(m_i)$ is the within-module node strength (i.e., the sum of the within-module weights of node i), and $\bar{s}(m_i)$ and $\sigma_{\bar{s}(m_i)}$ are the mean and standard deviation of the within-module strength of all nodes in module m_i, respectively (Fornito et al., 2012). The diversity coefficient describes the node's distribution of intermodular connectivity and it was calculated with the normalized Shannon entropy, specifically

$$h_i = \frac{1}{\log m} \sum_{uM} p_i(u) \log p_i(u)$$

[1]https://sites.google.com/a/brain-connectivity-toolbox.net/bct/

where $p_i(u) = \frac{s_i(u)}{s_i}$, $s_i(u)$ is the strength of node i in module u, and m is the number of modules in the partition M (Shannon, 1948; Rubinov and Sporns, 2011; Fornito et al., 2012). Thus, nodes with high z values are suggested to represent local intramodular hubs, while nodes with high h values, presenting an even distribution of connectivity across modules, are suggested to support functional integration between modules (Fornito et al., 2012).

We further characterized modularity at group level using the following procedure (Fornito et al., 2012). For each subject and condition, from the optimal modular decomposition, we constructed a 205 × 205 co-classification matrix (cC) in which the element $cC_{ij} = 1$ if nodes i and j belong to the same module and $cC_{ij} = 0$ otherwise. For each condition, we derived a group consistency matrix as the summation over all subjects of the co-classification matrices. Thus, the group consistency matrix represents the node co-classification frequency across subjects. The group consistency matrix was then subjected to a further modular decomposition in order to obtain an optimal group modularity matrix, for rest and task condition, respectively (also in this case the algorithm was iterated 10,000 times for testing degeneracies in the data and the resolution parameter was set to its default value). From the two optimal group modularity matrices, we determined the nodes that changed module membership from rest to task condition and we mapped them onto brain volume.

Similar to the subject-level analysis, for both conditions, we characterized the role of each node in the network at the group level by means of z and h computed on the optimal group modularity (Guimera and Amaral, 2005). At group level, nodes with high z values have highly conserved modular membership across subjects, while nodes with high h values have a variable membership identity across participants (Fornito et al., 2012).

Statistical Inference

To investigate the behavioral role of the degree of integration between modules, the diversity coefficient h of each node during task was correlated with subjects' accuracy in task execution via Pearson's correlation coefficient. Results were corrected for multiple comparisons across nodes via false discovery rate (FDR; Benjamini and Hochberg, 1995).

In order to assess the statistical significance of the topological configuration changes between rest and task conditions, we used a permutation test, using an approach similar to what proposed by Alexander-Bloch et al. (2012) and applied by Bordier et al. (2018). Specifically, we used the normalized mutual information (NMI, Kuncheva and Hadjitodorov, 2004) to assess the similarity between rest and task optimal group modularity matrices and compared it to a null distribution. If the change in topological configuration was driven by the experimental condition, then the experimental data should have yield a lower NMI value than those generated from the null distribution. To build the null distribution we repeated 10,000 times the process to generate the optimal group modularity matrices, each time randomly relabeling the rest and task conditions (permutations constrained via within-subject exchangeability blocks). The p-value was calculated as the number of times in which the NMI was lower than the NMI of the experimental data, divided by the number of permutations.

Unless otherwise stated, numerical results are given as mean ± standard deviation.

RESULTS

Behavioral Data

Behavioral data from three subjects could not be recorded for technical problems, leaving a total of 17 subjects for the behavioral analyses. For each subject, performances were evaluated in terms of accuracy, computed as the percentage of valid responses on the number of trials. Performances did not show significant change between the first and the second run of each session (paired t-test, $p > 0.57$) and was higher for the lower WM load, as expected (97% one-back, 84% two-back; $p < 10^{-5}$, paired t-test). For complete details, see Tommasin et al. (2018).

Modularity

The permutation test revealed a significant change in the topological configuration between rest and task ($p = 0.0017$). The optimal modular decomposition resulted in modularity across subjects of $Q = 0.36 \pm 0.06$ at rest and $Q = 0.31 \pm 0.09$ at task. The degree of segregation was significantly different across conditions (paired t-test, $N = 20$, $t = 3.9$, $p = 0.001$).

We identified three group-level modules both at task and at rest (**Figure 1**). The overall network structure showed a reorganization of nodes' module membership during the execution of the task, resulting in a Jaccard index of 0.71 between the two functional conditions. While module 2, which was mainly composed of nodes of the DMN (**Table 1**), was clearly preserved between task and rest, the other two modules showed large

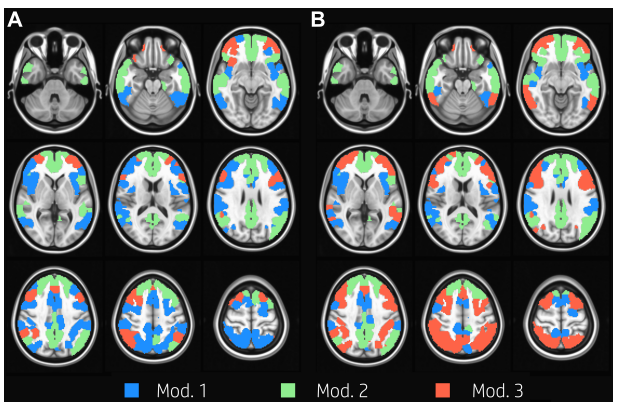

FIGURE 1 | Group modularity. Evenly spaced axial slices covering the whole brain for group modular membership at rest **(A)** and task **(B)**. Nodes are color-coded according to the module membership. Three group-level modules were identified for both task and at rest condition; module 2 was clearly preserved between task and rest, and it is mainly composed of nodes in the DMN, while the other two modules showed large reorganizations between rest and task.

TABLE 1 | Number of nodes and network membership of each module in both functional conditions.

Condition	Module	Number of nodes	Network membership			
			DAN	DMN	FPN	VAN
Rest	**1**	96	36	4	21	35
	2	82	1	77	2	2
	3	27	1	6	20	0
Task	**1**	52	11	6	2	33
	2	77	2	69	3	3
	3	76	25	12	38	1

reorganizations between rest and task. In particular, the resting condition was characterized by the presence of a large module (module 1, 96 nodes) mainly composed of VAN, DAN, and FPN nodes, and of a substantially smaller module (module 3, 27 nodes), whose nodes laid mainly in FPN. At task, the size of the two modules was more uniform (52 and 76 nodes, respectively). Module 1 was mainly composed of VAN nodes and to a lesser extent of DAN nodes. Module 3 grouped almost all FPN nodes and the majority of DAN nodes. In other words, FPN was equally shared between modules 1 and 3 at rest, and was mainly included in module 3 during the execution of the WM task, while DAN was mainly included in module 1 at rest and was shared between module 1 and 3 at task.

About 29% of nodes (60 nodes) changed modular membership between rest and task. These nodes represent a substantial amount of flexibility in modular composition. Nodes changing their membership were mainly located in the occipital cortex, temporal gyrus, postcentral and precentral gyrus, frontal gyrus, frontal pole, and cingulate gyrus (**Figure 2**).

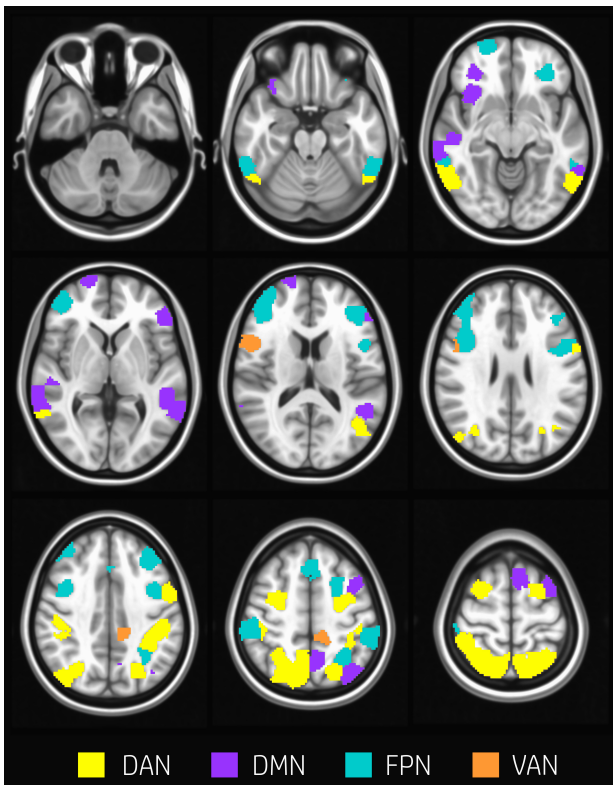

FIGURE 2 | Nodes changing modularity. Evenly spaced axial slices covering the whole brain for nodes changing modular membership between rest and task conditions. Nodes are color-coded according to network membership. About 29% of nodes (60 nodes) changed membership between rest and task. Nodes changing their membership were mainly located in occipital cortex, temporal gyrus, postcentral and precentral gyrus, frontal gyrus, frontal pole, and cingulate gyrus.

Nodes Functional Role

Figures 3A,B summarize the functional role of the nodes at rest and task in the *h*/*z* plane (diversity coefficient and within-module strength, respectively). The trajectories of each node between task and rest are shown in **Figure 3C**.

At rest, *z* showed a strong inverse correlation to *h* in modules 1 and 2 (**Figure 3A**, $r = -0.98$, $p < 10^{-10}$ for both). In module 3, the correlation was not significant but tended to be positive ($r = 0.18$, $p = 0.37$). Module 3 was indeed characterized by consistently high values of *h*. These nodes mainly belong to FPN and were located in the occipital and frontal cortex. At task, *z* and *h* were still inversely correlated both in module 1 and 2 (respectively $r = -0.59$ and $r = -0.95$, $p < 10^{-10}$ for both). During task, *z* and *h* of nodes belonging to module 3 become inversely correlated as well ($r = -0.89$, $p < 10^{-10}$). The correlation changed significantly from rest to task for modules 1 and 3 ($z = -10.8$, $p < 10^{-10}$ and $z = 5.6$, $p < 10^{-5}$, respectively, test on Fisher's Z transformed correlations). In other words, functional role of nodes in module 2 did not change between conditions, while module 1 and module 3 moved toward each other in plane *h*/*z*, going both toward higher *z* values, while *h* on average increased in module 1 (from 0.62 ± 0.15 to 0.905 ± 0.066) and decreased in module 3 (from 0.958 ± 0.032 to 0.797 ± 0.070). Taking into account the network composition of each module (see above), this behavior was determined by DAN, FPN, and VAN nodes in module 1, and by FPN and (to lesser extent) DMN in module 3 (see **Figure 3**, bottom plots).

Behavioral Scores

The overall degree of brain segregation, as quantified by Q, correlated inversely with subject accuracy, both at rest and task ($r = -0.61$ and $r = -0.54$, respectively. $p < 0.05$ for both). The change of segregation between rest and task, while significant in itself (see above), was not correlated with the behavioral performances. Significant positive correlations were found between h_t and subject accuracy ($p < 0.05$, FDR corrected) in temporal and frontal areas. These are summarized in **Table 2** and shown in **Figure 4**. These areas included regions of the left inferior and middle temporal gyrus, and regions across the precentral sulcus, including the anterior part of the precentral gyrus, and the posterior part of the middle and inferior frontal gyrus (bilaterally). A more rostral section of the left middle frontal gyrus and a section of the anterior cingulate gyrus were involved as well.

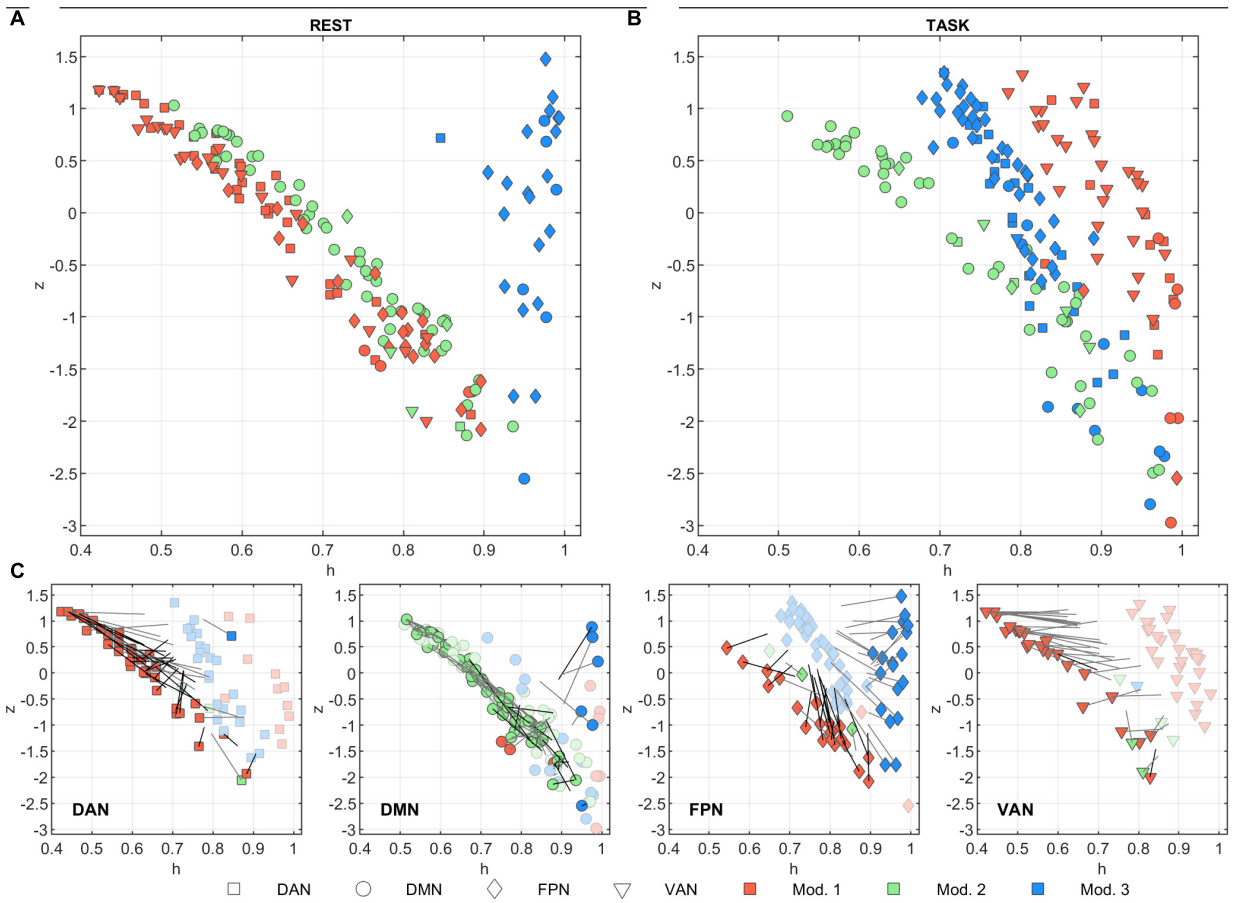

FIGURE 3 | Node functional role in the *h*/*z* plane. The within-module strength (*z*) is plotted as a function of the diversity coefficient (*h*) for each of the 205 nodes, separately for **(A)** rest and **(B)** task conditions. Nodes are color-coded according to module membership and shape-coded according to network membership. The change in module memberships and in the *h*/*z* positions can be appreciated in **(C)** where the *h*/*z* plots are shown separately for each network and separately for rest (darker color) and task (lighter color) conditions. Gray lines starting from rest nodes describe the trajectory vector of the node between task and rest. Note, however, that the length of the vector is halved for clarity purposes. Thus, each node position at task can be identified by doubling the length of the trajectory. Nodes that change module memberships between rest and task conditions are marked with darker trajectories.

TABLE 2 | Nodes showing significant correlation between h_T and subject accuracy ($p < 0.05$, FDR corrected).

Node	Network	Module		Label	h_T	
		Rest	Task		*r*	*p*
36	DAN	1	3	L Precentral Gyrus	0.7573	0.0004
188	VAN	1	1	L Precentral Gyrus (inf fro gy)	0.8199	0.0001
137	FPN	1	3	L Precentral Gyrus	0.7041	0.001
79	DMN	2	2	L Middle Temporal Gyrus	0.7020	0.001
130	FPN	1	3	L Inferior Temporal Gyrus	0.6902	0.002
161	FPN	1	1	L Middle Frontal Gyrus	0.7716	0.0003

For each node, the table reports network, module membership at rest and task, anatomical label, and r and p of correlation.

DISCUSSION

In our previous study, based on the same dataset, we found that the continuous performance of a sustained WM task is associated with large and widespread FC changes (Tommasin et al., 2018). The overall brain topology did not change between rest and task, but we found some evidence of task-driven dissociation between regions within VAN and modest network reorganization involving nodes within FPN, DAN, and DMN as well. In the present study, we investigated the exact features of these topological changes and the corresponding functional and behavioral correlates.

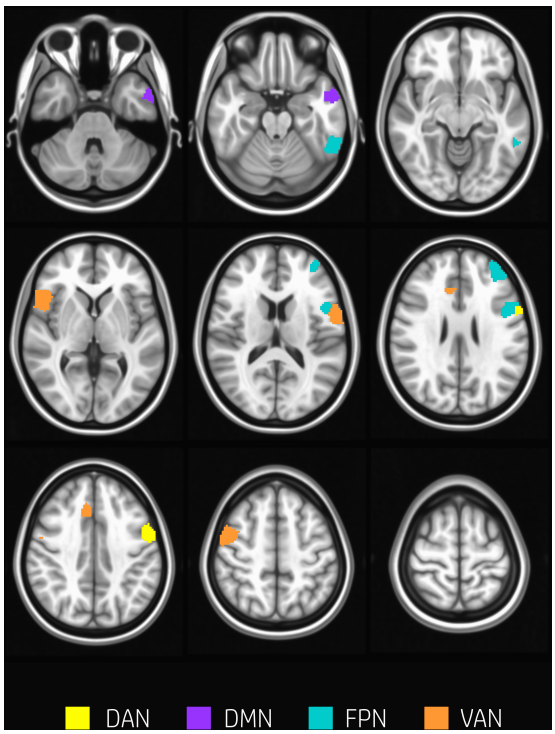

FIGURE 4 | Nodes correlating with performance. Nodes showing a significant positive correlation between h_t and subjects accuracy ($p < 0.05$, FDR corrected) are found in temporal and frontal areas including regions of the left inferior and middle temporal gyrus, and regions across the precentral sulcus, the anterior part of the precentral gyrus, and the posterior part of the middle and inferior frontal gyrus (bilaterally). A more rostral section of the left middle frontal gyrus and a section of the anterior cingulate gyrus were involved as well. Nodes are color-coded according to network membership.

During rest, DAN, VAN, and part of FPN coexisted in a common module, suggesting intrinsic dynamic collaboration of these networks (Damoiseaux et al., 2006; Fox et al., 2006; He et al., 2009). Modularity analysis showed that cognitive engagement entails a dynamic reorganization of several brain areas belonging to the investigated networks. The degree of brain segregation was significantly different between rest and task conditions, and task-performance was associated with a significant increase of brain global integration. Notably, the Q parameter, related to network segregation, was inversely correlated to subjects' accuracy in both conditions. This result is consistent with previous studies, using different techniques (Kitzbichler et al., 2011; Wen et al., 2015; Liang et al., 2016; Shine et al., 2016; Hearne et al., 2017; Zuo et al., 2018), and confirms that a brain topology suitable for integration of information is a prerequisite for the correct performance of a WM task.

Several previous works reported that task-driven (Braun et al., 2015; Hearne et al., 2017; Zuo et al., 2018) or dynamic (Shine et al., 2016; Fransson et al., 2018) reconfiguration of brain modular structure during task is driven by the flexibility of areas within FPN, DMN, DAN, and VAN. In our modular analysis, we found a high level of reorganization for nodes belonging to the TPNs, in particular for regions in frontal and temporal cortices (**Figure 2**). The only module overall unaffected by the task-performance was module 2, that included most of the DMN.

Module 1 included virtually the whole VAN (at least 89% of nodes), both at rest and at task, while participation of DAN and FPN nodes to this module changed between conditions. Specifically, at rest module 1 included all DAN and half of FPN nodes, at task it lost its FPN coverage and around 2/3 of the DAN nodes. On the other hand, FPN nodes converged to a single module, suggesting that the task is associated with a consolidation of FPN function.

This interpretation is corroborated by the analysis of changes in the h and z parameters. Indeed, nodes in DAN, VAN, and DMN changed their functional role rather uniformly, in agreement with the overall behavior of the pertaining modules. However, the split modularity of FPN at rest was mirrored by opposite changes in h, with nodes of modules 1 and 3 converging to a common module characterized by intermediate h values (**Figure 3**, bottom). These changes, taken together, indicate a task-dependent segregation of the functions carried out by the DAN and FPN nodes versus activities relying on VAN nodes. Considering the overall increase of integration during task, this effect indicates a tighter integration between areas belonging to DAN and FPN networks.

Our results show a clear task-driven dissociation between DAN and VAN: almost all the nodes within these networks were in the same module at rest, while during task 2/3 of DAN nodes transitioned to a third module that also included the FPN nodes. Indeed, albeit both structural (Umarova et al., 2009) and rsfMRI (Fox et al., 2006; He et al., 2007) studies have shown that DAN and VAN were plainly discernible, it has been repeatedly suggested that the attention control requires flexible and continuous collaboration between these networks (Fox et al., 2006; He et al., 2007; Macaluso, 2010; Chica et al., 2011; Vossel et al., 2014). The dissociation that we observed here could reflect the switching between reflexive (bottom up) and voluntary (top-down) attention during the task. Accordingly, many studies suggested that DAN and VAN have opposite pattern of activity during the execution of a WM task (Corbetta et al., 2000; Shulman et al., 2009; Asplund et al., 2010).

While the main topological reorganization associated with task-execution concerned the segregation of VAN modules from FPN and 2/3 of the DAN nodes, the inter-modular integration at task was found to be crucial for accurate performance. It is worth noting that eight of nine of the nodes where h_T correlated with behavior belong to either module 1 or 3, including three nodes that changed module during task (from 1 to 3).

This result confirms that the performance during WM was related to the capability of preserving intramodular integration in spite of modular reorganization.

The fact that no node had z (i.e., within-network hub properties) correlated to performance may indicate that integration between-modules is more crucial than within-network connections in the current WM task. From a network perspective, the execution of the WM task requires integration between DAN and FPN, but the performance was boosted by further integration with VAN.

Indeed, one of the key components of WM processing is the capacity of actively maintaining information no longer available and to manipulate this information for usage over short delays (Moser et al., 2018). This requires the integration of neuronal circuits on large scale, including regions in dorsolateral prefrontal cortex, parietal cortex, and dorsal anterior cingulate cortex (Liang et al., 2016). All of these regions are represented in the nodes characterized by correlation between h_T and performances (**Table 2** and **Figure 4**).

CONCLUSION

In conclusion, we have shown that the execution of an auditory WM task is associated with a switching between different topological configurations of FPN, VAN, and DAN nodes, involving a segregation of VAN nodes in the presence of increased overall integration. The correct execution of the task requires integration between components belonging to all the involved networks.

DATA AVAILABILITY STATEMENT

The datasets of this article are not publicly available because the authors lack the ethical consent to do that. Requests to access the datasets should be directed to the corresponding author.

ETHICS STATEMENT

The protocol of the study was approved by the Ethics Committee of Santa Lucia Foundation. All subjects gave written informed consent in accordance with the Declaration of Helsinki and with the European Union regulations.

AUTHOR CONTRIBUTIONS

MM acquired and processed the data prepared the figures and wrote the manuscript. DM acquired and processed the data and prepared the figures. ST acquired and processed the data. TG designed the study and programmed the stimulation. IH and MF performed the experiment. MD, RW, SM, and EM discussed the results and the manuscript and helped in the interpretation of the results. FG designed the study, interpreted the results, and coordinated the research. All authors edited the text and approved the final version.

FUNDING

This work was partially supported by the Italian Ministry of Health, with the Young Researcher Grant 2013 (GR-2013-02358177, to MF) and with Ricerca Corrente (MM, DM, TG, and FG).

REFERENCES

Alexander-Bloch, A., Lambiotte, R., Roberts, B., Giedd, J., Gogtay, N., and Bullmore, E. (2012). The discovery of population differences in network community structure: new methods and applications to brain functional networks in schizophrenia. *Neuroimage* 59, 3889–3900. doi: 10.1016/j.neuroimage.2011.11.035

Asplund, C. L., Todd, J. J., Snyder, A. P., and Marois, R. (2010). A central role for the lateral prefrontal cortex in goal-directed and stimulus-driven attention. *Nat. Neurosci.* 13, 507–512. doi: 10.1038/nn.2509

Behzadi, Y., Restom, K., Liau, J., and Liu, T. T. (2007). A component based noise correction method (CompCor) for BOLD and perfusion based fMRI. *Neuroimage* 37, 90–101. doi: 10.1016/j.neuroimage.2007.04.042

Benjamini, Y., and Hochberg, Y. (1995). Controlling the false discovery rate: a practical and powerful approach to multiple testing journal of the royal statistical society. *Series B* 57, 289–300. doi: 10.1111/j.2517-6161.1995.tb02031.x

Blondel, V. D., Guillaume, J.-L., Lambiotte, R., and Lefebvre, E. (2008). Fast unfolding of communities in large networks. *J. Stat. Mech. Theory E* 2008:10008.

Bluhm, R. L., Clark, C. R., McFarlane, A. C., Moores, K. A., Shaw, M. E., and Lanius, R. A. (2011). Default network connectivity during a working memory task. *Hum. Brain Mapp.* 32, 1029–1035. doi: 10.1002/hbm.21090

Bordier, C., Nicolini, C., Forcellini, G., and Bifone, A. (2018). Disrupted modular organization of primary sensory brain areas in schizophrenia. *Neuroimage Clin.* 18, 682–693. doi: 10.1016/j.nicl.2018.02.035

Braun, U., Schafer, A., Walter, H., Erk, S., Romanczuk-Seiferth, N., Haddad, L., et al. (2015). Dynamic reconfiguration of frontal brain networks during executive cognition in humans. *Proc. Natl. Acad. Sci. U.S.A.* 112, 11678–11683. doi: 10.1073/pnas.1422487112

Bray, S., Arnold, A. E. G. F., Levy, R. M., and Iaria, G. (2015). Spatial and temporal functional connectivity changes between resting and attentive states. *Hum. Brain Mapp.* 36, 549–565. doi: 10.1002/hbm.22646

Brueggen, K., Kasper, E., Dyrba, M., Bruno, D., Pomara, N., Ewers, M., et al. (2016). The primacy effect in amnestic mild cognitive impairment: associations with hippocampal functional connectivity. *Front. Aging Neurosci.* 8:244. doi: 10.3389/fnagi.2016.00244

Buckner, R. L., Andrews-Hanna, J. R., and Schacter, D. L. (2008). The brain's default network. *Ann. N. Y. Acad. Sci.* 1124, 1–38. doi: 10.1196/annals.1440.011

Bullmore, E. T., and Sporns, O. (2009). Complex brain networks: graph theoretical analysis of structural and functional systems. *Nat. Rev. Neurosci.* 10, 186–198. doi: 10.1038/nrn2575

Chica, A. B., Bartolomeo, P., and Valero-Cabre, A. (2011). Dorsal and ventral parietal contributions to spatial orienting in the human brain. *J. Neurosci.* 31, 8143–8149. doi: 10.1523/jneurosci.5463-10.2010

Corbetta, M., Kincade, J. M., Ollinger, J. M., Mcavoy, M. P., and Shulman, G. L. (2000). Voluntary orienting is dissociated from target detection in human posterior parietal cortex. *Nat. Neurosci.* 3, 292–297. doi: 10.1038/73009

Corbetta, M., Patel, G., and Shulman, G. L. (2008). The reorienting system of the human brain: from environment to theory of mind. *Neuron* 58, 306–324. doi: 10.1016/j.neuron.2008.04.017

Corbetta, M., and Shulman, G. L. (2002). Control of goal-directed and stimulus-driven attention in the brain. *Nat. Rev. Neurosci.* 3, 201–215. doi: 10.1038/nrn755

Cox, R. W. (1996). AFNI: software for analysis and visualization of functional magnetic resonance neuroimages. *Comput. Biomed. Res.* 29, 162–173. doi: 10.1006/cbmr.1996.0014

Craddock, R. C., James, G. A., Holtzheimer, P. E., Hu, X. P. P., and Mayberg, H. S. (2012). A whole brain fMRI atlas generated via spatially constrained spectral clustering. *Hum. Brain Mapp.* 33, 1914–1928. doi: 10.1002/hbm.21333

Crossley, N. A., Mechelli, A., Vertes, P. E., Winton-Brown, T. T., Patel, A. X., Ginestet, C. E., et al. (2013). Cognitive relevance of the community structure of the human brain functional coactivation network. *Proc. Natl. Acad. Sci. U.S.A.* 110, 11583–11588. doi: 10.1073/pnas.1220826110

Damoiseaux, J. S., Rombouts, S. A., Barkhof, F., Scheltens, P., Stam, C. J., Smith, S. M., et al. (2006). Consistent resting-state networks across healthy subjects.

Proc. Natl. Acad. Sci. U.S.A. 103, 13848–13853. doi: 10.1073/pnas.0601417103

Fornito, A., Harrison, B. J., Zalesky, A., and Simons, J. S. (2012). Competitive and cooperative dynamics of large-scale brain functional networks supporting recollection. *Proc. Natl. Acad. Sci. U.S.A.* 109, 12788–12793. doi: 10.1073/pnas.1204185109

Fox, M. D., Corbetta, M., Snyder, A. Z., Vincent, J. L., Raichle, M. E. (2006). Spontaneous neuronal activity distinguishes human dorsal and ventral attention systems. *PNAS* 103, 10046–10051. doi: 10.1073/pnas.0604187103

Fox, M. D., Snyder, A. Z., Vincent, J. L., Corbetta, M., Van Essen, D. C., and Raichle, M. E. (2005). The human brain is intrinsically organized into dynamic, anticorrelated functional networks. *Proc. Natl. Acad. Sci. U.S.A.* 102, 9673–9678. doi: 10.1073/pnas.0504136102

Fransson, P. (2006). How default is the default mode of brain function? Further evidence from intrinsic BOLD signal fluctuations. *Neuropsychologia* 44, 2836–2846.

Fransson, P., Schiffler, B. C., and Thompson, W. H. (2018). Brain network segregation and integration during an epoch-related working memory fMRI experiment. *Neuroimage* 178, 147–161. doi: 10.1016/j.neuroimage.2018.05.040

Friston, K. J. (1994). Functional and effective connectivity in neuroimaging: a synthesis. *Hum. Brain Mapp.* 2, 56–78. doi: 10.1002/hbm.460020107

Golland, Y., Golland, P., Bentin, S., and Malach, R. (2008). Data-driven clustering reveals a fundamental subdivision of the human cortex into two global systems. *Neuropsychologia* 46, 540–553. doi: 10.1016/j.neuropsychologia.2007.10.003

Gordon, E. M., Breeden, A. L., Bean, S. E., and Vaidya, C. J. (2014). Working memory–related changes in functional connectivity persist beyond task disengagement. *Hum. Brain Mapp.* 35, 1004–1017. doi: 10.1002/hbm.22230

Greicius, M. D., and Menon, V. (2004). Default-mode activity during a passive sensory task: uncoupled from deactivation but impacting activation. *J. Cogn. Neurosci.* 16, 1484–1492. doi: 10.1162/0898929042568532

Greicius, M. D., Srivastava, G., Reiss, A. L., and Menon, V. (2004). Default-mode network activity distinguishes Alzheimer's disease from healthy aging: evidence from functional MRI. *Proc. Natl. Acad. Sci. U.S.A.* 101, 4637–4642. doi: 10.1073/pnas.0308627101

Guimera, R., and Amaral, L. A. N. (2005). Functional cartography of complex metabolic networks. *Nature* 433, 895–900. doi: 10.1038/nature03288

Hampson, M., Driesen, N. R., Skudlarski, P., Gore, J. C., and Constable, R. T. (2006). Brain connectivity related to working memory performance. *J. Neurosci.* 26, 13338–13343. doi: 10.1523/jneurosci.3408-06.2006

Hampson, M., Peterson, B. S., Skudlarski, P., Gatenby, J. C., and Gore, J. C. (2002). Detection of functional connectivity using temporal correlations in MR images. *Hum. Brain Mapp.* 15, 247–262. doi: 10.1002/hbm.10022

Harrison, B. J., Pujol, J., Lopez-Sola, M., Hernandez-Ribas, R., Deus, J., Ortiz, H., et al. (2008). Consistency and functional specialization in the default mode brain network. *Proc. Natl. Acad. Sci. U.S.A.* 105, 9781–9786. doi: 10.1073/pnas.0711791105

He, B. J., Snyder, A. Z., Vincent, J. L., Epstein, A., Shulman, G. L., and Corbetta, M. (2007). Breakdown of functional connectivity in frontoparietal networks underlies behavioral deficits in spatial neglect. *Neuron* 53, 905–918. doi: 10.1016/j.neuron.2007.02.013

He, Y., Wang, J., Wang, L., Chen, Z. J., Yan, C., Yang, H., et al. (2009). Uncovering intrinsic modular organization of spontaneous brain activity in humans. *PLoS One* 4:e5226. doi: 10.1371/journal.pone.0005226

Hearne, L. J., Cocchi, L., Zalesky, A., and Mattingley, J. B. (2017). Reconfiguration of brain network architectures between resting-state and complexity-dependent cognitive reasoning. *J. Neurosci.* 37, 8399–8411. doi: 10.1523/JNEUROSCI.0485-17.2017

Horwitz, B. (2003). The elusive concept of brain connectivity. *Neuroimage* 19, 466–470. doi: 10.1016/s1053-8119(03)00112-5

Jo, H. J., Gotts, S. J., Reynolds, R. C., Bandettini, P. A., Martin, A., Cox, R. W., et al. (2013). Effective preprocessing procedures virtually eliminate distance-dependent motion artifacts in resting state FMRI. *J. Appl. Math.* 2013:935154. doi: 10.1155/2013/935154

Kelly, A. M. C., Uddin, L. Q., Biswal, B. B., Castellanos, F. X., and Milham, M. P. (2008). Competition between functional brain networks mediates behavioral variability. *Neuroimage* 39, 527–537. doi: 10.1016/j.neuroimage.2007.08.008

Kitzbichler, M. G., Henson, R. N., Smith, M. L., Nathan, P. J., and Bullmore, E. T. (2011). Cognitive effort drives workspace configuration of human brain functional networks. *J. Neurosci.* 31, 8259–8270. doi: 10.1523/JNEUROSCI.0440-11.2011

Kuncheva, L. I., and Hadjitodorov, S. T. (2004). "Using diversity in cluster ensembles," in *Proceedings of the 2004 IEEE International Conference on Systems, Man and Cybernetics (IEEE Cat. No. 04CH37583)*, (Piscataway, NJ: IEEE), 1214–1219.

Lebedev, A. V., Nilsson, J., and Lövdén, M. (2018). Working memory and reasoning benefit from different modes of large-scale brain dynamics in healthy older adults. *J. Cogn. Neurosci.* 30, 1033–1046. doi: 10.1162/jocn_a_01260

Leech, R., Kamourieh, S., Beckmann, C. F., and Sharp, D. J. (2011). Fractionating the default mode network: distinct contributions of the ventral and dorsal posterior cingulate cortex to cognitive control. *J. Neurosci.* 31, 3217–3224. doi: 10.1523/JNEUROSCI.5626-10.2011

Lerman-Sinkoff, D. B., and Barch, D. M. (2016). Network community structure alterations in adult schizophrenia: identification and localization of alterations. *Neuroimage Clin.* 10, 96–106. doi: 10.1016/j.nicl.2015.11.011

Liang, X., Zou, Q. H., He, Y., and Yang, Y. H. (2016). Topologically reorganized connectivity architecture of default-mode, executive-control, and salience networks across working memory task loads. *Cereb. Cortex* 26, 1501–1511. doi: 10.1093/cercor/bhu316

Lowe, M. J., Dzemidzic, M., Lurito, J. T., Mathews, V. P., and Phillips, M. D. (2000). Correlations in low-frequency BOLD fluctuations reflect cortico-cortical connections. *Neuroimage* 12, 582–587. doi: 10.1006/nimg.2000.0654

Macaluso, E. (2010). Orienting of spatial attention and the interplay between the senses. *Cortex* 46, 282–297. doi: 10.1016/j.cortex.2009.05.010

Mascali, D., Dinuzzo, M., Gili, T., Moraschi, M., Fratini, M., Maraviglia, B., et al. (2015). Intrinsic patterns of coupling between correlation and amplitude of low-frequency fMRI fluctuations are disrupted in degenerative dementia mainly due to functional disconnection. *PLoS One* 10:e0120988. doi: 10.1371/journal.pone.0120988

Moser, D. A., Doucet, G. E., Ing, A., Dima, D., Schumann, G., Bilder, R. M., et al. (2018). An integrated brain-behavior model for working memory. *Mol. Psychiatry* 23, 1974–1980. doi: 10.1038/mp.2017.247

Newton, A. T., Morgan, V. L., and Gore, J. C. (2007). Task demand modulation of steady-state functional connectivity to primary motor cortex. *Hum. Brain Mapp.* 28, 663–672. doi: 10.1002/hbm.20294

Piccoli, T., Valente, G., Linden, D. E. J., Re, M., Esposito, F., Sack, A. T., et al. (2015). The default mode network and the working memory network are not anti-correlated during all phases of a working memory task. *PLoS One* 10:e0123354. doi: 10.1371/journal.pone.0123354

Rogers, B. P., Morgan, V. L., Newton, A. T., and Gore, J. C. (2007). Assessing functional connectivity in the human brain by fMRI. *Magn. Reson. Imaging* 25, 1347–1357. doi: 10.1016/j.mri.2007.03.007

Rubinov, M., and Sporns, O. (2011). Weight-conserving characterization of complex functional brain networks. *Neuroimage* 56, 2068–2079. doi: 10.1016/j.neuroimage.2011.03.069

Sala-Llonch, R., Junque, C., Arenaza-Urquijo, E. M., Vidal-Pineiro, D., Valls-Pedret, C., Palacios, E. M., et al. (2014). Changes in whole-brain functional networks and memory performance in aging. *Neurobiol. Aging* 35, 2193–2202. doi: 10.1016/j.neurobiolaging.2014.04.007

Shannon, C. E. (1948). A mathematical theory of communication. *Bell Syst. Tech. J.* 27, 623–656.

Shine, J. M., Bissett, P. G., Bell, P. T., Koyejo, O., Balsters, J. H., Gorgolewski, K. J., et al. (2016). The dynamics of functional brain networks: integrated network states during cognitive task performance. *Neuron* 92, 544–554. doi: 10.1016/j.neuron.2016.09.018

Shulman, G. L., Astafiev, S. V., Franke, D., Pope, D. L., Snyder, A. Z., Mcavoy, M. P., et al. (2009). Interaction of stimulus-driven reorienting and expectation in ventral and dorsal frontoparietal and basal ganglia-cortical networks. *J. Neurosci.* 29, 4392–4407. doi: 10.1523/JNEUROSCI.5609-08.2009

Spreng, R. N., Stevens, W. D., Chamberlain, J. P., Gilmore, A. W., and Schacter, D. L. (2010). Default network activity, coupled with the frontoparietal control network, supports goal-directed cognition. *Neuroimage* 53, 303–317. doi: 10.1016/j.neuroimage.2010.06.016

Tommasin, S., Mascali, D., Moraschi, M., Gili, T., Hassan, I. E., Fratini, M., et al. (2018). Scale-invariant rearrangement of resting state networks in the human brain under sustained stimulation. *Neuroimage* 179, 570–581. doi: 10.1016/j.neuroimage.2018.06.006

Umarova, R. M., Saur, D., Schnell, S., Kaller, C. P., Vry, M. S., and Glauche, V. (2009). Structural connectivity for visuospatial attention: significance of ventral pathways. *Cereb. Cortex* 20, 121–129. doi: 10.1093/cercor/bhp086

van den Heuvel, M. P., and Hulshoff Pol, H. E. (2010). Exploring the brain network: a review on resting-state fMRI functional connectivity. *Eur. Neuropsychopharmacol.* 20, 519–534. doi: 10.1016/j.euroneuro.2010.03.008

Vatansever, D., Menon, D. K., Manktelow, A. E., Sahakian, B. J., and Stamatakis, E. A. (2015). Default mode network connectivity during task execution. *Neuroimage* 122, 96–104. doi: 10.1016/j.neuroimage.2015.07.053

Vossel, S., Geng, J. J., and Fink, G. R. (2014). Dorsal and ventral attention systems: distinct neural circuits but collaborative roles. *Neuroscientist* 20, 150–159. doi: 10.1177/1073858413494269

Wen, X., Zhang, D., Liang, B., Zhang, R., Wang, Z., Wang, J., et al. (2015). Reconfiguration of the brain functional network associated with visual task demands. *PLoS One* 10:e0132518. doi: 10.1371/journal.pone.0132518

Whitfield-Gabrieli, S., and Nieto-Castanon, A. (2012). Conn: a functional connectivity toolbox for correlated and anticorrelated brain networks. *Brain Connect.* 2, 125–141. doi: 10.1089/brain.2012.0073

Yeo, B. T., Krienen, F. M., Sepulcre, J., Sabuncu, M. R., Lashkari, D., Hollinshead, M., et al. (2011). The organization of the human cerebral cortex estimated by intrinsic functional connectivity. *J. Neurophysiol.* 106, 1125–1165. doi: 10.1152/jn.00338.2011

Zhao, Z., Jie, L., Jia, X., Chao, W., Han, Y., and Jia, J. (2014). Selective changes of resting-state brain oscillations in aMCI: an fMRI study using ALFF. *Biomed. Res. Int.* 2014:920902. doi: 10.1155/2014/920902

Zuo, N. M., Yang, Z. Y., Liu, Y., Li, J., and Jiang, T. Z. (2018). Both activated and less-activated regions identified by functional MRI reconfigure to support task executions. *Brain Behav.* 8:e00893. doi: 10.1002/brb3.893

Conflict of Interest: The authors declare that the research was conducted in the absence of any commercial or financial relationships that could be construed as a potential conflict of interest.

frontiers in Neuroscience

ORIGINAL RESEARCH
published: 12 May 2020
doi: 10.3389/fnins.2020.00429

Temperature Measurements in the Vicinity of Human Intracranial EEG Electrodes Exposed to Body-Coil RF for MRI at 1.5T

Hassan B. Hawsawi[1,2,3], Anastasia Papadaki[4,5], John S. Thornton[4,5], David W. Carmichael[6,7] and Louis Lemieux[1,2]*

[1] Department of Clinical and Experimental Epilepsy, UCL Queen Square Institute of Neurology, London, United Kingdom, [2] MRI Unit, Epilepsy Society, Buckinghamshire, United Kingdom, [3] Administartion of Medical Physics, King Abdullah Medical City, Makkah, Saudi Arabia, [4] Lysholm Department of Neuroradiology, National Hospital for Neurology and Neurosurgery, UCLH NHS Foundation Trust, Queen Square, London, United Kingdom, [5] Department of Brain Repair and Rehabilitation, UCL Queen Square Institute of Neurology, London, United Kingdom, [6] Developmental Imaging and Biophysics Section, UCL Great Ormond Street Institute of Child Health, London, United Kingdom, [7] Wellcome EPSRC Centre for Medical Engineering, King's College London, St Thomas' Hospital, London, United Kingdom

OPEN ACCESS

Edited by:
Marta Bianciardi, Harvard Medical School, United States

Reviewed by:
Richard Bowtell, University of Nottingham, United Kingdom
Lucia Navarro De Lara, Harvard Medical School, United States

***Correspondence:**
Hassan B. Hawsawi
hassan.hawsawi.15@ucl.ac.uk

Specialty section:
This article was submitted to Brain Imaging Methods, a section of the journal Frontiers in Neuroscience

Received: *20 September 2019*
Accepted: *07 April 2020*
Published: *12 May 2020*

Citation:
Hawsawi HB, Papadaki A, Thornton JS, Carmichael DW and Lemieux L (2020) Temperature Measurements in the Vicinity of Human Intracranial EEG Electrodes Exposed to Body-Coil RF for MRI at 1.5T. Front. Neurosci. 14:429. doi: 10.3389/fnins.2020.00429

The application of intracranial electroencephalography (icEEG) recording during functional magnetic resonance imaging (icEEG-fMRI) has allowed the study of the hemodynamic correlates of epileptic activity and of the neurophysiological basis of the blood oxygen level-dependent (BOLD) signal. However, the applicability of this technique is affected by data quality issues such as signal drop out in the vicinity of the implanted electrodes. In our center we have limited the technique to a quadrature head transmit and receive RF coil following the results of a safety evaluation. The purpose of this study is to gather further safety-related evidence for performing icEEG-fMRI using a body RF-transmit coil, to allow the greater flexibility afforded by the use of modern, high-density receive arrays, and therefore parallel imaging with benefits such as reduced signal drop-out and distortion artifact. Specifically, we performed a set of empirical temperature measurements on a 1.5T Siemens Avanto MRI scanner with the body RF-transmit coil in a range of electrode and connector cable configurations. The observed RF-induced heating during a high-SAR sequence was maximum in the immediate vicinity of a depth electrode located along the scanner's central axis (range: 0.2–2.4°C) and below 0.5°C at the other electrodes. Also for the high-SAR sequence, we observed excessive RF-related heating in connection cable configurations that deviate from our recommended setup. For the low-SAR sequence, the maximum observed temperature increase across all configurations was 0.3°C. This provides good evidence to allow simultaneous icEEG-fMRI to be performed utilizing the body transmit coil on the 1.5T Siemens Avanto MRI scanner at our center with acceptable additional risk by following a well-defined protocol.

Keywords: safety, intracranial, EEG, MRI, body transmit coil, icEEG-fMRI, RF heating

INTRODUCTION

Intracranial electroencephalography during functional magnetic resonance imaging (IcEEG-fMRI) has been used to map epileptic activities (Vulliemoz et al., 2011; Boucousis et al., 2012; Carmichael et al., 2012) with much greater sensitivity enabling more detailed, quantitative studies of interictal, preictal and ictal epileptogenic networks (Vulliemoz et al., 2011; Cunningham et al., 2012; Aghakhani et al., 2015; Beers et al., 2015; Chaudhary et al., 2016; Ridley et al., 2017; Sharma et al., 2019) and of neuronal events more generally (Murta et al., 2016, 2017; Saignavongs et al., 2016).

However, simultaneous icEEG-fMRI is prone to signal loss around the icEEG electrodes and more particularly when using echo-planar imaging (EPI) sequences due to magnetic susceptibility effects; using gradient echo EPI we found up to 50% signal drop at around 5 mm from the electrode contacts (Carmichael et al., 2012). Currently, our icEEG-fMRI acquisitions are limited to the head transmit and receive RF coil, in accordance with the conclusions of our previous investigations on the technique's feasibility (Carmichael et al., 2008, 2010, 2012). The use of the body transmit coil in conjunction with the use of a head receive coil array would allow the use of parallel imaging techniques to reduce scanning time and susceptibility effects (Pruessmann et al., 1999; Larkman et al., 2001; Griswold et al., 2002; Setsompop et al., 2012).

In terms of subject safety, the combination of icEEG-fMRI constitutes a particularly challenging imaging technique due to a number of health risks (in addition to the invasiveness of icEEG electrode placement), associated with the exposure of metallic implants to the three fields used in MRI, namely: static magnetic field (B_0), the radiofrequency (RF) field (B_1) and the switching gradient magnetic fields. In principle, the B_0 field can cause an implant to experience a net force (displacement) or rotational (torque), the RF field can result in heating of the tissues around the implants and the gradient fields can induce eddy currents resulting in neural stimulation (Carmichael et al., 2010; Hawsawi et al., 2017). The exhaustive safety and data quality tests (Carmichael et al., 2008, 2010, 2012) that preceded our implementation of icEEG-fMRI lead us to define a data acquisition protocol that limits us to use a head RF-transmit/receive coil [in addition to low SAR sequences and positioning of the electrode wires along the RF coil's central (Z) axis], with important implications for blood oxygen level-dependent (BOLD) sensitivity (Carmichael et al., 2012).

In view of further developing icEEG-fMRI by modifying our protocol to allow the use of our MRI scanner's body transmit RF coil, we undertook new phantom tests to assess the conditions under which the body RF-transmit coil could be used with an acceptable level of additional risk. This article focuses on characterizing the RF-induced heating in the vicinity of icEEG electrodes exposed to RF produced by our 1.5T MRI scanner's body transmit coil with different lead configurations and whether these were connected to the recording system or not.

MATERIALS AND METHODS

We measured RF-induced temperature changes in the immediate vicinity of icEEG electrodes placed in a standard test phantom exposed to a body transmit coil, over a range of lead placement and termination configurations. In line with our previous work on the safety of icEEG-fMRI (Carmichael et al., 2008, 2010) five icEEG electrodes were placed in the head part of the phantom to simulate a representative, realistic clinical scenario (see **Figure 1**).

Phantom Preparation

Following the ASTM F-2182-02a guidelines, we used a container made of acrylic with the following dimensions: head length = 290 mm, head width = 195 mm, torso length = 300 mm, torso width = 330 mm and height = 150 mm (**Figure 1**). It was filled with 0.70 g/L of NaCl, 8 g/L of polyacrylic acid (PAA) and 15 L of distilled water in order to simulate human brain tissue electrical conductivity of 0.26 S/m (Park et al., 2003).

EEG Electrode, Connecting Lead and Recording System Configurations

Three depth icEEG electrodes, two 8–contact (Ad-Tech model SD08R-SP10X-000; 8 platinum contacts, 10 mm spacing, 72 mm recording area and 380 mm total depth length) and one 10-contact (Ad-Tech model SD10R-SP10X-000, 10 platinum contacts, 10 mm spacing, 92 mm recording area, and 390 mm total depth length) were positioned as follows, along lateral trajectories mimicking a bilateral mesial temporal lobe implantation: *Depth 1* with eight contacts was positioned on the left hand side [9.86 cm from the superior aspect of the phantom (top of the head) and 5.5 cm from the anterior surface (face; depth from the gel's surface), with the deepest contact located 12 cm from the left lateral surface]; similarly, *Depth 2* with eight contacts was inserted (through a hole in the *Grid* electrode – see below) on the right hand side [9.28 cm from the superior aspect of the phantom (top of the head) and 5.5 cm from the anterior aspect (face; depth from the gel's surface), and the depth of 7.5 cm from the right lateral surface]; and *Depth 3* with 10 contacts in the left hand side located 10 mm superior to *Depth 1* in the same coronal plane and depth. A *Grid* electrode (Ad-Tech model FG64D-SS10X-0E2, 10 mm spacing, 64 platinum contacts, nichrome wire, and electrode total length of 455 mm) was placed in a para-sagittal plane in a location to emulate the placement of electrodes over the left cortical region and located 2 cm away from the head's lateral aspect. A *Strip* electrode (Ad-Tech model TS06R-AP10X-0W6, 6 platinum contacts, 10 mm spacing, 72 mm recording area and 380 mm total depth length) was located in an axial plane in the superior part of the phantom head (2.18 cm from the top of the head).

Lead extension wires (length = 90 cm), which are used to connect the electrode leads to the EEG digitization and amplification system [DAS; consisting of the electrode lead input box, battery pack and amplifier(s)] for the purpose of recording, were used in some of the heating tests.

Following our routine practice for patient scanning sand bags were placed on top of the electrode leads and cables along

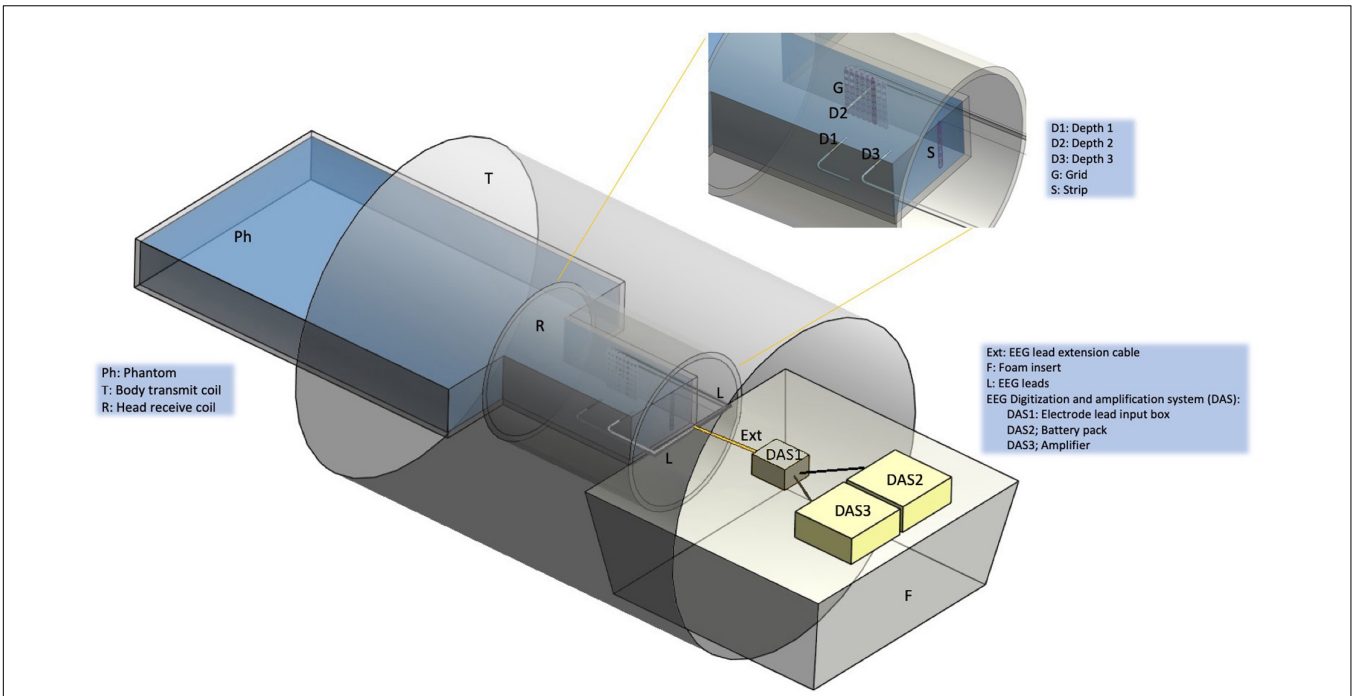

FIGURE 1 | Experimental set up. Schematic representation of the gel-filled phantom (Ph), scanner RF coils (T and R), foam insert (F) and EEG electrodes, leads and digitization and amplification system (DAS). The following icEEG electrode were placed in the gel-filled phantom: *Depth 1* (D1) orientated laterally, *Depth 2* (D2) (lateral), *Depth 3* (D3) (lateral), *Grid* (G) (para-sagittal), *Strip* (S) (anterior-posterior). Depending on the experimental configuration (see **Figure 2**), the electrodes were connected to leads (L), extension cables (Ext), and the DAS system [electrode lead input box (DAS1), battery pack (DAS2), amplifier (DAS3)]. Depending on the experimental configuration, the DAS system was placed either on top of a foam insert (F) or at the bottom of the scanner bore (no foam insert).

their path from the phantom to the DAS (Vulliemoz et al., 2011). In accordance with our icEEG-fMRI data acquisition protocol (Carmichael et al., 2012) a MRI scanner EEG equipment positioning foam insert manufactured by us, to be placed at the head end of the scanner bore (between the head coil and bore opening at the scanner far end) was used in the tests to ensure the reproducible and secure placement of the electrode lead tails and extensions, and EEG DAS in the scanner bore (**Figure 1**; Carmichael et al., 2012). The positioning foam insert consists of a hemi-cylinder (length: 79.7 cm) with a radius that matches the scanner bore's internal diameter, and has grooves and cut outs (depth: 0.8 cm) in its (top) flat surface to enable reproducible placement of the leads and DAS along the scanner's central (Z) axis, to minimize the coupling between the EEG system and RF *E* field, which by design is made to have the smallest possible magnitude on the Z-axis within the scanning field of view (Lemieux et al., 1997). In some of the tests described below, the effect of not using the positioning foam insert on the RF-induced heating was assessed; without the foam insert in place, the leads and EEG DAS rest on the bottom of the scanner bore (therefore away from the Z-axis, closer to the body coil).

Our previous work has demonstrated the effects of electrode and lead placement, and of electrical termination on the amount of RF-induced heating in the vicinity of icEEG electrodes (Carmichael et al., 2008, 2010). Two sets of measurements were performed: *Experiment 1* and *Experiment 2*; each set corresponding to a scanning session, and designed to provide an assessment of heating increases in the tissue surrounding the icEEG electrodes using different lead configurations for the body RF transmit coil, and assessing reproducibility by repeating some measurements. The configurations are labeled *A(i)* ($i = 1, 2, 3$) for *Experiment 1* and *B(i)* ($i = 1,\ldots, 5$) for *Experiment 2*.

Experiment 1

In this experiment, we set out to perform an evaluation of the effects of using the body transmit RF coil on the heating in the vicinity of icEEG (*Depth 1*, *Depth 2*, *Depth 3*, *Strip*, and *Grid*) electrodes located inside a water-based phantom. Previous studies (Carmichael et al., 2008, 2010; Boucousis et al., 2012; Ciumas et al., 2013) studied the effect of body transmit coil and concluded that body transmit coil produces significant temperature increase above the safety levels, and we sought to update this information for the configurations of electrodes, connecting leads and EEG DAS specified in our successfully implemented protocol (Carmichael et al., 2012). We also sought to explore slight variations on this arrangement and to obtain temperature measurement reproducibility data.

The three following electrode configurations were studied in *Experiment 1* (see **Figure 2**):

> ***A(1)***: With foam insert. No lead extensions. Electrodes unterminated with *Strip*, *Grid*, and *Depth 2* lead tails bundled together (using adhesive tape) on the right side of the superior aspect of the phantom head (right bundle) and

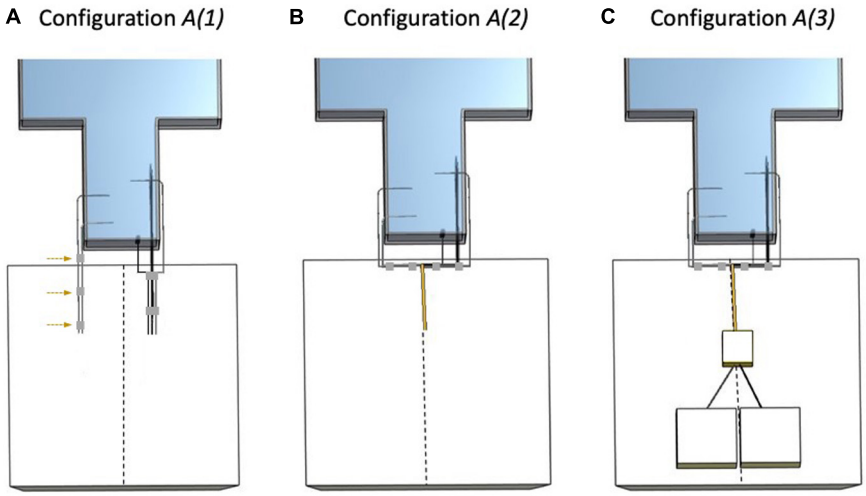

FIGURE 2 | Electrode configurations A (*Experiment 1*). The dashed line represents the scanner's central Z-axis as drawn on the foam insert. **(A)** Configuration *A(1)*: *Strip*, *Grid*, and *Depth 2* bundled together (right bundle) and separated from the left bundle (*Depth 1* and *Depth 3*) without lead extensions and with lead tails placed on top of the foam insert. The adhesive tape (gray) used to create the left bundle is highlighted with the dashed arrows. **(B)** Configuration *A(2)*: *Strip*, *Grid*, and *Depth 2* bundled together (right bundle), connected to 90 cm lead extensions and placed on top of the foam insert. *Depth 1* and *Depth 3* bundled together (left bundle) and unterminated with lead tails on top of the foam insert. **(C)** Configuration *A(3)*: *Strip*, *Grid*, and *Depth 2* bundled together (right bundle), connected and terminated by connection to the EEG DAS using the 90 cm lead extensions, placed on top of the foam insert. *Depth 1* and *Depth 3* bundled together (left bundle) and unterminated with lead tails on top of the foam insert.

Depth 1 and *Depth 3* lead tails bundled together on the left (left bundle) and separated from the right bundle.

A(2): With foam insert. Electrodes unterminated extended along the Z-axis and grouped into two bundles: *Strip*, *Grid*, and *Depth 2* with 90 cm lead extensions and *Depth 1* and *Depth 3* without lead extensions.

A(3): With foam insert. Electrodes extended along the Z-axis grouped into two bundles: *Strip*, *Grid*, and *Depth 2* with 90 cm lead extensions and connected to the EEG DAS (terminated), and *Depth 1* and *Depth 3* without lead extensions and unterminated.

The sequence of temperature measurements, with configuration, RF exposure sequence and manipulations, in *Experiment 1* are shown in **Table 1**.

Experiment 2

This experiment constitutes an elaboration of *Experiment 1*, designed to explore the heating that results from scenarios that deviate more from our protocol (therefore akin to fault conditions), in particular in relation to the placement of the leads relative to the scanner's central axis by not using the foam insert; also it provided additional (inter-session) reproducibility data.

The following five electrode configurations were studied in *Experiment 2* (see **Figure 3**):

B(1): A repetition of *A(2)* (*Experiment 1*).

B(2): With foam insert. Electrodes unterminated and placed away from the Z-axis. Grouped into two bundles: *Strip*, *Grid*, and *Depth 2* without lead extensions separated from each other, and *Depth 1* and *Depth 3* connected to the lead extensions.

B(3): Without foam insert. No lead extensions. Unterminated. All electrode leads separated from each other.

B(4): Without foam insert. Electrodes unterminated with *Depth 1* and *Depth 3* with lead extensions bundled together and *Strip*, *Grid*, and *Depth 2* without lead extensions separated from each other and from the other two.

B(5): Without foam insert. Electrodes *Depth 1* and *Depth 3* bundled together and connected to the lead extensions and the EEG DAS (terminated), and *Strip*, *Grid*, and *Depth 2* without lead extensions separated from each other and from the other two.

The sequence of measurements of heating with the specified icEEG leads configurations and the applied MRI sequence in *Experiment 2* are shown in **Table 2**.

MRI System and RF Exposure Sequences

The MRI scanner used in this investigation was a 1.5T Avanto (Siemens, Germany) in the Neuroradiology department of the National Hospital for Neurology and Neurosurgery (UCLH NHS Foundation Trust), London, United Kingdom; this is the scanner used for our icEEG-fMRI experiments on human subjects (Vulliemoz et al., 2011). All RF exposure in this work was performed using the scanner's standard body RF-transmit coil.

In accordance with our previous tests (Carmichael et al., 2010) the nominal RF exposure duration was 6 min. Two MRI sequences were used: (1) turbo spin echo (TSE) to maximize heating ("worst case" scenario): TR = 2850 ms, TE = 92 ms, slice thickness/slice gap = 2.5/1.25 mm, FOV = 300 × 300 mm,

TABLE 1 | Experiment 1 configurations, manipulations and RF exposure data.

Measurement #	Electrode configuration	Temperature probe locations	Other manipulations relative to previous measurement	RF exposure			
				Sequence type	SAR head (W/Kg) (% allowed maximum)	SAR whole-body (W/Kg) (% allowed maximum)	B_1 (μT) (% allowed maximum)
1.1	*A(1)*	Ref, D2, D3, G	–	TSE*	3.2 (100)	0.8 (34)	4.6 (67)
1.2	*A(1)*	Ref, D2, D3, G	None	EPI	0.1 (3)	0 (1)	0.9 (12)
1.3	*A(1)*	Ref, D2, D3, G	None	TSE*	3.2 (100)	0.8 (40)	4.7 (67)
1.4	*A(1)*	Ref, D2, D3, G	None	EPI	0.1 (3)	0 (1)	0.9 (12)
1.5	*A(2)*	Ref, D2, D3, G	Table out, cable repositioning and table in	TSE	2.6 (82)	0.7 (33)	4.1 (58)
1.6	*A(2)*	Ref, D2, D3, G	None	TSE*	3.2 (100)	0.8 (34)	4.6 (65)
1.7	*A(2)*	Ref, D2, D3, G	Table out, cable repositioning and table in	TSE	3.1 (98)	0.8 (39)	4.5 (64)
1.8	*A(3)*	Ref, D2, D3, G	None	TSE	2.6 (82)	0.7 (33)	4.1 (58)
1.9	*A(3)*	Ref, D2, D3, G	None	EPI*	0.1 (3)	0 (1)	0.9 (12)

The exposure duration was 6 min 9 s. Measurements 1.1 and 1.3, and 1.5, 1.6, and 1.7, respectively, constitute two sets of repeat measurements for configurations A(1) and A(2), respectively. TSE, turbo spin echo; EPI, echo-planar imaging; Ref, reference; D2, Depth 2; D3, Depth 3; G, Grid. *Measurement shortened to 4:37 for measurements 1.1, 1.3, 1.6, and 1.9, due to lack of appreciable heating and scanner time access limitations for this experiment.*

in-plane resolution = 0.9 × 0.8 mm, BW = 125 Hz/pixel, FA = 180° and duration = 6 min 9 s. In Experiment 1, for four of the measurements, the exposure was reduced to 4 min 32 s due to lack of appreciable heating and scanner time access constraints (see **Table 1**); (2) EPI as used for icEEG-fMRI scanning (Carmichael et al., 2012), with the following parameters: TR = 4480 ms, TE = 50 ms, slice thickness/slice gap = 2.0/1.0 mm, FOV = 192 × 192 mm, in-plane resolution = 3.0 × 3.0 mm, BW 2298 Hz/pixel, FA 90° and duration = 6 min 4 s.

Temperature Measurements

The temperature changes in the immediate vicinity of selected electrode contacts were monitored and recorded continuously using five fiber-optic sensors (model T1C-10-PP05 and model T1C-10-B05, Neoptix, Canada), connected to a 4-channel signal conditioner (Neoptix ReFlex—Neoptix, Canada). Based on prior experience we estimate the temperature measurement precision (standard deviation in the absence of heating) to be of the order of ±0.2°C. The temperature sensors were placed in five locations as follows: the tips of *Depth 1*, *Depth 2*, and *Depth 3*; contact number 48 of the *Grid* electrode which is located in the corner of the electrode and a reference location, at a depth of approximately 3 cm in the phantom gel, 10 cm away from all the electrodes corresponding roughly to the phantom's neck area.

Because we were limited to four temperature channels simultaneously, in some tests we repeated the measurement with alternative temperature probes. In particular, following *Experiment 1* (see **Table 3**), in which we did not measure the temperature at *Depth 1* based on the results of our previous work (Carmichael et al., 2010) which suggested that the heating would be greatest at *Depth 3*. We tested this assumption in the first three measurements of *Experiment 2* (see **Table 4**). This demonstrated that the heating was greater at *Depth 1* than *Depth 2* (see **Table 4**), and therefore decided to record at *Depth 1* for the rest of that experiment.

RESULTS

Experiment 1

The maximum observed temperatures for all measurements in the presence of the foam insert across configurations *A(1)–A(3)* at every location can be found in **Table 3**. **Figure 4** shows a typical temperature measurement series (measurement 1.1). The maximum temperature increase overall was 0.7°C at *Depth 2* for measurement 1.3, which was the electrode location of greatest heating for most measurements. In accordance with our expectations, the temperature increase values measured were greater for TSE than EPI; the maximum temperature changes for all EPI exposures were equal to, or below, 0.3°C, which is near the threshold of detectability (0.2°C), and comparable to the temperature increase at the reference position. Comparison of measurements 1.3 and 1.5–7 shows good reproducibility relative to phantom repositioning.

Experiment 2

Experiment 2 was performed one week after Experiment 1. The maximum observed temperature change values for all measurements are shown in **Table 4**. **Figure 5** illustrates temperature changes for measurement 2.1. For the high-SAR sequence, the highest temperature increase recorded was 4.5°C, at electrode *Depth 1* (measurement 2.8). For the EPI sequence (measurement 2.6), the maximum temperature increase was negligible.

Measurements 2.1–2.4 are two sets of repeat measurements with the foam insert and lead extensions [configurations *B(1)* and *B(2)*, with extensions laid along, and away from the Z-axis,

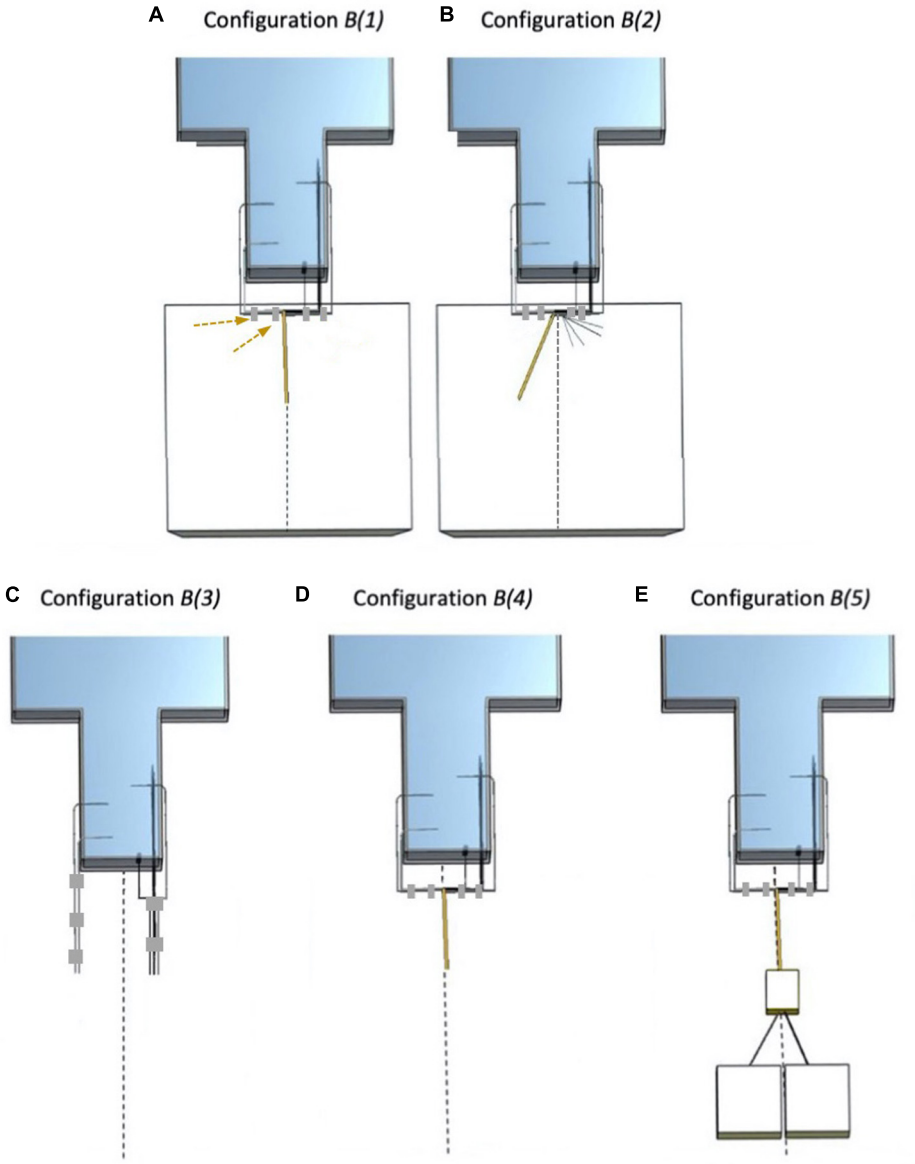

FIGURE 3 | Electrode configurations B (*Experiment 2*). The dashed line represents the scanner's central *Z*-axis. **(A)** Configuration *B(1)*: *Strip*, *Grid*, and *Depth 2* bundled together (right bundle), connected to 90 cm lead extensions and placed on top of the foam insert. *Depth 1* and *Depth 3* bundled together (left bundle) and unterminated with lead tails on top of the foam insert. The adhesive tape (gray) used to create the left bundle is highlighted with the dashed arrows. **(B)** Configuration *B(2)*: *Strip*, *Grid*, and *Depth 2* separated from each other and separated from *Depth 1* and *Depth 3. Depth 1* and *Depth 3* bundled together, connected to lead extensions (unterminated) and positioned a little away from the central Z-axis on top of the foam insert. **(C)** Configuration *B(3)*: *Strip*, *Grid*, *Depth 2*, *Depth 1*, and *Depth 3* leads without extensions, separated and unterminated; no foam insert. **(D)** Configuration *B(4)*: *Strip*, *Grid*, *Depth 2*, *Depth 1*, and *Depth 3* bundled together with *Depth 1* and *Depth 3* connected to the extensions (unterminated); no foam insert. **(E)** Configuration *B(5)*: *Strip*, *Grid*, *Depth 2*, *Depth 1*, and *Depth 3* bundled together, with *Depth 1* and *Depth 3* connected to the lead extensions and to the EEG DAS (extensions + terminated); no foam insert (i.e., EEG DAS placed on the bottom of the scanner bore).

respectively]; these resulted in maximum temperature increases in the range 0.2–2.4°C for the depth electrodes, 0.5–1°C for the *Grid*.

For the remaining measurements, due to the limited number of channels of our temperature signal conditioning unit, and our wish to sample temperatures simultaneously (*Depth 1* not sampled in Experiment 1), we used the temperature probe at *Depth 1* instead of *Depth 2*, due to the higher temperatures observed at the former in measurements 2.2 and 2.3. After removing the lead extensions and foam insert (measurements 2.5 and 2.6), the maximum temperature increase dropped to 0.4°C across all electrodes (for the high-SAR sequence; negligible for EPI). Reconnecting the electrodes to the lead extensions (without foam insert; measurement 2.7) resulted in greater maximum

TABLE 2 | Experiment 2 configurations, manipulations, and RF exposure data.

Measurement #	Electrode configuration	Temperature probe locations	Other manipulations relative to previous measurement	RF exposure			
				Sequence type	SAR head (W/Kg) (% allowed maximum)	SAR whole-body (W/Kg) (% allowed maximum)	B_1 (μT) (% allowed maximum)
2.1	*B(1)*	Ref, D1, G, D3	–	TSE	3.2 (99)	0.6 (28)	4.5 (64)
2.2	*B(1)*	Ref, D1, G, D2	None	TSE	3.2 (99)	0.6 (28)	4.5 (64)
2.3	*B(2)*	Ref, D1, G, D2	Table out, cable repositioning and table in	TSE	3.2 (99)	0.6 (28)	4.5 (64)
2.4	*B(2)*	Ref, D1, G, D3	None	TSE	3.2 (99)	0.6 (28)	4.5 (64)
2.5	*B(3)*	Ref, D1, G, D3	Table out, cable repositioning and table in	TSE	3.2 (99)	0.6 (28)	4.5 (64)
2.6	*B(3)*	Ref, D1, G, D3	Table out, cable repositioning and table in	EPI	0.1 (3)	0 (1)	0.9 (12)
2.7	*B(4)*	Ref, D1, G, D3	Table out, cable repositioning and table in	TSE	3.2 (99)	0.6 (28)	4.5 (64)
2.8	*B(5)*	Ref, D1, G, D3	None	TSE	3.2 (99)	0.6 (28)	4.5 (64)

Measurements 2.1 and 2.2, and 2.3 and 2.5, respectively, constitute two repeat measurements with different temperature probe locations (Depth 1 and Depth 2, respectively; see section "Temperature Measurements"). The exposure duration was 6 min 9 s. TSE, turbo spin echo; EPI, echo-planar imaging; Ref, reference; D1, Depth 1; D2, Depth 2; D3, Depth 3; G, Grid.

TABLE 3 | Experiment 1 results: maximum temperature increases.

Measurement #	Type of sequence, configuration	Maximum temperature increases (°C)			
		Depth 2	Depth 3	Grid	Reference
1.1	TSE, *A(1)*	0.6	0.3	0.1	0.1
1.2	EPI, *A(1)*	0.3	0.2	0.2	0.3
1.3	TSE, *A(1)*	0.7	0.2	0.3	0.3
1.4	EPI, *A(1)*	0.2	0.1	0	0.2
1.5	TSE, *A(2)*	0.3	0.2	0.4	0.4
1.6	TSE, *A(2)*	0.4	0.3	0.3	0.4
1.7	TSE, *A(2)*	0.2	0.2	0.3	0.5
1.8	TSE, *A(3)*	0.7	0.1	0.2	0.2
1.9	EPI, *A(3)*	0.3	0.2	0	0

temperature increases (1.9°C); connection to the digitization and amplification system (without foam insert; measurement 2.8) resulted in the maximum temperature increase of 4.5°C, at electrode *Depth 1*, the location of the greatest temperature increases in all measurements except 2.5.

DISCUSSION

We performed experiments to quantify the amount of heating induced in the immediate vicinity of a set of intracranial EEG electrodes by exposure to RF generated by a body transmit coil in a 1.5T MRI scanner. This work builds directly on our experience of acquiring concurrent icEEG-fMRI data using a quadrature head RF transmit coil in the MRI scanner (Vulliemoz et al., 2011; Chaudhary et al., 2016; Murta et al., 2016, 2017; Ridley et al., 2017; Sharma et al., 2019) and in particular the safety tests that made it possible (Carmichael et al., 2008) and associated scanning protocol (Carmichael et al., 2012). This protocol contains prescriptions on the choice of RF transmit coil, MR sequence, and the type, connection and positioning of the EEG wires and equipment, and relies to a large degree on the use of a scanner bore foam insert on which the EEG system can be placed precisely and consistently. In this work our objective was to confirm whether, based on the same protocol, the use of the body RF transmit coil instead of the head-only transmit coil in the same MRI scanner, would result in excessive heating. The electrodes were positioned inside a water-based gel phantom in a configuration that emulates a clinical scenario, in line with our previous tests (Carmichael et al., 2008) and subjected to trains of RF excitation pulses (low and high-SAR sequences)

TABLE 4 | Experiment 2 results: maximum temperature increases.

Measurement #	Type of sequence, configuration	Maximum temperature increases (°C)				
		Depth 1	Depth 2	Depth 3	Grid	Reference
2.1	TSE, *B(1)*	2.4	×	0.1	1	0.1
2.2	TSE, *B(1)*	2.1	0.2	×	0.5	0.4
2.3	TSE, *B(2)*	2.0	1.0	×	0.6	0.2
2.4	TSE, *B(2)*	1.7	×	0.2	0.5	0.3
2.5	TSE, *B(3)*	0.3	×	0.2	0.4	0.3
2.6	EPI, *B(3)*	0	×	0	0	0.1
2.7	TSE, *B(4)*	1.9	×	0.2	1	0.1
2.8	TSE, *B(5)*	4.5	×	0.1	1.1	0.1

×, *no measurement.*

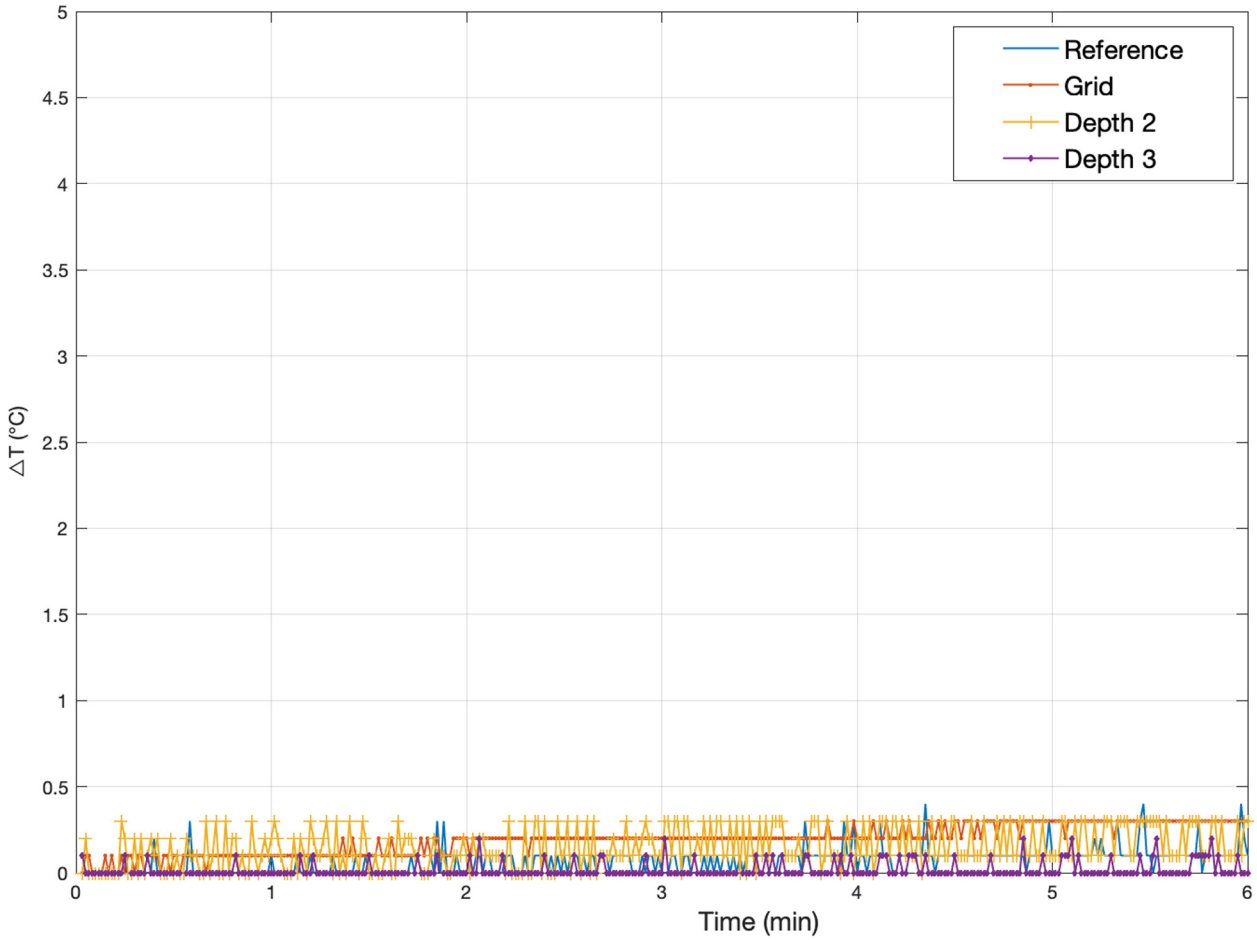

FIGURE 4 | Representative temperature changes for *Experiment 1*. Measurement 1.5: Temperature changes at *Grid*, *Depth 1*, and *Depth 3* [electrode configuration *A(2)*] following exposure to a high-SAR (TSE) sequence starting at Time = 0. The plot also serves to illustrate the precision of the measurements, of the order of ±0.2°C. The peak temperature increases for every Experiment 1 measurement are reported in **Table 3**.

through the body RF transmit coil. We explored a range of electrode lead configurations: length, placement relative to the scanner's central axis and termination; each a deviation from our previously defined protocol (Carmichael et al., 2012).

Current international guidelines recommend that MRI-induced heating should not cause temperature in the head to exceed 38°C, suggesting an allowable increase of ≤1°C (IEC, 2016).

In summary in this work, for the low-SAR (EPI) RF exposures prescribed in our protocol, the maximum observed temperature increase was 0.3°C across all tested configurations. This provides further evidence on the suitability of our established icEEG-fMRI protocol by extending its applicability to our 1.5T MRI scanner's body RF-transmit coil. We assessed reproducibility by performing a number of repeated measurements within each experiment, for the same configuration, either by simply repeating the RF exposure (considering the high-SAR measurements only: measurements 1.1 and 1.3, 1.5 and 1.6, 2.1 and 2.2, 2.3 and 2.4) or repeating the RF exposure after moving the phantom assembly in and out of the scanner bore (measurement pair 1.6 and 1.7). Furthermore, taken together, measurements 1.5, 1.6, 1.7, 2.1, and 2.2 constitute repeated measurements for the same (intended) configuration [*A(2)* and *B(1)*] between scanning sessions (*Experiments 1* and *2*, which took place one week apart). The results of these comparisons (mean and standard deviation of inter-measurement difference across all locations: 0.0 and 0.2°C, respectively) give an indication of the good reproducibility of our measurements (Bland and Altman, 1995), and which combined with the reference temperature measurements, suggest a detection threshold of the order of 0.5°C.

To our knowledge there has been a single previous investigation of the safety of using body transmit coil for icEEG during fMRI at 1.5T: Ciumas et al. (2013) performed temperature assessments in a water-gel phantom and rabbit cadavers using an EPI sequence for depth electrodes in two orientations: axial and lateral, showing temperature increases in the range of 0.2 and 1.3°C. Previously, we investigated RF-induced heating for a body transmit coil at 3T for a set of

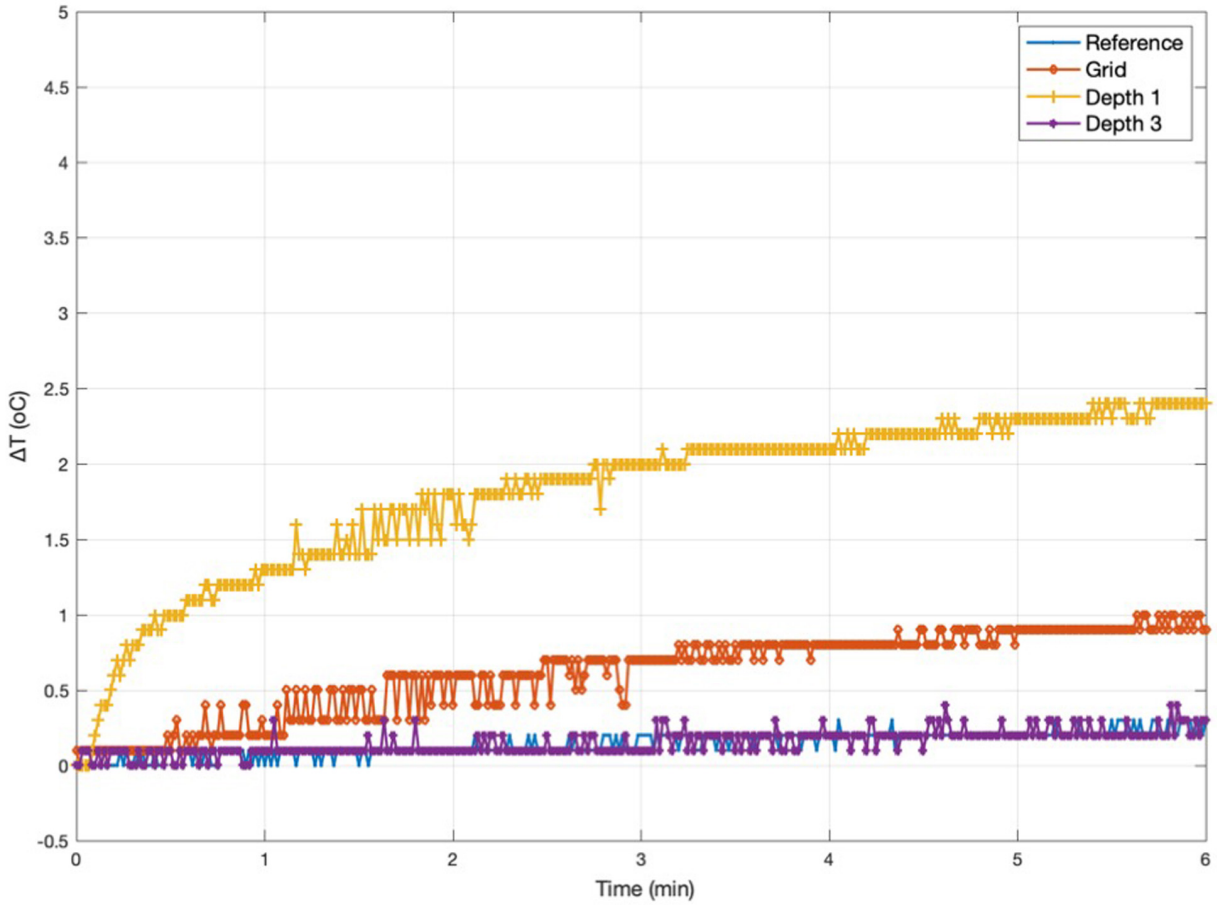

FIGURE 5 | Representative temperature changes for *Experiment 2*. Measurement 2.1: temperature changes at *Grid*, *Depth 1*, and *Depth 3* [electrode configuration *B(1)*] following exposure to a high-SAR (TSE) sequence starting at Time = 0. The peak temperature increases for every Experiment 2 measurement are reported in **Table 4**.

electrodes placed similarly to the set up used in this work. For high-SAR exposures maximum temperature increases of 6.4°C at the grid electrode and 0.7°C at the depth electrodes were observed when the electrode leads and extensions were separated ("open circuit" configuration), while the temperature increases were lower when gathering the leads and extensions together in a bundle "short circuit" (Carmichael et al., 2008). In addition, when placing the leads and extensions close to the scanner bore, the maximum heating at the grid was found to be 2.9 and 6.9°C at the depth electrodes (Carmichael et al., 2012). Boucousis et al. (2012), working at 3T and using the body RF-transmit coil, observed a maximum temperature increase of 4.9°C when applying high-SAR and 0.5°C for low-SAR (fMRI) sequences. Both studies concluded that high-SAR sequences should be avoided when performing icEEG-fMRI; however, Boucousis et al. (2012) concluded that low-SAR sequences with the body transmit coil do not pose an unacceptable risk for the patients.

The purpose of performing heating tests with high-SAR RF exposures, even for the evaluation of scanning protocols that preclude them, is manifold: (1) assess the risks associated with worst case scenarios (operator error during application of the protocol); (2) ensure that conclusions reached based on low-SAR tests do not simply reflect temperature measurement sensitivity limitations; and (3) reflects the requirements specified in the standard guidelines (ASTM F-2182-02a; ASTM, 2011). In this study, for the high-SAR (TSE) exposures the maximum observed temperature increase was 4.5°C, for a configuration in which the wires and lead extensions were far from the scanner central axis (lying at the bottom of the scanner bore: no foam insert). This compares with a maximum temperature increases of 2.4°C across all configurations with the wires lying along the scanner's Z-axis on top of our foam insert. We also note that this is much greater than the maximum increase of 0.7°C for the two configurations without lead extensions [*A(1)* and *B(3)*], thereby further confirming the important effect of lead length (Carmichael et al., 2010). Concerning the impact of circuit termination, which in our experiments tended to be associated with greater heating (measurements 1.8 vs 1.7 and 2.8 vs 2.7), this may result from this corresponding to a conductive loop, as opposed to capacitive effects between wires in close proximity.

Furthermore, "avoiding loops" is the usual guidance when placing electrophysiological leads in the MR environment (Lemieux et al., 1997; Kainz et al., 2002; Balasubramanian et al., 2017). Importantly, the lead extensions and connection to the EEG DAS are necessary for the application of icEEG-fMRI. Therefore, while they can affect the risk level adversely, in particular the use of lead extensions, our aim was to demonstrate that the amount of heating created in the "with extensions and connected" condition was acceptable and in what conditions relative to other factors (positioning, sequence, and coil types).

The generalization of the conclusions that can be reached from our measurements is limited by numerous factors, including: the representativeness (and quality of fabrication) of the phantom and of the electrode configuration, the specific characteristics of the MRI scanner, and temperature measurement capability (spatial sampling, limited by the number of available temperature probes) and measurement error. While some of these, in particular the variety of possible electrode implantations used in clinical practice, may be particularly challenging we believe that this study is in line with previously published empirical work and furthermore reflects the ASTM standard-level of evidence. Similarly, in relation to spatial sampling of the temperature changes, our use of four temperature probes is also in line with many other recent studies (Boucousis et al., 2012; Ciumas et al., 2013; Jorge et al., 2015; Balasubramanian et al., 2017). We tried to mitigate this limitation using prior knowledge; for example, while in retrospect it might have been preferable to record the temperature at *Depth 1* instead of *Depth 2* in *Experiment 1*, we do not believe that this significantly alters our conclusions because *Experiment 2* was specifically conceived as a series of worst-case scenarios (this in contrast to *Experiment 1* which is effectively a feasibility test for the body transmit coil, based on our recommended configurations (Carmichael et al., 2012).

Therefore, the guidance that can be provided based on our results can be summarized as follows: icEEG-fMRI is feasible with acceptable risk on a 1.5T MRI scanner (TIM Avanto, Siemens, Erlangen, Germany) using the standard body RF transmit coil if the following restrictions are applied: the EEG leads are brought together as close as possible to the top of the head and placed exactly along the scanner's central axis, and toward the back (head end) of the scanner, and connected to the EEG input box, itself placed on the scanner axis, which is connected to the EEG amplification units, also placed as close as possible to the scanner axis (this positioning can be facilitated by the use of a scanner foam insert (see Carmichael et al., 2012) and all scanning must be restricted to low-SAR gradient echo sequences.

CONCLUSION

In summary, this study provides good evidence for the feasibility of simultaneous icEEG-fMRI utilizing the body transmit coil on the 1.5T Siemens Avanto MRI scanner at our center. Careful consideration of the positioning of the electrode leads and EEG amplification system and choice of sequences is crucial, and should follow our established protocol (Carmichael et al., 2012).

DATA AVAILABILITY STATEMENT

The datasets generated for this study are available on request to the corresponding author.

AUTHOR CONTRIBUTIONS

HH, AP, DC, and LL prepared the phantom for the experiment. HH and LL prepared and analyzed the data. HH wrote the manuscript. All authors contributed editorially.

FUNDING

UCL-held UKRI funding and Wellcome Trust funding and the National Institute for Health Research University College London Hospitals Biomedical Research Centre.

REFERENCES

Aghakhani, Y., Beers, C. A., Pittman, D. J., and Gaxiola-valdez, I. (2015). Clinical Co-localization between the BOLD response and epileptiform discharges recorded by simultaneous intracranial EEG-fMRI at 3 T. *NeuroImage* 7, 755–763. doi: 10.1016/j.nicl.2015.03.002

ASTM (2011). *ASTM Standard F 2182-2002a Standard Test Method for Measurement of Radio Frequency Induced Heating Near Passive Implants During Magnetic Resonance Imaging*. West Conshohocken, PA: ASTM Int, 1–14.

Balasubramanian, M., Wells, W. M., Ives, J. R., Britz, P., Mulkern, R. V., and Orbach, D. B. (2017). RF heating of gold cup and conductive plastic electrodes during simultaneous EEG and MRI. *Neurodiagn. J.* 57, 69–83. doi: 10.1080/21646821.2017.1256722

Beers, C. A., Williams, R. J., Gaxiola-valdez, I., Pittman, D. J., Kang, A. T., Aghakhani, Y., et al. (2015). Patient specific hemodynamic response functions associated with interictal discharges recorded via simultaneous intracranial EEG-fMRI. *Hum. Brain Mapp.* 36, 5252–5264. doi: 10.1002/hbm.23008

Bland, J. M., and Altman, D. G. (1995). Comparing methods of measurement: why plotting difference against standard method is misleading. *Clin. Lab. Haematol.* 346, 1085–1087. doi: 10.1016/S0140-6736(95)91748-9

Boucousis, S. M., Beers, C. A., Cunningham, C. J. B., Gaxiola-Valdez, I., Pittman, D. J., Goodyear, B. G., et al. (2012). Feasibility of an intracranial EEG-fMRI protocol at 3T: Risk assessment and image quality. *Neuroimage* 63, 1237–1248. doi: 10.1016/j.neuroimage.2012.08.008

Carmichael, D. W., Thornton, J. S., Rodionov, R., Thornton, R., McEvoy, A., Allen, P. J., et al. (2008). Safety of localizing epilepsy monitoring intracranial electroencephalograph electrodes using MRI: radiofrequency-induced heating. *J. Magn. Reson. Imaging* 28, 1233–1244. doi: 10.1002/jmri.21583

Carmichael, D. W., Thornton, J. S., Rodionov, R., Thornton, R., McEvoy, A. W., Ordidge, R. J., et al. (2010). Feasibility of simultaneous intracranial EEG-fMRI in humans: a safety study. *Neuroimage* 49, 379–390. doi: 10.1016/j.neuroimage.2009.07.062

Carmichael, D. W., Vulliemoz, S., Rodionov, R., Thornton, J. S., Mcevoy, A. W., and Lemieux, L. (2012). Simultaneous intracranial EEG–fMRI in humans: protocol considerations and data quality. *Neuroimage* 63, 301–309. doi: 10.1016/j.neuroimage.2012.05.056

Chaudhary, U. J., Centeno, M., Thornton, R. C., Rodionov, R., Vulliemoz, S., McEvoy, A. W., et al. (2016). Mapping human preictal and ictal haemodynamic networks using simultaneous intracranial EEG-fMRI. *NeuroImage Clin.* 11, 486–493. doi: 10.1016/j.nicl.2016.03.010

Ciumas, C., Canet-Soulas, E., Ryvlin, P., Schaefers, G., Bouvard, S., Comte, J. C., et al. (2013). A phantom and animal study of temperature changes during fMRI with intracerebral depth electrodes. *Epilepsy Res.* 108, 57–65. doi: 10.1016/j.eplepsyres.2013.10.016

Cunningham, C. B. J., Goodyear, B. G., Badawy, R., Zaamout, F., Pittman, D. J., Beers, C. A., et al. (2012). Intracranial EEG-fMRI analysis of focal epileptiform discharges in humans. *Epilepsia* 53, 1636–1648. doi: 10.1111/j.1528-1167.2012.03601.x

Griswold, M. A., Jakob, P. M., Heidemann, R. M., Nittka, M., Jellus, V., Wang, J., et al. (2002). Generalized autocalibrating partially parallel acquisitions (GRAPPA). *Magn. Reson. Med.* 47, 1202–1210. doi: 10.1002/mrm.10171

Hawsawi, H. B., Carmichael, D. W., and Lemieux, L. (2017). Safety of Simultaneous Scalp Or Intracranial EEG during MRI: a review. *Front. Phys.* 5:42. doi: 10.3389/fphy.2017.00042

IEC (2016). *Medical electrical Equipment Part 2-4: Particular Requirements for the. 2011*. Geneva: IEC.

Jorge, J., Grouiller, F., Ipek, Ö, Stoermer, R., Michel, C. M., Figueiredo, P., et al. (2015). Simultaneous EEG-fMRI at ultra-high field: artifact prevention and safety assessment. *Neuroimage* 105, 132–144. doi: 10.1016/j.neuroimage.2014.10.055

Kainz, W., Neubauer, G., Überbacher, R., Alesch, F., and Chan, D. D. (2002). Temperature measurement on neurological pulse generators during MR scans. *Biomed. Eng. Online* 1, 1–8. doi: 10.1186/1475-925X-1-2

Larkman, D. J., Young, I. R., Hajnal, J. V., Ehnholm, G., Herlihy, A. H., and Coutts, G. A. (2001). Use of multicoil arrays for separation of signal from multiple slices simultaneously excited. *J. Magn. Reson. Imaging* 13, 313–317.

Lemieux, L., Allen, P. J., Franconi, F., Symms, M. R., and Fish, D. R. (1997). Recording of EEG during fMRI experiments: patient safety. *Magn. Reson. Med.* 38, 943–952. doi: 10.1002/mrm.1910380614

Murta, T., Chaudhary, U. J., Tierney, T. M., Dias, A., Leite, M., Carmichael, D. W., et al. (2017). Phase–amplitude coupling and the BOLD signal: a simultaneous intracranial EEG (icEEG) - fMRI study in humans performing a finger-tapping task. *Neuroimage* 146, 438–451. doi: 10.1016/J.NEUROIMAGE.2016.08.036

Murta, T., Hu, L., Tierney, T. M., Chaudhary, U. J., Walker, M. C., Carmichael, D. W., et al. (2016). A study of the electro-haemodynamic coupling using simultaneously acquired intracranial EEG and fMRI data in humans. *Neuroimage* 142, 371–380. doi: 10.1016/J.NEUROIMAGE.2016.08.001

Park, S. M., Nyenhuis, J. A., Smith, C. D., Lim, E. J., Foster, K. S., Baker, K. B., et al. (2003). Gelled versus nongelled phantom material for measurement of MRI-induced temperature increases with bioimplants. *IEEE Trans. Magn.* 39, 3367–3371. doi: 10.1109/TMAG.2003.816259 3367-3371.

Pruessmann, K. P., Weiger, M., Scheidegger, M. B., and Boesiger, P. (1999). SENSE: sensitivity encoding for fast MRI. *Magn. Reson. Med.* 42, 952–962.

Ridley, B., Wirsich, J., Bettus, G., Rodionov, R., Murta, T., Chaudhary, U., et al. (2017). Simultaneous intracranial EEG-fMRI shows inter-modality correlation in time-resolved connectivity within normal areas but not within epileptic regions. *Brain Topogr.* 30, 639–655. doi: 10.1007/s10548-017-0551-5

Saignavongs, M., Ciumas, C., Petton, M., Bouet, R., Boulogne, S., Rheims, S., et al. (2016). Neural activity elicited by a cognitive task can be detected in single-trials with simultaneous intracerebral EEG-fMRI Recordings. *Int. J. Neural Syst.* 27:1750001. doi: 10.1142/S0129065717500010

Setsompop, K., Gagoski, B. A., Polimeni, J. R., Witzel, T., Wedeen, V. J., and Wald, L. L. (2012). Blipped-controlled aliasing in parallel imaging for simultaneous multislice echo planar imaging with Reduced g -factor penalty. *Magn. Reson. Med* 1224, 1210–1224. doi: 10.1002/mrm.23097

Sharma, N. K., Pedreira, C., Chaudhary, U. J., Centeno, M., Carmichael, D. W., Yadee, T., et al. (2019). NeuroImage BOLD mapping of human epileptic spikes recorded during simultaneous intracranial EEG-fMRI: the impact of automated spike classification. *Neuroimage* 184, 981–992. doi: 10.1016/j.neuroimage.2018.09.065

Vulliemoz, S., Diehl, B., Walker, M. C., Rosenkranz, K., Rodionov, R., McEvoy, A. W., et al. (2011). Simultaneous intracranial EEG and fMRI of interictal epileptic discharges in humans. *Neuroimage* 54, 182–190. doi: 10.1016/j.neuroimage.2010.08.004

Conflict of Interest: The authors declare that the research was conducted in the absence of any commercial or financial relationships that could be construed as a potential conflict of interest.

Advantages of publishing in Frontiers

OPEN ACCESS
Articles are free to read for greatest visibility and readership

FAST PUBLICATION
Around 90 days from submission to decision

HIGH QUALITY PEER-REVIEW
Rigorous, collaborative, and constructive peer-review

TRANSPARENT PEER-REVIEW
Editors and reviewers acknowledged by name on published articles

Frontiers
Avenue du Tribunal-Fédéral 34
1005 Lausanne | Switzerland

Visit us: www.frontiersin.org
Contact us: frontiersin.org/about/contact

REPRODUCIBILITY OF RESEARCH
Support open data and methods to enhance research reproducibility

DIGITAL PUBLISHING
Articles designed for optimal readership across devices

FOLLOW US
@frontiersin

IMPACT METRICS
Advanced article metrics track visibility across digital media

EXTENSIVE PROMOTION
Marketing and promotion of impactful research

LOOP RESEARCH NETWORK
Our network increases your article's readership